New Directions in Mesoscopic Physics (Towards Nanoscience)

# NATO Science Series

*A Series presenting the results of scientific meetings supported under the NATO Science Programme.*

The Series is published by IOS Press, Amsterdam, and Kluwer Academic Publishers in conjunction with the NATO Scientific Affairs Division

*Sub-Series*

| | |
|---|---|
| **I. Life and Behavioural Sciences** | IOS Press |
| **II. Mathematics, Physics and Chemistry** | Kluwer Academic Publishers |
| **III. Computer and Systems Science** | IOS Press |
| **IV. Earth and Environmental Sciences** | Kluwer Academic Publishers |
| **V. Science and Technology Policy** | IOS Press |

The NATO Science Series continues the series of books published formerly as the NATO ASI Series.

The NATO Science Programme offers support for collaboration in civil science between scientists of countries of the Euro-Atlantic Partnership Council. The types of scientific meeting generally supported are "Advanced Study Institutes" and "Advanced Research Workshops", although other types of meeting are supported from time to time. The NATO Science Series collects together the results of these meetings. The meetings are co-organized bij scientists from NATO countries and scientists from NATO's Partner countries – countries of the CIS and Central and Eastern Europe.

**Advanced Study Institutes** are high-level tutorial courses offering in-depth study of latest advances in a field.
**Advanced Research Workshops** are expert meetings aimed at critical assessment of a field, and identification of directions for future action.

As a consequence of the restructuring of the NATO Science Programme in 1999, the NATO Science Series has been re-organised and there are currently Five Sub-series as noted above. Please consult the following web sites for information on previous volumes published in the Series, as well as details of earlier Sub-series.

http://www.nato.int/science
http://www.wkap.nl
http://www.iospress.nl
http://www.wtv-books.de/nato-pco.htm

**Series II: Mathematics, Physics and Chemistry – Vol. 125**

# New Directions in Mesoscopic Physics (Towards Nanoscience)

edited by

R. Fazio
Scuola Normale Superiore,
Pisa, Italy

V.F. Gantmakher
Institute for Solid State Physics,
Russian Academy of Sciences,
Chernogolovka, Moscow District, Russia

and

Y. Imry
Weizmann Institute of Science,
Department of Condensed Matter Physics,
Rehovot, Israel

Springer-Science+Business Media, B.V.

Proceedings of the NATO Advanced Study Institute on
New Directions in Mesoscopic Physics (Towards Nanoscience)
Erice, Sicily, Italy
20 July–1 August 2002

A C.I.P. Catalogue record for this book is available from the Library of Congress.

ISBN 978-1-4020-1665-3 ISBN 978-94-007-1021-4 (eBook)
DOI 10.1007/978-94-007-1021-4

*Printed on acid-free paper*

All Rights Reserved
© 2003 Springer Science+Business Media Dordrecht
Originally published by Kluwer Academic Publishers in 2003
Softcover reprint of the hardcover 1st edition 2003

No part of this work may be reproduced, stored in a retrieval system, or transmitted in any form or by any means, electronic, mechanical, photocopying, microfilming, recording or otherwise, without written permission from the Publisher, with the exception of any material supplied specifically for the purpose of being entered and executed on a computer system, for exclusive use by the purchaser of the work.

# TABLE OF CONTENTS

**Preface** vii

**List of Contributors** ix

**Lectures**

**D. E. Khmelnitskii** 1
Field theories in physics of disordered conductors

**C. Di Castro and S. Caprara** 39
Non-Fermi-liquid metals in low dimensions

**L. S. Levitov** 67
Counting statistics of mesoscopic noise

**L. I. Glazman and M. Pustilnik** 93
Coulomb blockade and Kondo effect in quantum dots

**H. Bouchiat, R. Deblock, M. Ferrier, S. Gueron, A. Kasumov, M. Kociak, and B. Reulet** 117
Quantum coherent transport: From mesoscopic circuits to molecular wires

**A. Silva and M. Heiblum** 149
Phase measurements in Quantum Dots

**D. Vion, A. Aassime, A. Cottet, P. Joyez, H. Pothier, C. Urbina, D. Esteve, and M. Devoret** 173
Superconducting quantum bit based on the Cooper pair box

**Yu. Makhlin, G. Schön and A. Shnirman** 197
Dissipation in Josephson qubits

**J.-M. Raimond** 225
Entanglement and decoherence studies in Cavity QED experiments

**Seminars**

**K. Schwab** 245
Quantum Electro-Mechanical Systems

**V.V. Afonin, J. Bergli, Y. M. Galperin, V.L. Gurevich, and V.I. Kozub** 259
Possible weak temperature dependence of electron dephasing

**M. Governale and U. Zülicke** 269
Momentum-resolved tunneling: Spectroscopic tool and basis for device applications

**B. Horovitz and A. Golub** 281
Edge states and quantum Hall effects in d+ id′ superconductors

**S. S. Murzin, M. Weiss, and A.G.M. Jansen** 291
Universal scaling flow diagram for magnetoconductance in disordered GaAs layers

**S. Kleff and J. von Delft** 303
Fluctuations of the anisotropy energy in nanoscale ferromagnetic particles

**J. Börlin, W. Belzig, and C. Bruder** 313
Full counting statistics in multi-terminal normal metal tunnel junction structures

**A.A. Clerk** 325
Resonant Cooper-Pair Tunneling: Counting Statistics and Frequency-Dependent Current Noise

**I.S. Beloborodov, F.W.J. Hekking and F. Pistolesi** 339
Influence of thermal fluctuations on an underdamped Josephson tunnel junction

**J.Q. You, J.S. Tsai and F. Nori** 351
Quantum computing with many superconducting qubits

**M. Rontani, G. Goldoni and E. Molinari** 361
Few-electron liquid and solid phases in artificial molecules at high magnetic field

**M. Y. Veillette** 373
Phase Coherence and Spin Dynamics

# PREFACE

Aim of this NATO Advanced Study Institute was to give an introduction and overview of the main debated issues in mesosocopic physics. Topics covered during the ASI include Quantum Hall effects, transport through quantum wires and dots, coherence in mesoscopic systems, spintronics, disordered systems, solid state quantum computation. Some lecturers were dedicated to the connections between nanoscience with biophysics and quantum optics.
Although the topics mentioned here have many aspects in common, they span large area of physics. In our opinion, it was especially important to provide occasions, in particular for young scientists, to acquire a broad view of this rapidly expanding field. Thanks to the excellent presentations given by the all lecturers and speakers, we hope that the school was successful both for young researchers who wanted to enter the field and, at the same time, was stimulating for more experienced people.

The ASI would not have been successfully without the support of many people and institutions that we would like to acknowledge. The funding by the NATO Science Programme made all this possible. Several grants were provided thanks to the financial support by Centro E. Majorana, NEST-INFM, and INFM - Sezione D. The hospitality of the Centro E. Majorana was important to have the pleasant atmosphere during the working days. Prof. G. Benedek encouraged us to organize this activity and helped us at all stages of the organization of this NATO-ASI and we warmly thank him for that. We would also like to thank Mr. Alessandro Romito for the help in the preparation of these Proceedings.

Last but not least we should thank all the speakers and lecturers for their interesting talks and all the participants that made the atmosphere of this ASI lively and stimulating.

Rosario Fazio
Vsevolod F. Gamtmakher
Yoseph Imry

# LIST OF CONTRIBUTORS

**Helene Bouchiat**
Laboratoire de Physique des Solides
Associé au CNRS, UMR 8502, Bat. 510
Université Paris–Sud, 91405 Orsay
France

**Christoph Bruder**
Department of Physics and Astronomy
University of Basel
CH-4056 Basel
Switzerland

**Aashish Clerk**
Departments of Applied Physics and Physics
Yale University
PO Box 208284, New Haven, CT 06520-8284
USA

**Michel Devoret**
Departments of Applied Physics and Physics
Yale University
PO Box 208284, New Haven, CT 06520-8284
USA

**Carlo Di Castro**
Dipartimento di Fisica
Università di Roma "La Sapienza"
Piazzale Aldo Moro, 2, I-00185 Roma
Italy

**Yuri M. Galperin**
Department of Physics
University of Oslo
P.O. Box 1048 Blindern, N-0316 Oslo
Norway

**Leonid I. Glazman**
Theoretical Physics Institute
University of Minnesota
Minneapolis, MN 55455
USA

**Michele Governale**
Scuola Normale Superiore
Piazza dei Cavalieri 7
56126 Pisa
Italy

**Moty Heiblum** Department of Condensed Matter Physics
The Weizmann Institute of Science
76100 Rehovot
Israel

**Frank W.J. Hekking**
Laboratoire de Physique et Modelisation des Milieux Condenses
Magistere-CNRS, BP 166, 38042 Grenoble-cedex 9
France

**Baruch Horovitz**
Department of Physics, Ben-Gurion
University of the Negev
Beer-Sheva 84105
Israel

**David E. Khmelnitskii**
Cavendish Labporatory
University of Cambridge
Cambrdge
United Kingdom

**Silvia Kleff**
Lehrstuhl fuer Theoretische Festkoerperphysik
Sektion Physik and Center for NanoScience
Ludwig-Maximilians-Universitaet Muenchen
Theresienstr. 37
80333 Muenchen
Germany

**Leonid S. Levitov**
Department of Physics
Massachusetts Institute of Technology
77 Massachusetts Ave
Cambridge, MA 02139
USA

**Sergey S. Murzin**
Institute of Solid State Physics RAS
142432, Chernogolovka

Moscow District
Russia

**Franco Nori**
Frontier Research System
The Institute of Physical and Chemical Research (RIKEN)
Wako-shi 351-0198
Japan

**Jean-Michel Raimond**
Laboratoire Kastler Brossel, Departement de Physique
Ecole Normale Superieure
Paris
France

**Massimo Rontani**
Dipartimento di Fisica
Università degli Studi di Modena e Reggio Emilia
Via Campi 213/A, 41100 Modena
Italy

**Gerd Schoen**
Institut fuer Theoretische Festkoerperphysik
Universitaet Karlsruhe
D-76128 Karlsruhe
Germany

**Keith Schwab**
Laboratory for Physical Sciences
National Security Agency
8050 Greenmead Drive
College Park, MD 20740
USA

**Martin Y. Veillette**
Department of Physics
University of California at Santa Barbara
CA 93106
USA

# FIELD THEORIES IN PHYSICS OF DISORDERED CONDUCTORS

*A Long list of Open Questions*

D.E.KHMELNITSKII
*Cavendish Labporatory, University of Cambridgee*
*Cambrdge, United Kingdom*
*and L.D.Landau Institute for Theoretical Physics*
*Moscow 17334 RUSSIA*



*R. Fazio et al. (eds.), New Directions in Mesoscopic Physics,* 1–37.
© 2003 *Kluwer Academic Publishers. Printed in the Netherlands.*

# Lecture 1.
# Electrons in weakly disordered metals

## Physics, problems and motivations

Physics of electrons in weakly disordered conductors is dominated by the simple qualitative picture which had been repeated many times: electrons are traveling from the source $S$ to the drain $D$ along numerous paths as shown in Fig1 a.

At low temperatures, the rate of all inelastic processes is very small and we can neglect it in the leading approximation. According to the general rule of Quantum Mechanics, an amplitude $A_i$ should be associated with every trajectory. The total probability $W$ of detecting electron is

$$W = |\sum_i A_i|^2 = \sum_i |A_i|^2 + \sum_{i \neq j} A_i A_j^* \tag{1}$$

The first term is a sum of classical probabilities of an electron moving along particular trajectories, while the second one takes care of the interference of partial amplitudes. The classical probabilities can be found from the Boltzmann equation. It leads to the classical diffusion with the coefficient $D = v^2\tau/d$, where $v$ is the velocity of electrons (the Fermi velocity $v_F$ under the condition of degeneracy), $\tau$ is the mean free time and $d$ is the dimension. The effect of interference is usually neglected. The reason for that is that the mean free path $l = v\tau$ is much larger than the wave length of electrons, $\lambda = \hbar/p_F$. Therefore, the second term in Eq (1) is a sum of strongly oscillating terms, which

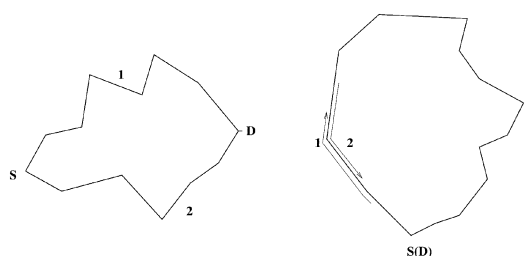


*Figure 1.* Typical diffusing trajectories from the source S to drain D

cancel each other, but they are not canceled completely. We may see this from a simple example of the case, when the source $S$ and detector $D$ are located at the same point. Then, every closed trajectory, that begins at $S$ and ends at $D$, can e traversed in two opposite directions: clockwise and counterclockwise. The amplitudes $A_1$ and $A_2$, corresponding to these directions, are coherent and the probability they give is $W = 4|A_1|^2$ instead of $2|A_1|^2$, one would expect from the classical analysis. Therefore, quantum effects contribute to the probability of returning to the initial point, of random walk, effectively diminish the conductivity $\sigma$ and diffusivity $D$. This contribution is large, but comes from those very rare trajectories, which return to the initial point.
In a precise quantum mechanical analysis, instead of trajectories, one has to consider the wave pipes of the radius equal to the wave length $\lambda$. "To return to initial point" means to achieve an intersection of the wave pipes, so, the initial point is located inside the intersecting pipe (see Fig). The classical probability $dW$ of passing at time $t$ through a volume element $dV$ at the distance $\mathbf{r}$ from the origin is equal to

$$dW \sim \frac{dV}{(Dt)^{d/2}} \exp\left[-\frac{r^2}{2Dt}\right]. \tag{2}$$

Finding effect of interference as an integral over the time $t$ of return and using Eq (2) at $\mathbf{r} = 0$, we obtain the following estimate of the relative correction to conductivity:

$$\frac{\delta\sigma}{\sigma} \sim -\int_{\tau}^{\tau_\phi} \frac{\lambda^{d-1} v dt}{(Dt)^{d/2}}. \tag{3}$$

The upper limit in this integral corresponds to the characteristic time $\tau_\phi$ of electron phase memory relaxation due to inelastic processes, the lower limit is the mean free time $\tau$, because there are no returns at times $t$, smaller than $\tau$. Taking into account the Einstein relation $\sigma = e^2 \nu D$ ($\nu$ is the density of states), we obtain

$$\delta\sigma \sim \frac{e^2}{\hbar} \begin{cases} L_\phi, & d = 1, \\ \log(\tau_\phi/\tau), & d = 2, \\ \text{const} - L_\phi^{-1}, & d = 3, \end{cases} \tag{4}$$

where $L_\phi = \sqrt{D\tau_\phi}$ is the characteristic length of coherent diffusive propagation.
Formulas (4) for the quantum correction to conductivity exhibit a phenomenon, called "Weak Localization": even in well conducting materials ($\sigma \gg e^2/\hbar$) quantum processes suppress conductivity. For $d = 1, 2$ these corrections are divergent at $\tau_\phi \to \infty$ , which means that all

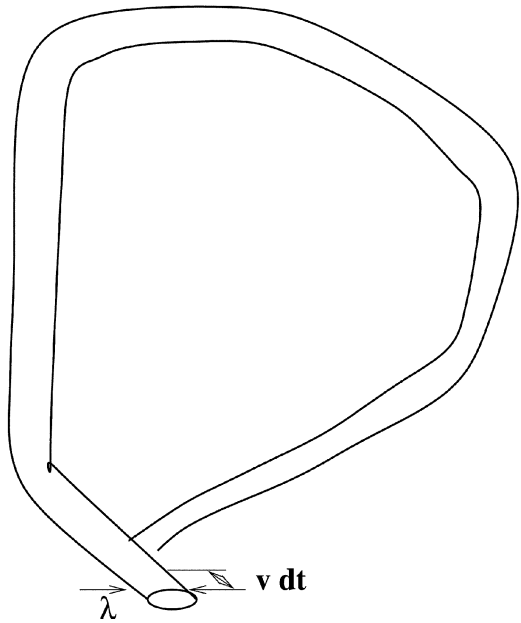


*Figure 2.* To the estimate of the quantum correction to conductivity

states are localized for an arbitrary weak disorder and, at $T = 0$, the conductance vanishes. For $d = 3$, the quantum correction is finite, so the conductance remains finite at $T = 0$, provided disorder is weak. If disorder is stronger, than a certain value, the electronic states are localized. This means that there is a transition from localized to extended states for $d = 3$ as a function of either Fermi energy or strength of disorder (the Anderson transition).

It is now natural to ask what the dimension $d$ in Eqs (3) and (4) means. To get an answer, let us consider random walk in a film of finite thickness $a \gg l$. At small times $t \ll a^2/D$, a diffusive trajectory returns back to its initial point with probability, proportional to $(Dt)^{-3/2}$. At larger times $t \gg a^2/D$, this probability is proportional to $(Dt)^{-1}$. Therefore, if phase breaking time $\tau_\phi$ is larger, than $a^2/D$, then this film behaves like a two-dimensional conductor. Otherwise, it is a bulk $3D$ conductor. The criteria for dimensional crossover looks like

$$a \to \begin{cases} < L_\phi, & d = 2, \\ > L_\phi, & d = 3. \end{cases} . \tag{5}$$

## Magnetoresistance

Now we are ready to analyze the effect of magnetic field on quantum corrections to conductivity. Despite of being small, this effect is so sensitive to magnetic field, that it determines the whole magnetoresistance. The magnetic field $B$ influences quantum mechanics of an electrons in two ways: i). the Lorentz force curves the electron's trajectory; as a result, the direction of the electron's momentum deviates from its initial direction; the deviation of momentum direction $\theta$ in the mean free time $\tau$ is of the order of

$$\Delta\theta \sim \frac{evB\tau}{cp} = \Omega\tau, \quad \Omega = \frac{eB}{mc};$$

ii). the amplitudes of traversing the loop clockwise and counterclockwise get extra phase factors (the Aharonov-Bohm effect):

$$A_{1,2} \to A_{1,2} \exp\left[\pm i \frac{e}{c\hbar} \int \mathbf{A} d\mathbf{r}\right].$$

As one can see, the mechanism i). is completely classical and is suppressed if the mean free time $\tau$ is short. The mechanism ii). is quantum and is not limited by any elastic processes. This is why the latter gives stronger dependence of the conductance on the magnetic field.
As a result of Aharonov-Bohm effect, the interference term in Eq (1) gets extra factor, $\cos(eBS/c\hbar)$, where $S$ is the area encircled by the loop. For a loop of length $\mathcal{L} = vt$, this area can be estimated as $S(t) \sim Dt$. So, the estimate for magnetoresistance is

$$\Delta\sigma^{(d)} = \sigma(B) - \sigma(0) \sim$$
$$\sim \frac{e^2}{\hbar} \cdot \int_0^{\tau_\phi} \frac{\lambda^{d-2} dt}{D^{(d-2)/2} t^{d/2}} \left[1 - \cos\left(\frac{eBDt}{c\hbar}\right)\right] \tag{6}$$

Introducing a dimensionless variable, we can simplify the expression on the right hand side of Eq (6):

$$\Delta\sigma^{(2)} \sim \frac{e^2}{\hbar} \cdot f_2\Big(\frac{eBD\tau_\phi}{c\hbar}\Big); \; f_2(x) = \int_0^x \frac{dz}{z}[1 - \cos z]; \tag{7}$$

$$\Delta\sigma^{(3)} \sim \frac{e^2}{\hbar}\sqrt{\frac{eB}{c\hbar}} \cdot f_3\Big(\frac{eBD\tau_\phi}{c\hbar}\Big); \; f_3(x) = \int_0^x \frac{dz}{z^{3/2}}[1 - \cos z]. \tag{8}$$

The functions $f_{2,3}(x)$ have the following asymptotes:

$$f_2(x) \sim \begin{cases} x^2, & x \ll 1, \\ \log x, & x \gg 1, \end{cases} \tag{9}$$

$$f_3(x) \sim \begin{cases} x^2, & x \ll 1, \\ x^{1/2}, & x \gg 1. \end{cases} \tag{10}$$

These formulas explain the mystery of the negative magnetoresistance: the conductivity consists of the Drude part $\sigma^{(0)}$ and a negative quantum correction $\delta\sigma$ due to weak localization; the Drude part is suppressed by magnetic field through the classical parameter $\Omega\tau$; the quantum correction is suppressed much stronger, which leads to enhancement of the conductivity. The magnetoresistance does not depend on the relative directions of the current and magnetic field, because it is determined by the loops, which can have any orientation, provided the sample is three-dimensional. In $2D$-systems the loops can be located only in the plane of the sample and, therefore, the conductance depends on the perpendicular component of the field only. The saturation in relatively weak fields and the temperature dependent behavior at extremely low fields can also bee attributed to the Aharonov-Bohm effect on the quantum correction. As it is seen from Eqs (7) and (8), the mean free time $\tau$ of elastic collisions does not enter the expressions (7) and (8) for magnetoresistance $\Delta\sigma(H)$. Instead, the magnetoresistance depends on phase breaking time $\tau_\phi$, which is much longer than $\tau$ and depends on temperature.

## Effect of Spin-Orbit Interaction

Recalling that electrons can have intrinsic quantum numbers, like spin projection, the energy band index, etc, one would naturally ask whether these factors can affect weak localization. The answer is:"They could", but let us go through it in the order.
Suppose that an electron can belong to one of two pockets (the index $\alpha$ takes on two values: either 1 or 2) in the momentum space (valleys of the energy spectrum). Then the amplitudes $A_{1,2}$ are matrices in the valley indexes: $A_{1,2}^{\alpha\beta}$. The quantum correction to conductivity can be expressed as

$$\int dt C^{\alpha\beta\beta\alpha}(r,r,t) \propto \mathrm{Re}\int dt A_1^{\alpha\beta}(r,-t;r,t)[A_2^{\beta\alpha}(r,-t;r,t)]^*,$$

where $C^{\alpha\beta\gamma\delta}(t)$ is the interference amplitude, the indexes of which correspond to time $-t$ (first two) and to time $t$. This matrix must be real and diagonal in these pairs of indexes:

$$C^{\alpha\beta\gamma\delta}(t) = C_s\delta^{\alpha\beta}\delta^{\gamma\delta}(t) + C_a\tau_3^{\alpha\beta}\tau_3^{\gamma\delta},$$

where $\tau_3$ is the Pauli matrix and $C_{s,a}$ are either symmetric ($s$) or antisymmetric ($a$)( with respect to the valley permutation ) phase correlators. If there is no inter-valley scattering and at time $-t$ only valley 1 is populated, then only $C^{1111}$ is not equal to zero. Therefore, at $t=0$

$$C_s = C_a = \frac{1}{2}.$$

At $t \neq 0$ the valley 1 remains populated and the valley 2 remains empty. So, both symmetric and antisymmetric correlators decay with the same phase

relaxation time $\tau_\phi$:

$$C_{s,a} \propto \frac{1}{2}\exp\left(-\frac{t}{\tau_\phi}\right)$$

If there is an inter-valley relaxation, the asymmetric correlator decays at its own rate $\tau_v^{-1}$ and

$$C^{\alpha\beta\beta\alpha} = \frac{1}{2}\left[\exp\left(-\frac{t}{\tau_\phi}\right) + \exp\left(-\frac{t}{\tau_\phi^*}\right)\right],$$

where

$$\frac{1}{\tau_\phi^*} = \frac{1}{\tau_\phi} + \frac{1}{\tau_v}.$$

Therefore, if $\tau_\phi \gg \tau_v$, then both the quantum correction and negative magnetoresistance are $N$ times smaller, where $N$ is the number of valleys.
Consider now an electron with spin and the indexes of $C$ as spin indexes. Then

$$C^{\alpha\beta\gamma\delta}(t) = C_s(t)\delta^{\alpha\beta}\delta^{\gamma\delta}(t) + C_t(t)\sigma^{\alpha\beta}\sigma^{\gamma\delta},$$

where $C_s$ and $C_t$ are phase correlators in spin-singlet and spin-triplet channels. Again, let us first assume that there is no spin relaxation, and the spins are polarized. Then their polarization is conserved and both triplet and singlet correlators decay with the same relaxation time $\tau_\phi$. There is, however, a difference between the cases of inter-valley and spin-orbit scattering: since there are three Pauli matrices, contribution of the triplet channel is three time larger, than that of the singlet channel. In order to give two spin projections, these 3 and 1 should be subtracted:

$$C(t) = \frac{1}{2}[3C_t(t) - C_s(t)]$$

and, therefore,

$$C_s \propto \exp\left(-\frac{t}{\tau_\phi}\right); \tag{11}$$

$$C_t \propto \exp\left(-\frac{t}{\tau_\phi^*}\right), \quad \frac{1}{\tau_\phi^*} = \frac{1}{\tau_\phi} + \frac{1}{\tau_{so}}, \tag{12}$$

where $\tau_{so}$ is the time of spin relaxation due to spin-orbit interaction.
Thus, the magnetoresistance in, say, two-dimensions is given by the formula

$$\Delta\sigma^{(2)} \sim \frac{e^2}{\hbar}\int_0^{\tau_\phi}\frac{dt}{t}\left[1-\cos\left(\frac{eDBt}{c\hbar}\right)\right]\left[\frac{3}{2}\exp\left(-\frac{t}{\tau_{so}}\right) - \frac{1}{2}\right]. \tag{13}$$

If $\tau_\phi \gg \tau_{so}$ then

$$\Delta\sigma^{(2)} \sim \frac{e^2}{\hbar}\begin{cases} -\frac{1}{2}\left(DeB\tau_\phi/c\hbar\right)^2, & \tau_\phi \ll c\hbar/DeB, \\ -\frac{1}{2}\log\left(DeB\tau_\phi/c\hbar\right), & \tau_{so} \ll c\hbar/DeB \ll \tau_\phi, \\ \log\left(DeB\tau_{so}/c\hbar\right), & \tau_{so} \gg c\hbar/DeB. \end{cases} \tag{14}$$

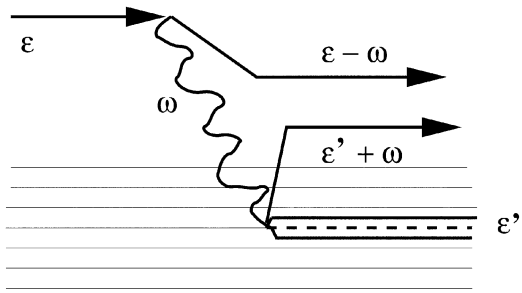


*Figure 3.* Transformation of an extra electron with energy $\epsilon$ into two electrons with energies $\epsilon - \omega$ and $\epsilon' + \omega$ and a hole with energy $\epsilon'$.

Therefore, the spin-orbit interaction leads to the change in the sign of magnetoresistance: positive in weak fields, it becomes negative with a twice as steep slope (in the logarithmic coordinates), as it is shown in Fig. Therefore, relatively simple measurements of magnetoresistance give a tool for determination of two relaxation times in disordered conductors: the phase breaking time $\tau_\phi$ and spin relaxation time $\tau_{so}$.

## Effect of interaction. Electron-electron collision rate

Effect of disorder is clearly seen on electron-electron collision rate $\tau_{ee}$. Consider an extra particle with energy $\epsilon > 0$ and momentum $\mathbf{p}$ which is interacting with the other electrons. Due to mentioned interaction, the wave function $\exp[i\mathbf{pr} - i\omega t]a^+_{\mathbf{p}}\ |0>$ is not an eigenfunction of the Hamiltonian and it decays into two electrons and one hole. As it is shown in Fig 3, this extra electron generates a Coulomb field with

Using the Fermi golden rule, write the rate of such a process as a sum over energy and momentum transfers:

$$\frac{1}{\tau_{ee}(\epsilon)} = 2\pi \int d\epsilon' d\omega (d\mathbf{p}')(d\mathbf{q}) |V(\omega, \mathbf{q})|^2 n_{\mathbf{p}'}(1 - n_{\mathbf{p}'+\mathbf{q}})(1 - n_{\mathbf{p}+\mathbf{q}})$$
$$\delta(\epsilon - \omega - \epsilon(\mathbf{p} - \mathbf{q}))\delta(\epsilon' - \epsilon(\mathbf{p}'))\delta(\epsilon' + \omega - \epsilon(\mathbf{p}' + \mathbf{q}))\delta(\epsilon - \epsilon(\mathbf{p})). \quad (15)$$

Since the collision rate does not depend on direction of momentum $\mathbf{p}$, it convenient to average the right-hand side of Eq (15) over these directions. This leads to the following form of Eq (15):

$$\frac{1}{\tau_{ee}(\epsilon)} = \frac{\pi\nu}{2} \int_0^\epsilon d\omega \int_{-\omega}^0 d\epsilon' \int_{-1}^1 dx \int_{-1}^1 dx' \int (d\mathbf{q}) |V(\omega, \mathbf{q})|^2$$

$$\delta(\omega - qv_F x')\delta(-\omega + qv_F x') = \frac{\pi\nu}{2} \int_0^\epsilon \omega \; d\omega \int (d\mathbf{q}) \frac{|V(\omega, \mathbf{q})|^2}{(qv_F)^2} \quad (16)$$

Interpretation of Eq (16) is very simple: the rate of collision is proportional to modulus square of the action of perturbation $V(\omega, \mathbf{q})$ which itself is equal to product of the strength of this perturbation to time of flight $t_f(q) = 1/v_F q$ of electron with velocity $v_F$ through the region of the size $1/q$, where potential is not vanished. This interpretation implies that electron moves ballistically, i.e. it is valid if $ql \gg 1$, where $l = v_F\tau$ is the mean free path and $\tau$ is the mean free time. If $ql \ll 1$, motion of electron is diffusive rather, than ballistic and, therefore,

$$t_f(q) = \begin{cases} (qv_F)^{-1}, & ql \gg 1; \\ |Dq^2 + i\omega|, & ql \ll 1 \end{cases} \quad (17)$$

Thus, the integral over momentum transfer in Eq (16) has the form

$$\int (d\mathbf{q}) |V(\omega, \mathbf{q}) t_f(q)|^2 \quad (18)$$

with $t_f(q)$ given by Eq (17). The mentioned integral over momentum transfer is determined by two regions, both situated far from $q \approx 1/l$. The contribution of the region $ql \gg 1$ is determined by $q \sim p_F$ and gives

$$\frac{1}{\tau_{ee}^{clean}(\epsilon)} \approx \left(\frac{e^2}{\hbar v_F}\right)^2 \int_0^\epsilon \frac{\omega \; d\omega}{\epsilon_F} = \left(\frac{e^2}{\hbar v_F}\right)^2 \frac{\epsilon^2}{\epsilon_F}, \quad (19)$$

while contribution of the region $ql \ll 1$ equals

$$\frac{1}{\tau_{ee}^{dirty}(\epsilon)} \approx \nu \; |V(\mathbf{q} = 0)|^2 \int_0^\epsilon \omega \; d\omega \int \frac{(d\mathbf{q})}{|Dq^2 - i\omega|^2} \quad (20)$$

Effective interaction at zero momentum transfer, surprisingly, does not depend on strength of Coulomb interaction:

$$V(\mathbf{q} = 0) = \frac{4\pi e^2}{\kappa^2} = \frac{4\pi e^2}{4\pi e^2 \nu} = \frac{1}{\nu}. \quad (21)$$

Performing integration in Eq (20), finally, obtain:

$$\frac{1}{\tau_{ee}^{dirty}(\epsilon)} \approx \begin{cases} \epsilon^{3/2} \; E_F^{-2} \; \tau^{-3/2}, & d = 3; \\ \epsilon \; E_F^{-1} \; \tau^{-1}, & d = 2; \\ \epsilon^{1/2} \; \tau^{-1/2}, & d = 1. \end{cases} \quad (22)$$

It is easy to see that $\tau_{ee}^{dirty}(\epsilon)$ is shorter, that $\tau_{ee}^{clean}(\epsilon)$, provided $\tau\epsilon \ll 1$. If the temperature $T$ is finite, then for all the energies $|\epsilon| \leq T$ in the

region of thermal smearing the Fermi distribution function the electron-electron collision rate depends on temperature rather than on energy and

$$\frac{1}{\tau_{ee}^{dirty}(T)} \approx \begin{cases} T^{3/2}\ E_F^{-2}\ \tau^{-3/2}, & d=3; \\ T\ E_F^{-1}\ \tau^{-1}, & d=2; \\ T^{1/2}\ \tau^{-1/2}, & d=1. \end{cases} \tag{23}$$

and this expression describes the dominant contribution to collision rate, provided $\tau T \ll 1$

## A Comment on Effective Dimension

Eqs (22, 23) contains effective dimension $d$ equal to 1, 2 or 3 without explanation what does that mean. For clarifying this point, consider a film of thickness $a$. At times $t < t_a = a^2/D$ initial density of electrons, position in the middle of this films thickness, diffuses in all three dimension. At times $t > t_a = a^2/D$ the density of electrons is roughly uniform across the film and diffuses in two dimensions along the films plane. Therefore, if the times $t_\epsilon = \hbar/\epsilon$ or $t_T = \hbar/T$ are shorter, than $t_a$, the film behaves as 3D sample. If $t_{\epsilon,T}$ are longer, than $t_a$, the film may be consider as a 2D sample. Thus, the crossover lengths

$$L_\epsilon = \sqrt{\frac{D\hbar}{\epsilon}}, \quad \text{and} \quad L_T = \sqrt{\frac{D\hbar}{T}}$$

determine whether $d$ in Eqs (22, 23) should be taken equal to 2 (when $a \ll L_{\epsilon,T}$), or to 3.

## Density of states for interacting electrons. Zero-bias anomaly.

Calculation of electron-electron collision rate gives an important insight:
1. Disordered metals bring a new phenomena associated with interaction with small momentum transfer $ql \ll 1$, for which motion of electrons should be considered as a diffusion. Despite of small range of these wave vectors, contribution of this range may dominate the total integral over momentums transfer.
2. An important role is played by time of flight of an electron through the region of interaction $t_f$, which leads to significant enhancement of effective interaction. Effective time of flight is especially long if the energy of an electron $\epsilon$ approaches the Fermi energy.
In the presence of interaction energy of every state with any quantum number (momentum $\mathbf{p}$ and spin projection $\sigma$, for instance) experiences a shift $\delta\epsilon$. In the leading order of perturbation theory, this shift is proportional to strength of interaction $V(\mathbf{q}=0)$ and contains integral over momentums transfer $\mathbf{q}$ (we know that it is dominated by the region $ql \ll 1$ ) and energy transfer $\omega$ (this

integral is taken in the limits $\epsilon > \omega > 0$.
Imaginary part of Green's function integrated over momentum $\mathbf{p}$ gives the density of states $\nu$. Correction to it gives correction to the density of states:

$$\delta\nu(\epsilon) \approx -V(0) \int_{\epsilon}^{+\infty} d\omega \int_{ql<1} \frac{(d\mathbf{q})}{|Dq^2 - i\omega|^2}. \tag{24}$$

Physical meaning of Eq (24) may be understood in the following manner: Repulsive interaction leads to a shift upward of all energy levels with positive energy $\epsilon > 0$ and downward with negative energy. This shift is not uniform, because the effective time of interaction is larger for energy levels with smaller modulus of the energy. This leads to a deep in density of states. Direct calculation of the integral in Eq (24) gives

$$\delta\nu(\epsilon) \approx -\nu_0 \begin{cases} \text{const} + \epsilon^{1/2}\ E_F^{-2}\ \tau^{-3/2}, & d = 3; \\ \ln(1/\epsilon\ \tau)\ E_F^{-1}\ \tau^{-1}, & d = 2; \\ (\epsilon\ \tau)^{-1/2}, & d = 1. \end{cases} \tag{25}$$

In the case of finite temperature the energy $\epsilon$ in Eq (25) should be substituted by $\max\{\epsilon, T\}$.

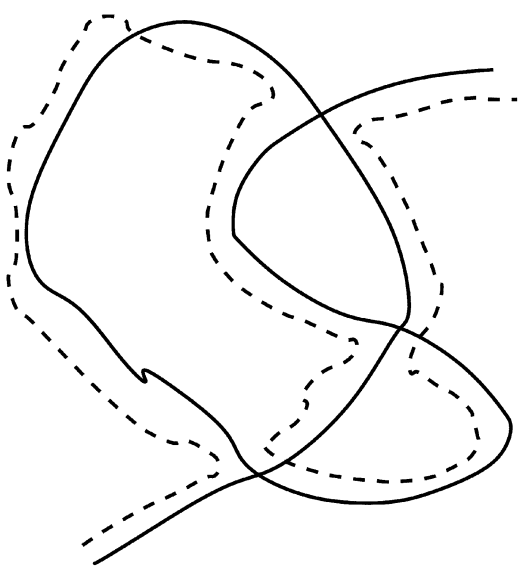

*Figure 4.* Typical self-crossing graph and distinctive ways of passing along it.

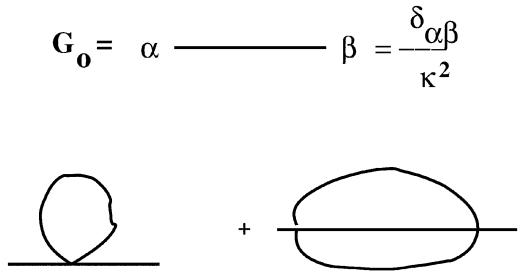


*Figure 5.* Typical Feynman graphs for self-interacting vector field.

## Motivations for Field Theory

It follows from our lengthy introduction that the target for analysis are trajectories shown in Fig 4, i.e. distinctive ways of passing along a self-crossing graphs. Physically, the contributions of these kinds reproduce the interference of semi-classical amplitudes. Our target, therefore, is the field theory which takes care of combinatorics of these merging and diverting double paths.

Consider an example of a field theory:

$$Z = \int \mathcal{D}\phi_\alpha e^{-F}; \quad F = \int d\mathbf{r} \left[ \frac{(\nabla\phi_\alpha)^2}{2} + \frac{\gamma}{4}(\phi_\alpha^2)^2 \right] \tag{26}$$

corresponding to a self-interacting vector field. Typical Feynman diagrams for this theory are shown in Fig 5. These diagrams correspond to a single rail with the vector index flowing along it.

Consider now the field theory for a matrix field with the action

$$Z = \int \mathcal{D}w_{\alpha\beta} e^{-F}; \; F = \int d\mathbf{r} \left[ \frac{(\nabla w_{\alpha\beta})^2}{2} + \frac{\gamma}{4}(w_{\alpha\beta} w_{\beta\gamma})^2 \right] \tag{27}$$

Typical diagrams for this theory are shown in Fig 6.

They have nearly all features needed for counting the combinatorics of the double-rail-paths. A very important disadvantage of this theory is the immanent presence of the graphs containing closed loops similar to one show and crossed at Fig 6. The physical motivation, which drove us, dealt with two long paths only without any loops. Let us assume

at this level that we have found the way of eliminating the loops from the perturbation expansion of the functional integral (27). A question remains which kind of a matrix field theory should be chosen. The hint comes from the fact that possible graphs of perturbation theory should include branching one double-rail-path into three, five and any other odd number.

A good example comes from thermodynamics of an isotropic ferromagnet. Consider a granular matter with $\mathbf{M}_i$ ($\mathbf{M}^2 = 1$) being spontaneous magnetization of a grain. The partition function is

$$Z = \int_{\mathbf{M}^2=1} \prod_i d\mathbf{M}_i e^{-F};\ F = -\sum_{ij} J_{ij}\mathbf{M}_i\mathbf{M}_j - \sum_i \mathbf{H}\mathbf{M}_i \tag{28}$$

At low temperatures, when $J \ll 1$, the magnetization varies very slowly in space, and the discrete version of Eq (28) could be replaced by the continuous version

$$Z = \int_{\mathbf{M}^2=1} \mathcal{D}\mathbf{M}_i e^{-F};\ F = \int d\mathbf{r} \left[\frac{\rho_s(\nabla\mathbf{M})^2}{2} - \mathbf{H}\mathbf{M}\right] \tag{29}$$

If the magnetization $\mathbf{M}(\mathbf{r})$ is parametrized as

$$\mathbf{M} = \left(\phi_x, \phi_y, 1 - \frac{\phi_x^2 + \phi_y^2}{2}\right),$$

Then the free energy $F$ in Eq (29) could be written in the form

$$F = \int d\mathbf{r} \left[\frac{\rho_s}{2}\ (\nabla\phi_\alpha)^2 + \frac{H}{2}\ \phi_\alpha^2 + \frac{\rho_s}{2}\ (\phi_\alpha\nabla\phi_\alpha)^2 + ...\right], \tag{30}$$

This gives the following expression for the bare correlator

$$\langle\phi_\alpha(\mathbf{q})\phi_\beta(-\mathbf{q})\rangle \sim \frac{\delta_{\alpha\beta}}{\rho_s q^2 + H}. \tag{31}$$

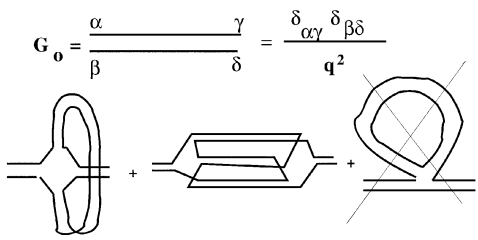


*Figure 6.* Typical Feynman graphs for self-interacting matrix field.

Free energy (30) contains all even powers of the vector field $\phi_\alpha$, which leads to the requested branchings. An important feature of the free energy (30) is that all higher powers contain gradients of the vector field. This originates in the symmetry at $\mathbf{H} = 0$ of initial Hamiltonian (28) with respect to the uniform rotation of magnetization $\mathbf{M}$.

Let us follow this example and suggest a hypothetical matrix model for granular metal

$$Z = \int_{Q_i^2=1} \prod_i dQ_i e^{-F};\ F = -\mathrm{tr} \sum_{ij} J_{ij} Q_i Q_j - \mathrm{tr} \sum_i \Lambda Q_i, \qquad (32)$$

where $Q_i$ is a matrix representing a single grain. Let us leave to different time the discussion of precise meaning of this matrix as well as the constant matrix $\Lambda$.

When $J \ll 1$, the matrices $\hat{Q}$ vary very slowly in space, and the discrete version of Eq (32) could be replaced by the continuous version

$$Z = \int_{Q^2=1} \mathcal{D}Q(\mathbf{r}) e^{-F}; F = \frac{\pi\nu}{4} \mathrm{tr} \int d\mathbf{r} \left[ D(\nabla Q)^2 - i\omega\Lambda Q \right], \qquad (33)$$

where $\nu$ is the density of states and $D$ is diffusion coefficient.

If the matrix $Q$ is parametrized as

$$\hat{Q} = \Lambda e^W$$

Then the free energy $F$ in Eq (29) could be written in the form

$$F = \frac{\pi\nu}{4} \mathrm{tr} \int d\mathbf{r} \left[ D(\nabla W)^2 - i\omega W^2 + D(W\nabla W)^2 + .. \right], \qquad (34)$$

This gives the following expression for the bare correlator

$$\langle W_{\alpha\beta}(\mathbf{q}) W_{\gamma\delta}(-\mathbf{q}) \rangle \sim \frac{\delta_{\alpha\gamma}\delta_{\beta\delta}}{Dq^2 - i\omega},$$

which represent a diffusive mode, while the Free energies(33) and (34) represent the effective Hamiltonians of interacting diffusive modes. Once again the higher powers of the matrix field $W$ contain the gradients of $W$. The origin of this extra gradients is the particle conservation law.

We stop here in order to return to analysis of the effect of this mode coupling in the next lecture.

## Lecture 2.
## Super-symmetric $\sigma$-model

Before going into great details let us look again at the $\sigma$-model:

$$Z = \int_{Q^2=1} \mathcal{D}Q(\mathbf{r})e^{-F}; F = \frac{\pi\nu}{4}\mathrm{tr}\int d\mathbf{r}\left[D(\nabla Q)^2 - i\omega\Lambda Q\right], \qquad (35)$$

Here the matrix $\Lambda$ has the block-diagonal form

$$\Lambda = \begin{pmatrix} I & 0 \\ 0 & -I \end{pmatrix}$$

The matrix $Q$ is $Q = U^{-1}\Lambda U$, where $U = \exp(W/2)$ and

$$W = \begin{pmatrix} 0 & B \\ -B^+ & 0 \end{pmatrix}. \qquad (36)$$

After these substitutions, we obtain

$$F = \frac{\pi\nu}{4}\mathrm{tr}\int d\mathbf{r}\left[D\nabla B\nabla B^+ - i\omega BB^+ + DB^+\nabla B\nabla B^+B\right], \qquad (37)$$

and

$$\langle B^+(\mathbf{q})B(-\mathbf{q})\rangle \sim \frac{1}{Dq^2 - i\omega},$$

In the following section we will discuss renormalization of this model and what does it bring.

### Renormalization Group

Thus, let us choose an intermediate scale $a' > a$, where $a$ is the lattice constant. Let

$$Q = U^{-1}V^{-1}\Lambda VU,$$

where

$$U = \begin{cases} I, & \frac{1}{a'} < k < \frac{1}{a} \\ U, & k < \frac{1}{a'} \end{cases} \qquad V = \begin{cases} e^W, & \frac{1}{a'} < k < \frac{1}{a} \\ I, & k < \frac{1}{a'} \end{cases}$$

If we perform the integration over matrices $B$ and $B^+$, using representation (36) and quadratic part of the action (37), the result will be that the action (35) remain valid, while the parameters in it change as :

$$\nu \to \nu, \qquad D \to D + \delta D \qquad (38)$$

In is convenient to introduce the dimensionless conductance

$$g = \frac{\hbar}{e^2} G = \frac{\hbar}{e^2} \sigma L^{d-2},$$

where the conductivity $\sigma$ is connected with the Diffusion coefficient through the Einstein relation $\sigma = e^2 \nu D$ Therefore, the result of renormalization is that the dimensionless conductance g changes obeying the equation

$$\frac{d \log g}{d \log L} = \beta(g), \tag{39}$$

where the so-called Gell-Mann-Low function $\beta(g)$ depends only on dimensionless conductance. We proceed now to the scaling theory of Anderson localization base upon Eq (39)

## Scaling Theory of Anderson Localization.

We know about two basic phases of a disordered metal: a conductor and an Anderson insulator. Transition between these two phases occurs when the Fermi energy $E_F$ of electrons coincides with the mobility edge $E_g$. The question of how d.c.conductivity $\sigma(0)$ vanishes and how localization length $L_c$ diverges when $E_F$ approaches $E_g$ remain un-answered. We bring here an interpolating theory, which unifies description of the both conducting and insulating phases and gives a description of the transition, which is supposed to be qualitatively correct.

In the center of the whole approach lies the concept of renormalization govern by Eq (39) and qualitative contemplation about the dimensionless conductance $g$ as a measure of disorder:
A good conductor has large conductance $g \gg 1$, while a bad conductor (an Anderson insulator) has a small conductance $g \ll 1$.
There are very few things we could calculate directly, but the fact that the scaling function $\beta$ depends only on dimensionless conductance $g$ allows to say a lot.

Let us assume that the dimensionless conductance of a sample of size (in all dimensions) $L$ is $g(L)$. Consider a sample of the size $2L$, which we might consider as composed from samples of size $L$. The law of composition could be pretty complicated. Nevertheless, it depends only on conductance itself:

$$\frac{d \log g}{d \log L} = \beta(g). \tag{40}$$

For $d = 2$ and $g \gg 1$, the theory of weak localization gives

$$\delta g = -\log L, \quad \beta(g) = -\frac{1}{g} + o\left(\frac{1}{g^2}\right) \tag{41}$$

For an arbitrary dimension $d$ and $g \gg 1$, the conductance is $g(L) = \sigma L^{d-2} + \delta\sigma L^{d-2}$ and, therefore, $\beta(g) = d - 2 - 1/g + ...$
Since small conductances $g \ll 1$ correspond to insulating phase, $g(L) \propto \exp(-L/L_c)$ and, therefore,

$$\beta(g) = \frac{d\log g}{d\log L} = -\frac{1}{L_c}\frac{d}{d\log L}\exp(\log L) = \log g + o(1). \tag{42}$$

The scaling functions $\beta(g)$ for different dimensions $d$ is plotted against $\log g$ on Fig 7. For given strength of disorder, conductance of the sample of the size of mean free path $g(l)$ determines the initial condition for the scaling equation (39). The result of renormalization is given by solution of this equation $g(l)$ with the mentioned initial condition. For instance, Fig shows that $\beta_d(g)$ for $d = 1, 2$ and all $g$ is negative. This means that independently from degree of disorder (the value of initial condition) for large enough distances $g(L) \propto \exp(-L/L_c)$. For $d = 2$, localization length $L_c \sim l\exp(\sigma\hbar/e^2)$.
For $d > 2$, the scaling $\beta(g)$ is positive at large conductances and negative at small conductances. Therefore, it vanishes at some critical conductance $g_c$. If the initial condition $g_i$ for the scaling equation (39) $g_i = g(l)$ is larger, than the critical value $g_c$, than the scaling function is positive $\beta(g_i) > 0$, the conductance is growing with increasing the sample size $L$ and, at large enough $L$, it follows the law

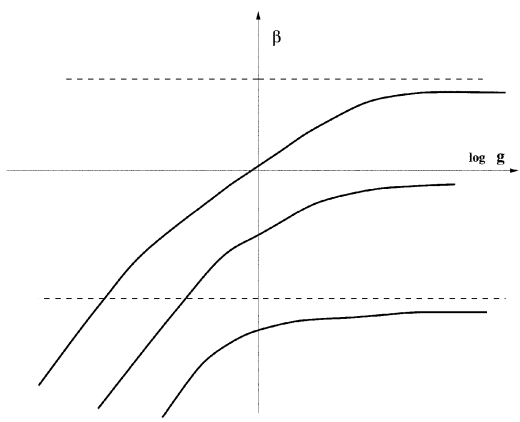


*Figure 7.* The Gell-Mann - Low function for localization theory

$g(L) = \sigma L^{d-2}$, characteristic for a conducting phase. If the scaling function near its zero has the Taylor expansion $\beta(g) \approx (g - g_c)/sg_c$, then, for $0 < g_i - g_c \ll 1$, solution of scaling equation is

$$\log \frac{L}{l} = \int_{g_i}^{g} \frac{dg}{g\beta(g)} \approx (d-2)^{-1} \log g - s \log(g_i - g_c); \tag{43}$$

$$g(L) \propto (g_i - g_c)^{s(d-2)} L^{d-2}; \qquad \sigma \propto (g_i - g_c)^{s(d-2)}. \tag{44}$$

If the initial condition $g_i$ is smaller, than the critical value $g_c$, than the scaling function is negative $\beta(g_i) > 0$, the conductance is decreasing with increasing the sample size $L$ and, at large enough $L$, it follows the law $g(L) \propto \exp(-L/L_C)$, characteristic for an insulating phase. For $0 < g_c - g_i \ll 1$, solution of scaling equation is

$$\log \frac{L}{l} = \int_{g}^{g_i} \frac{dg}{g\beta(g)} \approx s \log(g_i - g_c) - \log \log g; \tag{45}$$

$$g(L) \propto \exp\left[-\frac{L}{L_c}\right]; \qquad L_c \propto (g_i - g_c)^{-s(d-2)}. \tag{46}$$

It is natural to assume that $g_i - g_c$ varies linearly while the Fermi energy $E_F$ passes through the mobility edge $E_g$ ($g_i - g_c \propto E_F - E_g$). This assumption leads us to the following laws at the Anderson transition:

$$\sigma \propto (E_F - E_g)^{s(d-2)}, \; E_F > E_g; \tag{47}$$

$$L_c \propto (E_g - E_F)^{-s}, \; E_F < E_g. \tag{48}$$

Thus, the scaling predicts vanishing of d.c. conductivity $\sigma$ at the Anderson transition as a power of $E_F - E_g$ and divergence of localization length $L_c$ as the same (but negative) power.

## Localization in Magnetic field. Quantum Hall Effect

Localization in 2D in perpendicular magnetic field brings an interesting example of application of the $\sigma$ model and renormalization group. The $\sigma$ model (at $\omega$ =0) has in this case the following form :

$$Z = \int_{Q^2=1} \mathcal{D}Q(\mathbf{r}) e^{-F};$$

$$F = \frac{\pi}{8e^2} \text{ tr } \int d\mathbf{r} \left(\sigma_{xx}(\nabla Q)^2 + 2\sigma_{xy} Q[\nabla_x Q, \nabla_y Q]\right), \tag{49}$$

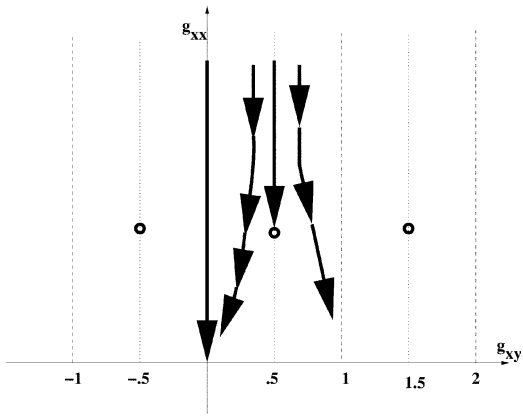


*Figure 8.* The flow diagram for the system of RG equations for 2D electrons in magnetic field.

which contains two conductivities $\sigma_{xx}$ and $\sigma_{xy}$ as two independent charges[1]. A remarkable property of Eq (49) is that

$$\mathrm{tr} \int d\mathbf{r}\ Q[\nabla_x Q, \nabla_y Q] = 16\ \pi i\ T,$$

where $T$ is an integer number characterizing the "winding" of the matrix $Q$ at the manifold of its definition when the coordinate $\mathbf{r}$ covers whole plane. As a result the contribution of the term with the hall conductivity into partition function is

$$\exp\left(2\pi i\ \frac{2\pi\sigma_{xy}}{e^2}\ T\right)$$

The action (49) gives rise to the system of renormalization group equations:

$$\frac{d\log g_{xx}}{d\log L} = \beta_{xx}(g_{xx}, g_{xy}), \tag{50}$$

$$\frac{d\log g_{xy}}{d\log L} = \beta_{xy}(g_{xx}, g_{xy}), \tag{51}$$

We know only very few general things about functions $\beta_{xx}$ and $\beta_{xy}$: both these functions are periodic with respect to $g_{xy}$ with period one, whole flow directed oppositely to the axis $g_{xx}$, there is an unstable fixed point at $(g_{xx} = g_0, g_{xy} = .5)$, which split the flow and direct it to the stable fixed points $(g_{xx} = 0, g_{xy} = n)$, where $n$ is an integer. The flow diagram in the plane $(g_{xx}, g_{xy})$ corresponding to this system is shown in Fig 8. The result of renormalization, which follows the Eqs (50) and (51) and the flow diagram of Fig 8, is shown

[1] More convenient to use dimensionless $g_{xx}$ and $g_{xy}$

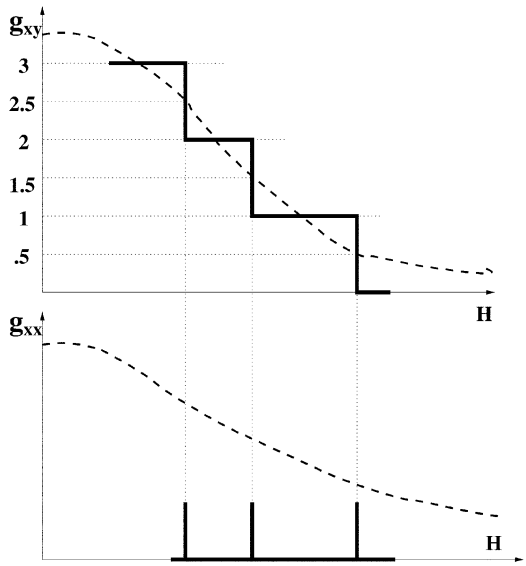


*Figure 9.* The result of renormalization for dissipative and the Hall conductances. The dashed lines corresponds to the values of conductances at short distances, the solid lines show the result of renormalization.

in Fig 9. One could see that it describes the phenomenology of th Quantum Hall Effect: broad plateaus and steep steps in $g_{xy}$ and deep minima of $g_{xx}$ in the middles of the plateaus and sharp spikes at positions of the steps.

## Derivation of the $\sigma$-model

After we discussed numerous consequences of the field theory for disordered conductors as a diffusion mode coupling theory, we pass now to a tedious job of deriving the non-linear $\sigma$-model. Let us begin with the Green's function $G_E(x, x')$ averaged over configurations of impurities. If the energy levels $E_n$ and the eigenfunctions $\chi_n(x)$ are known, then the Green's function (either retarded or advanced ) could be expressed as :

$$\langle\ G_E^{R(A)}(x, x')\ \rangle = \sum_n \frac{\chi_n(x)\chi_n^*(x')}{E - E_n \pm i\delta} \tag{52}$$

For the purpose of calculating the transport properties, one needs the two-particle Green's function $K^R_{E\omega}(x, x')$ which could be expressed

through the Green's functions

$$\langle \rho_E(x)\rho_E(x')\rangle^R_\omega = K^R_{E\omega}(x,x') = \\ \langle\ G^R_{E+\omega/2}(x,x')\ G^A_{E-\omega/2}(x',x)\ \rangle \tag{53}$$

To get a feeling of the problem, consider a toy model (TM)

$$\mathcal{K} = \langle\ \frac{1}{E+\frac{\omega}{2}-E_0+i\delta}\frac{1}{E+\frac{\omega}{2}-E_0+i\delta}\ \rangle \tag{54}$$

and super-toy model (STM)

$$\mathcal{G} = \langle\ \frac{1}{E-E_0+i\delta}\ \rangle \tag{55}$$

In STM, the expression (55) could be obtained using integration over fermions

$$\mathcal{G} = \langle \frac{\int d\bar\psi d\psi\psi\bar\psi e^{-\bar\psi(E-E_0+i\delta)\psi}}{\int d\bar\psi d\psi e^{-\bar\psi(E-E_0+i\delta)\psi}}\ \rangle\ ^2. \tag{56}$$

It is convenient to move the expression from denominator of Eq (56) into numerator, using integration over bosons instead of integration over fermions [3].

$$\mathcal{G} = \langle\ \int d\bar\psi d\psi d\bar\phi d\phi\psi\bar\psi e^{-\bar\psi(E-E_0+i\delta)\psi-\bar\phi(E-E_0+i\delta)\phi}\ \rangle \tag{57}$$

Equation (57) can be simplified if the super-vector notation

$$\Phi = \begin{pmatrix}\psi\\ \phi\end{pmatrix}, \quad \bar\Phi = (\bar\psi,\bar\phi) \tag{58}$$

[2] The standard rule for integration over fermions are

$$\int d\bar\psi d\psi = 0, \quad \int d\bar\psi d\psi\psi\bar\psi = 1$$

A the result, for instance

$$\int d\bar\psi d\psi e^{-a\bar\psi\psi} = a$$

and

$$\int \prod_i d\bar\psi_i d\psi_i e^{-\bar\psi_i A_{ij}\psi_j} = \det\hat{A}$$

[3] The rules are

$$\int d\bar\phi d\phi e^{-a\bar\phi\phi} = \frac{1}{a}$$

$$\int \prod_i d\bar\phi_i d\phi_i e^{-\bar\phi_i A_{ij}\phi_j} = \frac{1}{\det\hat{A}}$$

is used. It take now the following form

$$\mathcal{G} = \langle \int d\bar{\Phi} d\Phi \psi \bar{\psi} e^{-\bar{\Phi}(E-E_0+i\delta)\Phi} \rangle \tag{59}$$

Next stage is to obtain $G_E^R(x,x')$. Introducing the fields $\psi(x), \phi(x)$ and $\Phi(x)$ trough the substitution

$$\psi(x) = \sum_n \psi_n \chi_n(x), \quad \phi(x) = \sum_n \phi_n \chi_n(x), \tag{60}$$

$$\Phi(x) = \sum_n \Phi_n \chi_n(x), \tag{61}$$

we arrive at

$$G_E^R(x,x') = \int \mathcal{D}\bar{\Phi}\ \mathcal{D}\Phi \psi(x)\bar{\psi}(x') e^{-\int dz \bar{\Phi}(z)(E-\hat{H}+i\delta)\Phi(z)} \tag{62}$$

The passage to the two-particle Green's function $K_{E,\omega}^R(x,x')$ can be done by enlarging the size of super-vectors and super-matrices:

$$\Phi = \begin{pmatrix} \psi_R \\ \phi_R \\ \psi_A \\ \phi_A \end{pmatrix}, \qquad E - H \to (E-H)\hat{I} + \frac{\omega}{2}\hat{\Lambda}, \tag{63}$$

$$\Lambda = \begin{pmatrix} \hat{I} & 0 \\ 0 & -\hat{I} \end{pmatrix}. \tag{64}$$

Finally,

$$K_{E,\omega}(x,x') = \tag{65}$$

$$\int \mathcal{D}\bar{\Phi}\ \mathcal{D}\Phi \psi^R(x)\bar{\psi}_R(x')\psi^A(x')\bar{\psi}_A(x') e^{-\int dz \bar{\Phi}(z)(E-H)\Phi(z)} . \tag{66}$$

It is useful to recall at this stage that

$$H = H_0 + U(\mathbf{r}) = -\frac{\nabla^2}{2m}\hat{I} + U(\mathbf{r})\hat{I} - \frac{\omega}{2}\hat{\Lambda}$$

Absence of denominator in all expressions for the Green's functions is very convenient because it allows to perform averaging over impurities using the functional integration[4].

$$\langle A\{U(\mathbf{r})\}\rangle = \int \mathcal{D}U(\mathbf{r}) A\{U(\mathbf{r})\} \exp\left[-\frac{1}{2\gamma}\int U(\mathbf{r})^2 d\mathbf{r}\right], \tag{67}$$

[4] We can recall at this stage the problem of cancellation of closed loops. Formally, these loops appear in perturbative expansion in random potential $U(\mathbf{r})$, but the fermion loops come with the opposite sign to analogous boson loops and the total contribution of the loops vanishes

This averaging leads to the following new Free energy :

$$Z = \int \mathcal{D}\bar{\Phi}\ \mathcal{D}\Phi\ e^{-F} \qquad ; \tag{68}$$

$$F = \int d\mathbf{r}\bar{\Phi}(\mathbf{r})(E - H_0)\Phi(\mathbf{r}) - \gamma \int d\mathbf{r}\left[\bar{\Phi}(\mathbf{r})\Phi(\mathbf{r})\right]^2 \tag{69}$$

i.e. averaging over disorder induces an effective interaction of a $\Phi^4$ form between the components of the super-field $\Phi(\mathbf{r})$. It is convenient to decouple this quartic interaction using the identity

$$\exp\left\{\gamma \int d\mathbf{r}\left[\bar{\Phi}(\mathbf{r})\Phi(\mathbf{r})\right]^2\right\} =$$

$$\int \mathcal{D}Q(\mathbf{r}) \exp\left[\int d\mathbf{r}\bar{\Phi}(\mathbf{r})Q(\mathbf{r})\Phi(\mathbf{r}) - \frac{1}{2\gamma}\mathrm{str}\int d\mathbf{r}Q^2(\mathbf{r})\right] \qquad [5].$$

After mentioned decomposition of the quartic term performed, the superfield $\Phi$ enters the action only in a quadratic form. Calculation a Gaussian integral, we arrive finally at the following expression

$$Z = \int \mathcal{D}Q\Phi\ e^{-\mathcal{F}} \qquad ; \tag{70}$$

$$\mathcal{F} = \mathrm{str}\ln G^{-1} - \frac{1}{4\pi\nu\tau}\int d\mathbf{r}Q^2(\mathbf{r}), \tag{71}$$

$$G^{-1} = E + \frac{\omega}{2}\Lambda + \frac{\nabla^2}{2m} + i\ \frac{Q(\mathbf{r})}{2\tau}. \tag{72}$$

Thus, we arrived at a field theory operating with a super-matrix field $Q$. So far, no approximation we made. If we assume that disorder is weak ($E_F\tau \gg 1$), then the free energy $\mathcal{F}$ has a deep minimum t particular values of $Q$, and a steepest descend method can be applied to calculation the integral.

The condition

$$\frac{\delta\mathcal{F}}{\delta Q(\mathbf{r})} = 0$$

gives

$$\hat{Q}(\mathbf{r}) = \frac{1}{\pi\nu}\mathrm{Im}\hat{G}(\mathbf{r},\mathbf{r}\ |\{Q(\mathbf{r})\}). \tag{73}$$

If supermatrix $Q$ does not depend on coordinates, then Eq (73) could be re-written in following form

$$\hat{Q} = \frac{1}{\pi}\mathrm{Im}\int \frac{d\xi}{\xi + iQ/2\tau}\ \rightarrow\ Q = \mathrm{sign}\ Q, \tag{74}$$

[5] A new notion of super-trace str is used here: if the matrix $A$ has mixed fermionic and bosonic components, then $\mathrm{str}A = \mathrm{tr}A_{BB} - \mathrm{tr}A_{FF}$. The supertrace has the same property str $ABC$ = str $CAB$ with respect to supermatrices $A, B$ and $C$ as usual trace has with respect to conventional matrices.

where the second part of Eq (74) is written for eigenvalues $Q$ of the matrix $\hat{Q}$. This gives either 1 or $-1$ for these eigenvalues. If $Q = \Lambda$, then the Green's function takes a very familiar form:

$$G = \begin{pmatrix} G^R_{E+\omega/2} & 0 \\ 0 & G^A_{E-\omega/2} \end{pmatrix},$$

where

$$G^{R(A)}_E(\mathbf{p}) = \frac{1}{E - \epsilon(p) \pm i/2\tau}$$

We can conclude, therefore, that this familiar form corresponds to the minimum of Free energy $\mathcal{F}$ in the field theory. Condition of this minimum has, nevertheless, much mo general form $Q^2 = 1$ and any matrix of the form

$$Q = U^{-1}\Lambda U$$

obeys this condition. This means that if we consider deviation $\delta Q(\mathbf{r})$ from the stationary solution, this deviation could either change modulae of the eigenvalues of the matrix $Q$ or corresponds to its unitary transformation dependent on coordinates. The former has a gap of the order of $1/\tau$ in their spectrum and, therefore, are not interesting for further analysis. The latter obey the condition

$$Q\delta Q + \delta Q\ Q = 0 \tag{75}$$

correspond to the soft modes and will be considered. Calculating the second functional derivatives of $\mathcal{F}$ in $\delta Q(\mathbf{r})$ and using the condition (75)[6], obtain

$$\mathcal{F} = \mathcal{F}_0 + \mathrm{str} \int d\mathbf{q}\ \delta Q_{\mathbf{q}} \left\{ -1 + \int d\mathbf{p}\ G_{\mathbf{p}+\mathbf{q}}\ \tilde{G}_{\mathbf{p}} \right\}\ \delta Q_{-\mathbf{q}}, \tag{76}$$

which gives at $\omega\tau \ll 1$ and $ql \ll 1$

$$\mathcal{F} = \mathcal{F}_0 + \frac{\pi\nu}{4}\ \mathrm{str} \int d\mathbf{r}\ \left[ D(\nabla Q)^2 + i\omega\Lambda Q \right]. \tag{77}$$

This is exactly the proclaimed field theory - the non-linear supermatrix *sigma*-model. It is obtained now in a controlled way provided disorder is not too strong $E_F\tau gg1$.

The major subject of the theory is the supermatrix $Q$. In the case, used in the presented derivation, this is an $8 \times 8$ matrix: retarded-advanced, Fermi-Bose and the function and its conjugated doublets give $2\times2\times2 = 8$-structure called the orthogonal ensemble (OE). In the

[6] We use the notation $\tilde{G}\{Q\} = G\{-Q\}$

presence of magnetic field, the Hamiltonian is hermitian but not real. Therefore, the eigenfunctions of this Hamiltonian are complex functions and the mentioned the function and its conjugated degeneracy is destroyed. The matrix $Q$ in this case has the rank four (the unitary ensemble (UE)). Another case arises when the time-reversal symmetry is preserved but the spin-orbit interaction is taken into account. Spin adds one more dimension and the of the supermatrices is equal now to sixteen (the simplectic ensemble (UE)). These three universal ensembles resemble those by Dyson. We return to this connection very in the next lecture.

The standard field-theoretic methods allow to prove renormalizabiliy of the theory with the action (77). We discussed already numerous consequences of the scaling which emerge from this renormalizability.

In the next lecture we discuss the physics which could be naturally linked to this field theory.

# Lecture 3.
# In Zoo of $\sigma$-models

## Level Statistics

Consider first a metallic grain of a small size $L \gg l$. This size brings the typical time of flight $t_f \sim L^2/D$ and the Thouless energy $E_T \sim 1/t_f \sim D/L^2$. Small grain with randomly distributed impurities has random energy levels of electrons $\epsilon_i$. If we consider th density of states $\nu(\epsilon)$, it consist of the averaged part $\langle \nu(\epsilon) \rangle$ and the fluctuation $\delta\nu(\epsilon)$. Statistics of the energy levels is given by the correlation function

$$\mathcal{K}(\omega) = \frac{\langle \delta\nu(\epsilon+\omega)\delta\nu(\epsilon)\rangle}{\langle \nu(\epsilon)\rangle} = \delta(\omega) - \mathcal{P}\left(\frac{\omega}{\Delta}\right), \tag{78}$$

where $\Delta = 1/\nu V$ is the mean level spacing and $V \sim L^d$ is the volume of the grain.

Let us first concentrate the attention at the hermitian but not real random Hamiltonians, which correspond to the unitary ensemble. The levels repel each other, so the pair correlation function $\mathcal{P}(x)$ as a function of dimensionless distance between the levels $x = \pi\omega/\Delta$ is equal to

$$\mathcal{P}(x) = 1 - \frac{\sin^2 x}{x^2}, \quad x = \frac{\pi\omega}{\Delta} \tag{79}$$

and is shown in Fig 10. We can obtain a qualitative understanding of this form from the following consideration: if two levels are very close to each other, then the repulsion from all the other levels could be neglected. For these two levels the Hamiltonian has the following matrix form:

$$\mathcal{H} = \begin{pmatrix} h & v_1 + iv_2 \\ v_1 - iv_2 & -h \end{pmatrix}. \tag{80}$$

The energies corresponding to this Hamiltonian are equal to

$$\epsilon_\pm = \pm\sqrt{h^2 + v_1^2 + v_2^2},$$

and the probabilities to find small values of $h$, $v_1$, and $v_2$ do not depend on this values. Therefore, the pair correlation function is given by the following integral

$$\mathcal{P}(\omega) \sim \int dh dv_1 dv_2 \; \delta(\omega - 2\sqrt{h^2 + v_1^2 + v_2^2}) \sim$$
$$\int \rho \; d\rho \; \delta(\omega - 2\rho) \sim \omega^2 \tag{81}$$

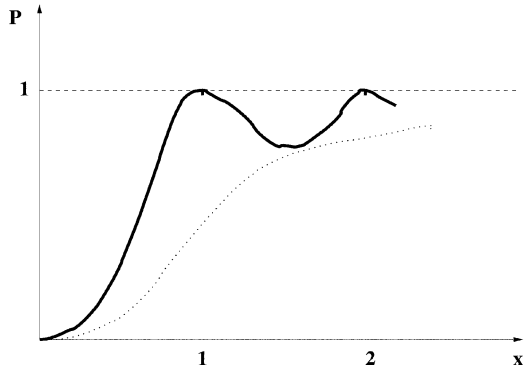


*Figure 10.* Pair correlation functions of the levels with the dimensionless energy difference $x = \pi\omega/\Delta$

[7] Another interesting feature of the curve of Fig 10 is its long tail at $x \to \infty$. At $x \to \infty$ the levels are nearly independent from each other and, therefore, $\mathcal{P} \to 1$. The fact that $\mathcal{P}$ approaches unity at $x \to \infty$ not exponentially but power-law shows that the levels staircase has certain rigidity and, therefore, keeps certain correlation even when $x \to \infty$.

How would we treat the level statistics, using the $\sigma$-model ?
Let us begin with the expression of the density of states through the Green's functions $G^{R(A)}$:

$$\nu(\epsilon) = \frac{1}{2\pi i V} \int d\mathbf{r} \left[ G^R_\epsilon(\mathbf{r},\mathbf{r}) - G^A_\epsilon(\mathbf{r},\mathbf{r}) \right] \tag{82}$$

Therefore, the correlator ( 78 ) contains an averaged product of two Green's functions at energies $\epsilon + \omega$ and $\epsilon$. It is not surprising that such a product can be calculated using the $\sigma$-model

$$Z = \int_{Q^2=1} \mathcal{D}Q e^{-F},\ F = \frac{\pi\nu}{2}\ \mathrm{str} \int d\mathbf{r} \left[ \mathcal{D}(\nabla Q)^2 + 2i\omega\Lambda Q \right] \tag{83}$$

The super-matrix $Q$ in this theory could be parametrized as $Q = U^{-1}\Lambda U$, where the unitary matrix $U$ depends on coordinates $\mathbf{r}$. The gradient term in the action (83) can be estimated as $D(\nabla Q)^2 \sim Dn^2/L^2 \sim n^2 E_T$. Therefore, if $\omega \ll E_T$ the dominant contribution comes from the mode with $n = 0$. This corresponds to the, so-called, zero-mode

[7] For OE a $\delta(v_2)$ should be added under integral and $\mathcal{P}(\omega) \propto \omega$. In SE case, all levels are presented by the Kramers' doublets. If one constructs the $4 \times 4$ matrix eigenvalues of which represent these doublets, then, integrating over the free parameters in the spirit of Eq(81), one obtains $\mathcal{P} \propto \omega^4$.

approximation, when $Q$ does not depend on coordinates. Therefore,

$$F = i\ \frac{\pi\omega}{\Delta}\ \mathrm{str}\ \Lambda Q \tag{84}$$

In zero-mode approximation, the calculation of the partition function $Z$ and the correlators is reduced to integration over final number of variables which characterized the super-matrix $Q$. Using the parametrization $Q = V^{-1}\hat{H}V$, where

$$V = \begin{pmatrix} u & 0 \\ 0 & v \end{pmatrix},\ \hat{H} = \begin{pmatrix} \cos\hat{\theta} & i\sin\hat{\theta} \\ -i\sin\hat{\theta} & -\cos\hat{\theta} \end{pmatrix} \tag{85}$$

while

$$\Lambda = \begin{pmatrix} 1 & 0 \\ 0 & -1 \end{pmatrix}. \tag{86}$$

and

$$\hat{\theta} = \begin{pmatrix} \theta \\ i\theta_1 \end{pmatrix}, \quad -\pi \le \theta \le \pi, \quad 0 \le \theta_1 < +\infty, \tag{87}$$

we can see that all integrals depend only on two parameters $\theta$ and $\theta_1$. The manifold of their variations is shown schematically at Fig 11 [8]. The expression for the action in zero-mode approximation looks as follows

$$F = i\ x\ \ (\cosh\theta_1 - \cos\theta) \tag{90}$$

At $x \gg 1$ the integral for partition function $Z$ with $F$ in exponential is determined by the contributions of two stationary points $\theta_1 = 0, \theta = 0$ and $\theta_1 = 0, \theta = \pi$. Their contributions 1 and $e^{2ix}$ hint about the origin of the oscillating part $\sin^2 x$ in Eq (79). Explicit integration gives precisely the expression (79) for the pair correlation function. It is difficult to explain now the excitement felt by those in 1982, who watched the formula (79) and the expressions for the pair correlation functions for different ensembles first time obtained not from Dyson phenomenology but directly from a macroscopic theory as a result of certain approximation. It gave a universal tool for treating numerous problems in Quantum Dots. As an example, the question:
- How a crossover from OE to UE occurs if a magnetic field is switched

[8] It is useful, at this stage, to return to our analogy with magnetism and trace how different aspects of the theory appear in these two cases. The partition function for a magnetic grain has the form

$$F_M = -\mathbf{MH} = -H\cos\theta, \tag{88}$$

$$Z = \frac{1}{2}\int_{-1}^{1} d\cos\theta \exp\left[-\frac{H}{T}\ \cos\theta\right] = \cosh\frac{H}{T}, \tag{89}$$

and is obtained by integration over single (compact) angle $\theta$

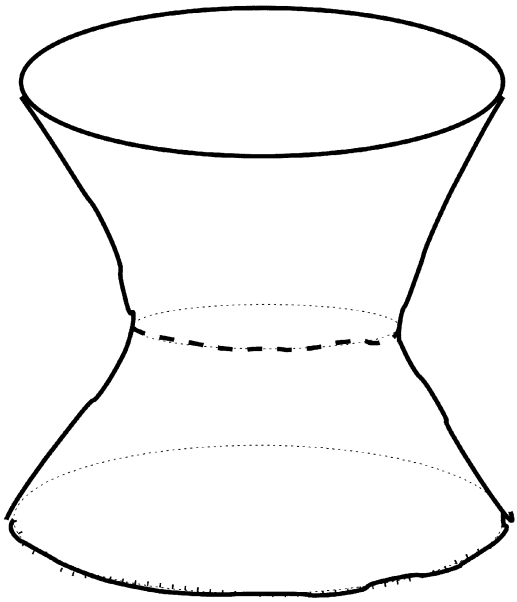

*Figure 11.* The manifold of variation of parameters, characterizing the super-matrix $\hat{Q}$

on -
has now a explicit answer: you have to replace the Hamiltonian $\mathcal{H} = -\nabla^2/2m$ by $\mathcal{H} = (-i\nabla - e\mathbf{A})^2/2m$ and, performing the whole derivation, arrive at

$$F = \frac{\pi\nu}{4}\,\mathrm{str}\int d\mathbf{r}\left[\mathcal{D}(\nabla Q - ie\mathbf{A}[\tau_3, Q])^2 + 2i\omega\Lambda Q\right], \tag{91}$$

which gives in the following zero mode approximation action

$$F = \frac{\pi}{4}\,\mathrm{str}\left[\frac{De^2}{\Delta}\langle\mathbf{A}^2\rangle[\tau_3, Q]^2 + i\frac{\omega}{\Delta}\Lambda Q\right], \tag{92}$$

where $\langle\mathbf{A}^2\rangle$ is the square of the vector-potential averaged over the Quantum Dot. If the super-matrix $Q$ is presented in the form

$$Q = \begin{pmatrix} \langle\phi\bar{\phi}\rangle & \langle\bar{\phi}\bar{\phi}\rangle \\ \langle\phi\phi\rangle & \langle\bar{\phi}\phi\rangle \end{pmatrix},$$

then fluctuations of diagonal and off-diagonal elements have very different rigidity: $\omega$ for diagonal and $1/\tau_H = De^2\langle\mathbf{A}^2\rangle$ for off-diagonal

elements. Introducing a proper parametrization and calculation this multiple, but still finite-dimensional integral, one arrives at an expression for the pair correlation function valid at arbitrary value of dimension-less parameter $\omega\tau_H$.

## Prelocalization - Rare Fluctuations

Zero-mode approximation as a method of treating the properties of Quantum Dots is only one of possible applications of the field theory. Another interesting direction is a study of rare events. Consider for example the following problem: we have a sample of a disordered conductor of the length $L$ and width $w < L$ as shown in Fig 12, attached to ideal bulk electrodes. Assume also that both these dimensions are longer that the mean free path $l$ ($L, w \gg l$). Electrons states in a very long wire are localized with localization length $L_c \sim l\ k_F\ w$. Let us assume that $L \ll L_c$. This means that the dimension-less conductance $g = \hbar G/e^2$ is large ($g \gg 1$).

For simplicity we assume that the electrons in this conductor do not interact with each other, the temperature is zero ($T = 0$) and there are no inelastic processes. The total current $I(t)$ at time $t$ depends upon the voltage $V(t)$ according to the Ohm law:

$$I(t) = \int_{-\infty}^{t} dt' G(t - t') V(t').$$

We are interested in the asymptotic form of the conductance $G(t)$ as $t \to \infty$. Its dependence on time is shown schematically in Fig 13. There are three time scales in the problem:

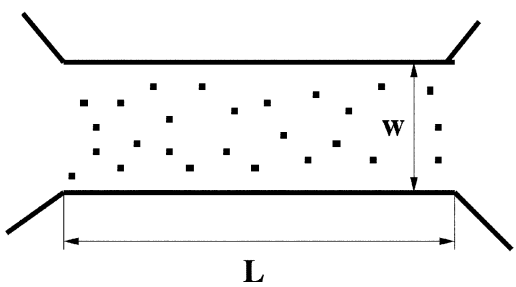


*Figure 12.* A disordered sample attached to bulk electrodes

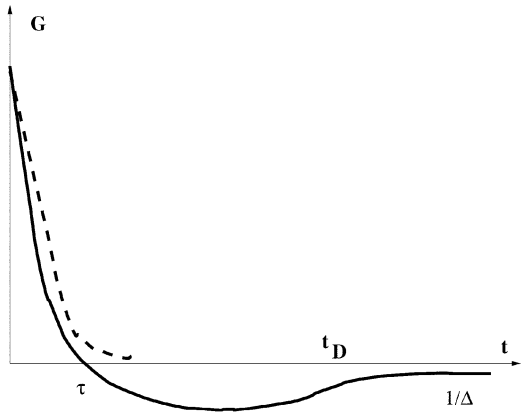


*Figure 13.* Time-dependent averaged conductance $G(t)$ of a disordered sample. The dashed line shows the classical Drude conductance

1. The mean free time $\tau = l/v_F$, where $v_F$ is the Fermi velocity and $l$ is the mean free path. This time scale determines the dispersion of the Drude conductivity $\sigma_0 \sim e^{-t/\tau}$

2. The time of diffusion through the sample $t_D = L^2/D$, where $D = l^2/3\tau$ is the diffusion coefficient, and $L$ is the sample size.

3. The inverse mean level spacing $1/\Delta = \nu V$, where $\nu$ is the density of states and $V = Lw$ is the volume of the sample.

In a macroscopic sample the inequality $\tau \ll t_D \ll \hbar/\Delta$ is valid, provided that $L \gg l$ and the disorder is weak. Indeed, the product $\Delta t_D$ is connected with the dimensionless conductance of the sample $g = 2\pi\hbar/(t_D\Delta)$, which is large for a weak disorder. The times $t_D$ and $\hbar/\Delta$ enter into time dispersion only due to quantum corrections to conductivity.

At times $t \ll \hbar/\Delta$ an electron can be considered a wave packet of many superimposed states propagating semi-clas-sically. Therefore, it is natural to assume that the conductance $G(t)$ is proportional to the probability of finding a Brownian trajectory that remains in the sample for the time $t$. For $t \gg t_D$ such a probability decays as $\exp[-t/t_D]$. Our calculations confirm this result.

In the opposite limit, for $t \gg \hbar/\Delta$, the conductance $G(t)$ is proportional to the probability of finding an electron state with the life time $t$. In order to trap an electron for a long time the state must be poorly connected with the leads (nearly localized). We show that the

probability of finding such a state decays non-exponentially with time. Namely, $G(t) \sim \exp\left[-g\log^2(t\Delta)\right]$ (for $d = 1$).

Instead of calculating the conductance as a function of time, we could have worked in the frequency representation. In that way we would have found a singularity in $G(\omega)$ as $\omega \to 0$. This singularity, however, does not affect the value of the d.c. conductance and therefore has an obscure physical meaning, while the time domain results have the direct interpretation.

Since the long time asymptote corresponds to the rare events when the electron is nearly trapped in the sample, it is natural to use the saddle-point approximation. We carry out the following program:

1. Express the averaged conductance as a functional integral over supermatrices

$$\begin{aligned} &G(t) = G_0 e^{-t/\tau} + \\ &\int \frac{d\omega}{2\pi} e^{-i\omega t} \int \mathcal{D}Q(r) P\{Q\} \exp\left[-A\right], \\ &A = \frac{\pi\nu}{8} \int dr\ \mathrm{Str}\{D(\nabla Q)^2 + 2i\omega\Lambda Q\}, \end{aligned} \tag{93}$$

2. Vary the action $A$ with respect to $Q$, taking into account the constraint $Q^2 = 1$, and obtain the saddle-point condition:

$$2D\nabla(Q\nabla Q) + i\omega\left[\Lambda, Q\right] = 0 \tag{94}$$

3. Derive the condition at the boundary with the lead

$$Q|_{\mathrm{lead}} = \Lambda. \tag{95}$$

4. Perform the integration over $\omega$ in Eq. (93) and obtain the self consistency condition

$$\int \frac{dr}{V}\ \mathrm{Str}(\Lambda Q) = -\frac{4t\Delta}{\pi\hbar} \tag{96}$$

   which allows us to exclude $\omega$ from Eq. (94).

5. Substitute the solution of Eq. (94) with boundary conditions (95) in Eq. (93) and obtain the results with exponential accuracy.

The $8 \times 8$ supermatrix $Q$ has commutative and anti-commutative matrix elements. Since $Q^2 = 1$ it can be chosen in the form:

$$Q = V^{-1} H V, \quad V = \begin{pmatrix} u & 0 \\ 0 & v \end{pmatrix},$$

$$\Lambda = \begin{pmatrix} 1 & 0 \\ 0 & -1 \end{pmatrix}, \quad H = \begin{pmatrix} \cos\hat{\theta} & i\sin\hat{\theta} \\ -i\sin\hat{\theta} & -\cos\hat{\theta} \end{pmatrix}, \tag{97}$$

$$\hat{\theta} = \begin{pmatrix} \theta_1 & 0 & 0 & 0 \\ 0 & \theta_1 & 0 & 0 \\ 0 & 0 & i\theta & 0 \\ 0 & 0 & 0 & i\theta \end{pmatrix}$$

This decomposition allows us to present the action $A$ in the form

$$A = \frac{\pi\nu}{8}\int dr\ \mathrm{Str}\{D(\nabla H)^2 + DM^2 + 2i\omega\Lambda H\}, \tag{98}$$

where $M = \left[V^{-1}\nabla V, H\right]$. The minimum action is reached for $V =$ const, and Eq. (98) may be expressed in terms of $\theta$-variables only:

$$\begin{aligned} A \ = \ & \frac{\pi\nu}{2}\int dr\{[D(\nabla\theta)^2 - 2i\omega\cosh\theta] \\ & +[D(\nabla\theta_1)^2 + 2i\omega\cos\theta_1]. \end{aligned} \tag{7}$$

Consequently, Eq. (2) has the form:

$$D\nabla^2\theta + i\omega\sinh\theta = 0, \tag{99}$$

$$D\nabla^2\theta_1 + i\omega\sin\theta_1 = 0 \tag{100}$$

The boundary condition (95) follows from the fact that $Q$ does not fluctuate in the bulk electrodes, $Q = \Lambda$. Hence, at the boundary with the ideal lead $\theta = \theta_1 = 0$ The time decay of the conductance $G(t) \sim \exp(-i\omega t)$ corresponds to real and positive values of $i\omega$. The permitted values of frequency $\omega$ in Eq. (100) are bounded from below by the value $\omega_1 \sim 1/t_D$, which corresponds to the linearized form of Eq. (100). For smaller frequencies $\omega < \omega_1$, which will turn out to be the only relevant ones, Eq. (100) has only trivial solutions $\theta_1 = 0$. Thus, the self-consistency equation (96) has the form:

$$\int \frac{dr}{V}\{\cosh\theta\ - 1\} = \frac{t\Delta}{\pi\hbar}. \tag{101}$$

The solutions of Eq. (99) depend on the sample geometry. We start by considering a one dimensional wire of length $L$, attached to ideal leads at $x = \pm L/2$. If $t\Delta \ll 1$, then, to satisfy the self-consistency condition (101) we must choose $\theta \ll 1$. Therefore, Eq. (99) can be linearized. The solutions that satisfy the boundary conditions is

$$\theta = C\cos(\pi n x/L), \quad \omega_n = \frac{-i\pi^2 n^2}{t_D}, \tag{102}$$

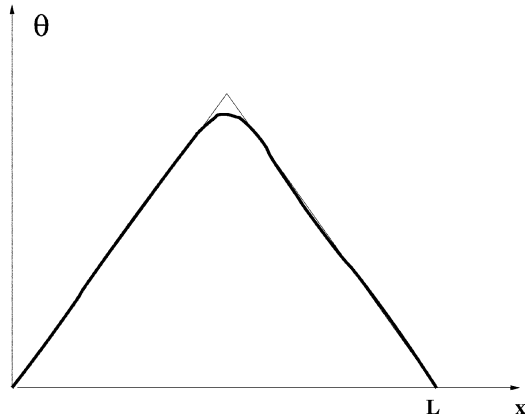


*Figure 14.* Saddle-point solution for the angle $\theta(x)$.

where $n$ is an arbitrary integer. The above formula for the frequency implies that in the discussed regime

$$G(t) \sim e^{-i\omega_1 t} = \exp\left(-\frac{\pi^2 t}{t_D}\right). \tag{103}$$

To obtain this result we determine the amplitude $C$ from the linearized self-consistency equation, and then substitute (102) into the action $A$.

For arbitrary times Eqs. (99) and (101) in dimensionless coordinates have the form:

$$\frac{d^2\theta}{dz^2} + \frac{\gamma^2}{2}\sinh\theta = 0, \quad z = \frac{x}{L}, \tag{104}$$

$$\int_{-1/2}^{1/2} dz[\cosh\theta - 1] = \frac{\Delta t}{\pi\hbar}, \quad \gamma^2 = 2i\omega t_D. \tag{105}$$

The solution of (104) is symmetric $\theta(z) = \theta(-z)$, and in the region $z > 0$ is given by the quadrature:

$$z = \frac{1}{\gamma}\int_{\theta(z)}^{\theta_0} \frac{d\theta'}{\sqrt{\cosh\theta_0 - \cosh\theta'}} \tag{106}$$

$$\theta_0 = \theta(0) = 2\log\frac{1}{\gamma} + 2\log\log\frac{1}{\gamma}, \text{ for } \gamma \ll 1 \tag{107}$$

Solution $\theta(x)$ is shown in Fig 14. The function $\theta(z)$ is almost linear $\theta = \theta_0(1 - 2|z|)$ everywhere except in the region $|z| < 1/\log(1/\gamma) \ll 1$.

Substituting Eq. (106) into Eqs. (101) and (93) we get

$$i\omega = \frac{2g}{t}\log\frac{t\Delta}{\hbar}, \quad G(t) \sim \exp\left[-g\log^2\frac{t\Delta}{\hbar}\right] \tag{108}$$

As mentioned earlier, the contribution from the individual nearly localized states dominates in $G(t)$ whenever $t\Delta/\hbar \gg 1$. The square modulus of the wave function for such a state $|\Psi|^2$ equals $\cosh\theta$. As we can see, this value decays exponentially towards the leads, where $|\Psi(x = \pm L/2)|^2 = \cosh\theta(\pm 1/2) = 1$. Because of the latter condition, the current through the wire is equal to unity. Therefore, the escape time $t$ is proportional to the normalization integral. This is exactly what is stated in the self-consistency condition (105) for $\theta \gg 1$. To summarize, the wave function is localized in the region $|x| \ll \xi \ll L$ with the localization length $\xi = L/\log(t\Delta/\hbar)$ and the probability to find such a state is given by Eq.(108).

It is worth mentioning, that the saddle point equation looks very similar to the well known Eilenberger-Usadell equation in the theory of dirty superconductors. If we introduce the matrix Green's function (obeying the Gor'kov equation) in the form

$$\hat{G}_\epsilon(\mathbf{r},\mathbf{r}') = \begin{pmatrix} G & F \\ -F^+ & G^+ \end{pmatrix}, \tag{109}$$

take a Furrier transfor of it

$$\hat{G}_\epsilon(\mathbf{r},\mathbf{r}') = \int (d\mathbf{p}) e^{i\mathbf{p}(\mathbf{r}-\mathbf{r}')}\hat{\mathcal{G}}_\epsilon\left(\mathbf{p}, \frac{\mathbf{r}+\mathbf{r}'}{2}\right)$$

and integrate over modulus $|\mathbf{p}|$ of momentum

$$\hat{g}_\epsilon(\mathbf{n},\mathbf{r}) = \int d|\mathbf{p}|\hat{\mathcal{G}}_\epsilon(\mathbf{p},\mathbf{r}), \quad \mathbf{n} = \frac{\mathbf{p}}{|\mathbf{p}|},$$

we arrive at the matrix function $\hat{g}_\epsilon(\mathbf{n},\mathbf{r})$ dependent on coordinate $\mathbf{r}$ and direction $\mathbf{n}$ of momentum. This function obeys the Eilenberger equation which reminds the Boltzmann equation for distribution function. If the space gradient at the mean free path is small $l\ \nabla\ \hat{g} \ll 1$, then the Eilenberger equation could be reduced to the diffusion-like form for the matrix function $g_\epsilon(\mathbf{r})$ dependent only on coordinate. This Usadell equation has the form

$$i\epsilon[\Lambda, g] + 2D\nabla(g\ \nabla g) + \Delta[\tau_3, g] = 0, \tag{110}$$

which strongly resembles Eq (94) at $\Delta = 0$. Significant diference between Eq (110) and Eq (94) is that the second one has twice larger rank because it operates with both fermions and bosons.

Therefore, the question:
- Which quantum action has the Usadell ( at $\Delta = 0$ ) equation as its saddle-point equation? -
has the following answer:
- There is no action for conventional matrices $\hat{g}$, but if the rank of the matrices is doubled adding to initial fermion variable, boson variable, then such an action simply coincides with super-symmetric $\sigma$-model.

## Further Developments and Open Questions

Discovery of parallelism between the semiclassical dynamics (Heisenberg-Usadell equations) and super-matrix field theory sends several exciting hints. First of all, we could take $\Delta \neq 0$ in the Usadell equation and find out the action corresponding to these dynamics. Such field theory describes a dirty superconductor. If $\langle \Delta \rangle = 0$ but $\delta\Delta \neq 0$, we arrive at a gap-less superconductor. We could study the level statistics in a small grain of such a material. When energy $\epsilon$ is larger than the level spacing then the level statistics in a superconductor does not differ from that in a normal metal. The satiation changers if $\epsilon$ is comparable with the level spacing. In this case, each level sees its mirror image at $-\epsilon$ and repels from it.

Even more interesting situation occurs when one begins to apply the instanton (rare fluctuations) technique to dirty superconductors. For instance, any concentration of paramagnetic impurities destroys the BCS relation between the gap in the spectrum of BCS quasi-particles and the critical temperature. It is well known from the mean field analysis that the large enough concentration of paramagnetic impurities leads to the gap-less situation. The instanton analysis shows that at any concentration of paramagnetic impurities, there is a finite density of states at all energies. Therefore, any superconductor with paramagnetic impurities is gap-less. The difference is that at the high concentration of impurities the states inside the BCS gap are conducting, while, if the concentration of impurities is low, then these states arise from the tail of the density of states and, therefore, they are localized.

A very exciting question is whether whole this knowledge allows to understand the nature of the transition between a superconductor and an insulator in thin films. So far, this question has no answer.

Returning down to the Earth from the heights and complexities of the theory of dirty superconductors, we find our old friend a single electron in a random potential. Do we understand all about it ? Not at all. Most important un-resolved question is what localization means in

the language of $\sigma$-model. The answer seems very close. When we learn it, a new horizon will open.

# Non-Fermi-liquid metals in low dimensions

C. Di Castro and S. Caprara (sergio.caprara@roma1.infn.it)
*Istituto Nazionale per la Fisica della Materia, SMC and Unità di Roma 1,*
*and Dipartimento di Fisica, Università di Roma "La Sapienza",*
*Piazzale Aldo Moro, 2 – I-00185 Roma, Italy*

**Abstract.** In low-dimensional metals the presence of massless excitations may lead to a breakdown of the Landau Fermi-liquid description, which successfully applies to higher-dimensional metals. This breakdown is mirrored by infrared divergences which plague the perturbative treatment of models for low-dimensional metals, despite the fact that the metallic phase is a stable liquid phase of the matter. However, the very condition of stability of the system implies exact cancellations among the singular terms in the response functions, controlled by additional Ward identities, which must be considered besides the standard Ward identities related to the conservation of the total particle and spin density. The combined use of renormalization group and of these Ward identities allows for the closure of the renormalization-group equations, leading to the description of the asymptotic (infrared) behavior of the low-dimensional metal.

**Keywords:** low-dimensional metals; non-Fermi-liquid systems

**PACS:** xxx

## 1. Introduction

The low-energy behavior of most interacting fermionic systems can be discussed within a small number of universality classes. This classification can be understood if one imagines to derive the effective asymptotic theory by means of an iterated elimination of the high-energy degrees of freedom within a Wilson renormalization-group scheme [1]. This procedure selects few types of dominant scattering processes near the Fermi surface [2, 3, 4, 5] and allows for a full description of the low-energy behavior of the system in terms of few parameters. For pure systems, and in the absence of symmetry breaking (e.g., magnetism, superconductivity,...) two types of metallic phases are well known: the "normal" Fermi-liquid phase in $d = 3$ [6], and the "anomalous" Luttinger-liquid phase in $d = 1$ [2].

The breakdown of the Fermi-liquid theory has been claimed to be relevant within many physical contexts. For instance, a number of experimental evidences indicates that the metallic phase of high-temperature superconducting cuprates is not a Fermi liquid [7]. These materials are insulating with antiferromagnetic long-range order when stoichiometric, and become metallic upon chemical doping, which introduces charge carriers (holes, in most cases) in the system. The cuprates are characterized by a strongly anisotropic crystal structure, based on copper-oxygen planes intercalated with rare-earth slabs,



*R. Fazio et al. (eds.), New Directions in Mesoscopic Physics,* 39–66.
© 2003 *Kluwer Academic Publishers. Printed in the Netherlands.*

which is mirrored by anisotropic (namely, quasi two-dimensional) electronic properties. For instance, the electrical resistivity in the direction perpendicular to the copper-oxygen planes, $\rho_\perp$, is much smaller than the resistivity within the planes, $\rho_\parallel$ ($\rho_\perp/\rho_\parallel \simeq 10^{-2} - 10^{-5}$). Contrary to what it is expected in a Fermi liquid, $\rho_\parallel$ increases linearly with the temperature $T$ over a wide temperature range [8], when the chemical doping (i.e., the density of charge carriers) is such that the superconducting critical temperature $T_c$ reaches the maximum value within each family of the cuprates (optimal doping). Moreover, at doping smaller than optimal doping, in the so-called underdoped regime, where the charge-carrier density is small, the anomalous behavior of the metallic state is much stronger and a pseudogap appears as a depletion of the low-energy excitation spectrum at a doping-dependent crossover temperature $T^*$, which manifests itself in various physical quantities [9].

Another evidence for a non-Fermi-liquid behavior comes from the linearity of the quasiparticle inverse scattering time, as a function of temperature and energy, $\tau_{\rm scatt}^{-1} \propto (T, \epsilon)$. This anomalous behavior is revealed, e.g., in angle-resolved photoemission spectroscopy [10] by the slow narrowing of the single-particle spectral density as the energy of the quasiparticle peak $\epsilon$ approaches the Fermi level, in contrast with the usual Fermi-liquid behavior $\tau_{\rm scatt}^{-1} \propto (T^2, \epsilon^2)$, which can be deduced by simple phase-space arguments for low-energy scattering processes near the Fermi surface [6], which are strongly constrained by the Pauli principle.

The clarification of the properties of the metallic phase from which high-temperature superconductivity emerges, apart from being an interesting problem by itself, may also give hints on the basic mechanism for the onset of superconductivity.

Suggestions for the anomalous behavior of the metallic phase are the breakdown of the Fermi liquid, as a direct extension of the Luttinger-liquid behavior, typical of interacting one-dimensional electron systems, to $d = 2$ (which is the dimensionality proper of the cuprates at some intermediate energy scale, due to their strong anisotropy) [7, 11, 12], or the onset of the marginal Fermi liquid [13], in which single-particle excitations are not well defined, as their inverse lifetime is of the same order as their energy. A third possibility is that the system is close to an instability, and that the critical fluctuations nearby couple to the charge carriers, giving rise to a singular effective interaction among the fermionic quasiparticles, which is strongly frequency-, momentum-, temperature-, and doping-dependent, and destroys the Fermi-liquid behavior [14]. Critical fluctuations can be associated with a charge instability (phase separation, or the onset of an incommensurate charge-density wave) [14], with a magnetic instability [15], or with a combination of the two, leading to a stripe-like modulation of the charge and spin density profile [16]. This modulation can be promoted by the tendency

of an antiferromagnetic background to expel doped charges carriers at low doping [17], or from an instability of the Fermi liquid towards the formation of a charge density modulation, which in turn enslaves a modulation of the spin density [14], and is reached upon reducing the doping, starting from the markedly metallic overdoped region.

The proposal that the Luttinger-liquid behavior can be extended to a two-dimensional system stems from the observation that all the high-temperature superconducting cuprates are insulators in the absence of doped charge carriers, and the ground state is antiferromagnetically ordered. Doping an antiferromagnet results in a frustrated state, since the spin of the doped charge carriers couples with the antiferromagnetically ordered spins, which are localized on the copper ions, thus disturbing the ordered state. This frustrated state, which in $d = 1$ is characterized by resonating spin singlets without magnetic long-range order (resonating-valence-bond state), no fermionic low-lying excitations, and decoupled charge and spin collective excitations, could then extend to $d = 2$ [11]. The underlying hypothesis is thus that the doped system never behaves as a Fermi liquid, and, in the absence of a symmetry breaking, rather reaches a new fixed point, characterized by a non-Fermi-liquid behavior.

The existence of (and the conditions leading to) this new fixed point will be the object of these notes. However, before addressing this relevant issue, we briefly review the theory of the normal Fermi liquid and of the Luttinger liquid. Then we discuss the dimensional crossover from a Luttinger liquid to a Fermi liquid, as soon as $d > 1$ [3, 18], unless singular long-range forces are present, which may extend the non-Fermi-liquid behavior to a higher dimension [19, 20, 21]. Our analysis is devoted to the ground-state properties at $T = 0$.

The physics of fermion systems in $d = 1$ is discussed in many papers, starting from the summary of the understanding of the problem at the end of the 1970s, by Sólyom [2]. More recent treatments can be found in Refs. [22, 23], whereas the case of interacting fermions in the presence of forward scattering is dealt with in Ref. [3], and a pedagogical exposition of the renormalization-group approach for Fermi systems is given in Ref. [5]. These notes closely follow Refs. [3, 24].

## 2. Normal Fermi liquid

The normal Fermi-liquid theory, which successfully applies to liquid $^3$He and to ordinary metals in $d = 3$, relies on the existence of well-defined fermionic low-lying excitations (quasiparticles), which are asymptotically free. From the point of view of the renormalization-group approach, the corresponding fixed-point Hamiltonian can be obtained by integrating out states far from the

Fermi surface, within a Wilson-like approach. All the momentum-transferring scattering processes in $d = 3$ become ineffective. The resulting effective Hamiltonian, representative of a metallic state (we do not consider here cases in which the symmetry is broken in the ground state, as in magnets or superconductors), describes the quasiparticles as a collection of free particles, with vanishing effective interactions, except for residual Hartree-like interactions, and can be written as

$$\mathcal{H} = \sum_{\mathbf{k}} \sum_{\sigma} \varepsilon_{\mathbf{k}\sigma} \delta n_{\mathbf{k}\sigma} + \frac{1}{V} \sum_{\mathbf{k},\mathbf{k}'} \sum_{\sigma,\sigma'} f_{\mathbf{k}\mathbf{k}'\sigma\sigma'} \delta n_{\mathbf{k}\sigma} \delta n_{\mathbf{k}'\sigma'},$$

where the first term represents the contribution from free quasiparticles with spin $\sigma = \uparrow, \downarrow$ and excitation energies $\varepsilon_{\mathbf{k}\sigma}$, the term $f_{\mathbf{k}\mathbf{k}'\sigma\sigma'}$ is the (weak) effective interaction which couples the changes in the occupation numbers of the quasiparticle states, $\delta n_{\mathbf{k}\sigma}$, and $V$ is the volume of the system. The presence of a residual interaction leads to various effects. The response functions change with respect to the Fermi gas, although, these changes are described by a small set of parameters, the so-called Landau parameters, related to the effective interaction $f_{\mathbf{k}\mathbf{k}'\sigma\sigma'}$. Once the modifications due to the presence of the Landau parameters are taken into account, the equilibrium properties of the system are similar to those of the Fermi gas, i.e., the specific-heat coefficient $\gamma = C_V/T$, the spin susceptibility $\chi$, and the compressibility $\kappa$ are temperature-independent, as long as the temperature is much smaller than the Fermi temperature. Moreover, quasiparticles have a finite inverse lifetime, associated with subleading corrections, which however vanishes as the square of the radial deviation of the momentum from the Fermi momentum $k_r = |\mathbf{k}| - k_F$, or the square of the temperature $T$, $\tau_{\rm scatt}^{-1} \simeq E_F^{-1} \max[(v_F k_r)^2, T^2]$, where $E_F = v_F k_F$ is the Fermi energy, $v_F$ is the Fermi velocity, and we here assumed that the properties of the liquid state are isotropic and spin-independent. As a consequence, for instance, a single-particle peak is observed in angle-resolved photoemission experiments, with a width which reduces as $k_r^2$ when $|\mathbf{k}| \to k_F$, and the resistivity due to electron-electron scattering at finite temperature is $\rho \propto T^2$ in ordinary metals. Finally, a finite wave-function renormalization $Z$ appears as the residual at the simple pole of the single-particle Green's function

$$G(\mathbf{k}, \epsilon) \simeq \frac{Z}{\epsilon - v_F k_r + i0^+ \mathrm{sgn}\epsilon}. \tag{1}$$

Together with the vanishing of the inverse lifetime near the Fermi energy [which is assumed in Eq. (1)], this implies that there still exists a Fermi surface, where the quasiparticle occupation number in momentum space at $T = 0$ is discontinuous, $n_{k_F - 0} - n_{k_F + 0} = Z < 1$ (see Fig. 1). In the Fermi gas $Z = 1$.

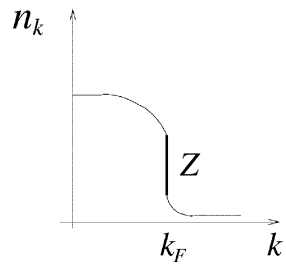


*Figure 1.* Quasiparticle occupation number in momentum space in a Fermi liquid, at $T = 0$. The discontinuity, indicated by the thicker solid line, marks the Fermi surface at $k = k_F$.

The Fermi-liquid theory breaks down in various systems, even in the absence of symmetry breaking. This is, for instance, the case of Kondo systems [25], or of electronic systems near the metal-insulator transition, in the presence of strong disorder [26].
In the Sec. 3, we discuss the breakdown of the Fermi liquid in clean electronic systems in $d = 1$, whereas the issue of the existence of a non-Fermi-liquid state in $d > 1$ is discussed in Sec. 4.

## 3. One-dimensional Luttinger liquids

The first signal of the breakdown of the Fermi-liquid theory in one-dimensional interacting systems is given by the appearance of logarithmic singularities in the second-order perturbative contribution to the single-particle self-energy and to the four-point vertex function, as a result of the relevant contribution of massless excitations near the Fermi energy in low dimensions. The first treatment of these divergences has been achieved within perturbative renormalization group [2], assuming a scaling form for the vertex functions, as the Fermi surface is approached by rescaling the fields and the coupling constants. Depending on the values of the bare coupling constants, the renormalized coupling constants flow either to strong coupling, out of the perturbative regime, or to the Luttinger model [27, 28], which is exactly solvable.
In the latter case the system is a Luttinger liquid [2, 27, 29, 30, 31, 32], i.e., a metallic phase with no symmetry breaking, in which the finite renormalizations of correlation functions ($C_V/T$, $\chi$, $\kappa$), and of the weight of the Drude peak in the optical conductivity, are characterized by changes in the values of the parameters, but not in the form, with respect to a Fermi liquid, whereas the wave-function renormalization $Z$ vanishes as the Fermi energy is approached, leading to a suppression of the discontinuity of the occupation number in momentum space, which is turned into an algebraic singularity

with a non-universal exponent, $n_{\mathbf{k}} - n_{k_F} \sim -\mathrm{sgn}(k_r)|k_r|^\eta$. Moreover, the single-particle density of states vanishes as $\epsilon^\eta$ at low energy. Thus, in a Luttinger liquid, the low-lying quasiparticle excitations are suppressed, and the low-energy behavior of the system is dominated by collective charge and spin excitations. As these have, in general, different velocities, the Luttinger liquid is characterized by the so-called charge and spin separation.
It is then evident that the collective properties of a Luttinger liquid in the hydrodynamic regime $|\mathbf{q}|, \omega \to 0$ are trivial as those obtained within the random-phase approximation or by means of the Landau-Boltzmann kinetic equation, whereas the single-particle properties are anomalous.
We give in Secs. 3.1, 3.2, 3.3 a detailed account of the properties of the Luttinger liquid in $d = 1$.

## 3.1. THE $g$-OLOGY MODEL

The peculiarity of one-dimensional system is that the "Fermi surface" consists of two disjoint points at $\pm k_F$. This, in turn, leads to the existence of few types of relevant scattering processes, which are incorporated into an effective low-energy model, known as the "$g$-ology" model [2]. This is a continuum model with a linear dispersion relation and simplified two-particle interactions, which describes the generic low-energy dynamics of a one-dimensional Fermi system. It can be written as $\mathcal{H} = \mathcal{H}_0 + \mathcal{H}_I$, where the free term

$$\mathcal{H}_0 = \sum_{|\mathbf{k}|<\lambda} \sum_{\sigma} \sum_{\alpha=\pm 1} \alpha v_F \mathbf{k}\, a^\dagger_{\alpha,\sigma}(\mathbf{k}) a_{\alpha,\sigma}(\mathbf{k}),$$

describes a linear band limited by a momentum cutoff $\lambda$, $a^\dagger_{\alpha,\sigma}(\mathbf{k})$ and $a_{\alpha,\sigma}(\mathbf{k})$ create and annihilate fermions with spin $\sigma$ close to $+k_F$ ($\alpha = +1$) and $-k_F$ ($\alpha = -1$). We adopt a boldface notation for the momentum $\mathbf{k}$, measured relative to $\pm k_F$, to distinguish it from the bi-vectors $k = (\mathbf{k}, \epsilon)$. The ultraviolet cutoff of the theory, $\lambda$, acts also as momentum-transfer cutoff in the interaction. The interaction Hamiltonian is $\mathcal{H}_I = \mathcal{H}_1 + \mathcal{H}_2 + \mathcal{H}_3 + \mathcal{H}_4$, where

$$\begin{aligned}
\mathcal{H}_1 &= \frac{1}{V} \sum_{\mathbf{q}} \sum_{\sigma\sigma'} g_1^{\sigma\sigma'} \rho^+_\sigma(\mathbf{q}) \rho^-_{\sigma'}(-\mathbf{q}), \\
\mathcal{H}_2 &= \frac{1}{V} \sum_{\mathbf{q}} \sum_{\sigma\sigma'} g_2^{\sigma\sigma'} \rho_{+1,\sigma}(\mathbf{q}) \rho_{-1,\sigma'}(-\mathbf{q}), \\
\mathcal{H}_3 &= \frac{1}{2V} \sum_{\mathbf{q}} \sum_{\sigma\sigma'} g_3^{\sigma\sigma'} [\rho^+_\sigma(\mathbf{q}) \rho^+_{\sigma'}(-\mathbf{q}) + \rho^-_\sigma(\mathbf{q}) \rho^-_{\sigma'}(-\mathbf{q})], \\
\mathcal{H}_4 &= \frac{1}{2V} \sum_{\mathbf{q}} \sum_{\sigma\sigma'} g_4^{\sigma\sigma'} [\rho_{+1,\sigma}(\mathbf{q}) \rho_{+1,\sigma'}(-\mathbf{q}) + \rho_{-1,\sigma}(\mathbf{q}) \rho_{-1,\sigma'}(-\mathbf{q})].
\end{aligned}$$

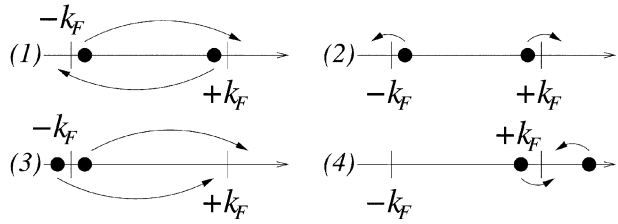


*Figure 2.* Scattering processes described by the interaction terms of the $g$-ology model. The numbers $(1), (2), (3)$ and $(4)$ refer to $\mathcal{H}_1, \mathcal{H}_2, \mathcal{H}_3$ and $\mathcal{H}_4$, respectively. The right and left Fermi points are indicated by $+k_F$ and $-k_F$.

In the above formulas, $V$ is the volume, which for $d = 1$ is understood as the length of the system, and

$$\begin{aligned}
\rho_\sigma^+(\mathbf{q}) &= \sum_{\mathbf{k}} a^\dagger_{+1,\sigma}(\mathbf{k}-\mathbf{q}) a_{-1,\sigma}(\mathbf{k}), \\
\rho_\sigma^-(\mathbf{q}) &= \sum_{\mathbf{k}} a^\dagger_{-1,\sigma}(\mathbf{k}-\mathbf{q}) a_{+1,\sigma}(\mathbf{k}), \\
\rho_{\alpha,\sigma}(\mathbf{q}) &= \sum_{\mathbf{k}} a^\dagger_{\alpha,\sigma}(\mathbf{k}-\mathbf{q}) a_{\alpha,\sigma}(\mathbf{k}) \qquad (\text{with } \alpha = \pm 1).
\end{aligned}$$

By definition, $\rho_{\pm 1,\sigma}$ are the density operators for right- $(+1)$ and left- $(-1)$ moving quasiparticles.
The interaction Hamiltonian $\mathcal{H}_I$ describes various scattering processes, shown in Fig. 2: the small-momentum-transfer processes ($\mathcal{H}_2$ and $\mathcal{H}_4$) are expressed in terms of $\rho_{\alpha,\sigma}$, the back scattering ($\mathcal{H}_1$) and the Umklapp scattering ($\mathcal{H}_3$) in terms of $\rho_\sigma^\pm$. The coupling constants, which are in general spin dependent, are parametrized as $g_i^{\sigma\sigma'} = g_{i\|}\delta_{\sigma\sigma'} + g_{i\perp}\delta_{\sigma,-\sigma'}$, where $g_{i\|}$ and $g_{i\perp}$ refer to processes involving parallel and opposite spins, respectively. Owing to momentum conservation, Umklapp processes described by $\mathcal{H}_3$ are relevant at low energy only if $4k_F$ is equal to a reciprocal-lattice vector $2\pi/a$ (where $a$ is the lattice spacing), as in the Hubbard model at half filling, and can be safely neglected in the case of a generic filling. In the case of Coulomb interactions (e.g., for repulsive Hubbard-like systems) all the $g_i$ are positive.
The physical properties of the $g$-ology model are extracted from the Green's functions defined as ground-state expectation values of the time-ordered operator products

$$\begin{aligned}
&G^{(2n,l)}_{\{\alpha,\sigma\}}(\{\mathbf{k},t\}) = (-i)^{n+l}\langle \mathcal{T} a_{\alpha_1,\sigma_1}(\mathbf{k}_1,t_1)\ldots a_{\alpha_n,\sigma_n}(\mathbf{k}_n,t_n) \\
&\times a^\dagger_{\alpha'_n,\sigma'_n}(\mathbf{k}'_n,t'_n)\ldots a^\dagger_{\alpha'_1,\sigma'_1}(\mathbf{k}'_1,t'_1)\rho_{\alpha''_1,\sigma''_1}(\mathbf{k}''_1,t''_1)\ldots\rho_{\alpha''_l,\sigma''_l}(\mathbf{k}''_l,t''_l)\rangle,
\end{aligned}$$

where $a_{\alpha,\sigma}$,$a^\dagger_{\alpha,\sigma}$, and $\rho_{\alpha,\sigma}$, are the operators in the Heisenberg representation, and $\mathcal{T}$ is the time-ordering operator. The Green's function in the frequency

representation will be denoted by $G^{(2n,l)}(\{k\})$, where $k = (\mathbf{k}, \epsilon)$, whereas $\Gamma^{(2n,l)}$ will denote the corresponding vertex functions, i.e., the one-particle irreducible contributions.
In the free case, the Fourier transform of the single-particle Green's function $G_{\alpha\sigma}(\mathbf{k}, t) \equiv G^{(2,0)}_{\alpha\sigma;\alpha\sigma} = -i\langle \mathcal{T} a_{\alpha,\sigma}(\mathbf{k}, t) a^{\dagger}_{\alpha,\sigma}(\mathbf{k}, 0)\rangle$ with respect to the time variable leads to the expression (1) with $Z = 1$. The functions $G^{(0,2)}_{\alpha\sigma,\alpha'\sigma'}$ describe the various charge- and spin-density correlations, which are dominated by the collective modes for small wave-vectors $|\mathbf{q}| \ll k_F$.
In $d = 1$ the distance of the two Fermi points in momentum space (which equals $2k_F$) plays no role. Thus the inverse momentum cutoff $\lambda^{-1}$ sets the only relevant length scale in the $g$-ology model, and all dimensionless quantities must depend on the momenta $k$ and on the cutoff $\lambda$ only through $k/\lambda$. Hence, the infrared limit $k \to 0$ is directly related to the ultraviolet limit $\lambda \to \infty$.
In general, an exact solution giving the expression of the correlation functions in the $g$-ology model is not possible. Moreover, as we have anticipated above, perturbation theory with respect to the coupling constants $g_i$ diverges at low energies. Indeed, simple dimensional analysis yields the canonical dimensions in inverse length: $[\mathcal{H}] = 1$, $[a(k)] = -1/2$, and therefore $[g_i] = 0$, i.e., the coupling constants are dimensionless. The bare propagator $G_0(k)$ has dimension $-1$. Each energy-momentum integration in a Feynman diagram introduces a power 2. Hence power counting predicts that primitive divergences may occur in $\Gamma^{(2,0)}$, $\Gamma^{(4,0)}$, $\Gamma^{(0,2)}$, and $\Gamma^{(2,1)}$, but not in higher-order vertex functions.
Then, assuming a scaling Ansatz for the vertex functions, the low-energy limit is approached by rescaling fields and coupling constants, e.g.,

$$\Gamma^{(2n,0)}(\ldots, \{g'_i\}, \lambda') = Z^n(\{g_i\}, \lambda'/\lambda)\Gamma^{(2n,0)}(\ldots, \{g_i\}, \lambda),$$

where $g'_i = g'_i(\{g_j\}, \lambda'/\lambda)$ is the running coupling constant, with a flow determined by the behavior of the function $\beta_i(\{g_j\}) = [\partial g'_i/\partial(\lambda'/\lambda)]_{\lambda'=\lambda}$. Depending on the values and on the signs of the bare coupling constant, or on whether $4k_F$ is equal to, or different from, a reciprocal lattice vector, the renormalized coupling constant may flow to strong coupling, or reach a fixed point. In the first case (e.g., $g_3 \neq 0$, $g_1 < 0$), the low-energy Hamiltonian undergoes a dramatic change, with dynamical generation of a gap in the charge and/or spin spectrum, while in the latter case (as for $g_i$ derived from repulsive Hubbard-like models, with $g_3 = 0$) one reaches a fixed-point Hamiltonian given by the Luttinger model [28, 29], where $g_2$ and $g_4$ only are present. Therefore the low-energy behavior of a generic one-dimensional fermion system interacting via repulsive interaction is well described in terms of the Luttinger model Hamiltonian $\mathcal{H} = \mathcal{H}_0 + \mathcal{H}_2 + \mathcal{H}_4$. The Luttinger model

is exactly solvable either by means of Ward identities [24, 32, 33], or by the bosonization procedure [27, 29, 30, 31].
Many features of the Luttinger liquids are already clear within perturbative renormalization-group calculations [2], as, for instance, the scaling behavior of the single-particle propagator $G(sk) = s^{\eta-1}G(k)$, with a non-universal anomalous dimension $\eta > 0$. As usual, the renormalization-group approach leads to a power-law resummation of the logarithmic singularities which affect the self-energy correction at second order in perturbation theory. At this order $\eta = (g_{2\|}^2 + g_{2\perp}^2)/(8\pi^2 v_F^2) + \mathcal{O}(g^3)$. We point out that $\eta$ depends on the value of the coupling constants of the model, since the $\beta$ function vanishes identically, owing to the peculiar left and right conservation (see below) [24, 34].
The exponent $\eta$ also characterizes the momentum distribution function $n_{\mathbf{k}} = -(1/2\pi^2)\sum_\sigma \int d\epsilon\, \mathrm{Im}G_{\alpha\sigma}(k) \propto |\mathbf{k}|^\eta$, and the single-particle spectral function $D(\epsilon) = -(1/2\pi^2)\sum_\sigma \int d\mathbf{k}\, \mathrm{Im}G_{\alpha\sigma}(k) \propto \epsilon^\eta$.
We explore in Sec. 3.2 the exact solution of the Luttinger model by exploiting the conservation laws and the related Ward identities, as reviewed in Refs. [3, 24].

### 3.2. Analysis of the Luttinger model via Ward identities

As usual, also in the $g$-ology model the *global* charge and spin conservation laws lead to Ward identities which yield relations between different functions of the skeleton structure, and some information on the asymptotic behavior of the correlation functions for small momentum and energy transfer.
Let us define the left ($\alpha = -1$) and the right ($\alpha = +1$) charge or spin density operators $\rho_\alpha^{c,s} = \rho_{\alpha,\uparrow} \pm \rho_{\alpha,\downarrow}$, which satisfy the commutation relations [24]

$$[\rho_\alpha^a(\mathbf{q}), \rho_{\alpha'}^a(\mathbf{q}')] = \frac{V}{2\pi}\delta_{\alpha\alpha'}\delta_{\mathbf{q},-\mathbf{q}'}\,\alpha\mathbf{q}, \tag{2}$$

where $a = c, s$ (observe that $|\mathbf{q}|V/2\pi$ gives the number of points in the segment $|\mathbf{q}|$). This non commutativity of the theory is a consequence of the restriction of the sums in momentum space up to a cutoff $\lambda$, within the $g$-ology model.
The Ward identities come from the continuity equation which is obtained by calculating the commutator of the $g$-ology Hamiltonian with the total charge (or spin) density operator at small $\mathbf{q}$, $\rho^a = \sum_\alpha \rho_\alpha^a$, with $a = c, s$, i.e.,

$$i\partial_t \rho^a(\mathbf{q}, t) = [\rho^a(\mathbf{q}, t), \mathcal{H}] = v^a \mathbf{q} j^a(\mathbf{q}, t), \tag{3}$$

where $j^a = \sum_\alpha \alpha\rho_\alpha^a$, is the current operator,

$$v^a = v_F + \frac{1}{\pi}(g_4^a - g_2^a), \tag{4}$$

is a coupling-dependent velocity, and $g_i^{c,s} = \frac{1}{2}(g_{i\|} \pm g_{i\perp})$. The physical current operator, $J^a = v^a j^a$ depends only on the forward scattering because $\rho^a$ commutes with $\mathcal{H}_1$ and $\mathcal{H}_3$. Eq. (3) is the continuity equation related to the conservation of the total charge or spin. From Eq. (3) one can derive the Ward identities for the vertex functions and the correlation functions, thus reducing the number of independent relevant structures to be considered within the renormalization-group treatment. We start by deriving the Ward identity for the correlation functions, $J^a_{\mu\nu}(\mathbf{q},t) = -iV^{-1}\langle \mathcal{T} j^a_\mu(\mathbf{q},t) j^a_\nu(-\mathbf{q},0)\rangle$, with $\mu,\nu = 0,1$, $j^a_0 = \rho^a$, and $j^a_1 = j^a$, so that $J^a_{00}$ is the density-density correlation function and $J^a_{11}$ is the current-current correlation function. Applying $i\partial_t$ to $J^a_{0\nu}$ and using the continuity equation, we find

$$i\partial_t J^a_{0\nu}(\mathbf{q},t-t') = -\frac{i}{V}\langle \mathcal{T} v^a \mathbf{q} j^a_1(\mathbf{q},t) j^a_\nu(-\mathbf{q},t')\rangle + \frac{1}{V}\delta(t-t')\langle [j^a_0, j^a_\nu]\rangle.$$

After Fourier-transforming, we obtain the following Ward identity

$$\omega J^a_{0\nu}(q) - v^a \mathbf{q} J^a_{1\nu}(q) = \frac{2}{\pi}\mathbf{q}\delta_{\nu,1}, \tag{5}$$

where $q = (\mathbf{q},\omega)$ and the commutators (2) have been used. This identity constrains the limiting behavior of charge and spin correlation functions for $q \to 0$. As in Fermi liquids, this limit depends on the ratio $r = |\mathbf{q}|/\omega$. The dynamic limit is defined as $J^a_{\mu\nu,0} = J^a_{\mu\nu}(q \to 0, r \to 0)$, whereas the static limit is $J^a_{\mu\nu,\infty} = J^a_{\mu\nu}(q \to 0, r \to \infty)$. Then, from Eq. (5), one finds $J^a_{00,0} = J^a_{01,0} = J^a_{10,\infty} = 0,\ J^a_{11,\infty} = -2/\pi v^a$.
The dynamic limit of the charge (or spin) density-density correlation function must always vanish, to ensure the conservation of the total particle number (or spin).
The Ward identity (5) does not constrain, instead, $J^a_{00,\infty}$ and $J^a_{11,0}$, which are related to the compressibility ($\kappa = -J^c_{00,\infty}$) and to the conductivity (via the Einstein relation). Therefore, as usual, the total charge (and spin) conservation cannot fully determine the physical behavior of the system.
The Ward identity for the charge and spin vertices can be derived from the equation of motion of the Green's function

$$F^a_{\alpha,\sigma;\mu}(\mathbf{k},t';\mathbf{q},t) = -\langle \mathcal{T} j^a_\mu(\mathbf{q},t) a_{\alpha,\sigma}(\mathbf{k}-\mathbf{q}/2,t') a^\dagger_{\alpha,\sigma}(\mathbf{k}+\mathbf{q}/2,t')\rangle.$$

Differentiating $F^a_{\alpha,\sigma;0}$ with respect to $t$ and using the continuity equation (3), we find $i\partial_t F^a_{\alpha,\sigma;0} = -\langle \mathcal{T} v^a \mathbf{q} j^a a a^\dagger\rangle - \delta(t-t')\langle [\rho^a, a a^\dagger]\rangle$, where, for simplicity, we omitted the arguments of the various operators. After transforming the previous relation to the frequency representation, we have

$$\omega F^a_{\alpha,\sigma;0}(k,q) - v^a \mathbf{q} F^a_{\alpha,\sigma;1}(k,q) = \epsilon^a_\sigma [G_{\alpha,\sigma}(k-q/2) - G_{\alpha,\sigma}(k+q/2)],$$

where $\epsilon^a_\sigma = -1$ for $a = s$ and $\sigma = \downarrow$, and $\epsilon^a_\sigma = +1$ otherwise. Introducing the vertex function $\Gamma^a_{\alpha,\sigma;\mu} = F^a_{\alpha,\sigma;\mu}/[G_{\alpha,\sigma}(k-q/2)G_{\alpha,\sigma}(k+q/2)]$, obtained

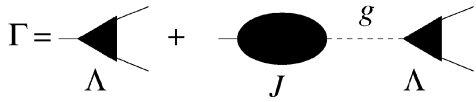


*Figure 3.* The diagrammatic representation of the Dyson equation (6) for $\Gamma$. The various indices and arguments are omitted for simplicity.

by truncating the external fermion lines in a diagrammatic representation, we have the following Ward identity

$$\omega\Gamma^a_{\alpha,\sigma;0}(k,q) - v^a\mathbf{q}\Gamma^a_{\alpha,\sigma;1}(k,q) = \epsilon^a_\sigma[G^{-1}_{\alpha,\sigma}(k+q/2) - G^{-1}_{\alpha,\sigma}(k-q/2)].$$

The vertex functions $\Gamma^a_{\alpha,\sigma;\mu}$ are reducible with respect to cutting single interaction lines in a diagrammatic representation. The skeleton structure of the $g$-ology model is obtained in terms of the charge and spin vertices $\Lambda^a_{\alpha,\sigma;\mu}$, which are *irreducible* with respect to cutting an interaction line, and are related to $\Gamma^a_{\alpha,\sigma;\mu}$ by the Dyson equation

$$\Gamma^a_{\alpha,\sigma;\mu}(k,q) = \Lambda^a_{\alpha,\sigma;\mu}(k,q) + \sum_\nu J^a_{\mu\nu}(q)g^a_{\nu\nu}\Lambda^a_{\alpha,\sigma;\nu}(k,q), \tag{6}$$

which is illustrated diagrammatically in Fig. 3. The coupling constants are given by $g^a_{00} = \frac{1}{2}(g^a_4 + g^a_2)$ and $g^a_{11} = \frac{1}{2}(g^a_4 - g^a_2)/2$. Using the Ward identity for $J^a_{\mu\nu}$ and $\Gamma^a_{\alpha,\sigma;\mu}$ we find

$$\begin{aligned}
&\omega\Gamma^a_{\alpha,\sigma;0}(k,q) - v^a\mathbf{q}\Gamma^a_{\alpha,\sigma;1}(k,q)\\
&= \omega\Lambda^a_{\alpha,\sigma;0}(k,q) - v^a\mathbf{q}\Lambda^a_{\alpha,\sigma;1}(k,q) + \frac{2}{\pi}\mathbf{q}g^a_{11}\Lambda^a_{\alpha,\sigma;1}(k,q)\\
&= \omega\Lambda^a_{\alpha,\sigma;0}(k,q) - v_F\mathbf{q}\Lambda^a_{\alpha,\sigma;1}(k,q)\\
&= \epsilon^a_\sigma[G^{-1}_{\alpha,\sigma}(k+q/2) - G^{-1}_{\alpha,\sigma}(k-q/2)],
\end{aligned} \tag{7}$$

where we used the expression (4) for $v^a$. Note that the final expression in Eq. (7) is independent of the coupling constant, i.e., it involves $v_F$ instead of $v^a$. Total charge and spin conservation also hold in Fermi liquids, and so do the Ward identities following from these properties. As we pointed out, the Ward identity (7), which relates the density and the current vertex functions to the single-particle Green's function, is generic of all systems conserving the total number of particles (or the total spin). By itself, it is not enough to solve any model.

In addition to the usual total charge and spin conservation, the discrete structure of the Fermi surface in $d = 1$ allows for more stringent conservation laws when large momentum scattering processes are absent ($g_1 = g_3 = 0$), i.e., in the Luttinger model: *charge (or spin) near the left and right Fermi points is conserved separately*. This separate conservation guarantees, even in the

presence of singularities in perturbation theory, the finiteness of charge- (or spin-) density response in normal one-dimensional metals, and the velocities associated to the corresponding currents provide a complete parametrization of the low-energy physics of the model.
Let us consider the charge (or spin) difference operators $\tilde{\rho}^a = \sum_\alpha \alpha \rho^a_\alpha$ within the Luttinger model, hereafter referred to as axial densities, which are now conserved, and obey the continuity equation

$$i\partial_t \tilde{\rho}^a(\mathbf{q}, t) = [\tilde{\rho}^a, \mathcal{H}] = \tilde{v}^a \mathbf{q} \tilde{j}^a(\mathbf{q}, t),$$

where $\tilde{j}^a = \sum_\alpha \rho^a_\alpha$ is the axial current operator, and $\tilde{v}^a = v_F + (g^a_4 + g^a_2)/\pi$. Note that $\tilde{\rho}^a = j^a$, and $\tilde{j}^a = \rho^a$.
In complete analogy with the case of total charge (or spin) conservation, we can define the axial correlation functions $\tilde{J}^a_{\mu\nu}$ and the vertices $\tilde{\Lambda}^a_{\alpha,\sigma;\mu}$. The continuity equation for the axial bi-current $\tilde{j}^a_\mu = (\tilde{\rho}^a, \tilde{j}^a)$ implies the Ward identities analogue to Eqs. (5) and (7), with $v^a$ substituted by $\tilde{v}^a$ and $\epsilon^a_\sigma$ by $\tilde{\epsilon}^a_{\alpha,\sigma} = \alpha \epsilon^a_\sigma$.
Combining the Ward identities from global and axial conservation laws one completely determines the correlation functions $J^a_{\mu\nu}$ and $\tilde{J}^a_{\mu\nu}$ in terms of $v^a$ and $\tilde{v}^a$. This yields an expression of the vertices as functions of the fermion propagator $G$. As a consequence of separate charge (and spin) left and right conservation, the density vertex $\Lambda^a_{\alpha,\sigma;0}$ and the current vertex $\Lambda^a_{\alpha,\sigma;1}$ are simply related $\Lambda^a_{\alpha,\sigma;1} = \alpha \Lambda^a_{\alpha,\sigma;0}$. Therefore the Ward identity, Eq. (7), reads

$$(\omega - \alpha v_F \mathbf{q}) \Lambda^a_{\alpha,\sigma;0} = \epsilon^a_\sigma \left[ G^{-1}_{\alpha,\sigma}(k + q/2) - G^{-1}_{\alpha,\sigma}(k - q/2) \right], \qquad (8)$$

and involves the density vertex only, which can now be eliminated in favor of the single-particle Green's function.

### 3.3. The Luttinger liquid as the solution of the Luttinger model

We start by discussing the left and right density-density correlation function

$$C_{\alpha\beta}(\mathbf{q}, t) \equiv J^c_{\alpha\beta;00} = -\frac{1}{V} \langle \mathcal{T} \rho^c_\alpha(\mathbf{q}, t) \rho^c_\beta(-\mathbf{q}, 0) \rangle.$$

We can proceed either by using the Ward identities for $C$ which follow from right and left conservation laws, or the Ward identity (8) for $\Lambda$, by considering its effect on the polarization bubble. We follow here this second procedure. $C$ can be expressed in terms of the polarization function $\Pi^c_{\alpha\alpha}(q)$ by the resummation of the geometric series analytically given by the Dyson equation $C_{\alpha\beta} = \Pi^c_{\alpha\beta}\delta_{\alpha\beta} + \Pi^c_{\alpha\alpha} \sum_\gamma g^c_{\alpha\gamma} C_{\gamma\beta}$, where $g^c_{\alpha\alpha} = g^c_4$ and $g^c_{\alpha,-\alpha} = g^c_2$, and we have used the condition $\Pi^c_{\alpha,-\alpha} = 0$. The charge polarization bubble can

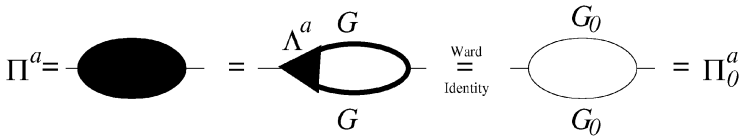


*Figure 4.* The Dyson equation for the polarization bubble $\Pi^a$; $\Lambda^a$ represents the bare density vertex ($a = c$ in the case under discussion). The thick lines represent the full Green's functions, whereas the thin lines represent the bare Green's functions.

be expressed in terms of the irreducible charge-density vertex $\Lambda^c$ and of the exact propagator $G$, as shown in Fig. 4,

$$\Pi^c_{\alpha\alpha}(q) = -i \sum_\sigma \int \frac{d^2k}{(2\pi)^2} \Lambda^c_{\alpha,\sigma;0}(2k+q,q) G_{\alpha,\sigma}(k) G_{\alpha,\sigma}(k+q).$$

$\Pi^c$ contains in principle singular contributions due to vertex and self-energy corrections. However, the Ward identity (8) for $\Lambda^c$ implies that

$$\Pi^c_{\alpha\alpha}(q) = \frac{-i}{\omega - \alpha v_F \mathbf{q}} \sum_\sigma \int \frac{d^2k}{(2\pi)^2} \left[ G_{\alpha,\sigma}(k) - G_{\alpha,\sigma}(k+q) \right].$$

Integrating over frequencies, and keeping in mind that all allowed momenta are restricted by a cutoff, $|\mathbf{k}|, |\mathbf{k}+\mathbf{q}| < \lambda$, one obtains, for $\mathbf{q} > 0$,

$$\Pi^c_{\alpha\alpha}(q) = \frac{1}{\omega - \alpha v_F \mathbf{q}} \sum_\sigma \int_{-\lambda}^{\lambda - q} \frac{d\mathbf{k}}{2\pi} \left[ n_{\alpha,\sigma}(\mathbf{k}) - n_{\alpha,\sigma}(\mathbf{k}+\mathbf{q}) \right],$$

where $n_{\alpha,\sigma}$ is the momentum distribution function of the interacting system. Shifting the integration variable in the second term by $-\mathbf{q}$, one obtains the same expression as for the noninteracting system

$$\Pi^c_{\alpha\alpha}(q) = \frac{1}{\pi v_F} \frac{\alpha v_F \mathbf{q}}{\omega - \alpha v_F \mathbf{q}}. \tag{9}$$

All vertex and self-energy corrections have cancelled each other, due to the peculiar conservation laws, and the density-density response is given by the simple random-phase approximation, with the appropriate coupling constants, and with the bare bubble

$$C(q) = \sum_{\alpha\beta} C_{\alpha\beta}(q) = \frac{2v^c}{\pi} \frac{|\mathbf{q}|^2}{\omega^2 - (u^c|\mathbf{q}|)^2},$$

where $u^c = (v^c \tilde{v}^c)^{1/2}$. Observe that $C(q)$ correctly vanishes as $|\mathbf{q}| \to 0$, at finite $\omega$. The density-density response function has poles at $\omega = \pm u^c \mathbf{q}$. A similar result holds also for the spin-spin correlation function, with $u^s =$

$(v^s\tilde{v}^s)^{1/2}$. The collective modes of the Luttinger liquid are therefore an undamped charge-density mode (zero sound) and an undamped spin-density mode, with velocity $u^c$ and $u^s$, respectively. The compressibility $\kappa = -C(|\mathbf{q}| \to 0, \omega = 0)$ is now fully determined $\kappa = 2/(\pi\tilde{v}^c)$. In the same way, the spin susceptibility is derived from the spin-spin correlation function, and reads $\chi = 2/(\pi\tilde{v}^s)$.

By using the generalized Einstein relation one can derive the electrical conductivity $\sigma(\omega)$ for the Luttinger liquid. The Drude weight is determined by $v^c$, $\mathrm{Re}\sigma(\omega) = 2v^c\delta(\omega)$.

Let us finally note that the continuity equations for $\rho^a$ and $\tilde{\rho}^a$ can be combined into a harmonic-oscillator equation for $\rho^a(\mathbf{q}, t)$, i.e.,

$$\partial_t^2\rho^a(\mathbf{q}, t) + v^a\tilde{v}^a|\mathbf{q}|^2\rho^a(\mathbf{q}, t) = 0,$$

describing undamped harmonic oscillations with frequency $u^a|\mathbf{q}|$. The low-temperature specific heat of the Luttinger liquid is therefore given by $C_V = (\pi T/6)\sum_a(u^a)^{-1}$, and is linear in temperature, as in the Fermi liquid, but with different coefficients, coming from the collective modes rather than from the fermion quasiparticles.

The most dramatic change of the Luttinger-liquid solution with respect to the Fermi liquid is in the single-particle Green's function. It can be calculated in the bosonization approach [27, 30]. We use here the Ward identity (8), derived in Sec. 3.2 via the separate charge and spin conservation at each Fermi point. The Ward identities obtained from the continuity equations associated to these conservation laws give a complete system of equations for any correlation function, and in particular we discussed the explicit calculation of the density-density correlation function. The same results are implied by another important property of the Luttinger model, the loop cancellation (see, e.g., Ref. [3]). For small momentum transfer Feynman diagrams involving fermion loops with more than two insertions cancel each other. This cancellation has been first exploited for the Luttinger model in Ref. [32]. As a consequence of loop cancellation, the effective interaction (dressed by the polarization bubbles) and response functions for small $\mathbf{q}$ are given by the random-phase approximation. Indeed, in general, the bubbles shown in Fig. 5 must be dressed by the self-energy and vertex corrections, however, as we have shown for the density-density correlation function, only the bare bubble remains, as the corrections involve fermion loops with more than two insertions, and must therefore cancel each other for small $\mathbf{q}$ and cutoff $\lambda$, at least at leading order in these small parameters.

The effective interaction $D$ for small $q$ is obtained by resummation of the diagrams illustrated in Fig. 5, $D^{\sigma\sigma'}_{\alpha\alpha'} = g^{\sigma\sigma'}_{\alpha\alpha'} + \sum_{\alpha'',\sigma''} g^{\sigma\sigma''}_{\alpha\alpha''}\Pi^c_{\alpha''\alpha''}D^{\sigma''\sigma'}_{\alpha''\alpha'}$, with $g^{\sigma\sigma'}_{\alpha\alpha} = g^{\sigma\sigma'}_4$, $g^{\sigma\sigma'}_{\alpha,-\alpha} = g^{\sigma\sigma'}_2$, and $\Pi^c_{\alpha\alpha}$ given by Eq. (9).

The effective interaction (for $\alpha = \alpha'$) $D(q)$ contains all the effect of the charge and spin collective modes via their velocities $u^a$, and can be cast in

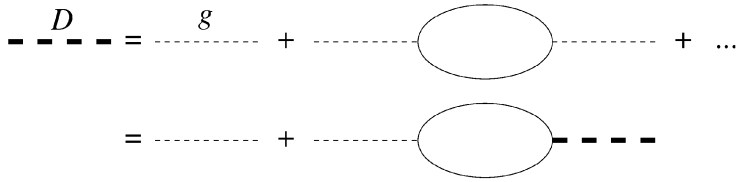


*Figure 5.* Dyson equation for the effective interaction $D$. Due to the cancellation of self-energy and vertex corrections, it reduces to the random-phase approximation with the bare fermion bubble, represented by the thin solid line. The thick and thin dashed lines represent the dressed $(D)$ and bare $(g)$ interaction respectively.

the form

$$D(q) = (\omega - \alpha v_F \mathbf{q})\pi \sum_{a=c,s} \left[ \frac{(2-\eta^a)(u^a - v_F)}{\omega - u^a \mathbf{q}} + \frac{\eta^a (u^a + v_F)}{\omega + u^a \mathbf{q}} \right], \quad (10)$$

where $\eta^a = (K^a - 2 + 1/K^a)/4$, and $K^a = (v^a/\tilde{v}^a)^{1/2}$.
Once $D$ is known, since the density vertex can be eliminated via the Ward identity (8), the Dyson equation for the single-particle propagator (Fig. 6) becomes a closed equation for $G$ [32]

$$(\epsilon - \alpha v_F \mathbf{p}) G(p) = 1 + i \int \frac{dq}{4\pi^2} \frac{D(q) G(p-q)}{\omega - \alpha v_F \mathbf{q}}.$$

The solution of the above integral equation can be obtained by transforming it to real space and time and with the Ansatz $G(\mathbf{r},t) = \exp[L(\mathbf{r},t) - L(0,0)]\, G_0(\mathbf{r},t)$, where $L(\mathbf{r},t)$ is the Fourier transform of $iD(q)[\omega - \alpha v_F \mathbf{q} + i0^+ \mathrm{sgn}(\omega)]^{-2}$, and $G_0(\mathbf{r},t) = (1/2\pi)[|\mathbf{r}| - v_F t + i0^+ \mathrm{sgn}(t)]^{-1}$. Using the expression (10) for $D$, we find that $L(\mathbf{r},t)$ behaves logarithmically in $|\mathbf{r}|$ and $t$, and since it appears at the exponent in the expression for $G$, it gives rise to a power-law behavior with anomalous exponents depending on $g_2$ and $g_4$ via $v^a$ and $\tilde{v}^a$. For large $|\mathbf{r}|$ and/or large $t$, one thus finds [2]

$$\begin{aligned} G(\mathbf{r},t) &= \frac{1}{2\pi\lambda^\eta} \prod_{a=c,s} \frac{1}{[|\mathbf{r}| - u^a t + i\mathrm{sgn}(t)/\lambda]^{1/2+\eta^a/2}} \\ &\times \frac{1}{[|\mathbf{r}| + u^a t - i\mathrm{sgn}(t)/\lambda]^{\eta^a/2}}, \end{aligned}$$

where $\lambda$ is the momentum-transfer cutoff, and $\eta = \eta^c + \eta^s$. The single-particle propagation is therefore realized in a very complex way, and results from the superposition of the collective charge and spin modes, which propagate with different velocities.
To summarize, in $d = 1$, all the scattering processes with small momentum transfer are marginal and the corresponding Luttinger model has been solved

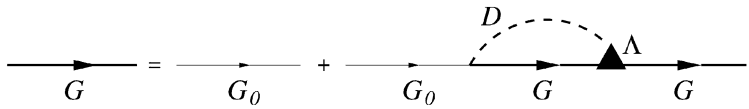


*Figure 6.* Dyson equation relating the dressed and bare fermion propagators $G$, and $G_0$, the effective interaction $D$, and the irreducible vertex $\Lambda$.

exactly via the Ward identities which, in addition to the total charge and spin conservation, specify the separate left and right conservation at each Fermi point. Due to these additional Ward identities, no sign of the infrared divergences is left in the response functions, giving rise to finite compressibility, spin susceptibility, Drude peak in the conductivity, and a specific heat which is linear in temperature.

The main anomalies appear in the single-particle propagator, with a power-law behavior and a vanishing wave-function renormalization $Z$ when approaching the Fermi points. The single-particle propagation is realized in a complex way, with velocities related to charge and spin collective modes and with vanishing low-energy spectral weight. The wave-function renormalization is the only true renormalization left, after the Ward identities have been applied.

We have not dealt with the properties of the charge and spin collective modes, and of the singlet and triplet superconducting fluctuations, for momenta close to $2k_F$. For the sake of completeness we recall [2] that the corresponding correlation functions are characterized by a power-law long-distance (and long-time-interval) decay. The exponents of the power-law behavior can be expressed through the parameters $K^c$ and $K^s$ defined above. These power-law behaviors translate into a power-law dependence on $T$ at finite temperature. Therefore, the Luttinger liquids are "critical" systems, although a symmetry breaking is forbidden by the one-dimensional character of the fluctuations. Predominantly repulsive ($g_2 > 0$) or attractive ($g_2 < 0$) Luttinger liquids have thus a tendency towards a spin- (charge-) density-wave, or triplet- (singlet-) superconducting instability, respectively.

## 4. Non-Fermi-liquid behavior in higher dimensions

As we emphasized in Sec. 1, the attempt to describe the anomalous properties of the metallic phase of high-temperature cuprate superconductors has motivated the search for metallic non-Fermi-liquid phases in $d > 1$, and in particular in $d = 2$ [11, 13]. In this section we address the issue of non-Fermi-liquid metals in $d > 1$, emphasizing in particular the role of Ward identities. The problem of finding metallic non-Fermi-liquid fixed points can be addressed in various ways, as, e.g., by considering a system of chains

coupled by an inter-chain-hopping $t_\perp$ much smaller than the intra-chain hopping [35, 36, 37], or by formally taking an isotropic system in dimension $1 \leq d < 2$, $d$ being an arbitrary real number, and trying to extend the one-dimensional solution to $d > 1$ [3, 18], or by considering singular interactions and long-range forces [19, 20, 21]. We shall discuss the last two points.

### 4.1. Tomographic Luttinger model

We want to determine at which dimension the Luttinger liquid crosses over to a Fermi liquid. To this purpose, we can generalize to $d > 1$ the method proposed by Dzyaloshinskii and Larkin [32], by showing how the additional Ward identities can still be used asymptotically near the Fermi surface, provided $1 \leq d < 2$. An alternative approach consists in extending the exact procedure from $d = 1$ to $d > 1$ via bosonization in $d = 2$ [38, 39].
In going from $d = 1$ to $d = 2$ many more coupling constants than in the $g$-ology model appear, although the low-energy properties of the metallic phase are still determined by the excitations close to the Fermi surface. For small momentum-transfer cutoff $\lambda$, the constraints imposed by momentum conservation in the narrow shell around the Fermi surface introduce strong simplifications and lead to a generalization of the $g$-ology model to $d > 1$. Consider the model given by $\mathcal{H} = \mathcal{H}_0 + \mathcal{H}_I$, where

$$\mathcal{H}_0 = \sum_{\mathbf{k}} \sum_{\sigma} v_F k_r a_\sigma^\dagger(\mathbf{k}) a_\sigma(\mathbf{k})$$

and

$$\mathcal{H}_I = \frac{1}{V} \sum_{\mathbf{k}\mathbf{k}'\mathbf{q}} \sum_{\sigma\sigma'} g_{\mathbf{k}\mathbf{k}'}^{\sigma\sigma'}(\mathbf{q}) a_\sigma^\dagger(\mathbf{k}+\mathbf{q}) a_\sigma(\mathbf{k}) a_{\sigma'}^\dagger(\mathbf{k}'-\mathbf{q}) a_{\sigma'}(\mathbf{k}'),$$

with transferred momentum $|\mathbf{q}| < \lambda \ll k_F$. Here $k_r = |\mathbf{k}| - k_F$ is the distance of $\mathbf{k}$ from the Fermi surface. The model represents an effective Hamiltonian for the excitations near the Fermi surface and we assume that $g_{\mathbf{k}\mathbf{k}'}^{\sigma\sigma'}$ is a slowly varying function of $\mathbf{k}$ and $\mathbf{k}'$ on the scale set up by $\lambda$. As $\mathbf{k}$ and $\mathbf{k}'$ are both near the Fermi surface, the scattering processes are severely restricted. We consider, for example, a spherical Fermi surface in $d = 2$. For incoming and outgoing particles strictly on the Fermi surface, there are three distinct scattering processes, which can be parametrized by a single angle: *forward (F)* scattering, $\mathbf{k_1} = \mathbf{k_1'}$ and $\mathbf{k_2'} = \mathbf{k_2}$; *exchange (E)* scattering, $\mathbf{k_1'} = \mathbf{k_2}$ and $\mathbf{k_2'} = \mathbf{k_1}$; *Cooper (C)* scattering, $\mathbf{k_1} + \mathbf{k_2} = \mathbf{0}$.
These processes are depicted in Figure 7. Forward and exchange scattering can be parametrized in terms of the angle between the momenta of the incoming particles $\theta = \angle(\mathbf{k_1}, \mathbf{k_2})$, while Copper scattering is parametrized by the angle defined by the momentum transfer $\phi = \angle(\mathbf{k_1}, \mathbf{k_1'})$. The asymptotic behavior is therefore described by three functions $g_F(\theta), g_E(\theta)$ and $g_C(\phi)$ as

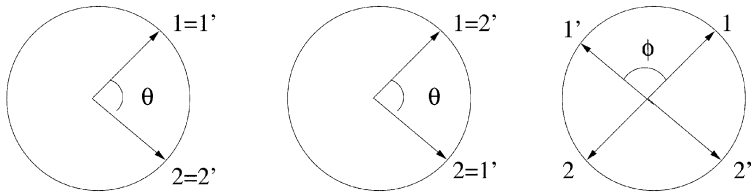


*Figure 7.* Scattering processes on the Fermi surface in $d = 2$: forward, exchange, and Cooper scattering, from left to right. The numbers $1, 1', 2, 2'$ label the momenta, according to the convention adopted in the text.

a generalization of the $g$-ology model in $d = 1$, where only two angles (0 and $\pi$) exist, with the following correspondence $g_F(0) = g_4,\ g_F(\pi) = g_2$, $g_E(0) = g_4,\ g_F(\pi) = g_1$, and $g_C(0) = g_2,\ g_C(\pi) = g_1$.
Since we want to discuss a normal metallic state, we do not consider the Cooper channel here. In a Fermi liquid, $g_F$ plays a special role, giving rise to Landau's quasiparticle interactions [6]. For parallel spins, exchange and forward scattering are asymptotically indistinguishable, while for opposite spins exchange scattering generalizes the spin backscattering process in $d = 1$, which renormalizes to zero for repulsive interactions. To our purpose, we would like to ignore both $g_C$ and $g_E$. In $d = 2$, for a system with dominant forward scattering the angle between particles involved in low-lying scattering processes is asymptotically conserved. This is the generalization of left and right charge and spin conservation, which determines the behavior of the Luttinger liquid in $d = 1$, to each point of the Fermi surface. Such a generalization allows to describe the low-energy properties of the system in terms of a tomographic Luttinger model, i.e., a collection of one-dimensional Luttinger models, each labelled by the angle $\theta$.

### 4.2. Dimensional crossover

The theory is extended to non-integer dimension $1 \leq d < 2$ by analytic continuation of the Feynman diagrams, defined for arbitrary $d$, to the complex $d$ plane, via the typical integral in momentum space

$$\int d^d\mathbf{k} f(|\mathbf{k}|, \mathbf{q}\cdot\mathbf{k}) = S_{d-1}\int d|\mathbf{k}|\,|\mathbf{k}|^{d-1}\int_0^\pi d\theta\,(\sin\theta)^{d-2} f(|\mathbf{k}|, |\mathbf{q}||\mathbf{k}|\cos\theta), \quad (11)$$

where $S_d = 2\pi^{d/2}/\Gamma(d/2)$ is the solid angle in $d$ dimensions. In the limit $d \to 1$, $S_{d-1} \to d-1$ and $S_{d-1}(\sin\theta)^{d-2} \to \delta(\theta) + \delta(\theta - \pi)$. The steps leading to the additional Ward identities of Sec. 3.2 in $d = 1$, and in particular to Eqs. (7),(8) are no longer strictly valid when $d > 1$. However, the geometric restrictions when $\mathbf{q}$ is small and the condition $d < 2$ make

both equations valid asymptotically for small exchanged momentum, since the typical integrals in Eq. (11) are still peaked at $\theta = 0, \pi$. In particular, since almost all relevant $\mathbf{k}$ vectors are still parallel or antiparallel, asymptotically close to the Fermi surface we can still write

$$\mathbf{\Lambda} \simeq v_F \widehat{\mathbf{k}} \Lambda^0, \tag{12}$$

where $\mathbf{\Lambda}$ and $\Lambda^0$ are the current and density vertex, respectively, and $\widehat{\mathbf{k}} = \mathbf{k}/k_F$. The same Ward identity for the density vertex, which controls the infinite resummation of possibly relevant terms, leading to the Luttinger liquid in $d = 1$, is therefore still asymptotically valid in $1 < d < 2$, and

$$\Lambda^0 = \frac{G^{-1}(p + q/2) - G^{-1}(p - q/2)}{\omega - v_F \widehat{\mathbf{k}} \cdot \mathbf{q}}. \tag{13}$$

Eq. (13) is valid apart from a correction in the denominator, which vanishes as $d \to 1$, and is small for $|\mathbf{q}| < \lambda \ll k_F$.
The insertion of the Eq. (13) into the Dyson equation, leads to an expression for the single-particle Green's function similar to that found for $d = 1$,

$$G_{\widehat{\mathbf{k}}}(\mathbf{r}, t) = \mathrm{e}^{L(\mathbf{r},t) - L(0,0)} G_0(\mathbf{r}, t), \tag{14}$$

where $L(\mathbf{r}, t)$ is the Fourier transform of $i\bar{D}(q)[\omega - v_F q_r + i0^+ \mathrm{sgn}(\omega)]^{-2}$, and $q_r = \widehat{\mathbf{k}} \cdot \mathbf{q}$ is the radial component of $\mathbf{q}$. The expression for $L(\mathbf{r}, t)$ involves now an *angular* average $\bar{D}$ of the effective dynamical interaction $D(q)$,

$$L(\mathbf{r}, t) = \frac{1}{(2\pi)^2} \int d\omega \int dq_r \, \mathrm{e}^{i(q_r|\mathbf{r}| - \omega t)} \frac{i\bar{D}_\lambda(q_r, \omega)}{[\omega - v_F q_r + i0^+ \mathrm{sgn}(\omega)]^2}, \tag{15}$$

where

$$\bar{D}_\lambda(q_r, \omega) = \frac{S_{d-1}}{(2\pi)^{d-1}} \int_0^{\sqrt{\lambda^2 - q_r^2}} dq_t \, q_t^{d-2} D\left(q_r, q_t, \omega\right). \tag{16}$$

In Eq. (16), we have integrated over the $d - 1$ components of the tangent momentum. The low-energy behavior of $G$ is now described in terms of a tomographic Luttinger model [12]. In the limit $d \to 1$, $\bar{D} \to D$ and one recovers the exact expression for the propagator of the Luttinger model in $d = 1$. In the case we considered (regular coupling, $1 < d < 2$) the effective interaction scales to zero at low-energy, since Eq. (16) implies the scaling relation $\bar{D}_{s\lambda}(sq_r, s\omega) = s^{d-1} \bar{D}_\lambda(q_r, \omega)$, i.e., $\bar{D}(q_r, \omega) \simeq \omega^{d-1} \bar{D}(q_r/\omega)$. This result clearly illustrates the marginality of small-$\mathbf{q}$ scattering processes in $d = 1$, and their irrelevance in $d > 1$, where the effective interaction has to be averaged over the angles. The physical origin of this irrelevance is therefore related to the reduction of the phase space for the scattering of the

particles by the collective modes at $d > 1$, where the Landau Fermi-liquid theory is recovered.
Fourier transforming $G(\mathbf{r}, 0)$ yields the momentum distribution $n_{\mathbf{k}}$ near the Fermi surface. A signature of the validity of the Fermi-liquid theory is given by a finite discontinuity at the Fermi surface, which vanishes only if $d \to 1$. The quasiparticle inverse lifetime is proportional to $k_r^d$ ($d < 2$), and is therefore anomalous when compared to the standard $k_r^2$ term present for $d > 2$. However, it is not sufficient to destroy the Fermi-liquid quasiparticle features as soon as $d > 1$.
The above results show that the mechanism leading to a non-Fermi-liquid behavior in $d = 1$ does not extend to $d > 1$ (specifically to $d = 2$). The small-$\mathbf{q}$ scattering processes, which generalize those leading to the Luttinger-liquid behavior in $d = 1$, can still be controlled by asymptotic Ward identities, and do not destroy the Fermi liquid, as soon as $d > 1$. A non-Fermi-liquid behavior in $d = 2$ must therefore have a different and more subtle origin than in $d = 1$. For example, strongly singular interaction can produce such an effect, as we discuss in Sec. 4.4.
The results presented in this section, which rely on Ward identities, are reproduced in $d = 2$ by various authors [38, 40], by extending the bosonization approach to $d = 2$, along the line proposed by Haldane [41], as we briefly discuss in Sec. 4.3.

## 4.3. Bosonization

For completeness, we give here a brief description of the bosonization procedure to treat systems whose low-energy physics is dominated by forward scattering. It consists in expressing the fermion creation and annihilation operators in terms of boson density-fluctuation operators. This technique has been originally invoked to analyze one-dimensional systems [27, 29, 30, 31]. A generalization to higher dimension has been pioneered by Haldane [41] and elaborated in detail for $d = 2$ in Refs. [38, 40], and later in Refs. [39, 42]. The basic conclusion is that the results obtained by bosonization are equivalent to those obtained by means of the asymptotic Ward identities.
Let us first assume spinless fermions for simplicity. The main idea behind the bosonization approach in $d = 1$ is that the particle-hole continuum is absent, and the particle-hole excitation created by the operator $a^\dagger_{\mathbf{k}+\mathbf{q}} a_{\mathbf{k}}$ has a definite energy $\epsilon_{\mathbf{k}+\mathbf{q}} - \epsilon_{\mathbf{k}} = v_F \mathbf{q}$, independent of $\mathbf{k}$. The idea is then to describe the non-interacting part of the Luttinger Hamiltonian for the right- ($\alpha = +1$) and left- ($\alpha = -1$) moving fermionic particles as a collection of free bosonic particles

$$\mathcal{H}_0 = \sum_{\mathbf{q}} \sum_{\alpha} \alpha v_F |\mathbf{q}| b^\dagger_\alpha(\mathbf{q}) b_\alpha(\mathbf{q}),$$

where $b_\alpha^\dagger$ and $b_\alpha$ satisfy the bosonic commutation relation $[b_\alpha(\mathbf{q}), b_{\alpha'}^\dagger(\mathbf{q}')] = \delta_{\alpha,\alpha'}\delta_{\mathbf{q},\mathbf{q}'}$. The correspondence between the density operators $\rho_\alpha(\mathbf{q})$, whose commutators are given, as in $d = 1$, by Eq. (2), and the boson operators is established via the relation

$$\begin{aligned} \rho_\alpha(\mathbf{q}) &= \sqrt{\frac{V|\mathbf{q}|}{2\pi}} b_\alpha(\alpha\mathbf{q}), \quad \mathbf{q} > 0, \\ \rho_\alpha(\mathbf{q}) &= \sqrt{\frac{V|\mathbf{q}|}{2\pi}} b_\alpha^\dagger(-\alpha\mathbf{q}), \quad \mathbf{q} < 0. \end{aligned} \tag{17}$$

The term $\mathcal{H}_4$ of the Luttinger model is also simply expressed in terms of $b^\dagger b$, whereas

$$\mathcal{H}_2 = \frac{g_2}{4\pi} \sum_{\mathbf{q}} \sum_{\alpha} |\mathbf{q}| \left[ b_\alpha^\dagger(\mathbf{q}) b_{-\alpha}^\dagger(-\mathbf{q}) + b_{-\alpha}(-\mathbf{q}) b_\alpha(\mathbf{q}) \right],$$

has an anomalous form, as it is expressed in terms of $b^\dagger b^\dagger$ and $bb$. Nonetheless, since the full Hamiltonian is bilinear in the bosonic operators, it can be cast in a diagonal form by a suitable Bogoljubov transformation, yielding the collective charge modes. In presence of spin variables we would have a correspondence between $\rho_\alpha^a$ and the boson operators $b_\alpha^a$, and the charge ($a = c$) and spin ($a = s$) sectors would decouple with charge and spin modes propagating with velocities $v^a$, leading to the charge and spin separation.
The extension of the bosonization approach to $d > 1$ relies on the decomposition of momentum space into $M$ disjoint sectors $K_\alpha$, $\alpha = 1, \ldots, M$, which correspond to a partition of the Fermi surface into patches. The area of each patch is $\lambda_\alpha^{d-1}$, and the condition $\lambda_\alpha \ll k_F$ ensures that the Fermi surface is locally flat and the velocity is constant within each patch. The condition for constant velocity in the patch is the same as the velocity conservation required by the Ward identities at each point of the Fermi surface. As in $d = 1$, the basic ingredient in the bosonization procedure is the density-fluctuation operator, that now is defined within each patch $\alpha$ as

$$\rho_\alpha(\mathbf{q}) = \sum_{\mathbf{k} \in \text{patch } \alpha} a_{\mathbf{k}-\mathbf{q}}^\dagger a_{\mathbf{k}}.$$

For $|\mathbf{q}| \ll \lambda_\alpha$, the above operators obey commutation relations [41, 40] which generalize Eq. (2), $[\rho_\alpha(\mathbf{q}), \rho_{\alpha'}(\mathbf{q}')] \simeq \Omega_\alpha \delta_{\alpha\alpha'} \delta_{\mathbf{q},-\mathbf{q}'}(\mathbf{n}_\alpha \cdot \mathbf{q})$, where $\Omega_\alpha = V\lambda_\alpha^{d-1}/(2\pi)^d$ is the number of states in the patch divided by the size $\lambda_\alpha$ in the radial direction, and $\mathbf{n}_\alpha$ is a unit vector normal to the patch. The density fluctuation operator $\rho_\alpha$ can be related to boson operators $b_\alpha$ and $b_\alpha^\dagger$ by the following generalization of Eq. (17),

$$\rho_\alpha(\mathbf{q}) = (\Omega_\alpha |\mathbf{n}_\alpha \cdot \mathbf{q}|)^{1/2} [\Theta(\mathbf{n}_\alpha \cdot \mathbf{q}) b_\alpha(\mathbf{q}) + \Theta(-\mathbf{n}_\alpha \cdot \mathbf{q}) b_\alpha^\dagger(-\mathbf{q})],$$

$\Theta$ being the characteristic function.
The main point of the bosonization procedure in $d > 1$ is that, if we consider forward scattering with momentum transfer restricted by $|\mathbf{q}| \ll \lambda_\alpha$, the interaction Hamiltonian can still be written in a quadratic form in terms of the density operators. Owing to the quadratic structure of the bosonized representation of the Hamiltonian, the dynamics of the operators $\rho_\alpha$ can be calculated exactly. The result in $d = 2$ is the same as that obtained by the Ward identities presented in Sec. 4.2. In particular, using the bosonic representation of fermion operators, the single-particle propagator $G_\alpha$ can be expressed in terms of the expectation value of the boson (density) operator for particles belonging to a small patch $\alpha$ of the Fermi surface. $G_\alpha$ coincides with the expression (14) derived via Ward identity, when calculated for $d = 2$. The only difference is that, instead of the radial variable, a vector is now present in Eq. (15). The bosonization approach, indeed, introduces an overcomplete set of fermion fields. The Ward-identity approach avoids instead the patch construction with artificial overcompletness of states and inter-patch scattering processes. Moreover the limitations of the bosonization approach in $d = 2$ are not so transparent as in the Ward-identity approach in $d = 2$. Indeed, in $d = 2$, the generic integrals (11) in momentum space are no longer peaked at $\theta = 0, \pi$. The relation between the current vertex and the density vertex and its consequences are therefore much less evident, when extended to $d = 2$. The dimensional crossover from Luttinger to Fermi liquid as $d > 1$, derived via Ward identities, is instead a firm result.

### 4.4. Singular interactions and long-range forces

We finally consider singular scattering as a possible source of non-Fermi-liquid behavior in $d > 1$. Singular scattering may plausibly occur in strongly correlated fermion systems [14]. Indeed, while in ordinary metals the kinetic-energy contribution is dominant and ensures a homogeneous phase, in the presence of strong correlation due, e.g., to a local Hubbard repulsion, this contribution is strongly suppressed, and additional forces of different nature (magnetic, nearest-neighbour repulsion, etc.) may lead to phase separation [43]. On the other hand, long-range Coulomb interactions forbid charge unbalance on a macroscopic scale, thus preventing the thermodynamic phase separation [44]. However, since Coulomb interaction is strongly effective at small $\mathbf{q}$, the way may still be open for an instability at finite wave-vectors $\mathbf{q} = \mathbf{q}_c$, with strong dynamic charge fluctuations. Informations about such an instability are indeed provided by the quasiparticle scattering amplitude $\Gamma(\omega, \mathbf{q})$. Near phase separation, in the absence of long-range Coulomb forces, $\Gamma$ is strongly singular at zero momentum. When long-range Coulomb forces are considered, there is still the possibility that $\Gamma$ is strongly singular at a finite momentum $\mathbf{q} = \mathbf{q}_c$, which signals an incommensurate charge-density-wave

instability [14]. A similar instability could be present in the magnetic sector, giving rise to strong magnetic fluctuations [15]. In both cases (short- and long-range forces) the singular interactions may lead to a breakdown of the Fermi-liquid picture in the metallic phase. Anomalous transport properties of the metal arise in a region determined by a crossover temperature, which depends in general on the density of charge carriers.

The previous analysis for the effective interaction $D$, can be pursued, for instance, in the presence of static long-range forces with spin independent singular coupling $g(\mathbf{q}) = g_0^2/|\mathbf{q}|^\alpha$, where $g_0^2$ is the strength of the interaction, which corresponds to a $|\mathbf{r}|^{-(d-\alpha)}$ behavior in real space [20]. One could expect that long-range forces change the scaling dimension of $\bar{D}$ from $d-1$ to $d-1-\alpha$. However, summing up the random-phase series for the effective (screened) dynamical interaction, the leading contribution in the asymptotic regime $|\mathbf{q}|/\omega \to 0$, which is relevant to the present problem, is found to be

$$D(q) = \frac{g_0^2\omega^2}{|\mathbf{q}|^\alpha(\omega^2 - C^2|\mathbf{q}|^{2-\alpha})}, \tag{18}$$

where $C = g_0\sqrt{v_F S_d k_F^{d-1}/d(2\pi)^d}$. From Eq. (18) one sees that the long-range forces change the dispersion of the collective mode from a sound mode $\omega_q \propto |\mathbf{q}|$ to a *plasma* mode $\omega_q \propto |\mathbf{q}|^{1-\alpha/2}$, which is massless as long as $\alpha < 2$. This changes the the dimension of $\omega$ from 1 to $1-\alpha/2$ and reduces the pole contribution to the integrand for $L$ in Eq. (15). The scaling dimension for $L(\mathbf{r}, t)$ is now $d-1-\alpha/2$. The outcome is that the breakdown of the Fermi liquid occurs only if the long-range interaction is strongly singular, $\alpha \geq 2d-2$ [19, 20].

### 4.5. Renormalization-group approach in the presence of singular forward scattering

The result discussed in Sec. 4.4 is based on the assumption that the random-phase approximation leading to the dynamically dressed effective interaction $D$ is still valid in the presence of a singular interaction. This amounts to say that (singular contributions associated with) self-energy and vertex corrections to the polarization bubble must cancel. This cancellation can be controlled by means of the Ward identities associated with the specific conservation laws of a system with singular forward scattering, within a perturbative renormalization-group approach.

To develop the renormalization-group approach in the case of long-range interaction [21], we exploit the equivalence with a problem of fermions interacting with a *scalar* boson field $\phi$. We consider spinless fermions for simplicity. The interaction Hamiltonian is

$$\mathcal{H}_I = ig_0 \int \frac{d^{d+1}k\, d^{d+1}q}{(2\pi)^{2d+2}} a^\dagger(k+q/2)\phi(q)a(k-q/2),$$

where the random-phase propagator of the field $\phi$ is given by $D^{LR} = D/g_0^2$, with $D$ given by Eq. (18), in the kinematic region $\omega \gg v_F|\mathbf{q}|$. If $\omega \ll v_F|\mathbf{q}|$ the effective interaction assumes the usual short-ranged expression due to the screening by the particle-hole fluctuations. Here we restrict to consider the regime $\omega \gg v_F|\mathbf{q}|$, in the case $\alpha < 2$ where the collective plasma mode is propagating and gapless.

Within a functional-integral formulation, by eliminating the fermions, one obtains an effective action for the field $\phi$

$$\mathcal{S}_{\text{eff}}[\phi] = \frac{1}{2}\int \frac{d^{d+1}q}{(2\pi)^{d+1}}\phi^*[D^{LR}]^{-1}\phi + \sum_{n\geq 3}\int \Gamma_n \phi^n,$$

where the first term in the right-hand side is the random-phase quadratic part, and the interacting part is symbolically represented by the second term, where the $n$-th contribution contains $n-1$ integrals over momenta and frequencies. The dimensional analysis yields the scaling dimensions $[q] = 1$, $[\omega] = 1 - \alpha/2$, $[\phi] = -(2d+2+\alpha)/4$. Thus $[\Gamma_n] = d+1+[(3n-2)\alpha - 2n(d+1)]/4$ and $\Gamma_n$ seems to be relevant for $d < (3n-2)\alpha/(2n-4) - 1$. However, the gauge transformation $\phi \to \mathbf{A} = -\mathbf{q}\phi/\omega$ from a scalar to a vector field, makes the momentum dependence explicit and shows that, for $n \geq 3$, $\Gamma_n$ vanishes at least as $\Gamma_n \sim (|\mathbf{q}|/\omega)^n$ in the dynamical regime $|\mathbf{q}|/\omega \to 0$, which is relevant in this context [21]. The expression for the $\phi$-field propagator is therefore not changed by corrections beyond the random-phase approximation, i.e., the field $\phi$ does not acquire an anomalous dimension with respect to its Gaussian form, and the wave-function renormalization $Z_\phi$ remains finite.

We are thus left with the problem of renormalizing the fermion Green's function $G$ and the fermion-boson vertex. We use conservation laws to establish relations among the various singularities of the theory, thus reducing the number of independent renormalization parameters. The first conservation law to be exploited is the conservation of the total number of particles which is generically valid. The corresponding Ward identity, which is the analogue of Eq. (7) for $a = c$, then reads

$$\mathbf{q}\cdot\mathbf{\Lambda}(k,q) - \omega\Lambda^0(k,q) = G^{-1}(k-q/2) - G^{-1}(k+q/2), \tag{19}$$

which allows to relate the renormalization parameters of the vertices with those of the fermion propagator.

Since frequency and momentum are inequivalent variables in the present problem, we introduce two renormalization parameters in the fermion propagator $G^{-1}(\mathbf{k},\epsilon) \equiv \epsilon - \xi_{\mathbf{k}} - \Sigma(\mathbf{k},\epsilon) = Z^{-1}\epsilon - (ZZ_{v_F})^{-1}\xi_{\mathbf{k}}$, where $\xi_{\mathbf{k}} \equiv (|\mathbf{k}|^2 - k_F^2)/2m \simeq v_F(|\mathbf{k}| - k_F)$ is the free-particle dispersion and $\Sigma$ is the fermion self-energy. The renormalization parameters are $Z^{-1} = 1 - \partial_\epsilon\Sigma$, $(ZZ_{v_F})^{-1} = 1 - v_F^{-1}\partial_{|\mathbf{k}|}\Sigma$, and must be related with the singular parts of the current and density vertices in the left-hand side of Eq. (19). In particular,

one has to extract the coefficient of $\mathbf{q}$ in the right-hand side of (19) and compare it with the static limit of the current vertex in the left-hand side. In that way, defining the renormalization of the current vertex $\mathbf{\Lambda}$ in the static limit, $Z_{\rm stat}^{-1}\mathbf{v}_F \equiv \mathbf{\Lambda}(\mathbf{k}, \mathbf{q} \to \mathbf{0}; \epsilon, \omega = 0)$, we find $Z_{\rm stat} = ZZ_{v_F}$.
Similarly, to extract the divergences of the frequency part of the propagator, one defines the dynamical limit of the density vertex

$$Z_{\rm dyn}^{-1} = \Lambda^0(\mathbf{k}, \mathbf{q} = \mathbf{0}; \epsilon, \omega \to 0),$$

and finds

$$Z_{\rm dyn} = Z. \tag{20}$$

As we show below, the renormalization which is relevant for the long-range case is Eq. (20).
The second conservation law to be considered is the conservation of the number of particles at each point of the Fermi surface, which is obviously approximate in $d > 1$ and holds if forward scattering is dominant at low energies, as in the tomographic Luttinger model. The associated Ward identity, as in Eq. (12), is $\mathbf{\Lambda}(k, q) = \mathbf{v}_F \Lambda^0(k, q)$.
Assuming the above approximate equation and combining it with Eq. (19) we can once again express the density vertex as a function of the single-particle propagator only. Finally, as it was shown in Sec. 3.3, by inserting this into the expression for the polarization bubble, the latter does not get dressed, since the vertex corrections exactly cancel the self-energy corrections, i.e., the validity of the random-phase approximation for the boson propagator is under control.
The renormalization parameters $Z$ and $Z_{v_F}$ are calculated through a perturbative expansion of the fermion self-energy $\Sigma$, and are defined in terms of $\Sigma$ at a proper normalization point $s$ in momentum space. The one-loop self-energy contribution due to the long-range singular interaction is such that in the dynamical limit $v_F^{-1}\left|\partial_{|\mathbf{k}|}\Sigma\right| \simeq |\partial_\epsilon \Sigma|$, i.e., the derivative of $\Sigma$ with respect to $\mathbf{k}$ and $\epsilon$ have the same singular infrared behavior [21]. Therefore $ZZ_{v_F} = Z$, i.e., $Z_{v_F}$ is finite and the Fermi velocity does not acquire singular corrections, as in the one-dimensional Luttinger model.
When considering the general expression for the fermion self-energy $\Sigma = ig\int \Lambda^0 D^{LR} G$, one realizes that the most singular contribution to this integral comes from the pole of the boson propagator $\omega^2 \simeq |\mathbf{q}|^{2-\alpha}$, i.e., $\omega \gg |\mathbf{q}|$. We introduce, therefore the renormalization parameter in the relevant kinematic regime $Z_{\rm dyn}^{-1}$. The renormalization of the coupling constant $g$ is now $g_0 = gZ_{\rm dyn}/Z$, which, using Eq. (20), becomes $g_0 = g$, i.e., the divergences in the vertex and self-energy diagrams cancel out thanks to the Ward identity coming from the conservation of the total number of particles. In conclusion, due to Ward identities, the Fermi velocity, the boson field, and the coupling constant do not get renormalized,

At one-loop level, one determines the effective coupling constant which appears in the skeleton structure of the perturbative expansion. The effective coupling is specified by observing that at the dominant pole $\omega = C|\mathbf{q}|^{1-\alpha/2}$, the energy of the internal fermion propagator is $\epsilon + C|\mathbf{q}|^{1-\alpha/2}$. But, since at small momenta and for $\alpha < 2$, $\xi_{\mathbf{k}+\mathbf{q}} - \xi_{\mathbf{k}} \ll C|\mathbf{q}|^{1-\alpha/2}$, one can neglect the contribution from $\xi_{\mathbf{k}+\mathbf{q}}$ when computing the contribution to $\Sigma$. As a consequence, the effective coupling coupling constant coincides with $g^2$ apart from a multiplicative factor coming from the integration in the diagram. Defining $u_0 \propto g_0^2$, the one-loop calculation of the self-energy [21] leads to the one-loop wave-function renormalization parameter

$$Z^{-1}(\epsilon) = 1 + u_0 \frac{2-\alpha}{2+\alpha-2d} |\epsilon|^{-\frac{2+\alpha-2d}{2-\alpha}}. \tag{21}$$

Since this quantity must be dimensionless, we can compute the scaling dimension of $u_0$, thus obtaining, for the dimensionless coupling constant, the expression

$$u = \frac{u_0}{s^{x_u}}, \tag{22}$$

where $s$ is a running momentum scale and $x_u = [\omega] \times (2+\alpha-2d)/(2-\alpha) = 1 - d + \alpha/2$. Thus $u$ does not acquire any anomalous dimension. Eq. (22) shows that a line of non-universal fixed points exist only for $x_u = 0$, i.e., for $d = d_c \equiv 1+\alpha/2$, while for $x_u > 0$ or $x_u < 0$ the effective coupling constant either scales to strong coupling or to the free fixed point $u^* = 0$. In the strong-coupling and non-universal fixed-point cases one obtains a non-Fermi-liquid behavior in agreement with the result discussed in Sec. 4.4.
From the one-loop result, Eq. (21), we can obtain a differential equation for $Z$, $\dot{Z} = -(1-\alpha/2)uZ$, where the dot indicates the derivative with respect to $-\log s$, and $\epsilon = s^{1-\alpha/2}$. The equation can be integrated, taking Eq. (22) into account, yielding $Z \sim \exp\left[-(2-\alpha)u_0|\epsilon|^{-(2+\alpha-2d)/(2-\alpha)}/(2+\alpha-2d)\right]$, i.e., $Z$ vanishes as a stretched exponential, for $d < d_c$. For $d = d_c$, instead, $Z \sim |\epsilon|^{u_0}$, vanishes with a non-universal exponent. We point out that, due to the absence of an anomalous dimension for the effective coupling constant, the solution of the renormalization-group equation for $Z$ corresponds to the exponentiation of the one-loop result, Eq. (21) [21].

## 5. Concluding remarks

In these lectures we have analyzed the metallic phase in low dimensions.
We have shown that a mere extension of the mechanism leading to the Luttinger liquid in $d = 1$ leads to a Fermi-liquid behavior as soon as $d > 1$. This result is controlled via Ward identities within the perturbative structure

of a tomographic Luttinger model, which generalizes the one-dimensional Luttinger model, where only forward scattering is considered, to $d > 1$.
A singular effective interaction among the fermionic quasiparticles is thus required to give a non-Fermi-liquid behavior in $d > 1$.
The combined use of Ward identities and renormalization group provides in this case the explicit expression for the vanishing of the wave-function renormalization and of the discontinuity of the occupation number in momentum space as the Fermi surface is approached.

## Acknowledgements

We acknowledge financial support from the Italian MIUR, Cofin 2001, prot. 20010203848, and from INFM, PA-G0-4.

## References

1. K. G. Wilson, *Phys. Rev.* **B 4**, 3174 (1971); *ibid.*, 3184 (1971).
2. J. Sólyom, *Adv. Phys.* **28**, 201 (1979).
3. W. Metzner, C. Castellani, and C. Di Castro, *Adv. Phys.* **47**, 317 (1998).
4. G. Benfatto and G. Gallavotti, *Phys. Rev.* **B 42**, 9967 (1990); *J. Stat. Phys.* **59**, 541 (1990).
5. R. Shankar, *Rev. Mod. Phys.* **66**, 129 (1994).
6. P. Nozières, *Theory of Interacting Fermi systems*, Benjamin, Amsterdam (1964); G. Baym and C. Pethick, in *The physics of liquid and solid Helium*, edited by K. H. Bennemann and J. H. Ketterson, John Wiley and Sons, New York (1978).
7. For a review see, e.g., P. W. Anderson, *The Theory of Superconductivity in the High $T_c$ Cuprates*, Princeton University Press, Princeton (1997).
8. S. Uchida, *J. Appl. Phys.* **32**, 3784 (1993).
9. For an overview on the pseudogap as measured in various experiments see, e.g., T. Timusk and B. Statt, *Rep. Prog. Phys.* **62**, 61 (1999).
10. T. Valla, A. V. Fedorov, P. D. Johnson, B. O. Wells, S. L. Hulbert, Q. Li, G. D. Gu, Sand N. Koshizuka, *Science* **285**, 2110 (1999).
11. P. W. Anderson, *Phys. Rev. Lett.* **64**, 1839 (1990); *ibid.* **65**, 2306 (1990).
12. P. W. Anderson, *Science* **235**, 1196 (1987).
13. C. M. Varma, P. B. Littlewood, S. Schmitt-Rink, E. Abrahams, and A. E. Ruckenstein, *Phys. Rev. Lett.* **63**, 1996 (1989).
14. C. Castellani, C. Di Castro, and M. Grilli, *Phys. Rev. Lett.* **75**, 4650 (1995); Z. Phys. B **103**, 137 (1997); for a recent review see, e.g., C. Di Castro, L. Benfatto, S. Caprara, C. Castellani, and M. Grilli, Physica **C 341-348**, 1715 (2000).
15. P. Monthoux, A. V. Balatsky, and D. Pines, *Phys. Rev.* **B 46**, 14803 (1992); A. Sokol and D. Pines, *Phys. Rev. Lett.* **71**, 2813 (1993); P. Monthoux and D. Pines, *Phys. Rev.* **B 50**, 16015 (1994); A. V. Chubukov, P. Monthoux, and D. K. Morr, *Phys. Rev.* **B 56**, 7789 (1997).
16. M. Tranquada, B. J. Sternlieb, J. D. Axe, Y. Nakamura, and S. Uchida, *Nature* **375**, 561 (1995); J. M. Tranquada, J. D. Axe, N. Ichikawa, Y. Nakamura, S. Uchida, and B. Nachumi, *Phys. Rev.* **B 54**, 7489 (1996).

17. V. J. Emery, S. A. Kievelson, and H. Q. Lin, *Phys. Rev. Lett.* **64**, 475 (1990).
18. C. Castellani, C. Di Castro, and W. Metzner, *Phys. Rev. Lett.* **72**, 316 (1994).
19. P. Bares and X. G. Wen, *Phys. Rev.* **B 48**, 8636 (1993).
20. C. Castellani and C. Di Castro, *Physica* **C 235-240**, 99 (1994).
21. C. Castellani, S. Caprara, C. Di Castro, and A. Maccarone, *Nucl. Phys.* **B 594**, 747 (2001).
22. H. J. Schulz, in *Proceedings of the Les Houches Summer School LXI*, Edited by E. Akkermans, G. Montambaux, J. L. Pichard, and J. Zinn-Justin, Elsevier, Amsterdam (1995).
23. J. Voit, *Rep. Prog. Phys.* **58**, 977 (1995).
24. W. Metzner and C. Di Castro, *Phys. Rev.* **B 47**, 16107 (1993).
25. P. Nozières and A. Blandin, *J. Phys.* (Paris) **41**, 193 (1980); for a review see, e.g., D. L. Cox and A. Zawadowski, *Adv. Phys.*, **47**, 599 (1998).
26. For a review see, e.g., P. A. Lee and T. V. Ramakrishnan, *Rev. Mod. Phys.* **57**, 787 (1985); D. Belitz and T. R. Kirkpatrick, *ibid.* **66**, 261 (1994).
27. A. Luther and I. Peschel, *Phys. Rev.* **B 9**, 2911 (1974).
28. S. Tomonaga, *Prog. Theor. Phys.* **5**, 544 (1950); J. M. Luttinger, *J. Math. Phys.* **4**, 1154 (1963).
29. D. C. Mattis and E. H. Lieb, *J. Math. Phys.* **6**, 304 (1965).
30. D. C. Mattis, *J. Math. Phys.* **15**, 609 (1974).
31. F. D. M. Haldane, *Phys. Rev. Lett.* **45**, 1358 (1980); *ibid.* **47**, 1840 (1981); *J. Phys.* **C 14**, 2585 (1981).
32. I. E. Dzyaloshinskii and A. I. Larkin, *Sov. Phys. JETP* **38**, 202 (1974).
33. H. U. Everts and H. Schulz, *Solid State Commun.* **15**, 1413 (1974).
34. C. Di Castro and W. Metzner, *Phys. Rev. Lett.* **67**, 3852 (1991).
35. C. Bourbonnais and L. G. Caron, *Int. J. Mod. Phys.* **B 5**, 1033 (1991).
36. C. Castellani, C. Di Castro, and W. Metzner, *Phys. Rev. Lett.* **69**, 1703 (1992).
37. M. Fabrizio, A. Parola, and E. Tosatti, *Phys. Rev.* **B 46**, 3159 (1992).
38. A. Houghton, H. -J. Kwon, and J. B. Marston, *Phys. Rev.* **B 50**, 1351 (1994).
39. P. Kopietz, *Bosonization of Interacting Fermions in Arbitrary Dimensions*, Springer, Berlin (1997).
40. A. Houghton and J. B. Marston, *Phys. Rev.* **B 48**, 7790 (1993).
41. F. D. M. Haldane, in *Proceedings of the International School of Physics 'Enrico Fermi'*, Course CXXI, edited by R.A. Broglia and J.R. Schrieffer, North-Holland, Amsterdam, (1994); *Elv. Phys. Acta* **65**, 152 (1992).
42. P. Kopietz and K. Schönhammer, *Z. Phys.* **B 100**, 561 (1996).
43. For a general overview and references see, e.g., *Proceedings of the Workshop on Phase Separation in Cuprate Superconductors*, Edited by K. A. Müller and G. Benedek, World Scientific, Singapore (1992).
44. V. J. Emery and S. A. Kivelson, in Ref. [43]; V. J. Emery and S. A. Kivelson, *Physica* **C 209**, 597 (1993).

# COUNTING STATISTICS OF MESOSCOPIC NOISE

L.S. Levitov
*Department of Physics, Massachusetts Institute of Technology, 77 Massachusetts Ave, Cambridge, MA 02139*

## 1. Introduction

The measurement performed by optical detectors, such as photon counters, is extended in the time domain, which makes it sensitive to temporal correlations of photons [1]. It has been known long ago in the theory of photodetection [2] that understanding photon counting distribution is essentially a problem of many-particle statistics. Similar considerations apply to the electrical noise measurement, which is fundamentally different from photodetection in that the electrons are not destroyed but just counted. The noise measurement, very much like photodetection, is a sensitive probe of temporal correlations between different transmitted electrons.

Fermi correlations in the electron noise were initially studied by Lesovik [3] (see also Ref.[4]) in a point contact, and then by Büttiker [5] in multiterminal systems, and by Beenakker and Büttiker [6] in mesoscopic conductors. Kane and Fisher proposed to employ the shot noise for detecting fractional quasiparticles in a Quantum Hall edge system [7]. Subsequent theoretical developments are summarized in a recent review [8].

Experimental studies of the shot noise, after first measurements in a point contact by Reznikov et al. [9] and Kumar et al. [10], focused on the quantum Hall regime. The fractional charges $e/3$ and $e/5$ were observed [11, 12, 13] at incompressible Landau level filling (see also recent work on noise at intermediate filling [14]). The shot noise in a mesoscopic conductor was observed by Steinbach et al. [15] and Schoelkopf et al. [16], who also studied noise in an ac driven phase-coherent mesoscopic conductor [17].

In this article we discuss counting statistics of electric noise and consider the probability distribution of charge transmitted in a fixed time interval [18, 19]. This distribution provides detailed information about current fluctuations. The counting statistics have been analyzed for the DC transport of free fermions [18, 20], in the photo-assisted transport [21], in the parametrically driven transport [19, 22], and in the mesoscopic regime [23] (also, see a review [24]). Nazarov developed



*R. Fazio et al. (eds.), New Directions in Mesoscopic Physics,* 67–91.
© 2003 *Kluwer Academic Publishers. Printed in the Netherlands.*

Keldysh formalism for the counting statistics problem and applied it to mesoscopic transport in a weak localization regime [25] and, together with Bagrets, in a multiterminal geometry [26]. Charge doubling due to Andreev scattering in NS junctions was considered by Muzykantskii and Khmelnitskii [27], and in mesoscopic NS systems by Belzig and Nazarov [28]. Andreev and Kamenev [29] studied the problem of mesoscopic pumping in view of the results of Ref.[19]. Taddei and Fazio discussed counting statistics of entangled electron sources [30]. Statistics of transport in a Coulomb blockade regime was studied by Bagrets and Nazarov [31]. Photon statistics was considered by Beenakker and Schomerus [32] and Kindermann et al. [33]. The problem of back influence of a charge detector on current fluctuations in the context of counting statistics measurement was studied by Nazarov and Kindermann [37].

The possibility of measuring counting statistics using a fast charge integrator scheme was considered recently [34]. From the measured distribution all moments of charge fluctuations can be calculated and, conversely, the knowledge of all moments is in principle sufficient for recovering the full distribution. However, due to the central limit theorem, high moments are probably difficult to access experimentally. Therefore recent literature focused primarily on the third moment. It was found that the third moment obeys a generalized Schottky relation which holds in the tunneling regime at both high and low temperature, but involves a temperature-dependent Fano factor in the mesoscopic regime [22, 35]. Gutman and Gefen [35] studied the third moment using a sigma model approach, while Nagaev [36] demonstrated that all moments are correctly reproduced by an extension of the Boltzmann-Langevin kinetic equation.

In this article, after introducing the counting distribution statistics (Sec.2), we review its microscopic definition based on a passive charge detector (Sec.2.1). Then we study statistics of tunneling in a generic many-body system (Sec.2.2). From the microscopic approach of Sec.2.1 we derive a bidirectional Poisson distribution for tunneling current, obtain a Schottky-like relation for the third moment and discuss its robustness. Then we briefly discuss the relation of the counting statistics theory and the theory of photo-detection (Sec.2.3). Then we proceed to the problem of mesoscopic transport. In Sec.3.1 we review the results on the DC transport and the derivation of a functional determinant formula for the counting distribution generating function. In Sec.3.3 we review the work on the AC transport statistics, and then consider the problem of mesoscopic pumping (Sec.3.4). The counting statistics for generic pumping strategy at weak pumping is given by a bidirectional

Poisson distribution. We show that the Fano factor varies between 0 and 1 as a function of the pumping fields phase difference.

## 2. General approach

The transmitted charge distribution can be characterized [18, 19] by electron counting probabilities $p_n$, usually accumulated in a generating function[1]

$$\chi(\lambda) = \sum e^{in\lambda} p_n \,. \tag{1}$$

The function $\chi(\lambda)$ is $2\pi$-periodic in the counting eld $\lambda$ and has the property $\chi(0) = 1$ which follows from the probability normalization $\sum_n p_n = 1$. The term "counting field" will be motivated in Sec.2.1, where a microscopic definition of $\chi(\lambda)$ is discussed in which $\lambda$ appears as a field that couples current fluctuations to a charge detector.

The generating function (1) is particularly well suited for characterizing statistics of the distribution $p_n$. The so-called irreducible correlators $\langle\langle \delta n^k \rangle\rangle$ (also known as cummulants) are expressed in terms of $\chi(\lambda)$ as

$$\ln \chi(\lambda) = \sum_{k=1}^{\infty} m_k \frac{(i\lambda)^k}{k!} \,, \qquad m_k \equiv \langle\langle \delta n^k \rangle\rangle \tag{2}$$

The first two correlators in (2) give the mean and the variance:

$$m_1 = \overline{n}, \qquad m_2 = \overline{\delta n^2} = \overline{n^2} - \overline{n}^2, \tag{3}$$

where $\overline{f(n)}$ stands for $\sum_n f(n) p_n$. The third correlator[2]

$$m_3 = \langle\langle \delta n^3 \rangle\rangle \equiv \overline{\delta n^3} = \overline{(n - \overline{n})^3} \tag{4}$$

characterizes the asymmetry (or skewness) of the distribution $p_n$.

To illustrate the notion of a generating function, let us consider a Poisson process. It describes charge transport at very low transmission, with subsequent transmission events uncorrelated. For the Poisson distribution

$$p_k = \begin{cases} e^{-\bar{n}}\, \bar{n}^k / k! & k \geq 0 \\ 0 & k < 0 \end{cases} \quad \text{and} \quad \chi(\lambda) = \exp\left( (e^{i\lambda} - 1)\bar{n} \right) \tag{5}$$

with $\bar{n} = It/e$ the average number of particles transmitted during the time interval $t$, where $I$ is the time-averaged current and $e$ is elementary

[1] The function $\chi(\lambda)$ is also called a characteristic function [1].

[2] The relation between cummulants and correlators is generally more complicated than Eq.(4) for the third cummulant. For example, $m_4 = \langle\langle \delta q^4 \rangle\rangle = \overline{\delta q^4} - 3\left(\overline{\delta q^2}\right)^2$.

charge. Comparing (5) with (2), one finds that all cummulants of the Poisson distribution are identical: $m_k = \bar{n}$.

Another useful example is binomial statistics. A binomial distribution arises when a fixed number $N$ of independent attempts to trasmit particles is made, each attempt successful or unsuccessful with probabilities $p$ and $q = 1 - p$. The probability to transmit $k$ particles in this case is determined by the number of $k$ successful outcomes, equal to $C_N^k = N!/(N-k)!k!$ each. The probability distribution and the generating function in this case are

$$p_k = C_N^k p^k q^{N-k} \quad \text{and} \quad \chi(\lambda) = \left(pe^{i\lambda} + q\right)^N \tag{6}$$

The cummulants of the binomial distribution can be found from (2) by expanding $\ln \chi$ in $\lambda$:

$$m_1 = pN, \quad m_2 = pqN, \quad m_3 = pq(q-p)N, \quad ... \tag{7}$$

The binomial distribution (6) describes counting distribution of DC current noise for a single channel scatterrer, such as point contact, at zero temperature (Sec.3.1).

Statistically independent processes result in a generating function given by a product of generating functions for constituing processes: $\chi(\lambda) = \chi_1(\lambda)...\chi_k(\lambda)$. For example, consider a biderectional Poisson distribution defined as a mixture of two independent Poisson processes transmitting particles in opposite directions with the rates $\bar{n}$ and $\bar{n}'$. In this case,

$$\chi_{2P}(\lambda) = \exp\left((e^{i\lambda} - 1)\bar{n}\right) \cdot \exp\left((e^{-i\lambda} - 1)\bar{n}'\right) \tag{8}$$

In Sec.2.2 we use the distribution (8) to describe statitics of tunneling current. In Sec.3.4 we show that it describes noise a mesoscopic pump.

## 2.1. A microscopic representation of $\chi(\lambda)$

Here we discuss a microscopic definition of counting statistics for a physical system. It will be shown that the generating fucntion can be written as a certain partition function in Keldysh field theory. Adopting an inductive approach, we shall start with a specific model of a current detector[20, 24]. We obtain $\chi(\lambda)$ for a particular current measurement scheme, and then argue that the result is universal.

In a realistic noise measurement, e.g. in a mesoscopic wire or a point contact, the current fluctuations are not detected directly. Instead, the measurement is performed on the electromagnetic fluctuations (basically, voltage noise) induced by current fluctuations in the system. The

electromagnetic fluctuations have to be amplified before detection. The conversion of underlying microscopic fluctuations due to fermions (electrons, fractional charges, etc.) into fluctuations of bosons (photons) is crucial, since Bose fields can be easily amplified without compromising noise statistics, while Fermi statistics does not allow amplification.

Our goal is a microscopic picture of current fluctuations, rather than a description of realistic measurements. Thus we choose a gedanken measurement scheme well suited for that purpose. Consider a spin 1/2 placed near an electron system and magnetically coupled to the electric current. We restrict the coupling to the spin $z$ component, so that the system in the presence of the spin is described by $\mathcal{H}(\mathbf{q}, \mathbf{p} - \mathbf{a}\sigma_3)$, where $\mathcal{H}(\mathbf{q}, \mathbf{p})$ is the electron Hamiltonian and $\mathbf{a}(r)$ is the spin vector potential scaled by $e/c$.

The scheme of current detection using the dynamics of a spin coupled to current can be motivated semiclassically. A spin coupled to a time-dependent classical current $I(t)$ by the interaction $\mathcal{H} = \frac{1}{2}\lambda\sigma_3 I(t)$ will precess at the rate proportional to current, which turns the spin into an analog galvanometer. Indeed, if the spin-current coupling is turned on at $t = 0$, the spin will start precessing around the $z$ axis with the precession angle $\theta(t) = \lambda \int_0^t I(t')dt'$ equal to the transmitted charge times $\lambda$. The coupling constant $\lambda$, so far arbitrary, will be associated with counting field below.

In a fully quantum-mechanical problem, the spin evolution can be obtained from $i\dot{\sigma} = [\sigma, \mathcal{H}]$. Since the spin-current coupling Hamiltonian commutes with $\sigma_3$, the spin dynamics can be found explicitly. For that we consider the transverse spin components $\sigma_\pm \equiv \sigma_1 \pm i\sigma_2$ and write the evolution equation $i\dot{\sigma}_\pm = [\sigma_\pm, \mathcal{H}]$ in the form

$$i\dot{\sigma}_+ = \sigma_+ P_\downarrow \mathcal{H}(\mathbf{q}, \mathbf{p} + \mathbf{a}) - \mathcal{H}(\mathbf{q}, \mathbf{p} - \mathbf{a}) P_\uparrow \sigma_+ \,, \tag{9}$$

$$i\dot{\sigma}_- = \sigma_- P_\uparrow \mathcal{H}(\mathbf{q}, \mathbf{p} - \mathbf{a}) - \mathcal{H}(\mathbf{q}, \mathbf{p} + \mathbf{a}) P_\downarrow \sigma_- \,, \tag{10}$$

with $P_{\uparrow,\downarrow} = \frac{1}{2}(1 + \sigma_3)$ the up and down spin projectors. Here we used the raising/lowering properties of the operators $\sigma_\pm$ and replaced $\sigma_3$ by 1 to the left of $\sigma_+$ and by $-1$ to the right of $\sigma_+$ (and similarly for the $\sigma_-$ equation).

We consider a measurement which is performed during time interval $0 < t' < t$, i.e. start with a spin decoupled from the electron system, $\mathbf{a}_{t<0} = 0$, maintain a finite coupling during $0 < t' < t$, and then make it zero again at $t' > t$. The expectation value of the transverse spin component at the time $t$, found by integrating Eqs. (9),(10), is

$$\langle \sigma_+(t) \rangle \;=\; \langle e^{i\mathcal{H}(\mathbf{q},\mathbf{p}-\mathbf{a})t} e^{-i\mathcal{H}(\mathbf{q},\mathbf{p}+\mathbf{a})t} \rangle_{\rm el} \, \langle \sigma_+(0) \rangle_{\rm spin}, \tag{11}$$

while $\langle \sigma_-(t) \rangle = \langle \sigma_+(t) \rangle^*$. Note that the result of the coupled spin and current evolution factors into a product of quantities that depend

separately on electron dynamics and on the initial state of the spin, as indicated by the subscripts.

The effect of current on spin precession is described by the dependence of the first term in Eq.(11) on the gauge field $\mathbf{a}$. To make contact with the semiclassical dicussion above, let us expand $\mathcal{H}$ in $\mathbf{a}$, assuming it to be small. The result is $\mathcal{H}(\mathbf{q}, \mathbf{p} \pm \mathbf{a}) = \mathcal{H}(\mathbf{q}, \mathbf{p}) \pm \mathbf{a}\mathbf{j}$, where $\mathbf{j}$ is electric current. Substituting this back in Eq.(11) and passing to the interaction representation with respect to the Hamiltonian of fermions uncoupled from the spin, we rewrite the average $\langle ... \rangle_{\rm el}$ in (11) as

$$\left\langle \mathrm{Texp}\left( i \int_t^0 \int \mathbf{a}\mathbf{j}(t') d^3 r\, dt' \right) \mathrm{Texp}\left( -i \int_0^t \int \mathbf{a}\mathbf{j}(t') d^3 r\, dt' \right) \right\rangle_{\rm el} \quad (12)$$

Let us consider a specific form of $\mathbf{a}$, taking it to be a pure gauge, $\oint \mathbf{a} d\mathbf{l} = 0$, within the electron system, and nonzero near a particular surface (e.g. a $\delta-$function on the surface). For a classical current, ignoring noncommutativity of current operators at different times, the expression (12) becomes

$$\left\langle e^{-i\theta(t)} \right\rangle_{\rm el} \quad \text{with} \quad \theta(t) = \lambda \int_0^t I(t') dt'. \quad (13)$$

Here $I(t)$ is the total current through the surface and $\lambda = -2 \int \mathbf{a} d\mathbf{l}$, where the integral is taken across the surface. The form of Eq.(13) agrees with what one expects for the precession phase factor averaged over classical current fluctuations. For $n$ electrons transmitted throught the system during the measurement time, the precession angle is $\theta(t) = \lambda n$. Thus one can relate the average in (13) with the transmitted charge distribution as

$$\left\langle e^{-i\theta(t)} \right\rangle_{\rm el} = \sum_n e^{i\lambda n} p_n \quad (14)$$

The relation with the spin precession in this case can be seen more clearly by combining the result (14) with Eq.(11), which gives

$$\langle \sigma_+(t) \rangle = \sum_n p_n \left( e^{i\lambda n} \langle \sigma_+(0) \rangle_{\rm spin} \right), \quad (15)$$

This way of writing the result of spin evolution confirms the expected relationship between the charge counting probability distribution and the distribution of the spin precession angles.

This discussion clarifies the meaning of the quantity $\langle ... \rangle_{\rm el}$ in Eq.(11), linking it with the counting distribution generating function. Motivated by this, we use this quantity to give a microscopic definition of counting statistics. We rewrite the quantity $\langle ... \rangle_{\rm el}$ as a Keldysh partition function

$$\chi(\lambda) = \left\langle \mathrm{T_K} \exp\left( -i \int_{C_{0,t}} \hat{\mathcal{H}}_\lambda(t') dt' \right) \right\rangle_{\rm el} \quad (16)$$

with the integral taken over the Keldysh time contour $C_{0,t} \equiv [0 \to t \to 0]$, first forward and then backward in time. The counting field $\lambda$ is related to the gauge field $\mathbf{a}$ via $\lambda = \mp\frac{1}{2}\int \mathbf{a}d\mathbf{l}$, where the integration path goes across the region where scattering takes place and noise is generated (e.g. across the barrier in the point contact). The sign $\mp$ indicates that the field $\mathbf{a}$ is antisymmetric on the upper and lower parts of the Keldysh contour. Because of that, even though $\mathbf{a}$ resembles in many ways an ordinary electromagnetic gauge field (allowing for gauge transformations, etc.), it has no such meaning. We emphasize that $\mathbf{a}$ is really an auxiliary field describing coupling with a `virtual`measurement device, such as the spin 1/2 above.

The microscopic formula (16), originating from the analysis of a coupling with spin 1/2, is in fact adequate for any ideal "passive charge detector" without internal dynamics. We shall use this formula below to obtain counting statistics for several physical situations of interest, including tunneling and mesoscopic transport.

This still leaves some questions about universality and limitations of Eq.(16). Nazarov and Kindermann [37] considered a more general scheme of charge detection and recovered the expression (16). Although this is reassuring, Ref.[37] concludes that the detector back action is inevitable. Thus it is still desirable to study more relistic models of noise detection that include conversion of microscopic current noise into electromagnetic field (photons) as well as an amplifier. The electron-to-photon noise conversion was partially addressed by Beenakker and Schomerus [32].

It is also of interest to compare the back action effects in different models. We argue that the above scheme is likely to describe noise measaurement with the least back action, since coupling to the precessing spin 1/2 affects only the phase of electron forward scattering amplitude, without changing scattering probabilities.

### 2.2. Statistics of the tunneling current

The problem of the tunneling current noise provides a simple test for the microscopic formula (16). The starting point of our analysis will be the tunneling Hamiltonian $\hat{\mathcal{H}} = \hat{\mathcal{H}}_1 + \hat{\mathcal{H}}_2 + \hat{V}$, where $\hat{\mathcal{H}}_{1,2}$ describe the leads and $\hat{V} = \hat{J}_{12} + \hat{J}_{21}$ is the tunneling operator. The specific form of the operators $\hat{J}_{12}$, $\hat{J}_{21}$ that describe tunneling of a quasiparticle between the leads will not be important for the most of our discussion. Both the discussion and the results for the tunneling current statistics obtained in this section are valid for a generic interacting many-body system.

The counting field $\mathbf{a}$ in this case can be taken localized on the barrier, entering the Hamiltonian through the phase factors $\exp(\pm i\int \mathbf{a}d\mathbf{l}) =$

$\exp(\pm i\lambda/2)$ of the operators $\hat{J}_{12}$, $\hat{J}_{21}$. The tunneling operator then is

$$\hat{V}_\lambda = e^{\frac{i}{2}\lambda(t)}\hat{J}_{12}(t) + e^{-\frac{i}{2}\lambda(t)}\hat{J}_{21}(t) \tag{17}$$

Here $\lambda(t) = \pm\lambda$ is antisymmetric on the Keldysh contour $C_{0,t}$.

In what follows we compute $\chi(\lambda)$ and establish a relation with the Kubo theorem for the tunneling current [39]. For that, we perform the usual gauge transformation turning the bias voltage into the tunneling operator phase factor as $\hat{J}_{12} \to \hat{J}_{12}e^{-ieVt}$, $\hat{J}_{21} \to \hat{J}_{21}e^{ieVt}$. Passing to the Keldysh interaction representation, we write

$$\chi(\lambda) = \left\langle \mathrm{T_K} \exp\left(-i\int_{C_{0,t}} \hat{V}_{\lambda(t')}(t')dt'\right)\right\rangle \tag{18}$$

Diagrammatically, the partition function (18) is a sum of linked cluster diagrams with appropriate combinatorial factors. To the lowest order in the tunneling operators $\hat{J}_{12}$, $\hat{J}_{21}$ we only need to consider linked clusters of the second order. This gives

$$\chi(\lambda) = e^{W(\lambda)}, \quad W(\lambda) = -\frac{1}{2}\iint_{C_{0,t}} \left\langle \mathrm{T_K}\hat{V}_{\lambda(t')}(t')\hat{V}_{\lambda(t'')}(t'')\right\rangle dt'dt'' \tag{19}$$

This result is correct for the measurement time $t$ much larger than the correlation time in the contacts that determines the characteristic time separation $t' - t''$ at which the correlator in (19) decays.

There are several different contributions to the integral in (19), arising from $t'$ and $t''$ taken on the forward or backward parts of the contour $C_{0,t}$. Evaluating them separately, we obtain

$$\begin{aligned} W(\lambda) = &\int_0^t\int_0^t \left\langle \hat{V}_{-\lambda}(t')\hat{V}_\lambda(t'')\right\rangle dt''dt' \\ &-\int_0^t\int_0^{t'} \left\langle \hat{V}_\lambda(t')\hat{V}_\lambda(t'')\right\rangle dt''dt' - \int_0^t\int_{t'}^t \left\langle \hat{V}_{-\lambda}(t')\hat{V}_{-\lambda}(t'')\right\rangle dt''dt' \end{aligned} \tag{20}$$

We substitute expression (17) in Eq.(20) and average by pairing $\hat{J}_{12}$ with $\hat{J}_{21}$. This gives

$$W(\lambda) = (e^{i\lambda}-1)N_{1\to 2}(t) + (e^{-i\lambda}-1)N_{2\to 1}(t) \tag{21}$$

with

$$N_{1\to 2} = \int_0^t\int_0^t \langle \hat{J}_{21}(t')\hat{J}_{12}(t'')\rangle\, dt'dt'', \tag{22}$$

$$N_{2\to 1} = \int_0^t\int_0^t \langle \hat{J}_{12}(t')\hat{J}_{21}(t'')\rangle\, dt'dt'' \tag{23}$$

where $N_{j\to k}(t) = g_{jk}t$ is the mean charge number transmitted from the contact $j$ to the contact $k$ in a time $t$. Exponentiating Eq.(21) gives nothing but the bidirectional Poisson distribution $\chi_{2P}(\lambda)$ defined by Eq.(8) with the transition rates given by $\bar{n} = N_{1\to 2} = g_{12}t$, $\bar{n}' = N_{2\to 1} = g_{21}t$, respectively.

Eq.(8) yields interesting relations between different statistics of the distribution. The cummulants $\langle\langle \delta n^k \rangle\rangle$, obtained by expanding $\ln \chi_{2P}(\lambda)$ in $\lambda$, are

$$m_k = \langle\langle \delta n^k \rangle\rangle = \begin{cases} (g_{12} - g_{21})t, & k \text{ odd} \\ (g_{12} + g_{21})t, & k \text{ even} \end{cases} \tag{24}$$

Setting $k = 1, 2$ we express $g_{12} \pm g_{21}$ through the time-averaged current and the low frequency noise spectral density[3]:

$$g_{12} - g_{21} = I/q_0, \quad g_{12} + g_{21} = \mathcal{S}_0/2q_0^2 \tag{25}$$

with $q_0$ the tunneling charge. Of special interest for us will be the third correlator of the transmitted charge

$$\langle\langle \delta q^3 \rangle\rangle \equiv \overline{\left(\delta q - \overline{\delta q}\right)^3} \tag{26}$$

For this correlator Eq. (24) gives $\langle\langle \delta q^3 \rangle\rangle = C_3 t$ with the coefficient $C_3$ ("spectral power") related to the current $I$ as

$$C_3 \equiv \langle\langle \delta q^3 \rangle\rangle / t = q_0^2 I \tag{27}$$

We note that the relation (27) holds for the distribution (8) at any ratio $(g_{12} - g_{21})/(g_{12} + g_{21})$ of the mean transmitted charge to the variance.

The quantities (22), (23) have several general properties. First, by writing the expectation values (22), (23) in a basis of exact microscopic states and using the detailed balance relation, we obtain

$$N_{1\to 2}/N_{2\to 1} \equiv g_{12}/g_{21} = \exp(eV/k_{\mathrm{B}}T) \tag{28}$$

where $V$ is the voltage applied between the contacts. Using this result to calculate the ratio of the first and second cummulants, Eq.(25), we have $(g_{12} - g_{21})/(g_{12} + g_{21}) = \tanh(eV/k_{\mathrm{B}}T)$. This gives the noise-current relation

$$\mathcal{S}_0 = 2q_0 \coth(eV/k_{\mathrm{B}}T)\, I \tag{29}$$

that holds for arbitrary $eV/k_{\mathrm{B}}T$. This relation was pointed out by Sukhorukov and Loss [38].

[3] The spectral density of the noise is defined through the symmetrized current correlator as $\mathcal{S}_\omega = \int \left\{\overline{\delta I(t), \delta I(0)}\right\}_+ e^{i\omega t} dt$. At $\omega = 0$, one can thus write $\mathcal{S}_0$ in terms of the variance of charge $q(\tau) = \int_t^{t+\tau} I(t')dt'$ transmitted during a long time $\tau$ as $\mathcal{S}_0 = \frac{2}{\tau}\overline{\delta q^2(\tau)}$.

Also, one can establish a relation of the quantities (22), (23) with the Kubo theorem. We consider the tunneling current operator

$$\hat{\mathcal{I}}(t) = -iq_0 \left( \hat{J}_{12}(t) - \hat{J}_{21}(t) \right). \tag{30}$$

From the Kubo theorem for the tunneling current [39], the mean integrated current $\int_0^t \langle \hat{\mathcal{I}}(t') \rangle dt'$ is

$$q_0 \int_0^t \int_0^t \left\langle \left[ \hat{J}_{21}(t'), \hat{J}_{12}(t'') \right] \right\rangle dt' dt'' = q_0 \left( N_{1\to 2} - N_{2\to 1} \right) \tag{31}$$

By writing $N_{j\to k} = g_{jk} t$, we confirm the first relation (25). To obtain the second relation (25) we consider the variance of the charge transmitted in time $t$. It is given by a time integral of an averaged symmetrized product of two current operators

$$\langle\langle \delta q^2 \rangle\rangle = q_0^2 \int_0^t \int_0^t \left\langle \left\{ \hat{\mathcal{I}}(t'), \hat{\mathcal{I}}(t'') \right\}_+ \right\rangle dt' dt'' \tag{32}$$

The integral in (32) can be rewritten as

$$\int_0^t \int_0^t \left\langle \left\{ \hat{J}_{12}(t'), \hat{J}_{21}(t'') \right\}_+ \right\rangle dt' dt'' = N_{1\to 2} + N_{2\to 1} \tag{33}$$

which immediately leads to the second relation (25).

We conclude that the tunneling current statistics, described by Eq.(8), are simpler than in a generic system. The current-noise relation, typically known in a generic system only at equilibrium (Nyquist) and in the fully out-of-equilibrium (Schottky) regimes, for the tunneling current is given by Eq.(29) at arbitrary $eV/k_{\mathrm{B}}T$.

In contrast, the relation (27) obeyed by the third correlator (4) is completely insensitive to the crossover between the Nyquist and Schottky noise regimes. The meaning of Eq.(27) is similar to that of the Schottky formula $\mathcal{S}_0 = 2\langle\langle \delta q^2 \rangle\rangle = 2q_0 I$. However, the Schottky current-noise relation is valid only when charge flow is unidirectional, i.e. at low temperatures $k_{\mathrm{B}}T \ll eV$, since $g_{12}/g_{21} = \exp(eV/k_{\mathrm{B}}T)$, while Eq.(27) holds at any $eV/k_{\mathrm{B}}T$.

In experiment, when the current-noise relation is used to determine the tunneling quasiparticle charge $q_0$ from the tunneling current noise, it is crucial to maintain low temperature $k_{\mathrm{B}}T \ll eV$. The requirement of a cold sample at a relatively high bias voltage is the origin of a well known difficulty in the noise measurement. In contrast, the relation (27) is not constrained by any requirement on sample temperature.

This property of the third moment, if confirmed experimentally, may prove to be quite useful for measuring quasiparticle charge. In

particular, this applies to the situations when the $I-V$ characteristic is strongly nonlinear, when it is usually difficult to unambiguously interpret the noise versus current dependence as a shot noise effect or as a result of thermal noise generated by non-linear conductance. This appears to be a completely general problem pertinent to any interacting system. Namely, in the systems such as Luttinger liquids, the $I-V$ nonlinearities arise at $eV \geq k_{\mathrm{B}}T$. However, it is exactly this voltage that has to be applied for measuring the shot noise in the Schottky regime.

Finally, we note that the ratio of the third moment to current is temperature-independent only in the tunneling regime. In other situations, such a point contact or a mesoscopic system, this ratio is not universal [34, 35, 36].

### 2.3. Relation to theory of photodetection

Here we discuss a relation of the above to the theory of photon detectors[1, 2]. Due to Bose statistics, photons entering a photo-counter are correlated in time, and this makes the theory of photon detection a problem of many-particle statistics. For a single normal mode of radiation field the probability $P_m$ to count $m$ photons over time $t$ is given by

$$P_m = \frac{(\eta t)^m}{m!} \langle : (a^+ a)^m e^{-\eta t a^+ a} : \rangle \ , \tag{34}$$

where $a^+$ and $a$ are Bose operators of the mode, $\eta$ is the counter efficiency parameter, and $\langle ... \rangle$ stands for the average over a quantum state. The normal ordering $: \ldots :$ is an important element of the formalism. Physically, it means that, after having been detected, each photon is destroyed, e.g., it is absorbed in the detector. Instead of the probabilities (34), it is more convenient to deal with the generating function

$$\chi(\lambda) = \sum_m P_m e^{i\lambda m} \ . \tag{35}$$

For the single normal mode Eq.(34) leads to

$$\chi(\lambda) = \langle : \exp \eta t (e^{i\lambda} - 1) a^+ a : \rangle \ . \tag{36}$$

Eqs.(34,35,36) account very well for numerous experimental situations. Particularly interesting is the case of a coherent state $|\mathrm{z}\rangle$, $a|\mathrm{z}\rangle = z\ |\mathrm{z}\rangle$, where $z$ is a complex number. It corresponds to the radiation field of an ideal laser, and with Eq.(36) one easily gets Poisson counting distribution,

$$P_m = \frac{(Jt)^m}{m!} e^{-Jt}, \qquad J = \eta |z|^2 \ , \tag{37}$$

which describes the so-called minimally bunched light source.

Similar to the photon detection, electric measurement is performed on a system containing an enormous number of particles — in this case fermions — and thus one expects the effects of Fermi statistics to be important. Also, the duration of electric measurement is typically much longer than the time it takes the system to transmit one electron by microscopic tunneling, scattering, or diffusion. Apart from these similarities, there is, however, a crucial difference from the photon counting: the number of electrons is not changed by the current measurement, since electric charge is conserved. This has to be contrasted with absorption of photons in photo-counters. Related to this, there is another important difference: at every detection of a photon, its energy $\hbar\omega$ is taken from the radiation field, which makes plain photodetectors insensitive to zero-point fluctuations of electromagnetic field. On the contrary, the measurement of current fluctuation is usually performed without changing energy of the system, which makes the zero-point noise an unavoidable component of any electric measurement. (Let us emphasize that the difference has nothing to do with the type of quantum statistics, Fermi or Bose. Rather it is the difference between the two kinds of measurement, e.g., see ... where counting of fermions was discussed using an optical-like counter that has to capture an electron in order to detect it.)

## 3. Counting statistics of mesoscopic transport

Here we consider the problem of counting statistics in a mesoscopic transport. From now on we adopt the noninteracting particle approximation and use the scattering approach [40], in which the system is characterized by a single particle scattering matrix. Depending on the nature of the problem, the matrix can be stationary or time-dependent. Even for noninteracting particles the problem of counting statistics remains nontrivial due to correlations between different particles arising from Fermi statistics.

The counting statistics can be analyzed using the microscopic formula (16). However, there is a more efficient way of handling the noninteracting problem. One can obtain a formula for the generating function $\chi(\lambda)$ in terms of a functional determinant that involves the scattering matrix and the density matrix of reservoirs. Then for each particular problem one must analyze and evaluate an appropriate determinant. Although functional determinats can be nontrivial to deal with, this approach is still much simpler than the one based directly on Eq.(16).

### 3.1. Statistics of DC transport

He we discuss the problem of time-independent scattering. We consider a conductor with $m$ scattering channels describing states within one or several current leads. The scattering is elastic and will be charcterized by a $m \times m$ matrix $S$. Although in applications so far the $2 \times 2$ matrices (i.e. two-channel problems) have been more common than larger matrices, the general determinant structure of $\chi(\lambda)$ will be revealed only for matrices of arbitrary size $m$.

In this case one can obtain $\chi(\lambda)$ from a quasiclassical argument. For elastic scattering, particles with different energies contribute to counting statistics independently, and thus one can "symbolically" write

$$\chi(\lambda) = \prod_{\epsilon} \chi_\epsilon(\lambda)\,, \quad \text{i.e.} \quad \chi(\lambda) = \exp\left(t \int \ln \chi_\epsilon(\lambda) \frac{d\epsilon}{2\pi\hbar}\right)\,, \tag{38}$$

where $\chi_\epsilon(\lambda)$ is the contribution of particles with energy $\epsilon$. The factor $2\pi\hbar$ is written based on the quasiclassical phase space volume normalization, $d\mathcal{V} = d\epsilon dt/2\pi\hbar$. The quantity $\chi_\epsilon(\lambda)$ depends on the scattering matrix $S$ and on the energy distribution $n_i(\epsilon)$ in the channels.

To obtain $\chi_\epsilon(\lambda)$ we introduce a vector of counting fields $\lambda_j$, $j = 1, ..., m$, one for each channel, and consider all possible multi-particle scattering processes at fixed energy. The processes can involve any number $k \leq m$ of particles each coming out of one of the $m$ channels and being scatterred into another channel. Since the particles are indistinguishable fermions, no two particles can share an incoming or outgoing channel. One can then write $\chi_\epsilon(\lambda)$ as a sum over all different multiparticle scattering processes:

$$\chi_\epsilon(\lambda) = \sum_{i_1,...,i_k,j_1,...,j_k} e^{\frac{i}{2}(\lambda_{i_1}+...+\lambda_{i_k}-\lambda_{j_1}-...-\lambda_{j_k})} P_{i_1,...,i_k\,|\,j_1,...,j_k}\,, \tag{39}$$

where the rate of $k$ particles transition from channels $i_1, ..., i_k$ into channels $j_1, ..., j_k$ is given by

$$P_{i_1,...,i_k\,|\,j_1,...,j_k} = \left|S^{j_1,...,j_k}_{i_1,...,i_k}\right|^2 \prod_{i \neq i_\alpha} (1 - n_i(\epsilon)) \prod_{i = i_\alpha} n_i(\epsilon)\,. \tag{40}$$

Here $S^{j_1,...,j_k}_{i_1,...,i_k}$ is an antisymmetrized product of $k$ single particle amplitudes, which is nothing but the minor of the matrix $S$ with rows $j_1, ..., j_k$ and columns $i_1, ..., i_k$. The product of $n_i$ and $1 - n_i$ gives the probability to have $k$ particles come out of the channels $i_1, ..., i_k$.

An important insight in the structure of the expression (39) can be obtained by noting that it has a form of a determinant:

$$\chi_\epsilon(\lambda) = \det\left(\hat{1} - \hat{n}_\epsilon + \hat{n}_\epsilon S^{-1}_{-\lambda} S_\lambda\right)\,. \tag{41}$$

Here $\hat{n}_\epsilon$ is a diagonal $m \times m$ matrix of channel occupancy at energy $\epsilon$ and the matrix $S_\lambda$ has matrix elements $e^{\frac{i}{4}(\lambda_j - \lambda_i)} S_{ji}$ with the counting field $\lambda_j$ in the phase factors. To demonstrate that the expressions (39) and (41) are identical one has to expand the determinant (41) and go through a bit of matrix algebra. The formula (41) is particularly useful because, as we shall see below, it can be generalized to a time-dependent problem.

Let us now focus on the simplest case $m = 2$ which describes transport in a point contact, with the two channels corresponding to current leads. The $2 \times 2$ scattering matrix $S$ contains reflection and tranmsmission amplitudes. In this case, since there are only six terms in Eq.(39), the determinat formula (41) is not necessary. In this case Eq.(39) takes the form

$$\begin{aligned}\chi_\epsilon(\lambda) = (1-n_1)(1-n_2) + (|S_{11}|^2 + e^{\frac{i}{2}(\lambda_2-\lambda_1)}|S_{21}|^2)n_1(1-n_2) \\ + (|S_{22}|^2 + e^{\frac{i}{2}(\lambda_1-\lambda_2)}|S_{12}|^2)n_2(1-n_1) + |\det S|^2 n_1 n_2\,, \quad (42)\end{aligned}$$

where the energy dependence of $n_j(\epsilon)$ is suppressed. By using the unitarity relations $|S_{1i}|^2 + |S_{2i}|^2 = 1$, $|\det S| = 1$, Eq.(42) can be simplified:

$$\chi_\epsilon(\lambda) = 1 + p(e^{i\lambda} - 1))n_1(1-n_2) + p(e^{-i\lambda} - 1))n_2(1-n_1) \qquad (43)$$

Here $p = |S_{21}|^2 = |S_{12}|^2$ is the transmission coefficient and $\lambda = \lambda_2 - \lambda_1$. (We denote transmission by $p$ instead of the traditional $t$ to avoid confusion with the measurement time.)

To obtain the full counting statistics integrated over all energies, one has to specify the energy distribution in the leads and use Eq.(38). We consider a barrier with energy-independent transmission and the leads at temperature $T$ biased by voltage $V$. Then $n_{1,2} = n_F(\epsilon \mp eV/2)$ with $n_F$ the Fermi fucntion.

At $T = 0$, since $n_F(\epsilon)$ takes values 0 and 1, for $V > 0$ we have

$$\chi_\epsilon(\lambda) = \begin{cases} e^{i\lambda}p + 1 - p\,, & |\epsilon| < \frac{1}{2}eV \\ 1\,, & |\epsilon| > \frac{1}{2}eV \end{cases} \qquad (44)$$

Doing the integral in Eq.(38) we obtain a binomial distribution $\chi_N(\lambda) = (e^{i\lambda}p + 1 - p)^N$ of the form (6) with the number of attempts $N(t) = eVt/2\pi\hbar$.

This means that, in agreement with intuition, in the energy window $eV$ the transport is just the single particle transmission and reflection, while the states with energies in the Fermi sea, populated in both reservoirs, are noiseless. (At $V < 0$ the result is similar, with $e^{i\lambda}$ replaced by $e^{-i\lambda}$, which corresponds to the DC current sign reversal.)

We note that the noninteger number of attempts $N(t) = eVt/2\pi\hbar$ is an artefact of a quasiclassical calculation. In a more careful analysis the number of attempts is characterized by a narrow distribution $P_N$ peaked at $\overline{N} = N(t)$, and the generating function is a weighted sum $\sum_N P_N \chi_N(\lambda)$. Since the peak width is a sublinear function of the measurement time $t$ (in fact, $\overline{\delta N^2} \propto \ln t$), the statistics to the leading order in $t$ are correctly described by the binomial distribution.

One can also consider the problem at arbitrary $k_{\rm B}T/eV$. The integral in Eq.(38), although less trivial, can still be carried out analytically, giving

$$\chi(\lambda) = \exp\left(-u_+ u_- N_T\right) , \quad N_T = t\, k_{\rm B}T/2\pi\hbar, \tag{45}$$

where

$$u_\pm = v \pm \cosh^{-1}(p\cosh(v+i\lambda) + (1-p)\cosh v), \quad v = eV/2k_{\rm B}T\,. \tag{46}$$

At low temperature $k_{\rm B}T \ll eV$, the expression (45) reproduces the binomial statistics. At low voltage $eV \ll k_{\rm B}T$ (or high temperature) Eq.(45) gives the counting statistics of the equilibrium Nyquist noise:

$$\chi(\lambda) = e^{-\lambda_*^2 N_T} , \qquad \sin(\lambda_*/2) = p^{1/2}\sin(\lambda/2)\ . \tag{47}$$

Interestingly, even at equilibrium the noise is non-gaussian, except for a special case of fully transmitting system, $p = 1$, $\lambda_* = \lambda$, when it is gaussian.

### 3.2. Statistics of time-dependent scattering

The time-dependent scattering problem describes photon-assisted transport. There are two groups of practically interesting problems: the ac-driven systems with static scattering potential, such as tunneling barriers or point contacts in the presence of a microwave field [17, 41], and the electron pumps with time-dependent scattering potential controlled externally, e.g. by gate voltages [42].

Typically, the time of individual particle transit through the scattering region is much shorter than the period at which the system is driven. This situation is described, in the instantaneous scattering approximation, by a time-dependent scattering matrix $S(t)$ that characterizes single particle scattering at time $t$. The question of interest is how Fermi statistics of many-body scattering states affects the counting statistics.

One can construct a theory of counting statistics of time-dependent scattering[19] by generalizing the results of Sec.3.1 for the statistics of a generic time-independent scattering. In particular, the determinant formula (41), along with (38), allows a straightforward extension to the

time-dependent case. In that, the generating function $\chi(\lambda)$ acquires a form of a functional determinant.

Let us consider a scattering matrix $S(t)$ varying periodically in time with the external (pumping) frequency $\Omega$. The analysis is most simple in the frequency representation[19], in which the scattering operator $S$ has off-diagonal matrix elements $S_{\omega',\omega}$ with a discrete frequency change $\omega' - \omega = n\Omega$. In this approach the energy axis is divided into intervals $n\Omega < \omega < (n+1)\Omega$ and each such interval is treated as a separate conduction channel. In doing so it is convenient (and some times necessary) to assign a separate counting field $\lambda_n$ to each frequency channel, so that the counting field may acquire frequency channel index in addition to the conduction channel dependence discussed above (see (41)).

Since the scattering operator conserves energy modulo multiple of $\hbar\Omega$, the scattering is elastic in the extended channel representation, which allows to employ the method of Sec.3.1. Now, we note that the form of the determinat in Eq.(41) is not particularly sensitive to the size of the scattering matrix. Thus one can use it even when the number of channels is infinite, provided that the determinat remains well defined. This procedure brings (41) to the form of a determinant of a matrix with an infinite number of rows and columns. This matrix is then truncated at very high and low frequencies, eliminating empty states and the states deep in the Fermi sea which do not contribute to noise.

Finally, we note that the product rule (38) for $\chi(\lambda)$ at all energies is consistent with the determinant structure, since scattering processes at energies different modulo $n\Omega$ are decoupled. This allows to keep the answer for $\chi(\lambda)$ in the form of the determinant (41), where now the scattering operator $S$ is considered in the entire frequency domain, rather than at discrete frequencies $\omega + n\Omega$. The resulting functional determinant has a simple form in the time representation:

$$\chi(\lambda) = \det\left(\hat{1} + n(t,t')\left(\hat{T}_\lambda(t) - \hat{1}\right)\right), \quad \hat{T}_\lambda(t) = S^\dagger_{-\lambda}(t) S_\lambda(t), \quad (48)$$

where $(S_\lambda)_{ji} = e^{\frac{i}{4}(\lambda_j - \lambda_i)} S_{ji}$ as above, and $\hat{n}$ is the density matrix of reservoirs. The operator $\hat{n}$, diagonal in the channel index, is given by

$$n_j(t,t') = \int n_j(\hbar\omega)\, e^{i\omega(t'-t)}\, d\omega/2\pi \quad (49)$$

In general $\hat{n}$ depends on the energy distribution parameters, such as temperature and bias voltage. In equlibrium, at finite $T$ and $V$, by taking Fourier transform of a Fermi function $n_F(\epsilon - eV)$, one obtains

$$n(t,t') = \frac{e^{-i\frac{e}{\hbar}V(t-t')}}{2\beta \sinh(\pi(t-t'+i\delta)/\beta)}, \quad \beta = \hbar/k_{\mathrm{B}}T \quad (50)$$

In equilibrium, at $T = 0$, $V = 0$, this gives $n(t, t') = i/(2\pi(t - t' + i\delta))$. The result (48) holds for an arbitrary (even nonequilibrium) energy distribution in reservoirs.

The functional determinant of an infinite matrix (48) should be handled carefully. One can show that, in a mathematical sense, the quantity (48) is well defined. For the states with energies deep in the Fermi sea, $\hat{n} = 1$ and, since $\det\left(\hat{T}_\lambda(t)\right) = 1$ due to unitarity of $S$, these states do not contribute to the determinant (48). Similarly, since $\hat{n} = 0$ for the states with very high energy, these states also do not affect the determinant. Effectively, the determinant is controlled by a group of states near the Fermi level, in agreement with intuition about transport in a driven system. The absence of ultraviolet divergences allows one to go freely between different representations, e.g. to switch from the frequency domain to the time domain, which facilitates calculations[24, 21].

The above derivation of the formula (48) based on a generalization of the result (41) for time-independent scattering might seem not entirely rigorous. A more mathematically sound derivation that starts directly from the microscopic expression (16) was proposed recently by Klich [43].

### 3.3. Case studies

Here we briefly review the time-dependent scattering problems for which the counting statistics have been studied. From several examples for which $\chi(\lambda)$ has been obtained it appears that the problem does not allow a general solution. Instead, the problem can be handled only for suitably chosen form of the time dependence $S(t)$.

In Ref.[19] a two channel problem was considered with $S(t)$ of the form

$$S(\tau) \equiv \begin{pmatrix} r & t' \\ t & r' \end{pmatrix} = \begin{pmatrix} B + be^{-i\Omega\tau} & \bar{A} + \bar{a}e^{i\Omega\tau} \\ A + ae^{-i\Omega\tau} & -\bar{B} - \bar{b}e^{i\Omega\tau} \end{pmatrix} \tag{51}$$

which is unitary for $|A|^2 + |a|^2 + |B|^2 + |b|^2 = 1$, $A\bar{a} + B\bar{b} = 0$. The problem was solved by using the extended channel representation in the frequency domain, in which each frequency interval $n\Omega < \omega < (n+1)\Omega$ is treated as a separate scattering channel, as discussed above.

For the reservoirs at zero temperature and without bias voltage the charge distribution for $m$ pumping cycles is described by

$$\chi(\lambda) = \left(1 + p_1(e^{i\lambda} - 1) + p_2(e^{-i\lambda} - 1)\right)^m \tag{52}$$

with $p_1 = |a|^4/(|a|^2 + |b|^2)$ and $p_2 = |b|^4/(|a|^2 + |b|^2)$. This result means that at each pumping cycle one electron is pumped in one direction

with probability $p_1$, or in the opposite direction with probability $p_2$, or no charge is pumped with probability $1 - p_1 - p_2$. The multiplicative dependence of $\chi(\lambda)$ on the number of pumping cycles $m$ means that the outcomes of different cycles are statistically independent. One can thus view (52) as a generalization of the binomial distribution (6).

**Results at finite bias voltage**

**Mesoscopic pumping**

Another kind of time-dependent problems for which solution can be obtained in a closed form is mesoscopic transport in the presence of an AC voltage[24]. The scatterer in this case is a time independent $2 \times 2$ matrix, while the voltage $V(t)$ contributes a phase factor to the density matrix in (48):

$$n_{1,2}(t,t') = e^{\pm\frac{i}{2}(\varphi(t')-\varphi(t))} n_{1,2}^{(0)}(t,t'), \quad \dot{\varphi}(t) = \tfrac{e}{\hbar} V(t) \tag{53}$$

(compare this with the formula (50) for constant bias voltage).

The counting distribution (48) for a family of such problems has been studied in Ref.[21]. It was noted earlier[44] that noise is minimized at fixed transmitted charge for a special form of time-dependent voltage:

$$V(t) = \frac{h}{e} \sum_{k=1,\ldots,m} \frac{2\tau_k}{(t-t_k)^2 + \tau_k^2} \tag{54}$$

Each of the Lorentzian voltage pulses (54) corresponds to a $2\pi$ phase change in $\varphi(t)$. Interestingly, the noise-minimizing pulses (54) have large degeneracy: they produce noise which is insensitive to the pulses' widths $\tau_k$ and peak positions $t_k$. This calls for an interpretation of the pulses (54) as independent attempts to transmit charge. Not surprisingly, the counting statistics for such pulses was found to be binomial:

$$\chi(\lambda) = (1 + t(e^{i\lambda} - 1))^m \tag{55}$$

with $t$ the transmission constant. The lowest possible noise for a current pumped by voltage pulses is thus equal to that of a DC current with the same transmitted charge.

The method of Ref.[21] also allows to find the distribution for an arbitrary sum of the pulses (54) with alternating signs. For example, two opposite pulses

$$V(t) = \frac{h}{e} \left( \frac{2\tau_1}{(t-t_1)^2 + \tau_1^2} - \frac{2\tau_2}{(t-t_2)^2 + \tau_2^2} \right) \tag{56}$$

give rise to the counting distribution

$$\chi(\lambda) = 1 - 2F + F(e^{i\lambda} + e^{-i\lambda}), \quad F = t(1-t) \left| \frac{z_1^* - z_2}{z_1 - z_2} \right|^2 \tag{57}$$

with $z_{1,2} = t_{1,2} + i\tau_{1,2}$. The quantity $|...|^2$ is a measure of pulses' overlap in time, varying between 0 for a full overlap and 1 for no overlap. For nonoverlapping pulses $\chi(\lambda)$ factors as $(t\,e^{i\lambda} + 1 - t)(t\,e^{-i\lambda} + 1 - t)$, in agreement with the interpretation of a binomial distribution for independent attempts

### 3.4. Mesoscopic pumping

A DC current in a mesoscopic system, such as an open quantum dot, can be induced by pumping, i.e. by modulating its area, shape, or other parameters[45, 47, 46]. After pumping was demonstrated experimentally[42], it become a popular subject mesoscopic transport literature (for references we refer to [48]). In particular, Brouwer made an interesting observation that time averaged pumped current is a purely geometric property of the path in the scattering matrix parameter space, insensitive to path parameterization.

Transport through a mesoscopic is described[40] by a scattering matrix $S$ which depends on externally driven parameters and varies cyclically with time. The matrix $S(t)$ defines a path in the space of all scattering matrices. For a system with $m$ scattering channels, the matrix space is the group $U(m) = SU(m) \times U(1)$. In an experiment one can, in principle, realize any path in the space of scattering matrices.

Counting distribution for a parametrically driven open system was discussed by Andreev and Kamenev who adapted the results [19] obtained for specific pumping cycles (see Sec.3.3). However, since the relation between the path in the scattering matrix space and the external pumping parametrs is generally unknown, only the results valid for generic paths are of interest in this problem.

Here we consider the weak pumping regime, when the path $S(t)$ is an arbitrary small loop, and show that in this case the counting distribution is universal [22], having the form of bidirectional Poisson distribution (8). From that, we obtain the dependence of the noise on the amplitude and relative phase of the voltages driving the pump.

Before turning to the calculation, we discuss general dependence of counting statistics on the path in matrix space. Different paths $S(t)$, in principle, give rise to different current and noise. However, there is a remarkable property of invariance with respect to group shifts. Any two paths,

$$S(t) \quad \text{and} \quad S'(t) = S(t)S_0, \tag{58}$$

where $S_0$ is a time-independent matrix in $U(m)$, give rise to the same counting statistics at zero temperature. We note that only the right shifts of the form (58) leave counting statistics invariant, whereas the left shifts generally change it. One can explain the result (58) qual-

itatively as follows. The change of scattering matrix, $S(t) \to S'(t) = S(t)S_0$, is equivalent to replacing states in the incoming scattering channels by their superpositions $\psi^\alpha = S^\alpha_{0\beta}\psi^\beta$. At zero temperature, however, Fermi reservoirs are noiseless and also such are any their superpositions. Correlation between superposition states of noiseless reservoirs is negligible, because all current fluctuations arise only during time-dependent scattering. Therefore, noise statistics remain unchanged. A simple formal proof of the result (58) is given below.

For a weak pumping field we shall evaluate (48) in the time domain by expanding $\ln\det(...)$ in powers of $\delta S$ and keeping non-vanishing terms of lowest order. In doing so, however, we preserve full functional dependence on $\lambda$ which gives all moments of counting statistics. We write $S(t) = e^{A(t)}S^{(0)}$ with antihermitian $A(t)$ representing small perturbation, $\mathrm{tr}A^\dagger A \ll 1$. Here $S^{(0)}$ is scattering matrix of the system in the absence of pumping. Substituting this into (48) one obtains

$$\hat{T}_\lambda(t) \equiv \hat{T}^{(0)}_\lambda + \delta T_\lambda(t) = S^{(0)\dagger}_{-\lambda} e^{-A_{-\lambda}(t)} e^{A_\lambda(t)} S^{(0)}_\lambda \tag{59}$$

with $\hat{T}^{(0)}_\lambda = S^{(0)\dagger}_{-\lambda} S^{(0)}_\lambda$ and $A_\lambda(t) = e^{i\frac{\lambda}{4}\sigma_3} A(t) e^{-i\frac{\lambda}{4}\sigma_3}$. Now, we expand (48):

$$\ln\chi(\lambda) = \ln\det Q_0 + \mathrm{tr}R - \frac{1}{2}\mathrm{tr}R^2 + \frac{1}{3}\mathrm{tr}R^3 - ... \tag{60}$$

where $Q_0 = 1 + \hat{n}(\hat{T}^{(0)}_\lambda - 1)$ and $R = Q_0^{-1}\hat{n}\delta T_\lambda$. At zero temperature, from $\hat{n}^2 = \hat{n}$ it follows that $\det Q_0 = 1$ and $R = S^{(0)\,-1}_\lambda \hat{n}\left(e^{-A_{-\lambda}(t)}e^{A_\lambda(t)} -1\right) S^{(0)}_\lambda$. Therefore,

$$\ln\chi(\lambda) = \mathrm{tr}\ \hat{n}\hat{M} - \frac{1}{2}\mathrm{tr}(\hat{n}\hat{M})^2 + \frac{1}{3}\mathrm{tr}(\hat{n}\hat{M})^3 - ... \tag{61}$$

where $\hat{M} = e^{-A_{-\lambda}(t)}e^{A_\lambda(t)} - 1$. Note that at this stage there is no dependence left on the constant matrix $S^{(0)}$, which proves the invariance under the group shifts (58).

We need to expand (61) in powers of the pumping field, which amounts to taking the lowest order terms of the expansion in powers of the matrix $A(t)$. One can check that the two $\mathcal{O}(A)$ terms arising from the first term on the RHS of (61) vanish. The $\mathcal{O}(A^2)$ terms arise from the first and second term in (61) and have the form

$$\ln\chi = \frac{1}{2}\mathrm{tr}\left(\hat{n}\left(A^2_{-\lambda} + A^2_\lambda - 2A_{-\lambda}A_\lambda\right)\right) - \frac{1}{2}\mathrm{tr}(\hat{n}B_\lambda)^2 \tag{62}$$

with $B_\lambda(t) = A_\lambda(t) - A_{-\lambda}(t)$. At zero temperature, by using $\hat{n}^2 = \hat{n}$, one can bring (62) to the form

$$\frac{1}{2}\,\mathrm{tr}\ (\hat{n}\,[A_\lambda, A_{-\lambda}]) + \frac{1}{2}\left(\mathrm{tr}\left(\hat{n}^2 B^2_\lambda\right) - \mathrm{tr}(\hat{n}B_\lambda)^2\right) \tag{63}$$

The first term of (63) has to be regularized in the Schwinger anomaly fashion, by splitting points, $t', t'' = t \pm \epsilon/2$, which gives

$$\frac{1}{2}\oint n(t',t'')\mathrm{tr}\left(A_{-\lambda}(t'')A_{\lambda}(t') - A_{\lambda}(t'')A_{-\lambda}(t')\right)dt \tag{64}$$

Averaging over small $\epsilon$ can be achieved either by inserting in (64) additional integrals over $t'$, $t''$, or simply by replacing $A_\lambda(t) \to \frac{1}{2}\left(A_\lambda(t) + A_\lambda(t')\right)$, etc. After taking the limit $\epsilon \to 0$, Eq.(64) becomes

$$\frac{i}{8\pi}\oint \mathrm{tr}\left(A_{-\lambda}\partial_t A_\lambda - A_\lambda \partial_t A_{-\lambda}\right)dt \tag{65}$$

The second term of (63) can be written as

$$\frac{1}{4(2\pi)^2}\oint\oint \frac{\mathrm{tr}\left(B_\lambda(t) - B_\lambda(t')\right)^2}{(t-t')^2}dtdt' \tag{66}$$

Now, we decompose $A = a_0 + z + z^\dagger$, so that $[\sigma_3, a_0] = 0$, $[\sigma_3, z] = -2z$, $\left[\sigma_3, z^\dagger\right] = 2z^\dagger$. Then

$$A_\lambda \equiv e^{-i\frac{\lambda}{4}\sigma_3}Ae^{i\frac{\lambda}{4}\sigma_3} = a_0 + e^{i\frac{\lambda}{2}}z^\dagger + e^{-i\frac{\lambda}{2}}z \tag{67}$$

$$B_\lambda = \left(e^{i\frac{\lambda}{2}} - e^{-i\frac{\lambda}{2}}\right)W, \quad W \equiv z^\dagger - z \tag{68}$$

Substituting this into (65) and (66) one finds that in terms of $W(t)$ these two expressions become

$$\frac{\sin\lambda}{8\pi}\oint \mathrm{tr}\left([\sigma_3, W]\,\partial_t W\right)dt \tag{69}$$

and

$$\frac{(1-\cos\lambda)}{2(2\pi)^2}\oint\oint \frac{\mathrm{tr}\left(W(t) - W(t')\right)^2}{(t-t')^2}dtdt' \tag{70}$$

Hence the counting distribution for one pumping cycle is

$$\chi(\lambda) = exp\left(u(e^{i\lambda} - 1) + v(e^{-i\lambda} - 1)\right) \tag{71}$$

with the average current per cycle $I = e(u - v)$ and the transmitted charge variance $J = e^2(u + v)$ (see Sec.2.2).

Eq.(69) is essentially identical to the result obtained by Brouwer for average pumped current[47]. The integral in (69) is invariant under reparameterization, and thus has a purely geometric character determined by the contour $S(t)$ in $U(m)$.

The parameters $u$ and $v$ in (71) can be expressed through $z(t)$ and $z^\dagger(t)$ as follows. Let us write $z(t)$ as $z_+(t) + z_-(t)$, where $z_+(t)$ and

$z_-(t)$ contain only positive or negative Fourier harmonics, respectively. Then

$$u = \frac{i}{4\pi} \oint \mathrm{tr} \left( z_-^\dagger \partial_t z_+ - z_+ \partial_t z_-^\dagger \right) dt = \sum_{\omega>0} \omega \ \mathrm{tr} z_{-\omega}^\dagger z_\omega, \tag{72}$$

$$v = \frac{i}{4\pi} \oint \mathrm{tr} \left( z_- \partial_t z_+^\dagger - z_+^\dagger \partial_t z_- \right) dt = - \sum_{\omega<0} \omega \ \mathrm{tr} z_{-\omega}^\dagger z_\omega \tag{73}$$

Note that $u \geq 0$ and $v \geq 0$. It is straightforward to show that (69) equals $i \sin \lambda (u - v)$, whereas (70) equals $(\cos \lambda - 1)(u + v)$.

Now we consider a single channel pump, $S(t) \in U(2)$. In this case, $z$ and $z^\dagger$ are complex numbers. For harmonic driving signal, without loss of generality, one can write

$$z(t) = z_1 V_1 \cos(\Omega t + \theta) + z_2 V_2 \cos(\Omega t), \tag{74}$$

where $V_{1,2}$ are pumping signal amplitudes, and complex parameters $z_{1,2}$ depend on microscopic details. From (72) we find the Poisson rates

$$u = \frac{1}{4} \left| z_1 V_1 e^{i\theta} + z_2 V_2 \right|^2, \ v = \frac{1}{4} \left| z_1 V_1 e^{-i\theta} + z_2 V_2 \right|^2 \tag{75}$$

Note that $u$ and $v$ vanish at particular signal amplitudes ratio $V_1/V_2$ and phase $\theta$. Once the two Poisson processes (71) are reduced to one, the current to noise ratio gives elementary charge, $I/J = \pm e^{-1}$. This happens at the extrema of $I/J$ as a function of $w = (V_1/V_2)e^{i\theta}$, for (75) reached at $w = -z_2/z_1, \ -\bar{z}_2/\bar{z}_1$.

Reducing the counting statistics (71) to purely Poissonian by varying pumping signal parameters, in principle, is possible for any number of channels $n$. However, since the number of parameters to be tuned is $2n^2$, this method is practical perhaps only for small channel numbers. Although the method is demonstrated for non-interacting fermions, we argue that it can be applied to interacting systems as well. Poisson statistics result from the absence of correlations of subsequently transmitted particles, which must be the case in any system at small pumping current. Using the dependence of Poisson rates $u$, $v$ on the driving signal to maximize $I/J$ allows to eliminate one of the two Poisson processes (71) and then obtain charge quantum in the standard way as $e = J/I$.

To summarize the results of this section, in the weak pumping regime the distribution of charge transmitted per cycle is of bidirectional Poisson form (8), i.e., it is fully characterized by only two parameters, average current and noise. The current to noise ratio $I/J$, scaled by elementary charge, varies between 1 and $-1$, depending on the relation between driving signals phases and amplitudes.

Thus the quantity $\max(|I|/J)$ gives the inverse of elementary charge without any fitting parameters. Polianski et al. [48] recently studied the dependence of $I/J$ on mesoscopic scattering ensemble parameters, and found that, within the random matrix theory, the nearly extremal values close to $\pm 1$ can be reached with finite probablity. This can make it possible to use noise in a pump to measure quasiparticle charge in open systems, such as Luttinger liquids.

## References


1. Mandel, L. and Wolf, E. (1995) *Optical Coherence and Quantum Optics*, Cambridge University Press, Cambridge
2. Glauber, R.J. (1963) Photon Correlations, *Phys. Rev. Lett.* **10**, pp. 84–86; The Quantum Theory of Optical Coherence, *Phys. Rev.* **130**, pp. 2529–2539
3. Lesovik, G.B. (1989) Excess Quantum Shot Noise in 2D Ballistic Point Contacts, *JETP Lett.*, **49**, pp. 592–594
4. Khlus, V.A. (1987) Current and Voltage Fluctuations in Microjunctions of Normal and Superconducting Metals, *Sov. Phys. JETP*, **66**, pp. 1243–?? [in Russian: *ZhETF*, **93** (6): 2179-2190 (1987)]
5. Büttiker, M. (1990) Scattering Theory of Thermal and Excess Noise in Open Conductors, *Phys. Rev. Lett.*, **65**, pp. 2901–2904
6. Beenakker, C.W.J. and Büttiker, M. (1992) Suppression of shot noise in metallic diffusive conductors, *Phys. Rev. B*, **46**, pp. 1889–1892
7. Kane, C.L. and Fisher, M.P.A. (1994) Nonequilibrium Noise and Fractional Charge in the Quantum Hall Effect, *Phys. Rev. Lett.*, **72**, pp. 724–727
8. Blanter, Ya.M. and Büttiker, M. (2000) Shot Noise in Mesoscopic Conductors, *Phys. Rep.* **336**, pp. 2-166
9. Reznikov, M., Heiblum, M., Shtrikman, H. and Mahalu, D. (1995) Temporal Correlation of Electrons: Suppression of Shot Noise in a Ballistic Quantum Point Contact, *Phys. Rev. Lett.*, **75**, pp. 3340–3343
10. Kumar, A., Saminadayar, L., Glattli, D.C., Jin, Y. and Etienne, B. (1996) Experimental Test of the Quantum Shot Noise Reduction Theory, *Phys. Rev. Lett.*, **76**, pp. 2778–2781
11. de-Picciotto, R., Reznikov, M., Heiblum, M., Umansky, V. Bunin, G. and Mahalu, D. (1997) Direct Observation of a Fractional Charge, *Nature*, **389**, pp. 162–164
12. Saminadayar, L., Glattli, D.C., Jin, Y. and Etienne, B. (1997) Observation of the *e/3* Fractionally Charged Laughlin Quasiparticles, *Phys. Rev. Lett.*, **79**, pp. 2526–2529
13. Reznikov, M., de-Picciotto, R., Griffiths, T.G., Heiblum, M. and Umansky, V. (1999) Observation of Quasiparticles with One-Fifth of an Electron's Charge, *Nature*, **399**, pp. 238–241
14. Griffiths, T.G., Comforti, E., Heiblum, M., Stern, A., Umansky, V. (2000) Evolution of Quasiparticle Charge in the Fractional Quantum Hall Regime, *Phys. Rev. Lett.*, **85**, pp. 3918–3921
15. Steinbach, A.H., Martinis, J.M., Devoret, M.H. (1996) Observation of Hot-Electron Shot Noise in a Metallic Resistor, *Phys. Rev. Lett.*, **76**, pp. 3806-3809

16. Schoelkopf, R.J., Burke, P.J., Kozhevnikov, A.A. and Prober, D.E. (1997) Frequency dependence of shot noise in a diffusive mesoscopic conductor, *Phys. Rev. Lett.*, **78**, pp. 3370–3373
17. Schoelkopf, R.J., Kozhevnikov, A.A., Prober, D.E. and Rooks, M. (1998) Observation of "Photon-Assisted" Shot Noise in a Phase-Coherent Conductor, *Phys. Rev. Lett.*, **80**, pp. 2437–2440
18. Levitov, L.S. and Lesovik, G.B. (1993) Charge Distribution in Quantum Shot Noise, *JETP Lett.*, **58**, pp. 230–235
19. Ivanov, D.A. and Levitov, L.S. (1993) Statistics of Charge Fluctuations in Quantum Transport in an Alternating Field, *JETP Lett.*, **58**, pp. 461–468
20. Levitov, L.S. and Lesovik, G.B. (1994) Quantum Measurement in Electric Circuit, cond-mat/9401004, unpublished
21. Ivanov, D.A., Lee, H.W., Levitov, L.S. (1997) Coherent States of Alternating Current, *Phys. Rev.*, B**56**, pp. 6839–6850
22. Levitov, L.S. (2001) Counting Statistics of Charge Pumping in an Open System, cond-mat/0103617, unpublished
23. Lee, H.W., Levitov, L.S. and Yakovets, A.Yu. (1995) Universal Statistics of Transport in Disordered Conductors" *Phys. Rev. B*, **51**, pp. 4079–4083
24. Levitov, L.S., Lee, H.W. and Lesovik, G.B. (1996) Electron counting statistics and coherent states of electric current," *J. of Math. Phys.*, **37**, pp. 4845–4866
25. Nazarov, Yu.V. (1999) Universalities of Weak Localization, *Ann. Phys. (Leipzig)*, **8**, SI-193; see also: cond-mat/9908143
26. Nazarov, Yu.V. and Bagrets, D.A. (2002) Circuit Theory for Full Counting Statistics in Multi-Terminal Circuits, *Phys. Rev. Lett.*, **88**, pp. 196801-196804
27. Muzykantskii, B.A. and Khmelnitskii, D.E. (1994) Quantum Shot Noise in a NS Point Contact, *Phys. Rev. B*, **50**, pp. 3982–5483
28. Belzig, W. and Nazarov, Yu.V. (2001) Full Current Statistics in Diffusive Normal-Superconductor Structures, *Phys. Rev. Lett.*, **87**, pp. 067006–067009
29. Andreev, A.V. and Kamenev, A. (2000) Counting Statistics of an Adiabatic Pump, *Phys. Rev. Lett.*, **85**, pp. 1294–1297
30. Taddei, F. and Fazio, R. (2002) Counting Statistics for Entangled Electrons, *Phys. Rev. B*, **65**, pp. 075317–075323
31. Bagrets, D.A. and Nazarov, Yu.V. (2002) Full Counting Statistics of Charge Transfer in Coulomb Blockade Systems, cond-mat/0207624
32. Beenakker, C.W.J. and Schomerus, H. (2001) Counting Statistics of Photons Produced by Electronic Shot Noise, *Phys. Rev. Lett.* **86**, pp. 700–703
33. Kindermann, M., Nazarov, Yu.V. and Beenakker, C.W.J. (2002) Manipulation of photon statistics of highly degenerate chaotic radiation, *Phys. Rev. Lett.*, **88**, pp. 063601–063604
34. Levitov, L.S. and Reznikov, M. (2001) Electron Shot Noise Beyond the Second Moment cond-mat/0111057, unpublished
35. Gutman, D.B. and Gefen, Y. (2002) Shot Noise at High Temperatures, cond-mat/0201007
36. Nagaev, K.E. (2002) Cascade Boltzmann-Langevin Approach to Higher-Order Current Correlations in Diffusive Metal Contacts, cond-mat/0203503
37. Nazarov, Yu.V. and Kindermann, M. (2001) Full Counting Statistics of a General Quantum Mechanical Variable, condmat/0107133
38. Sukhorukov, E. V. and Loss, D. (2001) Shot noise of weak cotunneling current: Non-equilibrium fluctuation-dissipation theorem, in: "Electronic Correlations: From meso- to nano-physics", edited by G. Montambaux and T. Martin, XXXVI Rencontres de Moriond; also: cond-mat/0106307

39. Mahan, G.D. (1981) *Many-Particle Physics*, Sec. 9.3. Plenum Press, New York
40. Beenakker, C.W.J. (1997) Random-matrix theory of quantum transport, *Rev. Mod. Phys.* **69**, pp. 731–808
41. Glattli D.C., Jin, Y., Reydellet, L.-H. and Roshe, P. (2002) Photo-Assisted Noise in Quantum Point Contacts, this volume
42. Switkes, M., Marcus, C.M., Campman, K. and Gossard, A.C. (1999) An Adiabatic Quantum Electron Pump, *Science* **283**, pp. 1905–1908
43. Klich, I. (2002) Full Counting Statistics, this volume
44. Lee, H.W. and Levitov, L.S. (1995) Estimate of Minimal Noise in a Quantum Conductor, preprint cond-mat/9507011, unpublished
45. Spivak, B. Zhou, F. and Beal Monod, M.T. (1995) Mesoscopic Mechanisms of the Photovoltaic Effect and Microwave Absorption in Granular Metals, *Phys. Rev. B* **51**, pp. 13226–13230
46. Altshuler, B.L. and Glazman, L.I. (1999) Condensed matter physics – Pumping electrons, *Science* **283**, pp. 1864–1865
47. Brouwer, P.W. (1998) Scattering approach to parametric pumping, Phys. Rev. **B58**, pp. 10135–10138
48. Polianski, M. L., Vavilov, M.G., Brouwer, P.W. (2002) Noise through Quantum Pumps, *Phys. Rev. B* **65**, pp. 245314–245322

# Coulomb blockade and Kondo effect in quantum dots

L.I. Glazman[1] and M. Pustilnik[2]
[1] *Theoretical Physics Institute, University of Minnesota, Minneapolis, MN 55455*
[2] *School of Physics, Georgia Institute of Technology, Atlanta, GA 30332*

**Abstract.** We review the mechanisms of low-temperature electron transport across a quantum dot weakly coupled to two conducting leads. Conduction in this case is controlled by the interaction between electrons. At temperatures moderately lower than the single-electron charging energy of the dot, the linear conductance is suppressed by the Coulomb blockade. Upon further lowering of the temperature, however, the conductance may start to increase again due to the Kondo effect. This increase occurs only if the dot has a non-zero spin $S$. We concentrate on the simplest case of $S = 1/2$, and discuss the conductance across the dot in a broad temperature range, which includes the Kondo temperature. Temperature dependence of the linear conductance in the Kondo regime is discussed in detail. We also consider a simple (but realistic) limit in which the differential conductance at a finite bias can be fully investigated.

## 1. Introduction

In this review, we define a quantum dot as a small paddle of electron liquid which is attached by tunnel junctions to two massive conductors (leads). The number of electrons on the dot in equilibrium $N$ can be controlled by varying the voltage applied to a gate – an auxiliary electrode coupled to the dot only capacitively (no tunneling occurs between the dot and gate). If the conductances of the lead-dot junctions are small compared to the conductance quantum $e^2/h$, and if the temperature $T$ is low enough, then $N$ is an integer at almost any gate voltage $V_g$. Exceptions are small intervals around the discrete set of values of $V_g$, at which an addition of a single electron to the dot does not change the electrostatic energy. Such a degeneracy between different charge states of a quantum dot allows for an activationless electron transfer through it, whereas for all other values of $V_g$ the activation energy for the conductance $G$ across the dot is finite. The resulting oscillatory dependence $G(V_g)$ is the hallmark of the Coulomb blockade phenomenon [1]. The contrast between the low- and high-conductance regions (Coulomb blockade valleys and peaks, respectively) gets sharper at lower temperatures. The described pattern of the $G(V_g, T)$ dependence is clearly observed down to the lowest attainable temperatures in experiments on tunneling through small metallic islands [2] However,



*R. Fazio et al. (eds.), New Directions in Mesoscopic Physics,* 93–115.
© 2003 *Kluwer Academic Publishers. Printed in the Netherlands.*

small quantum dots formed in GaAs heterostructures display a different behavior [3]: in some Coulomb blockade valleys the dependence $G(T)$ is not monotonic and has a minimum at a finite temperature. This minimum is similar in origin [4] to the well-known non-monotonic temperature dependence of the resistivity of a metal containing magnetic impurities [5] – the Kondo effect.

We present here an introduction to the theory of Kondo effect in quantum dots, concentrating on the so-called Constant Interaction Model. Despite its simplicity, the model allows one to describe the main conduction mechanisms, including the most important version of the Kondo effect in quantum dots.

## 2. Constant Interaction Model

The Hamiltonian of interacting electrons confined to a quantum dot has the following general form:

$$\hat{H}_{dot} = \sum_{ij;s} \mathcal{H}_{ij} d^\dagger_{is} d_{js} + \frac{1}{2} \sum_{ss'} \sum_{ijkl} \mathcal{H}_{ijkl} d^\dagger_{is} d^\dagger_{js'} d_{ks'} d_{ls}. \tag{1}$$

Here an operator $d^\dagger_{is}$ creates an electron with spin $s$ in the orbital state $\phi_i(\mathbf{r})$; $\mathcal{H}_{ij} = \mathcal{H}^*_{ji}$ is an Hermitian matrix describing the single-particle spectrum, and the matrix elements $\mathcal{H}_{ijkl}$ depend on the electron-electron interaction potential $V(\mathbf{r}_1 - \mathbf{r}_2)$ and on the chosen basis of orbital states:

$$\mathcal{H}_{ijkl} = \int d\mathbf{r}_1 d\mathbf{r}_2 V(\mathbf{r}_1 - \mathbf{r}_2) \phi_i(\mathbf{r}_1) \phi_j(\mathbf{r}_2) \phi^*_k(\mathbf{r}_2) \phi^*_l(\mathbf{r}_1). \tag{2}$$

Further simplification of the Hamiltonian (1) is possible if the following conditions are met:
(i) the electron-electron interaction within the dot is not too strong (the gas parameter characterizing the electron-electron interaction in a non-ideal Fermi gas $r_s \lesssim 1$) so that the Fermi liquid description is applicable;
(ii) the quasiparticle spectrum is not degenerate near the Fermi energy (which is satisfied, in general, if the motion of electrons within the dot is chaotic);
(iii) the dot is in the metallic regime, *i.e.* the Thouless energy of the dot $E_T$ exceeds the mean single-particle level spacing $\delta E$.

The Thouless energy $E_T$ is well-defined if the electron motion within it is chaotic due to either disorder or irregular shape of the dot. For a dot of linear size $L$ it equals

$$E_T \simeq \begin{cases} \hbar D/L^2, & l \ll L \\ \hbar v_F/L, & l \gg L \end{cases}, \tag{3}$$

where $l$ if the elastic mean free path and $D$ is the diffusion constant in a disordered dot. The average level spacing $\delta E$ can be estimated as

$$\delta E \simeq 1/\nu_d L^d. \tag{4}$$

Here $d$ is the dimensionality of the system ($d = 2$ for a quantum dot formed in a two-dimensional electron gas in a semiconductor heterostructure, and $d = 3$ for a metallic nanoparticle); $\nu_d$ is the density of states of the material. For a ballistic electron motion ($l \gg L$) the ratio

$$E_T/\delta E \sim L/\lambda_F \sim N^{1/d}$$

is large for large number of electrons $N$ on the dot.

If the conditions (i)-(iii) are met, then the Random Matrix Theory (RMT) is a good starting point for describing non-interacting quasiparticles, see [6] for a review; the matrix elements $\mathcal{H}_{ij}$ belong to a Gaussian ensemble [7]. The matrix elements do not depend on spin, and therefore each eigenvalue $\epsilon_n$ of the matrix $\mathcal{H}_{ij}$ represents a spin-degenerate energy level. The spacings $|\epsilon_{n+1} - \epsilon_n|$ between consecutive levels obey the Wigner-Dyson distribution [7]; the average value of $|\epsilon_{n+1} - \epsilon_n|$ is $\delta E$.

It turns out [8] that the vast majority of the matrix elements $\mathcal{H}_{ijkl}$ are small. In the limit $E_T/\delta E \to \infty$, only relatively few "most diagonal" elements remain finite. In this limit the interaction part $H_{int}$ of the Hamiltonian of a non-superconducting dot may be cast in the form [9]:

$$\hat{H}_{int} = E_C \left(\hat{N} - \mathcal{N}\right)^2 - E_S \hat{\mathbf{S}}^2. \tag{5}$$

Here

$$\hat{N} = \sum_{ns} d^\dagger_{ns} d_{ns}, \quad \hat{\mathbf{S}} = \sum_{nss'} d^\dagger_{ns} \frac{\sigma_{ss'}}{2} d_{ns'} \tag{6}$$

are the operators of total number of electrons and total spin on the dot. Obviously, the Hamiltonian (5) is invariant with respect to a change of the single-particle basis $\phi_i(\mathbf{r})$.

The first term in Eq. (5) represents the electrostatic energy of the dot. In the conventional equivalent circuit picture, see Fig. 1, the charging energy $E_C$ is related to the total capacitance $C$ of the grain, $E_C = e^2/2C$, and the dimensionless parameter $\mathcal{N}$ is proportional to the gate voltage, $\mathcal{N} = C_g V_g/e$, where $C_g$ is the capacitance between the dot and the gate. For a mesoscopic ($\lambda_F \ll L$) conductor, the charging energy is large compared to the level spacing $\delta E$. Indeed, using the estimate $C \sim \kappa L$, where $\kappa$ is the dielectric constant, we find

$$\frac{E_C}{\delta E} \sim \frac{e^2}{\kappa \hbar v_F} \left(\frac{L}{\lambda_F}\right)^{d-1} \sim \; r_s N^{d-1}, \tag{7}$$

where $v_F$ is the Fermi velocity, and $r_s$ is the conventional gas parameter. Except an exotic case of an extremely weak interaction, having a large number of electrons $N \sim (L/\lambda_F)^d \gg 1$ on a quantum dot guarantees that the inequality $E_C \gg \delta E$ is satisfied in dimensions $d = 2, 3$. For the smallest quantum dots formed in GaAs heterostructures, $E_C/\delta E \sim 10$ [3]; for a metallic nanoparticle with $L \simeq 5$ nm this ratio is about 100, see, *e.g.*, [10]. We should mention also that in the $d = 1$ case, the estimate (7) is of little help, as even a weak electron-electron interaction results in a formation of a Luttinger liquid [11], significantly affecting the nomenclature of the elementary excitations. In the case of a single-mode finite-length Luttinger liquid, the elementary excitations can be viewed as $1d$ plasmon waves in a confined geometry, so the corresponding level spacing is $\delta E \sim E_C$.

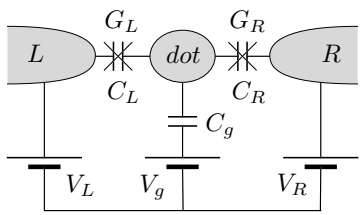


*Figure 1.* Equivalent circuit of a dot connected to two leads by tunnel junctions (with conductances $G_L$ and $G_R$) and coupled via a capacitor (with capacitance $C_g$) to the gate. The total capacitance of the dot is $C = C_L + C_R + C_g$.

The second term in Eq. (5) is the exchange interaction energy characterized by the exchange constant $E_S$. This constant is small in the case of weak electron-electron interaction: $E_S \sim r_s \delta E$ (there is an additional $\ln(1/r_s)$ factor in this estimate in the case of a $2d$ dot). Smallness of the ratio $E_S/\delta E$ guarantees the absence of a macroscopic (proportional to the volume of the dot) spin in the ground state, in accordance with the well-known Stoner criterion for the itinerant magnetism [12]. If all the orbital levels were equidistant, then the spin of an even-electron state would be zero, while an odd-electron state would have spin 1/2. However, the level spacings $|\epsilon_{n+1} - \epsilon_n|$ are random. If the spacing between some orbital levels is accidentally small, the dot may acquire a spin [13] exceeding 1/2. At small $r_s$, however, such states are rare, and in the following we disregard this possibility. This allows us to neglect the exchange term in the interaction Hamiltonian (5).

Keeping in mind that Eq. (5) is invariant with respect to the rotations of the basis of single-particle states, we can pick up the basis in which the first term in the Hamiltonian (1) is diagonal. Eq. (5) then

reduces to the Hamiltonian of the Constant Interaction Model,

$$\hat{H}_{dot} = \sum_{ns} \epsilon_n d^\dagger_{ns} d_{ns} + E_C \left(\hat{N} - \mathcal{N}\right)^2, \tag{8}$$

which is widely used in the analysis of the experimental data. We stress that the single-particle level spacings $|\epsilon_{n+1} - \epsilon_n| \sim \delta E$ here are small compared to the charging energy, and each single-particle state is spin-degenerate.

Electron transport through the dot occurs via two dot-lead junctions, see Fig. 1. As long as the conductances $G_L$ and $G_R$ of the left ($L$) and right ($R$) junctions are small compared to $e^2/h$, one may use the tunneling Hamiltonian to describe the junctions:

$$\hat{H}_t = \sum_{\alpha kns} t_{\alpha kn} c^\dagger_{\alpha ks} d_{ns} + \text{H.c.}, \quad \alpha = R, L. \tag{9}$$

Here $c^\dagger_{\alpha ks}$ are the creation operators of electrons in the leads, and $t_{\alpha kn}$ are the tunneling matrix elements (tunneling amplitudes) connecting state $n$ in the dot with the state $k$ in the lead $\alpha$. Usually it is adequate to consider the leads as reservoirs of free electrons:

$$\mathcal{H}_\alpha = \sum_{ks} \xi_{\alpha k} c^\dagger_{\alpha ks} c_{\alpha ks} \tag{10}$$

with continuous spectra $\xi_{\alpha k}$. In the following we will characterize these spectra by the density of states $\nu$, same for both leads.

The randomness of states $n$ translates into the randomness of the tunneling amplitudes $t_{\alpha kn}$. Similar to the single-particle spectrum of the dot, the tunneling amplitudes can be studied in the RMT framework. Regardless the details of the statistical properties of $t_{\alpha kn}$, the corresponding tunneling probabilities can be related to the average conductances $G_\alpha$ of the junctions:

$$\overline{|t^2_{\alpha kn}|} = \frac{\hbar G_\alpha}{4\pi e^2 \nu} \delta E. \tag{11}$$

The tunneling amplitudes determine also the rate $\Gamma_\alpha$ for an electron occupying a given discrete level in the dot to escape into the lead $\alpha = L, R$. The escape rates are determined by the tunneling amplitudes. With the help of Eq. (11) the average values of the rates are estimated to be $\Gamma_\alpha \sim (hG_\alpha/e^2)\delta E$.

## 3. Rate equations and conductance across the dot

At high temperatures, $T \gg E_C$, charging energy is negligible compared to the thermal energy of electrons. Therefore the conductance $G_\infty$ in this regime is not affected by charging and, independently of the gate voltage,

$$\frac{1}{G_\infty} = \frac{1}{G_L} + \frac{1}{G_R}. \tag{12}$$

At lower temperatures,

$$\delta E \ll T \ll E_C, \tag{13}$$

electron transport across the dot starts to depend on $\mathcal{N}$. The conductance is not suppressed only within narrow regions – Coulomb blockade peaks, *i.e.*, at the gate voltages tuned sufficiently close to points of charge degeneracy,

$$|\mathcal{N} - \mathcal{N}^*| \lesssim T/E_C; \tag{14}$$

here $\mathcal{N}^*$ is a half-integer number.

We will demonstrate this now using the method of rate equations. In addition to the constraint Eq. (13), we will assume that the inelastic electron relaxation rate $1/\tau_\varepsilon$ within the dot is large compared to the escape rates $\Gamma_\alpha$. In other words, electron transitions between discrete levels in the dot occur before the electron escapes to the leads[1]. Under this assumption the tunnelings across the two junctions can be treated independently of each other. The condition (14), on the other hand, allows us to take into account only two charge states of the dot which are almost degenerate in the vicinity of a Coulomb blockade peak. For $\mathcal{N}$ close to $\mathcal{N}^*$ these are the states with $N = \mathcal{N}^* \pm 1/2$ electrons on the dot. Hereafter we denote these states as $|N\rangle$ and $|N+1\rangle$. Finally, the condition (13) enables us to replace the discrete single-particle levels within the dot by a continuum with the density of states $1/\delta E$.

Applying the Fermi Golden Rule and using the described simplifications we may write the current $I_\alpha$ from the lead $\alpha$ into the dot as

$$\begin{aligned} I_\alpha \;=\; & \frac{2\pi}{\hbar} \sum_{kns} |t_{\alpha kn}|^2 \delta(\xi_k + eV_\alpha + E_N - \epsilon_n - E_{N+1}) \\ & \times \left\{ P_N f(\xi_k)[1 - f(\epsilon_n)] - P_{N+1} f(\epsilon_n)[1 - f(\xi_k)] \right\}. \end{aligned}$$

Here $f(\omega) = [\exp(\omega/T) + 1]^{-1}$ is the Fermi function, $V_\alpha$ is the potential on the lead $\alpha$, see Fig. 1, $E_N$ and $E_{N+1}$ are the electrostatic energies

[1] Note that a finite inelastic relaxation rate requires inclusion of mechanisms beyond the Constant Interaction Model, *e.g.*, electron-phonon collisions.

of the charge states $|N\rangle$ and $|N+1\rangle$, and $P_N$ and $P_{N+1}$ are the probabilities to find the dot in these states. Replacing the summations over $n$ and $k$ by integrations over the corresponding continua, we find

$$I_\alpha = \frac{G_L}{e}\left[P_N F(E_1 - E_0 - \mu_\alpha) - P_{N+1} F(E_0 - E_1 + \mu_\alpha)\right] \tag{15}$$

with $F(\omega) = \omega/[\exp(\omega/T) - 1]$. In equilibrium, the current Eq. (15) is zero by the detailed balance. When a finite current flows through the junction the probabilities $P_N$ and $P_{N+1}$ deviate from their equilibrium values. In the steady state, the currents across the two junctions satisfy

$$I = I_L = -I_R. \tag{16}$$

From Eqs. (15) and (16), supplemented by the obvious normalization condition $P_N + P_{N+1} = 1$, one finds the current across the dot $I$ in response to the applied bias $V = V_L - V_R$. The linear conductance across the dot $G = \lim_{V\to 0} dI/dV$ is then given by

$$G = G_\infty \frac{E_C(\mathcal{N} - \mathcal{N}^*)/T}{\sinh[2E_C(\mathcal{N} - \mathcal{N}^*)/T]}\,. \tag{17}$$

Here a half-integer $\mathcal{N} = \mathcal{N}^*$ corresponds to the Coulomb blockade peak. In the Coulomb blockade valleys ($\mathcal{N} \neq \mathcal{N}^*$), conductance falls off exponentially with the decreasing temperature, and all the valleys behave exactly the same way.

According to Eq. (17), all the Coulomb blockade peaks have the same height $G(\mathcal{N}^*) = G_\infty/2$ and are symmetric about $\mathcal{N} = \mathcal{N}^*$. Such equivalence of all the peaks occurs because for $T \gg \delta E$, see Eq. (13), many energy levels in the dot make a significant contribution to the conductance. Decrease of temperature below $\delta E$ brings about a modification of Eq. (17) in the vicinity of the Coulomb blockade peaks $|\mathcal{N} - \mathcal{N}^*| \ll \delta E/E_C$. In this regime the main contribution to the conductance comes from tunneling through a single energy level in the dot. The dependence $G(\mathcal{N}, T)$ can again be found from the proper rate equations with the result [9]

$$G \propto -G_\infty \frac{\delta E}{T}\frac{df(X)/dX}{1 + f(X)}, \qquad X = \frac{2E_C}{T}(\mathcal{N} - \mathcal{N}^*). \tag{18}$$

In writing Eq. (18) we neglected mesoscopic fluctuations of the peaks heights [14]. Note that according to Eq. (18) the shape of the peak is asymmetric. The asymmetry comes about from the difference in the spin states of the dots in two adjacent Coulomb blockade valleys: Eq. (18) is written for a peak separating the valley with $N = \mathcal{N}^* - 1/2 =$ odd number of electrons at $X < 0$ from the valley with $N = \mathcal{N}^* + 1/2 =$

even at $X > 0$. The validity of Eq. (18) is restricted to the vicinity of the Coulomb blockade peak, $|\mathcal{N} - \mathcal{N}^*| \ll \delta E/E_C$, and for temperatures in the interval $\Gamma_\alpha \ll T \ll \delta E$. When the temperature falls below the escape rates $\Gamma_\alpha$ the Coulomb blockade peaks are no longer well-defined due to the onset of the Kondo effect.

## 4. Activationless transport through a blockaded quantum dot

According to the rate equations theory [15], at low temperatures, $T \ll E_C$, conduction through the dot in the Coulomb blockade valleys is exponentially suppressed. This suppression occurs because the process of electron transport through the dot involves a *real transition* to the state in which the charge of the dot differs by $e$ from the thermodynamically most probable value. The probability of such fluctuation is proportional to $\exp[-E_C|\mathcal{N} - \mathcal{N}^*|/T]$, which explains the conductance suppression, see Eq. (17). Going beyond the lowest-order perturbation theory in conductances $G_\alpha$ allows one to consider processes in which states of the dot with a "wrong" charge participate in the tunneling process as *virtual states*. The existence of these higher-order contributions to the tunneling conductance was first envisioned by Giaever and Zeller [16]. The first quantitative theory of this effect, however, was developed much later [17].

The leading contributions to the activationless transport, according to Refs. [17], are provided by the processes of inelastic and elastic *co-tunneling*. Unlike the sequential tunneling, in the co-tunneling mechanism, the events of electron tunneling from one of the leads into the dot, and tunneling from the dot to the other lead occur as a single quantum process.

### 4.1. Inelastic co-tunneling

In the inelastic co-tunneling mechanism, an electron tunnels from the lead into one of the vacant single-particle levels in the dot, while it is an electron occupying some other level that tunnels out of the dot, see Fig. 2(a). As a result, transfer of charge $e$ between the leads is accompanied by a simultaneous creation of an electron-hole pair in the dot.

Here we will estimate the contribution of the inelastic co-tunneling to the conductance deep in the Coulomb blockade valley, *i.e.*, at almost integer $\mathcal{N}$. Consider an electron that tunnels into the dot from the lead $\alpha$. If the energy of the electron relative to the Fermi level $\omega$ is small

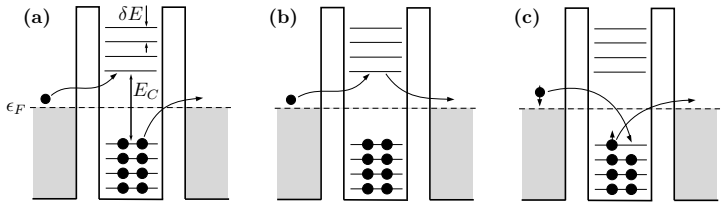


*Figure 2.* Examples of the co-tunneling processes.
(a) inelastic co-tunneling: transferring of an electron between the leads leaves behind an electron-hole pair in the dot; (b) elastic co-tunneling; (c) elastic co-tunneling with a flip of spin.

compared to the charging energy, $\omega \ll E_C$, then the energy of the virtual state involved in the co-tunneling process is close to $E_C$. The amplitude $A_{in}$ of the inelastic transition via this virtual state is then given by

$$\mathcal{A}^{in}_{\alpha\to\alpha'} = \frac{t^*_{\alpha kn} t_{\alpha' k' n'}}{E_C}. \tag{19}$$

The initial state of this transition has an extra electron in the single-particle state $k$ in the lead $\alpha$, while the final state has an extra electron in the state $k'$ in the lead $\alpha'$ and an electron-hole pair in the dot (state $n$ is occupied, state $n'$ is empty).

Given the energy of the initial state $\omega$, the number of available final states can be estimated from the phase space argument, familiar from the calculation of the quasiparticle lifetime in the Fermi liquid theory [18]. For $\omega \gg \delta E$ this number is of the order of $(\omega/\delta E)^2$. Since the typical value of $\omega$ is $T$, the inelastic co-tunneling contribution to the conductance can be estimated as

$$G_{in} \sim \frac{e^2}{h}\left(\frac{T}{\delta E}\right)^2 \nu^2 |\mathcal{A}^{in}_{L\to R}|^2.$$

Using Eqs. (19) and (11) we find [17]

$$G_{in} \sim \frac{h}{e^2} G_L G_R \left(\frac{T}{E_C}\right)^2. \tag{20}$$

A comparison of Eq. (20) with the result of the rate equations theory Eq. (17) shows that the inelastic co-tunneling takes over the thermally-activated hopping at moderately low temperatures

$$T \lesssim T_{in} = E_C \left[\ln\left(\frac{e^2/h}{G_L + G_R}\right)\right]^{-1}. \tag{21}$$

The smallest energy of the electron-hole pair is of the order of $\delta E$. At temperatures below this threshold the inelastic co-tunneling contribution to the conductance becomes exponentially small. It turns out, however, that even at much higher temperatures this mechanism becomes less effective than the elastic co-tunneling.

### 4.2. Elastic co-tunneling

In the process of elastic co-tunneling, transfer of charge between the leads is not accompanied by the creation of an electron-hole pair in the dot. In other words, occupation numbers of single-particle energy levels in the dot in the initial and final states of the co-tunneling process are exactly the same, see Fig. 2(b). Here we will estimate the elastic co-tunneling contribution to the conductance near the edge of a Coulomb-blockade valley,

$$\delta E/E_C \ll \mathcal{N} - \mathcal{N}^* \ll 1/2. \tag{22}$$

Under this condition, the average number of electrons on the dot $N = \mathcal{N}^* + 1/2$. A cost in electrostatic energy for a removal of a single electron from the dot, $E_- = 2E_C(\mathcal{N} - \mathcal{N}^*)$, see Eq. (8), is small compared to the cost to add an electron $E_+ \approx 2E_C$ [here we took into account the second inequality in Eq. (22)]. Therefore, only hole-like virtual states with $N-1$ electrons on the dot contribute to the co-tunneling amplitude:

$$\mathcal{A}^{el}_{\alpha\to\alpha'} = \sum_{\epsilon_n \le 0} A^n_{\alpha\to\alpha'}, \quad A^n_{\alpha\to\alpha'} = \frac{t^*_{\alpha kn} t_{\alpha' k' n}}{E_- + |\epsilon_n|}. \tag{23}$$

Here $A^n$ represent amplitudes of the processes in which a hole is virtually created on $n$th single-particle level. Creation of a hole is only possible if the level is occupied, hence the restriction of the sum in Eq. (23) to the levels below the Fermi level ($\epsilon_n \le 0$).

The elastic co-tunneling contribution to the conductance is

$$G_{el} = \frac{e^2}{\pi\hbar}\, \nu^2 \left|\mathcal{A}^{el}_{L\to R}\right|^2. \tag{24}$$

If the dot-leads junctions are point contacts, then $G_{el}$ exhibits strong mesoscopic fluctuations. Indeed, tunneling matrix elements entering Eq. (23) depend on the values of the electron wave functions at the points $\mathbf{r}_\alpha$ of the contacts, $t_{\alpha kn} \propto \varphi_n(\mathbf{r}_\alpha)$. In the RMT model, briefly discussed in Section 2, the electron wave functions in the dot $\varphi_n(\mathbf{r})$ are random and uncorrelated, $\overline{\varphi_n(\mathbf{r}_\alpha)\varphi_{n'}(\mathbf{r}_{\alpha'})} \propto \delta_{nn'}\delta_{\alpha\alpha'}$. Therefore, the partial amplitudes $A^n_{L\to R}$ are random and uncorrelated as well:

$$\overline{(A^n_{L\to R})^*\, A^m_{L\to R}} = \delta_{nm} \overline{|A^n_{L\to R}|^2}.$$

Eqs. (23),(24) and (11) then yield for the average conductance

$$\overline{G_{el}} = \frac{e^2}{\pi\hbar}\nu^2 \sum_{\epsilon_n \le 0} \overline{|\mathcal{A}^n_{L\to R}|^2} \sim \frac{h}{e^2} G_L G_R \sum_{\epsilon_n \le 0} \left[\frac{\delta E}{E_- + |\epsilon_n|}\right]^2 .$$

Since under the conditions (22) the number of terms making significant contribution to the sum over $n$ here is large, and since the sum is converging, one can replace the summation by an integral which results in [17]

$$\overline{G_{el}} \sim \frac{h}{e^2} G_L G_R \frac{\delta E}{E_C} \left[\frac{1}{\mathcal{N} - \mathcal{N}^*} + \frac{1}{\mathcal{N}^* - \mathcal{N} + 1}\right] . \tag{25}$$

Here we have included both the hole-like and electron-like contributions to the conductance and restored the explicit dependence on the gate voltage $\mathcal{N}$; Eq. (25) is valid for $|\mathcal{N} - \mathcal{N}^* - 1/2| \ll 1/2 - \delta E/E_C$. Comparison of Eq. (25) with Eq. (20) shows that the elastic co-tunneling dominates the electron transport already at temperatures

$$T \lesssim T_{el} = \sqrt{E_C \delta E}, \tag{26}$$

which may exceed significantly the level spacing.

Note that mesoscopic fluctuations of the elastic co-tunneling contribution to the conductance $G_{el}$ are of the order of its average and get stronger when the gate voltage is tuned closer to the middle of the Coulomb blockade valley [19]. Thus, although $\overline{G_{el}}$ is always positive, see Eq. (25), the sample-specific value of $G_{el}$ for a given gate voltage may vanish.

## 5. Kondo regime in transport through a blockaded quantum dot

Among the $E_C|\mathcal{N} - \mathcal{N}^*|/\delta E$ virtual states participating in the elastic co-tunneling through a blockaded dot, the top-most occupied single-particle level is special. If the number of electrons on the dot $N$ is odd, this level is filled by a single electron and is spin-degenerate. Therefore the ground state of the dot is characterized not only by the occupations of the single-particle energy levels, but also by the dot's spin. This opens a possibility of a co-tunneling process in which a transfer of an electron between the leads is accompanied by a flip of electron's spin with simultaneous flip of the spin on the dot, see Fig. 2(c). The amplitude of such a process, calculated in the fourth order in tunneling matrix elements, diverges logarithmically when the energy $\omega$ of an incoming electron approaches 0. Since $\omega \sim T$, the logarithmic singularity in the transmission amplitude translates into a dramatic enhancement of the conductance

$G$ across the dot at low temperatures: $G$ may reach values as high as the quantum limit $2e^2/h$ [20, 21]. This conductance enhancement is not really a surprise. Indeed, in the spin-flip co-tunneling process a quantum dot with odd $N$ behaves as $S = 1/2$ magnetic impurity embedded into a tunneling barrier separating two massive conductors. It is known [22] since mid-60's that the presence of such impurities leads to zero-bias anomalies in tunneling conductance [23], which are adequately explained [24] in the context of the Kondo effect [5].

For simplicity, we will assume here that the gate voltage $\mathcal{N}$ is tuned to the middle of the Coulomb blockade valley with $N =$ odd electrons on the dot. The tunneling (9) mixes this state with states having $N \pm 1$ electrons. The electrostatic energies of these states are high ($\sim E_C$), hence the transitions $N \to N \pm 1$ are virtual, and can be taken into account perturbatively in the second order in tunneling amplitudes. The resulting effective Hamiltonian, valid at energies well below the threshold ($\sim \delta E$) for spin excitations within the dot, has the form

$$H_{eff} = \sum_{\alpha ks} \xi_k c^\dagger_{\alpha ks} c_{\alpha ks} + \frac{4}{E_C} \sum_{\alpha\alpha'} \sum_{nn'} t^*_{\alpha n} t_{\alpha' n'} (\mathbf{s}_{\alpha'\alpha} \cdot \mathbf{S}_{nn'}). \tag{27}$$

Here

$$\mathbf{s}_{\alpha\alpha'} = \sum_{kk'ss'} c^\dagger_{\alpha ks} \frac{\sigma_{ss'}}{2} c_{\alpha' k' s'}, \quad \mathbf{S}_{nn'} = \mathcal{P} \left[ \sum_{ss'} d^\dagger_{ns} \frac{\sigma_{ss'}}{2} d_{n's'} \right] \mathcal{P},$$

and $\mathcal{P}$ is a projector onto the spin-degenerate ground state of an isolated dot. In the derivation of Eq. (27) we have replaced the tunneling amplitudes $t_{\alpha kn}$ by their values $t_{\alpha n}$ at the Fermi level. In addition, we have dropped the potential scattering terms associated with usual elastic co-tunneling. The latter approximation is well justified when the conductances of the dot-leads junctions are small, $G_\alpha \ll e^2/h$, in which case $G_{el}$ is also very small, see Eq. (25).

By $SU(2)$ symmetry, the operators $\mathbf{S}_{nn'}$ for any $n$ and $n'$ must be proportional to $\mathbf{S} = \mathcal{P}\hat{\mathbf{S}}\mathcal{P}$ with $\hat{\mathbf{S}}$ being the operator of the total spin on the dot introduced in Eq. (6) above: $\mathbf{S}_{nn'} = \lambda_{nn'}\mathbf{S}$. Substitution into Eq. (27) then yields [25]

$$H_{eff} = \sum_{\alpha ks} \xi_k c^\dagger_{\alpha ks} c_{\alpha ks} + \sum_{\alpha\alpha'} J_{\alpha\alpha'} (\mathbf{s}_{\alpha'\alpha} \cdot \mathbf{S}) \tag{28}$$

with

$$J_{\alpha\alpha'} = \frac{4}{E_C} \sum_{nn'} t^*_{\alpha n} \lambda_{nn'} t_{\alpha' n'}. \tag{29}$$

Under the conditions of applicability of the Constant Interaction Model Eq. (8), the effective exchange Hamiltonian (28) can be simplified even further. Indeed, in this case the ground state of an isolated

dot is a singlet or a doublet, depending only on the parity of $N$. If $N$ is odd, then $\mathbf{S}$ is spin-1/2 operator. The entire spin of the dot is now due to the only singly occupied single-particle energy level in it (denoted by $n = 0$ hereafter). The matrix $\lambda_{nn'}$ then reduces to $\lambda_{nn'} = \delta_{nn'}\delta_{n0}$, and Eq. (29) yields

$$J_{\alpha\alpha'} = \frac{4}{E_C} t^*_{\alpha 0} t_{\alpha' 0} \,. \tag{30}$$

The $2 \times 2$ Hermitian matrix $\hat{J}$ with elements given by Eq. (30) has an important property: since $\det \hat{J} = 0$, one of its eigenvalues vanishes, while the remaining eigenvalue,

$$J = \mathrm{Tr}\hat{J} = \frac{4}{E_C}\left(|t^2_{L0}| + |t^2_{R0}|\right), \tag{31}$$

is strictly positive. By an appropriate rotation in the $R - L$ space the Hamiltonian (28) can then be brought into the "block-diagonal" form

$$H_{eff} = H[\varphi] + H[\psi] \tag{32}$$

with

$$H[\varphi] = \sum_{ks} \xi_k \varphi^\dagger_{ks} \varphi_{ks}, \tag{33}$$

$$H[\psi] = \sum_{ks} \xi_k \psi^\dagger_{ks} \psi_{ks} + J(\mathbf{s}_\psi \cdot \mathbf{S}). \tag{34}$$

Here $\mathbf{s}_\psi = \sum_{kk'ss'} \psi^\dagger_{ks} (\sigma_{ss'}/2)\, \psi_{k's'}$, and the operators $\psi$ and $\varphi$ are certain linear combinations of the original operators $c_{R,L}$.

To get an idea about the physics of the Kondo model, let us first replace the operator $\mathbf{s}_\psi$ in Eq. (34) by spin-1/2 operator $\mathbf{S}_\psi$. The ground state of the resulting Hamiltonian of two spins $\widetilde{H} = J(\mathbf{S}_\psi \cdot \mathbf{S})$ is obviously a singlet. The excited state (a triplet) is separated from the ground state by the energy gap $J > 0$. This separation can be interpreted as the binding energy of the singlet. Unlike $\mathbf{S}_\psi$ in this simple example, the operator $\mathbf{s}_\psi$ in Eq. (34) is merely a spin density of the conduction electrons at the cite of the "magnetic impurity". Because conduction electrons are freely moving in space, it is hard for the impurity to "capture" an electron and form a singlet. Yet, even a weak local exchange interaction suffices to form a singlet ground state [28, 29]. However, the binding energy of this singlet is given not by the exchange amplitude $J$, but by the so-called Kondo temperature

$$T_K \sim \delta E \exp(-1/\nu J). \tag{35}$$

With the help of Eqs. (31) and (11) one obtains from Eq. (35) the estimate

$$\ln\left(\frac{\delta E}{T_K}\right) \sim \frac{1}{\nu J} \sim \frac{e^2/h}{G_L + G_R}\frac{E_C}{\delta E}. \tag{36}$$

Since $G_\alpha \ll e^2/h$, and $E_C \gg \delta E$, the r.h.s. of Eq. (36) is a product of two large parameters. Therefore, the Kondo temperature $T_K$ is small compared to the mean level spacing in the dot:

$$T_K \ll \delta E. \tag{37}$$

It is this separation of the energy scales that justifies the use of the effective low-energy Hamiltonian (27) for the description of the Kondo effect in a quantum dot system. The inequality (37) remains valid even if the conductances of the dot-leads junctions $G_\alpha$ are of the order of $2e^2/h$. However, in this case neither Eq. (31) nor the estimate Eq. (36) are applicable [30].

As it follows from Eqs. (33) and (34), one of the "channels" ($\varphi$) of conduction electrons completely decouples[2] from the dot, while the $\psi$-particles are described by the standard single-channel antiferromagnetic Kondo model [5]. Therefore, the thermodynamic properties of a quantum dot in the Kondo regime are identical to those of the conventional Kondo problem for a single magnetic impurity in a bulk metal; thermodynamics of the latter model is fully studied [26]. However, all the experiments addressing the Kondo effect in quantum dots test their transport properties rather then thermodynamics. The electron current operator is not diagonal in the $(\psi, \phi)$ representation, and the contributions of these two sub-systems to the conductanceare not additive. In the following we establish the relations of linear conductance and, in some special case, of the non-linear differential conductance as well, to the t-matrix of the conventional Kondo problem.

### 5.1. Linear response

The linear conductance can be calculated from the Kubo formula

$$G = \lim_{\omega\to 0} \frac{e^2}{\hbar}\frac{1}{\omega}\int_0^\infty dt e^{i\omega t}\left\langle [j(t), j(0)]\right\rangle, \tag{38}$$

where the particle current operator $j$ is given by

$$j = \frac{d}{dt}\frac{1}{2}\left(\hat{N}_R - \hat{N}_L\right). \tag{39}$$

[2] It should be emphasized that the decoupling is characteristic of the Constant Interaction Model rather than a generic property. In general, both electronic channels are coupled to the dot. This, however, does not lead to qualitative changes in the results if spin of the dot is 1/2, see [25].

Here $\hat{N}_\alpha = \sum_{ks} c^\dagger_{\alpha ks} c_{\alpha ks}$ is the operator of the total number of electrons in the lead $\alpha$. In order to take the full advantage of the decomposition (32)-(34), we need to rewrite $j$ in terms of the operators $\psi, \varphi$. These operators are related to the original operators $c_{R,L}$ representing the electrons in the right and left leads via

$$\begin{pmatrix} \psi_{ks} \\ \varphi_{ks} \end{pmatrix} = \hat{U}^* \begin{pmatrix} c_{Rks} \\ c_{Lks} \end{pmatrix}, \tag{40}$$

where $\hat{U}$ is $2 \times 2$ unitary matrix that diagonalizes the matrix of the exchange constants (29): $\hat{U}\hat{J}\hat{U}^\dagger = \mathrm{diag}\{J, 0\}$. The matrix $\hat{U}$ can be parametrized as

$$\hat{U} = e^{i\theta_0 \tau_y} e^{i\phi_0 \tau_z}, \tag{41}$$

where $\tau_i$ are the Pauli matrices acting in the R-L space ($\tau_+ = \tau_x + i\tau_y$ transforms $L$ to $R$) and the angle $\theta_0$ satisfies $\tan\theta_0 = |t_{L0}/t_{R0}|$. It follows from Eqs. (40) and (41) that, independently of $\phi_0$,

$$\hat{N}_R - \hat{N}_L = \cos(2\theta_0)\left(\hat{N}_\psi - \hat{N}_\varphi\right) - \sin(2\theta_0) \sum_{ks} \left(\psi^\dagger_{ks}\varphi_{ks} + \varphi^\dagger_{ks}\psi_{ks}\right). \tag{42}$$

Note that the current operator $j$ entering the Kubo formula (38) is to be calculated with the equilibrium Hamiltonian (32)-(34). Since both $\hat{N}_\psi$ and $\hat{N}_\varphi$ commute with $H_{eff}$, the first term in Eq. (42) makes no contribution to $j$. When the second term in (42) is substituted into Eq. (39) and then into Eq. (38), the result, after integration by parts, can be expressed via 2-particle correlation functions such as $\left\langle \psi^\dagger(t)\varphi(t)\varphi^\dagger(0)\psi(0)\right\rangle$. Due to the block-diagonal structure of $H_{eff}$, see Eq. (32), these correlation functions factorize into products of single-particle correlation functions describing the (free) $\varphi$-particles and the (interacting) $\psi$-particles. The result of the evaluation of the Kubo formula can then be written as[3]

$$G = G_0 \int d\omega \left(-df/d\omega\right) \frac{1}{2} \sum_s \left[-\pi\nu \mathrm{Im}\ T_s(\omega)\right]. \tag{43}$$

Here

$$G_0 = \frac{2e^2}{h}\sin^2(2\theta_0) = \frac{2e^2}{h}\left|\frac{2t_{L0}t_{R0}}{|t^2_{L0}| + |t^2_{R0}|}\right|^2, \tag{44}$$

$f(\omega)$ is the Fermi function, and $T_s$ is the t-matrix for the Kondo model Eq. (34). The t-matrix is related to the exact retarded Green function of the $\psi$-particles in the usual way:

$$G_{ks,k's'}(\omega) = G^0_k(\omega) + G^0_k(\omega)\left[\delta_{ss'}T_s(\omega)\right] G^0_{k'}(\omega), \tag{45}$$

[3] Further details about this calculation can be found, *e.g.*, in the Appendix B of Ref. [27].

Here $G_k^0(\omega) = (\omega - \xi_k + i0)^{-1}$ and $G_{ks,k's'}(\omega)$ is the Fourier transform of

$$G_{ks,k's'}(t) = -i\theta(t) \left\langle \left\{ \psi_{ks}(t), \psi^\dagger_{k's'} \right\} \right\rangle ,$$

where $\langle ... \rangle$ stands for the thermodynamic averaging with the Hamiltonian (34). In writing Eq. (45) we took into account the conservation of the total spin (which implies that $G_{ks,k's'}$ is diagonal in $s, s'$) and the fact that the interaction in Eq. (34) is local (which in turn means that the t-matrix is independent of $k$ and $k'$).

5.1.1. Weak coupling regime: $T_K \ll T \ll \delta E$

Kondo effect becomes important at low temperatures $T \sim T_K \ll \delta E$. The exchange term in the Hamiltonian (34), however, describes transitions between the electronic states within the band of the width $2D_0$ with $D_0 \sim \delta E$ centered at the Fermi level $\epsilon_F$. The transitions between the states close to $\epsilon_F$ and the states within a narrow strip of energies of the width $\delta D$ near the edges of the band are associated with high energy deficit $\sim \delta E \gg T$. Hence, these transitions are virtual and their influence on the states near $\epsilon_F$ can be taken into account perturbatively in the second order. This yields an effective Hamiltonian acting within the band of a reduced width $D = D_0 - \delta D$, which turns out to have the same form as Eq. (34), but with a modified value of the exchange amplitude $J$ [32]. Successive reductions of the bandwidth by small steps $\delta D$ can be viewed as a continuous process during which the initial Hamiltonian Eq. (34) is transformed to an effective low-energy Hamiltonian acting within the band of the width $D \ll D_0$. The evolution of the exchange amplitude during this transformation (known as the poor man's scaling [32]) can be cast into the form of an equation

$$\frac{dJ}{d\zeta} = \nu J^2, \quad \zeta = \ln\left(D_0/D\right).$$

The renormalization described by this equation can be continued until the bandwidth $D$ becomes of the order of the temperature $T$ or relevant electron energy $|\omega|$. The resulting effective exchange constant is $\omega$- and $T$-dependent [32, 33],

$$\nu J(\omega, T) = \left[ \ln \frac{\max\{|\omega|, T\}}{T_K} \right]^{-1}. \tag{46}$$

Calculation of the t-matrix in the lowest (second) order in $\nu J(\omega, T)$ results in

$$-\pi\nu \mathrm{Im} T_s(\omega) = \frac{3\pi^2}{16} \left[\nu J(\omega, T)\right]^2. \tag{47}$$

Substitution of (47) and (46) into Eq. (43) and evaluation of the integral over $\omega$ with the logarithmic accuracy then yield for the conductance across the dot

$$G = G_0 \frac{3\pi^2/16}{[\ln(T/T_K)]^2}, \quad T_K \ll T \ll \delta E. \tag{48}$$

Corrections to Eq. (48) contain higher powers of $1/\ln(T/T_K)$. Thus, it is often said that Eq. (48) represents the conductance in the leading logarithmic approximation.

5.1.2. Strong coupling regime: $T \ll T_K$

As temperature approaches $T_K$, the leading logarithmic approximation result diverges, see Eq. (48). This divergence signals the failure of the approximation, as the conductance in any case can not grow higher than $2e^2/h$. To obtain a more precise bound, we consider in this section the conductance in the strong coupling regime $T \ll T_K$.

We start with the zero-temperature limit $T = 0$. Since, as discussed above, the ground state of the Hamiltonian (34) is not degenerate, the scattering of conduction electrons by a quantum dot is completely characterized by the scattering phase shifts $\delta_s$ for electrons with spin $s$ at the Fermi level. The t-matrix is then given by the standard scattering theory expression

$$-\pi\nu T_s(0) = \frac{1}{2i}\left(e^{2i\delta_s} - 1\right) = e^{i\delta_s}\sin\delta_s. \tag{49}$$

In order to find the two phase shifts $\delta_s$, we need two independent relations. The first one follows from the invariance of the Kondo Hamiltonian (34) under the particle-hole transformation $\psi_{ks} \to s\psi^\dagger_{-k,-s}$ (here $s = \pm 1$ for spin-up/down electrons and $k$ is counted from $k_F$). The particle-hole symmetry implies the relation for the t-matrix

$$T_s(\omega) = -T^*_{-s}(-\omega),$$

valid at all $\omega$ and $T$. In view of Eq. (49), it translates into the relation for the phase shifts at the Fermi level ($\omega = 0$):

$$\delta_s + \delta_{-s} = 0 \pmod{\pi}. \tag{50}$$

Note that, as it is obvious from Eq. (49), the phase shifts are defined only modulo $\pi$ (that is, $\delta_s$ and $\delta_s + \pi$ describe equivalent scattering states). This ambiguity can be removed by setting the values of the phase shifts corresponding to $J = 0$ in Eq. (34) to zero. With this convention, Eq. (50) becomes

$$\delta_\uparrow + \delta_\downarrow = 0. \tag{51}$$

The second relation follows from the fact that the ground state of our system is a singlet at $J > 0$. In the absence of exchange ($J = 0$) and at $T = 0$, an infinitesimally small magnetic field acting on the dot's spin,

$$\delta H[\psi] = -BS^z, \quad B \to +0,$$

would polarize it. Since the free electron gas has zero spin in the ground state, the total spin in any large but finite region of space $\mathcal{V}$ surrounding the dot coincides with the spin of the dot, $\langle S^z \rangle_{J=0} = -1/2$. If the exchange with electron gas is now turned on, $J > 0$, the infinitesimally weak field will not prevent the formation of a singlet ground state. In this state, the total spin within the region $\mathcal{V}$ is zero. Such change of the spin is possible only if the numbers of spin-up and spin-down electrons in this region have changed in order to compensate for the spin of the dot:

$$\delta N_\uparrow - \delta N_\downarrow = 1, \quad \delta N_s = \langle \hat{N}_s \rangle_{J>0} - \langle \hat{N}_s \rangle_{J=0}. \tag{52}$$

Here $\hat{N}_s$ are operators of the number of electrons with spin $s$ within the region $\mathcal{V}$. By the Friedel sum rule, $\delta N_s$ are related to the scattering phase shifts: $\delta N_s = \delta_s/\pi$. Eq. (52) then gives

$$\delta_\uparrow - \delta_\downarrow = \pi. \tag{53}$$

Combining Eqs. (51) and (53), we find $|\delta_s| = \pi/2$. Eqs. (43) and (49) then yield for zero-temperature conductance across the dot [20]

$$G(0) = G_0 \frac{1}{2} \sum_s \sin^2 \delta_s = G_0. \tag{54}$$

Thus, the grows of the conductance across the dot with lowering the temperature is limited only by the value of $G_0$. This value, see Eq. (44), depends only on the ratio of the tunneling amplitudes $|t_{L0}/t_{R0}|$ between the leads and the last occupied single-particle energy level in the dot. If $|t_{L0}| = |t_{R0}|$, the conductance at $T = 0$ will reach the maximal value $G = 2e^2/h$ allowed by quantum mechanics [20].

The ground state of the Kondo Hamiltonian (34) is a singlet formed by the spin of the dot and a spin made up of the spins of conduction electrons. Finite-temperature correction to Eq. (55) can be found by considering virtual transitions from the singlet ground state to excited states in which the singlet is broken up [34]. The transitions can be studied by an expansion in inverse powers of the singlet binding energy $T_K$. The reader is referred to the original papers [34] for the details about this approach. Here we just quote the result for the imaginary part of the t-matrix [35]:

$$-\pi\nu \mathrm{Im}\ T_s(\omega) = 1 - \frac{3\omega^2 + \pi^2 T^2}{2T_K^2}, \quad |\omega|, T \ll T_K \tag{55}$$

Substitution of Eq. (55) into Eq. (43) yields

$$G = G_0 \left[1 - (\pi T/T_K)^2\right], \quad T \ll T_K \tag{56}$$

Accordingly, corrections to the conductance are quadratic in temperature – a typical result for the Fermi liquid theory [34].

The weak-coupling ($T \gg T_K$) and the strong-coupling ($T \ll T_K$) asymptotes of the conductance have a strikingly different structure. Nevertheless, since the Kondo effect is a crossover phenomenon rather than a phase transition [26, 28, 29], the dependence $G(T)$ is a smooth and featureless [36] function throughout the crossover region $T \sim T_K$.

Finally, note that both Eqs. (48) and (56) have been obtained here for the particle-hole symmetric model (34). This approximation is equivalent to neglecting the elastic co-tunneling contribution to the conductance $G_{el}$. The asymptotes (48),(54), however, remain qualitatively correct [25] as long as $G_{el}/G_0 \ll 1$. The overall temperature dependence of the linear conductance in the Coulomb blockade valley in the presence of the Kondo effect is sketched in Fig. 3.

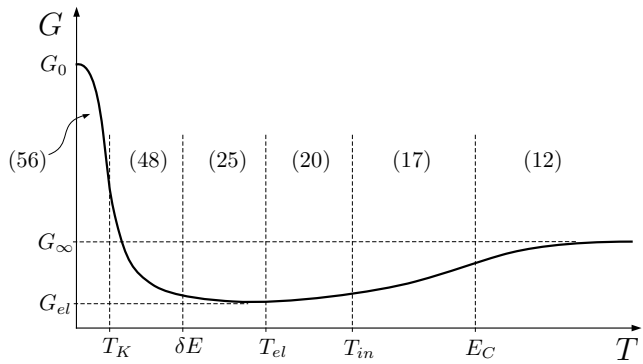


*Figure 3.* Schematic temperature dependence of the conductance in the middle of the Coulomb blockade valley with $N$ = odd electrons on the dot. The numbers in brackets refer to the corresponding equations in the text.

## 5.2. Beyond linear response

In order to study transport through a quantum dot away from equilibrium we add to the effective Hamiltonian (32)-(34) a term

$$H_V = \frac{eV}{2}\left(\hat{N}_L - \hat{N}_R\right)$$

describing a finite voltage bias $V$ applied between the left and right electrodes. Here we will evaluate the current across the dot at arbitrary

$V$ but under the simplifying assumption that the dot-lead junctions are strongly asymmetric: $G_L \ll G_R$. Under this condition the angle $\theta_0$ in Eq. (41) is small,

$$\theta_0 \approx |t_{L0}/t_{R0}| \ll 1.$$

Expanding Eq. (42) to the linear order in $\theta_0$ we obtain

$$\begin{aligned} H_V(\theta_0) &= \frac{eV}{2}\left(\hat{N}_\varphi - \hat{N}_\psi\right) + eV\theta_0\hat{A}, \\ \hat{A} &= \sum_{ks} \varphi^\dagger_{ks}\psi_{ks} + \text{H.c.} \end{aligned} \tag{57}$$

The first term in the r.h.s. of Eq. (57) describes the voltage bias between the reservoirs of $\varphi$ and $\psi$-particles, while the second term has an appearance of the $k$-conserving "tunneling" with $V$-dependent "tunneling amplitude". These two contributions correspond to the two terms in the r.h.s. of Eq. (42). Similarly, the current operator $j$, see Eq. (39), can be also split into two contributions:

$$\begin{aligned} j &= j_0 + \delta j, \\ j_0 &= \frac{i}{2}\left[H_{eff} + H_V, \hat{N}_\psi - \hat{N}_\varphi\right] = ieV\theta_0 \sum_{ks} \varphi^\dagger_{ks}\psi_{ks} + \text{H.c.}, \\ \delta j &= -\theta_0 \frac{d}{dt}\hat{A}. \end{aligned} \tag{58}$$

It turns out that $\delta j$ in Eq. (58) makes no contribution to the average current in the leading (second) order in $\theta_0$. Indeed, in this order

$$\langle \delta j \rangle = i\theta_0^2 eV \frac{d}{dt}\int_{-\infty}^{t} dt' \left\langle [\hat{A}(t), \hat{A}(t')] \right\rangle_0,$$

where $\langle ... \rangle_0$ denotes thermodynamic averaging with the Hamiltonian $H_0 = H_{eff} + H_V(0)$. The thermodynamic (equilibrium) averaging is well defined here because the "tunneling" term in Eq. (57) is absent at $\theta_0 = 0$. Taking into account that $\left\langle [\hat{A}(t'), \hat{A}(t)] \right\rangle_0$ depends only on $t - t' = \tau$, we find

$$\langle \delta j \rangle = i\theta_0^2 eV \frac{d}{dt}\int_0^{\infty} d\tau \left\langle [\hat{A}(\tau), \hat{A}(0)] \right\rangle_0 \equiv 0.$$

To the contrary, the term $j_0$ in Eq. (58) makes a finite contribution to the average current. Evaluation of this contribution in the leading order in $\theta_0$ proceeds similarly to the calculation of the tunneling current between two massive conductors (see, *e.g.*, [31]), and yields for the differential conductance across the dot

$$dI/dV = G_0 \int d\omega \, (-df/d\omega) \, \frac{1}{2}\sum_s \left[-\pi\nu \text{Im } T_s(\omega + eV)\right] \tag{59}$$

with

$$G_0 = \frac{2e^2}{h}(2\theta_0)^2 \approx \frac{8e^2}{h}\left|\frac{t_{L0}}{t_{R0}}\right|^2 .$$

Note that the $V \to 0$ limit of Eq. (59) coincides with the small $\theta_0$ limit of the linear response result Eq. (43). Using now Eqs. (46),(47),(55), and (59) we obtain for the differential conductance at $T \ll eV \ll \delta E$

$$\frac{dI}{dV} = \begin{cases} G_0\left[1 - \frac{3}{2}\left(\frac{eV}{T_K}\right)^2\right], & eV \ll T_K \\ G_0 \frac{3\pi^2/16}{[\ln(eV/T_K)]^2}, & eV \gg T_K \end{cases} \tag{60}$$

Thus, a large voltage bias $eV \gg T$ has qualitatively the same destructive effect on the Kondo physics as the temperature does. If temperature $T$ exceeds the bias, $T \gg eV$, the differential conductance $dI/dV$ coincides with the linear conductance $G$, see Eqs. (48),(56) above.

## 6. Conclusion

In the simplest form of the Kondo effect considered in this article, a quantum dot behaves essentially as a magnetic impurity with spin 1/2 coupled via exchange interaction to two conducting leads [24]. However, the characteristic energy scale for the intra-dot excitations is much smaller than the corresponding scale for a real magnetic impurity. This allows one to induce some degeneracies in the ground state of a dot which are more exotic than just the spin degeneracy considered above. One of the possibilities is to create a degeneracy between a singlet state and a component of a triplet state by applying a magnetic field to a dot with an even number of electrons. Depending on the relation between the Zeeman energy and the value of the diamagnetic shift of orbital levels in a magnetic field, this degeneracy gives rise to various "flavors" of the Kondo effect. A review of the corresponding experiments and theory can be found in [37]

In our discussion of the Kondo effect we assumed that the dot remains close to an equilibrium state even under the conditions of an electron transport experiment. In fact, this limitation led us to consider a very asymmetric setup of a quantum dot device in Sec. 5.2, where the non-linear electron transport is discussed. One of the advantages of quantum dots, however, is that these devices allow one to study the Kondo effect in truly out-of-equilibrium conditions. Such conditions may be created by applying a significant dc bias between the leads,

or by irradiating a dot by microwaves [38]. In the latter case one can monitor the "health" of the Kondo effect by measuring the linear dc conductance at the same time. It turns out that microwaves suppress the effect [38] by destroying the coherence of the spin state of the dot [39]. In the former case, one can apply a strong magnetic field in addition to biasing the dot. Zeeman splitting then leads to peaks in the differential conductance at a finite bias [40, 41]. Interest to this problem was recently revived, see, *e.g.*, [42] and references therein.

These are only a few out of many possible extensions of the simple model discussed in this review.

## Acknowledgements

This work is supported by NSF grants DMR97-31756, DMR02-37296, and EIA02-10736.

## References

1. L.P. Kouwenhoven *et. al.*, in *Mesoscopic Electron Transport*, eds. L.L. Sohn, L.P. Kouwenhoven, and G. Schön (Kluwer, Netherlands, 1997), p. 105.
2. P. Joyez *et. al.*, Phys. Rev. Lett. **79**, 1349 (1997).
3. D. Goldhaber-Gordon *et. al.*, Nature (London) **391**, 156 (1998); S.M. Cronenwett, T.H. Oosterkamp, and L.P. Kouwenhoven, Science **281**, 540 (1998); J. Schmid *et. al.*, Physica (Amsterdam) **256B-258B**, 182 (1998). Science **289**, 2105-2108 (2000).
4. L. Kouwenhoven and L. Glazman, Physics World **14**, 33 (2001).
5. J. Kondo, Prog. Theor. Phys. **32**, 37 (1964).
6. C.W.J. Beenakker, Rev. Mod. Phys. **69**, 731 (1997).
7. M.L. Mehta, *Random Matrices* (Academic Press, New York, 1991).
8. B.L. Altshuler *et. al.*, Phys. Rev. Lett. **78**, 2803 (1997); O. Agam *et. al.*, Phys. Rev. Lett. **78**, 1956 (1997); Ya.M. Blanter, Phys. Rev. B **54**, 12807 (1996); Ya.M. Blanter and A.D. Mirlin, Phys. Rev. E **55**, 6514 (1997); I.L. Aleiner and L.I. Glazman, Phys. Rev. B **57**, 9608 (1998).
9. I.L. Aleiner, P.W. Brouwer, and L.I. Glazman, Phys. Rep. **358**, 309 (2002).
10. D. Davidovic and M. Tinkham, Phys. Rev. Lett. **83**, 1644 (1999).
11. M.P.A. Fisher and L.I. Glazman, in *Mesoscopic Electron Transport*, eds. L.L. Sohn, L.P. Kouwenhoven, and G. Schön (Kluwer, Netherlands, 1997), p. 331.
12. J.M. Ziman, *Principles of the Theory of Solids*, (Cambridge University Press, Cambridge, 1972), p.339.
13. P.W. Brouwer, Y. Oreg, and B.I. Halperin, Phys. Rev. B **60**, R13 977 (1999); H.U. Baranger, D. Ullmo, and L.I. Glazman, Phys. Rev. B **61**, R2425 (2000); I.L. Kurland, I.L. Aleiner, and B.L. Altshuler, Phys. Rev. B **62**, 14886 (2000).
14. Y. Alhassid, Rev. Mod. Phys. **72**, 895 (2000).
15. I.O. Kulik and R.I. Shekhter, Sov. Phys. JETP **41**, 308 (1975); L.I. Glazman and R.I. Shekhter, J. Phys. Cond. Matt. **1**, 5811 (1989).

16. I. Giaever and H.R. Zeller, Phys. Rev. Lett. **20**, 1504 (1968); H.R. Zeller and I. Giaever, Phys. Rev. **181**, 789 (1969).
17. D.V. Averin and Yu.V. Nazarov, Phys. Rev. Lett. **65**, 2446 (1990).
18. A.A. Abrikosov, *Fundamentals of the Theory of Metals*, (North-Holland, Amsterdam, 1988), p. 620.
19. I.L. Aleiner and L.I. Glazman, Phys. Rev. Lett. **77**, 2057 (1996).
20. L.I. Glazman and M.E. Raikh, JETP Lett. **47**, 452 (1988); T.K. Ng and P.A. Lee, Phys. Rev. Lett. **61**, 1768 (1988).
21. W.G. van der Wiel *et. al.*, Phys. Rev. Lett. **88**, 126803 (2002).
22. C. B. Duke, *Tunneling in Solids* (Academic Press, New York, 1969); J. M. Rowell, in *Tunneling Phenomena in Solids*, eds. E. Burstein and S. Lundqvist (Plenum, New York, 1969), p. 385.
23. A.F.G. Wyatt, Phys. Rev. Lett. **13**, 401 (1964); R.A. Logan and J.M. Rowell, Phys. Rev. Lett. **13**, 404 (1964).
24. J. Appelbaum, Phys. Rev. Lett. **17**, 91 (1966); P.W. Anderson, Phys. Rev. Lett. **17**, 95 (1966).
25. M. Pustilnik and L.I. Glazman, Phys. Rev. Lett. **87**, 216601 (2001).
26. A.M. Tsvelick and P.B. Wiegmann, Advances in Phys. **32**, 453 (1983); N. Andrei, K. Furuya, and J.H. Lowenstein, Rev. Mod. Phys. **55**, 331 (1983).
27. M. Pustilnik and L.I. Glazman, Phys. Rev. B **64**, 045328 (2001).
28. P.W. Anderson, *Basic Notions of Condensed Matter Physics* (Addison-Wesley, Reading, 1997).
29. K.G. Wilson, Rev. Mod. Phys. **47**, 773 (1975).
30. L.I. Glazman, F.W.J. Hekking, and A.I. Larkin, Phys. Rev. Lett. **83**, 1830 (1999).
31. G.D. Mahan, *Many-Particle Physics* (Plenum, New York, 1990).
32. P.W. Anderson, J. Phys. C **3**, 2436 (1970).
33. A.A. Abrikosov, Physics **2**, 21 (1965).
34. P. Nozières, J. Low Temp. Phys. **17**, 31 (1974); J. Physique **39**, 1117 (1978).
35. I. Affleck and A.W.W. Ludwig, Phys. Rev. B **48**, 7297 (1993).
36. T.A. Costi, A.C. Hewson, and V. Zlatić, J. Phys.: Cond. Mat. **6**, 2519 (1994).
37. M. Pustilnik *et. al.*, Lecture Notes in Physics, **579**, 3 (2001).
38. J.M. Elzerman *et. al.*, J. Low Temp. Phys. **118**, 375 (2000).
39. A. Kaminski, Yu.V. Nazarov, and L.I. Glazman, Phys. Rev. Lett. **83**, 384 (1999).
40. J.A. Appelbaum, Phys. Rev. **154**, 633 (1967).
41. Y. Meir, N.S. Wingreen, and P.A. Lee, Phys. Rev. Lett. **70**, 2601 (1993).
42. A. Rosch, J. Kroha, P. Wolfle, Phys. Rev. Lett. **87**, 156802 (2001).

# Quantum coherent transport: From mesoscopic circuits to molecular wires

H. Bouchiat , R. Deblock , M.Ferrier , S.Gueron , A.Kasumov , M.Kociak and B. Reulet
*Laboratoire de Physique des Solides , Associé au CNRS, UMR 8502, Bât 510, Université Paris–Sud, 91405 Orsay France*

**Abstract.** The purpose of these lectures is to present some basic signatures of phase coherent transport in various electronic systems going from mesoscopic to nanoscopic scales, from micron size Aharonov Bohm rings to molecular wires such as DNA and carbon Nanotubes. The Aharonov Bohm geometry is well suitable for the investigation of phase coherence in mesoscopic rings which exhibit orbital magnetism and electrical polarisability reminding the magnetic and electric responses of molecules. This is particularly the case for semiconducting rings where energy spectrum can be resolved. On the other hand proximity induced superconductivity is a powerful tool to reveal phase coherence in molecular wires. This is specially interesting in the case of DNA where very little is known on the nature of electronic transport. In the case of carbon nanotubes the observation of high values of supercurrent strongly suggest the existence of intrinsic superconducting fluctuations as corroborated by experiments on long ropes of carbon nanotubes on normal contacts.



*R. Fazio et al. (eds.), New Directions in Mesoscopic Physics,* 117–148.
© 2003 *Kluwer Academic Publishers. Printed in the Netherlands.*

## 1. Introduction

Electronic transport in metals at low temperature presents various interesting features due to the coherence of the electronic wave functions. They depend on fundamental time and related length scales:

- The shortest length is the Fermi wave length $\lambda_F$. It varies between a few Å, in metals to a few hundred Å in lightly doped or heterostructured semiconductors.

- The disorder in the system is characterized by the elastic mean free path $l_e = v_F \tau_e$ where $v_F$ is the Fermi velocity and $\tau_e$ is the transport elastic scattering time. In disordered metals $l_e$ varies between a few hundred Å in polycristalline materials to a few Å in amorphous alloys. On the other hand in GaAs-GaAlAs heterostructures $l_e$ is of the order of $10\mu m$.

- The phase coherence length $L_\phi$ is the characteristic length for the interferences of the electronic wave functions. It is the typical length on which a wave packet can travel without loosing its phase coherence. $L_\phi$ increases with decreasing temperature and can be much larger than $l_e$ , i.e. of the order of few $\mu m$ for dirty metals and more than $20\mu_m$ in GaAs-GaAlAs heterostructures. It is the relevant length scale for mesoscopic physics.

  The inverse phase coherence time $\tau_\phi^{-1} = D/L_\phi^2$ where $D = v_F l_e$ is the diffusion coefficient, contains all possible physical mechanism susceptible to suppress quantum interference between electronic wave functions. In most cases $\tau_\phi$ is related to inelastic collisions like electron-phonon and at lower temperature electron-electron interactions. However phase breaking processes do not necessarily involve energy exchange between the interfering particle and environment degrees of freedom, but at least some modification of the environment state [1].

- The thermal length $L_T$, which is the typical length over which the different components of a wave packet of energy width $k_B T$ acquire a phase difference of the order of unity. (in a clean metal $L_T = \hbar v_F / k_B T$ and in a dirty metal $L_T = \sqrt{\hbar D / k_B T}$ where D is the electron diffusion coefficient).

One efficient tool to investigate phase coherence effects in electronic systems is to use the phase sensitivity of electronic wave functions to the magnetic field. More precisely the potential vector modifies the wave function $\Psi(r)$ according to $\Psi_A(\vec{r}) = \Psi(\vec{r}) \exp\left(2i\pi \int \vec{A}(\vec{r}\right) d\vec{r})$. As a result, the magnetoconductance of a phase coherent ring exhibits quantum oscillations whose periodicity corresponds to one flux quantum $\Phi_0 = h/e$ through the area of the sample [2]. The phase of the first harmonics of these oscillations are sample specific. They do not resist to ensemble average. On the other hand the second harmonics, have a contribution which resists to ensemble average. It results from the interference between time reversed paths around the ring (weak localisation contribution) [3]. These $h/2e$ periodic oscillations could be observed in long cylinders or connected arrays of rings [4]. Their sign corresponds to a positive magnetoconductance in zero field.
These oscillations constitute in general a small correction on the conductance of the mesoscopic ring which is at first approximation still given by the classical Drude conductance which in units of $e^2/h$ reads $g_D = Ml_e/L$. There also exist a number of experiments which can address electronic properties of mesoscopic samples without coupling to macroscopic wires. In particular it has been shown that in spite of its finite resistance, a mesoscopic ring pierced by an Aharonov Bohm flux exhibits persistent currents at equilibrium which can be investigates by measuring their magnetic susceptibility. These experiments will be discussed in parallel with electrical polarisability in the first part of this course. We show that in contrast with the connected case, the response of an isolated system can be dominated by quantum effects and presents some analogies with the electromagnetic response of a molecule. In the case of mesoscopic rings made from low electronic density GaAs/GaAlAs 2D electron gas the quasi discrete nature of the energy spectrum and the choice of the statistical ensemble (Canonical or Grand-Canonical) are new features of isolated mesoscopic systems.
Another way to probe phase coherence in a quantum mesoscopic wire is to investigate proximity induced superconductivity when connected to superconducting reservoirs which impose a phase shift on boundary conditions analogous with the Aharonov Bohm flux through a ring made from the same wire. In this spirit, we present in the second and third part of this lecture transport experiments on DNA molecules and carbon nanotubes connected to superconducting electrodes. . Observation of proximity induced superconductivity through DNA provides interesting information on the nature of transport in this molecule on which very little is known concerning electronic structure, however no Josephson currents were detected . On the other hand we show

that proximity induced superconductivity is surprisingly robust in carbon nanotubes. More over intrinsic superconductivity is observed in ropes containing 30 to 300 single walled carbon nanotubes connected to normal contacts provided that the distance between the normal electrodes is large enough, otherwise superconductivity is destroyed by (inverse) proximity effect. These experiments indicate the presence of attractive interactions in carbon nanotubes which overcome coulomb repulsive interactions at low temperature and enables investigation of superconductivity in a 1D limit never explored before.

## 2. Electromagnetic response of Isolated mesoscopic rings

An efficient way to probe the ac conductance of isolated mesoscopic objects is to couple them to a highly sensitive electromagnetic resonator, and investigate how the resonance is perturbed. Dissipation occurring in the samples affects the quality factor of the resonator, whereas the non dissipative part of the response affects the resonance frequency.
Considerations of coupling optimization between the samples and the detector, have led us to use the superconducting niobium resonator depicted in fig.1. The resonator is composed of an inductance (meander line) and a capacitance (comb-like structure), with the rings either on the inductive part either on the capacitive part. The detailed fabrication and characterization of this type of resonator is described in reference [5].
By measuring the shift of the resonance frequency $f$ of the resonator induced by the presence of the rings, we have access to $\chi_m$ $\chi_e$ the averaged magnetic , electric susceptibility of the rings, according to:

$$\frac{\delta f}{f} = -\frac{1}{2} N k_{m,e} \chi_{m,e} \tag{1}$$

where $N$ is the number of rings coupled to the resonator, $k_{m,e}$ are coefficients characterizing the coupling of one ring to the inductive, capacitive part of the resonator [5]. This quantity recorded as a function of the amplitude of a DC magnetic field yields the flux dependence of the susceptibility. It is also possible to detect the out of phase dissipative response from the quality factor.

### 2.1. Magnetic response: diamagnetic persistent currents

The magnetic response of a mesoscopic ring pierced by an Aharonov Bohm flux i.e. its orbital magnetism is directly related to persistent currents defined as $I = -\partial F/\partial \Phi$, which is a direct measurement of the

sensitivity of the coherent wave functions to a phase shit in boundary conditions function of $\Phi$ [6]. Persistent currents in mesoscopic rings have been studied for over 10 years theoretically [7, 8, 9, 10, 11, 12, 13] and experimentally addressing the question of either the typical current (measured on a single or a small number of rings) [14, 15, 16, 17], or of the ensemble averaged persistent current (measured on arrays of rings) [18, 19, 16, 5]. However we will see that theory and experiment still do not agree concerning the sign of the average value of these persistent currents.

Using the technique described in the preceeding paragraph, we have investigated the magnetic response of large arrays of disconnected metallic (silver) [20] and 2D semiconducting GaAS/GaAlAs rings [5] by coupling them to the inductive part of the resonator. In both cases the dimensions of the rings are chosen in order that their phase coherence length is larger than their circumference. They correspond however to very different physical limits. The GaAs rings contain typically 1000 electrons with a energy level spectrum which can be considered as discrete ( level spacing of the order of 80mK), the elastic mean free path is of the order of the circumference of the rings. Spin-orbit scattering in negligible. On the other hand Ag rings contain more than $10^9$ electrons and are deeply in the diffusive regime, with a mean free path of 30nm much smaller than the circumference. Further more they correspond to a rather strong spin-orbit scattering regime where the spin orbit scattering length is smaller that the phase coherence length.

The silver rings were fabricated on the same substrate than the resonator and aligned between the meanders of the inductive part, see fig.1. On the other hand the GaAs rings are sitting on a different substrate. The resonance frequency shift versus magnetic field is depicted in fig. 2for the Ag rings after substraction of the parabolic contribution of the bare resonator. At $T = 40$ mK oscillations are visible. At higher temperature ($T = 140$ mK) the oscillations are strongly reduced as also visible on the Fourier transform of the two previous curves. At low temperature the periodicity measured is consistent with half a flux quantum in the area enclosed in a ring, as expected for the average susceptibility [8, 21]. A similar signal has been measured on GaAs rings [5]. For both systems from the value of the maximum frequency shift $\delta_\Phi f = f(\Phi_0/4) - f(\Phi = 0)$ and given the coupling coefficient $k_m$ [5, 20] we deduce the amplitude of the variation with magnetic field of the magnetic susceptibility $\delta_\Phi \chi(\omega) = 5.3 \pm 0.9\, 10^{-24}$ m$^3$. In order to compare this value to existing theories on orbital magnetism we make the assumption that the signal measured is due to persistent currents:

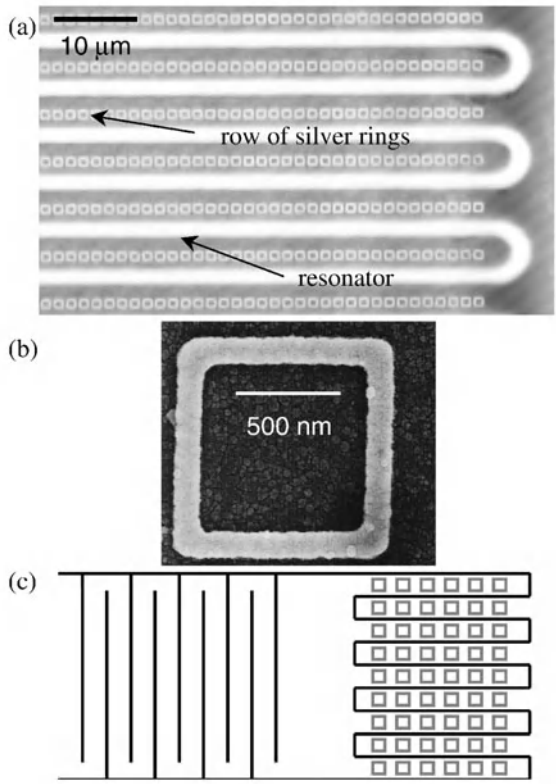


*Figure 1.* (a) Photograph of a part of the resonator with the silver rings. (b) Image obtained by scanning electron microscopy of one silver ring. (c) Schematic picture of the resonator with the square rings on the inductive part. The resonator has an inductive part (meander line) and a capacitive part (comb-like structure).

$$\frac{\partial I(\Phi)}{\partial \Phi} = -\frac{\delta f(\Phi)}{2f}\frac{\mathcal{L}}{N\mathcal{M}^2} \tag{2}$$

with $\mathcal{L} = 0.05\mu$H the estimated inductance of the resonator and $\mathcal{M} =$ 0.14 pH the calculated mutual inductance between one ring and the inductive part of the resonator. It is then possible for Ag rings to deduce the flux dependence of the average persistent current depicted

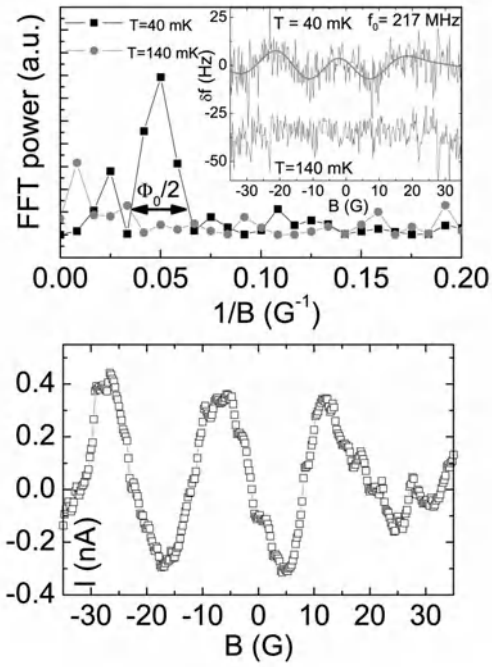


*Figure 2.* Top: Resonance frequency shift due to the silver rings at 40 mK and 140 mK versus magnetic field and Fourier transform of the same data . Bottom: Average persistent currents through the rings reconstituted from the field dependence of the resonance frequency according to expression 2 after high pass filtering at 0.025 $Gauss^{-1}$ and integration of the signal.

in Fig.2 which oscillates with a periodicity $\Phi_0/2$ and an amplitude $|I_0| = 0.33 \pm 0.05$ nA. Making a similar estimation for GaAs rings (taking into account in this case the misalignment of the rings with respect to the resonator) yields also average persistent currents of amplitude $|I_0| = 0.25 \pm 0.1$ nA. In both cases the current is diamagnetic at low field. Note that the sign of the susceptibility oscillations can be determined in a completely unambiguous way in this experiment, since it is directly related to the sign of the resonance frequency shift measured. Another check comes from the field dependence of the diamagnetic signal of the bare resonator. At the moment these experiments constitute the only one for which this question of sign can be really addressed. Previous experiments on arrays of Au rings [16] were not

conclusive concerning this sign because the current was not averaged on a sufficient number of rings.
We now compare our result with theoretical results. Predictions based on non-interacting electrons [12],lead to a current of amplitude $\Delta/\Phi_0$, and paramagnetic at low filed. More over these results would yield to a very small signal in Ag rings due to the very small value of the mean level spacing . In the case of interacting electrons [9], the expected value of the persistent current is of the order of $0.2E_c/\Phi_0 = 0.04$ nA, where $E_c = \hbar D/L^2$ is the Thouless energy for a ring of circumference L. This number is within an order of magnitude of the experimental value. However theory predicts in this case a paramagnetic current for repulsive interactions, with or without strong spin-orbit coupling [9, 10]. Considering instead attractive interactions, superconducting fluctuations in silver with a critical temperature of the order of 50 nK, would lead to a diamagnetic current (therefore in agreement with our experiment) with the same amplitude as the repulsive case. A similar explanation is however more doubtful for GaAs rings where superconducting fluctuations are a priori not expected.
All the previous analysis are valid in the limit of zero frequency. Our experiment however is performed at the resonance frequency of the resonator, above 200 MHz. In both systems this frequency is larger than $1/\tau_\Phi$ and not negligible compared to $1/\tau_D$ ($1/\tau_\Phi = 100$ MHz and $1/\tau_D = 1$ GHz). In this frequency range it is reasonable to expect extra contributions to the magnetic response of Aharonov-Bohm rings [20]. However these extra contributions are sensitive to spin orbit and are expected to give rise to magnetic susceptibilities of opposite sign for Ag and GaAs rings. The average diamagnetic sign of orbital magnetism in mesoscopic rings is still not easy to understand.

### 2.2. Electrical polarisability of GaAs rings

When an electric field $\mathbf{E}$ is applied to an isolated metallic sample, electron screening gives rise to an induced dipole $\mathbf{d}$. In the linear response regime :

$$\mathbf{d} = \alpha \mathbf{E} \tag{3}$$

where $\alpha$ is the electric polarizability. For a sample of typical size $a$ much larger than the Thomas-Fermi screening length $\lambda_s$, $\alpha$ is essentially determined by geometry, with a negative correction of the order of $\lambda_s/a$ [23]. The measurement of $\alpha$ yields information on the way electrons screen an external electric field. At the mesoscopic scale, when phase coherence through the sample is achieved, it is natural to expect that screening of an electric field should also be sensitive to this phase coherence, leading to a flux dependent mesoscopic correction to polarizability

[24, 25, 26]. In particular the polarizability of an Aharonov-Bohm ring is expected to exhibit oscillations as a function of the magnetic flux provided that the width W of the rings is not too large compared to the Thomas Fermi screening length which is the case for the GaAs rings described in the previous section corresponding to $\lambda_s/W$ 0.2. The experimental setup described in previous section is also adequate for the investigation of the effect of phase coherence on electric polarisability when the array of GaAs rings is placed on the top of the capacitive part of the resonator. The capacitance $C$ of the resonator is indeed modified by the non dissipative response $\alpha^{'}$ of the rings [27, 5]:

$$\frac{\delta C}{C} = kN_s\alpha^{'} \tag{4}$$

where $N_s$ is the number of rings coupled to the resonator and $k$ the electric coupling coefficient between a ring and the capacitance, which only depends on geometry. This change in $C$ shifts the resonance frequency.

$$\frac{\delta f}{f} = -\frac{1}{2}kN_s\alpha'(\omega), \tag{5}$$

We observe (see fig.3) like in the experiments depicted in the previous section, resonance frequency oscillations periodic in field with a period of 12.5 G which corresponds to half a flux quantum $\Phi_0/2 = h/2e$ in a ring. Their amplitude are however of the order of 100Hz that is more than an order of magnitude larger than the corresponding magnetic signal. From the amplitude of $\delta_\Phi f/f = (f(\Phi = \Phi_0/4) - f(\Phi = 0))/f$, is $-2.8\,10^{-7}$ and the estimation of the geometrical coupling factor $k_e$ [5] one obtains $\delta_\Phi\alpha'/\alpha_{1D} = 0.7\,10^{-3}$, where $\alpha_{1D} = \epsilon_0\pi^2R^3/\ln(R/W)$ is the polarizability of a ring of radius R and width W.

When comparing this result to theoretical predictions it is essential to take into account the finite frequency of the measurement compared to the average level spacing. There is indeed no flux dependent polarisability at equilibrium in a diffusive Aharonov Bohm ring. This can be shown easily [28] using the simple thermodynamic relation between the flux dependent polarisability and the second derivative of the persistent current with respect to a static electric field.

On the other hand when the frequency is much larger than the level spacing the polarisability is which can be expressed in terms of the average square of the matrix element of the screened potential inside the ring, which flux dependence gives rise to a $\phi_0/2$ periodic magnetopolarisability positive at low magnetic field of amplitude:

$$\frac{\delta_\Phi\alpha^{'}}{\alpha^{'}} = \frac{\epsilon}{16\pi^2\ln(R/W)}\frac{\Delta}{E_c}\frac{\lambda_s}{W} \tag{6}$$

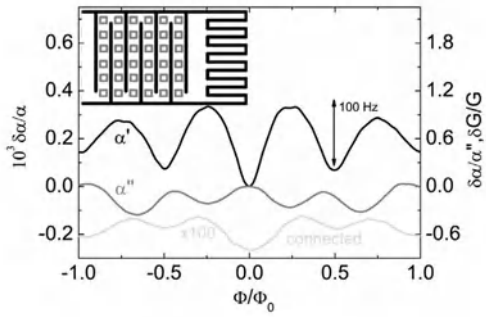


*Figure 3.* Magnetic field dependence of the in phase and out of phase polarisability obtained from the resonance frequency of the resonator and inverse quality factor 1/Q versus magnetic field . These quantities are directly proportional to the respectively non dissipative and dissipative ac magnetoconductance of the rings and can be compared to the same quantity measured on the same connected rings. Inset : schematic picture of the resonator and the rings on its capacitive part.

Where enters the ratio between the Thouless energy $E_c$ and the level spacing also identical to the dimensional conductance of the ring g. Our experiment corresponds to an intermediate situation where the frequency corresponds to $\hbar\omega/\Delta = 0.2$. The complete frequency dependence of the magnetopolarisability in the CE ensemble (corresponding to our experiment performed on isolated rings) has been recently derived by Blanter and Mirlin [29] from their results we could estimate a magnetopolarisability reduced by 50 % compared to the high frequency value (in the limit of small level broadening). As a consequence the expected value for $\delta_\Phi \alpha'_{CE}/\alpha_{1D}$ is then $6\,10^{-4}$ which is of the same order of magnitude than the experimental value. The agreement between experiment and theory is remarkably good for the dielectric response of the rings in contrast with the magnetic one discussed above. By measuring the quality factor of the resonator versus magnetic field, we have access to the flux dependent electric absorption The contribution due to the rings see fig.3 exhibits the same periodicity than the frequency shift, which corresponds to half a quantum flux in a ring. The low field signal decreases. It corresponds to a negative magnetoconductance, i.e. opposite to weak-localization observed in the same connected rings when their conductance is probed by connecting them to a voltage source. Electric absorption and conductance for an electric dipole are related through :

$$G_e = \frac{\omega\alpha''}{a^2} \tag{7}$$

This surprising sign was pointed out in the context of the magneto-conductance of rings submitted to an oscillating magnetic flux in the discrete spectrum limit [30, 31, 32].
The sign and amplitude of the average variation of electric absorption is then indeed related to the level spacing distributions function [33, 28, 5] which obeys universal rules of random matrix theory [35, 34] :

$$\frac{\delta_\Phi \alpha''}{\delta_\Phi \alpha'} = \frac{2\pi\omega}{\Delta}(R^{GUE}(\frac{\pi\omega}{\Delta}) - R^{GOE}(\frac{\pi\omega}{\Delta})) \tag{8}$$

$R^{GOE}$ is the two level correlation function in the orthogonal ensemble (in the presence of time reversal symmetry i.e. $\phi = 0, \Phi_0/2$ and $R^{GUE}$ in the unitary ensemble(corresponding to time reversal symmetry breaking i.e. for other values of flux) .
The strong negative magnetoconductance observed at frequencies smaller than the level spacing is then directly related to the fact that level repulsion in a disordered systems is higher in GUE than in GOE. It is clear that this effect is expected to disappear when the level broadening is comparable to the level spacing, and in particular in a connected ring where the electronic spectrum is continuous due to strong mixing between the electronic wave functions of the rings and those of the connection wires. The physics is then dominated by weak localisation which gives rise to smaller magnetoconductance oscillations reversed in sign, see fig.3.
To conclude this section we have shown that the ac response of isolated mesoscopic Aharonov Bohm rings is fundamentally different from the conductance of the same connected objects. It is always dominated by its non dissipative one which can be either related to the orbital magnetism (persistent currents) or to the magneto-polarisability which is the electric counter-part. For low density GaAs rings it was also possible to detect the dissipative dielectric response which flux dependence opposite in sign to the weak localisation oscillations observed on the same connected rings and can be related to the sensitivity of the energy spectrum statistics to time reversal symmetry breaking.

## 3. Proximity induced superconductivity in DNA molecules and carbon nanotubes

### 3.1. Proximity induced superconductivity as a probe of quantum transport

The hope to use molecules as the ultimate building blocks of electronic circuits motivates the quest to understand electronic transport

in molecular wires. However most molecules with delocalized electronic orbitals undergo a structural Peirls transition to an insulating state at low temperature[36]. Few systems are exceptions to this rule. Carbon nanotubes discussed in the next section are one of them [37]. The situation of DNA molecules is a lot more controversial. Optical experiments have indicated the possibility of charge transfer in DNA molecules [38]. As for transport measurements, some indicate that DNA molecules could be conducting [39, 40] and others that they are insulating [41, 42]. Motivated by this puzzle, we have performed transport experiments on DNA molecules connected to superconducting electrodes 0.5 $\mu m$ apart. Such an experiment does not only probe the conduction of DNA but also the coherent nature of the transport from the observation proximity induced superconductivity below the superconducting transition temperature of the electrodes. The proximity effect (PE), i.e. the penetration of superconducting correlations in a non superconducting (normal) conductor connected to it, has been extensively measured in metallic multilayers [43], mesoscopic wires made of noble metals [44]. A normal metal (N) in good contact with a macroscopic superconductor (S) is in the proximity effect regime: superconducting correlations will enter the normal metal over a characteristic length $L_N$ which is the smallest of either the phase coherence length in the normal metal $L_\phi$ or the thermal length $L_T$. Both lengths, of the order of a few $\mu m$, can be much longer than the superconducting coherence length $\xi = hv_F/\Delta$ or $\sqrt{\hbar D/\Delta}$ where $\Delta$ is the energy gap of the superconducting contacts. If the normal metal's length is less than $L_N$ and if the resistance of the NS interface is sufficiently small, a gap in the density of states is induced in the normal metal that is as large as the gap of the superconductor in the vicinity of the interface and decreases on the length scale $L_N$ . Consequently, a normal metal shorter than $L_N$ between two superconducting electrodes (a SNS junction) can have a critical temperature equal to that of the superconductor alone and exhibit a Josephson effect like tunnel junctions, i.e. a supercurrent at zero bias. The maximum low temperature value of the supercurrent (critical current) in such SNS junctions of normal state resistance $R_N$ is : $\pi\Delta/eR_N$ in the short junction limit $L << \xi$ or $\Delta << E_c$[45], and $\alpha E_c/eR_N$ , with $\alpha$ a numerical factor of the order of 10, in the limit of long junctions $L >> \xi$ or $E_c << \Delta$ [46]. Probing the proximity effect in a normal wire connected to superconducting electrodes and in particular the existence of a Josephson current constitutes a powerful tool for the investigation of phase coherent transport through this normal wire. It is interesting to note that the physical conditions for observing proximity induced superconducivity in a wire are the same than the one necessary to observe Aharonov Bohm effect in a loop of identical length. Observing

a PE in molecular wires implies not only that these molecules are conducting and form a low-resistance contact with the superconducting electrodes but also more fundamental, that both thermal length and phase coherence length are of the order of the length of the molecules.

### 3.2. DNA molecules

The experimental system consists of double-stranded 16$\mu m$-long $\lambda$-DNA molecules connecting two superconducting Re/C electrodes, deposited by r.f. diode sputtering on a freshly cleaved mica substrate. The Re film was 2 nm-thick. The same nominal thickness of C did not produce a smooth film, but rather a "forest" of individual fibers up to 40 nm-tall see fig.4. The resistance of this Re/C bilayer is $\sim$ 100 $\Omega$ per square and undergoes a superconducting transition around 1K. The thinness of the Re film was intended to minimize kinks in the DNA molecules at the edges of the metallic pads, since such kinks could hinder electronic transport from the contacts through the molecule. The deposited Re/C film was cut by focused laser beam in order to prepare 6 structures for transport measurements. Each structure consists of a double submicron slit which separates the Re/C film into two broad electrodes. The resistance of the structures was more than 1 G$\Omega$, and decreased to several k$\Omega$ after deposition of DNA molecules.
In order to obtain aligned DNA molecules across the submicron gaps, we first glow-discharged the Re/C covered mica substrate in the presence of pentylamine vapor, this treatment is essential since it promotes adhesion of the molecules with out squeezing them on the surface[47, 48]. We then combed the DNA molecules using a continuous flow of DNA solution [49, 50] and see fig.4. After deposition, the samples were imaged with an atomic force microscope (AFM). It was checked that the thickness of the molecules deposited within this technique is of the order of 2nm in contrast with much smaller values measured on molecules deposited on pure mica which exhibit a thickness smaller than 1nm. Strong correlation between thickness of deposited molecules and their conductivity have been evidenced recently from conducting AFM measurements [51]. The density of deposited DNA molecules depended on the duration of deposition.
We present low temperature transport measurements on 2 such structures: sample DNA1, with a 30 $\mu$m-wide unetched window, contains approximately 10 combed molecules as estimated from AFM observations; sample DNA2, with a 120 $\mu m$-wide window, has about 40 combed DNAs; . The room temperature resistances are respectively 17, 11 k$\Omega$ [52]. Magnetic fields up to 5 T could be applied perpendicularly to the contacts and the molecules. Down to 1 K, both samples present a mod-

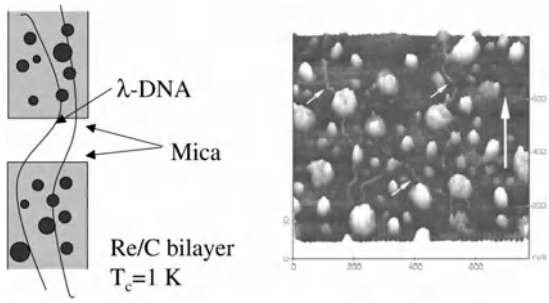


*Figure 4.* a. Schematic drawing of the measured sample with DNA molecules combed between Re/C electrodes on a mica substrate. b. Atomic force microscopy image showing DNA molecules combed on the Re/C bilayer. The large vertical arrow indicates the direction of the solution flow. The small arrows point toward the combed molecules. Note the forest structure of the carbon film.

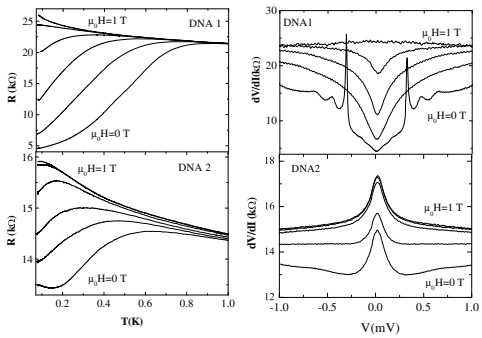


*Figure 5.* Left panel: dc resistance of DNA1 and DNA2 as a function of temperature, below 1K, for different values of the magnetic field. Right pannel Voltage dependence of the differential resistance measured at 50 mK in magnetic fields of 0,0.2,0.4,0.6,0.8 and 1T for the same samples. These measurements were done with an ac excitation current of 1nA at 30 Hz.

erate monotonous increase of resistance with decreasing temperature, which can be approximately fitted by a small negative exponent power law. In all this temperature range the transport is ohmic, the voltage drop across the samples is a linear function of voltage up to 10 mV which corresponds to a current in the $\mu A$ range.

The temperature dependence changes drastically below the superconducting transition of the Re/C contacts, around 1K. The resistances of DNA1 and DNA2 decrease, by 75% at 0.05K for DNA1 and by

15% for DNA2. The resistance of DNA2 increases slightly below 0.1K (see fig.5). The transition observed on DNA1 and DNA2 is shifted to lower temperature in a magnetic field, and disappears at fields higher than 1 T, where the resistance increases with decreasing temperature, and all curves overlap. We attribute these transitions to a lower state resistance to a proximity effect in the SNS systems constituted by DNA1 and DNA2 between the two superconducting electrodes. At low temperature the transport on these samples is non linear, as illustrated in fig. 5. In zero magnetic field, the differential resistance of DNA1 dips at low voltage, with two sharp peaks at 300 $\mu$V (close to the gap of Rhenium estimated around 200 $\mu V$ at zero magnetic field), followed by bumps at higher voltage. The normal state resistance is recovered above 1 mV. This low bias differential resistance dip becomes weaker and narrower at higher magnetic field and disappears around 1T. Above 1T the differential resistance is peaked at zero current . The behavior of DNA2 is intermediate, with a zero bias peak at all magnetic fields, within a larger dip which disappears around 1T. The differential resistance curve of DNA1 is very typical of incomplete proximity-induced superconductivity. The broad dip in DNA2 can also be interpreted as residual induced superconductivity. At this stage the most reasonable explanation for the different behaviours of the two samples is different transparencies of the contacts between the molecule and the superconducting film. It is also possible that the certainly different base sequences in the different samples play a role.

After the samples were warmed back to RT, micro-drops of a saline buffer (1 mM $CaCl_2$, 10 mM Tris) were continuously deposited on DNA1. The sample resistance remained identical to its initial value for more than half an hour of continuous buffer deposition. But when a DNAse enzyme was added to this buffer the resistance rapidly increased to about 1G$\Omega$ after 30s. This last experiment proves that the transport was indeed taking place through DNA molecules.

These experiments show that ohmic electric conduction can occur through DNA molecules on distances of the order of a few hundred nanometers, even at very low temperature. This result corroborates previous observations by Fink et al.[40], but we find resistance values one order of magnitude lower, for samples with comparable numbers of molecules. This is probably due to better contacts in our case. Observation of proximity induced superconductivity indicates that electronic quantum phase coherence is achieved in DNA molecules at low temperature on a length of the order of a few hundred nanometers. More precisely, the observation of a resistance drop by more than a factor 2 on DNA indicates that the thermal length at 0.1K is at least half of the length L of the molecules between superconducting contacts i.e. 100nm. This

argument also yields a lower bound for the Fermi velocity of carriers. $v_F > Lk_BT/\hbar \simeq 10^3 m/s$ assuming ballistic transport an even higher value of $v_F$ would be obtained using expressions for diffusive transport. However at the moment there is no clear understanding of what could be the physical mechanism involved in the conduction process. The electronic structure of the molecules is not a priori favorable to the existence of chains of delocalized $\pi$ orbitals along the molecule that would form a half filled conduction band, as is the case in carbon nanotubes. On the other hand, several authors have suggested [53, 54] that the structure of DNA with a $\pi$ electron system of four bases stacked upon each other can provide a mechanism of electron transfer along the DNA involving hole hopping from one Guanine base to the next. This conduction process is strongly dependent on the base sequence and is thermally activated, it should therefore lead to an exponential increase of resistance at low temperature, in strong disagreement with our experimental findings.

We should emphasize that the role of the contacts could be crucial in acting as strong electron or hole dopants. They could provide a sufficient number of carriers delocalized along the molecular wire because of the quasi-absence of electrostatic screening in one dimension [55]. A systematic investigation of the transport properties of DNA molecules connected to metal contacts with different electronic work functions should be a way to shed light on this issue. The influence of the substrate and the nature of ions trapped on the molecules may also be important.

### 3.3. Individual carbon nanotubes

Single wall carbon nanotubes are constituted by a single graphene plane wrapped into a cylinder. The Fermi surface of graphene is very particular, it is reduced to six discrete points at the corners of the first Brillouin zone. As a result, depending on their diameter and their helicity which determine the boundary conditions of the electronic wave functions around the tube, SWNT can be either semiconducting or metallic. When metallic they have only two conducting channels [37].

It has been shown that these two conduction modes of carbon nanotubes are only very weakly coupled by electron interactions. SWNT are thus expected to exhibit electronic properties similar to systems presenting 1D conducting ladders with very small transverse coupling .

Electron-electron interactions in 1D systems have been shown to determine their low temperature properties, with a non-Fermi liquid behavior characteristic of a Luttinger liquid state (LL) [56, 57] with

collective low energy plasmon-like excitations giving rise to anomalies in the single particle density of states, but no long range order. Proof of the validity of LL description with repulsive interactions in SWNT was given by the measurement of a resistance diverging as a power law with temperature down to 10 K [58] with an exponent depending on whether contacts are taken on the end or in the bulk of the tube. From these exponents it was possible to deduce the LL parameter $g$ measuring the strength of the interactions $g = 0.25 + -0.05$. This value which is much smaller than 1 indicates dominant repulsive interactions. The extrapolation of this power law behavior down to very low temperature would indicate an insulating state. However, these measurements were done on nanotubes separated from measuring leads by tunnel junctions. Because of Coulomb blockade [59], the low temperature and voltage transport regime could not be explored.

We have developed a technique in which measuring pads are connected through low resistance contact to suspended nanotubes [60]. It is then possible to obtain individual tubes with a resistance at room temperature no larger than 40 $k\Omega$, that increases only slightly at low temperatures (typically a 20% resistance increase between RT and 1 K. The current versus voltage ($IV$) curves also exhibit logarithmic non-linearities at low temperature. This weak temperature dependence has also recently been measured in samples where good contact to electrodes was achieved by burying the tube ends over a large distance under metallic electrodes fabricated with electron beam lithography [65]. It is on the other hand in stark contrast with the T dependence of tubes with tunnel contacts [58] , which exhibit power laws with much larger exponents (of the order of 0.3) at high temperature, and exponentially increasing resistance at lower temperature because of Coulomb blockade. It is not surprising that in addition to the intrinsic conducting properties of tubes (interactions, band structure, disorder), the way they are contacted should determine the temperature dependence of the resistance. For instance extrapolating the results obtained on Luttinger liquids between normal reservoirs [66], the resistance of a ballistic tube on perfect contacts is expected to be insensitive to interactions and to be given by $R_Q/2 = h/2e^2 = 6.5\ k\Omega$ at all temperatures.

We have observed proximity induced superconductivity in the three different isolated SWNT ST1,ST2 and ST4 . These samples are mounted on Ta/Au electrodes which are a bilayer (5 nm Ta, 100 nm Au) with a transition temperature of the order of 0.4 K. This value is strongly reduced compared to the transition temperature of bulk tantalum (4K) due to the large thickness of gold relative to tantalum.

For these three samples the temperature dependence of the zero bias resistance exhibits a broad transition around the superconducting trans-

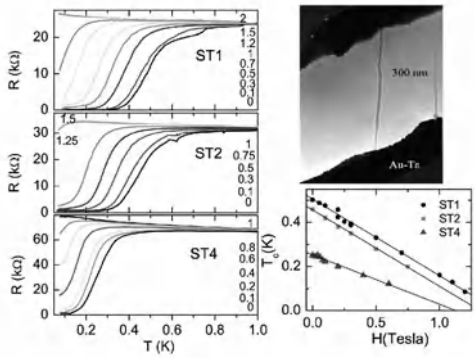


*Figure 6.* Temperature dependence of the resistance of 3 different single tubes $ST1, 2, 4$. mounted on TaAu measured for different values of the magnetic field perpendicular to the tube axis in the plane of the contacts. (The labels on the curves correspond to the value of magnetic field in Tesla). The arrow indicates the temperature below which the contact resistance is zero. Top Inset: Transmission electronic microscopy picture of the nanotube ST1 suspended between the two TaAu contacts . Bottom inset: Field dependence of the transition temperature (defined as the inflection point of R(T)).

ition temperature of the contacts and becomes zero at lower temperature except for the highest resistance sample ST4 ($R_N = 70\ k\Omega$) which has a residual resistance of 800 Ω. The transition is shifted to lower temperature when a magnetic field is applied in the plane of the contacts and perpendicular to the tube axis. Above 2 Tesla the resistance becomes field independent and slightly increases when the temperature is lowered below 0.2 $K$ as already mentioned in the previous section . The critical field, which can be also extracted as the inflection point of the magnetoresistance depicted in fig.3.3,is surprisingly high (of the order of 1 Tesla for all samples) and is ten times larger than the measured critical field of the contact (0.1 T). It is possible that these high values of critical field are due to local modifications of the bilayer Ta /Au film in the contact region due to the laser pulse, in particular the melted upper gold film is probably much thinner than the original one. It is however important to note that these values of critical field are nearly the same for the various samples measured. They all vary linearly with temperature up to $T_c$ .

The most striking signature of induced superconductivity which was not observed in DNA molecules, is the existence of Josephson supercurrents through the samples [61]. The existence of a supercurrent shows up in the voltage vs. current curves and differential resistance, as show

in Fig.3.3. For sample $ST_1$, the transition between the superconducting state (zero voltage drop through the sample) and the dissipative (resistive) state is quite abrupt and displays hysteresis at low temperature. It is characterised by a critical current $i_c = 0.14\mu A$ near zero temperature. The value of the product $R_N i_c$ at $T = 0$, for the 3 samples, varies between 1.6 and 3.5 mV. We find that the product is more than 10 times larger than the maximum expected value ($\pi\Delta/e = 0.06\ mV$), where we deduce $\Delta$ from the $T_c$ of the superconducting electrodes. (We find also that all samples are in the short junction limit $E_c > \Delta$). It may me interesting to compare the energy $R_N i_c$ to the gap of pure tantalum $\Delta_{Ta} = 0.7mV$. However it is difficult to understand why the induced gap could be the gap of pure tantalum while the resistance drop of the tube follows the transition of the bilayer.

Somewhat unexpectedly and uncharacteristic of metal SNS junctions, the normal state resistance is not recovered above the critical current, but the V(I) curve shows further hysteretic jumps at higher currents.

These features also appear in the differential resistance dV/dI measured with a small ac current superimposed to the dc one. The superconducting state corresponds to the zero differential resistance measured at low dc current. At the critical current the differential resistance displays a sharp peak followed by smaller ones at higher current. Each peak corresponds to a hysteretic feature in the dc V-I curve . The peaks are linearly shifted to lower current when increasing magnetic field and all disappear above 2T. The field dependence of the critical current is found to be precisely linear for all samples, with disappearance of critical current above a field equal to 1 T.

It is very difficult to understand these results in the framework of conventional proximity induced superconductivity. In particular we have also shown that IV characteristics exhibit non linearities together with persisting signs of superconductivity at very large bias, i.e. much larger than the gap of the Ta/Au contacts (and even the gap of pure tantalum!). This behavior, which is not expected in proximity induced superconductivity, is similar to that observed in long superconducting filaments [68]: Above $i_c$, small normal regions of size comparable to the inelastic length $L_N$ are nucleated around defects in the sample (phase slip centers).

Observation of strong proximity effect indicates that phase coherent transport takes place in carbon nanotubes on the micron scale, however in the case of single wall tubes the surprisingly high values of critical currents cannot be described by the theory of SNS junctions where N is a LL with repulsive interactions [69, 70].

Our data could indeed be explained by the existence of superconducting fluctuations intrinsic to SWNT [71, 72]. For an infinite nanotube,

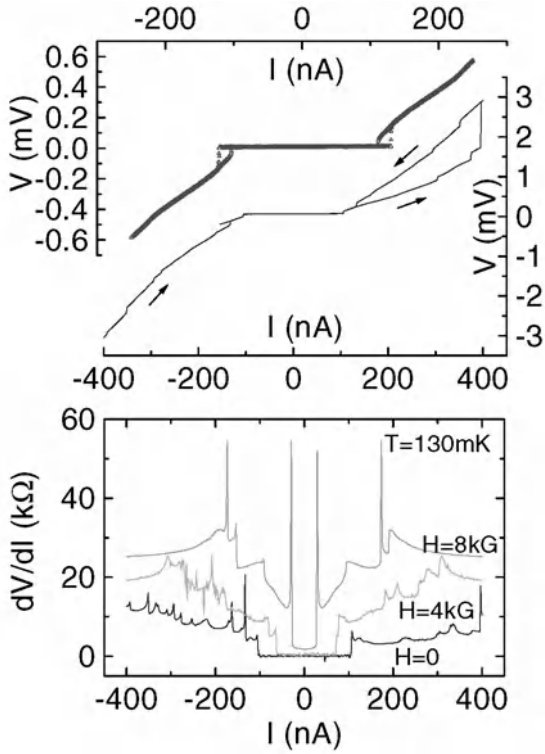


*Figure 7.* A) Upper curve, V(I) characteristics for the individual SWNT ST1 , from which the critical current is deduced. Lower curve, the same data on a wider current scale showing the existence of voltage steps for currents higher than $i_c$. B) Differential resistance measured with a small ac modulation of the current for various values of the magnetic field. It is clear from this data that the normal resistance $R_N = 25k\Omega$ is only recovered at currents much higher than $i_c$.

because of its 1D character, these fluctuations are not expected to give rise to a superconducting state at finite temperature. However, the superconducting state could be stabilized by the macroscopic superconductivity of the contacts. In such a situation, it is conceivable to expect the critical current to be enhanced compared to its value in a conventional SNS junction and to be identical with the critical current of a superconducting filament which reads $i_c = (4e^2/h)\Delta_t$ determined by the value of the superconducting pairing amplitude $\Delta_t$ inside the wire and independent of the normal state resistance of the nanotube (in the limit where the mean free path is larger than the superconducting coherence length). The existence of superconducting fluctuations

intrinsic to nanotubes may also help to explain the positive magnetoresistance observed in all our samples where the normal state resistance is recovered at fields much higher than the critical field of the contacts. We see in the next section that these statements are corroborated by the observation of intrinsic superconductivity in ropes of SWNT.

## 4. Intrinsic superconductivity in ropes of SWNT on normal contacts

Ropes of SWNT contacted using the same technique present a much wider range of resistance values than individual tubes: the resistances vary between less than 100 Ω and $10^5$ Ω at 300 K. There is also no systematic relation between the diameter of a rope and the value of its resistance. This may indicate that in certain cases only a small fraction of the tubes are connected. In contrast to individual nanotubes, the ropes seem to verify the Thouless criterion [73]: they strongly localize when their resistance is above 10 $k\Omega$ at room temperature and stay quasi-metallic otherwise. This behavior is very similar to what is observed in quasi 1D metallic wires. The temperature dependence of these ropes is also very weak. But for low resistance ropes ($R < 10k\ \Omega$) it is not monotonous, in contrast to individual tubes: The resistance decreases linearly as temperature decreases between room temperature and 30 K indicating the freezing-out of phonon modes, and then increases as T is further decreased, as in individual tubes.
In the following we discuss the low temperature transport (below 1K)of such suspended ropes of SWNT connected to normal electrodes. These electrodes consist of trilayers of sputtered $Al_2O_3/Pt/Au$ of respective thickness 5, 3 and 200 nm. They do not show any sign of superconductivity down to 50 mK.
As shown on figure, 8 depending on the samples various kinds of behavior are observed for the temperature dependence of the zero bias resistance. Some samples exhibit a weak monotonous increase of resistance as T is reduced, whereas others, on the other hand exhibit a resistance drop on a relatively wide temperature scale starting below a temperature $T^*$ between 0.4 and 0.1K. In particular the resistance of Pt2 decreases by more than two orders of magnitude, and reaches a constant value below 100 mK $R_r = 74\ \Omega$. This drop of resistance disappears when increasing magnetic field. For all the samples it is possible to define a critical field above which the normal state resistance is recovered. As shown on Fig.10 this critical field decreases linearly with temperature in a very similar way as observed in the previous section on tubes connected to superconducting contacts. We can define

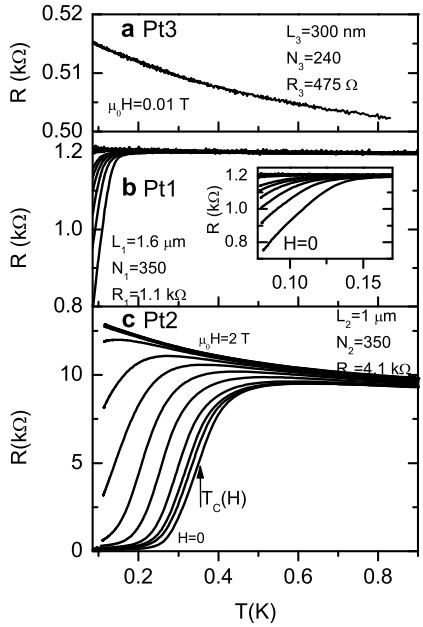


*Figure 8.* Resistance as a function of temperature for the three samples. The length L, number of tubes N and room temperature resistance R of each sample are given in the corresponding panel. a: Sample Pt3. b: Resistance of Pt1 in applied magnetic fields of $\mu_0 H$= 0, 0.02, 0.04, 0.06, 0.08, 0.1, 0.2, 0.4, 0.6, 0.8 and 1 T from bottom to top. Inset is a zoom of the low temperature region. c: Resistance of Pt2 at $\mu_0 H$=0, 0.05, 0.1, 0.2, 0.4, 0.6, 0.8, 1, 1.25, 1.5, 1.75, 2, 2.5 T from bottom to top.

a zero temperature critical field $H_c$ as the extrapolation of $Hc(T)$ to zero temperature.

In the temperature and field range where the zero-bias resistance drops, the differential resistance is strongly bias-dependent, with lower resistance at low bias (see Fig.9).

Although the experimental data of Pt2 seem similar to those of SWNT connected to superconducting contacts, there are major differences. In particular the $V(I), dV/dI(I)$ do not show any supercurrent because of the existence of a finite residual resistance.

Before going further in the data analysis it is important to note that it is the first time that superconductivity is observed in wires having a number of channels smaller than one hundred. Earlier experiments in

nanowires [74, 75] where dealing with at least a few thousand channels. So we expect a strong 1D behavior for the observed transition. In particular, the broadness of the resistance drop with temperature is due to large fluctuation of the superconducting order parameter in reduced dimension starting at the 3D transition temperature $T^*$. In the following we will try to explain the variety of behaviours observed taking into account several essential features: the large normal contacts, together with the finite length of the samples compared to relevant mesoscopic and superconducting scales, the number of tubes within a rope, the amount of disorder and intertube coupling. We first assume that all ropes are diffusive conductors but we will see that this hypothesis is probably not valid in the less disordered ropes.

We first recall that the resistance of any superconducting wire measured through normal contacts (an NSN junction) cannot be zero : a metallic SWNT, with 2 conducting channels, has a contact resistance of half the resistance quantum, $R_Q/2$ (where $R_Q = h/(2e^2)$=12.9 k$\Omega$), even if it is superconducting. A rope of $N_m$ parallel metallic SWNT will have a minimum resistance of $R_Q/(2N_m)$. Therefore we use the residual resistance $R_r$ to deduce a lower bound for the number of metallic tubes in the rope $N_m = R_Q/2R_r$. From the residual resistances equal to 74 $\Omega$ in sample Pt2 and below 200$\Omega$ in Pt1 we deduce that there are at least $\approx 90$ metallic tubes in Pt2 and $\approx 30$ in Pt1. In both cases that means that a large fraction of tubes participate to transport and justifies a posteriori the hypothesis that ropes are diffusive conductors.

### 4.1. Estimation of the superconducting coherence length.

We now estimate the superconducting gap through the BCS relation $\Delta = 1.76\ k_B T^*$ : $\Delta \approx 85\ \mu eV$ for Pt2. We can then deduce the superconducting coherence length along the rope in the diffusive limit :

$$\xi = \sqrt{\hbar v_F l_e / \Delta} \tag{9}$$

This expression yields $\xi_2 \approx 0.3\ \mu$m where $v_F$ is the longitudinal Fermi velocity $8 \times 10^5$ m/s. We now estimate the superconducting coherence length of the other samples, to explain the extent or absence of observed transition. Indeed, investigation of the proximity effect at high-transparency NS interfaces has shown that superconductivity resists the presence of normal contacts only if the length of the superconductor is much greater than $\xi$ [76]. This condition is nearly fulfilled in Pt2 ($\xi_2 \approx L_2/3$). Using the high temperature resistance values and assuming a gap $\Delta$ equal to that of Pt2 we find $\xi_1 \approx L_1/2$ and $\xi_3 \approx 2L_3$,. These values explain qualitatively reduced transition temperature for sample1 and the absence of a transition for sample

3. Moreover we can argue that the superconducting transitions we see are not due to a hidden proximity effect : if the $Al_2O_3/Pt/Au$ contacts were made superconducting by the laser pulse, the shortest ropes would become superconducting at temperatures higher than the longer ones. It is however not possible to explain the behavior of the sample 5 within the same kind of argument. Expression yields $\xi_5 =$ much shorter than the length of the sample. However no complete transition like in sample 2 is observed. We believe that this is due to the very strong value of disorder in this sample which is very close to localisation. One can see that the transition even disappeared after thermal cycling where an increase of room temperature resistance leaded to complete localisation at low temperature.

### 4.2. Role of the number of tubes.

Another a priori important parameter which is expected to strongly influence the superconducting transitions is the number of tubes in a rope. If we compare the two ropes in Fig. 11, it is clear that the transition both in temperature and magnetic field is much broader in the rope Pt4 containing only 40 tubes than in the rope Pt2 with 350 tubes. Moreover there is no inflexion point in the temperature dependence of the resistance in the thinner rope indicating a strictly 1D behavior. we also expect a stronger screening of e-e interaction in a thick rope compared to a thin one. This can also favour superconductivity as we will discuss below.

### 4.3. Role of disorder.

As already discussed above disorder is at the origin of a reduction of the superconducting coherence length in a diffusive sample compared to a ballistic one and can this way also decrease the destructive influence of the normal contacts. More subtle and specific to the physics of ropes, we have seen that disorder also enhances the intertube coupling, so it can increase the dimensionality of the superconducting transition: weakly disordered ropes like Pt1 and Pt4 will be more 1D like than the more disordered rope Pt2. Of course disorder must always be sufficiently small so as not to induce localisation. These considerations may explain the variety of behaviors oberved

Finally, disorder is the essential ingredient which reveals the difference between transport in a normal metal and in a superconductor. For a ballistic rope we would not expect to observe a variation of the resistance during a superconducting transition because for both cases the resistance of the rope is just the contact resistance. We have performed shot noise measurements in weakly disordered ropes like Pt1 and Pt4,

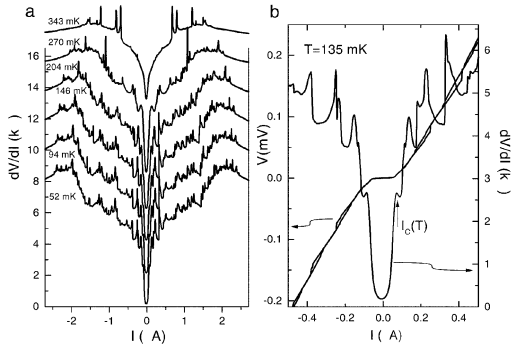


*Figure 9.* Left panel: Differential resistance of Pt2 vs. current at different temperatures. Curves are offset vertically for clarity. Right panel: V(I) and $\frac{dV}{dI}(I)$ curves showing the hysteretic behavior in V(I) at each peak in the $\frac{dV}{dI}(I)$ curve.

in the normal state. A surprising strong reduction by more than a factor 100 was observed which is still not well understood yet but would indicate that all the tubes in these ropes are either completely ballistic or completely localised [77], in strong apparent contradiction with the observation of a superconducting transition involving a 2/3 resistance drop.

It is however possible to explain different values of resistance between normal and superconducting states for these ropes, if the number of conducting channels is larger for Cooper Pairs than for individual electrons. In his recent theoretical investigation of superconductivity in ropes of SWNT Gonzalez [78] has shown the existence of a finite intertube tranfer for Cooper pairs having zero kinetic momentum even between two tubes of different helicities with no possibility of single electron transfer. It is possible that this mechanism can lead to the opening of new channels when a rope containing a mixture of insulating and ballistic tubes becomes superconducting .

### 4.4. 1D superconductivity

Reminiscent of measurements of narrow superconducting metal wires [74], we find jumps in the differential resistance as the current is increased. For sample 2 the differential resistance at low currents remains equal to $R_r$ up to 50 nA, where it strongly rises but does not recover its normal state value until 2.5 $\mu$A see Fig.9. The jump in resistance at the first step corresponds approximately to the normal state resistance of a length $\xi_2$ of sample2 . Each peak corresponds to a hysteretic feature in the V-I curve (Fig.9). These jumps are identified as phase slips

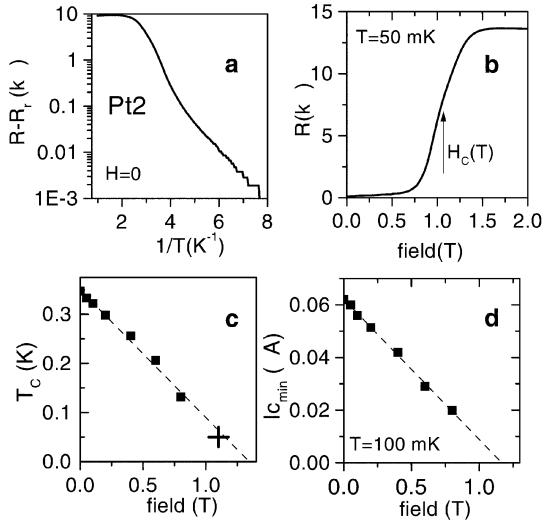


*Figure 10.* a Resistance of Pt2 plotted on a log scale as a function of the inverse temperature at H=0. We have subtracted the low temperature residual resistance (contact resistance). The slope yields an approximate activation energy of 0.8 K. b Magnetoresistance of Pt2 at 50 mK. We define the critical field as the inflection point of R(H): $\mu_0 H_C$(T= 50 mK)=1.1 T. c Transition line of Pt2 defined in the H,T plane by the inflection point of R(T) or equivalently by the inflection point of R(H). d Field dependence of the critical current of Pt2 defined as the current at which the first resistance jump occurs in the dV/dI curves of Fig.5. $I_C(H)$ extrapolates to a critical field of 1.2 T, in agreement with the linear extrapolation 1.3 T of $T_C(H)$.

[74, 68, 75], which are the occurrence of normal regions located around defects in the sample. Such phase slips can be thermally activated (TAPS), leading to an exponential decrease of the resistance instead of a sharp transition, in qualitative agreement with our experimental observation (Fig.10a). At sufficiently low temperature, TAPS are expected to be replaced by quantum phase slips (QPS), which, when tunneling through the sample, contribute an additional resistance to the zero temperature resistance.

For sample 2, the current above which the jumps disappear, 2.5 $\mu A$, is close to the critical current $I_C = \Delta/R_r e \approx 1$ $\mu$A of a superconducting wire without disorder and with the same number of conducting channels [75]. This large value of critical current would also be the maximum supercurrent in a structure with this same wire placed between superconducting contacts (with gap $\Delta_S$), and is much larger than the Ambegaokar-Baratoff prediction $R_N I_C = \Delta_S/e$. This might explain the anomalously large supercurrent measured in experiments depicted in the previous section, where nanotubes are connected to superconducting contacts.

### 4.5. Effect of magnetic field

It is difficult to say apriori what causes the disappearance of superconductivity in carbon nanotubes. The value of Hc(0) should be compared to the depairing field in a confined geometry [80], and corresponds to a flux quantum $\Phi_0$ through a length $\xi$ of an individual SWNT of diameter d, $\mu_0 H_C = \Phi_0/(2\sqrt{\pi} d\xi) = 1.35$ T. But $H_C(0)$ is also close to the field $\mu_0 H_p = \Delta/\mu_B = 1.43$ T at which a paramagnetic state becomes more favorable than the superconducting state [81, 82]. Note that this value is of the same order as the critical field that was measured on SWNT connected between superconducting contacts, i.e. much higher than the critical field of the contacts.
The linear dependence of the critical current with magnetic field observed in all samples is very similar to the data presented in the previous section on SWNT on superconducting contacts and appears strongly related to the linear dependence in Tc(H). This linear scaling with magnetic field is surprising since it is not expected to take place in a 1D system and is rather typical of 2D superconductivity [79]. A depairing mechanism based on spin splitting of the quasiparticle energy states could however provide a possible explanation. Experiments performed with various field directions compared to the tube are thus necessary for a better understanding of the influence of magnetic field on superconductivity in carbon nanotubes.

### 4.6. Conclusion:

Data depicted in the previous section show the existence of intrinsic superconductivity in ropes of carbon nanotubes which number of tubes varies between 30 and 400. The question of the existence of superconducting correlations in the limit of the individual tube cannot be answered yet. It is of course tempting to consider the high supercurrent measured on superconducting contacts as a strong indication that superconducting fluctuations are present also in individual carbon

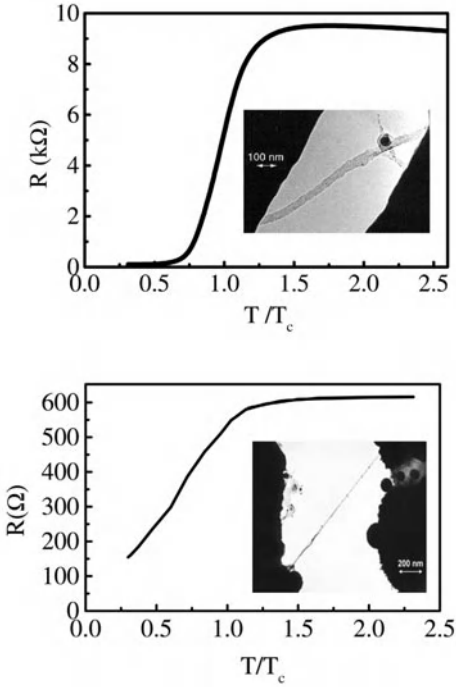


*Figure 11.* Resistance as a function of temperature and for 2 samples containing different number of tubes sample 2 contains approximately 350 tubes , sample 4 contains 30 tubes. Insets: TEM micrograph of the corresponding samples.

nanotubes. However since unscreened Coulomb repulsive interactions in these samples are expected to suppress superconductivity, precise investigations of individual carbon nanotubes on normal contacts are necessary. It is essential to investigate sufficiently long samples (like the ropes presently studied) in order that intrinsic superconductivity is not destroyed by the normal contacts. Note that recent magnetisation experiments [83] also strongly support the existence of superconducting fluctuations below 10K in very small diameter (0,4 nm) individual tubes grown in zeolites.

We now discuss what could be the relevant mechanism for superconductivity in carbon nanotubes. Observation of superconductivity in carbon based compounds has already been reported a long time ago. First in graphite intercalated with alkalis (Cs,K), superconducting trans-

itions where observed between 0.2 and 0.5 K [84]. Much higher temperatures were observed in alkali doped fullerenes [85] because of the coupling to higher energy phonons. In all these experiments it was essential to chemically dope the system to observe superconductivity. There is no such chemical dopants in the ropes of carbon nanotubes studied here. As shown in previous works there is some possibility of hole doping of the tubes by the gold metallic contacts which electronic work function is larger than in the tubes [86, 87]. However, if it is possible that this doping can slightly depopulate the highest occupied energy band in a semiconducting tube it is very unlikely that it is strong enough for depopulating other lower energy subbands for a metallic tube which diameter is in the nm range. More interesting would be a mechanism related to the 1D electronic structure of carbon nanotubes. A purely electronic coupling mechanism has been indeed shown to induce superconducting fluctuations in coupled double chain systems such as ladders. The relevance of this mechanism has been considered also in carbon nanotubes away from half filling but the very small order of magnitude for the energy scale of these superconducting fluctuations is not compatible with our findings [56].
Recent estimations of the electron phonon coupling coupling constants [78], [88] in carbon nanotubes seem to be more promising. It is shown that the breathing modes specific to carbon nanotubes can be at the origin of a strong electron phonon coupling giving rise to attractive interactions which can possibly overcome repulsive interactions in very small diameter tubes . The possible coupling of these rather high energy modes to low energy compression modes in the nanotube have been also considered, following the Wenzel Bardeen singularity scheme initially propose by Loss and Martin where low energy phonons are shown to turn repulsive interactions in a Luttinger liquid into attractive ones and drive the system towards a superconducting phase [89]. The suspended character of the samples may be essential in this mechanism.

## References


1. A. Stern, Y. Aharonov, and Y. Imry, Phys. Rev. A **41**, 3436 (1990).
2. S. Washburn and R. Webb, Advances in Physics **35**, 375 (1986).
3. B. L. Altshuler, A. G. Aronov and B. Z. Spivak, Pis'ma Zh. Eksp. Teor. Fiz. **33**, 101 (1981) [JETP Lett. **33**, 94 (1981)].
4. D. Y. Sharvin and Y. V. Sharvin, Pis'ma Zh. Eksp. Teor. Fiz. **34**, 285 (1981) [JETP Lett. **34**, 272 (1981)].
5. R. Deblock, Y. Noat, H. Bouchiat, B. Reulet and D.Mailly,Phys. Rev. B **65,** 075301 (2002).
6. M. Büttiker, Y. Imry and R. Landauer, Phys. Rev. **96A**, 365 (1983).
7. H. Cheung, E. Riedel and Y. Gefen, Phys. Rev. Lett. **62,** 587 (1989).

8. G. Montambaux, H. Bouchiat, D. Sigeti and R. Friesner, Phys. Rev. B **42,** 7647 (1990).
9. V. Ambegaokar and U. Eckern, Phys. Rev. Lett. **65**, 381 (1990). V. Ambegaokar and U. Eckern, Europhys. Lett. **13**(8), pp 733-738 (1990). U. Eckern, Z. Phys. B **82**, 393 (1991).
10. A. Schmid, Phys. Rev. Lett. **66**(1), 80 (1991).
11. F. Von Oppen and E. Riedel, Phys. Rev. Lett. **66,** 84 (1991).
12. B.L. Altshuler, Y. Gefen and Y. Imry, Phys. Rev. Lett. **66**, 88 (1991).
13. V.E. Kravtsov and B.L. Altshuler, Phys. Rev. Lett. **84**, 3394 (2000).
14. V. Chandrasekhar *et al.*, Phys. Rev. Lett. **67**, 3578 (1991).
15. D. Mailly, C. Chapelier and A. Benoit, Phys. Rev. Lett. **70**, 2020 (1993).
16. E.M.Q. Jariwala, P. Mohanty, M.B. Ketchen and R.A. Webb, Phys. Rev. Lett. **86**(8), 1594 (2001).
17. W.Rabaud *et al.* Phys. Rev. Lett. **86**, 3124 (2001).
18. L.P. Lévy, G. Dolan, J. Dunsmuir and H. Bouchiat, Phys. Rev. Lett. **64**, 2074 (1990). L.P. Lévy, Physica B **169**, 245-256 (1991).
19. B. Reulet, M. Ramin, H. Bouchiat and D. Mailly, Phys. Rev. Lett **75**, 124, (1995).
20. R. Deblock, R.Bel, H. Bouchiat, B. Reulet and D.Mailly,Phys. Rev. Lett. **89**, 206803(2002)
21. A. Kamenev and Y. Gefen, Phys. Rev. B **49**, 14474 (1994).
22. M. Schechter, Y. Oreg, Y. Imry, Y. Levinson, Phys. Rev. Lett. **90** 026805 (2003)
23. S. Strässler, M.J. Rice and P. Wyder, Phys. Rev. B **6**, 2575 (1972); M.J. Rice, W. R. Schneider and S. Strässler, Phys. Rev. B **8**, 474 (1973).
24. K.B. Efetov, Phys. Rev. Lett. **76**, 1908 (1996).
25. Y. Noat, B. Reulet and H. Bouchiat, Europhys. Lett. **36**(9), pp. 701-706 (1996).
26. Ya.M. Blanter and A.D. Mirlin, Phys. Rev. B **57**, 4566 (1998).
27. R. Deblock, Y. Noat, H. Bouchiat, B. Reulet and D.Mailly, Phys. Rev. Lett. **84**(23), 5379 (2000).
28. Y. Noat, R. Deblock, B. Reulet and H. Bouchiat, **65,** 075325 (2002).
29. Ya.M. Blanter and A.D. Mirlin, Phys. Rev. B **63** 113315 (2001).
30. N. Trivedi and D. A. Browne, Phys. Rev. B **38**, 9581 (1988).
31. B. Reulet and H. Bouchiat, Phys. Rev. B **50**, 2259 (1994).
32. A. Kamenev, B.Reulet, H. Bouchiat, and Y. Gefen, Europhysics Letters **28**, 391 (1994)
33. U. Sivan and Y. Imry, Phys. Rev. B, **35**, 6074, (1987).
34. M. L. Mehta, *Random Matrices and the Statistical Theory of Energy Levels.* New York : Academic Press 1967.
35. L.P. Gor'kov, G.M. Eliashberg, Sov. Phys.-JETP **21**, 940 (1965); B. I. Shklovskii, Pis'ma Zh. Eksp. Teor. Fiz. **36**, 287 (1982) [ JETP Lett. **36**, 352 (1982)].
36. D. Jérome and H.J. Schulz, *Adv. Phys.* **31** 299, (1982).
37. M.S. Dresselhaus, G. Dresselhaus, P.C. Eklund, *Science of Fullerenes and Carbon Nanotubes* (Academic, San Diego, 1996).
38. C. Wan, T.Fiebig, S.O. Kelley, C.R. Treadway, J.K. Barton and A.H. Zewail, *Proc. Natl. Acad. Sci. USA* **96**, 6014 (1999).
39. Y. Okahata, T. Kobayashi, H. Nakayama and K. Tanaka, *Supramolecular Science* **5**, 317 (1998).
40. H. W. Fink and C. Schoenenberger, *Nature* **398**, 407 (1999).
41. E. Braun, Y. Eichen, U. Sivan, G. Ben-Yoseph, *Nature* **391**, 775 (1998).
42. D. Porath, A. Bezryadin, S. de Vries and C. Dekker, *Nature* **403**, 635 (2000).

43. G. Deutscher and P.G. de Gennes in *Superconductivity* (Ed. R.D. Parks, Marcel Dekker Inc., 1969).
44. H.Courtois, Ph. Gandit, B. Panetier, *Phys. Rev.* **B 52** 1162 (1995).
45. For a review of suppercurrents through superconducting junctions see: K. Likharev, *Rev. Mod. Phys.* **51**,101 (1979).
46. P. Dubos, H. Courtois, B. Pannetier, F. K. Wilhelm, A. D. Zaikin, and G. Schn Phys. Rev. B **63**333, 064502 (2001)
47. D. V. Klinov *Nucleic Acids Res.* **26**, 4603 (1998).
48. V.V. Prokhorov, D.V. Klinov, and V.V. Demin, *Russian Journal of Bioorganic Chemistry* **25**, 211 (1999).
49. J. Dubochet, M. Ducommun, M. Zollinger, and E. Kellenberger, *J. Ultrastruct. Res.* **35**, 147 (1971).
50. Two leveled plastic tubes connected to the outlets of a peristatic pump (in order to control the flow-rate ) were fixed on the sample holder touching the mica surface. The DNA solution (0.1 ng/$\mu$ l DNA, 20 mM $NH_4CH_3COOH$, 7-9 mM $MgCl_2$) flowed from one tube into the other with a velocity of roughly 1-2 cm/sec.
51. A.Kasumov and D.Klinov to be published.
52. A. Yu . Kasumov, et al. Science **291**, 280 (2001).
53. M. Ratner, *Nature* **397**, 480 (1999).
54. J. Jordner, J. Bixon, M. Langenbacher, T. Michel-Beryerle, *Proc.Natl.Acad.Sci. USA* **95**12759 (1998).
55. A. A. Odinstov and Y. Tokura, to appear in *Physica B* (2000) .
56. R. Egger, A. Gogolin, Phys. Rev. Lett. **79**, 5082 (1997). R. Egger, Phys. Rev. Lett. **83**, 5547 (1999).
57. C. Kane, L. Balents, M. P. Fisher, Phys. Rev. Lett **79**, 5086 (1997).
58. M. Bockrath *et al.*, Nature **397**, 598 (1999).
59. H. Grabert and M. H. Devoret (eds), Single Charge Tunneling (Plenum, New-York, 1992); J. T. Tans *et al.*, Nature **386**, 474 (1997).
60. A.Yu. Kasumov, I.I. Khodos, P.M. Ajayan, C. Colliex, Europhys. Lett. **34**, 429 (1996); A.Yu. Kasumov *et al.*, Europhys. Lett. **43**, 89 (1998).
61. A.Yu. Kasumov *et al.*, Science **284**, 1508 (1999).
62. C. Journet, *et al.*, Nature **388**, 756 (1997).
63. L. Vaccarini, *et al.*, C.R.Acad.Sci.**327**, 925 (1999).
64. M. Burghard et al, *Electronic Properties of Novel Materials* (Eds H. Kuzmany et al,) AIP, New York (1998).
65. J. Nygard, D.H. Cobden and P.E. Lindelof, Nature **408**, 342 (2000).
66. I. Safi and H. J. Schulz, *Phys.Rev.B* **52**, R17040 (1995).
67. A.Yu. Kasumov et al., *Science* **284**, 1508 (1999).
68. J. Meyer, G. V. Minnigerode, Physics Letters, **38A**, 7, 529 (1972)
69. R. Fazio, F.W.J Hekking and A.A. Odintsov, *Phys. Rev.*, **B 53**, 6653 (1995).
70. D. Maslov, M. Stone, P.M. Goldbart, D. Loss Phys. Rev., **B 53,** 1548 (1995).
71. I. Affleck, J.B. Caux and A. Zagoskin *Phys. Rev.*, **B 62,** 1433 (2000).
72. J. Gonzalez, Phys. Rev. Lett. **87**, 136401 (2001).
73. D. J. Thouless, Phys. Rev. Lett. **39**, 1967 (1977).
74. N. Giordano, Phys. Rev. B **50**, 160 (1991).
75. Tinkham, M., Introduction to superconductivity, McGraw-Hill, 2d Ed. (Singapore, 1996).
76. W. Belzig, C. Bruder and G. Schön, Phys. Rev. B **54**, 9443 (1996).
77. P.Roche, M.Kociak, S.Gueron, A.Kasumov, B.Reulet and H.Bouchiat Eur.Phys.J.B.**28**,217-222 (2002).

78. J. Gonzalez, Phys. Rev. Lett. **88**, 076403 (2002) and to appear in Phys. Rev. B.
79. R. A. Smith, B. S. Handy, and V. Ambegaokar Phys. Rev. B **63**, 094513 (2001)
80. R. Meservey, P.M. Tedrow, Phys. Rep. **238**, no.4, 173 (1994).
81. A.M. Clogston, Phys. Rev. Lett. **9**, 266 (1962).
82. B.S. Chandrasekhar, Appl. Phys. Lett. **1**, 7 (1962).
83. Z.K. Tang et al. Science **292**, 2462 (2001).
84. N. B. Hannay *et al.*, Phys. Rev. Lett. **14**, 225 (1965).
85. O. Gunnarsson, Rev. Mod. Phys. **69**, 575 (1997).
86. L. C. Venema *et al.*, Science **283**, 52 (1999).
87. A.A. Odintsov , Phys. Rev. Lett. **85**, 150 (2000).
88. A. de Martino and R.Egger (to be published).
89. D. Loss, and T. Martin, Phys. Rev. B **50**, 12160 (1994).

# Phase measurements in Quantum Dots

Alessandro Silva and Moty Heiblum
*Department of Condensed Matter Physics, The Weizmann Institute of Science, 76100 Rehovot, Israel.*

**Abstract.** Recent measurements of the phase of the transmission amplitude through a quantum dot (QD) revealed interesting and unexpected physics. In particular, the phase evolution across a sequence of Coulomb Blockade (CB) peaks is demonstrated to have a peculiar structure, characterized by an increase of $\pi$ across each peak, followed by an abrupt phase lapse of $\pi$ in each CB valley. A simple theory accounting for the origin of such phase lapses as well as for their small scale is discussed, though a satisfactory explanation of the presence of a phase lapse in each CB valley is still lacking. As the temperature of the system is reduced, the Kondo effect develops in CB valleys with non-zero QD spin (Kondo valleys). The measured phase evolution in this regime is characterized by a plateau at $\pi$ in the valley, and a total increment of the phase close to $2\pi$ across the CB peak-Kondo valley-CB peak structure. This result contrast quantitatively with the theoretical prediction for the phase evolution based on the Anderson model, i.e. a plateau at $\pi/2$ in the Kondo valley and a total increment of $\pi$.

## 1. Introduction

A recent development in mesoscopic physics has been the possibility to study directly the phase coherence of electronic transport by means of Aharonov-Bohm interferometers [1]. The fabrication of these systems allowed the direct study of basic principles of quantum physics, such as the demonstration of Bohr's complementarity principle [2, 3], in electronic systems. However, apart from being a useful playground to address fundamental questions related to quantum physics, the technique of Aharonov-Bohm interferometry turned out to be a promising and innovative experimental tool to study transport through mesoscopic systems from the point of view of phase coherence. As an example transport through quantum dots (QD) was considered: starting with the demonstration of the (partial) coherence of transport through a QD in the Coulomb Blockade regime [4], the phase of the transmission amplitude through the dot was directly measured both in the Coulomb Blockade [5] and in the Kondo regimes [6, 7].

These experiments provided new (and sometimes unexpected) information on the physics of transport through QDs. Some of the experimental results we are going to discuss in the following sections of this review are still lacking a satisfactory theoretical explanation and are currently the subject of theoretical studies.



*R. Fazio et al. (eds.), New Directions in Mesoscopic Physics,* 149–172.
© 2003 *Kluwer Academic Publishers. Printed in the Netherlands.*

The review is organized as follows: in Sec.2 the experimental demonstration of the coherence of transport through a QD is discussed. In Sec. 3 it is introduced the logic behind the measurement of the complex transmission amplitude (magnitude and phase) through a QD, as well as the difference between two-terminal and four-terminal Aharonov-Bohm interferometers. In Sec. 4 the measurement of the transmission amplitude of a QD in the Coulomb Blockade (CB) regime is discussed, and in Sec. 5 a simple theoretical analysis of the phase evolution, following Ref. [8], is introduced. In particular, some of the experimental features, such as the so-called abrupt phase lapse in between CB peaks, are carefully analyzed theoretically. Finally, in Sec. 6 the measurement of the transmission phase of a QD in the Kondo regime is discussed.

## 2. Coherence of Transport through a Quantum Dot.

A QD is a small, confined, puddle of electrons, with two tunnel barriers coupling it to two electron reservoirs. The electrons in the puddle occupy a discrete ladder of energy levels, with average level spacing $\Delta$. A capacitively coupled metallic gate (plunger) is used to tune the energy levels in the dot. Resonant tunneling between the two reservoirs (through the tunnel barrier – puddle – tunnel barrier system) takes place and current flows when an energy level is aligned with the Fermi level in the leads. When one of the electronic levels drops below the Fermi level in the leads, it gets occupied and the number of electrons in the dot increases by one. However, due to the small capacitance $C$ of the QD and the discreteness of the electronic charge $e$, an additional, classical, charging energy $U_C = e^2/2C$ is needed in order to add a single electron into the dot. Effectively, the peak spacing in the conductance versus plunger gate voltage is $U_C + \Delta$, where typically $U_C \gg \Delta$. At low temperature $T$ ($k_B T \ll U_C$, with $k_B$ the Boltzmann constant), when the Fermi surface in the leads lays in the gap between levels, there is a well-defined number of electrons in the QD and current does not flow. This is the well-known Coulomb Blockade phenomenon, where periodic conductance peaks as a function of plunger voltage are separated by almost zero conductance valleys.

The Coulomb Blockade of transport in QDs has been the subject of intense experimental and theoretical studies in the past decades [9]. Experiments concentrated on transport measurements (conductance, $dI/dV$ characteristics) and spectral measurements (differential capacitance) of QD in the CB regime, while theoretical efforts have been mostly directed towards a detailed understanding of the CB peak spectra (e.g., peak spacing statistics) [10], the quantum effects on CB

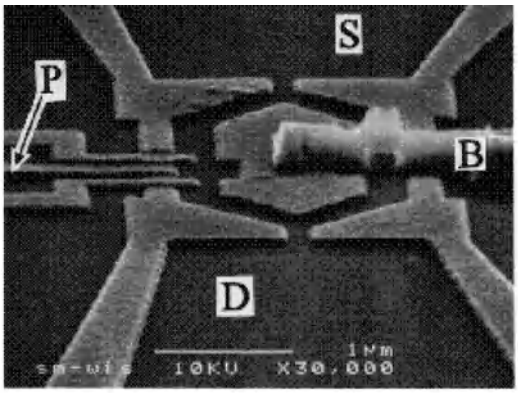


*Figure 1.* Electron micro-graph of the two-terminal AB interferometer used in Ref. [4]. The light grey regions represent metallic gates used to defined the interferometer in a two dimensional electron gas. In particular, an Aharonov-Bohm ring is created by biasing the central metallic island through an air bridge (B). Electrons flow from source (S) to drain (D) passing through the ring, whose left arm contains a quantum dot. From Ref. [4].

oscillations [11], as well as of the vanishing of the CB phenomenon resulting from the the coupling of the QD to its leads [12, 13, 14].

The first experimental study of phase coherent transport through a QD was realized in 1995 by Yacoby et al.[4]. The interferometer used for such experiment is shown in Fig. 1: it consisted of a small Aharonov-Bohm ring defined lithographically in a high mobility two dimensional electron gas at the interface of a GaAs-AlGaAs heterostructure. The circumference of the ring was smaller than the phase breaking length $L_\phi$ of electrons at the temperature at which the measurement was performed ($kT \approx 9\mu eV$). The ring was connected to two external reservoir, source (S) and drain (D), by means of two quantum point contacts (QPC). In one arm of the interferometer a QD was defined, whose electrostatic potential was controlled by a plunger gate (P) placed nearby. The QD had an average level spacing $\Delta \approx 40\mu eV$, charging energy $U \approx 0.5meV$, and was weakly coupled to the leads, the intrinsic broadening of the CB peaks being $\Gamma \approx 0.2\mu eV$. Therefore, pronounced CB oscillations of the QD conductance could be observed.

If transport through the QD is preserving the phase coherence of electrons, one should expect to observe Aharonov-Bohm oscillations of the S-D conductance as a function of a magnetic field applied perpendicular to the plane of the interferometer. This expectation revealed to be correct as shown in Fig. 2. Shown is the current passing through the ring at fixed magnetic field as a result of the application of a

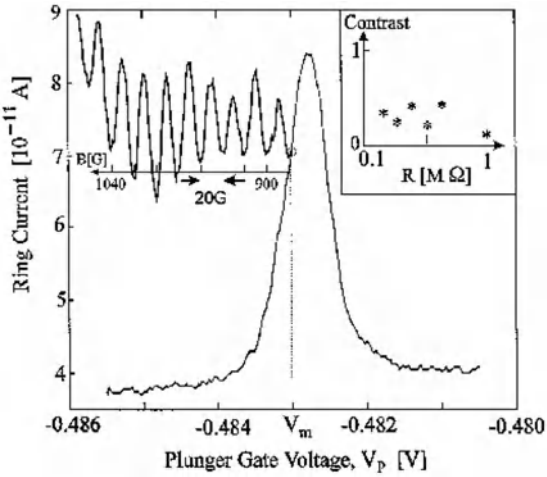


*Figure 2.* Current between source and drain as a function of the plunger gate voltage on the QD for a fixed source-drain bias and fixed magnetic field. A pronounced peak corresponding to a CB resonance in the QD is observed. The top left part shows the current signal versus magnetic field as for a given $V_P = V_m$. Inset: oscillation contrast (peak-to-peak over average current through the QD) versus resistance of the QD. From Ref. [4].

small S-D bias versus the plunger gate voltage on the QD. The CB in the QD manifest itself in a pronounced peak in the current signal on top of the background due to the transfer electrons through the arm without QD (reference arm ). It was observed that fixing the gate voltage at $V_P = V_m$ and sweeping the magnetic field, the current showed pronounced AB oscillations of period consistent with one flux quantum threading the area of the ring (see Fig. 2), therefore proving the coherence of transport through the QD . However, the contrast of AB oscillations, defined as the ratio between the amplitude of AB oscillations and the average current through the interferometer, was found to be in the range between 0.2 and 0.4, suggesting the presence of a incoherent background contributing to the current.

## 3. Phase of the Transmission Amplitude through a QD.

Once the coherence of transport through a QD is demonstrated, one may think of extracting information about the elastic transmission amplitude [15] through the QD (magnitude and phase) at different plunger gate voltages studying how the AB oscillatory pattern of the

current through the interferometer changes as the plunger gate voltage $V_P$ is swept through a series of CB peaks.

The logic of such measurement can be traced to the two slit experiment. Assuming fully coherent transport through the QD, as well as that, in a way similar to the two slit experiment, the transmission of electrons from source to drain is mediated by only two paths, one passing through the arm containing the QD and one passing through the reference arm, the source drain conductance is

$$G \propto | t_{ref} |^2 + | t_{QD} |^2 + 2 \, \mathrm{Re} \left[ \mathrm{t}^*_{\mathrm{ref}} \, \mathrm{t}_{\mathrm{QD}} \, \mathrm{e}^{2\pi \mathbf{\Phi}/\mathbf{\Phi_0}} \right] , \qquad (1)$$

where $t_{ref}$ is the transmission amplitude through the reference arm, $t_{QD}$ the transmission amplitude through the QD, $\mathbf{\Phi}$ is the magnetic flux threading the area enclosed by the two paths, and $\mathbf{\Phi_0}$ is the flux quantum [16].

The flux sensitive part of Eq. 1 can be written as

$$G_{osc} \propto 2 \; | t_{ref} | \, | t_{QD} | \cos \left( \varphi_{QD} - \varphi_{ref} + 2\pi \mathbf{\Phi}/\mathbf{\Phi_0} \right) , \qquad (2)$$

where $\varphi_{QD}$ and $\varphi_{ref}$ are the phases of $t_{QD}$ and $t_{ref}$, respectively. Notice that only $| t_{QD} |$ and $\varphi_{QD}$ are functions of the plunger gate voltage $V_P$. Therefore, the change in the amplitude of AB oscillations at different $V_P$ gives direct information on the change in the magnitude of $t_{QD}$ as a function of gate voltage. In a similar way, tracking the shift of the whole AB oscillations pattern as a function of $V_P$ one obtains direct information on the evolution of the transmission phase $\varphi_{QD}$.
Unfortunately, the two-terminal Aharonov-Bohm interferometer described in Sec.2 does not allow the direct measurement of the transmission phase $\varphi_{QD}$. The main reason is that one of the assumptions of the analysis leading to Eq.2, i.e. electrons going from source to drain can take only two paths, is simply not justified in the two-terminal geometry of Fig. 1. Indeed, in this case paths connecting source and drain and winding around the ring turn out to contribute as well to the conductance. In particular taking into account also these paths, one obtains that the conductance has to satisfy the Onsager relation $G(\mathbf{\Phi}) = G(-\mathbf{\Phi})$ [17], therefore locking the phase of the AB oscillatory patterns to be either 0 or $\pi$ [18].

In order to circumvent this limitation and perform a direct measurement of the phase of the transmission amplitude through a QD, a new class of interferometers was designed, whose main characteristic is to operate in a four-terminal configuration, therefore avoiding the symmetry relation $G(\mathbf{\Phi}) = G(-\mathbf{\Phi})$. A schematic view of a four terminal interferometer is shown in Fig. 3. The central element of this structure is again an Aharonov-Bohm ring containing a QD. The ring is connected

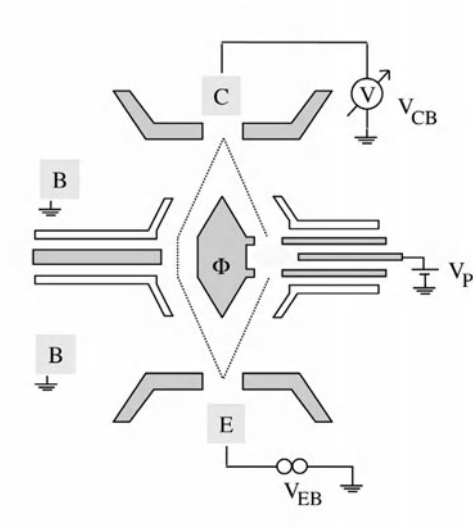


*Figure 3.* Schematic view of a four-terminal Aharonov-Bohm interferometer. Electrons are transmitted from the emitter (E) to the collector (C), crossing an Aharonov-Bohm ring, with a QD inserted in one of its arms. Additional contacts to a base region (B) allow the leakage of electrons traveling across the interferometer. As a result, only the two direct paths shown in the figure contribute to the conductance. Paths winding around the ring have higher probability to leak to the base region and are therefore suppressed.

to various contacts, an emitter (E), a collector (C) and a grounded base region (B). Electrons injected in the structure from the emitter can either cross the AB ring and enter the collector or can be absorbed and dispersed in the base region. In this way, the two paths shown in Fig. 3 and Fig. 4 contribute the most to the interferometer conductance, since paths winding around the AB ring have high probability to leak electrons to the base region.

In the next few sections the measurements of the transmission phase of a QD are discussed, both in the CB regime and in the Kondo regime.

## 4. Coulomb Blockade regime

The evolution of the phase of the transmission amplitude $\varphi_{QD}$ for a QD in the CB regime was measured in a beautiful experiment by Schuster et al. in 1997 [5]. An electron micrograph of the four terminal interferometer used for such measurement is shown in Fig. 4 The QD defined in one arm of the interferometer had average level spacing $\Delta \approx 55\mu eV$.

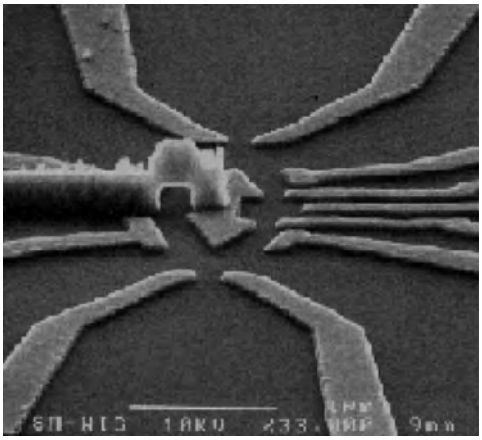

*Figure 4.* Electron micrograph of the four-terminal interferometer used by Schuster *et al.* [5].

Applying a finite bias between emitter and base region $V_{EB}$, electrons were injected into the interferometer. The resulting open circuit voltage drop between collector and base region $V_{CB}$ was then measured as a function of the plunger gate voltage $V_P$ on the QD and of magnetic field.

The result of such measurement is shown in Fig. 5. The collector-base voltage $V_{CB}$ measured as a function of $V_P$ for fixed magnetic field showed a peak structure, each peak corresponding to a CB resonance in the QD superimposed to the background due to conduction through the reference arm (Fig. 5(**a**)). Fixing $V_P$ to be close to a CB peak, the dependence of $V_{CB}$ on magnetic field was measured and showed clear oscillations consistent with the AB effect. Repeating this measurement for various values of plunger gate voltage, the AB oscillatory pattern was observed to shift (see Fig. 5 (**b**)), the shift being proportional to the phase of the transmission amplitude $\varphi_{QD}$ as in Eq. 2. The measurement of the shift of the AB oscillatory pattern as well as of the amplitude of AB oscillations allowed to extract the evolution of $\mid t_{QD} \mid^2$ and $\varphi_{QD}$ as a function of $V_P$ across a CB peak, as shown in Fig. 5(**c**). The observed behavior of the magnitude and phase of $t_{QD}$ across a CB peak is consistent with a model of resonant transmission through a Breit-Wigner resonance. In particular, the experimental data could be fitted accurately by the expression

$$t_{QD} = iC\frac{\Gamma/2}{\epsilon + i\Gamma/2}, \tag{3}$$

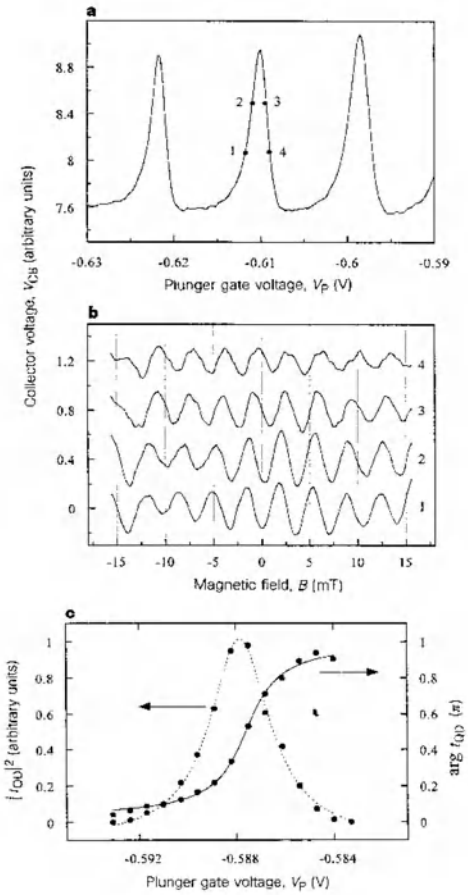


*Figure 5.* Evolution of the magnitude and phase of the transmission amplitude $t_{QD}$ along a CB peak. (a) Coulomb Blockade peaks in the collector-base voltage $V_{CB}$ as a function of plunger gate voltage $V_P$ at fixed magnetic field. (b) AB oscillations of $V_{CB}$ for fixed plunger gate voltage as a function of magnetic field. The four curves correspond to four different values of $V_P$ across the central CB peak. (c) Extracted magnitude and phase of $t_{QD}$. The dots represent actual data point, while the dashed and full curve are a fit of $\mid t_{QD} \mid^2$ and $\varphi_{QD}$ respectively, according to the Breit-Wigner formula Eq. 3. Taken from Ref. [5].

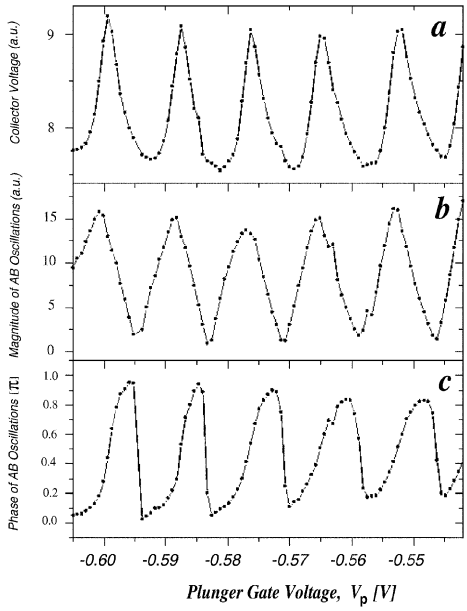


*Figure 6.* Evolution of the magnitude and phase of $t_{QD}$ as a function of plunger gate voltage, across a sequence of CB peaks. (a) Coulomb Blockade peaks in the collector-base voltage $V_{CB}$ versus plunger gate voltage $V_P$. (b) Amplitude of the AB oscillations. Notice the sharp minimum in each CB valley separating adjacent CB peaks. At the minimum, the amplitude is almost vanishing. (c) Phase evolution. Across each CB peak the phase evolution is well described by the Breit-Wigner formula Eq. 3. An unexpected, abrupt phase lapse of $\pi$ is observed in each CB valley, corresponding to a minimum of the amplitude of AB oscillations. Taken from Ref. [5]

where $\Gamma$ is the broadening of the resonance, $C$ is a complex amplitude independent on $V_P$ and $\epsilon$ is its position measured from the Fermi level in the leads. The broadening extracted from experimental data was found to be $\Gamma \approx 4kT$, where $T \approx 100mK$.

The most interesting result of this measurement was found by analyzing the behavior of the magnitude and phase of $t_{QD}$ across a sequence of a few CB peaks, shown in Fig. 6. The base-collector voltage and the amplitude of AB oscillations measured as a function of $V_P$ displayed a sequence of peaks, each one corresponding to a CB resonance. The evolution of the phase across every single peak is consistent with the Breit-Wigner formula in Eq. 3. However, in every CB valley separating adjacent CB peaks a sharp phase lapse of $\pi$ was observed. The

scale of this phase change turns out to be much smaller than both the temperature and the estimated level broadening $\Gamma$.

The phase lapse in between CB peaks turned out to be present in every resolved CB valley (see Fig. 6(**c**)). Moreover, this feature turns out to be ubiquitous: the measurement was repeated with many samples and the phase lapse was observed in every CB valley. Since its observation this phenomenon raised much theoretical interest [19], even though a satisfactory explanation of the evolution of the phase of the transmission amplitude in QDs and of the phase lapse in particular is still missing.

A theoretical explanation of the phase lapse phenomenon would require to give an answer to three questions:

1. What is the origin of the phase lapse ?
2. What is the scale of the phase lapse ?
3. What is the mechanism leading to the observation of a phase lapse in every CB valley analyzed experimentally ?

In the next section, a theoretical approach addressing the first two questions will be discussed.

## 5. Theoretical analysis

The purpose of this section is to discuss theoretically the origin of the phase lapse on the basis of a simple toy model describing a quantum dot connected to two leads. The main goal of the present discussion is to investigate the effect of the signs of the dot-lead coupling matrix elements on coherent transport through a QD. The underlying physics is related to the interference among different transmission amplitudes (say, from the left lead to the right lead), describing different traversal paths through different single particle levels. In particular, it is shown that, in addition to the strength of the coupling, $\Gamma$, the key to understand the behavior of the transmission phase as a function of $V_P$ (as well as other physical observables such as the conductance), is the relative phase of the coupling matrix elements of consecutive orbital levels in the QD to the leads.

We shall consider the Hamiltonian

$$\begin{aligned} H &= \sum \epsilon_{k,\alpha}\, c^{\dagger}_{k,\alpha} c_{k,\alpha} + \sum_j \epsilon_j d^{\dagger}_j d_j + \\ &\quad + \sum_{k,\alpha,j} \left[ V_{\alpha,j} c^{\dagger}_{k,\alpha} d_j + h.c. \right], \end{aligned} \tag{4}$$

where the operators $c_{k,\alpha}$ refer to electronic states in the leads ($\alpha = L, R$) and the operators $d_j$ describe the quantum dot levels ($j = 1, 2$) [20]. In order to simplify our discussion, we will assume the dot-lead couplings $V_{\alpha,j}$ to all have the same magnitude but possibly different phases. It is straightforward to see that three of these phases can be gauged out [21], absorbing them in the definitions of the operators $c_{k,\alpha}$ and $d_j$. Hence, we choose [22] $V_{L,1} = V_{R,1} = V_{L,2} = V$ and $V_{R,2} = e^{i\varphi}V$. When time reversal symmetry is present, the QD's wave functions can be chosen real, whereby, upon an appropriate gauge of the lead wave functions, the value of the relative phase $\varphi$ is either 0 or $\pi$, in other words $s \equiv e^{i\varphi} = \pm 1$.

We are interested in calculating the conductance and the phase of the transmission amplitude as a function of the plunger gate voltage $V_P$ in the two cases $s = \pm 1$. The latter can be described setting $\epsilon_{1,2} = -\epsilon \pm \Delta/2$, where $\Delta = \epsilon_1 - \epsilon_2$, and

$$\epsilon(V_P) = \epsilon(V_P = 0) + V_P. \tag{5}$$

Other than the level spacing, the scale coming into play is the strength of the coupling to the leads

$$\Gamma = 2\pi\rho V^2, \tag{6}$$

where $\rho$ is the density of states (DOS) of the leads.

The linear response conductance of the QD can be written in terms of the transmission amplitude $t(\omega)$ as

$$G = -\frac{e^2}{h}\int d\omega f'(\omega)\left|t(\omega)\right|^2, \tag{7}$$

where $f(\omega)$ is the Fermi function [23]. Moreover, the oscillating part of the conductance of an four terminal A-B interferometer with a QD in one of its arms can be expressed, at finite temperatures, as

$$G_{AB} \propto 2\,\mathrm{Re}\left[t^*_{\mathrm{ref}}\left(\int d\omega\ \left(-f'(\omega)\right)t(\omega)\right)e^{2\pi i\Phi/\Phi_0}\right], \tag{8}$$

where $t_{\mathrm{ref}}$ is the transmission amplitude through the reference arm, assumed to be $V_P$ independent ($t_{\mathrm{ref}}$ is taken energy independent as well); $\Phi_0 = hc/e$ is the flux quantum [24]. In general, it is thus possible, by means of such interference experiment, to extract information about the temperature weighted phase of the transmission amplitude[25] through the QD

$$\theta(T) = \arg\left[-\int d\omega\ f'(\omega)t(\omega)\right]. \tag{9}$$

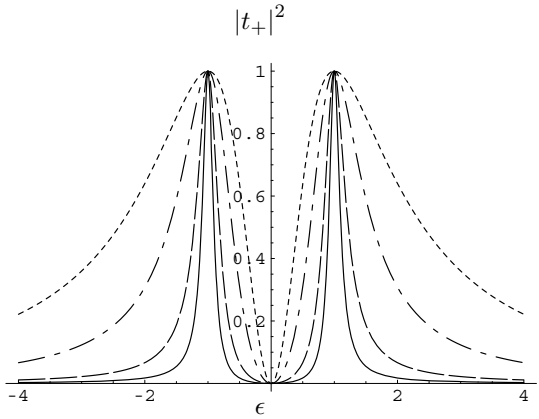


*Figure 7.* Transmission probability $|t_+|^2$ at the Fermi energy of the leads vs. $\epsilon$ for $s = +$. Here $\epsilon_1 - \epsilon_2 = 2$ and $\Gamma = 0.1$ (full), 0.2 (dashed), 0.5 (dash-dotted),1 (dotted). Notice that (i) at $\epsilon = 0$ the contributions to the transmission through to the two levels (including off-diagonal elements of the transmission matrix) add up destructively leading to an exact zero of the transmission probability; and (ii) the peak positions and maximal values (equal to 1) are insensitive to $\Gamma$. Taken from Ref. [8]

Since the Hamiltonian is free (quadratic), the calculation of $t(\omega)$ in the case where the two levels are in-phase ($t_{s=+1}(\omega)$) or out-of-phase ($t_{s=-1}(\omega)$) is straightforward. One readily obtains [8]

$$t_\pm(\omega) \;=\; \frac{\Gamma}{D_\pm(\omega)}\left[(\omega-\epsilon_1)\pm(\omega-\epsilon_2)\right], \tag{10}$$

where the denominator $D_\pm(\omega) \equiv (\omega-\epsilon_1)(\omega-\epsilon_2) + i\Gamma(2\omega-\epsilon_1-\epsilon_2) - \Gamma^2(1\mp 1)/2$.

As a first step in our analysis we consider the in-phase case, $s = +1$ [upper sign in Eqs. (10)] Starting with the zero temperature limit, all transport properties are determined by the value of $t(\omega)$ at the Fermi level, i.e., at $\omega = \epsilon_F \equiv 0$. From Eq. (10) the transmission amplitude at the Fermi level can be written as

$$t_{s=+}(0) \equiv t_+ = \frac{2\Gamma\epsilon}{\epsilon^2 - (\Delta/2)^2 + 2i\Gamma\epsilon}. \tag{11}$$

At zero temperature the Fermi function in Eq. (7) can be substituted by a Dirac delta function and $G$ is given by $G = (e^2/h)t_+$. The conductance $G$ is depicted in Fig. 7 for various values of the parameters.

The main feature to be noticed in Fig. 7 is the presence of an exact zero of the transmission probability between the two peaks, resulting

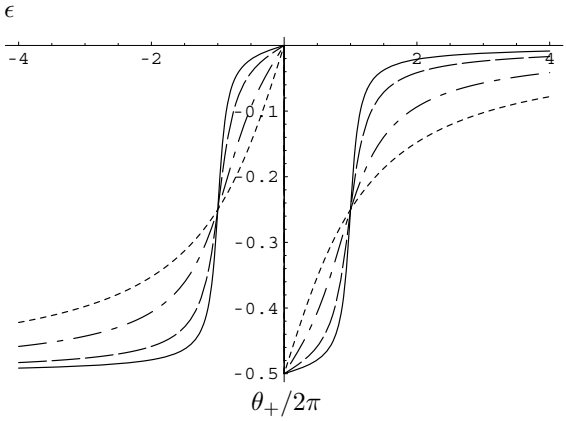


*Figure 8.* The transmission phase $\theta_+/2\pi$ at zero temperature vs. $\epsilon$ for $s = +$. Here, $\epsilon_1 - \epsilon_2 = 2$ and $\Gamma = 0.1$ (full), 0.2 (dashed), 0.5 (dash-dotted) and 1 (dotted). Note that the destructive interference of the transmission through the dot's levels leads to the vanishing of the conductance at $\epsilon = 0$ which, in turn, leads to an abrupt (without a scale) phase-lapse in the "conductance valley". As discussed below, the width of the phase lapse at finite temperatures is $\propto \Gamma T^2/\Delta^2$, introducing a new nontrivial energy scale. Taken from Ref. [8]

from the vanishing of the numerator in Eq. (11) at $\epsilon = 0$. Physically, that zero can be interpreted as the result of destructive interference between paths (left to right) traversing levels 1 and 2 of the dot respectively. As we demonstrate below, the interference pattern is sensitive to the relative sign $s$.

The existence of a zero in the transmission amplitude implies the existence of an abrupt (without a scale) phase lapse [5, 19, 27, 28] of $-\pi$ in the "conductance valley" between the two conductance peaks (cf. Fig. 8).

In terms of the AB oscillations pattern (i.e., the conductance measured as a function of $\Phi$) this implies that as $\epsilon$ varies from $0^-$ to $0^+$ $G(\Phi)$ shifts abruptly by half a period. Since at $T = 0$ this shift is abrupt, it is physically impossible to discuss its direction, i.e., whether the phase of the AB oscillations jumps by $-\pi$ (lapse) or by $+\pi$ (anti-lapse). Interestingly, at finite temperatures this ambiguity is resolved: the phase varies by $-\pi$ close to $\epsilon = 0$ (a lapse).

This conclusion can obtained by noting that the trajectory in the complex plane of $t_+$ [as a function of $\epsilon(V_g)$] is a closed curve tangential to the the abscissa at the origin (cf. the black line in Fig. 9), i.e., $\mathrm{Im}[\mathrm{t}(\omega)] \leq 0$. As $\epsilon$ is swept from $-\infty$ to $+\infty$, the transmission amplitude performs two full counterclockwise revolutions, starting from

$t(-\infty) = [0^-, 0^-]$ and ending at $t(\infty) = [0^+, 0^-]$. In the lower plot of Fig. 9 we show how $t_+(\epsilon)$ makes almost two full revolutions around the circle when $-4 < \epsilon < 4$. It starts (for $\epsilon = -4$) at $[\mathrm{Re}(t_+), \mathrm{Im}(t_+)] \approx [-0.3, -0.05]$, goes through point $(a)$ (cf. the upper plot of Fig. 9) then proceeds to point $(b)$ at the origin and goes around the circle through point $(c)$.

For a fixed $\epsilon$ at finite temperatures, one needs to average over the sections of the curve close to $t_+(\epsilon)$, with the appropriate statistical weight [cf. Eq. (9)]. The result is a trajectory (shown schematically as a grey contour in Fig. 9) which does not include the origin; the phase $\theta_+(T)$ evolves from $-\pi$ to 0 with a lapse of a finite width at $\epsilon = 0$. We note that by considering a vanishingly small (yet non-zero) temperature, it is possible to determine that the origin is not included within the closed contour, hence the transmission phase lapses by $-\pi$ (rather than by $+\pi$).

For $0 < T \ll \Delta, \Gamma$, the evolution of the phase $\theta_+$ for $\epsilon \approx 0$ is well approximated by [8]

$$\theta_+(\epsilon) \simeq \mathrm{ArcTan}\,[\epsilon/\lambda] - \frac{\pi}{2}. \tag{12}$$

The width of the phase lapse is therefore given by a nontrivial combination of $T$, $\Gamma$ and $\Delta$:

$$\lambda \simeq (8\pi^2/3)\,\Gamma\,T^2/\,\Delta^2. \tag{13}$$

We note that this contrasts with the width of the conductance peaks [9], $\lambda_{\mathrm{peak}} \sim \max[\Gamma, T]$. Therefore, the quadratic dependence of $\lambda$ on the $T$ leads at $T, \Gamma \ll \Delta$ to the inequality

$$\lambda \ll \lambda_{\mathrm{peak}} \text{ for } T, \Gamma \ll \Delta.$$

The smallness of $\lambda$ is in qualitative agreement with experimental observations [5].

As anticipated before, the behavior described above is not universal but depends crucially on the relative sign of the coupling constants, $s$. Indeed, the qualitative features for $s = -1$ are different from the ones described above for $s = +1$. We first consider the transmission probability depicted in Fig. 10. The features of the case $s = -1$ are markedly different from the previous $s = +1$ case. First, the transmission probability $|t_-|^2$ is always finite over the entire energy $(\epsilon)$ range, implying the absence of a phase lapse. Indeed, the phase evolves continuously from zero to $2\pi$ as $\epsilon$ is swept across the two resonances.

The analysis presented can be extended to include $N > 2$ in the QD, as well as interaction. Again, the key parameter determining the

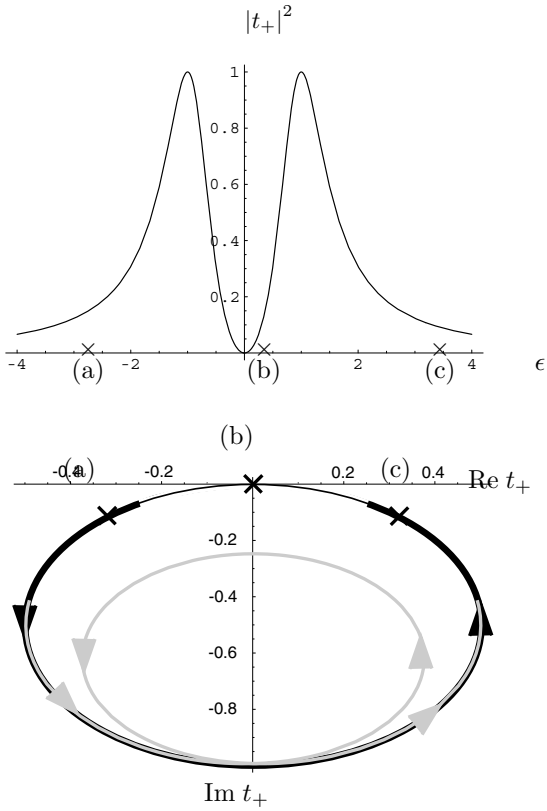


*Figure 9.* Plot of $|t_+(\epsilon)|^2$ vs. $\epsilon$ for $\epsilon_1 - \epsilon_2 = 2$ and $\Gamma = 0.5$ (upper plot) and of $t_+(\epsilon)$ in the complex plane (lower plot). At zero temperature the transmission amplitude evolves along a circle in the lower part of the complex plane (Im[t] $\leq 0$). As $\epsilon$ is increased, $t_+(\epsilon)$ evolves from point (a) traversing the origin at $\epsilon = 0$ [point (b)] and winds around the circle again up to point (c). The black thick line in the lower plot denotes that portion of the circle that is visited twice by $t_+(\epsilon)$ as $\epsilon$ varies from $-4$ to 4. Upon temperature averaging $t_+(\epsilon)$ evolves along a contour enclosed in the zero temperature circle (grey line in the lower plot). As a result, the finite temperature curve does not contain the origin, and the phase lapse of Fig. 7 is smeared. It is then easily concluded that as $T \to 0$ the transmission phase lapses by $-\pi$. Taken from Ref. [8].

behavior of the phase $\varphi$ as well as that of other physical quantities (conductance, differential capacitance) is found to be the relative phase between consecutive levels in the QD [8].

In conclusion, the evolution of the phase of the transmission amplitude in between two resonant peaks depends crucially on the relative

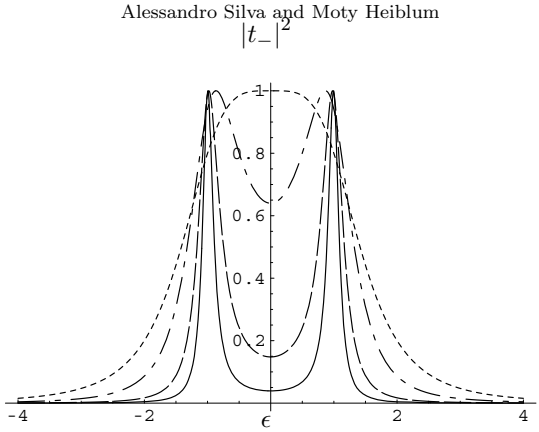


*Figure 10.* The transmission probability $|t_-|^2$ at the Fermi energy vs. $\epsilon$ for $s = -1$. Here, $\Delta = \epsilon_1 - \epsilon_2 = 2$ and $\Gamma = 0.1$ (full), 0.2 (dashed), 0.5 (dash-dotted),1 (dotted). Notice that in contrast to the zero at $\epsilon = 0$ for $s = +1$ (Fig. 7), here at large $\Gamma$ the conductance is peaked at $\epsilon = 0$. Taken from Ref. [8].

phase of the coupling matrix elements $s = \exp i\varphi$. Moreover, the behavior of the conductance as a function of $V_P$ at large $\Gamma$ is also strongly dependent on $s$: if the two levels are out-of-phase ($s = -1$) the two peaks tend to merge as $\Gamma$ is increased, becoming as single peak for $\Gamma = \Delta/2$. In contrast, if the two levels are in-phase ($s = +1$), the presence of a zero of the transmission amplitude keeps the two peaks apart, and the peak-valley-peak structure is preserved upon increasing $\Gamma$.

## 6. Kondo regime

The Kondo effect [29], a many body phenomenon, first discovered in metals slightly doped with magnetic impurities, has become one of the paradigms of strongly correlated systems. The effect results from an interaction of magnetic impurities with conduction electrons. In 1988 it was recognized [30] that the Kondo effect could also take place in a quantum dot[31] strongly coupled to an electron reservoir, whose lowest order theoretical description is based on the well known Anderson model [32]. In particular, when a QD is on the average occupied by an odd number of electrons and at temperatures below a characteristic scale $T_k$, the Kondo temperature, the strong Coulomb interaction produces a many-body resonance at the Fermi level [33] which manifests itself in an enhancement of the conductance through the QD. At temperatures $T \ll T_k$ the conductance $G$ reaches its unitary limit

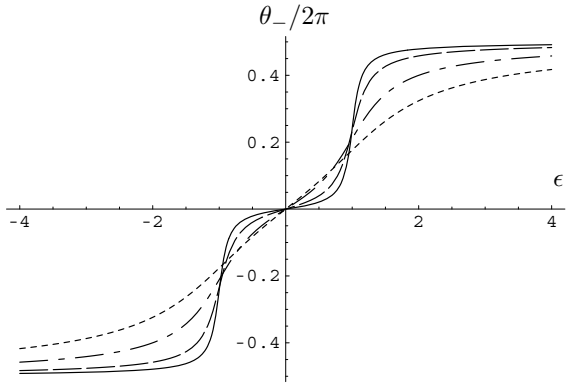


*Figure 11.* The transmission phase $\theta_-/2\pi$ at zero temperature vs. $\epsilon$ for $s = +1$. Here, $\Delta = \epsilon_1 - \epsilon_2 = 2$ and $\Gamma = 0.1$ (full), 0.2 (dashed), 0.5 (dash-dotted),1 (dotted). Notice that in contrast to Fig. 8 the phase evolves in the conductance valley continuously from zero to $2\pi$, hence no phase lapse. Taken from Ref. [8].

($G \approx 2e^2/h$). The realization of the Kondo effect in QD's permits the consideration of many aspects of Kondo physics (e.g., the Kondo effect out of equilibrium [34, 35]) whose study is experimentally difficult in traditional realizations of the Kondo effect, such as magnetic impurities in a bulk metallic host.

The Kondo effect was first observed in a mesoscopic QD by Goldhaber-Gordon et al. [36], who were able to control in situ many relevant parameters that affect Kondo correlation. This phenomenon was demonstrated and extensively studied through a direct measurement of the enhancement of the conductance in a CB valley upon lowering the temperature of the sample. The phenomenology observed in such transport measurements [37] in consistent with predictions based on the Anderson model [32, 38, 39].

One of the most fundamental properties of the Kondo effect is the prediction of a phase shift $\pi/2$ experienced by scattering electrons from the spin singlet [40][41]. This result is strictly related to the fact that in the Kondo regime transport is mediated by a resonance at the Fermi level. More recently, the evolution of the phase of the transmission amplitude through a QD in the Kondo regime as a function of gate voltage was studied theoretically on the basis of the Anderson model, leading to similar predictions [24].

The evolution of the transmission phase in the Kondo regime was addressed experimentally using the previously developed double-path

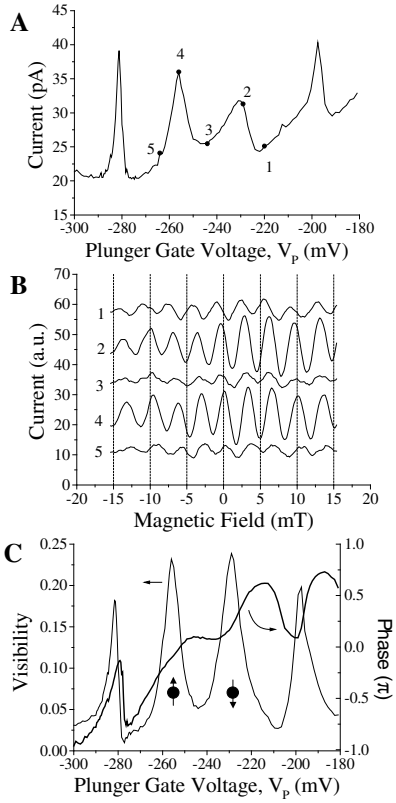


*Figure 12.* Complex transmission coefficient of the quantum dot in the Kondo regime measured via the Aharonov-Bohm (AB) effect. (**A**) Collector current as a function of *plunger* gate voltage at zero magnetic field. This current is very sensitive to magnetic field due to the AB effect, as shown in (**B**), when a series of interference patterns in the current collected by the drain (at specific points given in (A)), as a function of magnetic field (shifted vertically), taken at specific positions noted in (A). Trace 3, measured at center of the conductance valley between the Kondo pair, verifies coherency of electron transport in the Kondo valley. (**C**) Qualitative behavior of the magnitude (shown by the visibility of AB oscillation) and absolute value of the phase of the transmission coefficient of the QD — both obtained from the AB oscillations. Note that the phase evolves continuously through the Kondo pair while there is a phase lapse of $-\pi$ between the other consecutive peaks. Taken from Ref. [6].

electron interferometer with an embedded QD in one of its paths tuned to the Kondo regime.

The double path interferometer was similar to that used in the experiment by Schuster et al. [5] though the QD was made smaller than usual ($180nm \times 200nm$) to allow large energy level spacing, hence allowing strong coupling of the dot to the leads, without overlapping of the energy levels. The QD contained a few tens of electrons with average level spacing $\Delta \cong 0.5meV$ and a charging energy $U_C \cong 1.5meV$. Measurements were done in a dilution refrigerator with base temperature $T_{lattice} < 50mK$ and an electron temperature $T_{electron} \sim 90mK$. Current collected in the drain was measured with standard lock-in techniques, with an excitation voltage $10\mu V$ at $7Hz$, applied between the source and the nearby base contacts.

Once a Kondo valley was identified by means of standard experimental tests (enhacement of conductance upon decreasing of temperature, zero bias anomaly and its splitting in magnetic field), the measurement was performed in a way similar the experiments described in Sec. 4. The drain current, as a function of the plunger gate voltage, is shown in Fig. 12(A). Four CB peaks are clearly resolved on top of a large background, whose origin can be accounted for by the interference of the electron waves arriving from both of the interferometer arms. The central valley, was identified by means of conductance measurements as a Kondo valley.

Inducing a controlled phase difference between the two direct paths from source to drain by the application of a perpendicular magnetic field, the AB oscillations of the drain current were measured at different values of plunger gate voltage. The oscillation observed in the drain current (shown for example in five different points in Fig. 12(A) and 12(B)), with period 3.5 mT, immediately suggests coherency of transport in the QD current, when the dot is tuned to peaks or a valley of conductance. The high visibility ($5 - 25\%$), suggests that transport through the dot is highly coherent [4][5].

The visibility and the phase are shown as a function of plunger gate voltage in Fig. 12(C). While phase lapses, similar to those observed in Ref.[5], are observed between non-spin-degenerate levels ( the outer valleys near $V_P = -280$ mV, $-210$ mV), the phase in the spin-degenerate levels **evolves continuously and monotonously, with no sign of phase lapse.** The phase climbs through the spin up peak and saturates at $\pi$ in the valley, thereafter it continues and climbs by another $0.5\pi$ through the spin down peak. In other samples, not shown here, it was found that the climb through the spin down peak was also close to $\pi$. Most probably, the total phase change across a Kondo pair varies from one sample to another because of peaks overlapping depending on

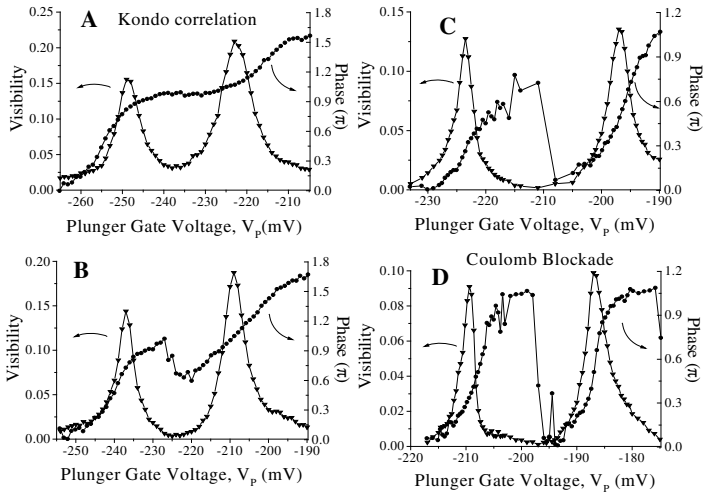


*Figure 13.* Phase lapse is formed as the coupling between the quantum dot and the leads is gradually reduced. When the coupling to the leads is strong (**A**), the phase evolution is continuous and the total phase change through the spin-degenerate pair is about $1.5\pi$. As the coupling gets weaker (from (**A**) to (**D**)), and the QD enters the Coulomb Blockade regime, the familiar phase lapse [5] is recovered and a full phase evolution of $\pi$ across each peak emerges. The peak position is shifting due to the influence of voltage applied to the gates that formed the two point contacts of the QD. Taken from Ref. [6].

their width and spacing. Hence, ideally, the phase seems to evolve by $\pi$ into the Kondo valley and by $2\pi$ across the two spin degenerate levels. This is in contradiction with the prediction of Gerland et al. [24], who predicted a $\pi/2$ and $\pi$ phase change, respectively.

In this device, due to the relatively high temperatures of the electrons, one could not reach the full Kondo enhancement, where the valley conductance reaches $2e^2/h$. However, it is worth noting that experiments performed with other devices close to the unitarity limit displaied an even more dramatic disagreement with theoretical prediction.

Since the Coulomb Blockade regime can be easily approached by reducing the coupling strength between the QD and the leads, such a procedure was followed with results shown in Fig. 13. As the coupling strength becomes gradually weaker (from Fig. 13(A) to Fig. 13(D)), the phase evolves from a continuous increase across the two spin-degenerate levels to a sudden appearance of a small phase lapse in the valley (even though the Kondo correlation was still apparent in that condition),

increasing eventually to a full $-\pi$ phase lapse — distinctive at Coulomb Blockade transport.

It is well known that increasing the temperature to be of the order of $T_K$ or applying a bias $eV \approx kT_k$ across the QD destroy the Kondo correlation. In Ref. [6] it was also demonstrated that the phase evolution, changes once again from that of a smooth and monotonic increase at low temperatures to that with a small phase lapse in the valley as temperature increases, the phase lapse reaching a full $-\pi$ drop at $1K$. Similarly, the application of a small DC bias across the QD leads to a similar change in the phase evolution, moving from a smooth increase to a phase lapse. In both cases Kondo correlation ceases to exist at $T \sim T_K \sim 1$ K and $eV_{DC} \sim k_B T_K \sim 100\mu eV$.

In this device, due to the relatively high temperatures of the electrons, one could not reach the full Kondo enhancement, where the valley conductance reaches $2e^2/h$. However, it is worth noting that experiments performed with other devices close to the unitarity limit displaied an even more dramatic disagreement with theoretical prediction, with a linear phase evolution between 0 and $2\pi$ across a fully enhanced Kondo valley.

The results presented above demonstrate a clear fingerprint of Kondo correlation in a QD with spin degenerate levels. As the correlation is being gradually suppressed, a gradual transition to the familiar behavior of the phase in the Coulomb Blockade regime emerges. The total phase change as the two spin-degenerate levels cross the Fermi energy in the leads is nearly $2\pi$ with a phase shift $\pi$ in the conduction valley. This does not agree with the prediction by Gerland et al. [24] of $\pi$ and $\pi/2$, respectively. Moreover, the phase evolution approaches to be highly sensitive to the onset of Kondo correlation. While the conductance is only a quantitative mark of the effect and has to be verified by changing temperature, voltage or coupling strength, the phase evolution has a distinctive behavior, which abruptly changes as one weakens the Kondo correlation while moving into the Coulomb Blockade regime.

## 7. Conclusions

In this review, we discussed the physics of coherent transport through a QD with particular emphasis on measurements of the phase of the transmission amplitude through the QD by means of modified Aharonov-Bohm interferometers. Such measurements revealed interesting and somewhat unexpected physics. In particular, the phase evolution across a sequence of CB peaks has a peculiar structure, whose main characteristic is an increase of $\pi$ across every CB peak followed by an abrupt

phase lapse of $\pi$ in every CB valley. The origin of such phase lapses as well as their small scale can be accounted for by a simple non interacting model of a QD. On the basis of this model one finds that at zero temperature the transmission amplitude vanishes exactly in between the two peaks of the conductance every time the relative phase of the coupling to the leads of the two consecutive levels is zero. Associated with a zero transmission is an abrupt phase lapse. The latter acquires a finite scale $\lambda$ at finite temperatures ($\lambda \propto \Gamma\, T^2/\, \Delta^2$). This simple theory accounts for the origin of the phase lapse and its scale. However, the observation of a phase lapse in every CB valley so far analyzed still lacks an accepted explanation.

Interestingly, the experiments devoted to the measurement of the transmission phase in the Kondo regime give a result which is in contrast with theoretical expectations. On the basis of the description of a QD in the Kondo regime by an Anderson model, the phase evolution as a function of plunger gate for a QD in the Kondo regime was predicted to be characterized by a plateau at $\pi/2$ in the Kondo valley and by total increment of the phase of $\pi$ across the CB peak-Kondo valley-CB peak structure. However, the measured plateau was observed at $\pi$, while the total increment was measured to be close to $2\pi$, in apparent contrast with theoretical predictions. Such discrepancy seems to indicate that the Anderson model, though able to account qualitatively for the conductance properties of a QD in the Kondo regime, does not describe accurately the physics of real QDs.

## References


1. Y. Aharonov and D. Bohm, Phys. Rev.**115** 485 (1959).
2. N. Bohr, Discussion with Einstein on Epistemological Problems in Atomic Physics, in Albert Einstein: Philosopher - Scientist (Ed. P. A. Schilpp) 200-241 (Library of Living Philosophers, Evanston, 1949).
3. E. Buks, R. Schuster, M. Heiblum, D. Mahalu and V. Umansky, Nature **391** , 871 (1998); D. Sprinzak, E. Buks , M. Heiblum, H. Shtrikman, Phys. Rev. Lett. **84**, 5820 (2000).
4. A. Yacoby, M. Heiblum, D. Mahalu, and H. Shtrikman, Phys. Rev. Lett. **74**, 4047 (1995).
5. R. Schuster, E. Buks, M. Heiblum, D. Mahalu, V. Umansky, and H. Shtrikman, Nature **385**, 417 (1997).
6. Yang Ji, M. Heiblum, D. Sprinzak, D. Mahalu, H. Shtrikman, Science **290** , 779 (2000).
7. Yang Ji, M. Heiblum, H. Shtrikman, Phys. Rev. Lett. **88** 076601 (2002).
8. Alessandro Silva, Yuval Oreg, and Yuval Gefen, Phys. Rev. B **66** , 195316 (2002).

9. L. P Kouwenhoven, C. M. Marcus, P. L. McEuen, S. Tarucha, R. M. Westervelt, and N. S. Wingreen, in *Mesoscopic Electron Transport*, edited by L. L. Sohn, L. P. Kouwenhoven, and G. Schon (Kluwer, Dordrecht, 1997).
10. Y. Alhassid, Rev. Mod. Phys. **69**, 731 (1997).
11. I. L. Aleiner , P. W. Brouwer, I. L. Glazman, Phys. Rep. **35 8**, 309 (2002).
12. K. A. Matveev, Phys. Rev. B **51**, 1743 (1995).
13. Yu. V. Nazarov, Phys. Rev. Lett. **82**, 1245 (1999).
14. A. Kamenev, Phys. Rev. Lett. **85**, 4160-4163 (2000).
15. Indeed, only the elastic component of the transmission through the interferometer contributes to the interference signal, see e.g. A. Stern, Y. Aharonov and Y. Imry, Phys. Rev. A **41**, 3436 (1990).
16. Y. Imry, Introduction to Mesoscopic Physics (Oxford University Press, Oxford 1997).
17. L. Onsager, Phys. Rev. **38** , 2265 (1931).
18. This relation is general and valid in a two terminal geometry, even in the presence of inelastic scattering, not taken into account in our analysis. See M. Büttiker, Phys. Rev. Lett, **57** , 1761 (1986); M. Büttiker, IBM J. Res. Dev. **32** , 317 (1988).
19. Y. Oreg and Y. Gefen, Phys. Rev. B **55**, 13726 (1997). H.-W. Lee, Phys. Rev. Lett. **82**, 2358 (1999); A. Levy Yeyati and M. Buttiker, Phys. Rev. B **62**, 7307 (2000); P. G. Silvestrov and Y. Imry, Phys. Rev. Lett. **85**, 2565 (2000).
20. O. Entin-Wohlman, C. Hartzstein, and Y. Imry, Phys. Rev. B *34*, 921 (1986).
21. Indeed, starting with a different phase for each coupling ($V_{\alpha,j} = V \exp[i\varphi_{\alpha,j}]$), and applying the change of variab les, $\tilde{c}_{k,\alpha} = \exp[-i\varphi_{\alpha,1}]\ c_{k,\alpha}$, $\tilde{d}_2 = \exp[i(\varphi_{L,2} - \varphi_{L,1})]\ d_2$, and $\tilde{d}_1 = d_1$, one obtains an Hamiltonian of the form of Eq. 4 with hybridization couplings given by $V_{L,1} = V_{R,1} = V_{L,2} = V$ and $V_{R,2} = e^{i\varphi}V$, where $\varphi = (\varphi_{R,1} - \varphi_{R,2} - \varphi_{L,2} + \varphi_{L,1})$.
22. Allowing the four couplings to have different magnitudes leads t o two main effects. If $V_{L,1} = V_{L,2} \neq V_{R,1} = V_{R,2}$ (left/right asymmetry) the conductance is suppressed as a whole, but all the features described in the text (*e.g.*, zero of the conductance, the appearance of a phase lapse and the merging of the spectral density peaks for $s = +1$) are still present. The other possible asymmetry, $V_{L,1} = V_{R,1} \neq V_{R,2} = V_{L,2}$ (level asymmetry), spoils the symmetry of the conductance curve with respect to the point $\epsilon = 0$. The qualitative features discussed here remain intact, including the zero of the conductance (which is now shifted with respect to the $\epsilon = 0$ point).
23. Y. Meir and N. S. Wingreen, Phys. Rev. Lett. **68**, 2512 (1992).
24. U. Gerland, J. von Delft, T. A. Costi and Y. Oreg, Phys. Rev. Lett. **84**, 3710 (2000).
25. We note that the "transmission phase" so measured may not reflect the actual transmission phase through the QD, but might be affected by multiple reflection paths, reflection from any of the terminals of the interferometer and deviations from unitarity [26].
26. A. Aharony, O. Entin-Wohlman, B. I. Halperin, and Y. Imry, Phys. Rev. B **66**, 115311 (2002) ; O. Entin-Wohlman, A. Aharony, Y. Imry, Y. Levinson, and A. Schiller, Phys. Rev. Lett. **88**, 166801 (2002).
27. R. Berkovits, Y. Gefen, O. Entin-Wohlman, Philos. Mag. B **77**, 1123 (1998).
28. G. Hackenbroich, W. D. Heiss, H. A. Weidenmuller, Philos. Mag. B **77**, 1255 (1998).

29. J. Kondo, in Solid State Physics, Eds. H. Ehrenreicht, F. Seitz, D. Turnbull, Academic Press, New York, **Vol. 23**, 13 (1969); L. Kouwenhoven and L. Glazman, Physics World, **14**, Jan., 33 (2001).
30. L. I. Glazman and M. E. Raikh, JETP Lett. **47**, 452 (1988); T. K. Ng and P. A. Lee, Phys. Rev. Lett. **61**, 1768 (1988).
31. U. Meirav, E. B. Foxman, *Semicond. Sci. Technol.* **10**, 255 (1995).
32. P. W. Anderson, Phys. Rev. **124**, 41 (1961).
33. A. C. Hewson, The Kondo Problem to Heavy Fermions (Cambridge University Press, Cambridge, 1993).
34. N. S. Wingreen and Y. Meir, Phys. Rev. B **49**, 11040 (1993 ).
35. A. Kaminski, Yu. V. Nazarov, and L. I. Glazman, Phys. Rev. Lett. **83**, 384 (1999); A. Kaminski, Yu. V. Nazarov, and L.I. Gl azman, Phys. Rev. B **62**, 8154 (2000); J. M. Elzerman et al., J. Low Temp. Phys **118**, 375 (2000).
36. D. Goldhaber-Gordon, H. Shtrikman, D. Mahalu, D. Abusch-Magder, U. Meirav, M. A. Kastner, Nature **391**, 156 (1998).
37. S. M. Cronenwett, T. H. Oosterkamp, L. P. Kouwenhoven, Science, **281**, 540 (1998); D. Goldhaber-Gordon,J. Göres,M. A. Kastner, H. Shtrikman, D. Mahalu, and U. Meirav , Phys. Rev. Lett. **81**, 5225 (1998); F. Simmel, R. H. Blick, J. P. Kotthaus, W. Wegscheider, and M. Bichler, Phys. Rev. Lett. **83**, 804 (1999); J. Schmid, J. Weis, K. Erbel, and K. von Klitzing, Phys. Rev. Lett. **84**, 5824 (2000); S. Sasaki, S. De Franceschi, J. M. Elzerman, W. G. van der Wiel, M. Eto, S. Tarucha, and L. P. Kouwenhoven, Nature **405**, 764 (2000).
38. Y. Meir, N. S. Wingreen, P. A. Lee, *Phys. Rev. Lett.* **70**, 2601 (1993).
39. N. S. Wingreen, Y. Meir, *Phys. Rev.* **B49**, 11040 (1994).
40. D. C. Langreth, *Phys. Rev.* **150**, 516 (1966).
41. P. A. Nozieres, *J. Low Temp. Phys.* **17**, 31 (1974).

# Superconducting quantum bit based on the Cooper pair box

D. Vion, A. Aassime, A. Cottet, P. Joyez, H. Pothier, and C. Urbina, D. Esteve and M.H. Devoret
*Quantronics Group*
*Service de Physique de l'Etat Condensé, CEA-Saclay*
*F-91191 Gif-sur-Yvette cedex, France*

## 1. Introduction

The more advanced proposals so far for the implementation of qubits and quantum gates for quantum computation[1] are based on ions or atoms in vacuum [2, 3]. These systems have been manipulated individually in a controlled fashion for about 20 years and techniques have reached a high level of sophistication. However, it is not clear yet if these proposals can be extended to the fabrication of a quantum processor which would be "scalable", a jargon term referring to the situation where fabrication costs scale sufficiently "gently" with the number of quantum bits and gates that quantum computation can overpower its classical counterpart.

This is why there is currently interest in various solid-state implementations of qubits [4, 5, 6, 7, 8, 9, 10, 11, 12, 13, 14] which could be fabricated in parallel by lithography methods, hence benefiting of the technological advances that have made classical processors so powerful today.

In these notes we focus on one particular solid-state implementation for which a lot of experience on feasibility has been gathered experimentally, namely qubits based on superconducting tunnel circuits.

Ion systems have remarkable level structures. The ground state is split by the hyperfine interaction, thus yielding basis states for the qubit, while well-resolved excited states hovers well above the ground state at energies corresponding to visible or infra-red photons, thus providing a very good isolation between the degrees of freedom representing the qubits and perturbing ones. At the same time, the ground-to-excited states transitions can be exploited to readout the value of the qubit by fluorescence photons which can be easily detected.

A similar, although not as ideal situation, is encountered with a superconducting junction, i.e. two superconducting electrode separated by an oxide layer acting as a tunnel barrier. Here we suppose that



*R. Fazio et al. (eds.), New Directions in Mesoscopic Physics,* 173–195.
© 2003 *Kluwer Academic Publishers. Printed in the Netherlands.*

the electrodes are sufficiently small that the superconducting order parameter is homogeneous inside the electrode. In order to describe the degrees of freedom of this so-called Josephson tunnel junction, it is useful to first begin with only one isolated BCS-type superconducting electrode with an even number of electrons. This system has a unique many-body ground state. Excited states of the electrode have a minimum energy of $2\Delta$, where $\Delta$ is the superconducting quasiparticle gap, an energy of the order of a few kelvin which we suppose large in comparison with all the environmental energies like temperature fluctuations energies. The energy $2\Delta$, needed to break a Cooper pair into independent quasiparticles, is equivalent to the energy difference between ground and excited state of the ion. If we now imagine having two such isolated electrodes come together until they become separated only by a tunnel barrier, we will have a combined system possessing a set of quasi-degenerate ground states corresponding to all the possible number $N$ of pairs of electrons which can be transferred from one electrode to the other. The degree of freedom corresponding to $N$ has to be understood as an operator and will thus be noted $\hat{N}$. We will use the usual Dirac notation for the eigenstates and eigenvalues of $\hat{N}$.

$$\hat{N}\left|N\right\rangle = N\left|N\right\rangle \tag{1}$$

The degeneracy between the eigenstates of $\hat{N}$, the so-called charge states, is lifted by two energy terms which play the role in the junction of the hyperfine interaction in ions.

The first term is the Coulomb energy, whose origin is the electric field in the tunnel oxide due to the charge on the two electrodes (note on offset charge). With the previously introduced notation the Coulomb hamiltonian can be written

$$H_C = 4E_C \sum_p \left(\hat{N} - q\right)^2 \left|N\right\rangle \left\langle N\right| \tag{2}$$

where the Coulomb energy

$$E_C = \frac{e^2}{2C_j} \tag{3}$$

corresponds to the electrostatic energy of one charge quantum on the capacitance $C_j = \epsilon A/d$ of the tunnel junction, which we suppose here to be well described by a parallel-plate capacitor with area $A$, dielectric constant $\epsilon$ and dielectric thickness $d$. The charge $q$ , which in general is not a integer, corresponds to the offset charge on the tunnel junction and reflects the fact that even when two electrodes are neutral, there can be a non-zero electric field between them due to the

difference in their work function. We suppose that the temperature $T$ and the superconducting gap $\Delta$ satisfy $k_B T \ll \Delta / \ln \mathsf{N}$ and $E_C < \Delta$, where $\mathsf{N}$ is the total number of pair states. When these conditions are satisfied, there are no unpaired electrons in the electrodes, provided we start of course with an even total number of electrons[15, 16].

The second term is the Josephson energy. It correspond to the delocalization energy of Cooper pairs through the tunnel barrier.

The Josephson hamiltonian has the form

$$H_J = \frac{E_J}{2} \sum_p |N+1\rangle \langle N| + h.c. \tag{4}$$

The Josephson energy

$$E_J = \frac{1}{8} \frac{G_t}{e^2/h} \Delta \tag{5}$$

is simply proportional, via the tunnel conductance of the barrier,

$$G_t = \frac{e^2}{h} M \mathcal{T} \tag{6}$$

to the transparency $\mathcal{T}$ of the barrier and the number of independent electronic $M$ modes passing through it. The constant $\frac{e^2}{h}$appearing here is the conductance quantum. The number of modes is proportional to the area $A$ of the junction and inversely proportional to the Fermi wavelength $\lambda_F$

$$M = \frac{4A}{\lambda_F^2} \tag{7}$$

It is worth noting that the operator $\hat{N}$ is a macroscopic quantum variable: its dynamics is governed by quantum mechanics, but the parameters appearing in the hamiltonian are not God-given constants like the Rydberg constant or the Bohr magneton. They correspond to macroscopic parameters like the junction area which can be engineered by nanolithography. Also, the various $N$ states correspond to a complete rearrangement of the charge on the electrode, and not to the filling of single electron wavefunctions. The $\hat{N}$ operator is a collective variable like the angular momentum of a top.

It is useful at this point to introduce the operator $\hat{\theta}$ canonically conjugate to $\hat{N}$. Since $\hat{N}$ has integer eigenvalues, some care is needed in the definition of $\hat{\theta}$

$$\mathrm{e}^{i\alpha\hat{\theta}} \mathrm{e}^{-i\alpha\hat{\theta}} = \hat{N} - \alpha \tag{8}$$

The operator $\hat{\theta}$ is called the phase difference between the two electrodes. At this level, the name "phase" can be misleading. Its meaning is that of a position variable in a cyclic system, like the center of mass of a ball constrained to roll in a circle-shaped groove, not the phase of a single-particle wavefunction. In the $\hat{\theta}$ representation, the Josephson hamiltonian is diagonal and takes a very simple form

$$H_J = -E_J \cos\hat{\theta} \tag{9}$$

The pair number $\hat{N}$ and the phase difference $\hat{\theta}$ bear some resemblance with the photon number and the phase operators of a cavity mode in quantum optics. However, one must realize that the pair number eigenvalues can take both positive and negative values whereas the photon number is always non-negative. This difference is fundamental. The topology of the Hilbert space spanned by $\hat{N}$ and $\hat{\theta}$ is that of a cylinder and is intrinsically curved, while the harmonic oscillator Hilbert space is flat.

The Josephson tunnel junction is the unique quantum non-linear electric system. Although many other non-linear electrical system exist, their internal degrees of freedom all get frozen by the time one reaches the temperatures at which quantum effects implying collective variables like charge can be observed.

If we express the total tunnel junction hamiltonian in terms of the "macrovariable" operators,

$$H_0 = 4E_C\left(\hat{N} - q\right)^2 - E_J \cos\hat{\theta} \tag{10}$$

we see that the Josephson term plays the role of a potential term while the Coulomb energy corresponds to a kinetic energy term.

If $E_C \ll E_J$, we can forget about the discreetness of $\hat{N}$, associated with the cyclic property of $\hat{\theta}$. If furthermore $q = 0$, the hamiltonian $H_0$ becomes the hamiltonian of a anharmonic oscillator, the quadratic potential term being replaced by a sinusoidal one. We have then an hamiltonian analogous to that of a pendulum making an angle $\hat{\theta}$ with the vertical.

$$H_0 = 8E_C\frac{\hat{N}^2}{2} + E_J\frac{\left(2\sin\frac{\hat{\theta}}{2}\right)^2}{2} \tag{11}$$

The small oscillation frequency is thus given by

$$\omega_p = \frac{\sqrt{8E_C E_J}}{\hbar} \tag{12}$$

This quantity is called the plasma frequency of the junction. The junction surface scales out of this parameter which is essentially only

determined by the oxide thickness and dielectric constant (the Fermi wavelength does not vary much from one metal to another). In practice its value is in the 5-50 GHz range.

In the limit $E_C \ll E_J$ the mean square fluctuations of $\hat{\theta}$ in the ground state is given by

$$\left\langle \hat{\theta}^2 \right\rangle_0 = \sqrt{\frac{2E_C}{E_J}} \tag{13}$$

We can thus see the ratio $E_C/E_J$ as a sort of "quanticity" parameter. If $E_C \ll E_J$, the junction behaves as a semiclassical anharmonic oscillator and $\theta$ is a good quantum number. If $E_C \gg E_J$, it behaves as a free particle on a one-dimensional ring and its momentum $N$ is a good quantum number. Neither the charge nor the phase are good quantum numbers when $E_C/E_J \sim 1$.

The Josephson junction is thus a macroscopic one-dimensional atom.

We will see in the next section that we can manipulate the states of this macroatom with electric signals traveling along "wires" instead of light.

We have so far a "bare" junction with certain macrostates. How can we address them? We need fields that couples to the junction macrovariables. There are three types of fields we can impose, each one of them corresponding to a different type of electrical bias. We can impose a current through the junction and get the so-called current biased Josephson junction[17]. We can also link the to sides of the junction by a superconducting loop and impose an external magnetic flux through the loop: this forms the so-called RF-SQUID. Finally, the simplest form of bias has been proposed theoretically by Büttiker in 1989[18], well after the initial developments of the Josephson effect. It was realized experimentally several years later by our group[19]. The associated device is called the single Cooper pair box.

## 2. The single Cooper pair box

The idea of Büttiker was to subject the Josephson junction superconducting electrodes to a minimally invasive influence: the junction is placed beween two capacitor plates connected to a voltage source. By electrostatic influence, this applied voltage induces surface charge on the junction electrodes and modify the offset charge.

$$H_U = 4E_C \left(\hat{N} - C_g U/2e\right)^2 - E_J \cos\hat{\delta} \tag{14}$$

Here, we have lumped into the voltage $U$ the effect of the junction intrinsic offset charge. The value $U = 0$ corresponds here to a nulling out of the offset charge, not necessarily to zero voltage applied to the capacitor plates. The parameter $C_g$ is called the gate capacitance. It is half the value of the capacitance between plate and junction electrode, if they influence each other completely. In practice, we do not need two capacitors on each side of the junction. In the Cooper pair box, the voltage $U$ is applied between one junction electrode and the gate capacitor (see Fig. 1). Note that for the box the value of the Coulomb energy now takes the form

$$E_C = \frac{e^2}{2C_\Sigma} \tag{15}$$

where $C_\Sigma = C_j + C_g$.

In Fig. 2 we show the eigenvalues of hamiltonian (14) as a function of the reduced gate charge $n_g = C_g U/e$ for different values of the ratio $E_J/\ E_C$. When $E_C \gg E_J$ the Cooper pair number is almost everywhere a good quantum number, except at the degeneracy points of the electrostatic part of the hamiltonian, i.e. for odd values of $n_g$. In the vicinity of these degeneracy points, we can limit our analysis to two neighboring charge states $|N_0\rangle$ and $|N_0 + 1\rangle$, which are coupled by the Josephson energy and which play the role of the 2 basis states of an effective spin 1/2. Since the hamiltonian is invariant under the transformation $\hat{N} \to \hat{N} - N_0$, we can limit ourselves to the reduced Hilbert space spanned by $|N = 0\rangle$ and $|N = 1\rangle$.

In this reduced Hilbert space, we have a spin hamiltonian

$$H = -\overrightarrow{h} \cdot \overrightarrow{s} \tag{16}$$

where the spin $\overrightarrow{s}$ is given by

$$\overrightarrow{s} = \frac{1}{2}\left(\sigma_X \overrightarrow{X} + \sigma_Y \overrightarrow{Y} + \sigma_Z \overrightarrow{Z}\right) \tag{17}$$

with the Pauli spin matrices $\sigma_{X,Y,Z}$ given by

$$\begin{aligned} \sigma_X &= \begin{bmatrix} 0 & 1 \\ 1 & 0 \end{bmatrix} \\ \sigma_Y &= \begin{bmatrix} 0 & i \\ -i & 0 \end{bmatrix} \\ \sigma_Z &= \begin{bmatrix} 1 & 0 \\ 0 & -1 \end{bmatrix} \end{aligned}$$

and where the effective field $\overrightarrow{h}$ is given

$$\overrightarrow{h} = 4E_C\left(n_g - 1\right)\overrightarrow{X} + E_J\overrightarrow{Z} \tag{18}$$

If we compare our system to a magnetic spin like in ESR or NMR, the Josephson energy plays thus the role the Zeeman energy, while the the applied voltage plays the role of the transverse field.

At $T = 0$, the effective spin points in the direction of the effective field. This latter has a direction $\overrightarrow{\zeta}$ whose angle $\alpha$ with $\overrightarrow{Z}$ is given by

$$\tan\alpha = \frac{4E_C\left(n_g - 1\right)}{E_J} \tag{19}$$

and an intensity

$$h_\zeta = \sqrt{E_J^2 + \left[4E_C\left(n_g - 1\right)\right]^2} \tag{20}$$

The spin density matrix can thus be written as

$$\rho = \frac{1}{2}\left[1 + \overrightarrow{m}.\overrightarrow{\sigma}\right] \tag{21}$$

with

$$\overrightarrow{m} = \overrightarrow{\zeta}\tanh\frac{h_\zeta}{2k_BT} \tag{22}$$

The average Cooper pair number is directly proportional to the polarization of the spin along the $X$ axis.

$$\langle\hat{p}\rangle = \frac{m_X + 1}{2} \tag{23}$$

with

$$m_X = \tanh\left(\frac{h_\zeta}{2k_BT}\right)\cdot\sin\alpha \tag{24}$$

As we vary $U$, the average Cooper pair number varies in a step-wise fashion, with the shape of the step being described by expression (24). At $T = 0$, the width of the step is broadened by the quantum fluctuations of the charge governed by the Josephson energy. This behavior has been measured experimentally[19].

Rabi oscillations between two charge states of the box have subsequently been measured[8], thus further demonstrating the macrospin character of the system and its promising features for the implementation of a qubit.

## 3. Flux-tuned Cooper pair box

We now consider a Cooper pair box in which the junction is replaced by a so-called DC SQUID, i.e. two junctions in a loop through which a flux $\Phi$ can be threaded by an applied magnetic field. The two junctions are not supposed to be identical and we denote their Josephson energy $E_{J1}$ and $E_{J2}$. Likewise their capacitance is denoted $C_{j1}$ and $C_{j2}$.

The Josephson energy term in the hamiltonian now takes the form

$$E_{J1}\cos\hat{\theta}_1 + E_{J2}\cos\hat{\theta}_2 \tag{25}$$

where the two phases $\theta_1$ and $\theta_2$ obey $\theta_1 - \theta_2 = \theta$ and $\theta_1 + \theta_2 = \delta$, the phase $\delta$ denoting the phase of the series combination of the two junctions. This latter phase is related to the the flux $\Phi$ by

$$\delta + \gamma = 2\pi\frac{\Phi}{\Phi_0} \tag{26}$$

where $\gamma$ is the phase across the inductor, which is related to the current $I_{loop}$flowing around the loop by

$$\frac{\hbar}{2e}\gamma = LI_{loop} \tag{27}$$

Using some algebra we can rewrite the Josephson energy as:

$$E_J^{eff}\cos\left(\hat{\theta} + \beta\right) \tag{28}$$

where

$$E_J^{eff} = \sqrt{(E_{J1} + E_{J2})^2\left(\frac{1+\cos\delta}{2}\right) + (E_{J1} - E_{J2})^2\left(\frac{1-\cos\delta}{2}\right)} \tag{29}$$

and

$$\tan\beta = \frac{E_{J1} - E_{J2}}{E_{J1} + E_{J2}} \tag{30}$$

Note that small variations in the flux $\Phi$ will induce small field components along the three $X$, $Y$ and $Z$ axes if the two junctions are not symmetrical.

## 4. Cooper pair box with orthogonal write and read ports

Unlike the electric dipoles of isolated atoms or ions, the state variables of a circuit like voltages and currents usually undergo rapid quantum decoherence [20] because, in general, they are coupled to an environment with a large number of uncontrolled degrees of freedom [7]. Tunnel junction circuits [21, 8, 9, 10, 13] have displayed so far coherence quality factors $Q_\varphi$ of several hundreds [14]. Here, the coherence quality factor for a pair of quantum levels $|a\rangle$ and $|b\rangle$ is defined by $Q_\varphi = \pi\nu_{ab}T_\varphi$ where $\nu_{ab}$ is the transition frequency and $T_\varphi$ is the inverse of decoherence rate of quantum superpositions of these two states. In the following, we describe an experiment performed by our group which has shown that coherence quality factors of more than $10^4$ can experimentally be achieved in a new circuit built around the Cooper pair box. Two orthogonal access ports are used for preparing and measuring the quantum state [27, 22]. This lead us to an improvement of decoherence time by a factor of more than $10^2$compared to the best previously published results [8].

In our experiment $E_J \simeq 5E_C$ (see upper right panel in Fig. 2) and neither $\hat{N}$ or $\hat{\theta}$ are good quantum numbers. However, we can still restrict ourselves to the Hilbert space spanned by the ground $|0\rangle$ and first excited energy eigenstate $|1\rangle$ since the system is sufficiently non-harmonic. The effective spin $\vec{s}$ has a Zeeman energy $h\nu_{01}$ which goes to the minimal value $E_J$ when $N_g = 1/2$. The spin up ($s_z = 1/2$, state $|0\rangle$) and down ($s_z = -1/2$, state $|1\rangle$) states are there approximately $(|N=0\rangle \pm |N=1\rangle)/2$. Both states have the same average charge $\left\langle \hat{N} \right\rangle = 1/2$, and consequently the system is immune to first order fluctuations of the gate charge. With appropriate NMR-like microwave pulses on the gate $u(t) = U_{\mu w}(t)\sin 2\pi\nu t$, where $\nu \simeq \nu_{01}$, any superposition $|\Psi\rangle = \alpha\,|0\rangle + \beta\,|1\rangle$ can be prepared [23].

For readout, instead of measuring the charge $\left\langle \hat{N} \right\rangle$ which requires moving away from $N_g = 1/2$ [8, 24], we entangle $\vec{s}$ with a new degree of freedom more advantageous to measure. For this purpose, the single junction of the basic Cooper pair box has been split into two nominally identical junctions inserted into a superconducting loop (see Fig. 3). The new degree of freedom is the phase difference $\hat{\delta}$ across the two junctions, and the Josephson energy $E_J$ in Eq. (14) becomes $E_J\cos(\hat{\delta}/2)$ [25]. The information about $\vec{s}$ is transferred onto $\hat{\delta}$ through the supercurrent in the loop $\hat{I} = (2e/\hbar)\partial\hat{H}/\partial\hat{\delta} \simeq i_0 s_z \sin(\hat{\delta}/2)$ where $i_0 = eE_J/\hbar$. The currents $\left\langle 0 \left| \hat{I} \right| 0 \right\rangle$ and $\left\langle 1 \left| \hat{I} \right| 1 \right\rangle$ in the two states grow with opposite signs when $\delta = \left\langle \hat{\delta} \right\rangle$ moves away from zero.

Our readout strategy is to exploit the two corresponding evolutions of $\delta$ generated by its entanglement with $\vec{s}$. It has been implemented by inserting in the loop a large Josephson junction biased with a current $I_b$ [26]. This junction has a Josephson energy $E_{J0}$ which is about 20 times larger than $E_J$. Its phase difference is denoted by $\hat{\gamma}$. We have designed the loop dimensions to be as small as possible, thus making the loop inductance much smaller than the effective inductance of all junctions. This condition imposes the constraint $\hat{\delta} = \phi + \hat{\gamma}$, where $\phi = 2e\Phi/\hbar$, $\Phi$ being the externally imposed flux through the loop. By placing a large capacitance $C$ in parallel with the large junction so that $(2e)^2/2C \ll E_{J0}$, the phase $\hat{\gamma}$, and consequently $\hat{\delta}$, can be treated in first approximation as classical variables. Under these conditions, $\delta \simeq \phi + \arcsin(I_b/I_0)$, neglecting terms of order $i_0/2I_0 \simeq 0.01$ where $I_0 = 2eE_{J0}/\hbar$. Just as the system is immune to charge noise at $N_g = 1/2$, it is immune to flux and current noise at $\phi = 0$ and $I_b = 0$, where $\hat{I} = 0$. The preparation of the quantum state and its manipulation are therefore performed at this working point in charge-flux-current space. Readout is then achieved by displacing the system adiabatically along the $I_b$ axis to make the loop supercurrent non-zero.

In practice, a trapezoidal pulse of current with amplitude slightly below $I_0$ is applied to the large junction (see Fig. 4). Depending on whether the effective spin $\vec{s}$ is up or down, a value of order $i_0/2$ will be subtracted or added to $I_b$ in the large junction. The junction is extremely sensitive to the total current running through it when a value close to $\gamma = \pi/2$ is reached at the top of the pulse. A small excess current induces the switching of the junction from the zero-voltage state to the finite voltage state. With a precise adjustment of the amplitude and duration of the $I_b(t)$ pulse, the large junction switches to the voltage state with a large probability if $s_z = -1/2$ and with a small probability if $s_z = +1/2$ [27]. For the parameters given above, the efficiency of this projective measurement should be $\eta = p_1 - p_0 = 0.95$, where $p_1$ and $p_0$ are the switching probabilities in the excited and ground states, respectively, for optimum readout conditions.

The readout is also designed so as to minimize the relaxation of $\vec{s}$ using a Wheatstone-bridge-like symmetry. The large ratios $E_{J0}/E_J$ and $C/C_j$ provide further protection from the environment.

It is worthwhile to develop analogies between our experiment on an electrical circuit and experiments on atoms. Our circuit can be viewed as an artificial two-level atom, which we have nicknamed "quantronium". The gate voltage and the magnetic flux through the loop, the two bias parameters used to tune the transition frequency, play a role similar to that of the static electric and magnetic fields for atoms.

Like in many atomic physics experiments, transitions are induced by microwave pulses. Finally, the readout scheme can be compared with a Stern and Gerlach experiment: $\vec{s}$ is the analog of the spin of the Ag atom while the applied bias current is the analog of the magnetic field gradient. The loop current response is to be compared with the transverse acceleration of the Ag atom, the phase $\gamma$ being the analog of the transverse position of the atom. The presence or absence of the voltage pulse corresponds to the impact of the Ag atom in the upper or lower spot of the "screen".

The actual sample on which measurements have been performed is shown in the bottom of Fig. 3. Tunnel junctions have been fabricated using the standard technique of Al evaporation through a shadow-mask obtained by e-beam lithography [28]. With the external microwave circuit capacitor $C = 1$ pF, the plasma frequency of the large junction with $I_0 = 0.77$ $\mu$A is $\omega_p/2\pi \simeq 8$ GHz. The sample and last filtering stage were anchored to the mixing chamber of a dilution refrigerator with 15 mK base temperature. The switching of the large junction to the voltage state is detected by measuring the voltage across it with a room temperature preamplifier followed by a discriminator with a threshold voltage $V_{th}$ well above the noise level (Fig. 4). By repeating the experiment, we can determine the switching probability, and hence, the occupation probabilities $|\alpha|^2$ and $|\beta|^2$.

We have first tested the readout part of the circuit by measuring at thermal equilibrium, for a current pulse duration of $\tau_r = 100$ ns, the switching probability $p$ as a function of the pulse height $I_p$. We have found that the discrimination between the currents corresponding to the $|0\rangle$ and $|1\rangle$ states had an efficiency of $\eta = 0.6$, lower than the expected $\eta = 0.95$. Measurements of the switching probability as a function of temperature and repetition rate indicate that the discrepancy between the theoretical and experimental readout efficiency could be due to an incomplete thermalization of our last filtering stage in the bias current line.

We have then performed spectroscopic measurements of $\nu_{01}$ by applying to the gate a weak continuous microwave irradiation suppressed just before the readout current pulse. The variations of the switching probability as a function of the irradiation frequency display a resonance whose center frequency evolves as a function of the dc gate voltage and flux as the Hamiltonian (1) predicts, reaching $\nu_{01} \simeq 16.5$ GHz at the optimal working point (see Fig. 5). We attribute the small discrepancy between theory and experiment to a residual flux penetration in the small junctions not taken into account in the model. We have used these spectroscopic data to determine precisely the relevant circuit parameters and found $i_0 = 18.1$ nA and $E_J/E_C = 5.08$. At the optimal

working point, the linewidth was found to be minimal with a 0.8 MHz full width at half-maximum. When varying the delay between the end of the irradiation and the measurement pulse, the peak height decays with a time constant $T_1 = 1.8$ $\mu$s (see Fig. 6). Supposing that the energy relaxation of the system is only due to the bias circuitry, a calculation along the lines of Ref. [29] predicts that $T_1 \sim 10$ $\mu$s for a crude discrete element model. This result shows that no detrimental sources of dissipation have been seriously overlooked in our circuit design.

We have then addressed the fidelity of controlled rotations of $\vec{s}$ around an axis $x$ perpendicular to the quantization axis $z$. Prior to readout, a single pulse at the transition frequency with variable amplitude $U_{\mu w}$ and duration $\tau$ was applied. The resulting change in switching probability is an oscillatory function of the product $U_{\mu w}\tau$ (see Fig. 7), in agreement with the theory of Rabi oscillations [30, 23]. It provides direct evidence that the resonance indeed corresponds to an effective spin rather than to a spurious harmonic oscillator resonance in the circuit. The proportionality ratio between the Rabi period and $U_{\mu w}\tau$ was used to calibrate microwave pulses for the application of controlled rotations of $\vec{s}$.

The main result of this paper, the coherence time of $\vec{s}$ during free evolution, was obtained by performing the classic Ramsey fringes experiment [31] on which atomic clocks are based. One applies on the gate two phase coherent microwave pulses corresponding each to a $\pi/2$ rotation around $x$ [32] and separated by a delay $\Delta t$ during which the spin precesses freely around $z$. For a given detuning of the pulse center frequency, we have observed decaying oscillations of the switching probability as a function of $\Delta t$ (see Fig. 8), which correspond to the "beating" of the spin precession with the external microwave field. The oscillation period agrees exactly with the inverse of the detuning, allowing a measurement of the transition frequency with an accuracy of $6 \times 10^{-6}$ [33]. The envelope of the oscillations yields the decoherence time $T_\varphi \simeq 0.5$ $\mu$s. Given the transition period $1/\nu_{01} \simeq 60$ ps, this means that $\vec{s}$ can perform on average 8000 coherent free precession turns.

In all our time domain experiments, the oscillation period of the switching probability closely agrees with theory, meaning a precise control of the preparation of $\vec{s}$ and of its evolution. However, the amplitude of the oscillations is smaller than expected by a factor of three to four. This loss of contrast is likely to be due to a relaxation of the level population during the measurement itself. In principle the current pulse, whose rise time is 50 ns, is sufficiently adiabatic not to induce transitions directly between the two levels. Nevertheless, it is possible that the readout or even the preparation pulses excite resonances in the

bias circuitry which in turn could induce transitions in our two-level manifold. Experiments using better shaped readout pulses and a bias circuitry with better controlled high-frequency impedance are needed to clarify this point.

In order to understand what limits the coherence time of the circuit, we have performed measurements of the linewidth $\Delta\nu_{01}$ of the resonant peak as a function of $U$ and $\Phi$. The linewidth varies linearly when departing from the optimal point ($N_g = 1/2$, $\phi = 0$, $I_b = 0$), the proportionality coefficients being $\partial\Delta\nu_{01}/\partial N_g \simeq 250$ MHz and $\partial\Delta\nu_{01}/\partial(\phi/2\pi) \simeq 430$ MHz. These values can be translated into RMS deviations $\Delta N_g = 0.004$ and $\Delta(\phi/2\pi) = 0.002$ of the transition frequency during the time needed to record the resonance. The residual linewidth at the optimal working point is well-explained by the second order contribution of these noises and is not therefore limited by any fundamental factor or unknown noise sources. The amplitude of the charge noise is in agreement with measurements of 1/f charge noise [34], and its effect could be minimized by increasing the $E_J/E_C$ ratio. By contrast, the amplitude of the flux noise is unusually large [35], and we think that implementation of magnetic shielding and better Al layer configuration will significantly reduce it. An improvement of $Q_\varphi$ by an order of magnitude seems thus possible [36].

Acknowledgements: The indispensable technical work of Pief Orfila is gratefully acknowledged. This work has greatly benefited from direct inputs from J. M. Martinis and Y. Nakamura. The authors acknowledge discussions with P. Delsing, G. Falci, D. Haviland, H. Mooij, R. Schoelkopf, G. Schön and G. Wendin. This work is partly supported by the European Union through contract IST-10673 SQUBIT.

## References

1. D. P. DiVincenzo, "Quantum gates and circuits," Proc. R. Soc. Lond. A 454, 261-76 (1998)
2. D. Bouwmeester, A. Ekert, and A. Zeilinger, (Eds) "The Physics of Quantum Information: Quantum Cryptography, Quantum Teleportation, Quantum Computation" (Springer Verlag, Berlin, 2000)
3. J. M. Raimond, M. Brune, and S. Haroche, "Manipulating quantum entanglement with atoms and photons in a cavity," Rev. Mod. Phys. **73**, 565 (2001)
4. M.F Bocko, A. M. Herr and M.F. Feldman, IEEE Trans. Applied Supercond. **7,** 3638-3641(1997)
5. B. E. Kane, Nature **393,** 133-137 (1998)
6. D. Loss and D.P. DiVincenzo, Phys. Rev. **A 57**,120-126 (1998)
7. Yu. Makhlin, G. Schoen and A. Shnirman, Nature **398,** 786-789 (1999); Y. Makhlin, G. Schön, A. Shnirman, Rev. Mod. Phys. **73**, 357 (2001).

8. Y. Nakamura, Yu. A. Pashkin and J. S. Tsai, Nature **398**, 786-788 (1999); Phys. Rev. Lett. **87**, 246601 (2001); ibid. to be published [cond-mat/0111402].
9. J.E. Mooij, *et al.*, Science **285**, 1036 (1999); Caspar H. van der Wal *et al.*, Science **290**, 773 (2000).
10. Siyuan-Han, R. Rouse, J. E. Lukens, Phys. Rev. Lett. **84**, 1300 (2000).
11. B.E. Kane, N.S. McAlpine, A.S. Dzurak, R.G. Clark, G.J. Milburn, He Be Sun, and H. Wiseman, Phys. Rev. **B 61**, 2961 (2000)
12. D. Vion, A. Aassime, A. Cottet, P. Joyez, H. Pothier, C. Urbina, D. Esteve, and M.H. Devoret, Science **296**, 286-280 (2002)
13. Y. Yu, S. Han, Xi Chu, S. Chu and Z. Wang, Science **296,** 889 (2002)
14. J. M. Martinis, S. Nam, J. Aumentado, and C. Urbina, Phys. Rev. Lett. **89**, 117901 (2002)
15. M. T. Tuominen, J. M. Hergenrother, T. S. Tighe, and M. Tinkham, Phys. Rev. Lett. **69**, 1997 (1992).
16. P. Lafarge, P. Joyez, D. Esteve, C. Urbina, and M.H. Devoret, Nature **365**, 422 (1993).
17. K.K. Likharev, "Dynamics of Josephson junctions and Circuits" (Gordon and Breach, New York, 1986).
18. M. Büttiker, Phys. Rev. B **36**, 3548 (1987).
19. V. Bouchiat, D. Vion, P. Joyez, D. Esteve, M. H. Devoret, Phys. Scr. **T76**, 165-170 (1998).
20. W. H. Zurek, Physics Today **44**, 36 (1991); W. H. Zurek and J. P. Paz, in *Coherent atomic matter waves*, edited by R. Kaiser, C. Westbrook and F. David, (Springer-Verlag Heidelberg 2000) [quant-ph/0010011].
21. J. M. Martinis, M. H. Devoret, and J. Clarke, Phys. Rev. B **35**, 4682-4698 (1987); M. H. Devoret, D. Esteve , C. Urbina, J. M. Martinis , A. N. Cleland, and J. Clarke, in *Quantum Tunneling in Condensed Media* edited by Y. Kagan and A.J. Leggett (Elsevier Science Publishers, 1992).
22. Another two-port design has been proposed by A. B. Zorin (cond-mat/0112351; to be published in Physica C)
23. A. Abragam, *The principles of nuclear magnetism* (Oxford University Press, 1961).
24. A. Aassime, G. Johansson, G. Wendin, R. J. Schoelkopf, and P. Delsing, Phys. Rev. Lett. **86**, 3376 (2001).
25. D. V. Averin and K. K. Likharev, in *Mesoscopic Phenomena in Solids*, edited by B. L. Altshuler, P. A. Lee, and R. A. Webb (Elsevier, Amsterdam, 1991).
26. A different Cooper pair box readout scheme using a large Josephson junction is discussed by F. W. J. Hekking, O. Buisson, F. Balestro, and M. G. Vergniory, in *Electronic Correlations: from Meso- to Nanophysics*, T. Martin, G. Montambaux and J. Trân Thanh Vân, eds. (EDPSciences, 2001), p. 515.
27. A. Cottet, D. Vion, A. Aassime, P. Joyez, D. Esteve, M.H Devoret., Physica **C367**, 197 (2002)
28. G. J. Dolan and J. H. Dunsmuir, Physica **B152**, 7 (1988).
29. A. Cottet, A. H. Steinbach, P. Joyez, D. Vion, H. Pothier, D. Esteve, and M. E. Huber, in *Macroscopic quantum coherence and quantum computing*, edited by D. V. Averin, B. Ruggiero, and P. Silvestrini, Kluwer Academic, Plenum publishers, New-York, 2001, p. 111-125.
30. I. I. Rabi, Phys. Rev. 51, 652 (1937).
31. N. F. Ramsey, Phys. Rev. **78**, 695 (1950).

32. In practice, the rotation axis does not need to be $x$, but the rotation angle of the two pulses is always adjusted so as to bring a spin initially along $z$ into a plane perpendicular to $z$.
33. At fixed $\Delta t$, the switching probability displays a decaying oscillation as a function of detuning, the maximum corresponding to zero detuning.
34. H. Wolf, F.-J. Ahlers, J. Niemeyer, H. Scherer, Th. Weimann, A. B. Zorin, V. A. Krupenin, S. V. Lotkhov, D. E. Presnov, IEEE Trans. on Instrum. and Measurement 46, 303 (1997).
35. F. C. Wellstood, C. Urbina, and J. Clarke, Appl. Phys. Lett. **50**, 772-774 (1987).
36. Critical current noise [B. Savo, F. C. Wellstood, and J. Clarke, Appl. Phys. Lett. **50**, 1758-1760 (1987)] seems to be of a lesser concern since none of our results forces us to invoke it.

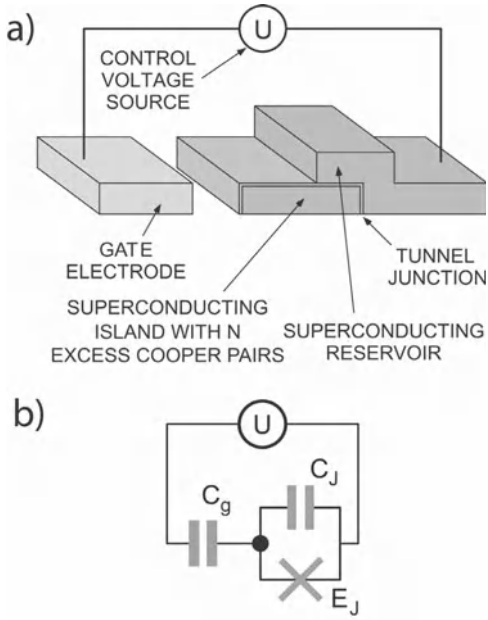


*Figure 1.* a) Schematic representation of single Cooper pair box. b) Equivalent circuit diagram for single Cooper pair box. The capacitances $C_g$ and $C_j$ correspond to the gate and junction, respectively. $E_J$ is the Josephson energy of the tunnel junction.

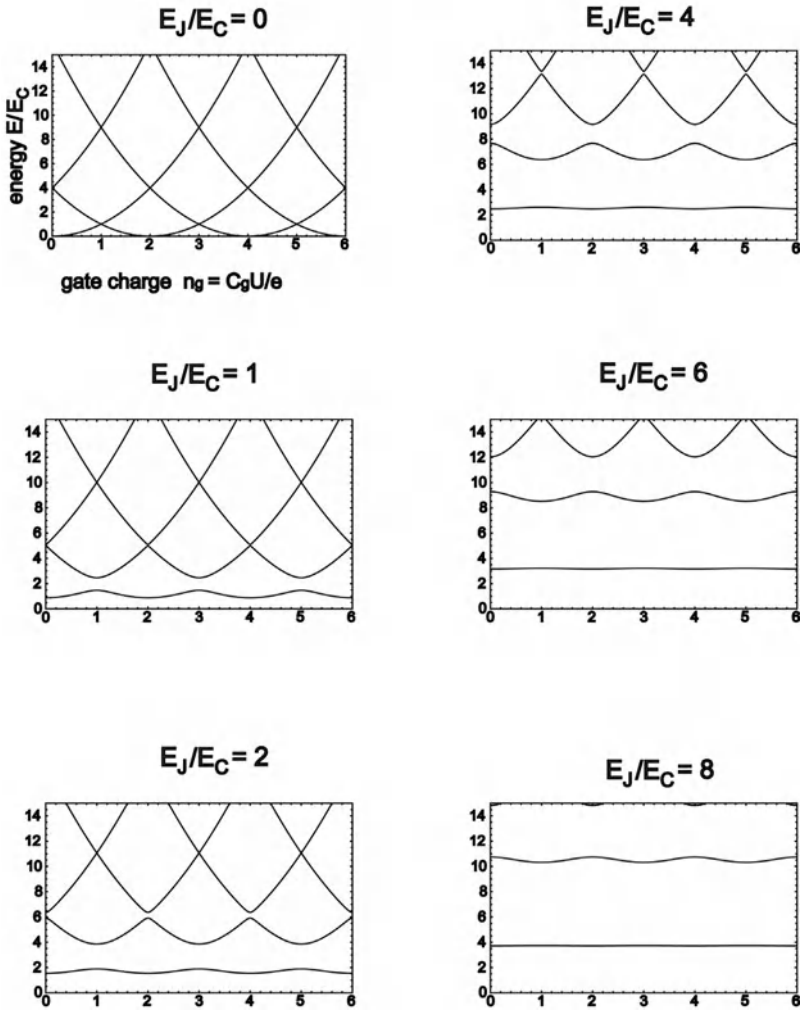


*Figure 2.* Energy spectrum of the single Cooper pair box as a function of the gate charge $n_g = C_g U/e$, for several values of the ratio $E_J/E_C$.

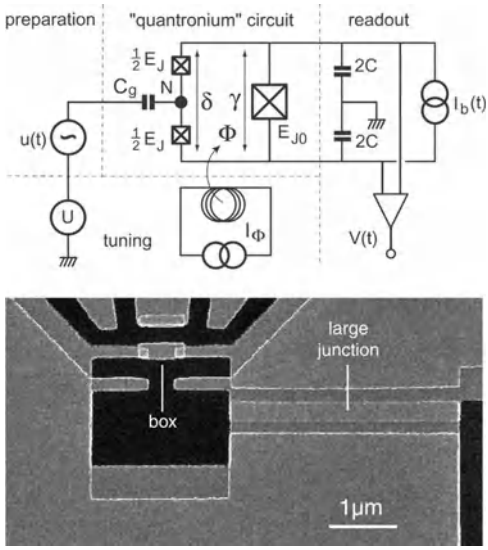


*Figure 3.* schematic diagram of quantum coherent circuit with its tuning, preparation and readout blocks. The coherent circuit, nicknamed "quantronium", consists of a Cooper pair box island (black node) delimited by two small Josephson junctions (cross symbols) in a superconducting loop. The loop also includes a third, much larger Josephson junction shunted by a capacitance $C$. The Josephson energy of the box and the large junction are $E_J$ and $E_{J0}$. The Cooper pair number $N$ and the phases $\delta$ and $\gamma$ are the degrees of freedom of the circuit. A dc voltage $U$ applied to the gate capacitance $C_g$ and a dc current $I_\phi$ applied to a coil producing a flux $\Phi$ in the circuit loop tune the quantum energy levels. Microwave pulses $u(t)$ applied to the gate prepare arbitrary quantum states of the circuit. The states are readout by applying a current pulse $I_b(t)$ to the large junction and by monitoring the voltage $V(t)$. Filters in the microwave and dc lines have not been represented for simplicity. Bottom: scanning electron micrograph of a quantronium sample.

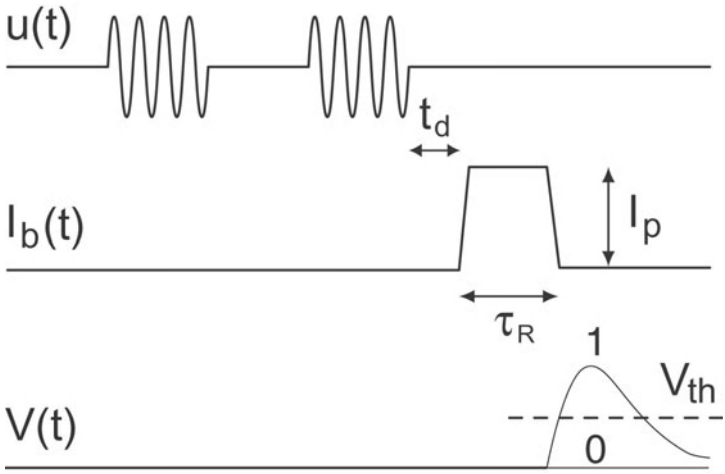


*Figure 4.* Signals involved in quantum state manipulations and measurement of the "quantronium". Top: microwave voltage pulses are applied to the gate for state manipulation. Middle: a readout current pulse $I_b(t)$ with amplitude $I_p$ is applied to the large junction $t_d$ after the last microwave pulse. Bottom: voltage $V(t)$ across the junction. The occurence of a pulse depends on the occupation probabilities of the energy eigenstates. A discriminator with threshold $V_{th}$ converts $V(t)$ into a boolean 0/1 output for statistical analysis.

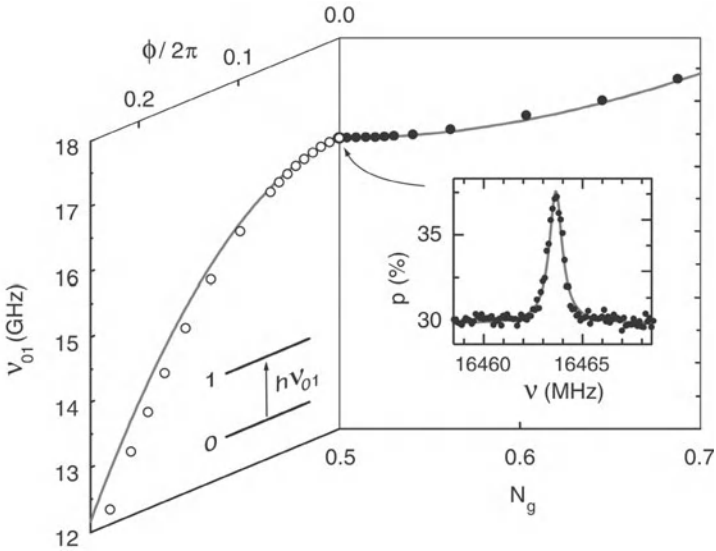


*Figure 5.* Measured center frequency (symbols) of the resonance as a function of reduced gate charge $N_g$ for reduced flux $\phi = 0$ (right panel) and as a function of $\phi$ for $N_g = 0.5$ (left panel), at 15 mK. Spectroscopy is performed by measuring the switching probability $p$ ($10^5$ events) when a continuous microwave irradiation of variable frequency is applied to the gate before readout ($t_d < 100$ ns). Continuous line: theoretical best fit (see text). Inset: minimum width lineshape measured at the optimal working point $\phi = 0$ and $N_g = 0.5$ (dots). Lorentzian fit with a FWHM $\Delta\nu_{01} = 0.8$ MHz and a center frequency $\nu_{01} = 16463.5$ MHz (curve).

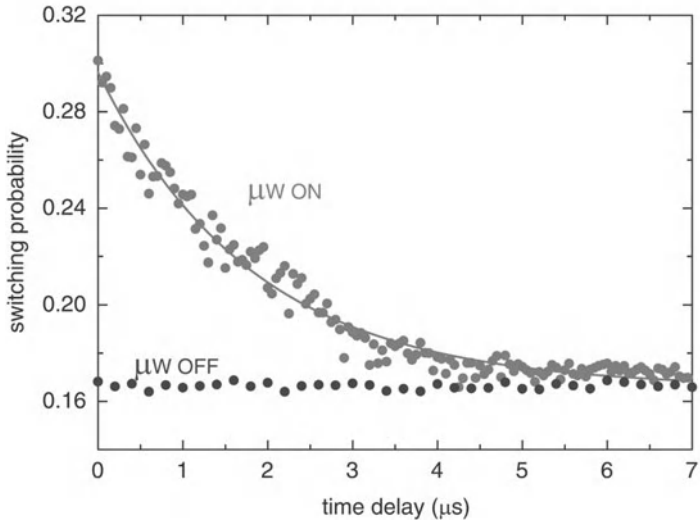


*Figure 6.* Decay of the switching probability as a function of the delay time after a continuous excitation at the center frequency of the line shown in the inset of Fig. 3 (data points labeled "$\mu$W ON"). A control experiment has been performed by doing the same measurement as a function of the delay time, but without excitation (data points labeled "$\mu$W OFF").

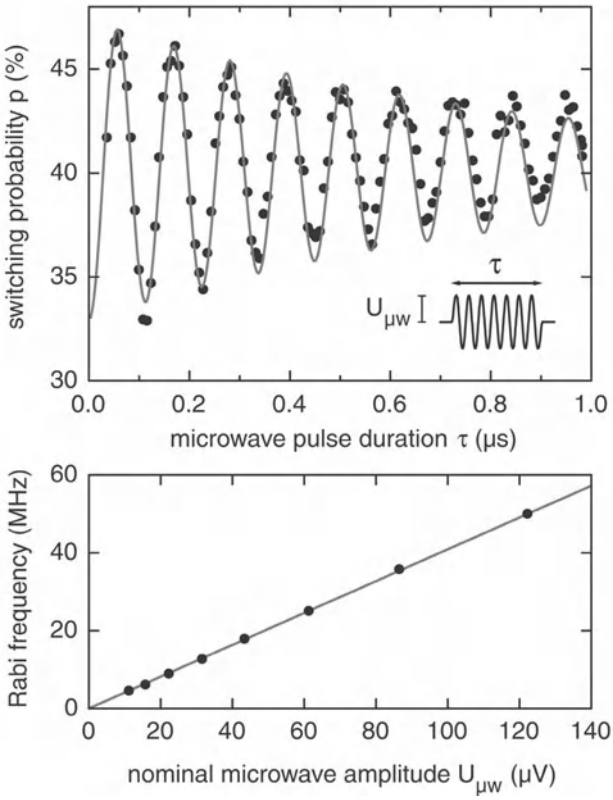


*Figure 7.* Top: Rabi oscillations of the switching probability $p$ ($5 \times 10^4$ events) measured just after a resonant microwave pulse of duration $\tau$. Data taken at 15mK for a nominal pulse amplitude $U_V$ (dots). The Rabi frequency is extracted from an exponentially damped sinusoidal fit (continuous line). Bottom: the measured Rabi frequency (dots) varies linearly with $U_{\mu w}$, as expected.

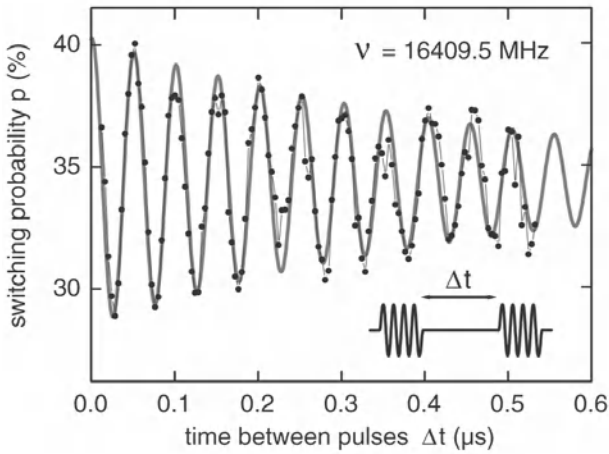


*Figure 8.* Ramsey fringes of the switching probability $p$ ($5 \times 10^4$ events) after two phase coherent microwave pulses separated by $\Delta t$. Dots: data at 15mK; The total acquisition time was 5 mn. Continuous line: fit by exponentially damped sinusoid with time constant $T_\varphi = 500 \pm 50$ ns. The oscillation corresponds to the "beating" of the free evolution of the spin with the external microwave field. Its period indeed coincides with the inverse of the detuning frequency (here $\nu - \nu_{01} = 20.6$ MHz).

# DISSIPATION IN JOSEPHSON QUBITS

Yuriy MAKHLIN[1,2], Gerd SCHÖN[1,3] and Alexander SHNIRMAN[1]
[1]*Institut für Theoretische Festkörperphysik, Universität Karlsruhe, D-76128 Karlsruhe, Germany.* [2]*Landau Institute for Theoretical Physics, Kosygin st. 2, 117940 Moscow, Russia.* [3]*Forschungszentrum Karlsruhe, Institut für Nanotechnologie, D-76021 Karlsruhe, Germany.*

**Abstract.** Josephson-junction systems have been studied as potential realizations of quantum bits. For their operation as qubits it is crucial to maintain quantum phase coherence for long times. Frequently relaxation and dephasing effects are described in the frame of the Bloch equations. Recent experiments demonstrate the importance of $1/f$ noise, or operate at points where the linear coupling to noise sources is suppressed. This requires generalizations and extensions of known methods and results. In this tutorial we present the Hamiltonian for Josephson qubits in a dissipative environment and review the derivation of the Bloch equations as well as systematic generalizations. We discuss $1/f$ noise, nonlinear coupling to the noise source, and effects of strong pulses on the dissipative dynamics. The examples illustrate the renormalization of qubit parameters by the high-frequency noise spectrum as well as non-exponential decay governed by low-frequency modes.

## 1. Introduction

Quantum-state engineering requires coherent manipulations of suitable quantum systems. The needed quantum manipulations can be performed if we have sufficient control over the fields which couple to the quantum degrees of freedom, as well as the interactions. The effects of external noise sources have to be minimized in order to achieve long phase coherence times. In this tutorial we review the requirements for suitable physical realizations of qubits – with emphasis on Josephson circuits – and discuss ways to analyze the dissipative effects.

As has been stressed by DiVincenzo (DiVincenzo, 1997) any physical system, considered as a candidate for quantum computation, should satisfy the following five criteria: (i) One needs well-defined two-state quantum systems (qubits). (ii) One should be able to prepare the initial state of the qubits with sufficient accuracy. (iii) A long phase coherence time is needed, sufficient to allow for a large number (depending on details, say, $\geq 10^4$) of coherent manipulations. (iv) Control over the qubits' Hamiltonian is required to perform the necessary unitary transformations. (v) Finally, a quantum measurement is needed to read out the quantum information.

The listed requirements may be satisfied by a system of spins – or quantum degrees of freedom which under certain conditions effectively reduce to two-state quantum systems – which are governed by a Hamiltonian of the form

$$H = H_{\rm ctrl}(t) + H_{\rm meas}(t) + H_{\rm res}\,. \tag{1}$$



*R. Fazio et al. (eds.), New Directions in Mesoscopic Physics,* 197–224.
© 2003 *Kluwer Academic Publishers. Printed in the Netherlands.*

The first term, $H_{\rm ctrl}(t)$, describes the control fields and interactions,

$$H_{\rm ctrl}(t) = -\frac{1}{2}\sum_{i,a} B_a^i(t)\sigma_a^i + \sum_{i\neq j;a,b} J_{ab}^{ij}(t)\sigma_a^i\sigma_b^j \ . \tag{2}$$

Here $\sigma_a$ (with $a,b = x,y,z$) are Pauli matrices in the basis of states $|\uparrow\rangle = \binom{1}{0}$ and $|\downarrow\rangle = \binom{0}{1}$. Full control of the unitary quantum dynamics of individual spins is achieved if the effective 'magnetic field' $\vec{B}^i(t)$ can be switched arbitrarily at each site $i$. For most purposes control over two of the field components is sufficient, e.g., $H_{\rm ctrl}(t) = -\frac{1}{2}\sum_i \left[B_z^i(t)\sigma_z^i + B_x^i(t)\sigma_x^i\right]$.
In order to perform logic operations, e.g. for quantum computing, one also needs two-qubit operations. They can be controlled if the coupling, $J_{ab}^{ij}(t)$, between the qubits can be switched. Examples for a suitable couplings are an Ising $zz$-coupling or a spin-flip $xy$-coupling (see below).
The measurement device and the residual interactions with the environment are accounted for by extra terms $H_{\rm meas}(t)$ and $H_{\rm res}$, respectively. Ideally the measurement device should be switchable as well and be kept in the off-state during manipulations. The residual interaction $H_{\rm res}$ leads to dephasing and relaxation processes. It has to be weak in order to allow for a series of coherent manipulations.
A typical experiment involves preparation of an initial quantum state, switching the fields $\vec{B}^i(t)$ and coupling energies $J_{ab}^{ij}(t)$ to effect a specified unitary evolution of the wave function, and the measurement of the final state.
The initial state can be prepared by keeping the system at low temperatures in strong enough fields, $B_z^i \gg k_{\rm B}T$, for sufficient time such that the residual interaction, $H_{\rm res}$, relaxes each qubit to its ground state, $|\uparrow\rangle$.
A single-bit operation on a selected qubit $i$ can be performed, e.g., by turning on the field $B_x^i(t)$ for a time span $\tau$. As a result the spin state evolves according to the unitary transformation

$$U_x^i(\alpha) = \exp\left(\frac{iB_x^i\tau\sigma_x^i}{2\hbar}\right) = \begin{pmatrix} \cos\frac{\alpha}{2} & i\sin\frac{\alpha}{2} \\ i\sin\frac{\alpha}{2} & \cos\frac{\alpha}{2} \end{pmatrix} , \tag{3}$$

where $\alpha = B_x^i\tau/\hbar$. By appropriate choice of the parameters an $\alpha = \pi$- or an $\pi/2$-rotation can be induced, producing a spin flip (NOT-operation) or (starting from the ground state $|\uparrow\rangle$) an equal-weight superposition of spin states, respectively. Turning on $B_z^i(t)$ for some time $\tau$ produces another needed single-bit operation, a phase shift between $|\uparrow\rangle$ and $|\downarrow\rangle$, described by $U_z^i(\beta) = \exp\left(iB_z^i\tau\sigma_z^i/2\hbar\right)$ where $\beta = B_z^i\tau/\hbar$. With a sequence of $x$- and $z$-rotations any unitary transformation of the single-qubit state can be achieved.
A two-bit operation on qubits $i$ and $j$ is induced by turning on the corresponding coupling $J_{ab}^{ij}(t)$. For instance, for the $xy$-coupling $J^{ij}(\sigma_x^i\sigma_x^j + \sigma_y^i\sigma_y^j)$ the

result is described, in the basis $|\uparrow_i\uparrow_j\rangle$, $|\uparrow_i\downarrow_j\rangle$, $|\downarrow_i\uparrow_j\rangle$, $|\downarrow_i\downarrow_j\rangle$, by the unitary operator

$$U_{2\mathrm{b}}^{ij}(\gamma) = \begin{pmatrix} 1 & 0 & 0 & 0 \\ 0 & \cos\gamma & i\sin\gamma & 0 \\ 0 & i\sin\gamma & \cos\gamma & 0 \\ 0 & 0 & 0 & 1 \end{pmatrix}, \tag{4}$$

with $\gamma \equiv 2J^{ij}\tau/\hbar$. For $\gamma = \pi/2$ the operation leads to a swap of the states $|\uparrow_i\downarrow_j\rangle$ and $|\downarrow_i\uparrow_j\rangle$ (and multiplication by $i$), while for $\gamma = \pi/4$ it transforms the state $|\uparrow_i\downarrow_j\rangle$ into an entangled state $\frac{1}{\sqrt{2}}(|\uparrow_i\downarrow_j\rangle + i\,|\downarrow_i\uparrow_j\rangle)$.

Instead of the sudden switching of $B_{z,x}^i(t)$ and $J^{ij}(t)$, discussed above for illustration, one can use other techniques to implement single- or two-bit operations. For instance, ac resonance signals can induce Rabi oscillations between different states of a qubit or qubit pairs. Both switching and ac-techniques have been applied for Josephson qubits, e.g. in Refs. (Nakamura et al., 1999) and (Vion et al., 2002; Chiorescu et al., 2003), respectively.

The coupling to the environment, described by $H_{\mathrm{res}}$, leads to dephasing and relaxation processes. In this tutorial we will first derive in Section 2 the proper form of $H_{\mathrm{res}}$ for the case where a Josephson charge qubit is coupled to an electromagnetic environment characterized by an arbitrary impedance. In Section 3 we present a systematic perturbative approach, derive the Bloch equations and discuss their validity range. In particular, we find expressions for the relaxation and dephasing rates. In the following Section 4 we use the Bloch equations to study several problems of interest. Section 5 deals with extensions beyond the Bloch-Redfield description.

## 2. Dissipation in Josephson circuits

### 2.1. Josephson qubits, the Hamiltonian and the dissipation

Fig. 1 shows an example of a 'Josephson charge qubit' built from superconducting tunnel junctions. All Josephson qubits have in common that they are nanometer-size electronic elements embedded into and manipulated by electrical circuits. The electromagnetic environment, which can not be avoided if we want to control the qubit, leads also to dissipation. This environment plays a crucial role in many contexts, e.g., the physics of the Coulomb blockade in tunnel junctions, for which the appropriate theory is reviewed in Ref. (Ingold and Nazarov, 1992). In the spirit of this analysis we will analyze the effects of the environment on Josephson qubits.

We first consider a superconducting single-charge box shown in Fig. 1a in the absence of dissipation. We further choose parameters such that single-electron tunneling is suppressed and only Cooper-pair charges tunnel across the junction. This situation is realized if the superconducting gap $\Delta$ is larger

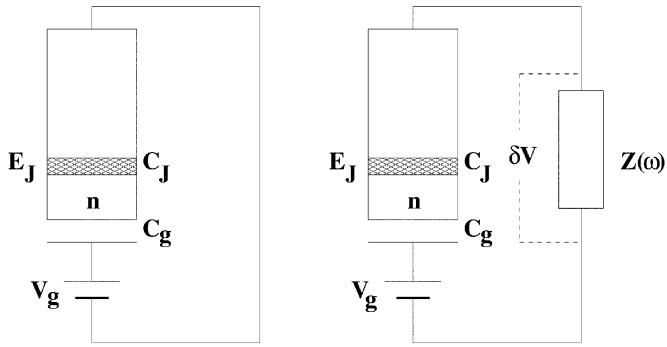


*Figure 1.* a) A Josephson charge qubit in its simplest design formed by a superconducting single-charge box. b) A qubit with the electromagnetic environment represented by the impedance $Z(\omega)$.

than the charging energy scale $E_{\rm C}$ (defined below) and the temperature $k_{\rm B}T$. In this case superconducting charge box is described by the Hamiltonian

$$H_{\rm box} = 4E_{\rm C}\left(n - \frac{Q_{\rm g}}{2e}\right)^2 - E_{\rm J}\cos\theta\,. \tag{5}$$

Here n is the operator counting the number of excess Cooper pairs on the island relative to a neutral reference state. It is conjugate to $\theta$, the phase difference of the superconducting order parameter across the junction. Charge quantization requires that physical quantities are $2\pi$-periodic functions of $\theta$, for instance $e^{i\theta}$, with $e^{i\theta}|n\rangle = |n+1\rangle$. The 'gate charge' $Q_{\rm g} \equiv C_{\rm g}V_{\rm g}$ is controlled by the gate voltage, and $E_{\rm C} \equiv e^2/2(C_{\rm J}+C_{\rm g})$, which depends on the junction and gate capacitances, is the single-electron charging energy scale. Interactions with charges in the substrate induced by stray capacitances, leads to additional contributions to the gate charge.

Next we account for the dissipation due to electromagnetic fluctuations. They can be modeled by an effective impedance $Z(\omega)$, placed in series with the voltage source (see Fig. 1b) and producing a fluctuating voltage. The sum $V_{\rm g} + \delta V(t)$ couples to the charge in the circuit. For an impedance with open leads the Johnson-Nyquist expression relates the voltage fluctuations between its terminals to $Z(\omega)$. In the present case the impedance is embedded in a circuit, which further modifies the spectrum of voltage fluctuations. Neglecting for a moment the Josephson tunneling (i.e., treating the Josephson junction as a capacitor) we obtain from the fluctuation-dissipation theorem (FDT)

$$S_V(\omega) \equiv \frac{1}{2}\int dt\, e^{i\omega t}\langle\{\delta V(t), \delta V(0)\}\rangle = {\rm Re}Z_{\rm t}(\omega)\,\hbar\omega\coth\frac{\hbar\omega}{2k_{\rm B}T}\,. \tag{6}$$

Here $Z_{\rm t}(\omega) \equiv \left[-i\omega C_{\rm t} + Z^{-1}(\omega)\right]^{-1}$ and $C_{\rm t}^{-1} = C_{\rm J}^{-1} + C_{\rm g}^{-1}$ are the total impedance and capacitance as seen from the terminals of $Z(\omega)$, respectively.

For many purposes it is sufficient to characterize the environment by its noise spectrum and the corresponding response function. In general one should take into account that the environment itself is also a quantum system with many degrees of freedom. As argued before (Caldeira and Leggett, 1983), in a generic setting one can think of a linear environment as of a large set of harmonic oscillators, each of which interacts weakly with the system of interest. I.e., $H_{\rm bath} \equiv \sum_a \left[\frac{p_a^2}{2m_a} + \frac{m_a\omega_a^2}{2}x_a^2\right]$, and the qubit is coupled to the fluctuation variable $\delta V = \sum_a \lambda_a x_a$. The Johnson-Nyquist relation (6) is reproduced if one chooses the bath 'spectral density' as $J_V(\omega) \equiv \frac{\pi}{2}\sum_a \frac{\lambda_a^2}{m_a\omega_a}\delta(\omega-\omega_a) = \omega\,{\rm Re}Z_{\rm t}(\omega)$. The Hamiltonian of the whole system then reads[1]

$$H = H_{\rm box} - 2en\frac{C_{\rm t}}{C_{\rm J}}\,\delta V + H_{\rm bath} + \frac{1}{2\tilde{C}_{\rm t}}\left(2en\frac{C_{\rm t}}{C_{\rm J}}\right)^2 . \tag{7}$$

The last 'counter-term' is introduced to cancel the renormalization of the qubit's charging energy by the environment. The capacitance $\tilde{C}_{\rm t}$ is defined by $\int_0^\infty d\omega\, J_V(\omega)/\omega \equiv \pi/(2\tilde{C}_{\rm t})$. Because of the analytic properties of response functions it also equals $\tilde{C}_{\rm t} = C_{\rm t} + \lim_{\omega\to\infty} i/(\omega Z(\omega))$. For a pure resistor $Z(\omega) = R$ it reduces to $C_{\rm t}$. The last three terms in (7) can be lumped as

$$H = H_{\rm box} + \sum_a \left[\frac{p_a^2}{2m_a} + \frac{m_a\omega_a^2}{2}\left(x_a - \frac{\lambda_a}{m_a\omega_a^2}\,2en\frac{C_{\rm t}}{C_{\rm J}}\right)^2\right] .$$

## 2.2. Reduction to a two-level system

If we bias the superconducting charge box near a degeneracy point of the charging energy, e.g. at a voltage close to $e/C_{\rm t}$, and choose all other parameters (temperature, frequency and strength of control pulses) appropriate, only two charge states play a role, $|n=0\rangle$ and $|n=1\rangle$, which we denote as $|\uparrow\rangle$ and $|\downarrow\rangle$, respectively. The leakage to higher charge states can be kept at a low level (Fazio et al., 1999). In spin notation, the number operator becomes $n = \frac{1}{2}(1-\sigma_z)$, while $\cos\theta = \frac{1}{2}\sigma_x$, and the effective spin Hamiltonian reads

$$H = -\frac{1}{2}B_z(V_{\rm g})\,\sigma_z - \frac{1}{2}B_x\,\sigma_x - \frac{1}{2}X\,\sigma_z + H_{\rm bath}\ , \tag{8}$$

where $X = \frac{C_{\rm t}}{C_{\rm J}}\,2e\delta V$ , $B_x = E_{\rm J}$, and

$$B_z = \frac{2e}{C_{\rm J}+C_{\rm g}}(e - C_{\rm g}V_{\rm g}) = 4E_{\rm C}\left(1 - \frac{Q_{\rm g}}{e}\right) . \tag{9}$$

[1] Here we 'postulate' the model based on experience with dissipation in quantum systems. For the reader who is less familiar with these ideas we present in the appendix a more detailed derivation of the Hamiltonian for a particular model of the electromagnetic environment, namely a resistor modeled as a transmission line.

The spectral density of the fluctuating field $X$ is related to the power spectrum of voltage fluctuations by

$$S_X(\omega) = \frac{1}{2}\left(\left\langle X_\omega^2\right\rangle + \left\langle X_{-\omega}^2\right\rangle\right) = \left(2e\,\frac{C_\mathrm{t}}{C_\mathrm{J}}\right)^2 S_V(\omega)\,. \tag{10}$$

Here we defined $\langle X_\omega^2\rangle \equiv \int dt\, e^{i\omega t}\,\langle X(t)X(0)\rangle$. For the calculation of many properties of the two-level system the knowledge of the symmetrized noise correlator, $S_X$, is sufficient. In general, however, the anti-symmetric part $A_X(\omega) \equiv \frac{1}{2}\,\langle[X(t), X(0)]\rangle_\omega$ is needed as well. It is related to the response function of the bath, $X = \chi f$, to a perturbing force, $H_\mathrm{p} = -fX$, given by $\chi(t) = (i/\hbar)\theta(t)\langle[X(t), X(0)]\rangle$. The function $A_X(\omega)$ is related to the imaginary part of the response function, $A_X(\omega) = \hbar\chi''(\omega)$, and in equilibrium the FDT fixes $S_X(\omega) = A_X(\omega)\coth(\hbar\omega/2k_\mathrm{B}T)$.
To simplify the comparison with the literature on the Caldeira-Leggett model we include the prefactor in (10) into the definition of the spectral density, $J_X(\omega) \equiv (2eC_\mathrm{t}/C_\mathrm{J})^2 J_V(\omega) = \chi''(\omega)$. The generic low-frequency behavior is a power-law, $J_X(\omega) = 2\pi\hbar\alpha\omega_0^{1-s}\omega^s$, where $\omega_0$ is a frequency scale and $\alpha$ the dimensionless strength of the dissipation. Of particular interest is the Ohmic case ($s = 1$), obtained if $Z(\omega) = R$ and, hence, $\mathrm{Re}\, Z_\mathrm{t}(\omega) \approx R$, for $\omega \ll (RC_\mathrm{t})^{-1}$. In this case we have $J_X = 2\pi\hbar\alpha\omega$ and

$$S_X(\omega) = 2\pi\hbar\alpha\omega\coth\frac{\hbar\omega}{2k_\mathrm{B}T}\,, \tag{11}$$

with

$$\alpha = \frac{R}{R_\mathrm{Q}}\left(\frac{C_\mathrm{t}}{C_\mathrm{J}}\right)^2\,, \tag{12}$$

and $R_\mathrm{Q} \equiv (2e)^2/h$ is the (superconducting) resistance quantum.

## 3. Dissipative dynamics

### 3.1. Bloch equations

The dissipative dynamics of spins has been the subject of extensive research in the context of the nuclear magnetic resonance (NMR). One of the main tools in this field are the Bloch equations. These kinetic equations were first formulated, on phenomenological grounds, by (Bloch, 1946) for the case of nuclei in a magnetic field $\vec{B} = \vec{B}_\parallel + \delta\vec{B}_\perp(t)$, which is the sum of a strong static field $\vec{B}_\parallel$ in the $z$-direction, and a weak, time-dependent, transverse perturbation $\delta\vec{B}_\perp(t)$. The latter may be chosen to oscillate in resonance with the Larmor frequency $B_\parallel/\hbar$ to induce spin flips. The Bloch equations describe

the dynamics of the magnetization in the 'anisotropic $\tau$-approximation':

$$\frac{d}{dt}\vec{M} = -\vec{B} \times \vec{M} - \frac{1}{T_1}(M_z - M_0)\vec{z} - \frac{1}{T_2}(M_x\vec{x} + M_y\vec{y}) \ . \tag{13}$$

The two relaxation times, $T_1$ and $T_2$, characterize the relaxation of the longitudinal component of the magnetization $M_z$ to $M_0$, which is the equilibrium magnetization in the static field $\vec{B}_{\|}$, and the transverse components ($M_x$, $M_y$) to zero, respectively. Eq. (13) describes the evolution of a two-level system in terms of its 'magnetization' $\vec{M} \propto \langle\vec{\sigma}\rangle$, and at the same time it describes the time evolution of the components of its density matrix, related to the magnetization by $\langle\sigma_z\rangle = \rho_{00} - \rho_{11}$ and $\langle\sigma_x + i\sigma_y\rangle = \rho_{10}$. Here 0 and 1 denote the ground state, $|\uparrow_z\rangle$, and excited state, $|\downarrow_z\rangle$, in the field $B_{\|}$, respectively.
Using the normalization, $\mathrm{tr}\,\hat{\rho} = \rho_{00} + \rho_{11} = 1$, one can rewrite Eq. (13) as equations of motion for the density matrix:

$$\begin{aligned} \dot{\rho}_{00} &= -\Gamma_\uparrow\rho_{00} + \Gamma_\downarrow\rho_{11} \ , \\ \dot{\rho}_{11} &= \Gamma_\uparrow\rho_{00} - \Gamma_\downarrow\rho_{11} \ , \\ \dot{\rho}_{01} &= -iB_{\|}\rho_{01} - \frac{1}{T_2}\rho_{01} \ , \end{aligned} \tag{14}$$

where the excitation rate $\Gamma_\uparrow$ and relaxation rate $\Gamma_\downarrow$ are related to $T_1$ and the equilibrium value $\langle\sigma_z\rangle_0$ by $1/T_1 = \Gamma_\downarrow + \Gamma_\uparrow$ and $\langle\sigma_z\rangle_0 = T_1(\Gamma_\downarrow - \Gamma_\uparrow)$.
A series of papers were devoted to the derivation and generalization of the Bloch equations (Wangsness and Bloch, 1953; Bloch, 1957; Redfield, 1957). Below we will illustrate the derivation from the model (8) in several limits of the qubit's dynamics. We can anticipate two different regimes: The *Hamiltonian-dominated* regime where the dissipative effects are slow compared to the Larmor precession. In this case it is convenient to describe the dynamics in the eigenbasis of the spin's Hamiltonian. The other, *dissipation-dominated* regime, arises, when the total magnetic field is weak. Then the dissipation dominates, and the preferred eigenbasis is that of the dissipative part of the Hamiltonian ($\propto \sigma_z$).

### 3.2. Golden Rule and the Bloch equations

In the eigenbasis of the spin (qubit) the Hamiltonian (8) reads

$$H = -\frac{1}{2}\Delta E\ \sigma_z - \frac{1}{2}X\ (\cos\eta\ \sigma_z - \sin\eta\ \sigma_x) + H_{\mathrm{bath}} \ , \tag{15}$$

where $\Delta E \equiv \sqrt{B_z^2 + B_x^2}$ and $\tan\eta = B_x/B_z$. We denote the ground and excited states of the free qubit by $|0\rangle$ and $|1\rangle$, respectively. The coupling to the bath is a sum of a transverse ($\propto \sin\eta$) and a longitudinal ($\propto \cos\eta$) term. Only the transverse part can cause spin flips. In the weak-noise limit we consider

$X$ as a perturbation and apply Fermi's golden rule to obtain the relaxation rate, $\Gamma_\downarrow = \Gamma_{|1\rangle\to|0\rangle}$, and excitation rate, $\Gamma_\uparrow = \Gamma_{|0\rangle\to|1\rangle}$. E.g., for $\Gamma_\downarrow$ we obtain

$$\begin{aligned}
\Gamma_\downarrow &= \frac{2\pi}{\hbar}\,\frac{\sin^2\eta}{4}\,\sum_{i,f}\rho_i\,|\,\langle i|\,X\,|f\rangle\,|^2\,\delta(E_i+\Delta E-E_f)\\
&= \frac{2\pi}{\hbar}\,\frac{\sin^2\eta}{4}\,\sum_{i,f}\rho_i\;\langle i|\,X\,|f\rangle\,\langle f|\,X\,|i\rangle\;\frac{1}{2\pi\hbar}\int dt\;e^{i\frac{t}{\hbar}\,(E_i+\Delta E-E_f)}\\
&= \frac{\sin^2\eta}{4\hbar^2}\int dt\,\sum_i\rho_i\;\langle i|\,X(t)X\,|i\rangle\;e^{i\frac{t}{\hbar}\,\Delta E}\\
&= \frac{\sin^2\eta}{4\hbar^2}\,\langle X^2_{\omega=\Delta E/\hbar}\rangle\,. \qquad (16)
\end{aligned}$$

Here $|i\rangle$ and $|f\rangle$ are the initial and the final states of the bath and $\rho_i$ is the probabilities for the bath to be initially in the state $|i\rangle$. Similarly, we obtain

$$\Gamma_\uparrow = \frac{\sin^2\eta}{4\hbar^2}\,\langle X^2_{\omega=-\Delta E/\hbar}\rangle\,. \qquad (17)$$

For the relaxation time we thus find

$$\frac{1}{T_1} = \Gamma_\downarrow + \Gamma_\uparrow = \frac{\sin^2\eta}{2\hbar^2}\,S_X(\omega=\Delta E/\hbar)\,, \qquad (18)$$

and for the equilibrium magnetization

$$\langle\sigma_z\rangle_0 = \frac{\Gamma_\downarrow-\Gamma_\uparrow}{\Gamma_\downarrow+\Gamma_\uparrow} = \frac{A_X(\omega=\Delta E/\hbar)}{S_X(\omega=\Delta E/\hbar)} = \tanh\frac{\Delta E}{2k_{\mathrm{B}}T}\,. \qquad (19)$$

The golden rule can also be used to evaluate the dephasing time. Here we skip the derivation since it will be performed in Section 3.5 in the framework of the Bloch-Redfield approximation. The result is

$$T_2^{-1} = \frac{1}{2}T_1^{-1} + \frac{1}{2\hbar^2}\cos^2\eta\,S_X(\omega=0)\,. \qquad (20)$$

Note that the first term $\propto S(\omega=\Delta E/\hbar)$ in Eq. (20) is the result of the transverse noise, which involves transitions between the qubit's states with the energy change of $\Delta E$. The second term $\propto S(\omega=0)$ is associated with the longitudinal noise, which does not flip the spin and therefore involves only transitions in the bath without energy transfer. It produces a random contribution to energy differences, and hence to the accumulated phase difference. This contribution to the dephasing rate is sometimes called the "pure-dephasing" rate, $1/T_2^*$, so that $T_2^{-1} = \frac{1}{2}\,T_1^{-1} + (T_2^*)^{-1}$.

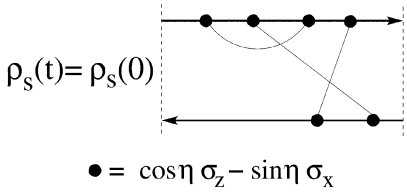


*Figure 2.* Diagrammatic representation of Π.

### 3.3. DIAGRAMMATIC TECHNIQUE

We proceed with a systematic perturbative analysis of the time evolution of the qubit's density matrix based on the Keldysh diagrammatic technique. We derive the Bloch equations and the corresponding dissipative times within the so-called Bloch-Redfield approximation, which may be thought of as a generalized golden rule. The systematic extensions allow us to analyze effects of higher orders in the noise and of long-time noise correlations. We will also determine the limits of applicability of the Bloch equations.

To begin with we briefly sketch the derivation of the master equation for the evolution of the density matrix, based on the formalism developed in Ref. (Schoeller and Schön, 1994). With the interaction Hamiltonian

$$H_{\rm int} = -\frac{1}{2}\, X\, (\cos\eta\, \sigma_z - \sin\eta\, \sigma_x) \tag{21}$$

the time evolution of the density matrix in the interaction representation follows from

$$\rho(t) = T e^{-\frac{i}{\hbar}\int_{t_0}^{t} H_{\rm int}(t')dt'}\, \rho(t_0)\, \tilde{T} e^{\frac{i}{\hbar}\int_{t_0}^{t} H_{\rm int}(t')dt'} . \tag{22}$$

Assuming that initially, at $t = t_0$, the density matrix is factorized, $\hat{\rho}(t_0) = \rho_s(t_0) \otimes \rho_{\rm bath}$, we trace Eq. (22) over the bath degrees of freedom and obtain a perturbative expansion for the propagator $\Pi$ of the spin's density matrix $\rho_{\rm s}(t) = \Pi(t, t_0)\rho_{\rm s}(t_0)$. On one hand, the assumption of a factorized initial condition allows us to introduce the characteristics of the bath, e.g. its temperature. On the other hand, it may introduce transient behavior and even artifacts. In general we find for $\rho_{\rm s}$ a non-Markovian (nonlocal in time) time evolution equation such that the behavior at a time $t$ involves knowledge of $\rho_{\rm s}$ at earlier times. However, the kernel of this integral equation has a limited range $\tau_{\rm c}$ and does not depend on the initial spin state. Thus, the simple assumption about the initial density matrix should be justified if we are interested in the asymptotic time evolution.

By tracing out the bath degrees of freedom in Eq. (22) and expanding in $H_{\rm int}$, one obtains a perturbative series. A typical contribution to $\Pi$ is shown in

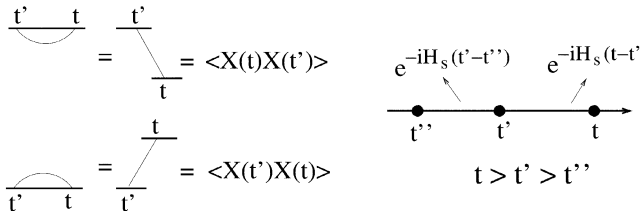


*Figure 3.* Basic elements of the diagrammatic technique.

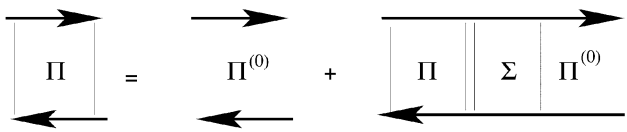


*Figure 4.* The Dyson equation for the propagator $\Pi$.

Fig. 2. The upper line contains vertices (the terms $H_{\rm int}$) from the first, time-ordered exponent in Eq. (22), and the lower one contains vertices from the other, inversely time-ordered exponent. As one can see from Eq. (21), each vertex in the diagrams contains one bath operator $X$. The emerging averages of their products reduce, due to Wick's theorem, in a standard way to pairwise averages, which are shown by the dashed lines in the figure. The horizontal solid lines describe explicitly the evolution of the spin degree of freedom, each line corresponding to (a $2\times 2$ operator) $\exp[\pm iH_{\rm s}(t-t')]$ with different signs for the upper and lower lines.

The propagator $\Pi$ satisfies the Dyson equation shown in Fig. 4. Taking the time derivative one arrives at the master (kinetic) equation

$$\begin{aligned}\frac{d}{dt}\rho_{\rm s}(t) &= \frac{i}{\hbar}\,[\rho_{\rm s}(t), H_{\rm s}] + \int_0^t dt'\;\Sigma(t-t')\;\rho_{\rm s}(t') \\ &= L_{\rm s}\rho_{\rm s}(t) + \int_0^t dt'\;\Sigma(t-t')\;\rho_{\rm s}(t')\;. \end{aligned} \tag{23}$$

We introduced the Liouville operator $L_{\rm s}\rho_{\rm s} \equiv (i/\hbar)\;[\rho_{\rm s}, H_{\rm s}]$. The self-energy $\Sigma$ is defined as the sum of all irreducible diagrams, i.e., diagrams that can not be divided by cutting the upper and lower solid lines at the same time (see an example in Fig. 5). It is an operator in the space of density matrices, i.e., a tensor of rank four. We denote its components by $\Sigma_{nn'\leftarrow mm'}$, implying the following action on density matrices: $(\Sigma\rho_{\rm s})_{nn'} = \sum_{mm'}\Sigma_{nn'\leftarrow mm'}\,(\rho_{\rm s})_{mm'}$.

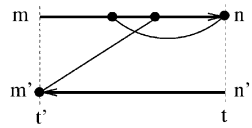


*Figure 5.* A second-order contribution to $\Sigma_{nn' \leftarrow mm'}(t - t')$.

### 3.4. Bloch-Redfield and the rotating-wave approximations

Under certain conditions Eq. (23) may be approximated by a simpler equation which is local in time. Indeed, the self-energy (which in lowest order is proportional to the noise correlator) in the last term on the right hand side decays on time differences $t - t'$ of the order of $\tau_{\rm c}$. If this time is much shorter than the dissipative dephasing and relaxation times we may replace the density matrix in the integral from $t'$ to $t$ by the leading term

$$\rho_{\rm s}(t') \approx e^{-L_{\rm s}(t-t')}\, \rho_{\rm s}(t)\ , \tag{24}$$

and obtain a Markovian evolution equation

$$\frac{d}{dt}\rho_{\rm s}(t) = L_{\rm s}\, \rho_{\rm s}(t) + \hat{\Gamma}\, \rho_{\rm s}(t)\, . \tag{25}$$

It involves the 'Bloch-Redfield tensor'

$$\hat{\Gamma} \equiv \int_{-\infty}^{\infty} dt\, \hat{\Sigma}(t)\, e^{-L_{\rm s}t}\, . \tag{26}$$

To simplify the Fourier analysis here and in the following, the definition of the self-energy is extended to negative times with $\hat{\Sigma}(t < 0) = 0$. In the eigenbasis of $H_{\rm s}$ the Liouvillian $L_{\rm s}$ is diagonal, $[L_{\rm s}]_{mm' \leftarrow mm'} = i(E_m - E_{m'})\hbar$, and the components of the Bloch-Redfield tensor are related to the self-energy: $\Gamma_{nn' \leftarrow mm'} = \Sigma_{nn' \leftarrow mm'}(\hbar\omega = E_m - E_{m'})$.
To verify the validity of the Bloch-Redfield approximation one should check whether the dissipative times $T_1$, $T_2$ in the resulting Bloch equations are indeed much longer than the correlation time $\tau_{\rm c}$ of the integrand in Eq. (26) [more precisely, whether the integral is dominated by times shorter than $T_1$ and $T_2$]. [2]
In certain cases the equations of motion can be simplified further by employing the rotating-wave approximation (RWA). It is based on the following

[2] Note that due to differences in the oscillatory factors different components of the matrix integral in Eq. (26) can be dominated by different time scales. Within the RWA the influence of dissipative terms on the $nn'$-component of the density matrix is dominated by the behavior of the bath spectral power close to $\hbar\omega = E_n - E_{n'}$. One finds that the validity of the Bloch-Redfield approximation requires that the spectrum does not change much on the scale given by the respective component of $\hat{\Gamma}$.

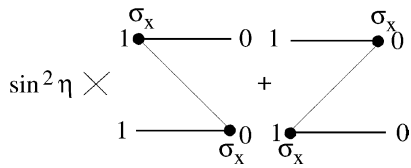


*Figure 6.* Leading order contributions to $\Gamma_{00\leftarrow 11}$.

considerations: if the dissipation is weak and the dynamics of the components of the density matrix close to the unperturbed dynamics, the spectral weight of $\rho_{nn'}(t)$ is located in the vicinity of $\omega = (E_n - E_{n'})/\hbar \equiv \omega^0_{nn'}$. The rhs of the $nn'$-component of the equation of motion (25) contains contributions from all components $mm'$ of the density matrix. However, if $\omega^0_{mm'} \neq \omega^0_{nn'}$ this contribution averages out fast (on the time scale $\hbar/(\omega^0_{mm'} - \omega^0_{nn'})$) and can be neglected. I.e., one truncates the terms $\Gamma_{nn'\leftarrow mm'}\rho_{mm'}$ on the rhs of the equation of motion: for the diagonal elements $\rho_{nn}$ one keeps only the diagonal entries, while for the off-diagonal elements, e.g. $\rho_{01}$, one keeps only the contribution from the same entry, e.g. the component $\Gamma_{01\leftarrow 01}$. The latter are, in general, complex numbers, with a real part describing dephasing and an imaginary part corresponding to a renormalization of the energy.
If the system is subject to a strong pulse, Eq. (25) may not be sufficient. Typically the initial evolution for a certain period of time $\sim \tau_{\rm c}$ needs to be described by other methods. However, the following time evolution is governed by (25). We will discuss examples in Section 5.3. Another situation, where Eq. (25) may be not sufficient is the case where the noise shows long-range correlations (cf. the discussion of the 1/f noise in Section 5.1).

### 3.5. $T_1$ AND $T_2$

As an example and demonstration of the diagrammatic expansion we rederive the expressions for $T_1$ and $T_2$, obtained before by golden rule arguments in Section 3.2. The lowest-order contributions to the rate $\Gamma_{00\leftarrow 11} = \Gamma_\downarrow$ are shown in Fig. 6. We obtain

$$\Sigma_{00\leftarrow 11}(t-t') = \frac{\sin^2\eta}{4\hbar^2}\left[\langle X(t)X(t')\rangle e^{\frac{i}{\hbar}\Delta E(t-t')} + c.c.\right] , \qquad (27)$$

and thus, from Eq. (26) and the fact that $(L_{\rm s})_{11\leftarrow 11} = 0$, we get

$$\begin{aligned}&\Gamma_\downarrow = \Gamma_{00\leftarrow 11} = \Sigma_{00\leftarrow 11}(\omega = 0) = \\ &\mathrm{Re}\left[-\frac{i\sin^2\eta}{2\hbar^2}\int\frac{d\omega'}{2\pi}\,\frac{\langle X^2_{\omega'}\rangle}{\omega' - (\Delta E/\hbar) - i0}\right] = \\ &\frac{\sin^2\eta}{4\hbar^2}\,\langle X^2_{\omega=\Delta E/\hbar}\rangle\,. \end{aligned} \qquad (28)$$

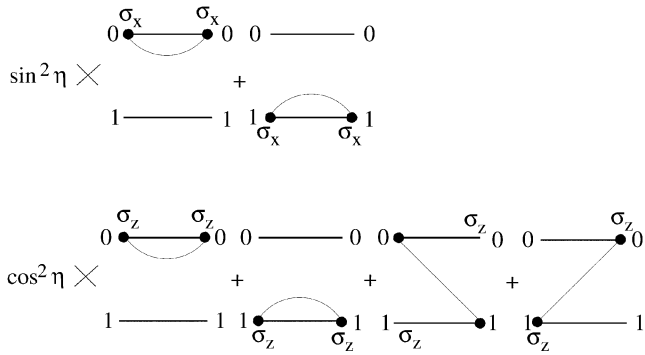


*Figure 7.* Leading order contributions to $\Gamma_{01\leftarrow 01}$.

In the same way one can obtain the excitation rate $\Gamma_{11\leftarrow 00} \equiv \Gamma_{\uparrow}$, and hence $T_1$, as well as the rates $\Gamma_{00\leftarrow 00} = -\Gamma_{11\leftarrow 00}$ and $\Gamma_{11\leftarrow 11} = -\Gamma_{00\leftarrow 11}$.
As for the dephasing time $T_2$, the relevant lowest-order contributions to $\Gamma_{01\leftarrow 01}$ are shown in Fig. 7. The upper row of the diagrams shows the contribution of the transverse fluctuations $\Sigma^{\perp}_{01\leftarrow 01}$ and the lower row shows that of the longitudinal fluctuations $\Sigma^{\parallel}_{01\leftarrow 01}$, so that $\Sigma_{01\leftarrow 01} = \Sigma^{\perp}_{01\leftarrow 01} + \Sigma^{\parallel}_{01\leftarrow 01}$. The transverse and longitudinal contributions give:

$$\Sigma^{\perp}_{01\leftarrow 01}(t-t') = -\frac{\sin^2\eta}{2\hbar^2}\, S(t-t')\,, \tag{29}$$

$$\Sigma^{\parallel}_{01\leftarrow 01}(t-t') = -\frac{\cos^2\eta}{\hbar^2}\, S(t-t')\, e^{\frac{i}{\hbar}\,\Delta E(t-t')}\,. \tag{30}$$

Noting that $(L_{\rm s})_{01\leftarrow 01} = i\Delta E/\hbar$ we obtain from Eq. (26)

$$\Gamma^{\perp}_{01\leftarrow 01} \;=\; \frac{i\sin^2\eta}{2\hbar^2}\int\frac{d\omega}{2\pi}\,\frac{S_X(\omega)}{\omega + (\Delta E/\hbar) - i0}\,, \tag{31}$$

$$\Gamma^{\parallel}_{01\leftarrow 01} \;=\; \frac{i\cos^2\eta}{\hbar^2}\int\frac{d\omega}{2\pi}\,\frac{S_X(\omega)}{\omega - i0}\,, \tag{32}$$

and $\Gamma_{01\leftarrow 01} = \Gamma^{\perp}_{01\leftarrow 01} + \Gamma^{\parallel}_{01\leftarrow 01}$. The real part of these entries of the Redfield tensor, $\mathrm{Re}\,\Gamma_{01\leftarrow 01} = -T_2^{-1}$, reproduces the dephasing rate (20).

### 3.6. Energy renormalization

The analysis of the preceding subsection also shows that the qubit's level splitting is renormalized by the bath. This effect is the analogue of the Lamb shift, i.e. the renormalization of the level splitting in atoms due to the coupling to the electromagnetic radiation. As can be seen from Eq. (25) an imaginary

part of $\Gamma_{01\leftarrow 01}$ gives rise to such a renormalization. Only the transverse noise contributes to this renormalization. From Eq. (31) we obtain

$$\operatorname{Im}\Gamma_{01\to 01} = -\frac{\sin^2\eta}{2\hbar^2}\,\mathrm{P}\int\frac{d\omega}{2\pi}\,\frac{S_X(\omega)}{\omega-(\Delta E/\hbar)}\,. \tag{33}$$

As an example we consider an oscillator bath with Ohmic spectral density up to a high-frequency cut-off, $J(\omega) = 2\pi\alpha\hbar\omega\Theta(\omega_c - \omega)$, at low temperature $k_\mathrm{B}T \ll \Delta E$ where $S(\Delta E) = J(\Delta E)\coth\frac{\Delta E}{2k_\mathrm{B}T} \approx J(\Delta E)$, which is coupled purely transversely, $\eta = \pi/2$. Then the integral in (33) is dominated by high frequencies $\omega > \Delta E$ and gives the following correction to the energy splitting: $\Delta E \to \Delta E(1 - \alpha\ln(\omega_c/\Delta E))$. This result indicates that the small parameter of the perturbative expansion is $\alpha\ln(\omega_c/\Delta E)$, rather than $\alpha$. Also for general bath spectra the high-frequency part of the spectrum typically leads to a renormalized Hamiltonian. The effect can be calculated perturbatively as shown above or in the frame of a renormalization-group approach, which accounts for all orders in the small parameter. It turns out that in such a situation only the component of the field perpendicular to the direction of the fluctuating field is affected by the renormalization (Leggett et al., 1987; Weiss, 1999).

The effect of low-frequency fluctuations can be treated adiabatically: They do not induce transitions between the qubit states, but they change their energy splitting since the fluctuations of the transverse component of the 'magnetic field' $X^\perp$ increase the average magnitude of the field.

Even if the bare Hamiltonian is time-dependent the contribution of the high-frequency modes ($\hbar\omega \gg \Delta E$) of the environment can be absorbed in a renormalization of the Hamiltonian. In contrast, the analysis of the effect of low-frequency modes depends on further details.

## 4. Applications

### 4.1. Ohmic dissipation in real devices

For an Ohmic environment we obtain from Eqs. (18) and (20)

$$T_1^{-1} = \pi\alpha\,\sin^2\eta\,\frac{\Delta E}{\hbar}\coth\frac{\Delta E}{2k_\mathrm{B}T}\,, \tag{34}$$

$$T_2^{-1} = \frac{1}{2}\,T_1^{-1} + \pi\alpha\,\cos^2\eta\,\frac{2k_\mathrm{B}T}{\hbar}\,. \tag{35}$$

For the charge qubit the coupling constant $\alpha$ is given by Eq. (12). The typical impedance of the control line is $R \approx 50\ \Omega$. Since $R_\mathrm{Q} \approx 6.5\ \mathrm{k}\Omega$ we obtain $\alpha \approx 10^{-2}(C_\mathrm{t}/C_\mathrm{J})^2$. With the typical values of the capacitances $C_\mathrm{J} \approx 10^{-16}\mathrm{F}$ and $C_\mathrm{g} \approx 10^{-18}\mathrm{F}$ their ratio can be made as small as

$10^{-2}$. Thus $\alpha$ can be as small as $10^{-6}$. At temperature $T \approx 10$ mK and for $\Delta E/k_{\rm B} \approx 1$ K, we estimate the pure dephasing time $T_2^* \approx 100\ \mu$s (for $\eta = 0$) and the relaxation time $T_1 \approx 1\ \mu$s (for $\eta = \pi/2$). In recent experiments (Vion et al., 2002; Chiorescu et al., 2003) similar values of $T_1$ have been observed, however $T_2$ was much shorter. This has been attributed to the contribution of the $1/f$ noise (i.e. dominated by low-frequencies), which we discuss below.

### 4.2. Validity of the Bloch-Redfield approximation in the Ohmic case

As mentioned above, after having solved the Bloch equations one should verify the validity of the Bloch-Redfield approximation by checking the self-consistency. Let us consider the example of a weakly coupled Ohmic environment, $\alpha \ll 1$. The Bloch-Redfield approximation is justified provided the integral in Eq. (26) converges on a time scale short compared to the appropriate dissipative time $T_1$ or $T_2$.
(i) For the evaluation of $T_1^{-1} \propto S(\Delta E/\hbar)\sin^2\eta$ consistency requires that the noise power in the vicinity of $\omega = \Delta E/\hbar$ varies smoothly on the scale $T_1^{-1}$. For the Ohmic bath this condition is always satisfied: in the limit $\Delta E \gg k_{\rm B}T$ it reduces to $\alpha\Delta E \ll \Delta E$ and in the opposite limit to $\alpha T \ll T$.
(ii) For the evaluation of $T_2^{-1} = \frac{1}{2}T_1^{-1} + (T_2^*)^{-1} \propto \frac{1}{2}S(\Delta E)\sin^2\eta + S(0)\cos^2\eta$ the condition may differ only if the rate is dominated by the second term, $T_2^*$. Then the condition is that the noise power varies weakly on the scale of $(T_2^*)^{-1} \sim \alpha T(k_{\rm B}/\hbar) \ll T(k_{\rm B}/\hbar)$ around zero frequency, which is always true.
We conclude that for $\alpha \ll 1$ the Bloch-Redfield approximation is valid.

### 4.3. Environment-dominated dynamics

Consider a Hamiltonian with purely transverse coupling, $\eta = \pi/2$:

$$H = -\frac{1}{2}\Delta E\ \sigma_z - \frac{1}{2}X\ \sigma_x + H_{\rm bath}\ . \tag{36}$$

For this model the Bloch-Redfield tensor becomes:

$$\frac{d}{dt}\begin{pmatrix}\rho_{00}\\ \rho_{11}\\ \rho_{01}\\ \rho_{10}\end{pmatrix} = \begin{pmatrix}-\Gamma_\uparrow & \Gamma_\downarrow & 0 & 0\\ \Gamma_\uparrow & -\Gamma_\downarrow & 0 & 0\\ 0 & 0 & i\Delta E - \Gamma_\varphi & \Gamma_\varphi^*\\ 0 & 0 & \Gamma_\varphi & -i\Delta E - \Gamma_\varphi^*\end{pmatrix}\begin{pmatrix}\rho_{00}\\ \rho_{11}\\ \rho_{01}\\ \rho_{10}\end{pmatrix}\ . \tag{37}$$

Here $\Gamma_\varphi \equiv -\Gamma_{01\leftarrow 01}$. If the two-level system is almost degenerate, $\Delta E \ll \hbar\Gamma_\varphi$, the RWA is not valid, and one can not neglect the off-diagonal entries (obtained from diagrams similar to those in Fig. 6). Notice that the degeneracy condition, $\Delta E \ll \Gamma_\varphi$, may still be consistent with the validity condition

of the Bloch-Redfield approximation, $1/\tau_{\rm c} \gg \Gamma_\varphi$. For instance, for an Ohmic bath in the weak-coupling limit, $\alpha \ll 1$, one finds $1/\tau_{\rm c} \sim (k_{\rm B}/\hbar)T \gg \alpha(k_{\rm B}/\hbar)T \sim \Gamma_\varphi$ (the latter equality is valid provided $\Delta E \ll k_{\rm B}T$).
In this regime, $\Delta E \ll \hbar\Gamma_\varphi$, Eq. (37) has a very slowly decaying eigenmode, with $\hat\rho \propto \hat\sigma_x$, with the relaxation rate $(\Delta E)^2/2\Gamma_\varphi$ ($\Gamma_\varphi$ is almost real). This phenomenon is called the quantum Zeno effect (Misra and Sudarshan, 1977). The environment "observes" $\sigma_x$ and prevents it from relaxing. The effect has the remarkable property that the stronger the dephasing, $\Gamma_\varphi$, the slower the relaxation.
In general, in the dissipation-dominated regime it is more convenient to treat the spin Hamiltonian as a perturbation on top of the dissipative dynamics.

### 4.4. Time-dependent driving: Rabi oscillations

For a general time-dependent magnetic field $\vec{B}(t)$ the description of the dissipative dynamics is more complicated. Here we discuss an example for which the Bloch-Redfield approximation does not apply in the laboratory frame but can be used in the rotating frame (or, equivalently, in the interaction representation).
Consider a situation with the purely longitudinal coupling,

$$H = -\frac{1}{2}\Delta E\ \sigma_z - \frac{1}{2}X\ \sigma_z + H_{\rm bath}\ , \tag{38}$$

for which Eqs. (18) and (20) give $T_1^{-1} = 0$ and $T_2^{-1} = (1/2\hbar^2)\, S_X(\omega = 0)$. Let us now apply a resonant transverse driving field:

$$H = -\frac{1}{2}\Delta E\ \sigma_z - \frac{1}{2}\Omega_{\rm R}\ (\cos\omega t\, \sigma_x - \sin\omega t\, \sigma_y) - \frac{1}{2}X\ \sigma_z + H_{\rm bath}\,. \tag{39}$$

The subscript R indicates that this field can induce the so-called Rabi oscillations between the levels. As follows from the discussion in Section 3.4, one can still use the Bloch equations as long as the driving is weak enough, $\Omega_{\rm R}\tau_{\rm c} \ll 1$. For a stronger driving these equations may fail. However, the transformation to the rotating frame [$H \to \tilde{H} = \hbar\dot{U}U + UHU^\dagger$, with $U = \exp(-i\omega\sigma_z\, t/2)$ and $\hbar\omega = \Delta E$] makes the Hamiltonian time-independent:

$$H = -\frac{1}{2}\Omega_{\rm R}\ \sigma_x - \frac{1}{2}X\ \sigma_z + H_{\rm bath}\ . \tag{40}$$

The first term on the rhs of Eq. (40) induces coherent oscillations in the rotating frame, with the spin performing an oscillatory motion between the up- and down-states. Furthermore, using Eqs. (18) and (20), we find that the relaxation of the $x$-component of the spin in the rotating frame occurs on the time scale $T_1^{-1} = (1/2\hbar^2)\, S_X(\omega = \Omega_{\rm R})$, and the decay of the transverse ($y$- and $z$-) components on the time scale $T_2^{-1} = 1/(2T_1)$. One may verify that in

the weak-driving limit ($\Omega_{\rm R}\tau_{\rm c} \ll 1$) this result in consistent with the standard Bloch equations in the laboratory frame.
We summarize, strong or fast variations of the Hamiltonian (e.g., the field $\vec{B}(t)$) may invalidate the Bloch equations, but in certain situations one may still reduce the problem to another one for which these equation can be applied. The resulting dissipative times $T_1$, $T_2$ may, however, differ from those in the original Bloch equations.

## 5. Beyond the Bloch-Redfield (golden-rule) approximation

### 5.1. 1/F NOISE

Several experiments with Josephson circuits have revealed at low frequencies the presence of $1/f$ noise. While the origin of this noise may be different in different circuits, it appears that in several cases (especially in the charge devices) it derives from "background charge fluctuations". This noise is usually presented as an effective noise of the gate charge (see Eq.(5)), i.e., $S_{Q_{\rm g}}(\omega) = \alpha_{1/f} e^2/|\omega|$. Recent experiments (cf. (Nakamura et al., 2002) and references therein) yield $\alpha_{1/f} \sim 10^{-7}$–$10^{-6}$. We translate this noise into fluctuations of the effective magnetic field $X$ with

$$S_X(\omega) = \frac{E_{1/f}^2}{|\omega|} \ , \tag{41}$$

and by comparison with Eq. (9) find $E_{1/f} = 4E_{\rm C}\sqrt{\alpha_{1/f}}$.
The Bloch-Redfield result (20) predicts a divergent rate $T_2^{-1} \to \infty$, unless $\eta = \pi/2$, and clearly fails in this case. This can be attributed to the very slow (logarithmic) time decay of the function $S_X(t)$. It is easy, though, to describe the dephasing due to $1/f$ noise rigorously, if it couples purely longitudinally ($\eta = 0$) and is Gaussian distributed. Treating $X$ as a classical variable one obtains (Cottet et al., 2001)

$$\begin{aligned}\langle\sigma_+(t)\rangle &\propto \left\langle e^{-\frac{i}{\hbar}\int_0^t dt'\, X(t')} \right\rangle = e^{-\frac{1}{2\hbar^2}\int_0^t dt' \int_0^t dt'' \langle X(t')X(t'')\rangle} \\ &= \exp\left(-\frac{1}{2\hbar^2}\int \frac{d\omega}{2\pi}\, S_X(\omega)\, \frac{\sin^2(\omega t/2)}{(\omega/2)^2}\right) \ . \end{aligned} \tag{42}$$

This result coincides with the real part of Eq. (55) obtained in a quantum description. For a regular low-frequency spectrum one may replace the last fraction in (42) by $2\pi\delta(\omega)\, t$ and obtain the golden-rule result for the dephasing time. For the $1/f$ noise one obtains with logarithmic accuracy (Cottet

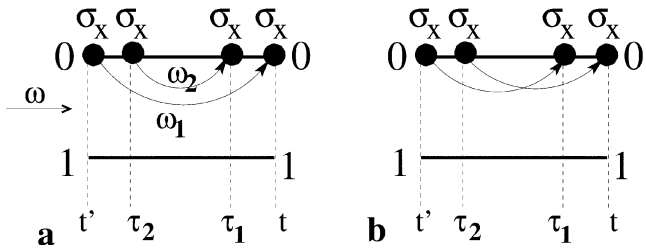


*Figure 8.* Second order contributions. One can obtain all 16 second-order diagrams by shifting an even number of the vertices in **a** or **b** to the lower line.

et al., 2001)

$$\langle \sigma_+(t) \rangle \propto \exp\left( -\frac{E_{1/f}^2}{2\pi\hbar^2}\, t^2 \,|\ln t\omega_{\rm ir}| \right) , \tag{43}$$

where $\omega_{\rm ir}$ is the infrared cutoff frequency for the $1/f$ noise. [3] From this decay law one can deduce the dephasing time scale,

$$\frac{1}{T_2^*} \approx \frac{1}{\hbar}\, E_{1/f} \sqrt{\frac{1}{2\pi} \ln \frac{E_{1/f}}{\omega_{\rm ir}}} \, . \tag{44}$$

Using experimental parameters for an estimate one obtains $T_2$ in the range from fractions to a few nanoseconds, which is close to the dephasing time observed in the experiments away from the special point $\eta = \pi/2$. We also see that this source of dephasing dominates over the Ohmic noise.

### 5.2. Contribution of higher orders

In this section we consider a further situation where the lowest-order Bloch equations are not sufficient. The dissipative times (18, 20) in the Bloch equations are dominated by the noise power at specific frequencies (0 and $\Delta E/\hbar$). As an example, consider the purely transverse case, $\eta = \pi/2$, where the first-order Bloch-Redfield formulas give $T_1^{-1} = 2T_2^{-1} = \frac{1}{2\hbar^2} S_X(\omega = \frac{\Delta E}{\hbar})$. In higher orders of the perturbative expansion (cf. Section 3.3) the noise power in other frequency ranges may be involved. If the noise power in these ranges is much stronger, higher-order contributions may compete with the lowest-order. An important example is the case of $1/f$ noise. Here the strong noise at low frequencies contributes in higher order to the dissipative rates.
To illustrate the importance of higher orders, consider the contribution to the second-order self-energy $\Sigma^{(2)}_{01\leftarrow 01}$ shown in Fig. 8a,

[3] In an experiment with averaging over repetitive measurements the infrared cutoff may be determined by the time interval $t_{\rm av}$ over which the averaging is performed (Vion et al., 2002). In a spin-echo experiment it may be set by the echo frequency (Nakamura et al., 2002).

$$\delta\Sigma^{(2)}_{01\leftarrow 01} = \frac{1}{(2\hbar)^4}\int_{t'}^{t} d\tau_1 \int_{t'}^{\tau_1} d\tau_2 \, \langle X(t)X(t')\rangle \, \langle X(\tau_1)X(\tau_2)\rangle e^{i\Delta E(\tau_1-\tau_2)/\hbar} \, . \tag{45}$$

The factor $e^{\frac{i\Delta E}{\hbar}(\tau_1-\tau_2)}$ is due to the difference in energy of the state on the upper ($|0\rangle$) and lower ($|1\rangle$) lines in the time interval between $\tau_1$ to $\tau_2$. The Fourier transform of Eq. (45) reads

$$\begin{aligned}\delta\Sigma^{(2)}_{01\leftarrow 01}(\omega) = \quad & \frac{-i}{(2\hbar)^4}\int_{-\infty}^{\infty} \frac{d\omega_1 d\omega_2}{(2\pi)^2} \, \langle X^2_{\omega_1}\rangle\langle X^2_{\omega_2}\rangle \\ & \times \frac{1}{(\omega-\omega_1+i0)^2(\omega-\omega_1-\omega_2+\Delta E/\hbar+i0)} \, .\end{aligned} \tag{46}$$

Comparison of Eq. (46) and Fig. 8a elucidates the diagrammatic rules: the bath lines carry the frequencies $\omega_1$ and $\omega_2$, while pairs of horizontal solid lines contribute factors of the type $1/(\omega - \sum \omega_n - i\hat{L}_{\rm s})$, where the summation is over all the bath lines in the interval and the matrix element of $L_{\rm s}$ is determined by the spin states on the upper and lower lines.

There are in total 16 second-order diagrams (see Fig. 8), which contribute to $\Sigma_{01\leftarrow 01}$. They add up to

$$\begin{aligned}\Sigma^{(2)}_{01\leftarrow 01}(\omega) = \quad & \frac{-2i}{(2\hbar)^4}\int_{-\infty}^{\infty} \frac{d\omega_1 d\omega_2}{(2\pi)^2} \left[\frac{1}{\omega-\omega_1+i0} + \frac{1}{\omega-\omega_2+i0}\right] \\ & \times \frac{1}{\omega-\omega_1+i0}\left[\frac{\langle X^2_{\omega_1}\rangle\langle X^2_{\omega_2}\rangle + \langle X^2_{-\omega_1}\rangle\langle X^2_{-\omega_2}\rangle}{\omega-\omega_1-\omega_2+\Delta E/\hbar+i0}\right. \\ & \left. + \frac{\langle X^2_{\omega_1}\rangle\langle X^2_{-\omega_2}\rangle + \langle X^2_{-\omega_1}\rangle\langle X^2_{\omega_2}\rangle}{\omega-\omega_1-\omega_2-\Delta E/\hbar+i0}\right] \, .\end{aligned} \tag{47}$$

We evaluate the behavior of the self-energy in the vicinity of the level splitting, $\Sigma^{(2)}_{01\leftarrow 01}(\omega = -\Delta E/\hbar - \omega' + i0)$, where $\omega' \ll \Delta E/\hbar$. If the integral (47) is dominated by low frequencies, we obtain:

$$\begin{aligned}\mathrm{Re}\,\Sigma^{(2)}_{01\leftarrow 01}\Big(\omega \quad & = -\frac{\Delta E}{\hbar} - \omega' + i0\Big) \\ & \approx -\frac{1}{8\hbar^2\Delta E^2}\int_{-\infty}^{\infty}\frac{d\nu}{2\pi}\left[\langle X^2_{\nu+\omega'}\rangle\langle X^2_{-\nu}\rangle + \langle X^2_{\nu-\omega'}\rangle\langle X^2_{-\nu}\rangle\right] \\ & = -\frac{1}{2\hbar^2}S_{X_2}(\omega') \, ,\end{aligned} \tag{48}$$

where $S_{X_2}$ is the symmetrized correlator of $X_2 \equiv X^2/(2\Delta E)$.

To understand the origin of this result (48) consider the effect of the low-frequency fluctuations (which, we assumed, dominate the dephasing).

Starting from the Hamiltonian (15) with the transverse coupling to the noise source, $\eta = \pi/2$, we see that in the adiabatic limit of very slow fluctuations the dynamics reduces to an accumulation of the relative phase between the eigenstates, $\int dt\, \Delta E_X(t)/\hbar$, where $\Delta E(X) = \sqrt{\Delta E^2 + X^2} \approx \Delta E + X^2/(2\Delta E)$. Thus the problem reduces to the longitudinal case. The calculation above confirms this reduction in the lowest order. More precisely, the second-order contribution to $\Sigma^{(2)}_{01\leftarrow 01}$ for the transversely coupled $X$ coincides with the lowest-order contribution for the longitudinally coupled $X_2$.

Notice also that the fluctuating field $X_2$ has a nonzero average which provides a (low-frequency contribution to the) renormalization of the level splitting (cf. Section 3.6).

Generally speaking, the result (48) does not allow one to evaluate the dephasing decay law but may be used for qualitative estimates. Consider the example of the $1/f$ noise. In this case the low-frequency behavior of the second-order self-energy is singular and it may compete with the first-order contribution. Higher-order contributions require further analysis (both in the linear transverse and quadratic longitudinal cases). However, one can show that at high enough frequencies the higher-order contributions to $\Sigma$ may be neglected. Thus, the result (48) permits an analysis of the decay law at short times. Extrapolating this law to longer times, one can estimate the typical dephasing time. Qualitatively, this amounts to solving the equation $T_2^{-1} \sim -\Sigma^{(2)}_{01\leftarrow 01}(\omega = T_2^{-1})$. For $1/f$ spectrum (41) we obtain

$$S_{X_2}(\omega) \sim \frac{E^4_{1/f}}{(\Delta E)^2}\,\frac{1}{|\omega|}\ln\frac{|\omega|}{\omega_{\rm ir}}\,, \tag{49}$$

i.e., this noise power is again of the $1/f$ type. This gives the estimate $T_2^{-1} \sim (E^2_{1/f}/\hbar\Delta E)\ln(E^2_{1/f}/\hbar\Delta E\omega_{\rm ir})$.

### 5.3. Effect of strong pulses

In this section we discuss the effects of a strong pulse of the magnetic field on the dissipative dynamics of the spin. The derivation of the Bloch equations (cf. the discussion in Section 3.4) relied on the slowness of the spin's dynamics, which may be violated if a strong or a fast-oscillating field is applied. In this case for a period of order $\tau_{\rm c}$ a different description beyond the Bloch-Redfield approximation is needed.

As an example we consider the 'initial-state preparation' of a gedanken experiment designed to observe the effects of dephasing on the spin precession. Specifically, we assume that initially the spin was kept at low temperatures in a field $B_z\hat{z}$ and has relaxed to the ground state $|\uparrow\rangle$. Then it is rotated by a strong short $\pi/2$-pulse of the transverse field and starts a free precession in

the field $B_z\hat{z}$. Under the influence of the bath the relative phase between the spin-up and -down states will not only have a contribution which grows linear in time due to the Zeeman splitting $B_z$ but also a random contribution from the noise, which destroys the phase coherence.

The effect of the pulse on the spin's dynamics, as compared to the Bloch equations, is an additional unitary evolution and dephasing. The former effect is an extra phase acquired by the spin due to the initial polarization of the bath. The latter is the dephasing due to the initial partial disentanglement of the bath and the spin (which amounts to a partial factorization of the initial density matrix).

During the relaxation stage of the spin to the ground state $|\uparrow\rangle$ the oscillators have also relaxed to the corresponding ground state. I.e., the initial state of the whole system is given by the density matrix $\rho_0 = |\uparrow\rangle\langle\uparrow| \otimes \rho_\uparrow$ with $\rho_\uparrow \propto \exp(-H_\uparrow/k_\mathrm{B}T)$ and $H_\uparrow \equiv H_\mathrm{bath} - X/2$. In this state the bath operator $X$ provides a finite average field. Its expectation value $\langle X\rangle$ can be calculated as a linear response of the bath to the perturbation $H_\mathrm{pert} = -fX$ with $f = 1/2$. Thus we obtain $\langle X\rangle = \chi(\omega = 0)f = \chi'(\omega = 0)/2$. For an Ohmic spectrum, $\chi''(\omega) = 2\pi\alpha\hbar\omega$ up to a cutoff $\omega_\mathrm{c}$, we have $\langle X\rangle = \chi'(\omega = 0)/2 = \int(d\nu\,\chi''(\nu))/(2\pi\nu) \sim \alpha\hbar\omega_\mathrm{c}$. We note that this expectation value depends strongly on the high-frequency cutoff $\omega_\mathrm{c}$ of the bath spectrum. The field produced by each bath mode averages out after its typical oscillation period; still during a short initial period of length $\sim \omega^{-1}$ it affects the spin dynamics. Depending on the spectral density of the bath, the resulting effect may be dominated by low or high frequencies.

Now we apply a $\pi/2$-pulse to rotate the spin to a position perpendicular to the original state, i.e. into the superposition $(|\uparrow\rangle+|\downarrow\rangle)/\sqrt{2}$. If the pulse duration is very short, the state of the bath does not change during the pulse. If the pulse takes a finite time, $\omega_p^{-1}$, the bath oscillators partially adjust to the changing spin state. For the high-frequency oscillators, $\omega \gg \omega_p$, the spin evolution during the pulse (and afterwards) is adiabatic; they just 'dress' the spin, renormalizing its parameters (e.g., its $g$-factor (Shnirman et al., 2002)). In contrast, the slow oscillators, with $\omega \ll \omega_p$, do not have time to react on this short time interval and start to change their states only after the pulse. They react differently for the spin-up and spin-down components, thus contributing to the dephasing. Neglecting, for a qualitative discussion, the oscillators at intermediate frequencies, we find the system in the state $\rho_0 = \frac{1}{2}\left|\tilde{\uparrow} + \tilde{\downarrow}\right\rangle\left\langle\tilde{\uparrow} + \tilde{\downarrow}\right| \otimes \tilde{\rho}_\uparrow$. Here the state $\left|\tilde{\uparrow}\right\rangle$ denotes the state of the dressed spin, i.e. the product state of $|\uparrow\rangle$ and the equilibrium states of high frequency oscillators under the influence of the spin up (i.e. with the Hamiltonian $H_\uparrow$), and similarly for the state $\left|\tilde{\downarrow}\right\rangle$. After this initial preparation, the spin starts a precession in the field $B_z\hat{z}$. To describe the time evolution in the presence of the bath we split the

Hamiltonian (8) as

$$H = -\frac{1}{2}B_z\sigma_z - \frac{1}{2}X(\sigma_z - 1) + H_\uparrow \tag{50}$$

and extract explicitly the average $\langle X\rangle$ with the intention to treat the part proportional to $\delta X$ as a perturbation. Hence

$$H = -\frac{1}{2}B_z\sigma_z - \frac{1}{2}\langle X\rangle(\sigma_z - 1) - \frac{1}{2}\delta X(\sigma_z - 1) + H_\uparrow\,. \tag{51}$$

At $t = 0$ the spin is subject to the additional field $\langle X\rangle$. We expect that this field relaxes, on the time scale $\omega^{-1}$ for oscillators with frequency $\omega$. Nevertheless, before the field vanishes, it leaves a trace. Clearly, the Hamiltonian (50) does not couple the spin-up and spin-down states, and the problem can be treated by means of the 'polaron transformation' (see, e.g., (Leggett et al., 1987; Weiss, 1999)). Here we present a different derivation. We calculate the time evolution of the off-diagonal element of the qubit's density matrix:

$$\langle\sigma_+(t)\rangle = e^{-\frac{iB_z t}{\hbar}}\ \mathrm{Tr}\left[\sigma_+\, S(t,0)\rho_0\ S^\dagger(t,0)\right]\ , \tag{52}$$

where

$$S(t,0) \equiv T e^{\frac{i}{\hbar}\int\limits_0^t \frac{\delta X(t')}{2}(\sigma_z - 1)\,dt'}\ . \tag{53}$$

Obviously, the evolution operators $S$ and $S^\dagger$ do not flip the spin, while the operator $\sigma_+$ in Eq. (52) imposes a selection rule such that the spin is in the state $|\downarrow\rangle$ on the forward Keldysh contour (i.e., in $S(t,0)$) and in the state $|\uparrow\rangle$ on the backward contour (i.e., in $S^\dagger(t,0)$). Since $\langle\uparrow|\,\sigma_z - 1\,|\uparrow\rangle = 0$ the contribution of the backward contour vanishes. From $\langle\downarrow|\,\sigma_z - 1\,|\downarrow\rangle = -2$ we obtain $\langle\sigma_+(t)\rangle = P(t)\exp(-iB_z t/\hbar)\langle\sigma_+(0)\rangle$, where

$$P(t) \equiv \langle T\exp\left(-\frac{i}{\hbar}\int\limits_0^t \delta X(t')dt'\right)\rangle\ . \tag{54}$$

Due to the harmonic nature of the bath the equilibrium correlation functions of $\delta X$ for a bath with the Hamiltonian $H_\uparrow$ coincide with those for $X$ and $H_{\mathrm{bath}}$. Using the fact that the fluctuations of $\delta X$ are Gaussian, we arrive at

$$\begin{aligned}\ln P(t) &= -\frac{i}{2\hbar^2}\int\limits_0^t\int\limits_0^t dt_1 dt_2 G^c(t_1 - t_2)\\ &= -\frac{i}{2\hbar^2}\int \frac{d\omega}{2\pi}\,G^c(\omega)\,\frac{\sin^2(\omega t/2)}{(\omega/2)^2}\ .\end{aligned} \tag{55}$$

In equilibrium the Green function $G^c(t-t') = -i\langle T\delta X(t)\delta X(t')\rangle$ is related to the noise by the fluctuation-dissipation theorem:

$$G^c(\omega) = -\hbar\left(\chi'(\omega) + i\chi''(\omega)\coth\frac{\omega}{2T}\right) = -\hbar\chi'(\omega) - iS(\omega)\ . \qquad (56)$$

If we substituted $\sin^2(\omega t/2)/(\omega/2)^2 \ \rightarrow\ 2\pi\delta(\omega)\,t$ in Eq. (55) we would obtain

$$\ln P(t) = -\frac{1}{2\hbar^2}S_X(\omega=0)\ t + \frac{i}{2\hbar}\chi'(\omega=0)\ t\ . \qquad (57)$$

The first term in Eq. (57) yields the usual longitudinal dephasing rate $1/T_2^* = 2\pi\alpha k_{\rm B}T/\hbar$, while the second term exactly cancels the effect of the additional magnetic field $\langle X\rangle$. Thus, the golden-rule approximation predicts that there is no dephasing at $T=0$, and there is no net effect due to the initial preparation. However, the golden-rule substitution described above is justified only if $G^c(\omega)$ has no structure at low frequencies $\omega \sim 1/t$. This condition is violated for not too long times, still small compared to the inverse temperature $\omega_p^{-1} < t < \hbar/k_{\rm B}T$ (cf. e.g., Ref. (Shnirman et al., 2002)). In this time range we find $\mathrm{Re}\ [\ln P(t)] \approx -2\alpha|\ln(\omega_{\rm p}t)|$, which implies a power-law decay

$$|\langle\sigma_+(t)\rangle| = (\omega_{\rm p}t)^{-2\alpha}|\langle\sigma_+(0)\rangle|\ . \qquad (58)$$

Thus even at $T=0$, when $S_X(\omega=0)=0$, the off-diagonal elements of the density matrix decay in time. The reason is the excitation of the low-frequency ($\omega < \omega_p$) modes of the environment by the initial strong pulse, and only the excited modes contribute to the dephasing. From this viewpoint, the effect of the initial pulse is similar to heating.

Finally, the extra phase contribution $\delta\Phi(t) \equiv \mathrm{Im}\ [\ln P(t)] - \langle X\rangle\, t/\hbar$ is

$$\begin{aligned}\delta\Phi &= \frac{1}{2\hbar}\int\frac{d\omega}{2\pi}\,\chi'(\omega)\left[\frac{\sin^2(\omega t/2)}{(\omega/2)^2} - 2\pi\delta(\omega)\,t\right]\\ &= -\frac{1}{\hbar}\int\frac{d\omega}{2\pi}\,\frac{\chi''(\omega)}{\omega^2}\,\sin\omega t\ . \qquad (59)\end{aligned}$$

In deriving Eq. (59) we have used the analyticity of $\chi$ in the upper half-plane. For the Ohmic bath, $\delta\Phi \rightarrow -\pi\alpha$ for $t \gg \omega_{\rm p}^{-1}$. Thus the extra phase is acquired during a short period of time of order $\omega_{\rm p}^{-1}$. This extra phase is the result of an additional magnetic field $\langle X\rangle$ produced by the excited modes in the bath. Note also that the time, over which the extra phase is acquired, may depend on the power spectrum of the noise.

After a period of free precession we assume that a measurement of the final spin state is performed. If we perform a 'low-energy measurement', which does not break the adiabaticity condition for the high-frequency modes, it reads out the state of the dressed spin.

### 5.4. 'OPTIMAL' OPERATION POINTS AND NONLINEAR COUPLING

In the presence of $1/f$ noise, its longitudinal component typically dominates dephasing (see Section 5.1). By adjusting the system control parameters to a point where the longitudinal coupling to the low-frequency noise is tuned to zero one should be able to increase the coherence time. This increase was observed, indeed, in recent experiments (Vion et al., 2002). The qubit in this experiment was subject to several electromagnetic noise sources, including charge and flux noise. When tuned to the optimal operation point the remaining coupling to the noise is linear transverse for one part, $X$, of the noise sources and quadratic longitudinal for the rest, $Y$. In the mentioned experiments $X$ refers to the charge noise, while $Y$ describes flux noise. The resulting Hamiltonian reads

$$H = -\frac{1}{2}\left(\Delta E\,\sigma_z + X\,\sigma_x + Y_2\,\sigma_z\right)\,. \tag{60}$$

Here, analog to the discussion after Eq. (48), we introduced $Y_2 \equiv Y^2/(2E_Y)$. The energy scale $E_Y$, needed since $Y$ has dimensions of energy, characterizes the strength of the quadratic coupling to the noise source $Y$. For the setup of Ref. (Vion et al., 2002) $E_Y$ is of the order of the qubit's Josephson energy.
For noise spectra with much weight at low frequencies, both the transverse linear and the longitudinal quadratic coupling should be treated on an equal footing. As discussed in Section 5.2 for a purely transverse linear coupling to a low frequency noise source it may be necessary to account for higher-order contributions in the calculation of the dissipative rates. In particular, we have seen that the transverse contribution noise $X$ in second-order effectively reduces to a longitudinal coupling to the field $X_2 = X^2/(2\Delta E)$. Thus, both the linear transverse coupling and the quadratic longitudinal coupling in (60) have similar effects on the dephasing. The effective, low frequency Hamiltonian now reads

$$H = -\frac{1}{2}\Delta E\,\sigma_z - \frac{1}{2}(X_2 + Y_2)\,\sigma_z\,. \tag{61}$$

If $X$ and $Y$ are statistically independent, their effects in the framework of the Hamiltonian (61) are independent as well. That is, we can write $\langle\sigma_+(t)\rangle \propto P_{X_2}(t)P_{Y_2}(t)$, where the functions $P_{X_2}$ and $P_{Y_2}$ characterize the dephasing due to the corresponding noise sources. As an example we estimate $P_{X_2}(t)$. The noise power of the variable $X_2$ is given in Eq. (49). Treating $X_2$ as Gaussian distributed we obtain by substituting Eq. (49) in Eq. (42) the decay law (see Table I)

$$P_{X_2}(t)\rangle \approx \exp\left(-\frac{E_{1/f}^4}{\hbar^2\Delta E^2}\,t^2\ln^2(\omega_{\rm ir}t)\right) \tag{62}$$

Table I. The decay law for the off-diagonal (in the qubit's eigenbasis) entries of the qubit's density matrix. The Bloch-Redfield approximation predicts an exponential decay with dephasing time $\propto S^{-1}(\omega = 0)$. Three examples are listed where this time vanishes or diverges and a more careful analysis is required. The sign $\|$ indicates the longitudinal coupling ($\eta = 0$).

| | Bloch-Redfield<br>Sections 3, 4 | $1/f$, $\|$<br>$S(\omega) \propto E_{1/f}^2/\omega$<br>Section 5.1 | $X^2$, $1/f$, $\|$<br>$S_{X_2}(\omega) \propto \ln \frac{\lvert\omega\rvert}{\omega_{\rm ir}}/\omega$<br>Section 5.4 | Ohmic, $\|$<br>$S(\omega) \propto \alpha\omega$<br>Section 5.3 |
|---|---|---|---|---|
| $\rho_{01} \propto$ | $e^{-t/T_2}$ | $e^{-E_{1/f}^2 t^2 \lvert \ln(\omega_{\rm ir} t)\rvert}$ | $e^{-\frac{E_{1/f}^4}{\Delta E^2} t^2 \ln^2(\omega_{\rm ir} t)}$ | $(\omega t)^{-2\alpha}$<br>for $t < \frac{\hbar}{k_{\rm B} T}$ |

and an estimate for the dephasing rate, $1/T_2^* \sim (E_{1/f}^2/\hbar\Delta E)\ln[E_{1/f}^2/\Delta E\omega_{\rm ir}]$. Note, however, that the result (62) is valid at short times only. At longer times the non-Gaussian nature of the fluctuations of $X_2$ becomes important. These, however, are not expected to substantially modify the estimate for the dephasing time scale obtained from an extrapolation of (62). In conclusion, we note that for $\Delta E \gg E_{1/f}$ the dephasing due to $1/f$ noise at the optimal point is substantially reduced as compared to the general case where $X$ is coupled linearly to $\sigma_z$.

## 6. Summary

In this tutorial we have discussed the issue of dissipation in solid-state qubits due to the coupling to the environment. First, the electromagnetic environment of the charge qubit was described and the coupling Hamiltonian was derived, and the relevant Caldeira-Leggett model was introduced. For weak dissipation the description by the Bloch equations is sufficient in many situations. We have presented the calculation of the relaxation and dephasing times, $T_1$ and $T_2$, in the Bloch-Redfield approximation and analyzed their validity range. We have also considered examples where the Bloch-equation description is not sufficient. This includes the effects of the strong pulses and dephasing due to $1/f$ noise. Some of the examples analyzed are illustrated in Table I. It includes situations in which the Bloch-Redfield approximation is insufficient since it would produce vanishing or diverging dephasing rates.

The work is part of the EU IST Project SQUBIT and of the **CFN** (Center for Functional Nanostructures) which is supported by the DFG (German Science Foundation). Y.M. was supported by the Humboldt foundation, the BMBF, and the ZIP Programme of the German government.

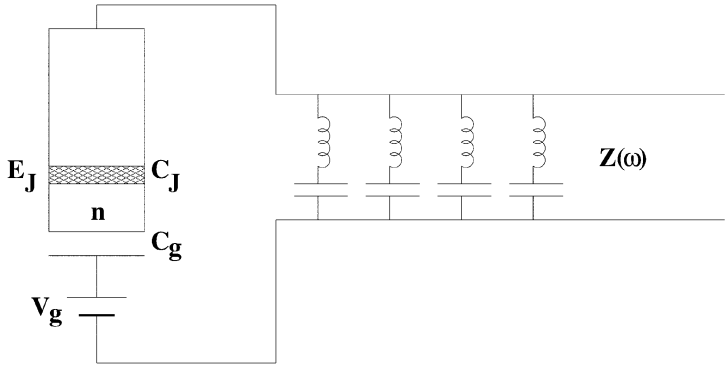


*Figure 9.* The qubit's environment modeled by a transmission line.

## 7. Appendix: derivation of the Hamiltonian

In this section we present a way of introducing the environment following Ref. (Ingold and Nazarov, 1992), in which the bath is modeled by a transmission line. Even if a real device is not coupled to an $LC$-line or a resistor, in generic situations the effect of the fluctuations on the system (qubit) can be *modeled* by an $LC$-line. The transmission line is also equivalent to an oscillator bath model introduced by Caldeira and Leggett. The purpose of the following is to present a particular model which might clarify some ideas behind the Caldeira-Leggett approach. A similar analysis for a slightly different model was presented in Ref. (Paladino et al., 2003).

Consider a transmission line, or $LC$-line, shown in Fig. 9. It amounts to an impedance $Z(\omega)$

$$Z^{-1}(\omega) = \sum_a \left(-i\omega L_a - \frac{1}{i\omega C_a} + 0\right)^{-1} = \sum_a \frac{i\omega}{L_a(\omega^2 - \omega_a^2 + i0\,\mathrm{sign}\,\omega)}\,, \tag{63}$$

with $\omega_a \equiv 1/\sqrt{L_a C_a}$ (index $a$ counts the $LC$ elements of the transmission line). The infinitesimal resistance in each $LC$-element serves to regularize the model. One way to derive the Hamiltonian is to start by introducing the degrees of freedom (the phase drops at circuit elements), writing the Lagrangian of the system (a combination of the charging and Josephson energies), and then performing the Legendre transformation. For convenience instead of the phase variables $\theta_k$ ($k$ being any index) we use the dimensionfull flux variables $\phi_k = \Phi_0\theta_k/2\pi$ (defined as time integrals of respective voltage drops; here $\Phi_0 = h/2e$), to which we still refer as 'phases'. As independent variables one can use the phase on the Josephson junction $\phi_{\mathrm{J}}$, the phase between the terminals of the impedance $\phi$ and the phases on the capacitors of the $LC$ elements of the transmission line $\phi_a$. Then the phases on the inductances of

the $LC$ elements are given by $\phi - \phi_a$, while the phase on the gate capacitor is given by the Kirchhof rule $\phi_{\rm g} = -(\phi_{\rm J} + \phi + \int V_{\rm g} dt')$. The Lagrangian of the system reads

$$L = \frac{C_{\rm J}\,\dot{\phi}_{\rm J}^2}{2} + \frac{C_{\rm g}\,(\dot{\phi}_{\rm J} + \dot{\phi} + V_{\rm g})^2}{2} + E_{\rm J}\cos\left(2\pi\frac{\phi_{\rm J}}{\Phi_0}\right) + L_Z(\phi)\,, \qquad (64)$$

where

$$L_Z(\phi) \equiv \sum_a \left[\frac{C_a\dot{\phi}_a^2}{2} - \frac{(\phi_a - \phi)^2}{2L_a}\right]\,. \qquad (65)$$

From here it is straightforward to derive the Hamiltonian of the system,

$$H = \frac{(2en - q)^2}{2C_{\rm J}} - E_{\rm J}\cos\theta + \frac{(q - C_{\rm g}V_{\rm g})^2}{2C_{\rm g}} + H_Z(\phi)\,, \qquad (66)$$

where

$$H_Z(\phi) \equiv \sum_a \left[\frac{q_a^2}{2C_a} + \frac{(\phi_a - \phi)^2}{2L_a}\right]\,. \qquad (67)$$

Here $(n, \theta)$, $(q, \phi)$, $(q_a, \phi_a)$ are the pairs of conjugate variables, and $q = -C_{\rm g}\dot{\phi}_g$ is the charge on the gate capacitor. We assumed that the charge of the island $2en$ is completely located on the plates of the capacitors $C_{\rm J}$ and $C_{\rm g}$, and neglected the so-called offset charge induced by parasitic voltages due, e.g., to extra charges in the substrate. Introducing the new charge $\tilde{q} \equiv q - C_{\rm t}V_{\rm g}$ we obtain

$$H = \frac{(2en - C_{\rm t}V_{\rm g})^2}{2C_{\rm J}} - E_{\rm J}\cos\theta - \frac{2e}{C_{\rm J}}n\tilde{q} + C_{\rm t}\dot{V}_{\rm g}\phi + \frac{\tilde{q}^2}{2C_{\rm t}} + H_Z(\phi)\,, \quad (68)$$

thus recovering Eq. (7).

Indeed, the degrees of freedom $q_a, \phi_a$ and $q, \phi$ play the part of the oscillator bath, its Hamiltonian being given by the last two terms in Eq. (68) (its eigenmodes are not given explicitly). Further, $\tilde{q}/C_{\rm t} = \delta V$ corresponds to the voltage fluctuations, and the first term in Eq. (68) coincides with the sum of the first and the last terms in Eq. (7). Notice that the last two terms in Eq. (68) describe a parallel connection of the impedance and an effective capacitance $C_{\rm t}$. Accordingly – one can check this also by an explicit calculation – the produced noise is given by Eq. (6), i.e., the bath 'corresponds' to the impedance $Z_{\rm t}$ rather than $Z$.

In this model one can also observe the result of an abrupt change of the gate voltage. It is most easily seen from Eqs. (66, 67) that the gate voltage is coupled to the qubit's degree of freedom $n$ only via the damped mode $(q, \phi)$. As a result, for a pure resistor $Z(\omega) = R$ changes of $V_{\rm g}$ influence the qubit only after a delay time, of order $RC_{\rm t}$. In the form (68) the term proportional to the time derivative of $V_{\rm g}$ is responsible for this delay.

## References

Bloch, F.: 1946, 'Nuclear Induction'. *Phys. Rev.* **70**, 460.

Bloch, F.: 1957, 'Generalized Theory of Relaxation'. *Phys. Rev.* **105**, 1206.

Caldeira, A. O. and A. J. Leggett: 1983, 'Quantum tunnelling in a dissipative system'. *Ann. Phys. (NY)* **149**, 374.

Chiorescu, I., Y. Nakamura, C. J. P. M. Harmans, and J. E. Mooij: 2003, 'Coherent Quantum Dynamics of a Superconducting Flux Qubit'. *Science* **299**, 1869.

Cottet, A., A. Steinbach, P. Joyez, D. Vion, H. Pothier, and M. E. Huber: 2001, 'Superconducting Electrometer for Measuring the Single Cooper Pair Box'. In: D. V. Averin, B. Ruggiero, and P. Silvestrini (eds.): *Macroscopic Quantum Coherence and Quantum Computing*. New York, p. 111, Kluwer Academic/Plenum Publ.

DiVincenzo, D.: 1997, 'Topics in Quantum Computers'. In: L. Kouwenhoven, G. Schön, and L. Sohn (eds.): *Mesoscopic Electron Transport*, Vol. 345 of *NATO ASI Series E: Applied Sciences*. Dordrecht, p. 657, Kluwer Ac. Publ.

Fazio, R., G. M. Palma, and J. Siewert: 1999, 'Fidelity and leakage of Josephson qubits'. *Phys. Rev. Lett.* **83**, 5385.

Ingold, G.-L. and Y. V. Nazarov: 1992, 'Charge Tunneling Rates in Ultrasmall Junctions'. In: H. Grabert and M. H. Devoret (eds.): *Single Charge Tunneling*. N.Y., Plenum Press.

Leggett, A. J., S. Chakravarty, A. T. Dorsey, M. P. A. Fisher, A. Garg, and W. Zwerger: 1987, 'Dynamics of the dissipative two-state system'. *Rev. Mod. Phys.* **59**, 1.

Misra, B. and E. Sudarshan: 1977, 'The Zeno's Paradox in quantum theory'. *J. Math. Phys.* **18**, 756.

Nakamura, Y., Yu. A. Pashkin, and J. S. Tsai: 1999, 'Coherent control of macroscopic quantum states in a single-Cooper-pair box'. *Nature* **398**, 786.

Nakamura, Y., Yu. A. Pashkin, T. Yamamoto, and J. S. Tsai: 2002, 'Charge echo in a Cooper-pair box'. *Phys. Rev. Lett.* **88**, 047901.

Paladino, E., F. Taddei, G. Giaquinta, and G. Falci: 2003, 'Josephson nanocircuit in the presense of linear quantum noise'. *cond-mat/0301363*.

Redfield, A. G.: 1957, 'On the Theory of Relaxation Processes'. *IBM J. Res. Dev.* **1**, 19.

Schoeller, H. and G. Schön: 1994, 'Mesoscopic quantum transport: resonant tunneling in the presence of strong Coulomb interaction'. *Phys. Rev. B* **50**, 18436.

Shnirman, A., Y. Makhlin, and G. Schön: 2002, 'Noise and Decoherence in Quantum Two-Level Systems'. *Physica Scripta* **T102**, 147.

Vion, D., A. Aassime, A. Cottet, P. Joyez, H. Pothier, C. Urbina, D. Esteve, and M. H. Devoret: 2002, 'Manipulating the quantum state of an electrical circuit'. *Science* **296**, 886.

Wangsness, R. K. and F. Bloch: 1953, 'The Dynamical Theory of Nuclear Induction'. *Phys. Rev.* **89**, 728.

Weiss, U.: 1999, *Quantum dissipative systems*. Singapore: World Scientific, 2nd edition.

# Entanglement and decoherence studies in Cavity QED experiments

J.M. Raimond
*Laboratoire Kastler Brossel, Département de Physique, Ecole Normale Supérieure*

**Abstract.** Circular Rydberg atoms and superconducting millimeter-wave cavities make it possible to realize the simplest matter-field system: a single atom interacting with a few photons in a single radiation mode. These experiments can thus be used to test the most intimate features of the quantum world: superposition, measurement and entanglement. They lead also to demonstrations of elementary quantum information processing functions. Finally, mesoscopic fields stored in the cavity can be used to explore experimentally the quantum/classical border and the decoherence phenomenon.

## 1. Introduction

Quantum mechanics describes a microscopic world which is quite at odds with our intuition, forged by our macroscopic environment. One of the most intriguing aspect of the quantum world is the superposition principle, which allows a system to be "suspended" between two different classical realities. The simplest quantum experiment, the Young's slits device, illustrates vividly the weirdness of quantum superpositions. The particle is in a superposition of two different classical paths, corresponding to the two slits. The interference results from the superposition of the two associated probability amplitudes. This situation leads to the important concept of complementarity. In the simple Young's slits experiment, the fringes disappear as soon as an unambiguous information about the path followed by the particle ("which-path information") is recorded, for instance by a detector placed near one slit. The which-path information and the interferences fringes are thus complementary and never appear simultaneously.

Entanglement is another counterintuitive feature of the quantum world. After a non-trivial interaction, two quantum systems are generally in a non-separable state. They are described by a single state vector, which cannot be cast, under any representation, as a tensor product of two separate states pertaining to the two systems. This entails strong correlations between quantum measurements performed on the two systems, irrespective of the physical distance between them. The non-local nature of quantum mechanics, discussed for the first time by Einstein, Podolsky and Rosen (1935), has been vindicated



*R. Fazio et al. (eds.), New Directions in Mesoscopic Physics,* 225–244.
© 2003 *Kluwer Academic Publishers. Printed in the Netherlands.*

since them in many experiments (Aspect et al., 1982; Zeilinger, 1999) observing a violation of the Bell inequalities (Bell, 1964), which should be verified by any local theory.

Superposition and non-locality, ever present in the microscopic world, are, however, never observed at macroscopic scales. There is never, following Schrödinger's (1935) provocative wording, a cat in a quantum superposition of the "dead" and "alive" states. In fact, we observe only a tiny fraction of all possible quantum states for large objects. The emergence of classicality in the quantum world can be understood in terms of decoherence (Zurek, 1991). A large object, such as a cat, is strongly coupled to a complex environment. In all simple relaxation models, some states (the "preferred basis") are relatively stable with respect to relaxation. All other states, quantum superpositions of preferred states, are blured by the coupling to the environment and transformed into mere statistical mixtures. The decoherence time scale decreases when the "distance" between the superposed states increases. It is thus an extremely efficient process for large objects. It plays an essential role in the quantum measurement process, by preventing the macroscopic meters from being finally in a quantum superposition of all possible answers. It is also a terrible obstacle for any application of quantum mechanics superpositions at a large scale.

All these questions have been intensively discussed since the foundation of quantum mechanics. They received recently a renewed interest. The experimental progresses, mainly in the field of quantum optics, make it possible now to experiment with individual quantum systems placed in a carefully controlled environment. We are able to realize some of the gedankenexperiments used by the founding fathers to assess their interpretation of the formalism. We can thus deepen our understanding of basic quantum phenomena.

Beyond this fundamental interest, the weird quantum features could be used to realize new functions for information processing or transmission (Bouwmeester et al., 2000; Nielsen and Chuang, 2000). Quantum information relies on the replacement of the ordinary bits (either zero *or* one) by qubits, quantum two-level systems. They can be in the basis states $|0\rangle$ or $|1\rangle$, but also in any quantum superposition of these "logical" states (zero *and* one at the same time). Superposition, entanglement and non-locality open a whole new realm of possibilities for information processing.

Quantum key distribution schemes for cryptographic systems, for instance, may use EPR correlations between two qubits (Ekert, 1991; Ekert et al., 1992). Measurements performed by two remote observers on these qubits provide them with random but highly correlated data. Any attempt to eavesdrop on this quantum communication channel

involves a quantum measurement performed on one of the particles and an unavoidable perturbation of the quantum correlations, which can be easily detected. The unconditionnally secret common data can then be used as a key in an secure cryptosystem (Vernam code or one-time-pad). Quantum teleportation (Bennett et al., 1993; Bouwmeester et al., 1997) relies on the same EPR correlations to transmit at a distance the unknown quantum state of a qubit.

More ambitiously, quantum computing envisions a computer manipulating entanglement between many qubits (Nielsen and Chuang, 2000). It could thus perform all calculations at the same time, in a quantum superposition of the states corresponding to all possible inputs. Such a machine could be, for some problems, exponentially more efficient than any classical computer. Quantum computers could, for instance, factor easily large numbers (Shor, 1994), with far reaching consequences for classical cryptographic schemes. A possible organization for a quantum computer is quite reminiscent of the one of a classical machine. It involves an array of "quantum gates", elementary entangling machines, performing simple unitary transformations on two qubits. In these gates, the qubits experience a conditional dynamics, controlled by the initial state of both qubits.

These fascinating perspectives have boosted the interest for fundamental quantum physics experiments. There are, however, strong requirements on experimental systems to process complex entangled state. The qubits should be individually addressable, prepared in a well defined state. Their final state must be analyzable. They should be very well isolated from the outside world to minimize the adverse effects of decoherence and, at the same time, strongly coupled together to provide the conditional dynamics of the quantum gates. Up to now, few systems only demonstrated convincing qubit implementations, and even fewer actually achieved entanglement manipulations in quantum gates. Among the latter, let us quote Nuclear Magnetic Resonance based systems (Gershenfeld and Chuang, 1997; Vandersypen et al., 2001), ion traps (Sackett et al., 2000) and cavity quantum electrodynamics (CQED) (Raimond et al., 2001). Let us mention also the impressive recent progresses in the field of mesoscopic circuits. Convincing qubits have been realized recently (Vion et al., 2002) and quantum gates are within reach (see the chapter by M. Devoret in this book).

We describe shortly here the CQED experiments performed at ENS. They realize the simplest matter-field system, with a single atom coupled to a single radiation mode containing a few photons. With circular Rydberg atoms and superconducting cavities, the atom-cavity coupling overwhelms dissipative processes (strong coupling regime of CQED). The system can be used to generate the dynamics of a quantum gate

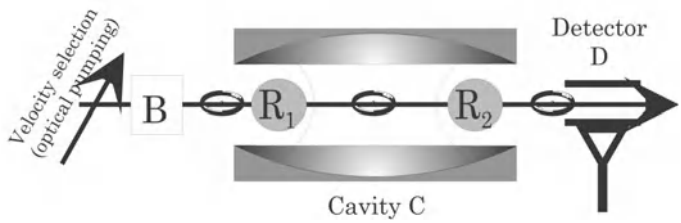


*Figure 1.* General scheme of our cavity QED set-up.

and to tailor complex entangled states. With small coherent semi-classical fields stored in the cavity, they can also be used for an exploration of the quantum-classical boundary and of the decoherence phenomenon.

We start by a brief description of the experimental tools. We switch then to entanglement and quantum information experiments based on resonant atom-field coupling. We discuss finally experiments on complementarity and decoherence at the quantum/classical borderline. The limited size of this chapter does not allow an in-depth description of these topics. Additional information can be found in a variety of review papers (Haroche, 1992; Haroche and Raimond, 1994; Raimond et al., 2001).

## 2. Experimental tools

The general scheme of our experimental set-up is depicted in figure 1. The circular Rydberg atoms, prepared in box $B$, cross the superconducting cavity $C$ before being detected in $D$. We give in the following paragraphs a brief description of the main parts of this set-up.

### 2.1. Atoms

Circular Rydberg atoms are almost ideal tools for matter-field coupling experiments. In an alkali atom (rubidium here), the outer electron is promoted to a level with a very high principal quantum number and maximum orbital and magnetic quantum numbers. In a classical picture, the electron orbit is then the circular Bohr one. We use in our experiments three states. The cavity-resonant transition takes place between $g$ (principal quantum number 50) and $e$ (51). The $e \Leftrightarrow g$ transition is at 51.1 GHz, in the millimeter-wave domain. Another level $i$ (principal quantum number 49) may be used as a reference.

The circular states have very long radiative lifetimes (30 ms for $e$, $g$ or $i$). The millimeter-wave transitions between adjacent circular levels

implement, to an excellent approximation, an ideal two-level system. The dipole matrix element on these transitions is huge, thousands of atomic units, due to the large size of the orbit. The transition frequency can be conveniently tuned through Stark effect. It is thus easy to control, with a good time resolution, the atom-cavity resonance condition. Circular atoms can be detected in a selective and sensitive way by field-ionization. The detection efficiency is of the order of 40%. Moreover, the rapid dependence of the ionizing field with the principal quantum number makes it possible to assess the atomic state at detection time with a 2% error rate only.

The preparation of these states is a complex process, involving up to 53 laser, radiofrequency and microwave photons. In spite of this complexity, it is very selective, preparing either $e$ or $g$ with a 98% purity. The atoms are prepared at a given time, with a velocity selected by laser optical pumping and time-of-flight techniques. The position of the atomic sample at any time during its 20 cm transit through the apparatus is thus known within a millimeter. This is an essential point to allow for a proper addressing of individual atomic samples.

Most experiments require a single atom in each sample. This is simply achieved by preparing much less than one atom on the average. When one atom is detected, the probability for another atom in the same sample escaping detection is quite low. At the expense of very long data taking times for experiments involving many atomic samples, we are thus able to operate with a reasonable approximation of one-atom samples.

Since the Rydberg atoms are utterly sensitive to millimeter-wave fields, they should be carefully protected from the blackbody radiation. The whole atomic path is thus enclosed in a 1K cryostat, also needed for the superconducting cavity operation.

Note that the two-level atomic transition can be conveniently represented by a spin-1/2. Spin pointing up or down on the $Oz$ axis represents an atom in the upper or lower state of the transition. A spin pointing in an arbitrary direction on the "Bloch sphere" represents a quantum superposition of the two states. The field ionization amounts to detecting the atomic spin along the $Oz$ axis. This analogy is extremely useful in the discussion of the following experiments.

### 2.2. Cavity

The superconducting cavity $C$ is a Fabry Perot, realized with spherical niobium mirrors facing each other. A static electric field can thus be applied across the cavity mirrors to stabilize the atomic orbit plane and to tune the transition frequency through Stark effect. The cavity

sustains a gaussian mode, with a 6mm waist. The mode frequency can be tuned close to the atomic resonance by displacing the mirrors. The photon lifetime, $T_r$, is of the order of 1 ms. This is short compared to the 30 ms atomic lifetime, but still much longer than the time necessary to create an atom-cavity entanglement (see below).

The cavity can be prepared initially in the vacuum state $|0\rangle$. Residual thermal fields or photons left over by previous experimental sequences can be conveniently removed by sending through $C$ a train of absorbing atoms, prepared in the lower state of the cavity resonant transition.

A coherent source can be coupled to $C$ through a small hole pierced in one mirror. This allows us to feed in $C$ a coherent semi-classical state $|\alpha\rangle$. This state is defined, as a classical field, by an amplitude $\alpha$ defined in the Fresnel complex plane. The average photon number is $|\alpha|^2$. Quantum fluctuations are superposed to this classical amplitude. Pictorially, these fluctuations can be represented as a small uncertainty disk (with radius unity) at the tip of the classical amplitude. For small average photon numbers (of the order of one), the quantum fluctuations are important both for the field phase and energy. For large fields, the classical amplitude is much greater than quantum fluctuations. The field has then a well-defined energy and phase. The size of such fields can thus be varied from a microscopic to a mesoscopic regime.

### 2.3. Ramsey interferometer

The atoms are prepared initially either in $e$ or $g$. They can be put, before entering $C$, in any coherent superposition of $e$ and $g$ (or $g$ and $i$) by a classical microwave pulse applied in zone $R_1$ (see Fig.1), resonant on the proper atomic transition. In terms of spin-1/2, this pulse performs a tunable rotation of the atomic spin on the Bloch sphere. In terms of quantum information, it performs a one-qubit quantum gate (Nielsen and Chuang, 2000). A similar rotation performed in zone $R_2$ immediately before detection along $Oz$ in $D$ makes it possible to detect the atomic spin along any axis.

In most experiments, $R_1$ and $R_2$ are tuned to perform $\pi/2$ rotations. Their association constitutes then a Ramsey atomic interferometer (Ramsey, 1985). The final atomic transfer probability is modulated with the relative phase $\phi$ of the two pulses. Ramsey fringes obtained on the $g \Leftrightarrow i$ transition are shown on figure 2(a). The 90% contrast gives a good indication of the achieved fidelity for single qubit transformations. These fringes are, of course, extremely sensitive to any modification of the atomic state between $R_1$ and $R_2$. They are thus a convenient tool to reveal the effects of the atom-cavity interaction.

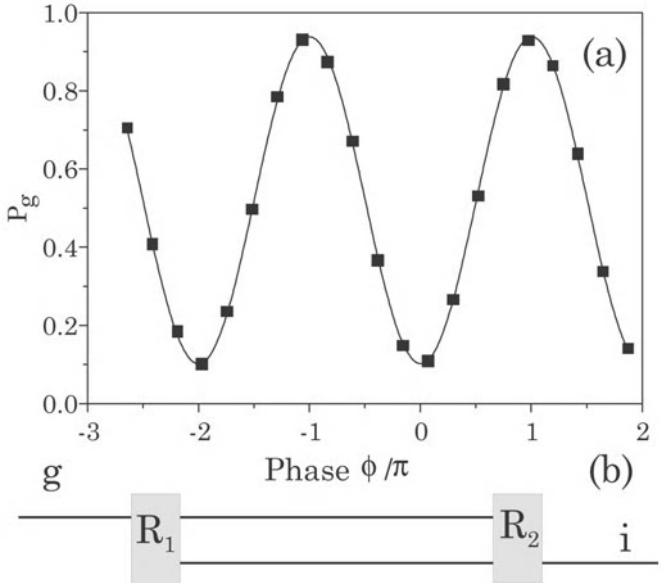


*Figure 2.* Ramsey fringes. (a) signal observed for the $g \Leftrightarrow i$ transition. Probability $P_g$ for detecting the atom in $g$ versus the relative pulse phase $\phi/\pi$. The points are experimental, the line is a sine fit. (b) Diagram depicting the two paths followed by the atom in the Ramsey interferometer.

The Ramsey fringes result in fact from an atomic interference process [see figure 2(b)]. When the atom undergoes a transition from $g$ to $i$, it can emit a photon either in $R_1$ or in $R_2$. Both Ramsey pulses involve a large photon number. The emission of a single photon does not change noticeably these fields. The two paths are thus indistinguishable and quantum interferences result from their superposition. Note the topological analogy between this atomic interferometer and a Mach-Zehnder optical interferometer.

## 3. Resonant atom-cavity entanglement manipulations

Most of our experiments on quantum information and entanglement processing rely on the resonant atom-cavity interaction. Before reviewing briefly our achievements, we give thus a brief account of this important phenomenon.

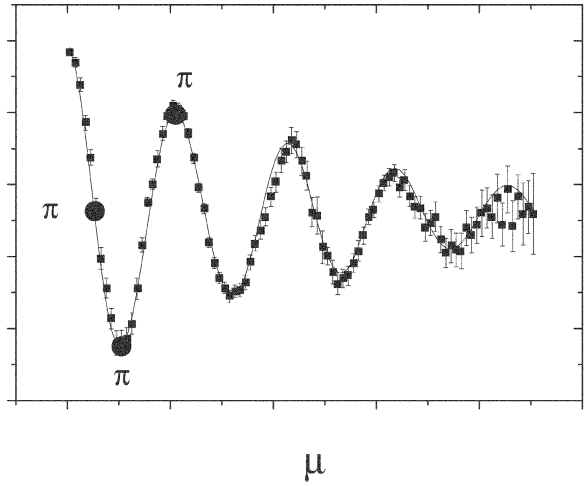


*Figure 3.* Vacuum Rabi oscillations. Plot of the probability for detecting the atom in $e$, $P_e$, as a function of the effective interaction time $t_i$. Three important interaction times (corresponding to the $\pi/2$, $\pi$ and $2\pi$ Rabi rotations) are indicated.

### 3.1. Quantum Rabi oscillation

We consider here the simplest situation. The atom enters the empty cavity in the upper state $e$ of the $e \Leftrightarrow g$ transition, tuned at exact resonance with the cavity mode. The initial state $|e, 0\rangle$ is obviously coupled to $|g, 1\rangle$, representing an atom in the lower state with one photon in the mode. A Rabi oscillation between these two levels should thus take place, at an angular frequency $\Omega$ measuring the strength of the atom-field coupling. In our experiments, $\Omega/2\pi \approx 50$ kHz (Brune et al., 1996b).

In simpler terms, the atom emits a photon in $C$. The trapped photon remains coupled to the atom. It is thus absorbed and then emitted again. In a high finesse cavity, spontaneous emission becomes a reversible, oscillatory process. The experimental "vacuum Rabi oscillations" (Brune et al., 1996b) are plotted on figure 3. It represents the probability $P_e$ for finding the atom in the intial level, $e$, after an effective interaction time $t_i$, as a function of $t_i$. This effective interaction time takes into account the cavity mode gaussian geometry. It is changed by tuning the atomic velocity and by making use of the Stark effect to detune the atoms from the cavity resonance after a preset amount of time. The observation of up to four complete oscillations shows that we reach the strong coupling regime of CQED.

It is interesting to consider in more details the state transformations undergone by the atom-cavity system at peculiar times during this quantum Rabi oscillation (the corresponding times are indicated by dots on figure 3).

After a quarter of a period ("$\pi/2$ quantum Rabi pulse"), the atom-cavity system is in the state $(|e,0\rangle + |g,1\rangle)/\sqrt{2}$, an entangled state of the EPR type. Note that the time needed to prepare this state (about 5 $\mu$s) is much shorter than its lifetime, about 1 ms, limited by cavity damping. The entanglement created by the interaction will thus survive atom-cavity separation in a non-local form.

After half a period ("$\pi$ quantum Rabi pulse"), the atom and the cavity have exchanged their excitation. More generally, this pulse performs the transformation $(c_e|e\rangle + c_g|g\rangle)|0\rangle \mapsto |g\rangle(c_e|1\rangle + c_g|0\rangle)$. It copies the atomic state onto the cavity one (in terms of quantum information, it transfers a qubit from the atom to the cavity). It provides a convenient way to initialize the cavity qubit in an arbitrary state. The transformation can be reversed to read out the cavity state. An atom entering $C$ in $g$ and performing a $\pi$ quantum Rabi pulse carries away the intial cavity state.

Finally, after a complete period ("$2\pi$ quantum Rabi pulse"), the atom and cavity energies return to the initial values. However, the global wavefunction undergoes a $\pi$-phase shift $(|e,0\rangle \mapsto -|e,0\rangle)$, similar to the sign change experienced by a spin-1/2 undergoing a $2\pi$ rotation in real space. The same phase shift applies when the initial state is $|g,1\rangle$. Note, however, that no evolution occurs when the initial state is $|g,0\rangle$ (there is no excitation to be exchanged between the atom and the cavity). This phase shift is thus conditioned to the atom and cavity states, a conditional dynamics reminiscent of a quantum gate.

We combine these three transformations as elementary stitches to knit complex entangled states. In the following paragraphs, we review briefly some of these experiments.

### 3.2. Creation of an atomic EPR pair

In the simplest entanglement manipulation experiment, we prepare an atom pair in an EPR entangled state (Hagley et al., 1997). A first atom, $A_1$, initially prepared in the upper level $e$, interacts with the initially empty cavity for a $\pi/2$ quantum Rabi pulse. It thus gets entangled with $C$. This entanglement cannot be revealed directly, the cavity state being not directly accessible in our experiments. We thus send, through $C$, a second atom, $A_2$, initially prepared in the lower state $g$. Undergoing a $\pi$ quantum Rabi pulse, $A_2$ copies the cavity state and, hence, its entanglement with $A_1$. The two atoms end up in the state $(|e,g\rangle -$

$|g,e\rangle)/\sqrt{2}$, the spin singlet state in terms of the spins 1/2 associated to both atoms. Note that the cavity ends up in its initial vacuum state. It thus plays the role of a catalyst for the two-atoms entanglement.

The atomic entanglement can be checked by verifying the fundamental property of the spin singlet state: whatever the detection axis chosen, the two spins are always found pointing in opposite directions. Two measurements, corresponding to two sets of non-commuting spin observables are necessary to assess entanglement. The energy correlations (when one atom is found in $e$ the other is always found in $g$) alone, for instance, could be understood in classical terms.

We have thus realized two complementary experiments: measurements of the spins along the $Oz$ axis (corresponding to a direct energy detection) and measurements of the spins along two axes in the horizontal plane. We will not describe them in details here. Additional information can be found in other papers (Hagley et al., 1997; Raimond et al., 2001). The results show that we prepare and analyze EPR pairs with a fidelity close to 50%.

Such atomic EPR pairs, prepared with an improved fidelity, could be used for new tests of quantum non-locality and of Bell inequalities violation. Since Rydberg atoms can, in principle, be detected with a high efficiency, it could be possible to close, as in ion traps experiments (Rowe et al., 2001), the "detection efficiency loophole" (not all photon pairs are detected in most Bell inequalities experiments so far), which still leaves a narrow gap for "hidden variable" local models.

### 3.3. A quantum logic gate

The experiment described above cannot be easily extended, since the cavity finally returns to its initial vacuum state. A full-fledged quantum gate is required to prepare more complex entangled states. We have realized a quantum phase gate, based on the resonant $2\pi$ quantum Rabi pulse (Rauschenbeutel et al., 1999). One of the qubits is carried by an atom, with $g$ and $i$ as the two "logical" levels. The other qubit corresponds to the zero and one photon states in the cavity.

When the atom is in $i$, nothing happens during the interaction, since the $i \Leftrightarrow g$ transition is far off-resonance from $C$. When the atom enters in $g$ the empty cavity, no evolution takes place as well since there is no energy to be exchanged. The only evolution occurs when the initial state is $|g,1\rangle$. With an interaction time tuned for a $2\pi$ quantum Rabi pulse, the state evolves into $-|g,1\rangle$.

The atom/cavity state undergoes a global phase shift only when both systems are in their upper energy state. This conditional dynamics is the one of a "quantum phase gate". Note that combining quantum

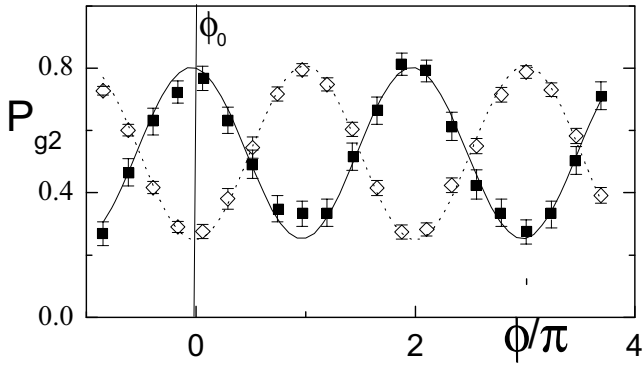


*Figure 4.* Test of the quantum phase gate. Probability $P_{g_2}$ for detecting atom $A_2$ in state $g$ versus the phase $\phi$ of the Ramsey interferometer (units of $\pi$). Open diamonds: empty cavity. Solid squares: cavity containing one photon. The error bars reflect the statistical variance. The lines are sine fits. For phase $\phi_0 = 0$, indicated by a vertical line, the atomic state is directly correlated to the photon number.

phase gates with single qubit gates (Ramsey pulses in our case) makes it possible, in principle, to realize any quantum logic operation.

In order to check the coherent operation of this gate, we have performed two complementary experiments (Rauschenbeutel et al., 1999). In the first, we check that a single photon stored in $C$ phase-shifts by $\pi$ a $g/i$ atomic coherence, according to $|1\rangle(|i\rangle+|g\rangle)/\sqrt{2} \mapsto |1\rangle(|i\rangle-|g\rangle)/\sqrt{2}$.

The single-photon state is created in $C$ by a first atom, $A_1$, initially in $e$, performing a $\pi$ quantum Rabi pulse. A second atom, $A_2$, is prepared in a $g/i$ superposition by a first Ramsey pulse $R_1$. It interacts with $C$ for a $2\pi$ quantum Rabi pulse. The final atomic coherence is analyzed by a second Ramsey pulse $R_2$. Due to the phase shift experienced by the atomic coherence, the Ramsey fringes obtained for an empty cavity (no atom $A_1$ sent) and with one photon in $C$ are expected to be in phase opposition.

The observation of this phase shift (see figure 4) clearly exhibits the single-photon sensitivity of our atomic interferometer. In another experiment, we detected the complementary $\pi$-phase shift produced on a superposition of zero- and one-photon states by an atom in $g$. These two experiments together prove the coherent operation of the quantum gate.

Note that, for the interferometer phase $\phi_0$ depicted by a vertical line in figure 4, the atomic state is, ideally, correlated to the presence of a photon in $C$: $i$ when $C$ is empty and $g$ when $C$ contains one photon. The

atom thus realizes a measurement of the cavity field intensity. Contrary to most photo-detections, the photon is still in $C$ after its measurement by the atom. This detection is thus an absorption-free or Quantum Non Demolition (QND) measurement of a single photon (Nogues et al., 1999), which opens interesting perspectives for fundamental quantum measurement studies.

### 3.4. Controlled entanglement of three quantum systems

The most complex entanglement manipulation realized so far with this set-up is the creation of a three-qubit entangled state (Rauschenbeutel et al., 2000). This experiment is a natural extension of the EPR pair creation. A first atom, $A_1$, prepared in $e$, gets entangled with the intially empty cavity through a $\pi/2$ quantum Rabi pulse. A second atom $A_2$, initially prepared in a superposition of $g$ and $i$, performs then a quantum phase gate operation with the cavity field. It thus gets entangled with $C$, and, hence, with $A_1$ too. The resulting $A_1 - A_2 - C$ state can be written, with proper spin-1/2 conventions, $(|+_1, +_2, +_C\rangle - |-_1, -_2, -_C\rangle)/\sqrt{2}$. This is a maximally entangled state, considered for the first time by Greenberger, Horne and Zeilinger (1990) (GHZ) in the context of new tests of quantum non locality.

As in the EPR pair case, two complementary experiments corresponding to detections of the spins along perpendicular axes, are necessary to estimate the entanglement fidelity. A third atom, $A_3$, copies the cavity state. Ramsey pulses are then applied on the three atoms before detection to access the required detection directions. We will not describe in details here these experiments. Their detailed analysis (Rauschenbeutel et al., 2000; Raimond et al., 2001) shows that we prepare the GHZ state with a 54% fidelity. This value is incompatible with any classical explanation for the observed correlations.

Altogether, state preparation and detection imply up to six operations (three one-qubit and three two-qubit gates) on four systems (three atoms and the cavity). It is the most complex quantum entanglement manipulation so far performed on individually addressed quantum systems. This entanglement scheme could, in principle, be extended to an arbitrary number of atoms performing successive quantum phase gate operations with $C$. The limited individual gate fidelity and the acquisition time growing exponentially with the atom number preclude, however, a direct extension of this experiment with the present set-up.

## 4. Exploring the microscopic/ macroscopic boundary

The experiments discussed so far rely on the manipulation of zero- and one-photon states in $C$. The cavity is also well suited for the manipulation of coherent semi-classical fields. When the photon number is close to one, such a field is a quantum obect with important quantum flucuations, whereas it turns into an almost classical field with negligible quantum fluctuations for mesoscopic photon numbers (of the order of ten). This allows an experimental exploration of the fuzzy boundary between the classical and quantum worlds. We describe in this section two such experiments: a direct illustration of the complementarity concept (Bertet et al., 2001) and the realization of a laboratory version of the "Schrödinger cat" experiment (Brune et al., 1996a).

### 4.1. An experiment on complementarity

In a quantum interference process, resulting from the superposition of two probability amplitudes corresponding to two paths from the initial to the final state, the observation of interferences is incompatible with any unambiguous information about the path followed by the system. This is a simple application of the complementarity concept, discussed by Bohr since the early days of quantum theory.

In one of his famous Solvay discussions with Einstein, Bohr illustrated this situation with a Young's slit device (Bohr, 1983). One of the slits is mobile. When the interfering particle passes through it, the slit receives a momentum kick which changes its motional state. When the slit is very massive (usual case), the kick is negligible. The interferometer stores no which-path information, and interference fringes are observed. On the contrary, when the slit is a microscopic object, its motional state is appreciably changed when the particle crosses it and the interferometer stores an unambiguous which-path information. The fringes should thus disappear. Intermediate situations, with a partial which-path information and fringes with a reduced contrast can be envisioned in the case of a mesoscopic slit. This thought-experiment illustrates one of Bohr's requirement: a *bona fide* measurement device or interferometer should be a macroscopic object.

The vanishing fringes contrast for a microscopic slit can be understood in terms of entanglement. When the slit is microscopic, it gets entangled with the particle path. Tracing out the slit's variables reduces the particle state to a statistical mixture of the two different paths and the fringes disappear. Entanglement of the interfering particle, either with the interferometer itself, with an external which-path detector, or even with the environment (decoherence) reduces fringes visibility.

The Bohr proposal is obviously quite unrealistic. We have realized a very similar experiment using a Ramsey interferometer device (Bertet et al., 2001). The two interfering paths correspond to an atom emitting a photon either in the first or in the second pulse. In ordinary Ramsey set-ups, the fields are macroscopic and a single photon emission does not change appreciably the field state. No which-path information is stored in the Ramsey zones and fringes are routinely observed.

In this experiment, the atom, initially in $e$, undergoes two Ramsey pulses on the $e \Leftrightarrow g$ transition. The first is produced by a small coherent field $|\alpha\rangle$ stored in $C$. The interaction time is tuned, according to the field amplitude, to achieve a $\pi/2$ pulse. Note that this condition can be fulfilled even when the cavity is empty, thanks to the quantum Rabi oscillation phenomenon. The second pulse is an ordinary one, performed outside $C$.

When the photon number in $C$ is small, the resonant atom-field interaction changes the cavity state. After $C$ and before $R_2$, the atom-cavity system is in state $(|e, \alpha_e\rangle + |g, \alpha_g\rangle)/\sqrt{2}$. Note that the cavity state may be changed even when the atom exits $C$ it in $e$. Getting finally the atom in $e$ is incompatible with the photon numbers which would produce and exact $\pi$-pulse on the atomic transition. The atom thus carries away a partial information on the cavity field, even when no emission takes place. The atom and the cavity are thus entangled, at least partially. The final fringes contrast is $|\langle\alpha_e|\alpha_g\rangle|$. When the field is large, both final cavity states, $|\alpha_e\rangle$ and $|\alpha_g\rangle$, are close to the initial one and the contrast is maximal. When the cavity is initially empty, $|\alpha_e\rangle = |0\rangle$ and $|\alpha_g\rangle = |1\rangle$, two orthogonal states. The atom is fully entangled with $C$ and the fringes contrast vanishes. The initial average photon number $n = |\alpha|^2$ in $C$ thus plays the role of the slit's mass in Bohr's proposal.

The experimental results are shown as dots on figure 5 as a function of $n$. For large photon numbers, the contrast saturates at 72%, limited by the experimental imperfections. When $n$ decreases, the contrast decreases also and finally cancels when the cavity is initially empty. The solid line presents the results of the simple model outlined above, with no adjustable parameter but an overall contrast reduction factor. The agreement with the data is quite good, providing a vivid illustration of the complementarity concept in a situation quite close to the initial Bohr's proposal.

### 4.2. A laboratory version of the "Schrödinger cat"

In the preceding experiment, the which-path detector is part of the interferometer itself. Another interesting situation arises when a which-

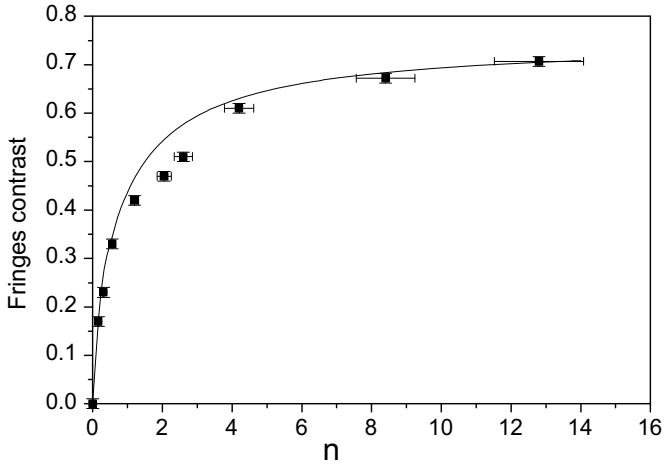


*Figure 5.* Contrast of the Ramsey interferometer versus the average photon number $n$ in $C$. The dots are experimental and the line is a theoretical fit.

path detector external to the interferometer is used. In this experiment (Brune et al., 1996a), we use a standard Ramsey interferometer on the $e \Leftrightarrow g$ transition, with two classical Ramsey pulses $R_1$ and $R_2$. The cavity $C$, containing a small coherent field $|\alpha\rangle$, is used between $R_1$ and $R_2$ as a which-path detector.

The cavity field should act as a measurement device for the atomic state. We use thus a non-resonant interaction. Atom and cavity cannot exchange energy. The non-resonant atom is equivalent to a piece of transparent dielectric for the cavity field. It changes the effective cavity length and its resonant frequency. Due to the strong atom-cavity coupling, the cavity frequency changes by more than the mode's spectral width. This transient frequency change results finally in a modification of the classical phase of the cavity field. For an atom in $e$, the phase change, $\Phi$, can be easily adjusted to small or large values by changing the atom-cavity detuning $\delta$ ($\Phi$ is proportional to $1/\delta$). An atom in $g$ produces an opposite phase shift, $-\Phi$. The cavity field acts thus as a meter's needle evolving in the Fresnel plane of complex amplitudes, pointing finally towards different directions for $e$ and $g$.

The atom-cavity state after the interaction is thus $(|e, \alpha \exp i\Phi\rangle + |g, \alpha \exp -i\Phi\rangle)/\sqrt{2}$ [we omit here phase factors which are not relevant for the following qualitative discussion (Maître et al., 1997)]. When the phase shift $\Phi$ is much greater than the phase quantum fluctuations in $|\alpha\rangle$ (small detuning), the atom is fully entangled with $C$. The Ramsey fringes contrast thus vanishes. On the contrary, when $\Phi$ is much

smaller than the quantum phase fluctuations (large detunings), the two final cavity states overlap and no which-path information is acquired. Contrasted Ramsey interferences are then observed. The only effect of $C$ is then a phase shift of the Ramsey fringes pattern, resulting from the light shifts experienced by the atomic transition in the cavity field. The measurement of this phase shift provides a convenient and precise calibration of the average photon number in $C$ (Brune et al., 1994). We have observed this other manifestation of complementarity and checked that the contrast of the fringes varies as expected with $\Phi$ (Brune et al., 1996a).

It is quite interesting to consider the cavity state at the end of this interference experiment. Since $R_2$ erases all information about the atomic state during cavity crossing, the atomic detection projects $C$ onto a superposition of the states corresponding to an atom in $e$ or $g$ : $(|\alpha \exp i\Phi\rangle + |\alpha \exp -i\Phi\rangle)/N$, where $N$ is a proper normalization factor. This state is a quantum superposition of two mesoscopic fields differing trough a classical parameter, the phase. It is obviously an highly non-classical state, having the two phases "at the same time" in a quantum superposition, a close analog of the famous Schrödinger cat (Schrödinger, 1935).

The decoherence process, due to cavity relaxation, is bound to transform rapidly this superposition into a mere statistical mixture of two coherent fields with different phases (either one phase or the other). Since we are dealing here with mesoscopic photon numbers and since $C$ is well isolated from the outside world, the decoherence dynamics is slow enough to be resolved. In order to monitor the decoherence process , we send a probe in $C$ (a quantum "mouse"). A quantum interference process involving the cavity field itself then provides an information about the nature of the cavity state (quantum superposition or statistical mixture).

The "mouse" is a second atom crossing the cavity a delay $\tau$ after the first one, which prepared the cat. We extract, from the detection of the two atoms, a correlation signal $\eta$. It is non-zero (ideally 0.5) when the cavity field is in a quantum superposition. It is zero if the cavity field has been reduced to a statistical mixture.

Figure 6 presents the results of the measurement of $\eta$ as a function of $\tau$, expressed in units of the cavity damping time $T_r$ (Brune et al., 1996a). The initial cavity field contains 3.3 photons. Two atom-field detunings $\delta$ are used, corresponding to phase configurations pictorially shown in the insets (the lines represent the classical amplitude, the disks represent the quantum fluctuations).

At short times, the correlation signal is non-valishing, showing that the field state left by the first atom is an highly non-classical "cat"

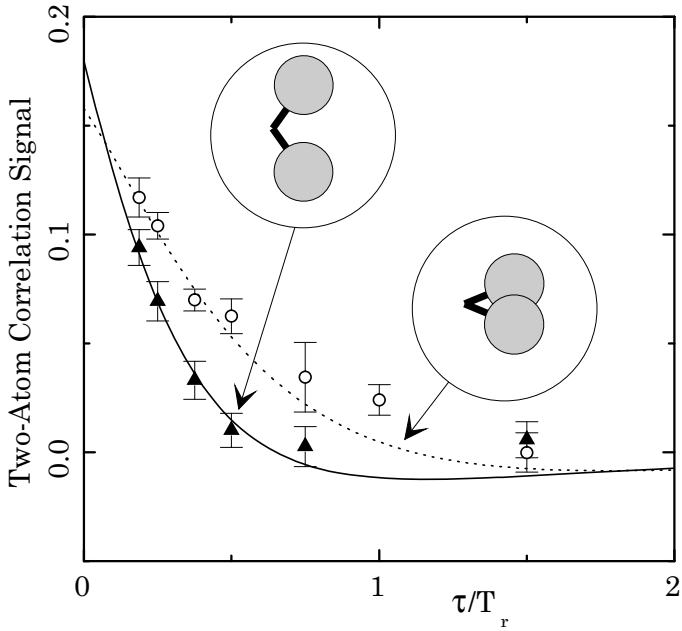


*Figure 6.* Decoherence experiment. Correlation signal $\eta$ plotted versus the delay between the two atoms, $\tau$, in units of the cavity damping time $T_r$. The initial coherent field contains 3.3 photons on the average. Experimental results for two different values of the field components separation are shown here (circles and triangles). The phase shifts, corresponding to $\delta/2\pi = 170$ and 70 kHz respectively, are depicted in the insets. The curves result from a simple analytical model.

state. The quantum superposition disappears rapidly versus $\tau$. This reduction to a statistical mixture is faster than the cavity damping time (unit of time on figure 6) and gets faster and faster when the distance between the two superposed states increases.

This experiment reveals an essential aspect of the decoherence process. Its time scale is much faster than the natural relaxation time scale. The more distant the superposed states, the faster the decoherence process. Decoherence is thus a non-trivial relaxation mechanism, whose peculiar features are due to the mesoscopic nature of the states under consideration. Note that, in spite of being non-trivial, decoherence in this simple situation is well described by quantum relaxation theory (Maître et al., 1997). The solid lines in figure 6 correspond to the predictions of a simple model (Raimond et al., 1997). They are in quite good agreement with the experimental data.

This experiment, which reveals the progressive decoherence of the field acting as a meter measuring the first atom's state, provides an

exploration of an essential process in quantum measurement. It also clearly exhibits the extreme efficiency of the decoherence process, which precludes any quantum superposition from entering the macroscopic world.

## 5. Conclusion

Circular Rydberg atoms and superconducting millimeter-wave cavities are excellent tools to explore fundamental quantum features. They make it possible to test elementary quantum logics functions and to manipulate complex entangled states, up to three systems. They are also well adapted to the exploration of the boundary between microscopic and macrosopic worlds.

Some experimental improvements, in progress, could lead to the realization of even more complex experiments. Cavities with a larger photon holding time, a better detection efficiency and a much better control of the atomic external degrees of freedom, based on laser cooling techniques, could make it possible to manipulate entangled states with a larger number of qubits. Elementary quantum algorithms could be implemented. It should be possible also to test simple quantum error correction codes (Steane, 1996), making it possible to counteract up to some extent the effects of decoherence.

With better cavities, precise quantitative tests of the decoherence models would be accessible, using cats involving a few tens of photons. A probe atom could be used to measure directly the complete Wigner function of the relaxing Schrödinger cat (Bertet et al., 2002). The determination of this quasi-probability distribution in phase space would provide a very stringent test of our understanding of the decoherence phenomenon. We are also envisioning an experiment with two microwave cavities. A single atom crossing the two cavities containing coherent fields could prepare an unprecedented quantum state: a nonlocal cat, or, in other words, an EPR pair involving mesoscopic objects instead of spins 1/2 (Davidovich et al., 1993). The study of this state's decoherence would be a severe test of our understanding of this basic quantum phenomenon.

## References

Aspect, A., J. Dalibard, and G. Roger: 1982, 'Experimental test of Bell's inequalities using time-varying analysers'. *Phys. Rev. Lett.* **49**(25), 1804.

Bell, J. S.: 1964, 'On the Einstein Podolsky Rosen paradox'. *Phys. (N.Y.)* **1**(3), 195.

Bennett, C. H., G. Brassard, C. Crépeau, R. Jozsa, A. Peres, and W. K. Wootters: 1993, 'Teleporting an unknown quantum state via dual classical and Einstein-Podolsky-Rosen channels'. *Phys. Rev. Lett.* **70**(13), 1895.

Bertet, P., A. Auffeves, P. Maioli, S. Osnaghi, T. Meunier, M. Brune, J.-M. Raimond, and S. Haroche: 2002, 'Direct Measurement of the Wigner function of a one-photon Fock state in a Cavity'. *Phys. Rev. Lett.* **89**, 200402.

Bertet, P., S. Osnaghi, A. Rauschenbeutel, G. Nogues, A. Auffeves, M. Brune, J.-M. Raimond, and S. Haroche: 2001, 'A complementarity experiment with an interferometer at the quantum-classical boundary'. *Nature (London)* **411**, 166.

Bohr, N.: 1983. In: *Quantum Theory and Measurement.* Princeton, p. 9, Princeton University Press.

Bouwmeester, D., A. Ekert, and A. Zeilinger: 2000, *The physics of quantum information.* Berlin: Springer.

Bouwmeester, D., J.-W. Pan, K. Mattle, M. Eibl, H. Weinfurter, and A. Zeilinger: 1997, 'Experimental quantum teleportation'. *Nature (London)* **390**, 575.

Brune, M., E. Hagley, J. Dreyer, X. Maître, A. Maali, C. Wunderlich, J.-M. Raimond, and S. Haroche: 1996a, 'Observing the progressive decoherence of the meter in a quantum measurement'. *Phys. Rev. Lett.* **77**, 4887.

Brune, M., P. Nussenzveig, F. Schmidt-Kaler, F. Bernardot, A. Maali, J.-M. Raimond, and S. Haroche: 1994, 'From Lamb Shifts to Light Shifts: Vacuum and Subphoton Cavity fields Measured by Atomic Phase Sensitive Detection'. *Phys. Rev. Lett.* **72**, 3339.

Brune, M., F. Schmidt-Kaler, A. Maali, J. Dreyer, E. Hagley, J.-M. Raimond, and S. Haroche: 1996b, 'Quantum Rabi Oscillation: a Direct Test of Field Quantization in a Cavity'. *Phys. Rev. Lett.* **76**, 1800.

Davidovich, L., A. Maali, M. Brune, J.-M. Raimond, and S. Haroche: 1993, 'Quantum Switches and Non-Local Microwave Fields'. *Phys. Rev. Lett* **71**, 2360.

Einstein, A., B. Podolsky, and N. Rosen: 1935, 'Can quantum mechanical description of physical reality be considered complete?'. *Phys. Rev.* **47**, 777.

Ekert, A.: 1991, 'Quantum Cryptography Based on Bell's Theorem'. *Phys. Rev. Lett.* **67**, 661.

Ekert, A., J. Rarity, P. Tapster, and G. Palma: 1992, 'Practical Quantum Cryptography Based on Two-Photon Interferometry'. *Phys. Rev. Lett.* **69**, 1293.

Gershenfeld, N. A. and I. L. Chuang: 1997, 'Bulk spin-resonance quantum computation'. *Science* **275**, 350.

Greenberger, D. M., M. Horne, and A. Zeilinger: 1990, 'Bell's theorem without inequalities'. *Am. J. Phys.* **58**, 1131.

Hagley, E., X. Maître, G. Nogues, C. Wunderlich, M. Brune, J.-M. Raimond, and S. Haroche: 1997, 'Generation of Einstein-Podolsky-Rosen pairs of atoms'. *Phys. Rev. Lett.* **79**, 1.

Haroche, S.: 1992, 'Cavity Quantum Electrodynamics'. In: J. Dalibard, J.-M. Raimond, and J. Zinn-Justin (eds.): *Fundamental Systems in Quantum Optics, Les Houches Summer School, Session LIII.* Amsterdam: North Holland, p. 767.

Haroche, S. and J.-M. Raimond: 1994, 'Manipulation of Non-Classical Field States in a Cavity by Atom Interferometry'. In: P. Berman (ed.): *Advances in Atomic and Molecular Physics, supplement 2.* New York: Academic Press, p. 123.

Maître, X., E. Hagley, J. Dreyer, A. Maali, C. Wunderlich, M. Brune, J.-M. Raimond, and S. Haroche: 1997, 'An experimental study of a Schrödinger's cat decoherence with atoms and cavities'. *J. Mod. Opt.* **44**, 2023.

Nielsen, M. and I. Chuang: 2000, *Quantum computation and quantum information.* Cambridge: Cambridge University Press.

Nogues, G., A. Rauschenbeutel, S. Osnaghi, M. Brune, J.-M. Raimond, and S. Haroche: 1999, 'Seeing a single photon without destroying it'. *Nature (London)* **400**, 239.

Raimond, J.-M., M. Brune, and S. Haroche: 1997, 'Reversible decoherence of a mesoscopic superposition of field states'. *Phys. Rev. Lett.* **79**, 1964.

Raimond, J.-M., M. Brune, and S. Haroche: 2001, 'Manipulating quantum entanglement with atoms and photons in a cavity'. *Rev. Mod. Phys.* **73**, 565.

Ramsey, N. F.: 1985, *Molecular beams*, International series of monographs on physics. Oxford.

Rauschenbeutel, A., G. Nogues, S. Osnaghi, P. Bertet, M. Brune, J.-M. Raimond, and S. Haroche: 1999, 'Coherent operation of a tunable quantum phase gate in cavity QED'. *Phys. Rev. Lett.* **83**, 5166.

Rauschenbeutel, A., G. Nogues, S. Osnaghi, P. Bertet, M. Brune, J.-M. Raimond, and S. Haroche: 2000, 'Step-by-step engineered multiparticle entanglement'. *Science* **288**, 2024.

Rowe, M. A., D. Kielpinski, V. Meyer, C. A. Sackett, W. M. Itano, C. Monroe, and D. J. Wineland: 2001, 'Experimental violation of a Bell's inequality with efficient detection'. *Nature (London)* **409**(6822), 791.

Sackett, C. A., D. Kielpinski, B. E. King, C. Langer, V. Meyer, C. J. Myatt, M. Rowe, Q. A. Turchette, W. M. Itano, D. J. Wineland, and C. Monroe: 2000, 'Experimental entanglement of four particles'. *Nature (London)* **404**, 256.

Schrödinger, E.: 1935, 'Die Gegenwärtige Situation in der Quantenmechanik'. *Naturwissenschaften* **23**, 807, 823, 844.

Shor, P. W.: 1994. In: *Proceedings of the 35$^{th}$ Annual Symposium on the Foundations of Computer Science*. New York, p. 124, IEEE Comput. Soc. Press.

Steane, A.: 1996, 'Error correcting codes in quantum theory'. *Phys. Rev. Lett.* **77**, 793.

Vandersypen, L., M. Steffen, G. Breyta, C. Yannoni, M. Sherwood, and I. Chuang: 2001, 'Experimental realization of Shor's quantum factoring algorithm using nuclear magnetic resonance'. *Nature (London)* **414**, 883.

Vion, D., A. Aassime, A. Cottet, P. Joyez, H. Pothier, C. Urbina, D. Esteve, and M. Devoret: 2002, 'Manipulating the quantum state of an electrical circuit'. *Science* **296**, 886.

Zeilinger, A.: 1999, 'Experiment and the foundations of quantum physics'. *Rev. Mod. Phys.* **71**, S288.

Zurek, W. H.: 1991, 'Decoherence and the transition from quantum to classical'. *Phys. Today* **44**(10), 36.

# QUANTUM ELECTRO-MECHANICAL SYSTEMS

Recipe to make a mechanical device interfere with itself

KEITH SCHWAB
Laboratory for Physical Sciences
8050 Greenmead Drive
College Park, MD 20740 USA

## 1. Introduction

A dominant theme of modern physics is to show that quantum mechanics is a valid description of the world, from atomic lengths scales and upward. This pursuit is aimed at both answering questions about the apparent boundary between the classical and quantum world, and at exploiting quantum behavior for technological purpose. As a result of the intense effort in quantum computing, nano-electronic devices have entered this realm and shown themselves to be fully quantum mechanical. Single electron devices and SQUIDs have recently exhibited quantized energy levels, Schrodinger evolution, and superposition states (Nakamura et al., 1999; Friedman et al., 2000; Vion et al., 2002).

Despite all of this progress, behavior in mechanical devices remain essentially classical. Only recently has there been a hint of the quantum nature of a mechanical device measured through energy transport on a suspended microstructure (Schwab et al., 2000; Schwab et al., 2001), and in the electronic transport through molecular systems (Park et al., 2000).

Although the simple harmonic oscillator is an elementary system which we teach to all of our undergraduate students, it still receives attention from the precision measurement and gravitational wave research communities as it is often the front-end of ultra-sensitive detectors. Quantum measurement strategies such as quantum non-demolition and quantum squeezing of mechanical resonators have been theoretically explored since the early 1980's (Caves et al., 1980; Bocko and Onofrio, 1996) yet still have not been realized and largely remain unexplored for two reasons. The large mass of gravitational wave detectors, $10 - 1000Kg$ gives a very small uncertainty



*R. Fazio et al. (eds.), New Directions in Mesoscopic Physics,* 245–258.
© 2003 *Kluwer Academic Publishers. Printed in the Netherlands.*

principle limit of $\Delta X_{SQL} = \sqrt{\frac{\hbar}{2m\omega}} \sim 10^{-19}m$ (Braginsky and Khalili, 1992). In addition, the low frequency of most mechanical detectors yields an extraordinarily small freeze-out temperature: $T_Q = \hbar\omega/k_B$. A $20kHz$ resonator freezes-out to the ground state at $T_Q = 1\mu K$.

Nanomechanical resonators, as shown in Figure 1, are ideal to approach quantum limits. Resonant frequencies of up to $1GHz$ have been realized and can be prepared in the ground state at $\approx 50mK$. In addition, the mass is very low, $10^{-15} - 10^{-16}Kg$, which gives a much larger zero-point motion, $\Delta X_{SQL} \sim 10^{-14}m$. These facts has been realized by a number of researchers (Blencowe and Wybourne, 1999; Carr et al., 2001; Schwab, 2001). It is hoped that nanomechanical systems can be a testbed for these advanced strategies which will find their use throughout the precision measurement community, from single-spin detection (Sidles et al., 1995) to quantum computing devices to gravitational wave physics.

The quantum effects we would like to demonstrate are quantized energy, evidence for zero-point motion, formation of superposition states, and the creation of entangled states with other quantum devices. However, to show a mechanical device is in fact quantum mechanical is non-trivial since a harmonic oscillator has equally spaced energy levels. If one resonantly drives a linear oscillator, coherent states are produced which are essentially indistinguishable from the classical oscillating states. On the contrary, if one drives a quantum two-state system with a resonant excitation, one finds that the probability to occupy the upper or lower state oscillates, the well-known Rabi oscillations. As a result of the tremendous progress with single-electronics there exists viable schemes to demonstrate all of the phenomena listed above.

The purpose of this chapter is to briefly touch upon and give references to the physics which is possible with coupled nanomechanical and single-electron systems, Quantum Electro-Mechanical systems. This chapter is arranged as follows. Section 2 will argue why it is believed that these mechanical devices can be prepared at the quantum limit. Section 3 will discuss the linear coupling of a nanomechanical resonator to a single-electron transistor, a position detection scheme which is expected to approach the uncertainty principle-limit. The last sections will describe some of the physics that is possible by electrostatically coupling a nanomechanical resonator to coherent two-level system, a Cooper-Pair Box (CPB). These ideas borrow heavily from the strategies and physics that is observed in cavity quantum electro-dynamics (CQED) where an atom interacts with a single mode of an electromagnetic cavity. This coupled system is expected to provide evidence of the zero-point motion of the mechanics through an energy shift of the CPB, and a means to prepare and monitor mechanical Fock states (Irish and Schwab, 2003). Most exciting is the possibility for this system to pro-

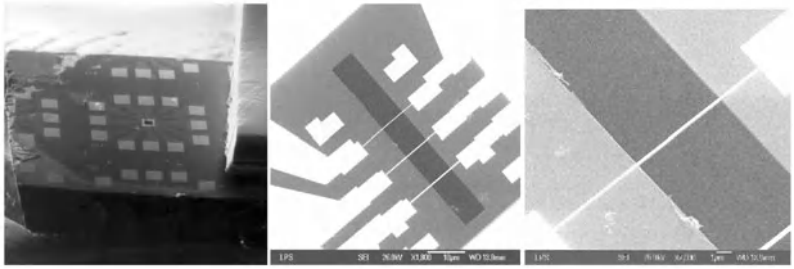

*Figure 1.* The scanning electron micrograph on the left shows the $3mm$ x $3mm$ silicon chip with $80\mu m$ x $80\mu m$ silicon nitride membrane in center. Center micrograph shows a close up of the membrane with three nanomechanical resonators which have been formed by plasma etching. Right micrograph shows a resonator which is coated with $30nm$ of Au. The resonator shown is $8\mu m$ long, $200nm$ wide, and $150nm$ thick, with resonant frequency of $30MHz$ and quality factor of $\sim 10,000$ at $4.2K$. Device fabricated by Matt LaHaye and Alex Hutchinson.

duce entangled CPB-mechanical states and strangely, to produce quantum interference of the mechanical device with itself.

## 2. Why Will They Behave in a Quantum Way?

In order to understand when a simple harmonic oscillator should behave quantum mechanically, we should ask at least two questions: Can we prepare the resonator into the ground state? Is the lifetime of a superposition state long enough to effect measurements? On theoretical grounds it appears that the answer to both questions is yes, but this has yet to be confirmed experimentally.

Figure 2 shows the thermal occupation versus frequency for a variety of nanomechanical resonator frequencies: $N_{TH} = 1/(e^{\hbar\omega/k_B T} - 1)$. It is clear that a $\omega/2\pi = 100MHz - 1GHz$ resonator should occupy the ground state for temperatures which are routinely achieved on a dilution refrigerator, $10mK$. This is well within the reach of current nanoresonators where $1GHz$ has recently been demonstrated (Huang et al., 2003).

Thermalization of single, high-$Q$ nanomechanical modes is still not understood (Cross and Lifshitz, 2001) and it is not yet known how difficult it will be to cool small mechanical devices to milli-kelvin temperatures. Given the vanishingly small thermal conductance through mechanical channels at very low temperatures(Schwab et al., 2000), passive cooling will eventually fail. For example, nanoelectronic systems are usually heated to $\sim 30 - 50mK$ while measured. Active cooling by feeding-back on the

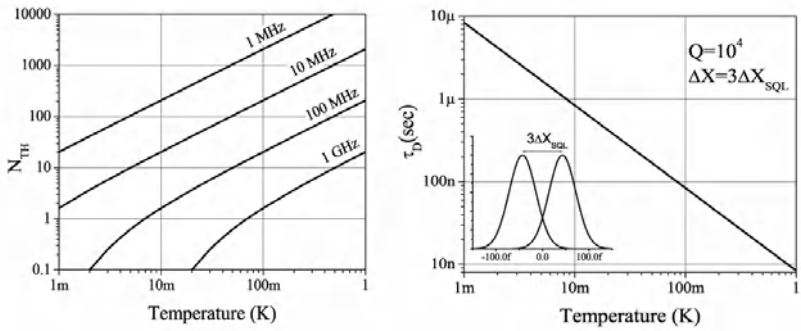


*Figure 2.* Figure on left shows the thermal occupation factor, $N_{TH}$, versus temperature for various resonant frequencies. Figure on right shows the expected decoherence time for a superposition to two coherent states displaced by $3\Delta X_{SQL}$ for a $100MHz$, $10^{-16}Kg$ resonator. Inset shows spacial probability density of a superposition of two coherent states separated by $3\Delta X_{SQL}$.

resonator using an SET position detector might be a possible technique to overcome this limitation (Hopkins et al., 2003).

Figure 2 shows the expected decoherence time for a superposition of coherent states separated by $\Delta X = 3\Delta X_{SQL}$ interacting with a thermal environment. It is thought that the environment selects coherent states as the habitual states of the oscillator (Zurek et al., 1993), states that are essentially classical. Other quantum states such as Fock states (the number states) or superpositions of coherent states will decay to the environmentally selected coherent states with a finite lifetime, $\tau_D$:

$$\tau_D = Q\frac{\hbar}{k_B T}\Big[\frac{\Delta X_{SQL}}{\Delta X}\Big]^2.$$

As shown in the figure, the expected lifetime at $10mK$ is $\sim 1\mu sec$ which is surprisingly long. Whether all other sources of decoherence can be avoided, other than through the above linear dissipation, remains to be seen.

The Fock states, $|N\rangle$, which are the eigenstates of the simple harmonic oscillator, can be produced by interaction with a two-state system (Irish and Schwab, 2003), and should have a lifetime given by $\tau_N = Q/(\omega N)$, similar to the lifetime of photon number states in an optical cavity (Lu, 1989). Thus we expect lifetimes in excess of microseconds for the lowest lying Fock states of a $100MHz$, $Q = 10,000$ resonator.

## 3. Position Detection at the Uncertainty Principle Limit

Single-electron transistors (SET) coupled to nanomechanical resonators promise position sensitivity near the uncertainty principle limit (Blencowe and Wybourne, 1999; Zhang and Blencowe, 2001; Schwab, 2001). In this scheme, a metalized nanomechanical resonator is fabricated in close proximity to the central island of the SET. Motion of the resonator will modulate the coupling capacitance. With a large voltage bias on the resonator, $V_g$, this capacitance change will change the potential of the island, which in turn modifies the conductance of the SET, the measured quantity. Figure 3 shows a device fabricated in our laboratory to explore this scheme.

The enabling technology of this scheme is the rf SET (Schoelkopf et al., 1998). This technique uses a microwave tank circuit to match the relatively high impedance of the SET, $20 - 100k\Omega$, to a $50\Omega$ transmission line and ultra-low noise preamplifier. This scheme has yielded charge sensitivity which approaches the uncertainty principle and bandwidths of $50MHz$ (Devoret and Schoelkopf, 2000; Aassime et al., 2001).

Figure 3 shows the expected dependence of the displacement resolution versus coupling voltage, $V_g$. For small values of the coupling, the sensitivity improves as the coupling is increased; the responsivity, $\partial I_{SET}/\partial x$, increases with increasing bias. However, for large values of the coupling, above $2V$ in Figure 3, the back-action of the SET onto the resonator dominates which results in a decrease in sensitivity as the coupling bias is increased. This back-action is a caused by the fluctuations of the island potential caused by the random charging and discharging of the island by $\delta V = e/C_\Sigma \approx 100\mu V$ each time an electron arrives or leaves the island, where $e$ is the electron charge and $C_\Sigma$ is the SET total capacitance. The spectral distribution of the island potential fluctuations is thought to be white and extends to a frequency given by the inverse tunneling time $1/RC_\Sigma \sim 10GHz$, where $R$ is the junction resistance (Korotkov, 1994).

In addition to position detection, a coupled SET-nanomechanical system my produce novel interactions such as non-linear and periodic potentials (Schwab, 2002). More advanced single-electron devices relying on the Josephson effect is expected to have a much lower white noise back-action as a result of the coherent transport at the Josephson frequency (Zorin, 1996). This could provide a means of engineering the detector back-action.

## 4. Coupling to Two-State Systems

Although we have shown that it is possible to prepare resonators at the quantum limit, this does not solve the difficult problem of how to show that the resonator is in fact a quantum system. We learn from the exper-

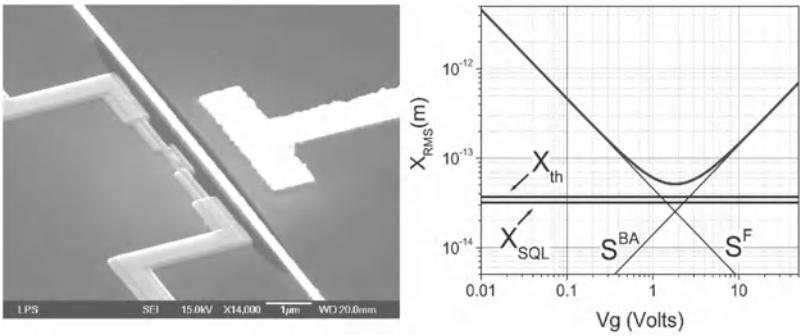


*Figure 3.* Scanning electron micrograph on left shows our current state-of-the-art device with silicon nitride nanomechanical resonator shown in the center with a $30nm$ Au coating. Single electron transistor fabricated from aluminum using double angle evaporation is shown at the center-left. Gate to actuate the resonator is shown at the center-right. This device was fabricated by Matt LaHaye and Benedetta Camarota. Plot on the right shows expected position sensitivity versus coupling voltage for an optimal SET. $X_{th}$ is the thermal noise at $10mK$ for a $50MHz$ and $Q = 10^4$ resonator. $X_{SQL}$ is the standard quantum limit.

ience of the atomic physics and quantum optics community where they have utilized the exquisite control over and measurement of atomic states to study the quantum mechanics of a single electromagnetic mode in a microwave or optical cavity (Haroche and Raimond, 1994; Kimble, 1994). Using the two-state atom as a quantum probe, they have been able to measure the zero-point energy of a single field mode(Brune et al., 1994), prepare and measure electromagnetic Fock states without destruction of the state(Nogues et al., 1999), and produce entangled states usable for quantum information (Nagerl et al., 2000).

A solid state analogy of the atom-cavity system is a Cooper-Pair Box (CPB) coupled to a mechanical resonator. A CPB is an nanoelectronic, two-state device which has shown superposition states of charge (Nakamura et al., 1999; Nakamura et al., 2002), long-lived phase superpositions (Cottet et al., 2002; Vion et al., 2002), and Schrodinger evolution. Strong coupling to the CPB can be accomplished by placing a nanomechanical resonator in close proximity and biasing the resonator with a large voltage. The force, $\hat{F}$, between the CPB and the resonator depends upon the charge state of the CPB and the position of the resonator, $\hat{x}$.

Near the CPB degeneracy point, the Hamiltonian description of the coupled system has the following simple form:

$$H_{TOTAL} = H_{CPB} + H_R + H_{INT}$$

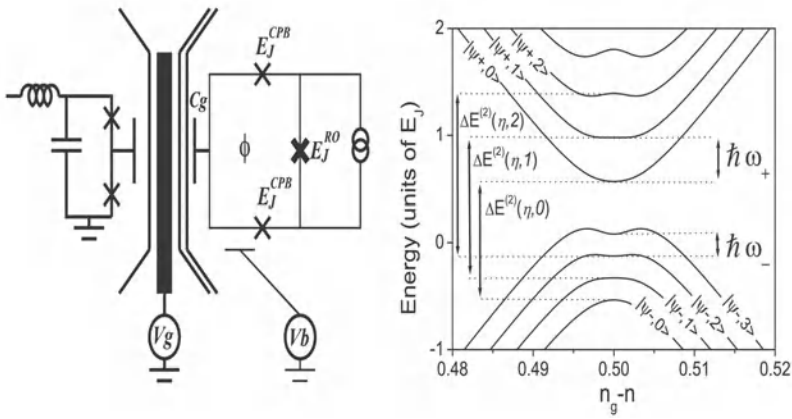


*Figure 4.* Figure on left shows a schematic of the coupled CPB-resonator system. Figure on right shows the manifold of energy levels of this system versus the CPB gate voltage $n_g - n$, near the CPB degeneracy point. The $\psi_\pm$ indicates the upper/lower CPB state and the number indicates the resonator number state (only lowest four number states are shown.) We have assumed $E_C = 25E_J$ and $\hbar\omega_0 = E_J/3$ and $\lambda = 1$. Transitions defining the mechanical frequencies $\hbar\omega_\pm$, and the CPB transitions $\Delta E^{(2)}(\eta, N)$ are shown with arrows.

$$H_{CPB} = 4E_C(n_g - n - \frac{1}{2})\hat{\sigma}_z - \frac{E_J}{2}\hat{\sigma}_x$$
$$H_R = \hbar\omega\hat{a}^\dagger\hat{a}$$
$$H_{INT} = \hat{x}\hat{F} = \lambda(\hat{a}^\dagger + \hat{a})\hat{\sigma}_z$$

where $\hat{a}^\dagger, \hat{a}$ are raising and lowering operators which act only on the resonator; $\hat{\sigma}_z, \hat{\sigma}_x$ are Pauli spin matrices operating on the CPB; $n$ is an integer which labels the charge states of the CPB; $n_g = \frac{C_g V_g}{2e}$ where $C_g$ and $V_g$ are the capacitance and voltage between the resonator and the CPB; $E_C$ and $E_J$ are the Coulomb and Josephson energies; $\omega$ is the unperturbed mechanical frequency; and $\lambda = -4E_C n_g \frac{\Delta x_{ZP}}{d}$ where $\Delta x_{ZP} = \sqrt{\frac{\hbar}{2m\omega}}$, which is the zero-point uncertainty of the resonator ground state.

Figure 4 shows the energy manifold of the coupled system near the CPB degeneracy point, where the CPB-resonator states are labeled $|\psi\pm, N\rangle$. Second order corrections to the energy eigenvalues from the interaction cause the spectrum to deviate from a manifold of CPB hyperbolas. It is easy to show that both the CPB and the resonator shift their transition frequency based on the state of the other. CPB transitions are labeled $\Delta E^{(2)}(\eta, N)$, and mechanical frequencies $\omega_\pm$. This has been explored by

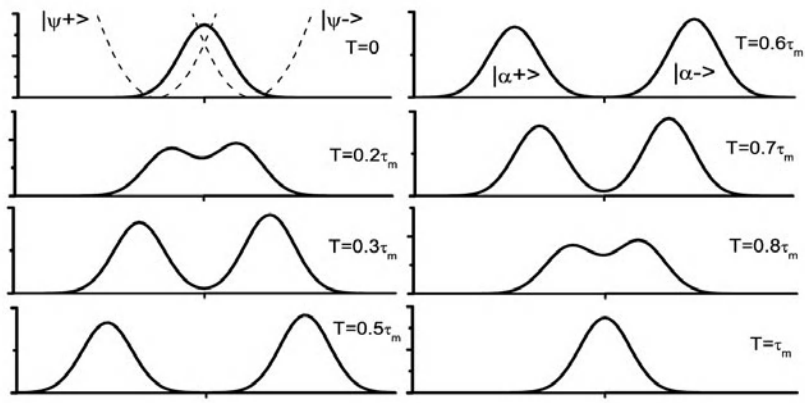


*Figure 5.* These figures show the calculated probability density of the mechanical resonator center-of-mass coordinate versus position for different moments in time. The upper left figure shows the initial condition of the resonator and the dotted lines show the potential energy for the two CPB states, $|\psi\pm\rangle$. The CPB state is $(|\psi+\rangle + i|\psi-\rangle)/\sqrt{2}$. The upper right figure shows the two coherent states that develop after interaction with the CPB superposition state, labeled $|\alpha\pm\rangle$. Conditions for simulation are $E_C = 100\mu V$, $E_J = 40\mu V$, $\lambda = 1$.

Irish, et al., 2003 and is expected to be the basis for the preparation and quantum non-demolition measurement of the resonator number state, mechanical readout of the CPB phase states, and a Lamb shift effect on the CPB from the resonator which reveals the zero-point motion of the mechanical resonator(Armour et al., 2002).

The equilibrium position of the resonator depends on the charge state of the box. Each Cooper-pair on the box produces a force $F = 4n_g E_C/d$. For reasonable parameter choices, two distinguishable resonator states can be created by the presence or absence of a single Cooper-Pair: $\Delta X = 4n_g E_C/kd > \Delta X_{SQL}$, where $k$ is the resonator spring constant. Figure 5 shows two parabolas which indicate the resonator potential energy for two CPB charge states.

Entangled states can be produced as follows. Suppose the CPB is biased away from the degeneracy point where the quantum states, $|\psi-\rangle$ and $|\psi+\rangle$, are essentially that of charge and the initial system state is $|\psi_S\rangle = |\psi-\rangle|\alpha(0)\rangle$. At $t = 0$ we apply a $\pi/2$ pulse to CPB. Since the resonator responds on a much slower time scale, this forms the state $[|\psi-\rangle + i|\psi+\rangle]|\alpha(0)\rangle$. As

time evolves, an entangled state is formed as a result of the interaction and the fact that the resonator must respond to both CPB states: $|\psi_S\rangle = [|\psi-\rangle|\alpha_-(t)\rangle + e^{i\phi(t)}|\psi+\rangle|\alpha_+(t)\rangle]/\sqrt{2}$, where $|\alpha_-(t)\rangle$ and $|\alpha_+(t)\rangle$ are a coherent state oscillating about the equilibrium position for the charge state $|\psi-\rangle$ and $|\psi+\rangle$, respectively. If the coupling is large enough, these mechanical states will be distinct at a time $T = \tau_m/2$, $\langle\alpha_+(\tau_m/2)|\alpha_-(\tau_m/2)\rangle \approx 0$. More details of this situation and how we expect to detect this dynamics can be found in Armour, et al., 2002a.

## 5. Quantum Interference

Figure 5 shows snap shots of the resonator probability distribution as it responds to the CPB charge superposition. It is apparent from the plots that when the two coherent states collide, they do not interfere. This can easily be understood by calculating the expectation value of the resonator position $\langle\hat{x}\rangle$:

$$\begin{aligned}\langle\hat{x}\rangle = \langle\psi_S|\hat{x}|\psi_S\rangle \; &= \tfrac{1}{2}\Big[\langle\alpha_-|\hat{x}|\alpha_-\rangle\langle\psi-|\psi-\rangle + \langle\alpha_+|\hat{x}|\alpha_+\rangle\langle\psi+|\psi+\rangle + \\ &\qquad \langle\alpha_-|\hat{x}|\alpha_+\rangle\langle\psi-|\psi+\rangle + \langle\alpha_+|\hat{x}|\alpha_-\rangle\langle\psi+|\psi-\rangle\Big]\end{aligned}$$

The last two terms are clearly zero since $\langle\psi+|\psi-\rangle = 0$, which gives $\langle\hat{x}\rangle = \frac{1}{2}[\langle\alpha_-|\hat{x}|\alpha_-\rangle + \langle\alpha_+|\hat{x}|\alpha_+\rangle]$, an incoherent sum of the probability from each coherent state. This is a result of the fact that each coherent state is entangled with an orthogonal CPB states. The CPB is a witness to the position of the resonator and, as in a Young's double slit experiment with detectors at each slit, the interference terms vanish.

Can we create interference of these mechanical states? The answer is yes and can be accomplished following the sequence shown in Figure 6 which shows the evolution of the resonator probability distribution. The initial preparation and evolution up to $T = \tau_m/2$ is identical to that in Figure 5 where the state evolves to $|\psi_S\rangle = [|\psi-\rangle|\alpha_-(t)\rangle + e^{i\phi(t)}|\psi+\rangle|\alpha_+(t)\rangle]/\sqrt{2}$. At this time, if we apply an additional $\pi/2$ pulse the state becomes:

$$|\psi_S\rangle = \frac{1}{2}\Big[|\psi-\rangle\Big[|\alpha_-(t)\rangle + |\alpha_+(t)\rangle\Big] + ie^{i\phi(t)}|\psi+\rangle\Big[|\alpha_-(t)\rangle - |\alpha_+(t)\rangle\Big]\Big]$$

As time continues to evolve,

$$|\psi_S\rangle = \frac{1}{2}\Big[|\psi-\rangle\Big[|\alpha_{--}\rangle + |\alpha_{+-}\rangle\Big] + ie^{i\phi(t)}|\psi+\rangle\Big[|\alpha_{-+}\rangle - |\alpha_{++}\rangle\Big]\Big]$$

with four distinct coherent states $|\alpha_{--}\rangle$, $|\alpha_{+-}\rangle$, $|\alpha_{-+}\rangle$, and $|\alpha_{++}\rangle$. Given the form of the above state, it is clear that the expectation value of position

will produce interfering terms such as $\langle\alpha_{--}|x\rangle\langle x|\alpha_{+-}\rangle$. Figure 6 shows this interference at time $\sim 0.75\tau_m$ as the states $|\alpha_{+-}\rangle$ and $|\alpha_{-+}\rangle$ cross through the origin.

As can be seen from the results of simulation in Figure 6, the dynamics of this interference is very quick and it is not clear at this time how this might be measured. However, it is fascinating to think that one can indeed cause mechanical interference without sending the object around a topological boundary, like a wire or around two slits which is the usual design for interference with electrons or photons. The CPB in a charge superposition state acts as an analogy of two slits or a beam-splitter for the resonator to scatter off of; one resonator state in $\rightarrow$ superposition of two resonator states out.

It is interesting to point out that a pure mechanical superposition is produced if a projective measurement of the CPB charge state were made after the $\pi/2$ pulse.

## 6. Comments and Conclusions

What is exciting about these schemes is not the uniqueness of the physics; all of the concepts such as uncertainty principle limited detection, superpositions and entanglement, and quantum interference, have been developed or observed in other systems. What is exciting is that the schemes discussed here appear to be viable for nanomechanical devices, this is new. For instance, other schemes to produce mechanical superpositions or quantum non-demolition measurements have been proposed but are not within experimental reach (Thorne et al., 1978; Bose et al., 1999).

Our experimental plans to show the true quantum nature of mechanics rely heavily upon single-electronics. It is clear that as progress is made in nanoelectronics, especially devices intended for quantum computing, new schemes and strategies will emerge, offering more possibilities such as longer decoherence times and tighter coupling.

The impact of these experiments is hoped to be wide reaching, both technological and fundamental. Quantum Computation: If coherent quantum behavior can be achieved, it may be possible to use nanomechanical systems as a 'bus' for the entanglement of solid state qubits (Irish and Schwab, 2003) much in the same way entanglement is accomplished in ion traps or CQED experiments (Cirac and Zoller, 1995; Haroche and Raimond, 1994). Force Detection: Ultra-sensitive mechanical detection is essential for schemes to probe single electron or nuclear spins (Sidles et al., 1995). Advanced Mechanical Materials: In order to achieve the highest frequency with the largest coupling to a CPB, we are investigating the low temperature properties of crystalline diamond resonators. This is thought to be the ultimate ma-

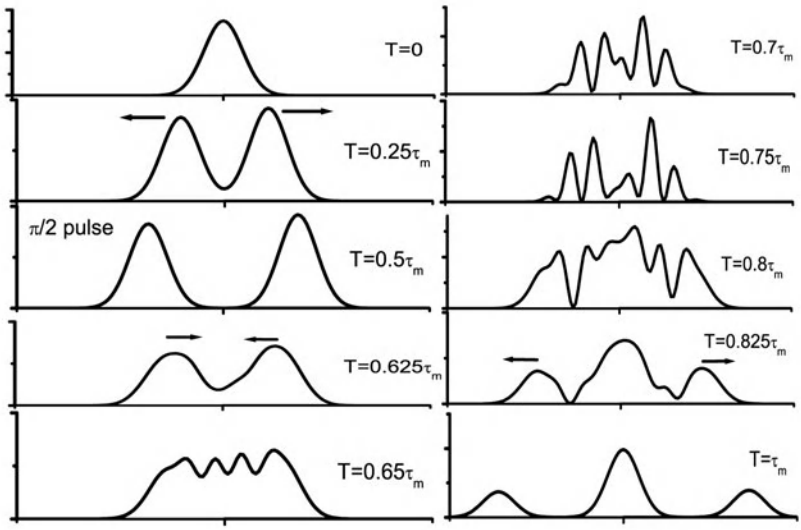


*Figure 6.* These figures show the calculated probability density of the mechanical resonator center-of-mass coordinate versus position for different moments in time. The upper left figure shows the initial condition of the resonator. The initial CPB state is $(|\psi+\rangle + i|\psi-\rangle)/\sqrt{2}$. The arrows show the direction of motion. Note $\pi/2$ pulse to CPB at $T = 0.5\tau_M$. $|\alpha_{+-}\rangle$, $|\alpha_{-+}\rangle$ are the most extreme peaks in the bottom right figure. Conditions for simulation are $E_C = 100\mu V$, $E_J = 40\mu V$, $\lambda = 1$.

terial for approaching nanomechanical quantum limits since it produces the highest frequency for a given geometry as a result of the extremely high Young's modulus and moderate density. We have recently observed a $13MHz$, $Q = 5,000$, diamond nanoresonator at $4.2K$(Sekaric et al., 2002).

The most lofty goal is to illuminate some of the fundamental questions we have about quantum mechanics, such as, why do we not observe truly quantum behavior at the macroscale (Leggett, 2002), or how measurement induces a quantum-to-classical transition (Mozyrsky and Martin, 2002). The nanomechanical systems we are working with are indeed small, but would constitute the largest coherent quantum object, composed of $\sim 10^{10}$ atoms. Success would push the quantum world above the micron scale and tempt us to push to larger scales. Failure would force us to ask if we have run into a fundamental boundary.

**Acknowledgments**

The experiments and theory described here are vigorously pursued at the Laboratory for Physical Sciences and is a result of interaction with many scientist: Matt LaHaye, Carlos Sanchez, Olivier Buu, Benedetta Camarota, Elinor Irish, Michael Roukes, Miles Blencowe, Andrew Armour, Kurt Jacobs, Asa Hopkins, and Salman Habib. This work is dedicated to the brave souls of the Columbia.

## References


Aassime, A., D. Gunnarsson, K. Bladh, P. Delsing, and R. Schoelkopf: 2001, 'Radio-frequency single-electron transistor: toward the shot-noise limit'. *Applied Physics Letters* **79**(24), 4031–4033.

Armour, A., M. Blencowe, and K. Schwab: 2002, 'Mechanical Lamb-shift analogue for the Cooper-pair box'. *Physica B* **316**, 406–407.

Blencowe, M. and M. Wybourne: 1999, 'Quantum Squeezing of Mechanical Motion for Micron-Sized Cantilevers'. *Physica B* **280**(1-4), 555–556.

Bocko, M. F. and R. Onofrio: 1996, 'On the measurement of a weak classical force coupled to a harmonic oscillator: experimental progress'. *Reviews of Modern Physics* **68**(3), 755–799.

Bose, S., K. Jacobs, and P. Knight: 1999, 'Scheme to probe the decoherence of a macroscopic object'. *Physical Review A* **59**(5), 3204–3210.

Braginsky, V. B. and F. Y. Khalili: 1992, *Quantum Measurement*. Cambridge University Press.

Brune, M., P. Nussenzveig, F. Schmidt-Kaler, F. Bernardot, A. Maali, J. Raimond, and S. Haroche: 1994, 'From Lamb Shift to Light Shifts: Vacuum and Subphoton Cavity Fields Measured by Atomic Phase Sensitive Detection'. *Physical Review Letters* **72**, 3339–3342.

Carr, S., W. Lawrence, and M. Wybourne: 2001, 'Accessibility of quantum effects in mesomechanical systems'. *Physical Review B* **64**, 220101.

Caves, C. M., K. S. Thorne, R. W. Dreaver, V. D. Sandberg, and M. Zimmermann: 1980, 'On the measurement of a weak classical force coupled to a quantum-mechanical oscillator: I. Issues of principle'. *Reviews of Modern Physics* **52**(2), 341–392.

Cirac, J. and P. Zoller: 1995, 'Quantum Computing with Cold Trapped Ions'. *Physical Review Letters* **74**(20), 4091–4094.

Cottet, A., D. Vion, A. Assime, P. Joyez, D. Esteve, and M. Devoret: 2002, 'Implementation of a combined charge-phase quantum bit in a superconducting circuit'. *Physica C* **367**, 197–203.

Cross, M. and R. Lifshitz: 2001, 'Elastic wave transmission at an abrupt junction in a thin plate with applications to heat transport and vibrations in mesoscopic systems'. *Phys. Rev. B* **64**, 0854324.

Devoret, M. H. and R. J. Schoelkopf: 2000, 'Amplifying quantum signals with the single electron transistor'. *Nature* **406**, 19–26.

Friedman, J. R., V. Patel, W. Chen, S. Tolpygo, and J. Lukens: 2000, 'Quantum superposition of distinct macroscopic states'. *Nature* **406**, 43–46.

Haroche, S. and J. Raimond: 1994, 'Manipulation of Nonclassical Field States in a Cavity by Atom Interferometry'. In: P. Berman (ed.): *Cavity Quantum Electrodynamics*. Acedemic Press, Inc., p. 123.

Hopkins, A., K. Jacobs, S. Habib, and K. Schwab: 2003, 'Feedback cooling of a nanomechanical resonator'. Submitted to Phys. Rev. B.

Huang, X. M. H., C. A. Zorman, M. Mehregany, and M. L. Roukes: 2003, 'Nanodevice motion at microwave frequencies'. *Nature* **421**, 496.

Irish, E. K. and K. Schwab: 2003, 'Quantum Measurements with a coupled nanomechanical resonator-cooper pair box system'. submitted to Physical Review B.

Kimble, H.: 1994, 'Structure and Dynamics of Cavity Quantum Electrodynamics'. In: P. Berman (ed.): *Cavity Quantum Electrodynamics*. Acedemic Press, Inc., p. 203.

Korotkov, A. N.: 1994, 'Instrinsic noise of the single electron transistor'. *Physical Review B* **49**(15), 10381–10392.

Leggett, A.: 2002, 'Testing the Limits of Quantum Mechanics: Motivation, State of Play, Prospects'. *Journal of Physics Condensed Matter* **14**, R415–R451.

Lu, N.: 1989, 'Effects of dissipation on photon statistics and the lifetime of a pure number state'. *Physical Review A* **40**, 1707–1708.

Mozyrsky, D. and I. Martin: 2002, 'Quantum-classical transition induced by electrical measurement'. *Phys. Rev. Lett.* **89**, 018301.

Nagerl, H., D. Leibfried, F. Schmidt-Kaler, J. Eschner, R. Blatt, M. Brune, J. Raimond, and S. Haroche: 2000, 'Cavity QED-Experiments: Atoms in Cavities and Trapped Ions'. In: D. Bouwmeester, A. Ekert, and A. Zeilinger (eds.): *The Physics of Quantum Information*. New York: Springer.

Nakamura, Y., Y. Pashkin, and J. Tsai: 1999, 'Coherent control of a macroscopic quantum states in a single-Cooper-pair box'. *Nature* **398**, 786–788.

Nakamura, Y., Y. Pashkin, T. Yamamoto, and J. Tsai: 2002, 'Charge Echo in a Cooper-Pair Box'. *Phys. Rev. Lett.* **88**, 047901.

Nogues, G., A. Rauschenbeutel, S. Osnaghi, M. Brune, J. M. Raimond, and S. Haroche: 1999, 'Seeing a single photon without destroying it'. *Nature* **400**, 239–242.

Park, H., J. Park, A. K. Lim, E. H. Anderson, A. P. Alivisatos, and P. McEuen: 2000, 'Nanomechanical oscillations in a single-C60 transistor'. *Nature* **407**, 57–60.

Schoelkopf, R., P. Wahlgren, A. Kozhevnikov, P. Delsing, and D. Prober: 1998, 'The radio-frequency single-electron transistor (RF-SET): A fast and ultrasensitive electrometer'. *Science* **280**(5367), 1238–1242.

Schwab, K.: 2001, 'Quantum Measurement with Nanomechanical Systems'. In: R. Clark (ed.): *Proceedings of the 1st International Conference on Experimental Implementation of Quantum Computing*. pp. 189–194.

Schwab, K.: 2002, 'Frequency and Disipation Control of a Nanomechanical Resonator using a Single-electron Transistor'. *Appl. Phys. Lett.* **88**, 047901.

Schwab, K., J. Arlett, J. Worlock, and M. Roukes: 2001, 'Thermal Conductance through discrete quantum channels'. *Physica E* **9**(1), 60–68.

Schwab, K., E. Henriksen, J. Worlock, and M. Roukes: 2000, 'Measurement of the quantum of thermal conductance'. *Nature* **404**(6781), 974–977.

Sekaric, L., J. Parpia, H. Craighead, T. Feygelson, B. Houston, and J. Butler: 2002, 'Nanomechanical resonant structures in nanocrystallline diamond'. *Appl. Phys. Lett.* **81**, 4455–4457.

Sidles, J., J. Garbini, K. Bruland, D. Rugar, O. Zuger, S. Hoen, and C. Yannoni: 1995, 'Magnetic resonance force microscopy'. *Reviews of Modern Physics* **67**, 249–265.

Thorne, K. S., R. W. P. Drever, and C. M. Caves: 1978, 'Quantum Nondemolition Measurements of Harmonic Oscillators'. *Physical Review Letters* **40**(11), 667–671.

Vion, D., A. Aassime, A. Cottet, P. Joyez, H. Pothier, C. Urbina, D. Esteve, and M. Devoret: 2002, 'Manipulating the quantum state of an electrical circuit'. *Science* **296**, 886–889.

Zhang, Y. and M. Blencowe: 2001, 'Intrinsic noise of a micro-mechanical displacement detector based on the radio-frequency single-electron transistor'. *Journal of Applied Physics* **91**, 4249–4255.

Zorin, A.: 1996, 'Quantum-Limited Electrometer Based on Single Cooper-Pair Tunneling'. *Physical Review Letters* **76**(23), 4408–4411.

Zurek, W. H., S. Habib, and J. P. Paz: 1993, 'Coherent States via Decoherence'. *Physical Review Letters* **70**(9), 1187–1190.

# Possible weak temperature dependence of electron dephasing

V.V. Afonin,[1] J. Bergli,[2] Y.M. Galperin,[1–3]
V.L. Gurevich[1], V.I. Kozub,[1,3]
[1]*Solid State Division, A. F. Ioffe Physico-Technical Institute, 194021 St. Petersburg, Russia;*
[2] *Department of Physics, University of Oslo, P. O. Box 1048 Blindern, N 0316 Oslo, Norway*
[3]*Argonne National Laboratory, 9700 S. Cass av., Argonne, IL 60439, USA*

**Abstract.** The first-principle theory of electron dephasing by disorder-induced two state fluctuators is developed. There exist two mechanisms of dephasing. First, dephasing occurs due to direct transitions between the defect levels caused by inelastic electron-defect scattering. The second mechanism is due to violation of the time reversal symmetry caused by time-dependent fluctuations of the scattering potential. These fluctuations originate from an interaction between the dynamic defects and conduction electrons forming a thermal bath. The first contribution to the dephasing rate saturates as temperature decreases. The second contribution does not saturate, although its temperature dependence is rather weak, $\propto T^{1/3}$. The quantitative estimates based on the experimental data show that these mechanisms considered can explain the weak temperature dependence of the dephasing rate in some temperature interval. However, below some temperature dependent on the model of dynamic defects the dephasing rate tends rapidly to zero. The relation to earlier studies of the dephasing caused by the dynamical defects is discussed.

## 1. Introduction

The problem of dephasing of electron states in low-dimensional structures is in focus of interests of many research groups. This is due to novel experiments on the Aharonov-Bohm effect in specially designed mesoscopic circuits [1, 2] and on weak localization magnetoresistance in low-dimensional samples [3], as well as to new theoretical discussions of dephasing [4, 5, 6, 7, 8, 9]. In particular, dephasing due to defects with internal degrees of freedom as a source of dephasing were recently addressed [6, 7]. According to the model discussed in Ref. [7], a temperature interval can exist in which the dephasing rate is almost temperature-independent.

In this work we revisit the dephasing due to dynamic defects which interact with electrons and tunnel between their two states due to interaction with some thermal bath. Examples of such defects are disorder-induced two-state fluctuators [10, 11] present in any disordered material, impurities with a non-compensated spin, etc. These defects produce



*R. Fazio et al. (eds.), New Directions in Mesoscopic Physics,* 259–268.
© 2003 *Kluwer Academic Publishers. Printed in the Netherlands.*

a random time-dependent field and in this way they violate the time-reversal symmetry of the problem. According to a conventional opinion, this property is sufficient to produce dephasing. However, this is true only under the condition that a typical defect relaxation time is shorter that the time during which the electron interference pattern is formed. Indeed, if the defects do not change their state during the pattern formation they act as static ones and can contribute to the interference only in a constructive way [7].

The purpose of this work is to develop a systematic theory of weak localization with dephasing due to dynamic defects interacting with electrons which results in a smooth temperature dependence at relatively low temperatures $T$. The dynamic defects are specified as two-level tunneling states (TLS) that exist in any crystalline metal.

The main message of this work is the following. There exist two mechanisms of electron dephasing due to dynamic defects. The first one is due to direct inelastic transitions between the levels of the TLS leading to the possibility of determining the actual path of the electron, and consequently to loss of interference. The second one is due to relaxation dynamics of dynamic defects which fluctuate due to interaction with the thermal bath. Time dependence of the electron scattering crossection due to the defects' fluctuations lead to violation of the time-reversal symmetry and, as a consequence, to decoherence. To our knowledge, the theory relevant to the second mechanism has not been developed. However, there exists a temperature interval where this relaxation mechanism is dominating.

Below we will give physical considerations to describe dephasing by dynamic defects, which will be then confirmed by a diagrammatic approach, see [12]. In this section the model for electron-TLS interaction will be formulated. This model will be used to calculate the dephasing rate due to identical TLSs, and, finally, an average procedure over different TLSs will be considered. Estimates and discussion will be given and the conclusions will be drawn.

## 2. Qualitative considerations

Let us start with a toy model which illustrates the essence of the physics involved. Consider the electron motion in a slowly varying potential field $U(\mathbf{r}, t)$. Let us calculate the phase difference $\Delta\varphi$ between the electron waves moving from the same point $C$ along the same closed path clockwise and counterclockwise. We begin with evaluation of the variation $\Delta S$ of the electron's action $S$ due to the time variation of potential $U$. We assume that an electron during its motion along the

trajectory experiences many scattering events against both static and dynamic defects, so that the trajectory can be approximated by a smooth curve. We have where $\mathbf{n} = \mathbf{p}/p$ is a unit vector parallel to the tangent to the trajectory $ds$ is its length element. This can also be written $S = \int ds\sqrt{2m(\mathcal{E} - U)}$, $\mathcal{E} = p^2/2m$ being the electron kinetic energy while $m$ is the electron effective mass. Expanding this equation in powers of the potential energy $U$ assumed small, one gets

$$\Delta S = -\int \frac{ds}{v} U(s,t) = -\int dt\, U(s_t, t).$$

Here $s_t$ is the electron's coordinate on the trajectory parameterized by time $t$. So $U$ depends on time both via the space coordinate $s_t$ and explicitly.

Let now $t_0$ be the total time of the motion of an electron along the loop. Then the phase variations for a clockwise/counterclockwise motion are:

$$(\Delta\varphi)_+ = -\frac{1}{\hbar}\int_0^{t_0} dt\, U(s_t, t)\,, \quad (\Delta\varphi)_- = -\frac{1}{\hbar}\int_0^{t_0} dt\, U(s_{t_0-t}, t)\,. \quad (1)$$

The dephasing means a non-vanishing phase difference $\Delta\varphi \equiv (\Delta\varphi)_+ - (\Delta\varphi)_-$. Thus, $\overline{(\Delta\varphi)^2} = \sum_\pm \left[\overline{(\Delta\varphi)^2_\pm} - \overline{(\Delta\varphi)_\pm(\Delta\varphi)_\mp}\right]$. Using Eqs. (1) the above expression is expressed through $\int_0^{t_0} dt \int_0^{t_0} dt' \, \overline{U(s_{t_i}, t) U(s_{t'_k}, t')}$ where $i, k = \pm,\ t_+ \equiv t,\ t_- \equiv t_0 - t$. We assume that there is no spatial correlation between the scattering centers, $\overline{U(s_t,t)U(s_{t'},t')} \propto \delta(s_t - s_{t'})$, that implies

$$\begin{aligned}
\overline{U(s_{t_\pm}, t) U(s_{t'_\pm}, t')} &\propto \overline{U^2(s,t)}\, \delta(t - t')\,, \\
\overline{U(s_{t_\pm}, t) U(s_{t'_\mp}, t')} &\propto \overline{U(s,t) U(s, t_0 - t)}\, \delta(t + t' - t_0)\,.
\end{aligned}$$

Using these expressions and introducing the time correlation function of the time-dependent random potential as

$$\overline{U(s,t)U(s,t')} \equiv \overline{U^2} f(t - t')\,,\ \overline{U^2} \equiv \overline{U^2(s,t)}\,,\ f(0) = 1\,,$$

one obtains $\overline{(\Delta\varphi)^2} \propto \overline{U^2} \int_0^{t_0} dt\, [1 - f(2t - t_0)]$. If there are several mechanisms responsible for dephasing characterized by different coupling strengths and different correlation functions the resulting phase variance can be expressed as

$$\overline{(\Delta\varphi)^2} \propto \sum_s \int_0^{t_0} \frac{dt}{\tau_s}\, [1 - f_s(2t - t_0)]\ . \quad (2)$$

Here we have absorbed the random scattering potential into the partial relaxation rates $\tau_s^{-1}$. They, as well as the correlation functions, depend

on the properties of dynamic defects. We wish to emphasize that Eq. (2) demonstrates the following point indicated above. If the defect has not relaxed during the time $2t - t_0$ between two acts of scattering then in spite of non-invariance of the Hamiltonian respective to the time reversal there is no phase relaxation.

We distinguish two mechanisms of dephasing. The first, which we call the resonant mechanism, is connected to interactions which cause real transitions between different states of the environment. This can be illustrated by the famous double slit experiment. If we send electrons at the double slit, it will pass through both slits and interfere with itself, creating an interference pattern on the screen. Putting detectors to determine which slit the electron really passed through will destroy the interference pattern. If the interaction with the environment in any way allows us to determine the path of the electron, interference is lost. The second mechanism of dephasing is related to a change in the state of the environment due to its own internal dynamics. A dynamic environment leads to a difference in a scattering potential "felt" by an electron state during clockwise and counterclockwise motion. As a result, time-reversal symmetry is broken and the interference pattern decays. We call this mechanism the relaxational mechanism, because it is caused by the relaxation of the environmental states which results when the environment is considered to be in contact with a thermal bath.

At this point we would like to compare our description to the one given in Ref. [13] where it is proved that the dephasing can be described in two equivalent ways. Either you consider the change in the electron phase of you consider the change of state of the environment, where complete dephasing corresponds to the environment being in orthogonal states. The last point of view would imply the existence of only the first mechanism of dephasing that we consider, resonant transitions of environment states. We want to emphasize that our second, relaxational mechanism is not in conflict with this, but is a result of our description of the process. In Ref. [13] the environment is considered as a mechanical system evolving according to its own Hamiltonian, whereas we consider the environment to be a statistical system at some temperature. That is, we calculate the action of the environment on the electrons, but do not consider the action of the electrons on the environment. In principle, if one were to follow all the complex dynamics of the environment one would find that it does indeed evolve into orthogonal states as the electron dephases according to the relaxational mechanism, and it would be seen that this is only the resonant mechanism in disguise. However, as the environment consists of a macroscopic number of degrees of freedom is it more natural to

treat it statistically as a thermal bath. In other words, the phase of an electron state forming a Cooperon trajectory decays due to real transitions in the thermal bath formed by other electrons assisted by virtual processes involving dynamic defects. In a perturbative approach these processes occur in the fourth order in the electron-defect coupling constant. In particular, they do not enter the second-order calculation of defect-enhanced electron-electron interaction [14]. However, it will be shown that they play an important role in dephasing.

A different classification can be made by discriminating between the two different regimes of phase dynamics – phase jumps and phase wandering (or phase diffusion). To understand this, let us consider the resonant mechanism. Consider the case of interest for weak localization, that of one electron traveling around a closed loop both in the clockwise and counterclockwise direction, and interferes with itself after completing a full circuit. If we can determine which direction the electron went, we will not get interference. If we are unable to do so, it will appear. As a detector we use a two level system that is placed at a point on the right hand side of the loop, the distance from the starting (and ending) point being a fraction $\alpha < \frac{1}{2}$ of the total circumference.

The energy splitting of the two level system is $E$, and it starts out in the lower state. When the electron passes, it excites the two level system. We determine the direction of the electron by measuring the time at which this happens. The accuracy with which we can make this measurement is limited by the uncertainty principle $\Delta t \Delta E > \hbar$. If $E$ is large there is no problem, and the interference is destroyed by a single detection event. This case we call a phase jump. In the opposite case where $E$ is small we can not determine with certainty which direction the electron went, and the interference pattern will be smeared out, but not lost entirely. In this case we need the interaction with a number of two level systems along the path, and the combined result of all the detection times can be put together to determine the direction. In this case we speak about phase wandering or phase diffusion, since the random contributions of the difference two level systems makes the electron phase change in a diffusive way.

Let us estimate the dephasing rates in the different cases. Consider first the resonant mechanism where we have inelastic electron scattering due to direct transitions between the two TLS's states. We emphasize that the inelasticity is not essential to this channel of dephasing. The important point is that there is a real transition between orthogonal states of the TLS. Since we are not considering degenerate states this will mean inelastic scattering in our case. If the energy transfer $E$ is large enough, the phase relaxation time $\tau_\varphi$ is equal to the typical inelastic relaxation time $\tau_1$, which is a function of the defect parameters.

The criterion of "large" $E$ in this case is given as $E\tau_1/\hbar >> 1$. For smaller $E$ one deals with a phase diffusion or wandering. To estimate the dephasing time for this case let us recall that the phase coherence for any two-level system is conserved during the time $t < \hbar/E$. While traversing the trajectory during the time $t$ an electron appears to be coupled with $\bar{N} \sim t/\tau_1$ dynamic defects. The evolution of the electron wave function due to coupling with any of these defects is described by a phase factor $\exp(\pm iEt/\hbar)$ where $\pm$ corresponds to the sign of the energy transfer. If $T \gtrsim E$ the probabilities of the both defect states are almost equal, and the correlation function of the time-dependent random potential is $f(t) = \cos(Et/\hbar)$, see the calculation later. The resulting electron phase shift turns out to be $\bar{N}^{1/2}Et/\hbar$. Consequently, the phase relaxation time can be estimated as $\tau_\varphi \sim \hbar^{2/3}\tau_1^{1/3}/E^{2/3}$. A similar expression for the dephasing time has been introduced in Refs. [15] in connection with decoherence due to quasielastic electron-electron scattering and in Refs. [16, 17] in connection with decoherence by low-frequency phonons. In the following we will call this regime the phase wandering. Summarizing, we can express the contribution of inelastic processes as

$$\tau_\varphi^{(1)} = \max\left\{\tau_1, \tau_1^{1/3}(\hbar/E)^{2/3}\right\} . \tag{3}$$

Moving to the relaxational mechanism, we find that the simplest way to evaluate this contribution is note that $\tau_\varphi$ has a sense of the time at which $\Delta\varphi(t) \approx 1$ provided all the involved defects would suffer a transition. It is clear that if the phase shift $\delta\varphi$ due to transition of a single defect is $\gtrsim 1$ then a single TLS is enough to produce the dephasing. For $\delta\varphi << 1$ the significant phase evolution is possible only with the help of many defects. The actual dephasing time, $\tau_\varphi$, is also sensitive to the defect transition rate $\gamma$. Indeed, the correlation function $f(t)$ for statistically independent defects is expected to have a form $f(t) = e^{-2\gamma|t|}$.

If $\gamma\tau_3 \gtrsim 1$, then with a help of Eq. 2 one obtains $\overline{(\Delta\varphi)^2} = t_0/\tau_3$ (for the reasons which will be clear later we ascribe the subscript 3 for the relaxation mechanism) . If $\gamma\tau_3 << 1$, one has $\overline{(\Delta\varphi)^2} \sim \gamma t_0^2/\tau_3$. We observe that there is a phase wandering regime also for this relaxation mechanism. Again, defining $\tau_\varphi$ as a time at which $\overline{(\Delta\varphi)^2} \sim 1$ one has

$$\tau_\varphi^{(3)} = \max\left\{\tau_3, (\tau_3/\gamma)^{1/2}\right\} . \tag{4}$$

To calculate the quantum contribution to conductance one has to sum over different dynamic defects. In the previous considerations we have assumed that the dynamical defects are modeled by the Hamilto-

nian

$$\tilde{\mathcal{H}}_{\rm d} = (\Delta\,\sigma_3 - \Lambda\,\sigma_1)/2 \tag{5}$$

and all dynamic defects have the same diagonal interlevel splitting, $\Delta$, and the same tunneling amplitude, $\Lambda$, the interlevel spacing being $E = \sqrt{\Delta^2 + \Lambda^2}$. Consequently, the summation over different defects has been allowed for by the factor $n_d$ in the expressions for the relaxation times $\tau_1$ and $\tau_3$. However, in realistic systems both $\Delta$ and $\Lambda$ can be distributed over a significant range. Since the number of dynamic defects at a typical electron trajectory is assumed to be large the summation over different defects can be replaced by a proper average. To calculate the latter it is necessary to specify the distribution function $\mathcal{P}(E, \Lambda)$ which we assume to be normalized to 1. To specify this function, let us come back to the effective Hamiltonian (5). Since $\Delta$ is determined by the defect's neighborhood while $\Lambda$ is determined by the distance between two metastable states it is natural to assume $\Delta$ and $\Lambda$ to be uncorrelated, $\mathcal{P}(\Delta, \Lambda) = \mathcal{P}_\Delta(\Delta)\mathcal{P}_\Lambda(\Lambda)$.

Below we will assume the "tunneling-states-model" (TM) is more appropriate for crystalline materials. There the tunneling integrals $\Lambda$ is determined by the crystalline structure and are almost the same for all dynamical defects. On the other hand, the parameter $\Delta$ is determined by long-range interactions, and it is assumed distributed smoothly within some band, cf. with Ref. [18]. Then

$$\mathcal{P}_{TM}(E, \Lambda) = \frac{\Theta(E^* - E)}{E^*}\,\frac{E}{\sqrt{E^2 - \Lambda_0^2}}\,\delta(\Lambda - \Lambda_0)\,. \tag{6}$$

In the following we will assume that the dynamical defects are characterized by $\Lambda_0 \ll T$. Using this distribution one obtains for the contribution of direct (resonant) transitions [12]:

$$\frac{1}{\tau_\varphi^{(1)}} \approx \frac{1}{\tau_\Lambda}\frac{\Lambda_0}{T_\Lambda}\begin{cases} \min\{(T/T_\Lambda)^{1/3}, 1\}\,, & T_\Lambda \gg \Lambda_0\,, \\ T_\Lambda/\Lambda_0 & T_\Lambda \ll \Lambda_0\,. \end{cases} \tag{7}$$

where $T_\Lambda = (\hbar\Lambda_0/\tau_\Lambda)^{1/2}$, $\tau_\Lambda = \tau_i(E^*/\Lambda_0)$.

For the relaxation processes, it is convenient to introduce the characteristic temperature $T_\alpha = \hbar/\chi\tau_\Lambda$. Then

$$1/\tau_\varphi^{(3)} = \tau_\Lambda^{-1}(T/T_\alpha)^{1/3}\,. \tag{8}$$

Another important characteristic energy is the temperature $T_\beta$ defined as $T_\beta = \Lambda_0^{3/2}/T_\alpha^{1/2}$ The ratio $T_\alpha/T_\beta = (\chi\Lambda_0\tau_\Lambda/\hbar)^{3/2}$ can be arbitrary.

One can show (see [12]) that at $T \geq T_\alpha, T_\beta$ the relaxation contribution dominates, and the dephasing rate is

$$\tau_\varphi^{-1} = \tau_\Lambda^{-1}[(T/T_\alpha)^{1/3} + \zeta] \tag{9}$$

where $\zeta$ is a constant of the order 1 originating from the resonant contribution.

At low temperatures both contributions can be important, their interplay depending on the relationship between the temperature $T$ and the characteristic energies $\Lambda_0$, $T_\Lambda$, $T_\alpha$ and $T_\beta$. For both mechanisms the dephasing rate vanishes as $T \to 0$ and there is is a region in which the dephasing rate is proportional to $T^{1/3}$ .

As it is seen, can the suggested mechanism indeed exhibit saturation-like behavior in some temperature region. Unfortunately the existing experimental data are obtained in a relatively narrow temperature interval (typically no more than 2 decades) which does not allow one to determine the temperature dependence with an accuracy that is sufficient to prove or disprove equation (9).

## 3. Estimates, discussion and conclusions

The key parameter of our theory, $\tau_\Lambda$, is given as $\tau_\Lambda^{-1} = \Lambda_0 P_d \sigma_{\rm in} v_F$ where $P_d = n_d/E^*$ is the density of states of the dynamic defects. The density of states $P_d$ can be, in principle, estimated for a given material on the basis of point contact measurements. Namely, metallic point contacts are known to exhibit, first, telegraph resistance noise [26] and, second, zero-bias anomalies [27]; both effects are expected to be associated with the dynamic defects [26, 27, 18]. Although we appreciate that the material preparation procedure can significantly affect the defect system, we believe that such experiments can provide more or less reasonable estimates for $P_d$. The telegraph noise studies [26] for a Co nanoconstriction with a size of $\sim 10$ nm revealed the presence of about several dynamic defects at energies less than 10 mV. This would give us the value $P_d \sim (3-5) \times 10^{32}$ erg$^{-1}$cm$^{-3}$. However, the telegraph noise is related to TLS with rather slow relaxation rates ($\lesssim 10^3$ s$^{-1}$) while we are interested in the defects with switching times of the order of $10^{-9}$ s. Consequently, these estimates most probably significantly underestimate $P_d$. What is more instructive, the magnitude of the resistance noise revealed rather large defect asymmetry corresponding to the estimate $\sigma_{\rm in} \sim \sigma_e^{\rm d} \sim 10^{-15}$ cm$^2$. We believe that the zero bias anomalies can give more reliable information concerning $P_d$. The magnitude of these anomalies for Co nanoconstrictions [27] of the same type as mentioned above corresponds to a presence of several tens of TLS at the energy region about 1 meV [27, 18]. Correspondingly, one obtains $P_d \sim (3-5) \times 10^{34}$ erg$^{-1}$cm$^{-3}$. Based on these estimates and taking $P_d \approx 10^{34}$ erg$^{-1}$cm$^{-3}$, $\sigma_{\rm in} \approx 10^{-15}$ cm$^2$, $v_F \approx 10^8$ cm/s, and $\Lambda_0 \approx 10$ mK we obtain $\tau_\Lambda \approx 10^{-9}$ s and $T_\Lambda \simeq \Lambda_0$. Thus at temperatures

larger than $T_\Lambda \approx \Lambda_0 \approx 10$ mK one expects, according to Eq. (7), temperature-independent contribution of resonant processes.

For the relaxation channel, one obtains $T_\alpha \approx T_\beta \approx 10$ mK. Consequently, at $T \gtrsim T_\alpha \approx T_\Lambda \approx 10$ mK one expects that dephasing rate obeys Eq. (9) with $\tau_\Lambda \approx 10^{-9}$ s.

Summarizing, we can conclude that for realistic parameters of the dynamic defects one can indeed expect a slow temperature dependence of the dephasing rate given by Eq. (9) crossing over to a rapid decrease at low temperatures. The crossover temperature, as well as the behavior below that temperature, depends on the distribution of $\Lambda$. For a delta-like distribution (6) the TLS spectrum has a gap of $\Lambda_0$. Thus the TLS contribution to dephasing rate is exponentially frozen out at for $T < \Lambda_0$, and we are left with the "standard" mechanisms like electron-electron scattering.

Although some papers, e. g. Refs. [9, 28], stated that to explain the dephasing saturation by a TLS contribution one would need an unreasonably large concentration of the TLS, this conclusion was mainly based on the "glassy" model of the TLS while we exploited the tunneling state model of Refs. [18, 20]. In general, to obtain independent information concerning the TLS concentration based on "bulk" measurements like acoustic measurements or heat capacity measurements in conductors is rather difficult due to a presence of electronic contributions. In particular, the value $P_d \sim 10^{34}$ erg$^{-1}$ cm$^{-3}$ exploited above is still less than the electron density of states ($\sim 10^{35}$ erg$^{-1}$cm$^{-3}$ for Co) and so the TLS are not expected to affect significantly the properties of the material, like heat capacity.

It is worthwhile to mention that similar ideas were used to explain the magnetoresistance of polymers [30]. Polymer systems exhibiting rather large fraction of free volume are expected to form readily mobile and metastable defects of different types.

To conclude, we have shown that the dynamic defects can be responsible for the slowing down of the temperature dependence of the dephasing rate at low temperatures.

There are two mechanisms of dephasing. The first one corresponds to direct inelastic scattering of electrons by the defects, while the second one is due to violation of the time reversal symmetry caused by fluctuations of the scattering potential. The first mechanism can indeed lead to the saturation, while the second one still contains a temperature dependence although a weak one. However, when $T \lesssim \Lambda_0$ the dephasing rate rapidly tends to 0.

We thank Y. Imry for discussions. This research is partly supported by the Norwegian Research Council and partly by the US DOE Office of Science under contract No. W-31-109-ENG-38.

## References


1. E. Buks, R. Schuster, M. Heiblum, D. Mahalu, V. Umansky and H. Shtrikman, Phys. Rev. Lett. **77**, 4664 (1996).
2. A. Yacoby, M. Heiblum, D. Mahalu, Hadas Shtrikman, Phys. Rev. Lett. **74**, 4047 (1995).
3. P. Mohanty, E. M. Q. Jariwala, and R. A. Webb, Phys. Rev. Lett. **78**, 3366 (1997).
4. D. S. Golubev and A. D. Zaikin, Phys. Rev. Lett. , **81**, 1074 (1998).
5. I. L. Aleiner, B. L. Altshuler, and M. E. Gershenson, Phys. Rev. Lett. **82**,3190 (1999).
6. P. Mello, Y. Imry, B. Shapiro, Phys. Rev. B **61**, 16570 (2000).
7. Y. Imry, H. Fukyama, and P. Schwab, Europhys. Letters, **47**, 608 (1999).
8. A. Zawadowski, Jan von Delft and D. C. Ralph, Phys. Rev. Lett. **83**, 2632 (1999).
9. Kagn-Hun Ahn, P. Mohanty, Phys. Rev. B **63**, 195301 (2001)
10. P. W. Anderson, B. I. Halperin, and C. M. Varma, Philos. Mag. **25**, 1 (1972).
11. J. L. Black, in *Glassy Metals 1*, edited by H. J. Günterodt and H. Beck (Springer, Berlin 1981).
12. V. V. Afonin, J. Bergli, Y. M. Galperin, V. L. Gurevich, V. I. Kozub, Phys. Rev. B (in press), cond-mat/0205438.
13. A. Stern, Y. Aharonov, and Y. Imry, Phys. Rev. B **41**, 3436 (1990); Y. Imry, *Introduction to Mesoscopic Physics*, (Oxford University Press, 1997).
14. P. Schwab, Eur. Phys. J. B **18**, 189 (2000)
15. B. L. Altshuler, A. G. Aronov, and D. E. Khmelnitskii, J. Phys. C **15**, 7367 (1982); see also B. L. Altshuler, A. G. Aronov, A. I. Larkin, D. E. Khmelnitskii, Sov. Phys. JETP **54**, 411 (1981). [Zh. Eksp. Teor. Fiz. **81**, 768 (1981)].
16. V. V. Afonin, Y. M. Galperin, and V. L. Gurevich, Sov. Phys. JETP **61**,1130 (1985)[Zh. Eksp. Teor. Fiz. **88** 1906 (1985)].
17. V. V. Afonin, Y. M. Galperin, and V. L. Gurevich, Phys. Rev. B **40**, 2598 (1989).
18. V. I. Kozub and A. M. Rudin, Phys. Rev. B **55**, 259 (1997).
19. Y. Imry, in: *Tunneling in Solids, Proceedings of the 1967 NATO Conference.* edited by E. Burstein and S. Lundquist (Plenum Press, New York) ch. 35 (1969).
20. W. A. Phillips, Phys. Rev. Lett. **61**, 2632 (1988).
21. A. A. Abrikosov, Physics **2** 21(1965).
22. S. V. Maleev, Sov. Phys. JETP, **57**, 149 (1983)[Zh. Eksp. Teor. Fiz. **84**, 260 (1983)].
23. S. V. Maleev, Theor. and Math. Physics, **4**, 694 (1970) [Teor. Mat. Fiz. **4**, 86 (1970)].
24. G. C. Evans, Rend. R./Accad. dei Lincei **20**, 453 (1911).
25. W. A. Phillips, J. Low Temp. Phys. **7**, 351 (1972).
26. K. S. Ralls and R. A. Buhrman, Phys. Rev. Lett. **60**, 2434 (1988)
27. D. C. Ralph and R. A. Buhrman, Phys. Rev. Lett. **69**, 2118 (1992).
28. I. L. Aleiner, B. L. Altshuler, Y .M. Galperin, Phys. Rev. B **63**, 201401(R) (2001).
29. I. L. Aleiner, B. L. Altshuler, Y. M. Galperin, and T. A. Shutenko, Phys. Rev. Lett. **86**, 2629 (2000).
30. A. N. Aleshin, V. I. Kozub, D.-S. Suh, Y. W. Park, Phys. Rev. B **64** (2001).

# Momentum–resolved tunneling: Spectroscopic tool and basis for device applications

M. Governale and U. Zülicke
*Institut für Theoretische Festkörperphysik,*
*Universität Karlsruhe, D-76128 Karlsruhe, Germany*

**Abstract.** Recent advances in nanofabrication techniques have enabled the creation of extended uniform tunnel barriers between low–dimensional electron systems. Translational invariance implies approximate conservation of the component of canonical momentum parallel to the barrier in a single tunneling event. We briefly review possibilities to utilize momentum–resolved tunneling for novel spectroscopic and device applications. In particular, it is shown how the interplay between momentum–resolved tunneling and spin–orbit coupling enables the design of a novel spin–filter device without using magnets.

## 1. Introduction

Tunneling spectroscopy has long been a premier tool for investigating electronic properties of solids [Wolf, 1985]. While tunneling is basically a one–particle process, the probability for it to happen depends sensitively on electron correlations. It is easiest to use a perturbative picture to elucidate this. A system with two separate parts labelled, e.g., L and R coupled by a barrier is left in an excited many–body state after the transfer of an electron between L and R. Assuming both subsystems to be independent except for the tunnel coupling, one of them (e.g., R) will be in an electron–like excited state with energy $\varepsilon$, and the other one (L) in a hole–like excited state with energy $\varepsilon'$. Energy conservation requires the total excitation energy to equal the electrochemical–potential difference at the barrier: $\varepsilon + \varepsilon' = \mu_{\rm L} - \mu_{\rm R} \equiv -eV$. (See Fig. 1.) The tunneling current $I(V)$ is a measure for the number of excited states of the total system in an energy window $|eV|$ that are compatible with an electron having tunneled from one subsystem to the other. It reads explicitly [Mahan, 1990]:

$$I(V) = \frac{e}{\hbar} \sum_{\substack{\{q_{\rm L}\} \\ \{q_{\rm R}\}}} \left| t^{\{q_{\rm R}\}}_{\{q_{\rm L}\}} \right|^2 \int \frac{d\varepsilon}{2\pi} \mathcal{A}_{\rm L}\left(\{q_{\rm L}\}, \varepsilon + eV\right) \mathcal{A}_{\rm R}\left(\{q_{\rm R}\}, \varepsilon\right) \left[f_{\varepsilon+eV} - f_\varepsilon\right]. \tag{1}$$

Here $e$ denotes the electron's charge, and $f_\varepsilon = 1/(\exp\{\varepsilon/k_{\rm B}T\} + 1)$ the Fermi function. The quantity $\mathcal{A}_\alpha\left(\{q_\alpha\}, \varepsilon\right)$ is the single–electron spectral function for system $\alpha$ in the representation of one–body states



*R. Fazio et al. (eds.), New Directions in Mesoscopic Physics,* 269–279.
© 2003 *Kluwer Academic Publishers. Printed in the Netherlands.*

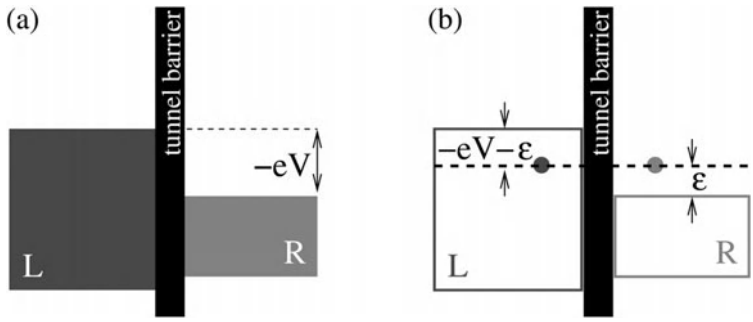


*Figure 1.* Two metallic systems, labelled L and R, are coupled via a tunnel barrier. (a) Initially, both systems are in their respective ground states. Then a voltage $V > 0$ is applied. (b) Upon tunneling of an electron from L to R, the L system ends up in an excited state with one quasihole, while the R system is in an excited quasielectron state. The total excitation energy equals $-eV$. When the two systems are also coupled by interactions, more complicated many–body excited states may be generated.

labelled by the set of quantum numbers $\{q_\alpha\}$. Formally defined as $-2$ times the imaginary part of the retarded single–electron Greens function [Mahan, 1990], the spectral function has a clear physical meaning: $\mathcal{A}_\alpha\left(\{q_\alpha\},\varepsilon\right)\frac{d\varepsilon}{2\pi}$ is the probability to find the system $\alpha$ in an excited state with energy in the interval $\varepsilon\ldots\varepsilon+d\varepsilon$ after an electron with quantum numbers $\{q_\alpha\}$ has been added to it. In a noninteracting system $\alpha$ with electrochemical potential $\mu_\alpha$, $\mathcal{A}_\alpha^{(0)}\left(\{q_\alpha\},\varepsilon\right)=2\pi\delta(\varepsilon+\mu_\alpha-E_{\{q_\alpha\}})$ if $\{q_\alpha\}$ is a one–body eigenstate with energy $E_{\{q_\alpha\}}$. The matrix elements $t_{\{q_{\rm L}\}}^{\{q_{\rm R}\}}$ for tunneling of an electron from the state $\{q_{\rm L}\}$ in subsystem L to the state $\{q_{\rm R}\}$ in subsystem R is determined by, e.g., geometric, details of the tunnel barrier. For example, consider a point contact between two metals in zero magnetic field where electron states are labelled by spin $\sigma$ and wave vector $\vec{k}$. Spatial localization of a tunneling electron in the point contact implies approximately constant tunneling matrix elements in reciprocal space, i.e., $t_{\vec{k}\sigma}^{\vec{k}'\sigma'}\approx t\,\delta_{\sigma\sigma'}$. In this case, $I(V)$ cannot display any momentum–resolved features and is only measuring the so–called tunneling density of states $\mathcal{N}_\alpha(\varepsilon)=\sum_{\vec{k}}\mathcal{A}_\alpha\left(\vec{k},\varepsilon\right)$.

As soon as the barrier is extended and uniform in one or more spatial directions, translational invariance implies conservation of the component $\vec{p}_\parallel$ of canonical momentum parallel to the barrier. This additional selection rule severely restricts phase space for tunneling and can result in strong resonances[1] exhibited by tunneling conduct-

[1] An example to the contrary will be mentioned in Sec. 3 below.

ances. Such resonances have been used to measure subband energies in 2D [Smoliner et al., 1989] and 1D [Eugster et al., 1994] electron systems as well as the band structure of 1D superlattices [Kardynał et al., 1996]. The possibility to tune canonical momentum $\vec{p}$ versus kinetic momentum $\vec{\pi} = \vec{p} - e\vec{A}(\vec{r}_\perp)$ by an external magnetic field $\vec{B} = \vec{\nabla} \times \vec{A}(\vec{r}_\perp)$ opened up a new arena for truly momentum–resolved tunneling spectroscopy. ($\vec{r}_\perp$ is perpendicular to the barrier.) For example, 2D Fermi surfaces were mapped [Eisenstein et al., 1991], the life time of 2D Fermi–liquid quasiparticles measured [Murphy et al., 1995], and the shape of 1D [Kardynał et al., 1997] and 0D [Vdovin et al., 2000] quantum confinement determined quantitatively. Most recently, the method of cleaved–edge overgrowth [Pfeiffer et al., 1990] was used to create uniform extended tunnel barriers between parallel quantum wires [Auslaender et al., 2002] and mutually perpendicular 2D quantum wells [Huber et al., 2001]. Progress in nanofabrication techniques has inspired theoretical works [Altland et al., 1999; Zülicke and Governale, 2002; Carpentier et al., 2002] proposing momentum–resolved tunneling probes to directly observe the, so far elusive, dynamical separation of the electron's spin and charge degrees of freedom that is expected [Voit, 1994] to occur in interacting 1D electron systems. In a similar spirit, it was suggested [Zülicke and MacDonald, 1996; Zülicke et al., 2002] to verify chiral–Luttinger–liquid behavior [Wen, 1992] of quantum–Hall edge states in a momentum–resolved tunneling setup.

Here we focus on two examples of novel momentum–resolved tunneling geometries. In the following Section 2, we discuss how electronic dispersion relations can be obtained in tunnel–coupled parallel quantum wires. In Sec. 3, it is described how Landau levels for a 2D electron system in a perpendicular magnetic field can be measured from tunneling resonances in mutually perpendicular quantum wells. As an example for interesting device applications, we show the design of a spin filter involving no magnets at all in Sec. 4 before presenting our conclusions.

All results presented here are based on a perturbative treatment of tunneling. We would like to remark that, for ideal momentum–resolved tunneling geometries, such an approach cannot be justified [Jungwirth and MacDonald, 1996; Boese et al., 2001]. Only if momentum conservation is actually violated on a scale larger than $|t|/(\hbar v)$ where $v$ is the characteristic velocity of electrons parallel to the barrier does it make sense to use Eq. (1). In a ballistic system, this implies that the barrier length has to be $\ll \pi\hbar v/|t|$. Otherwise, electrons will be able to tunnel coherently back and forth between the two systems before being swept out to external reservoirs.

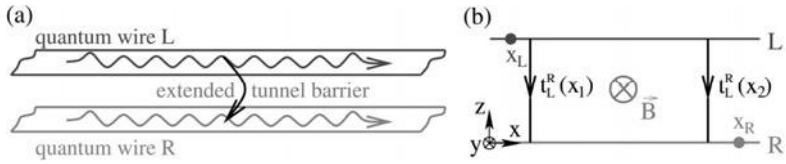


*Figure 2.* System of two tunnel–coupled parallel quantum wires. (a) In contrast to a point–like barrier, electrons tunnel between extended plane–wave states with the same 1D wave number in the L and R wires. (b) The tunneling matrix element in real space has uniform modulus but a spatially varying phase factor that is proportional to the strength of the perpendicular magnetic field. This ensures that quantum amplitudes for any two tunneling paths between arbitrary fixed locations $x_{\rm L}$ and $x_{\rm R}$ differ by a phase proportional to the enclosed flux, as prescribed by the Aharonov–Bohm effect.

## 2. Quasiparticle–dispersion spectroscopy in quantum wires

A system of two parallel tunnel–coupled quantum wires, shown schematically in Fig. 2(a), is an ideal example for the power of momentum–resolved tunneling. Translational invariance implies conservation of 1D canonical momentum or, equivalently, uniformity of the matrix element for tunneling from the L wire to the R wire in real space. In an external magnetic field that is perpendicular to the wires' plane, the real–space tunneling matrix element aquires a nontrivial coordinate–dependent phase factor: $t_{\rm L}^{\rm R}(x) = t\exp\{ieBx(z_{\rm L} - z_{\rm R})/\hbar\}$. This can be easily understood by referring to the Aharonov–Bohm phases accumulated for different tunneling paths; see Fig. 2(b). Expressing tunneling matrix elements in reciprocal space yields $t_{k_{\rm L}\sigma}^{k_{\rm R}\sigma'} = t\,\delta_{k_{\rm R}+p_B,k_{\rm L}}\delta_{\sigma\sigma'}$, with $p_B = -eBd/\hbar$. (Here $d = z_{\rm L} - z_{\rm R}$ is the wire separation.) Tunability of the momentum transfer $\hbar p_B$ in a single tunneling event is the basis for momentum–resolved tunneling spectroscopy. Let us assume, for the moment, zero temperature, Fermi–liquid–like quasiparticle excitations in the two wires with dispersions $E_{\rm L,R}(k,\sigma)$ which, per definition, include any band shifts due to applied voltages, and neglect life–time broadening. Inspection of Eq. (1) reveals that only those pairs of states $\{\vec{k}_{\rm R},\sigma\}$, $\{\vec{k}_{\rm L},\sigma'\}$ from the two wires contribute to the tunneling current for which (i) $\sigma = \sigma'$, (ii) $k_{\rm L} = k_{\rm R} + p_B$, (iii) $E_{\rm L}(k_{\rm L},\sigma) = E_{\rm R}(k_{\rm R},\sigma')$, and (iv) $E_{\rm L}(k_{\rm L},\sigma) \in [\mu_{\rm R},\mu_{\rm L}]$. It is instructive to visualize conditions (ii) and (iii) by plotting the quasiparticle dispersions as a function of $k_{\rm R}$. This is done in Fig. 3(a) for the case where applied voltages are entirely absorbed into shifts of the electronic band bottoms. Conditions (ii) and (iii) are fulfilled for those states where the dispersion curves in that plot coincide. If such a state is occupied in one wire and empty in the other one, i.e., condition (iv) is fulfilled, that state will contribute

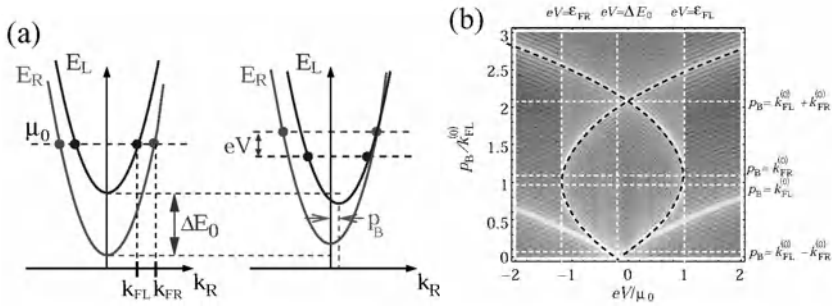


*Figure 3.* Simultaneous conservation of energy and momentum results in strong resonances in the differential tunneling conductance that map electronic quasiparticle dispersions in Fermi–liquid wires. (a) Coincidences of the wires' dispersion curves can be induced by applying a magnetic field and/or a voltage. Shown here is the case where a voltage induces band shifts only, i.e., the wires are never charged. (b) Logarithmic gray–scale plot of the calculated differential tunneling conductance as a function of the magnetic–field–induced momentum transfer $p_B$ and transport voltage $V$. Special points are identified that allow for determination of wire parameters as, e.g., density and Fermi energy in the ideal case when no charging occurs in response to applied voltages, and when the finite width of the wires can be neglected. The width of resonant features is determined by the finite length of the barrier ($100/k_{FL}$ here).

to the tunneling current. Hence, whenever a Fermi point of one wire coincides with the dispersion curve of the other, the current is suddenly switched on (off) because condition (iv) is satisfied for the first time (not anymore). This will lead to strong resonant features in the differential tunneling conductance $dI/dV$ that map, as a function of magnetic field and transport voltage, the wires' quasiparticle dispersions. Basically, each of the two Fermi points for a wire acts as a probe for the dispersion curve of the other, creating two identical images of it in the $dI/dV$ that are shifted, in magnetic–field direction, by an amount $2k_{F\alpha}$. In Fig. 3(b), we show a logarithimc gray–scale plot of $|dI/dV|$ calculated from Eq. (1) for the case of a finite–length barrier, parabolic quasiparticle dispersions, and zero charging due to applied voltages. Main resonance lines map the dispersion curves and allow for the direct determination of Fermi wave vectors and energies. Due to the finite size of the barrier, secondary resonances appear that are like fringes in a diffraction pattern.

The ideal situation discussed above enables a momentum–resolved spectroscopy analogous to photoemission. In real experiments, however, several deviations from that ideal behavior are important, which we discuss now. First, wave–vector resolution is limited by momentum–relaxing processes induced, e.g., by the finite barrier length and elastic

scattering from impurities or surface roughness. A finite life time for quasiparticles in the wires also degrades momentum resolution via the broadening of spectral functions. Any resonance features in $dI/dV$ will therefore aquire a finite width $2\pi/L_{\rm rel}$ in their wave–vector dependence, with the length $L_{\rm rel}$ being the smallest among barrier length and scattering mean free paths. Second, low–dimensional systems like quantum wires are no perfect metals and get, in general, charged when connected to external voltage sources [Sablikov et al., 2000]. In the presence of charging, Fermi wave vectors are voltage–dependent and, therefore, the location of tunneling resonances in $p_{\rm B}$–$eV$ space is affected. As a result, the shape of resonance lines in $dI/dV$ changes [Boese et al., 2001]. Finally, at low energies, interacting 1D electron systems exhibit strong non–Fermi–liquid behavior signified, e.g., by a double–peak structure in the electronic spectral function [Voit, 1994]. The two peaks can be associated with the separate dynamics of wave packets formed from independent spin and charge–density fluctuations that are the low–lying excitations in such strongly correlated 1D systems dubbed `Luttinger liquids`. Deviations from simple Fermi–liquid behavior observed in recent experiments [Auslaender et al., 2002; Tserkovnyak et al., 2002] may be a signature of Luttinger–liquid physics.

## 3. Landau–level spectroscopy in mutually orthogonal 2D systems

Tunneling between contacts with different spatial dimensionality can be momentum–resolved [Snell et al., 1987; Kardynał et al., 1997] if the spectral function of the higher–dimensional contact retains a strong dependence on the momentum component $\vec{p}_{\parallel}$ parallel to the barrier after being summed over the components perpendicular to it. (An example where this is `not` the case is tunneling between a 3D Fermi–liquid contact and a 1D system. Summation over transverse wave vectors in the 3D contact yields an energy–independent 2D density–of–states factor, thereby losing momentum resolution despite unbroken translational invariance in the direction parallel to the 1D system.) In recently fabricated samples with mutually orthogonal 2D quantum wells, features of momentum resolution in tunneling has been observed [Huber et al., 2001]. While both systems are 2D, the geometric arrangement implies the conservation of only one momentum component. (See Fig. 4.) If a magnetic field is applied such that it is perpendicular to one of the 2D electron systems (2DES$_\perp$) and parallel to the other one (2DES$_\parallel$), the character of electron states is very different in both systems. Neglecting the finite width of the 2D quantum wells, states in 2DES$_\parallel$ are labelled

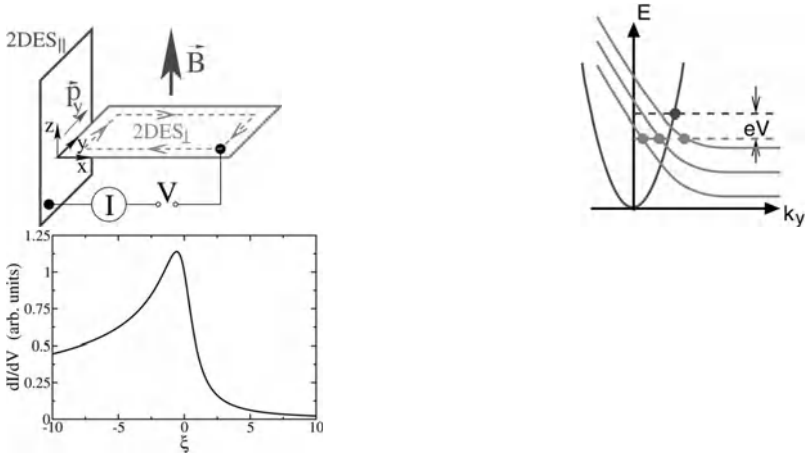


*Figure 4.* Spectroscopy of Landau levels in mutually orthogonal quantum wells. A schematic sample layout is shown in the left panel. The momentum component $p_y$ parallel to the tunnel barrier is conserved. In an external magnetic field perpendicular to one of the 2D systems ($2\mathrm{DES}_\perp$), edge channels run parallel to the tunnel barrier. Each of them corresponds to the Fermi point of a Landau level in $2\mathrm{DES}_\perp$ (middle panel). An effective 1D spectral function of $2\mathrm{DES}_\parallel$ (visualized as the parabola in the middle panel) allows for a direct map of Landau–level dispersions much the same way as in the case of parallel quantum wires. The resonance line shape is different from that case, however, because the tunneling current has contributions from states with different $k_z$. It is shown in the right panel for finite life–time broadening $\hbar/\tau$ in $2\mathrm{DES}_\parallel$. The variable $\xi = 2\tau e[V - V_{\mathrm{res}}(B)]/\hbar$ measures the distance to a resonant–tunneling point $V_{\mathrm{res}}(B)$.

by a 2D wave vector $\vec{k} = (k_y, k_z)$. (We assume full spin polarization of electrons in both quantum wells due to the large applied magnetic field.) In $2\mathrm{DES}_\perp$, quantum numbers of one–body eigenstates are the Landau–level index $n$ and, using the appropriate Landau gauge that preserves translational invariance along the barrier, the guiding–center coordinate $X \equiv k_y \ell^2$. (Here $\ell = \sqrt{\hbar/|eB|}$ is the magnetic length.) Landau–level states with guiding centers located far enough away from the barrier, i.e., having $X \gg \ell$, are degenerate in energy. However, they acquire a dispersion in $X \propto k_y$ close to it [MacDonald and Středa, 1984], as shown schematically in Fig. 4. Each occupied Landau level represents a chiral 1D electron system with a separate Fermi point. In contrast, there exist many states at fixed $k_y < k_{\mathrm{F}\parallel}$ in $2\mathrm{DES}_\parallel$ that simultaneously contribute to tunneling. Assuming the life time of electron

in 2DES$_\perp$ to be large, we find from Eq. (1)

$$I(V) \;=\; e\frac{\sqrt{2m}L_z}{\hbar^2}\sum_{n,k_y}|t_{n,k_y}|^2\mathcal{N}_{1\mathrm{D}}\left(E_\perp(n,k_y\ell^2)-\frac{\hbar^2k_y^2}{2m}-E_{0\|}(V)\right) \times\left[f_{E_\perp(n,k_y\ell^2)-\mu_\|}-f_{E_\perp(n,k_y\ell^2)-\mu_\perp}\right]\;. \quad (2)$$

Here $E_\perp(n,X)$ is the energy of $n^{\mathrm{th}}$–Landau–level eigenstates including the, in general, voltage–dependent energy of the subband bottom in 2DES$_\perp$, $E_{0\|}(V)$ is the subband energy of 2DES$_\|$, and $\mathcal{N}_{1\mathrm{D}}(\varepsilon) = \sum_{k_z}\mathcal{A}_\|(\vec{k},\epsilon)$ denotes the effective 1D density of states obtained from the spectral function for electrons in 2DES$_\|$ after summing over its wave–vector component perpendicular to the barrier. We included the dependence of the tunneling matrix element on $n$ and $k_y$ which is important, however, only for Landau–level states in the bulk of 2DES$_\perp$, i.e., those with guiding–center location $X \equiv k_y\ell^2 \gg \ell$. The peaked line shape of $\mathcal{N}_{1\mathrm{D}}(\varepsilon)$ is directly observed as resonances in the differential tunneling conductance. We show the expected line shape in Fig. 4 for the case when life–time broadening in 2DES$_\|$ is included. Such resonances occur at values of magnetic field and voltage whenever (i) a Landau–level Fermi point coincides with the quasi–1D dispersion $E_\|^{(0)}+\hbar^2k_y^2/2m$, or (ii) the point $k_y = k_{\mathrm{F}\|}$, $k_z = 0$ on the Fermi circle of 2DES$_\|$ coincides with a point on the Landau levels in 2DES$_\perp$. Except for the resonance line shape being much broader, this is analogous to dispersion spectroscopy in the double–wire system of Sec. 2. An exact analog to spin–charge separation in quantum wires occurs when the lowest Landau level is filled to a certain fraction, e.g, 2/5. This should be observable in using the momentum–resolved tunneling setup discussed here [Zülicke et al., 2002].

## 4. Spin filter without magnets

Momentum–resolved tunneling has been suggested as the basis for possible device applications. In particular, assuming the possibility to engineer external control of barrier height and/or width, coherent tunneling of electrons between two parallel wires could be used to build a switching device called directional coupler [del Alamo and Eugster, 1990] or quantum logical gates [Bertoni et al., 2000]. We have recently extended the list of possible applications by proposing the design for a spin–selective device that works without any magnetic part [Governale et al., 2002]. It is based on the interplay between momentum–resolved tunneling between parallel quantum wires and the intrinsic Rashba

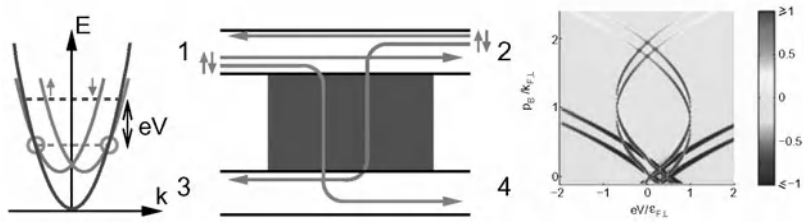


*Figure 5.* Spin filter based on momentum–resolved tunneling between parallel quantum wires. We show here the special case where only one of the wires has a Rashba–spin–split dispersion curve (left panel). Applying a voltage induces crossing points, e.g., for spin–up right–movers and spin–down left–movers. (Circled in the left panel.) Hence, the unpolarized current through the tunnel barrier is separated into spin–up and down parts which end up in opposite terminals (labelled 3 and 4 in the middle panel). Dispersion spectroscopy as described in Sec. 2 would enable direct observation of Rashba spin splitting in quantum wires (right panel).

spin splitting [Bychkov and Rashba, 1984] experienced by electrons in low–dimensional semiconductor structures.

Electrons can be confined in 2D quantum wells created by conduction–band bending in semiconductor heterostructures. If the confinement is asymmetric with respect to inversion in the growth ($z$) direction, an intrinsic spin–orbit coupling of the 2D electrons results [Winkler, 2000] that has the form $H_{\rm so} = \hbar k_{\rm so}\left(\sigma_x p_y - \sigma_y p_x\right)/m$ with a characteristic momentum scale $\hbar k_{\rm so}$. Further confinement of electronic motion results in the formation of a quantum wire with spin–split subbands. To elucidate our spin–filter design, we consider here the simplest case of an ideal, i.e., zero–width 1D system which has a dispersion relation $E(k,\sigma) = E_0 - \Delta_{\rm so} + \hbar^2(k - \sigma k_{\rm so})^2/2m$. Here $\Delta_{\rm so} = \hbar k_{\rm so}^2/2m$, and the spin quantization axis of eigenstates is perpendicular to the wire. Dispersion curves for the two spin species are uniformly shifted in wave–vector direction. Addressing them separately can be done most effectively using a momentum–selective method.

One possible way is illustrated in Fig. 5. Its essential ingredient consists of two parallel tunnel–coupled quantum wires having a different Rashba spin splitting. We assume in the following that only one of the wires has a Rashba–split dispersion while the other one is spin degenerate. Application of a transport voltage induces crossing points, simultaneously allowing tunneling for, e.g., spin–up right–movers and spin–down left–movers. (At a different voltage, the direction of propagation for spin species allowed to tunnel will be reversed.) Sufficient momentum selectivity for addressing different spin bands requires the momentum–relaxation length $L_{\rm rel}$ of Sec. 2 to be larger than $\pi/\Delta k_{\rm so}$ where $\Delta k_{\rm so}$ is the difference of Rashba spin splittings in

the two wires. Then electrons ending up in opposite terminals of the receiving wire will have opposite spins. The tunnel barrier acts as a spin splitter, and a Stern–Gerlach–type experiment can be performed by switching on a voltage instead of a magnetic field.

In the context of spintronics [Wolf et al., 2001], nonmagnetic spin filters are an intriguing and, perhaps, useful alternative. In addition to potential device applications, a direct mapping of spin–spit dispersion curves would enable the first direct observation and study of the Rashba effect [Bychkov and Rashba, 1984] in semiconductor nanostructures.

## 5. Conclusions

Momentum–resolved tunneling enables detailed study of electronic excitations in low–dimensional systems. In particular, dispersion curves for quantum wires and quantum–Hall edge states can be directly measured. Spin splitting due to the Rashba effect can be utilized to separate the tunneling current between parallel quantum wires into spin–polarized parts.

## Acknowledgment

We thank D. Boese, A. Rosch, C. Schroll, and E. Shimshoni for collaborating with us on projects related to momentum–resolved tunneling and numerous other colleagues for discussions. Financial support from DFG within the Center for Functional Nanostructures is gratefully acknowledged.

## References

Altland, A., C. H. W. Barnes, F. W. J. Hekking, and A. J. Schofield: 1999, *Phys. Rev. Lett.* **83**, 1203–1206.

Auslaender, O. M., A. Yacoby, R. de Picciotto, K. W. Baldwin, L. N. Pfeiffer, and K. W. West: 2002, *Science* **295**(5556), 825–828.

Bertoni, A., P. Bordone, R. Brunetti, C. Jacoboni, and S. Reggiani: 2000, *Phys. Rev. Lett.* **84**, 5912–5915.

Boese, D., M. Governale, A. Rosch, and U. Zülicke: 2001, *Phys. Rev. B* **64**, 085315.

Bychkov, Y. A. and E. I. Rashba: 1984, *J. Phys. C* **17**, 6039–6045.

Carpentier, D., C. Peça, and L. Balents: 2002, *Phys. Rev. B* **66**, 153304.

del Alamo, J. A. and C. C. Eugster: 1990, *Appl. Phys. Lett.* **56**, 78–80.

Eisenstein, J. P., T. J. Gramila, L. N. Pfeiffer, and K. W. West: 1991, *Phys. Rev. B* **44**, 6511–6514.

Eugster, C. C., J. A. del Alamo, M. J. Rooks, and M. R. Melloch: 1994, *Appl. Phys. Lett.* **64**, 3157–3159.

Governale, M., D. Boese, U. Zülicke, and C. Schroll: 2002, *Phys. Rev. B* **65**, 140403(R).

Huber, M., M. Grayson, M. Rother, R. Deutschmann, W. Biberacher, W. Wegscheider, M. Bichler, and G. Abstreiter: 2001, *Physica E* **12**, 125–128.

Jungwirth, T. and A. H. MacDonald: 1996, *Phys. Rev. B* **53**, 7403–7412.

Kardynał, B., C. H. W. Barnes, E. H. Linfield, D. A. Ritchie, K. M. Brown, G. A. C. Jones, and M. Pepper: 1996, *Phys. Rev. Lett.* **76**, 3802–3805.

Kardynał, B., C. H. W. Barnes, E. H. Linfield, D. A. Ritchie, J. T. Nicholls, K. M. Brown, G. A. C. Jones, and M. Pepper: 1997, *Phys. Rev. B* **55**, R1966–R1969.

MacDonald, A. H. and P. Středa: 1984, *Phys. Rev. B* **29**, 1616–1619.

Mahan, G. D.: 1990, *Many-Particle Physics*. New York: Plenum Press.

Murphy, S. Q., J. P. Eisenstein, L. N. Pfeiffer, and K. W. West: 1995, *Phys. Rev. B* **52**, 14825–14828.

Pfeiffer, L., K. W. West, H. L. Störmer, J. P. Eisenstein, K. W. Baldwin, D. Gershoni, and J. Spector: 1990, *Appl. Phys. Lett.* **56**, 1697–1699.

Sablikov, V. A., S. V. Polyakov, and M. Büttiker: 2000, *Phys. Rev. B* **61**, 13763–13773.

Smoliner, J., W. Demmerle, G. Berthold, E. Gornik, G. Weimann, and W. Schlapp: 1989, *Phys. Rev. Lett.* **63**, 2116–2119.

Snell, B. R., K. S. Chan, F. W. Sheard, L. Eaves, G. A. Toombs, D. K. Maude, J. C. Portal, S. J. Bass, P. Claxtona, G. Hill, and M. A. Pate: 1987, *Phys. Rev. Lett.* **59**, 2806–2809.

Tserkovnyak, Y., B. I. Halperin, O. M. Auslaender, and A. Yacoby: 2002, *Phys. Rev. Lett.* **89**, 136805.

Vdovin, E. E., A. Levin, A. Patanè, L. Eaves, P. C. Main, Yu. N. Khanin, Yu. V. Dubrovskii, M. Henini, and G. Hill: 2000, *Science* **290**(5489), 122–124.

Voit, J.: 1994, *Rep. Prog. Phys.* **57**, 977–1116.

Wen, X. G.: 1992, *Int. J. Mod. Phys. B* **6**, 1711–1762.

Winkler, R.: 2000, *Phys. Rev. B* **62**, 4245.

Wolf, E. L.: 1985, *Principles of Electron Tunneling Spectroscopy*, Vol. 71 of *International Series of Monographs in Physics*. New York: Oxford University Press.

Wolf, S. A., D. D. Awschalom, R. A. Buhrmann, J. M. Daughton, S. von Molnár, M. L. Roukes, A. Y. Chtchelkanova, and D. M. Treger: 2001, *Science* **294**, 1488–1495.

Zülicke, U. and M. Governale: 2002, *Phys. Rev. B* **65**, 205304.

Zülicke, U. and A. H. MacDonald: 1996, *Phys. Rev. B* **54**, R8349–R8352.

Zülicke, U., E. Shimshoni, and M. Governale: 2002, *Phys. Rev. B* **65**, 241315(R).

# Edge states and quantum Hall effects in d+id' superconductors

Baruch Horovitz and Anatoly Golub
*Department of Physics, Ben-Gurion University of the Negev Beer-Sheva 84105, Israel*

**Abstract.** Broken time reversal symmetry (BTRS) in d wave superconductors is studied and is shown to yield current carrying surface states. We evaluate the temperature and thickness dependence of the resulting spontaneous magnetization and show a marked difference between weak and strong BTRS. We also derive the Hall conductance which vanishes at zero wavevector $q$ and finite frequency $\omega$, however at finite $q, \omega$ it has an unusual structure. The chirality of the surface states leads to quantum Hall effects for spin and heat transport. Simulations of a network model show a new universality class for the corresponding Hall transition.

## 1. Introduction

Recent data on the high $T_c$ superconductor $YBa_2Cu_3O_x$ (YBCO) has supported the presence of broken time reversal symmetry (BTRS) [1, 2, 3]. A d wave superconductor would show Andreev bound states at zero bias, however tunnelling data shows in some cases states away from zero bias [1, 2], in particular in overdoped YBCO [2], consistent with BTRS. Spontaneous magnetization in the absence of an external field has been observed in YBCO [3], setting in abruptly at $T_c$ and is almost temperature ($T$) independent below $T_c$. The phenomenon has been attributed to either a $d_{x^2-y^2} + id_{xy}$ state or to formation of $\pi$ junctions. No microscopic reason was given, however, for the spontaneous magnetization being independent of both $T$ and of film thickness [3].

It has been shown theoretically that BTRS can occur locally in a $d_{x^2-y^2}$ superconductor at certain surfaces [8, 9, 10] or it is due to the paramegnetic nature of the surface states [6, 7]. In both cases the onset of such BTRS is expected to be well below $T_c$ and therefore does not correspond to the spontaneous magnetization data [3].

Of further theoretical interest is the relation of the BTRS state to quantum Hall systems with a variety of Hall effects [11, 12, 13, 14, 15]. In particular a finite charge hall conductance has been suggested [11], though this has been questioned [14].

In the present work we assume that BTRS is a bulk property, i.e. both components of an order parameter $d_{x^2-y^2} + id_{xy}$ set in at $T_c$; this is a plausible scenario which can account for the data. In section 2 we



*R. Fazio et al. (eds.), New Directions in Mesoscopic Physics,* 281–290.
© 2003 *Kluwer Academic Publishers. Printed in the Netherlands.*

discuss properties of the surface currents. In previous works [8, 9, 10] surface states appear due to a surface induced $id_{xy}$ component. We find, however, the less anticipated result that the bulk state $d_{x^2-y^2} + id_{xy}$ leads to surface states with finite surface current densities. The latter situation was found in the bulk p wave state [16] and for the total current was inferred from topological considerations [17]. We then evaluate the spontaneous magnetization and show that it is dominated by (100) surfaces; for thin films it increases with the ratio $\Delta'/\Delta$ ($\Delta$ and $\Delta'$ are the amplitudes of $d_{x^2-y^2}$ and $d_{xy}$, respectively) while for thick films it has a maximum at $\lambda/\xi' \approx 1$ where $\xi, \xi'$ are the coherence lengths associated with $\Delta$, $\Delta'$, respectively ($\xi'$ =Fermi velocity/$\Delta'$, similarly for $\xi$) and $\lambda$ is the magnetic penetration length. The maximum for YBCO is at $\Delta'/\Delta \approx \xi/\lambda \approx 0.01$. Throughout we assume an exterme type II superconductor, i.e. $\xi \ll \lambda$, while $\xi'/\lambda$ is arbitrary. We show that for weak BTRS, $\lambda/\xi' < 1$, the spontaneous magnetization is $T$ and thickness independent, while for strong BTRS thickness and $T$ dependence may occur, as well as a transition to a paramagnetic state close to $T_c$. For the sample of Ref [3] we estimate $\Delta'/\Delta \approx 10^{-4}$, i.e. weak BTRS.

In section 3 we derive the effective action and identify the Hall coefficient which has an unusual wavevector and frequency dependence. We also discuss the quantum Hall effect associated with spin and heat transport. At weak disorder the Hall conductance has two units of a quantized value; as disorder increases the Hall conductance jumps to zero. This quantum Hall transition is of a new universality class. In presence of a electron-hole symmetry breaking the transition splits into two transitions of one unit each, belonging to the universality class of the conventional quantum Hall effect.

## 2. edge states

Consider the Bogoluibov-de Gennes (BdG) Hamiltonian for a singlet superconductor

$$\mathcal{H}_S = \sum_{ij} \begin{pmatrix} c^\dagger_{i\uparrow} & c_{i\downarrow} \end{pmatrix} \begin{pmatrix} h_{ij} & \Delta_{ij} \\ \Delta^*_{i,j} & -h^T_{ij} \end{pmatrix} \begin{pmatrix} c_{j\uparrow} \\ c^\dagger_{j\downarrow} \end{pmatrix} \tag{1}$$

where $c^\dagger$, $c$ are creation and annihilation operators for electrons at sites $i, j$ with spin $\uparrow$ or $\downarrow$. $h_{ij}$ is the Hamiltonian in the normal state, including a vector potential, while $\Delta_{ij} \sim \langle c_{i\uparrow} c_{j\downarrow} \rangle$ is the superconducting order parameter. For singlet pairing $\langle c_{i\uparrow} c_{j\downarrow} \rangle = -\langle c_{i\downarrow} c_{j\uparrow} \rangle = \langle c_{j\uparrow} c_{i\downarrow} \rangle$, hence $\Delta_{ij} = \Delta_{ji}$ is symmetric while $h_{i,j}$ is hermitian . The Hamiltonian has

therefore the symmetry $\mathbf{Q}\mathcal{H}_S\mathbf{Q}^{-1} = -\mathcal{H}_S$, where here $\mathbf{Q} = i\tau_y K$, $\tau_y$ acts on the particle-hole spinor of Eq. (1) and $K$ is complex conjugation. This symmetry identifies the system as class C ensemble in the scheme of Altland and Zirnbauer [18]. We will return to this general Hamiltonian in section 3, while here we consider a clean system with a surface. Fourier transforming the relative coordinates $i-j$ gives the dependence on momentum $\mathbf{k} = k_F(\cos\zeta, \sin\zeta)$, where $k_F$ is the Fermi momentum and $\zeta$ is the angle on the Fermi circle. For a d wave superconductor

$$\Delta(\zeta) = \Delta \sin(2\zeta) \tag{2}$$

The d wave is maximal along the principal axes, hence its lobes are at angle $\zeta = \pm\pi/4$ relative to a (110) surface as shown in Fig. 1. Under specular reflection from the (110) surface $\zeta \to -\zeta$ so that $\Delta(\zeta)$ changes sign. This scenario is well known from $\pi$ junctions leading to a bound state at energy $\epsilon = 0$. All incident angles yield the same zero energy which results in a strong zero bias anomaly in tunneling data. The eigenfunctions decay as $\exp[-x|\sin\zeta|/\xi]$ where $\xi = v_F/\Delta$ and $x$ is a coordinate perpendicular to the surface. The presence of BTRS is signalled by a complex order parameter of the form

$$\Delta(\zeta) = \Delta \sin(2\zeta) + i\Delta' \cos(2\zeta)\,. \tag{3}$$

The zero energy condition $\Delta(\zeta) = -\Delta(-\zeta)$ is now satisfied only at $\zeta = \pm\pi/4$. This symemtry breaking is maximal at $\zeta = \pm\pi/4$ is $\Delta'$; hence the positive energy solutions cover the range $0 < \epsilon < \Delta'$. A detailed solution of the corresponding BdG equations is given in Ref. [19].

The symmetry under sign change of $k_y$ is now broken and the states are current carrying. Both branches near $\epsilon = 0$ increase with $k_y$ demonstrating the chiral nature of these edge states.

In presence of a (100) surface Fig. 1 applies with $\Delta$ and $\Delta'$ interchanged. The spectrum now extends in the much bigger range $0 < \epsilon < \Delta$, the eigenfunctions decay more slowly as $\exp[-x|\sin\zeta|/\xi']$ where $\xi' = v_F/\Delta'$, the currents are larger and so is the spontaneous magnetization. For the expectation value of the current density in the y direction and the charge density at temperature $T$ we obtain [19]

$$\begin{aligned}
\frac{4\pi}{c} j_{edge}(x) &= \frac{4\phi_0}{\pi\xi'\lambda_0^2}\int_0^{\pi/2} d\zeta \cos\zeta \sin^2\zeta e^{-2x\sin\zeta/\xi'} \times \\
&\quad \tanh\left(\frac{\Delta\cos 2\zeta + (e/c)v_F \sin\zeta A_y(x)}{2T}\right) \\
n_{edge}(x) &= \frac{ek_F}{\pi d\xi'}\int_0^{\pi/2} d\zeta \cos\zeta \sin\zeta e^{-2x\sin\zeta/\xi'}
\end{aligned} \tag{4}$$

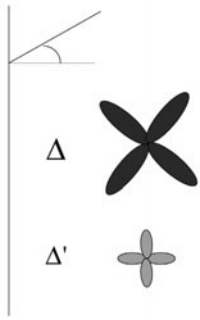


*Figure 1.* d and d' wave order parameters near a (110) boundary. For a (100) boundary interchange $\Delta$ and $\Delta'$.

where $A_y$ is a vector potential, $\lambda_0 = (mc^2 d/2k_F^2 e^2)^{1/2} = \lambda(T=0)$ is the $T=0$ penetration length , m is the electron mass and $d$ is the spacing between layers. We note that the integrated current $\int_0^\infty j_{edge}(x)dx$ vanishes, unlike the p wave case [16].

We solve next London's equation for which $j_{edge}(x)$ is a source term with boundary condition of zero magnetic field,

$$-\nabla^2 A_y(x) = [-(1/\lambda^2)A_y(x) + (4\pi/c)j_{edge}(x)]\theta(x) \tag{5}$$

where $\theta(x)$ is a step function.

We consider solutions where the Doppler shift $\sim A_y$ on the right hand side of Eq (4) is neglected; [the latter may be observable as a paramagnetic effect near $T_c$ in thin films [19]]. This is solved by the Greens' function $G(x,x') = -(\lambda/2)[\exp(-|x-x'|/\lambda)+\exp(-|x+x'|/\lambda)]$ resulting at $T \to T_c$ in the solution

$$A_y(0) = (2\phi_0\lambda\Delta/\pi\lambda_0^2 T_c)\int_0^{\pi/2} d\zeta \cos\zeta \sin^2\zeta \cos 2\zeta (2\sin\zeta + \xi'/\lambda)^{-1} \tag{6}$$

The total spontaneous flux is $\Phi = A_y(0)L_y$ where $L_y$ is the length of the boundary. The ratio $\tilde{\Phi} = -\Phi/(2\phi_0 L_y \lambda\Delta/\pi\lambda_0^2 T_c)$ is shown in Fig. 2. It varies between $\xi'/12\lambda$ at $\lambda \gg \xi'$ to $\lambda/15\xi'$ at $\lambda \ll \xi'$ with a maximum of

0.014 at $\lambda \approx \xi'$. For a (110) surface $\tilde{\Phi} = \xi\Delta'/12\lambda\Delta$, much smaller than for a (100) surface. We note that $\Phi$ is $T$ independent up to $T_c$ since the product $\lambda\Delta$ is finite at $T \to 0$, consistent with the spontaneous magnetization data [3].

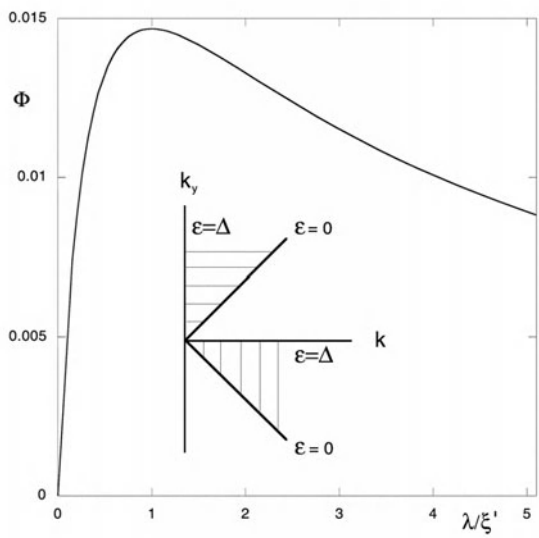


*Figure 2.* Spontaneous flux for a (100) boundary in thick films ($\xi' < \bar{d}$) in units of $2\phi_0 L_y \lambda\Delta/\pi\lambda_0^2 T_c$. For thin films the spontaneous flux is a straight line tangent to the latter curve at the origin. The hatched areas in the inset show the allowed directions $(k, k_y)$ of (positive energy) bound states. Their spectra spans the range $\epsilon = 0$ (diagonal lines) up to $\epsilon = \Delta$ as shown.

The above refers to thick films with thickness $\bar{d} > \xi'$. For thin films the right hand side of Eq. (5) is multiplied by $\bar{d}\delta(z)$. For $A_y(x) \equiv A_y(x, z = 0)$ this yields

$$A_y(x) - A_y(0) = \int_0^\infty dx' \ln|(x-x')/x'|[-1/\lambda^2)A_y(x') + (4\pi/c)j_{edge}(x')]\bar{d} \tag{7}$$

which implies a slow (non-exponential) decay of $A_y(x)$. To avoid divergence of $dA_y(x)/dx|_{x=0}$ the relation $A_y(0) = \lambda^2(4\pi/c)j_{edge}(0)$ must hold. This, interestingly, yields for $\Phi$ the previous result of the $\lambda \ll \xi'$ case, i.e. $\tilde{\Phi} = \lambda/15\xi'$; in Fig. 2 this is the tangent line to the thick film curve at the origin. Hence we can define two regimes: Weak BTRS with $\lambda/\xi' < 1$ where the spontaneous flux is $T$ and $\bar{d}$ independent, and strong BTRS with $\lambda/\xi' > 1$ where film thickness matters. In the latter

case $T$ dependence is induced as $\xi' < \bar{d}$ changes to the thin film case $\xi' > \bar{d}$ as $T \to T_c$.

## 3. quantum Hall effects

We consider first the usual charge conduction. In the absence of an external field, and given that the surface fields decay in the bulk, Ampére's law implies a zero net current, i.e. a net Hall conductance $\sigma_{xy} = 0$. It is interesting, however, to look for the frequency and wavevecor dependence of this conductance. We consider then the effective action of a bulk $d_{x^2-y^2} + id_{xy}$ superconductor. In terms of the Nambu spinors $\psi^\dagger(\mathbf{r}) = [u^*(\mathbf{r}), u^*(\mathbf{r})]$, the superconducting phase $\theta(\mathbf{r})$ and Pauli matrices $\tau_i$, the transformation $\psi(\mathbf{r}) \to exp[i\tau_3\theta(\mathbf{r})/2]\psi(\mathbf{r})$ yields the off-diagonal Hamiltonian $\int d^2r\psi^\dagger(\mathbf{r})h_\Delta\psi(\mathbf{r})$ where

$$h_\Delta = -[\Delta(-\partial_x^2 + \partial_y^2)\tau_1 + \Delta'\partial_x\partial_y\tau_2]/k_F^2 \tag{8}$$

and we neglect terms with $\nabla\theta << k_F$. The action in presence of electromagnetic potentials $\mathbf{A}, \varphi$ is then

$$\begin{aligned} S &= \int d^2rdt\psi^\dagger(i\partial_t - \tau_3\epsilon(\hat{p}) - h_\Delta - \Sigma)\psi \\ \Sigma &= \tau_3(a_0 + \mathbf{a}^2/2m) + \mathbf{a}\cdot\mathbf{p}/m - i\boldsymbol{\nabla}\cdot\mathbf{a}/2m \end{aligned} \tag{9}$$

where $\epsilon(\hat{p}) = (\hat{p}^2 - k_F^2)/2m$ and we introduce the gauge invariant potentials $\mathbf{a} = \frac{1}{2}\boldsymbol{\nabla}\theta - e\mathbf{A}$ and $a_0 = \frac{1}{2}\frac{\partial}{\partial t}\theta - e\varphi$. Expansion to 2nd order in $\mathbf{a}, a_0$ leads to the effective action

$$S_{eff} = \int \frac{d^2qd\omega}{(2\pi)^3} P_{\mu\nu}(\mathbf{q},\omega)a_\mu(\mathbf{q},\omega))a_\nu(-\mathbf{q},\omega)) \tag{10}$$

At $T = 0$ and $\mathbf{q}, \omega \to 0$ we obtain $P_{00} = N_0$ (density of states which is $N_0 = m/2\pi$ in two dimensions), $P_{ij} = -N_0c_s^2$ where $c_s^2 = v_F/\sqrt{2}$, while $P_{0j}(q) = isign(\Delta\Delta')\epsilon_{0ij}q_i/(4\pi)$ and $\epsilon_{0ij}$ is the antisymmetric unit tensor. The latter term reflects BTRS and is derived for $\Delta' \ll \Delta$.

Integrating out the phase $\theta$ we obtain the effective action in terms of the electromagnetic potentials $\mathbf{A}, \varphi$

$$\begin{aligned} S_{eff}\{\mathbf{A},\varphi\} = e^2\int \frac{d^2qd\omega}{(2\pi)^3} \ \{ & \frac{c_s^2\mathbf{q}^2}{c_s^2\mathbf{q}^2 - \omega^2}[P_{00}|\varphi(\mathbf{q},\omega)|^2 \\ & - \frac{i}{4\pi}\epsilon_{0ij}q_i\varphi(\mathbf{q},\omega)A_j(-\mathbf{q},-\omega) \\ & + O(\omega^2|\mathbf{A}|^2)] - P_{00}(\frac{c_s}{c})^2|\mathbf{A}(\mathbf{q},\omega)|^2\} \end{aligned} \tag{11}$$

The total electromagnetic action includes also the Maxwell field part $S_M = \int d^2r dt(\vec{E}^2 - \vec{H}^2)/8\pi$. E.g., for $\omega \neq 0$, $q \to 0$ the propagator for $\varphi$ yields the plasmon mode at $\omega_p = c/\lambda_0$. The Hall current $J_y$ is identified by a functional derivative with respect to $A_x$ leading to the Hall coefficient

$$\sigma_{xy}(\mathbf{q}, \omega) = sign(\Delta\Delta')\frac{e^2}{4\pi\hbar}\frac{c_s^2 q^2}{c_s^2 q^2 - \omega^2} \tag{12}$$

Transport is defined by taking the $q \to 0$ limit first, i.e. $\sigma_{xy} = 0$. Hence the conventional Hall coefficient vanishes, as expected from Galilean invariance [14]. A limit in which $\omega \to 0$ is taken first yields a quantized "static" conductance $e^2/2h$ which was argued to correspond to $\sigma_{xy} \neq 0$ in presence of a boundary [11]. It is intriguing that $\sigma_{xy}(\mathbf{q}, \omega)$ has a nontrivial structure and space resolved measurement of a Hall current could then probe the full Eq. (12). We note that a result similar to Eq. (12) was obtained for superfluid $^3$He [15].

We consider now the spin and thermal Hall effects. These were shown to be quantized first by a network model simulations [12] and then by the relation to edge states [13]. We have studied above the chiral edge states. Near $k_y = \pm k_F/\sqrt{2}$ their dispersion can be linearized with a velocity $v = \sqrt{8}\Delta'/k_F$ (for the (110) edge). The Hamiltonian has then the form

$$\mathcal{H} = \int dy \Psi^\dagger(y)[-iv\partial_y + V(y)\sigma_1]\Psi(y) \tag{13}$$

where $\Psi(y)$ is a spinor representing the two chiral branches near $\pm k_F/\sqrt{2}$, respectively, and $V(y)$ is a weak random potential which scatters between these branches via the Pauli $\sigma_1$ matrix. [Strong disorder which couples opposite edges is discussed below]. The chirality implies that backscattering is ineffective, i.e. no states to backscatter to. Formally, $V(y)$ can be gauged away by the transformation

$$\Psi(y) \to \exp[i\sigma_1 \int^y V(y')dy'/v]\Psi(y) \tag{14}$$

Therefore, the edge states act as ideal 1D gas.

To evaluate the spin Hall conductance, we define a spin voltage $V_s(x)$ (x is a coordinate perpendicular to the edge) such that $(\hbar/2)\rho_s(x)V_s(x)$ is the coupling energy density to a density $\rho_s(x)$ of $\hbar/2$ spins. This can be represented by a Zeeman term with $V_s(x) = eB_z(x)/mc$ where $m$ is the electron mass; the corresponding force in the $x$ direction is $(e/mc)dB_z(x)/dx$. The spin current along the edge is $I_s = (\hbar/2)\rho_s v_s$ where $v_s$ is the velocity of the spin carriers. The unit of spin conduction, in analogy with $e^2/h$ of the charge conduction is $(\hbar/2)^2/h = \hbar/8\pi$.

Hence the spin Hall conductance $\sigma_{xy}^{spin} = I_s/V_s$ is

$$\sigma_{xy}^{spin} = 2\frac{\hbar}{8\pi}\mathrm{sign}(\Delta\Delta') \tag{15}$$

The thermal Hall conduction is derived in a similar way from the heat conduction of an ideal gas, yielding

$$K_{xy}/T = 2\pi^2 k_B^2/3h \tag{16}$$

Hence $K_{xy}/T$ is also quantized in this weakly disordered system.

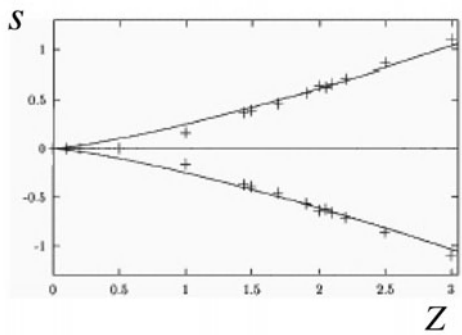


*Figure 3.* Phase diagram of quantum Hall effects. The + symbols indicate positions of extended states, and the fitted lines are $\epsilon = \pm 0.25\Delta^{1.3}$. $S$ measures the disorder strength while $Z$ is the electron-hole symmetry breaking parameter. The Hall coefficient is 0,1,2 in the 3 regions, changing by 2 units on the Z=0 line.

We reconsider now the effect of disorder on the spin Hall conductance. Imagine many random Hall systems, each with their own localized chiral states which are weakly coupled. If the couplings are too weak we expect no currents between the systems so overall $\sigma_{xy}^{spin} = 0$. As the coupling strength increases we expect a finite current to circulate around the ensemble of grains, leading to Eqs. (15,16). The transition is in fact induced by disorder: For weak disorder the argument of Eq. (14) holds and the Hall coefficients have their quantized values, Eqs. (15,16) values. As disorder increases, opposite chiral channels get

coupled leading to formation of localized chiral loops which eventually have an insulating behavior, i.e. the Hall conduction vanishes.

We have simulated this quantum Hall plateau transition [12] by a network model. The transfer on links of the network correspond to the time evolution of an electron-hole spinor with the Hamiltonian Eq. (1), i.e. $T = \exp[i\mathcal{H}_s t]$. The symmetry $\mathbf{Q}\mathcal{H}_S\mathbf{Q}^{-1} = -\mathcal{H}_S$ becomes $\mathbf{Q}T\mathbf{Q}^{-1} = T$ identifying $T$ as SU(2) matrices. Thus the links have a transfer matrix which is randomly chosen among SU(2) matrices. The transfer matrix between grains, i.e. at nodes of the network, measures the transmission across the node. A symmetry point, where transmission and reflections are equal, defines the transition. The node matrix is symmetric in particle and hole space; if this symmetry is broken, e.g. by a Zeeman term $Z$, then the critical point splits into two branches, each with universality of the usual quantum Hall, as shown in Fig. 3. The quantum Hall transition at $Z = 0$ is of a new universality class. Finite size scaling has shown new critical indices, e.g. for the localization length $\mu \approx 1.4$, in contrast with the usual quantum Hall which has $\mu \approx 2.5$.

## 4. conclusions

In conclusion, we have shown that surface states of a $d_{x^2-y^2}+id_{xy}$ superconductor lead to spontaneous magnetization which is $T$ independent and thickness independent for weak BTRS, $\lambda/\xi' < 1$, in accord with the data [3]. For strong BTRS, $\lambda/\xi' > 1$, as expected in overdoped YBCO [2] , a crossover from thick to thin film behavior can lead to $T$ and thickness dependence, as well as to an observable paramagnetic anomaly near $T_c$. We also find that the Hall conductance has an unusual $\sigma_{xy}(\mathbf{q}, \omega)$ dependence, though its conventional transport value vanishes.

We have also shown that the edge states lead to quantized spin Hall and thermal Hall transport. For strong disorder there is a quantum Hall plateau transition to an insulator with vanishing Hall coefficients. Network model simulations show a new universality class for this transition.

## References

1. Covington M. et al. (1997) *Phys. Rev. Lett.* **79**, 277.
2. Deutscher G., Dagan Y., Kohen A. and Krupke R. (2001) *Physica C* **341-348**1629; Dagan Y. and Deutscher G. (2001) *Phys. Rev. Lett* **87**, 177004; *Phys. Rev. B* **64**, 092509.
3. Carmi R., Polturak E., Koren G., and Averbach A. (2000) *Nature* **404**, 853.

4. Alff L. et al. (1998) *European Phys. J. B* **5**, 423.
5. Sharoni A., Koren G. and Millo O. (2001) *Europhysics Letts.***54**, 675; Sharoni A. et al. (2001) *cond-mat/0111156*.
6. Higashitani S. (1997) *J. Phys. Soc. Japan* **66**, 2556.
7. Barash Yu. S., Kalenkov M. S. and Kurkijärvi J. (2000) *Phys. Rev. B* **62** 6665.
8. Sigrist M., Bailey D. B. and Laughlin R. B. (1995) *Phys. Rev. Lett.* **74**, 3249.
9. Matsumoto M. and Shiba H. (1995) *J. Phys. Soc. Jpn.* **64**, 3384; *ibid***64**, 4867.
10. Fogelstrom M., Rainer D., and Sauls J. A. (1997) *Phys. Rev. Lett.* **79**, 281.
11. Goryo J. and Ishikawa K. (1999) *Phys. Letts. A* **260**, 294.
12. Kagalovsky V., Horovitz B., Avishay Y. and Chalker J. T. (1999) *Phys. Rev. Lett.* **82**, 3516.
13. Senthil T., Marston J. B. and Fisher M. P. A., Phys. Rev. B (1999) *Phys. Rev. B*, 4245.
14. Read N. and Green D. (2000) *Phys.Rev. B* **61**, 10267.
15. Goryo J. and Ishikawa K. (1998) *Phys.Lett. A* **246**, 549.
16. Furusaki A., Matsumoto M. and Sigrist M. (2001) *Phys. Rev. B* **64**, 054514.
17. Volovik G. E. (1997) *JETP Lett.* **66**, 522.
18. Altland A. and Zirnbauer M. R., (1997) *Phys. Rev. B* **55**, 1142.
19. Horovitz B. and Golub A., (2002) *EuroPhys. Lett.*, **57**, 892.

# Universal scaling flow diagram for magnetoconductance in disordered GaAs layers

S.S. Murzin (murzin@issp.ac.ru) *
*Institute of Solid State Physics RAS, 142432, Chernogolovka, Moscow District, Russia*

M. Weiss and A.G.M. Jansen
*Grenoble High Magnetic Field Laboratory, Max-Planck-Institut für Festkörperforschung and Centre National de la Recherche Scientifique, BP 166, F-38042, Grenoble Cedex 9, France*

**Abstract.** Development of the unified scaling theory for the integer and the fractional quantum Hall effect resulted in the derivation of exact expressions for the flow lines of the coupled evolution of the Hall ($G_{xy}$) and diagonal ($G_{xx}$) conductance components with decreasing temperature [B.P. Dolan (1999)]. The lines have a universal shape independent of details of the two-dimensional system. In strongly disordered GaAs layers, the temperature driven flow lines are accurately described by the theory.

**Keywords:** quantum Hall

**Abbreviations:** QHE – quantum Hall effect

## 1. INTRODUCTION.

In spite of great efforts made over many years by researchers studying the integer and fractional quantum Hall effect (QHE) theoretically and experimentally, the understanding of its evolution with decreasing temperature is, nonetheless, far from satisfactory at the moment, and it is still unclear under which conditions the QHE could exist at zero temperature. Usually the QHE is observed at high magnetic fields, $\omega_c\tau \gg 1$ ($\omega_c = eB/m$ is the cyclotron frequency, $\tau$ is the transport relaxation time). One of the basic unsolved problems is the determination of the weakest fields at which the QHE could exist at zero temperature. About 20 years ago, the scaling treatment of the integer QHE was presented graphically by the flow diagram [1, 2] in order to suggest a solution of the problem. The flow diagram, which is shown in Fig. 1, depicts the coupled evolution of the diagonal ($G_{xx}$) and Hall ($G_{xy}$) conductance components with the increasing sample size $L$ (or, which is equivalent, increasing phase breaking length $L_\phi(T)$ for the

* This e-mail address is available for all problems and questions.



*R. Fazio et al. (eds.), New Directions in Mesoscopic Physics,* 291–301.
© 2003 *Kluwer Academic Publishers. Printed in the Netherlands.*

finite decreasing temperature). The scaling theory leads to quite an unexpected conclusion: the integer QHE does not require the Landau quantization of the electron spectrum. It should exist even in a two-dimensional system at low magnetic fields, $\omega_c\tau \ll 1$, and in a film whose thickness $d$ is much larger than the electron's transport free path $l$, i.e. $d \gg l$, at both low and high magnetic fields. Although these important predictions have been derived from the scaling theory, the latter is far from complete. Only a sketch of the flow diagram showing its symmetry was plotted in Ref. [1, 2].

The similarity between numerous features of the fractional and integer QHE stimulated the creation of a unified theory [3, 4, 5]. As a result of this development, which incorporated the symmetry of the problem, exact expressions for the flow lines of the integer and fractional QHE were deduced recently [5]. Their shape is universal, i.e. not depending on specific parameters of a totally spin polarized 2D electron system.

Here we give a description of the scaling treatment of the integer QHE (section II), show experimental magnetotransport data for disordered heavily Si-doped GaAs layers with a plot of the temperature driven flow diagram of $G_{xx}(T)$ versus $G_{xy}(T)$ [6] (section III), present quantitative outcomes of unified theory [5] for the integer and fractional QHE with a comparison to the experimental results (section IV). For the investigated disordered GaAs layers a good quantitative agreement between experiment and scaling theory is found.

## 2. SCALING TREATMENT OF THE INTEGER QHE.

The scaling theory is developed on the basis of the field-theory approach. Presently there is no microscopic understanding of the integer QHE at low magnetic fields $\omega_c\tau \ll 1$ and in thick films $d \gg l$ in terms of wave functions, scattering, or tunneling. Nevertheless, the predictions of the scaling theory in these limiting cases seem quite natural if we believe that the dissipative conductance $G_{xx}$ (per square) tends to zero as the temperature decreases, and that the Hall conductance $G_{xy}$ should be quantized when $G_{xx} = 0$ [7, 8]. For a large dissipative conductance $G_{xx} \gg 1$ (throughout the paper $G_{xx}$ and $G_{xy}$ will be expressed in units $e^2/h$), $G_{xx}$ decreases with temperature $T$ due to diffusive interference effects (quantum corrections). These weak localization (single-particle) corrections are suppressed in a magnetic field $B$ and reduce to [9]

$$G_{xx}(L_\varphi) = G_{xx}^0 - \frac{2}{\pi^2 G_{xx}^0} \ln\left[L_\phi(T)/L_0\right], \tag{1}$$

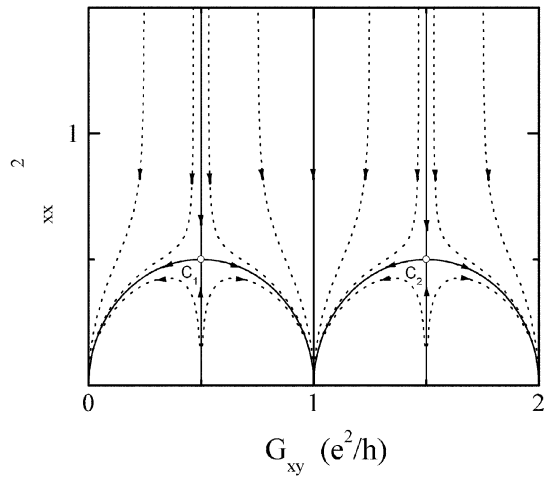


*Figure 1.* The flow diagram (dotted lines) describing the coupled evolution of the diagonal ($G_{xx}$) and Hall ($G_{xy}$) conductance components for increasing sample size $L$ (or, which is equivalent, increasing phase breaking length $L_\phi(T)$ for finite decreasing temperatures).

where $G^0_{xx}$ is the "bare" diagonal conductance, which corresponds to diffusive motion of electrons without interference effects over a distance larger than diffusive length $L_0$. The corrections in a magnetic field are much smaller ($\pi h G^0_{xx}/e^2$ times) than those in the absence of the field. In high magnetic fields, the quantum corrections to $G_{xx}$ due to the electron-electron interaction are of the same order as in zero magnetic field [10]:

$$G_{xx}(L_T) = G^0_{xx} - \frac{\lambda}{\pi}\ln(T_0/T), \tag{2}$$

Here , $\lambda < 1$ is the constant of interaction and $T_0 = \hbar/k_B\tau_D$ with $\tau_D$ the time of an electron displacement through the diffusive length. However, the electron-electron interaction corrections are much larger than the single-particle corrections of Eq.2. In a magnetic field, the interference effects, both of single particles and of correlated particles, do not affect the Hall conductance $G_{xy}$. Therefore, the flow lines $G_{xx}(G_{xy})$ are vertical in the region of large $G_{xx}$ as is shown in Fig. 1. Since $\ln(1/T) \to \infty$, as $T \to 0$, there is good reason to expect that finally $G_{xx}$ should vanish. When $G_{xx} = 0$ the Hall conductance is expected to be quantized with $G_{xy} = i$ ($i$ is an integer) [7, 8]. Therefore, the flow lines should deviate from the vertical at $G_{xx} \sim 1$. Since $G_{xy}$ tends to different quantum values for different starting values $G^0_{xy}$, transitional values of $G^0_{xy} = G^{c,i}_{xy}$ $= i+1/2$ should exist, for which $G_{xx}$ tends to a finite value $G^c_{xx}$ and $G_{xy}$

is not quantized. The nonzero $G_{xx}$ implies that the electronic states are extended at the Fermi level.

So, with the increasing system size ($L \to \infty$) $G_{xx}$ tends to zero ($G_{xx} \to 0$), while $G_{xy}$ becomes quantized ($G_{xy} \to i$). The points $[G_{xx}(L), G_{xy}(L)]$ flow on lines merging into the integer QHE plateau states characterized by one of the fixed points $(0, i)$. The regions relating different Hall plateaus are separated by vertical lines with Hall conductance $G_{xy} = i + 1/2$ for all $L$ terminating at unfixed critical points $(G^c_{xx}, i + 1/2)$. As one can see in Fig. 1, the points $[G_{xx}(L), G_{xy}(L)]$ move along the lines merging into the integer QHE plateau states even from a region of starting points $\left(G^0_{xy}, G^0_{xx}\right)$ where $G^0_{xy}/G^0_{xx} = \omega_c\tau \ll 1$.

At finite low temperature, wide plateaus with a precisely quantized Hall conductance $G_{xy}$ and resistance $R_{xy}$ should exist with the diagonal conductance $G_{xx}$ and resistance per square $R_{xx}$ exponentially small. In the transition region between plateaus $G_{xx} \sim 1$. The width of the transition tends to zero as the temperature decreases, and the maximum value of $\partial G_{xy}/\partial B \propto \partial R_{xy}/\partial B \propto T^{-\mu}$, where $\mu$ is the universal critical exponent.

The values of $G^c_{xx}$ and $\mu$ were not found in the initial scaling theory [1, 2]. According to the unified theory [3, 4, 5], the merging into the insulator or the QHE state at low temperatures occurs along a semicircular separatrix

$$G^2_{xx} + [G_{xy} - (i + 1/2)]^2 = 1/4, \tag{3}$$

which is divided by the critical points at $(G^c_{xy}, G^c_{xx}) = (1/2, i + 1/2)$. Previously, numerical calculations for a system of non-interacting electrons at high magnetic fields in the lowest Landau level gave $G^c_{xx} \approx 1/2$ in the presence of different random potentials [11]. The semicircle equation (3) for the separatrix in the case of a smooth disorder potential was derived in Ref.[12].

The phase diagram of the integer QHE at zero temperature can be easily obtained in the plane of the "bare" resistances $(R^0_{xy}, R^0_{xx})$ from the flow diagram. This is done solely by maintaining the Hall conductance $G_{xy} = i + 1/2$ for all $L$. The phase boundaries are semicircles [4] described by the right-hand part of the equation $G^0_{xy} = R^0_{xy}/\left[(R^0_{xx})^2 + (R^0_{xy})^2\right] = i + 1/2$.

Although QHE experiments reveal certain aspects of the two-parameter scaling behavior the picture has not yet been fully confirmed. The QHE at low magnetic fields $\omega_c\tau \ll 1$ has never been observed because very low temperatures are required [13]. Magnetotransport studies of the flow diagram [14] clearly demonstrate the quantization of $G_{xy}$ but do not show essential features of the scaling picture, such as the sym-

metry about the vertical lines $G_{xy} = i$ and $i+1/2$ or the correct values of $G^c_{xx} = 1/2$ and $G^c_{xy} = i+1/2$. The values of the critical exponent $\mu$, extracted from experimental data are different, varying over the range $0.41 \div 0.57$. Moreover, the authors of many papers claimed that their results were in a glaring contradiction with the scaling theory. It seems, however, that these claims are groundless [13, 15]. On the other part, the integer QHE in thick films $d \gg l$ was observed [16]. $G^c_{xx} \approx 1/2$ and $G^c_{xy} \approx i+1/2$ were found at the point of transition from the insulator to the quantum Hall state in $\delta$-doped GaAs [17] and between two integer QHE plateaus with $G_{xy} = 1$ and 2 ($i = 1$) in a Si-Ge hole system [18]. In most experiments, however, these values differ significantly from $1/2$ and $i + 1/2$, respectively.

There are several causes of the quantitative difference between theoretical predictions and experimental data. First of all, the theory was developed for spinless (or totally spin polarized) electrons and does not apply directly to any given 2D system. Secondly, it could be applied when the conductance depends on the temperature only owing to the diffusive interference effects, in particular, the temperature should be low as compared with the Landau level broadening due to disorder. Thirdly, the increase in the current density near the edges does not need to be very large. Fourthly, the theory was developed for idealized, absolutely random disorder. Macroscopic inhomogeneity of a sample could result in an essential discrepancy of the experiments and theory.

Since the theory was developed for spinless or totally spin polarized electrons, the most favorable candidate for an experimental study of the flow diagram under integer QHE conditions is a disordered system with a small $g$-factor such that the spin-splitting $g\mu_B B$ ($\mu_B$ is the Bohr magneton) is small as compared with the disorder broadening and will only show up in the flow diagram at relatively low temperatures [19]. For non-interacting electrons, and in the absence of spin-flip scattering, electrons with different spin can be considered as two independent, totally spin polarized electron systems. In such a situation, one should substitute $G_{ij}$ by $G_{ij}/2$ in the theoretical expressions. For interacting electrons at $k_B T \ll \mu_B g B$ ($k_B$ is the Boltzmann constant), only interaction of electrons with the same spin leads to a renormalization of the conductance [20]. Therefore, it seems that the electrons with different spin projections can be considered as two independent systems.

## 3. EXPERIMENT.

### 3.1. Samples.

The investigated heavily Si-doped n-type GaAs layers sandwiched between undoped GaAs were prepared by molecular-beam epitaxy. The nominal thicknesses of the layers are $d = 27, 30, 34$, and 40 nm and the Si-donor bulk concentration equals to $1.5 \times 10^{17}$ cm$^{-3}$. The number given in this paper to indicate a particular sample corresponds to the thickness of its doped layer. The electron densities per square as derived from the slope of the Hall resistance $R_{xy}$ in weak magnetic fields ($0.5 \div 3$ T) at $T = 4.2$ K are $N_s = 3.7, 4, 5.5$, and $6.2 \times 10^{11}$ cm$^{-2}$ for samples 27, 30, 34, and 40, respectively. The "bare" high-temperature mobilities $\mu_0$ are about $1300, 1400, 1900$, and 2300 cm$^2$/Vs. Previous experimental studies of the flow diagram have been performed on much purer samples with at least an order of magnitude of higher mobility.

### 3.2. Magnetotransport.

Samples 34 and 40 reveal a wide QHE plateau from $\approx 6$ up to $\approx 11$ T with the value $R_{xy} = h/2e^2$ (i.e., $i = 2$ for a spin degenerate lowest Landau-level occupation) accompanied by an exponentially small value of $R_{xx}$ at low temperatures $T \lesssim 0.3$ K. The magnetoresistance data of sample 40 are presented in Ref.[21].

In Fig. 2(a) the magnetotransport data of the diagonal ($R_{xx}$, per square) and Hall ($R_{xy}$) resistance (both given in units of $h/e^2$), and of the diagonal ($G_{xx}$) and Hall ($G_{xy}$) conductance have been plotted for sample 30. At $T = 4.2$ K, $R_{xx}$ depends on magnetic field rather weakly and has only a weak minimum at $B = 6$ T, and $R_{xy}$ increases linearly up to 5 T with a slightly smaller slope at higher fields. Such a behavior is typical for bulk samples in the extreme quantum limit. At the lowest temperatures, the layer is insulating ($R \geq 100$) in zero magnetic field. At low magnetic fields up to 0.5 T, the diagonal resistance $R_{xx}$ drops abruptly and continues to decrease more slowly between 0.5 and 4 T. For fields between 5 and 7 T, a minimum is observed with a QHE plateau in the Hall resistance with $R_{xy} = 1/2$. The same QHE structure around 6 T can be observed in the plotted conductance data. In the minimum of $G_{xx}$ near $B = 6$ T, the Hall conductance $G_{xy}$ increases from a value higher than 1 (at 4.2 K) towards 2 at the lowest temperatures. The curves $G_{xy}(B)$ for different temperatures cross at one point with $G_{xy} = 1$ at $B_c = 4.9$ T. The diagonal conductance $G_{xx}$ tends towards 1 for decreasing temperature at this critical field. For curves at $T > 0.2$ K there is a second crossing point at $B = 7$ T with $G_{xy} \approx 1$. The second peak in $G_{xx}(B)$ has an amplitude smaller than

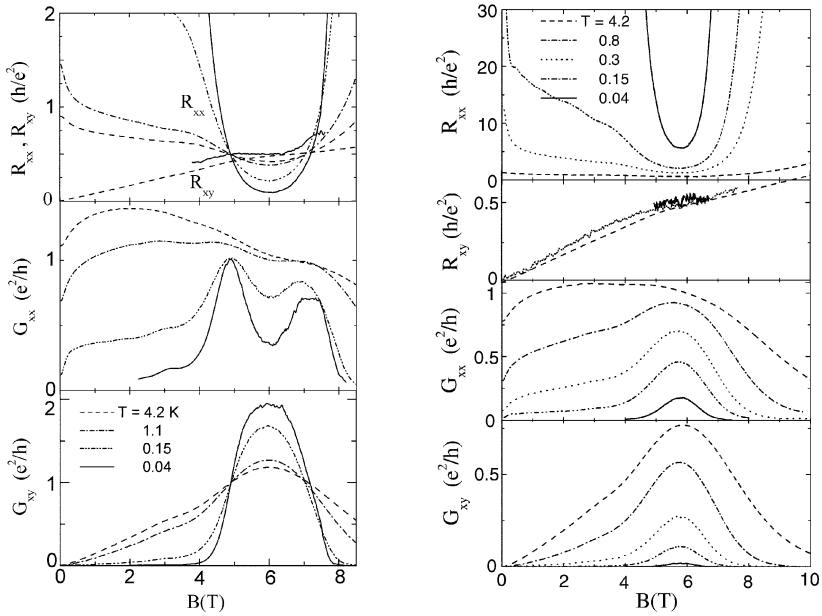


(a) (b)

*Figure 2.* Magnetic-field dependence of the diagonal ($R_{xx}$, per square) and Hall ($R_{xy}$) resistance and the diagonal ($G_{xx}$) and Hall ($G_{xy}$ ) conductance for samples 30 (a) and 27 (b) in a magnetic field perpendicular to the heavily doped GaAs layer at different temperatures.

$e^2/h$ and is broader than the first one. We believe that this peculiar structure of the second peak is a manifestation of spin-splitting.

In Fig. 2(b), the magnetotransport data have been plotted for sample 27. At $T = 4.2$ K, these data are similar to the data for sample 30. However, sample 27 shows insulating behavior ($R_{xx}$ increases with decreasing temperature) at all magnetic fields with a rather deep and narrow minimum in the field dependence $R_{xx}(B)$ at low temperatures. Note that at the lowest temperature we can measure $R_{xy}$ only near the minimum of $R_{xx}$ since outside this region $R_{xy} \ll R_{xx}$. Within our accuracy, the sample reveals a Hall-insulator state ($R_{xy} = 0.5$) [4] in this region. $G_{xx}$ and $G_{xy}$ have peaks at $B \approx 6$ T.

The QHE in sample 30 is much less pronounced than in samples 34 and 40 due to the fact that the maximum of the high temperature Hall conductance $G^0_{xy}(B)$ has a value of $\approx 1.2$ close to 1. For $G^0_{xy} \to 1$, the localization length diverges, and the system is in the dissipative, non-quantized state. For samples 34 and 40 with a maximum of $G^0_{xy}(B)$ close

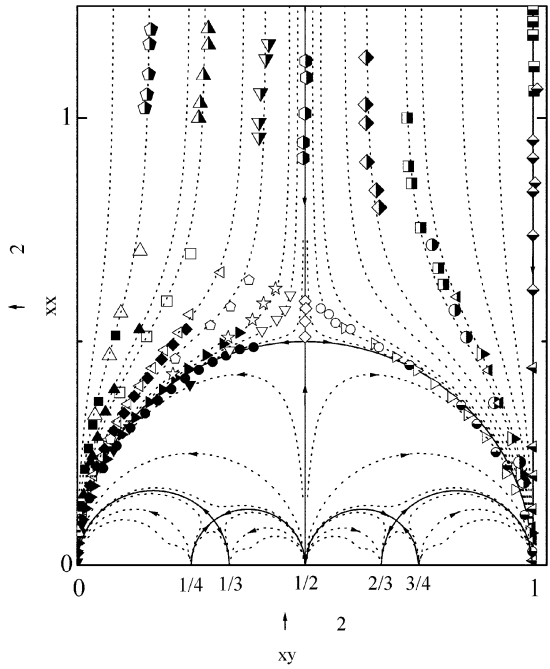


*Figure 3.* Flow diagram of the $[G_{xx}(T), G_{xy}(T)]$ data points for the investigated heavily doped GaAs layers with different thickness (filled symbols sample 27 ($B = 1.7 \div 6.1$ T); open, sample 30 ($B = 1.62 \div 5.8$ T); half right filled, sample 34 ($B = 0.9 \div 5.8$ T); and half bottom filled, sample 40 ($B = 3.3 \div 6$ T). Different magnetic field values are indicated by different types of symbols. Dotted lines show the theoretical flow lines. Solid lines display the separatrix for the integer and partially for the fractional QHE.

to 2, quantization at $G_{xy} = 2$ develops already at higher temperatures. Although insulating for all fields, sample 27 shows a minimum in $R_{xx}$ and a maximum in $G_{xx}$ due to the proximity of $G^0_{xy}(B)$ to 1 on the insulator side, giving a large localization length at its maximum.

The value of the critical exponent $\mu$ can be extracted for sample 30 from the temperature dependence of $\partial G_{xy}/\partial B$ at the critical field $B = 4.9$ T. With the experimental accuracy, the best fit yields $\mu = 0.48 \pm 0.05$.

### 3.3. Flow diagram.

In Fig. 3 the temperature evolution of the points $(G^{\uparrow}_{xx}(T), G^{\uparrow}_{xy}(T))$ of the conductance per spin $G^{\uparrow}_{ij} = G_{ij}/2$ has been plotted for the different samples at different magnetic fields with temperature ranging from 4.2

down to 0.04 and 0.1 K except for the flow lines of sample 34 in weak magnetic fields (1.4 − 2.4 T) which start only at 1.1 K. Only data below $B = 6.2$ T have been plotted because in higher magnetic fields spin-splitting starts to affect the magnetotransport properties. A distinct signature of spin-splitting has been observed in samples 40 and 34, and will be subject of a separate publication. The data points at the lowest temperatures approach and, subsequently, follow the semicircle dependence given in Eq. (3). Their final low-temperature limiting value depends on the initial high temperature Hall conductance $G_{xy}^{\uparrow 0}$ with respect to $G_{xy}^{\uparrow} = 1/2$. Data points starting on the semicircle follow this semicircle. The points starting for high temperatures at $G_{xy}^{\uparrow} = 1/2$ terminate at the lowest temperatures very close to $(G_{xx}^{c}, G_{xy}^{c}) = (1/2, 1/2)$. The presented data on disordered GaAs layers follow the trends expected from the theory [5].

## 4. OUTCOMES OF UNIFIED SCALING THEORY FOR INTEGER AND FRACTIONAL QHE.

According to Ref. [5] the phase of the complex function

$$f = -\vartheta_3^4 \vartheta_4^4 / \vartheta_2^8, \tag{4}$$

with the Jacobi $\vartheta$ functions

$$\vartheta_2(q) = 2\sum_{n=0}^{\infty} q^{(n+1/2)^2}, \quad \vartheta_3(q) = \sum_{n=-\infty}^{\infty} q^{n^2}, \quad \vartheta_4(q) = \sum_{n=-\infty}^{\infty} (-1)^n q^{n^2} \tag{5}$$

for $q = \exp(i\pi G)$, is constant along the flow lines ($G \equiv G_{xy} + iG_{xx}$ is the complex conductance). Results of a numerical solution of equation $\arg(f) = \alpha$ for various $\alpha$ are plotted in Fig. 3 by dotted lines. For flow lines above the semicircle given by Eq.(3), the value $\alpha$ corresponds to the Hall conductance $G_{xy}^{\infty}$ for large $G_{xx}$, where the flow lines are vertical, with $\alpha = \pi(1 - G_{xy}^{\infty})$. The theoretical flow-lines are in a very good agreement with the experimental data for $G_{xx}^{\uparrow}(G_{xy}^{\uparrow})$ and are universally determined by the limiting $G_{xy}^{\infty}$ values. The solutions of the above equations describe the flow lines for both the integer and the fractional QHE shown partially in Fig. 3. The flow lines above the semicircle for the integer QHE can be mapped into the flow lines of the fractional QHE using a transformation $\bar{G} \longleftrightarrow (aG + b)/(cG + d)$, where $a, b, d$ are the integers, $c$ is the even integer, $ad - bc = 1$.

As was mentioned above, for $k_B T \ll \mu_B g B$ only interaction of electrons with the same spin leads to a renormalization of the conductance.

In our experiments $\mu_B gB/k_B T = 0.01 \div 3$. It seems that even for $k_B T \gtrsim \mu_B gB$, the flow lines remain unchanged while the interaction of electrons with different spins may be important for the flow rate. For large values of $G_{xx}$, its temperature dependence is mostly due to electron-electron interaction.

## 5. SUMMARY.

The flow diagram of coupled evolution of the diagonal and Hall components of the conductance tensor for strongly disordered GaAs layers is accurately described by the scaling theory. While electron-electron interaction affects the flow rate, which depends on the constant of interaction $\lambda$ for the case under study, it seems not to change the shape of the flow lines. This last conclusion is of importance for the problem of the flow diagram by considering the interaction between electrons with different spin projections.

## References


1. H. Levine, S. B. Libby, and A. M. M. Pruisken, Phys. Rev. Lett. **51**, 1915 (1983); A. M. M. Pruisken, in *The Quantum Hall Effect*, edited by R. E. Prange and S. M. Girven, Springer-Verlag, 1990.
2. D. E. Khmel'nitskiĭ, Pis'ma Zh. Eksp. Teor. Fiz. **38**, 454 (1983) [JETP Lett. **38**, 552 (1983)]; Phys. Lett. A **106**, 182 (1984).
3. J. K. Jain, Phys. Rev. Lett. **63**, 199 (1989); C.A. Lütken and G.G. Ross, Rev. B **45**, 11837 (1992); **48**, 2500 (1993); C. P. Burgess, R. Dib, and B. P. Dolan, Phys. Rev. B **62**, 15359 (2000); C. P. Burgess, and B. P. Dolan, Phys. Rev. B **63**, 155309 (2001).
4. S. Kivelson, D. Lee, and S. Zang, Phys. Rev. B **46**, 2223 (1992).
5. B. P. Dolan, Nucl. Phys. B **460**[FS], 297 (1999); cond-mat/980929.
6. S. S. Murzin, M. Weiss, A. G. M. Jansen and K. Eberl, Phys. Rev. B **66**, 233314 (2002).
7. R. B. Laughlin, Phys. Rev. B **23**, 5632 (1981).
8. H. Aoki and T. Ando, Phys. Rev. Lett. **57**, 3093 (1986).
9. S. Hikami, Phys. Rev. B **24**, 2671 (1981); K. B. Efetov, Adv. Phys. **32**, 53 (1983).
10. B. L. Al'tshuler and A. G. Aronov, in *Electron-Electron Interaction in Disordered Systems*, edited by A. L. Efros and M. Pollak, North-Holland, Amsterdam, 1987.
11. Y. Huo, R. E. Hetzel, and R. N. Bhatt, Phys. Rev. Lett. **70**, 481 (1993).
12. Igor Ruzin and Shechao Feng, Phys Rev. Lett. **74**, 154 (1995).
13. Bodo Huckestein, Phys. Rev. Lett. **84**, 3141 (2000).
14. H. P. Wei et al., Phys. Rev. B **33**, 1488 (1988); Surf. Sci. **229**, 34 (1990); Phys. Rev.B **45**, 3926 (1992); M.Yamane et al., J. Phys. Soc. Japan **58**, 1899 (1989); S. V. Kravchenko et al., Pis'ma Zh. Eksp. Teor. Fiz. **50**, 65 (1989); S. Koch

et al., Phys. Rev. B **43**, 6828 (1991); V. T. Dolgopolov et al., Zh. Eksp. Teor. Fiz. **99**, 201 (1991) [Sov. Phys. JETP **72**, 113, (1991).
15. S. S. Murzin, cond-mat/0212111.
16. S. S. Murzin et al., Phys. Rev. Lett. **80**, 2681 (1998); Pis'ma Zh. Eksp. Teor. Fiz. **68**, 305 (1998) [JETP Lett. **68** (1998)]; Phys. Rev. B **59**, 7330 (1999).
17. R. J. F. Hughes et al, J. Phys.: Condens Matter. **6**, 4763 (1994).
18. R.B. Dunford, N. Griffin, and M. Pepper et al., Physica E **6**, 297 (2000).
19. D. E. Khmel'nitskiĭ, Helv. Phys. Acta **65**, 164 (1992).
20. A. M. Finkelstein, Zh. Eksp. Teor. Fiz. **86**, 367 (1984) [Sov. Phys. JETP **59**, 212 (1984)].
21. S. S. Murzin, M. Weiss, A. G. M. Jansen and K. Eberl, Phys. Rev. B **64**, 233309 (2001).

# Fluctuations of the anisotropy energy in nanoscale ferromagnetic particles

Silvia Kleff and Jan von Delft
*Lehrstuhl für Theoretische Festkörperphysik*
*Sektion Physik and Center for NanoScience*
*Ludwig-Maximilians-Universität München*
*Theresienstr. 37*
*80333 München*
*Germany*

## 1. Introduction

What are the properties of individual states in the electronic spectrum of a nanometer size ferromagnetic particle? – Besides the intrinsic scientific interest in understanding ferromagnetism on the nanometer scale, this question might also be of technological interest, since the size of memory elements in magnetic storage technologies is decreasing extremely rapidly [1], and particles as small as 4 nm are coming under investigation [2]. In a ferromagnetic single electron transistor (SET) with leads and/or island made from itinerant ferromagnetic materials such as Co, Fe or Ni, which have different densities of states for spin-up (majority band) and spin-down (minority band) electrons, transport becomes spin dependent. This leads to a number of interesting new phenomena, such as tunneling magneto resistance, TMR [3], (the resistance of the SET depends on the relative orientation of the magnetic moments of leads and island) or Coulomb oscillations as a function of the applied magnetic field [4]. Such single electron tunneling effects in ferromagnetic systems are part of a new branch in mesoscopic physics called magneto electronics or spintronics, bringing together magnetism (spin) and electronics.

An important milestone in the study of itinerant ferromagnetism on the nanometer scale was reached during the last three years, when Deshmukh, Guéron, Ralph et al. (DGR) [5, 6], using single-electron tunneling spectroscopy [7], succeeded for the first time in resolving discrete resonances in the tunneling spectrum through individual ferromagnetic single-domain cobalt nanograins, with diameters between 1 and 4 nm. Their work goes beyond previous studies of ferromagnetic single electron transistors [8, 9, 10, 11], which elucidated the interplay of ferromagnetism and charging effects: the fact that DGR's Co grains



*R. Fazio et al. (eds.), New Directions in Mesoscopic Physics,* 303–312.
© 2003 *Kluwer Academic Publishers. Printed in the Netherlands.*

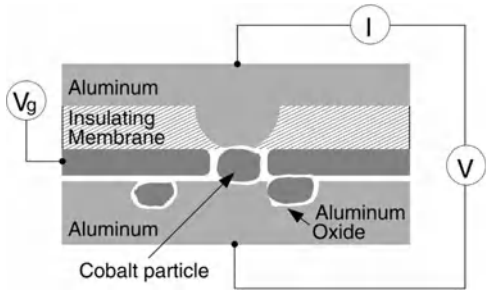


*Figure 1.* Schematic setup of DGR's experiment: A single electron transistor with a Cobalt grain as a central island.

were sufficiently small such that discrete resonances could be resolved means that they were probing the true quantum states participating in electron tunneling, which allows the nature of electron correlations in itinerant ferromagnets to be studied in unprecedented detail. They found complex nonmonotonic and hysteretic energy level shifts of individual resonances as the magnetic moment (spin) of the grain rotates in an applied magnetic field. Magnetization reversal in small single-domain magnetic particles have usually been described using a classical theory in which the energy is a function of the direction of the magnetization of the particle. The dynamics of the magnetization is governed by the competition between anisotropies that separate different easy axes directions and an applied magnetic field. At the nanometer scale, however, the discreteness of the particle's quantum energy spectrum plays an important role. To this end a simple phenomenological model was recently introduced by the present authors et al. [6, 12, 13] and independently by Canali and MacDonald [14].

The origin of magnetic anisotropies lies in spin-orbit interaction, which should give energy shifts of different size for the discrete states inside a nanoscale magnetic grain. Therefore changing the state of the grain by adding additional electrons to it, as in tunnel spectroscopy experiments, should result in a change of the anisotropy energy. In Refs. [6] and [12] the present authors et al. showed that large changes of the anisotropy energy as function of the electron number on the grain lead to a nontrivial magnetic field dependence of tunneling resonances that resembles experimental behavior [6]. Recently Cehovin, Canali, and MacDonald [15], using a microscopic tight binding model with spin-orbit interaction demonstrated that, indeed, such surprisingly large changes in anisotropy energies of nanoscale particles can occur.

In this article we will discuss fluctuations of the anisotropy energy in nanoscale ferromagnetic particles. First we will summarize some

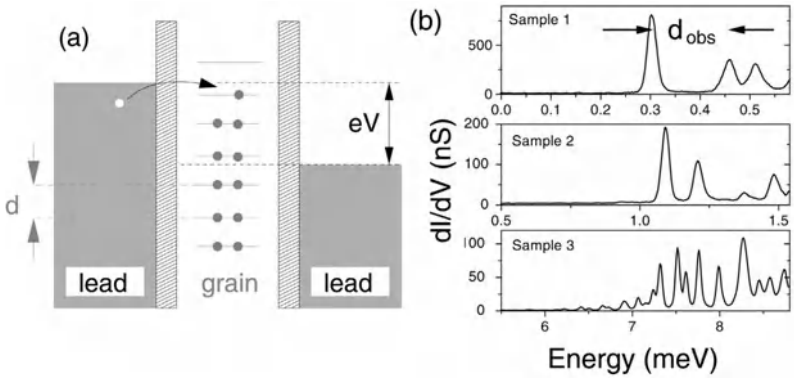


*Figure 2.* (a) Cartoon picture of an $dI/dV$ measurement. (b) Tunneling spectra of three different samples taken from Ref. [5]: $dI/dV$ as a function of energy (transport voltage times a known capacitance ratio) for samples without gate. Peaks can be associated with transitions between discrete states in the nanoparticle.

of the experimental results by DGR dealing with the magnetic field dependence of individual eigenenergies of discrete states inside Co nanoparticles. Before discussing fluctuations of the anisotropy energy in those grains we will give a brief review of the classical theory of magnetization reversal in small magnetic particles.

## 2. Experimental results

In DGR's tunnel spectroscopy experiments a nanoscale cobalt grain was used as a central island in a single electron transistor (SET) as shown in Fig. 1. The grain was connected via tunnel barriers to external leads. The electronic spectrum of the particle was determined by measuring the tunnel conductance through the grain as a function of transport voltage ($V$), gate voltage ($V_g$) and magnetic field $\mu_0 H$ . The diameters of the Co-grains were estimated to be 1-4 nm. Assuming a roughly hemispherical shape, the number of atoms in each grain then is in the range $N_a \approx 20$–$1500$. This implies a total spin of $s_0 \approx 0.83 N_a \approx$ 17–1250.

At $\lesssim$ 90 mK the tunneling conductance, $dI/dV$, as a function of transport voltage $V$ consists of individual peaks associated with transitions between discrete electronic states in the nanoparticle [see Fig. 2(b)]. Since the charging energy ($>$ 30 meV) was very much larger than typical values of the transport voltage ($eV <$ 9 meV) and the temperature, the number of electrons on the grain, $N$, can fluctuate only by one (between $N$ and $N-1$ or $N$ and $N+1$). The energy

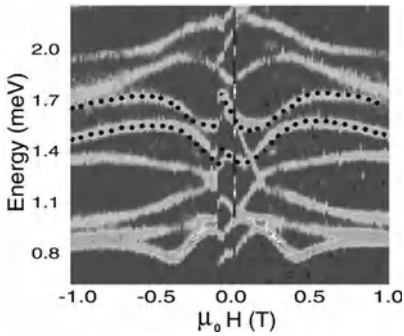


*Figure 3.* Grey-scale plot of the differential conductance, $dI/dV$, as a function of energy (transport voltage times a known capacitance ratio) and magnetic field for tunneling resonances in a cobalt nanoparticle. The field is varied from positive to negative values (taken from Ref. [6]).

balance condition that determines through which eigenstates of the grain electrons can tunnel for given values of transport (and gate) voltage thus involve differences between eigenenergies of a grain with a fixed particle number of $N$ and $N \pm 1$ [16],

$$\Delta E_{fi}^{\pm} \equiv E_f^{N\pm 1} - E_i^N \,, \tag{1}$$

each corresponding to the energy cost of an electron tunneling process onto $(N \to N+1)$ or off $(N \to N-1)$ the grain. $E_i^N$ is the eigenenergy of the discrete initial eigenstate of a grain with $N$ electrons, etc. The differential conductance $dI/dV$ as a function of $V$ at a fixed $V_g$ has a peak whenever the transport voltage $eV$ (times a known capacitance ratio) is equal to one of the $\Delta E_{fi}^{\pm}$'s [Fig. 2(b)], at which point another channel for carrying tunneling current through the grain opens up as schematically illustrated in Fig. 2(a).

Figure 3 shows the energies of tunneling resonances for a Co particle as a function of magnetic field $H$. The tunneling resonance energies show a strong non-linear dependence on $H$, with hysteresis and jumps at the switching field $|H_{\rm sw}|$. $H_{\rm sw}$ can be identified with magnetic switching, i.e., a sudden change in the direction of the magnetic moment of the nanoparticle (see Sec. 3.1). For fields beyond the switching field, the levels can exhibit nonmonotonic variations as a function of $H$, with each level behaving differently, suggesting that the anisotropy energy fluctuates significantly from eigenstate to eigenstate.

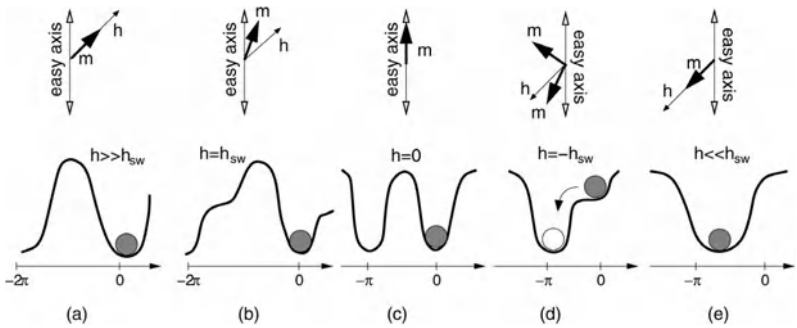


*Figure 4.* Cartoon pictures of the energy $E(\phi)$ as a function of $\phi$ for different values of the magnetic field: The easy axis lies in $z$ direction and the magnetic field $\vec{h}$ makes an angle $\theta = \pi/4$ with the easy axis. The magnetic moment vector $\vec{m}$ changes its orientation as the magnetic field is ramped from large positive ($\theta = \pi/4$) (a) to large negative ($\theta = 5\pi/4$)(e). The ball indicates the local minimum of $E(\phi)$ that determines the direction of $\vec{m}$.

## 3. Classical micromagnetic theory

### 3.1. Stoner-Wohlfarth model

For single-domain particles the magnetization is expected to reverse by uniform (coherent) rotation of magnetization in the presence of a changing magnetic field. The corresponding model, developed by Stoner and Wohlfahrth [17], is the simplest classical model describing magnetization reversal. One considers a single-domain, uniaxial, magnetic particle with magnetic moment $\vec{m}$. The magnetic moment changes its orientation due to a competition between the anisotropy energy of the particle and the effect of an applied magnetic field, but has a constant magnitude. This is justified for very small particles, where the exchange energy holds all spins parallel to each other. The energy is a function of the angle $\phi$ between magnetic moment vector $\vec{m}$ and easy axis [1], and $\theta$, the angle the magnetic field makes with the easy axis:

$$E(\phi) = -k\, m \cos^2 \phi - h\, m \cos(\theta - \phi). \tag{2}$$

Here the first term represents a uniaxial anisotropy energy with $k$ being a phenomenological anisotropy constant. The second term is the Zeeman energy, describing the interaction of $\vec{m}$ with the applied magnetic field $\vec{h}$.

In Figure 4 (a)-(e) cartoon pictures of the energy as a function of $\phi$ illustrate the evolution of the magnetic moment as the magnetic field

[1] The easy axis is the preferred direction of the magnetic moment in absence of an applied magnetic field.

is changed. The direction of the magnetic moment is determined by a local minimum of $E(\phi)$ (indicated by the ball). If the applied magnetic field $h$ is changed, with $\theta$ fixed, the positions of the local minima vary continuously as well. For large magnetic field (a) the magnetic moment points along $\vec{h}$ . As $h$ is reduced $\vec{m}$ moves towards the easy axis (b). For zero magnetic field $\vec{m}$ passes the easy axis (c); there are two local minima in the orientation dependence of the energy, namely, at $\phi = 0$ and $\phi = \pi$. As the field is ramped further there exists one particular field (d) where the barrier between the metastable minimum and the stable minimum will disappear by merging with a saddle point. At this so-called switching field, $h_{\mathrm{sw}}$, the orientation of $\vec{m}$ varies discontinuously, jumping to the other minimum. For a large negative magnetic field $\vec{m}$ again lies in the $\vec{h}$ direction (e). The condition defining the switching field $h_{\mathrm{sw}}$, namely, that $E(\phi)$ has a saddle point

$$\left(\frac{\partial^2 E}{\partial \phi^2}\right) = \left(\frac{\partial E}{\partial \phi}\right) = 0 \tag{3}$$

yields $\tan\phi = -(\tan\theta)^{\frac{1}{3}}$ and hence the switching field is

$$h_{\mathrm{sw}} = \pm \frac{2k}{\left((\sin\theta)^{\frac{2}{3}} + (\cos\theta)^{\frac{2}{3}}\right)^{\frac{3}{2}}} \,. \tag{4}$$

### 3.2. Real systems

The original Stoner-Wohlfarth model [17] assumed only one anisotropy contribution, namely, a uniaxial anisotropy of second order as in Eq. (2). In real systems, however, the anisotropy has several contributions, e.g., shape, surface, magnetocrystalline, magnetoeleastic anisotropy, etc.. A generalization of the Stoner-Wohlfarth model for an arbitrary effective anisotropy was introduced by Thiaville [18]. By calculating the energy of the particle one is able to determine the switching field for all angles of the applied magnetic field, i.e., the critical surface of the switching field.

The magnetization reversal of 3 nm cobalt particles was studied by Jamet et al. [19] using a micro-SQUID technique. The measured angular dependence of the switching field was used to determine the different contributions to the magnetic anisotropy of the nanoparticle by fitting it to the generalized Stoner-Wohlfarth model by Thiaville [18]. The measured critical surface of nearly all Co particles revealed a dominating uniaxial anisotropy due to surface anisotropy. The difficulty in observing stronger higher order terms lies in the fact that nearly

all structural defects in the particle lead to a dominating uniaxial anisotropy [19].

## 4. Anisotropy fluctuations

### 4.1. Phenomenological model

In Refs. [6, 12, 13, 14] a phenomenological model for nanoscale ferromagnetic grains was introduced. The magnetic field dependent part of the Hamiltonian introduced there, namely

$$\mathcal{H}_{\text{anis}} + \mathcal{H}_{\text{Zee}} = -k_N(\vec{S} \cdot \hat{z})^2/s_0 - \vec{h} \cdot \vec{S} \tag{5}$$

consists, analogous to Eq. (2), of a uniaxial anisotropy and a Zeeman term with the classical magnetic moment replaced by the total spin of the grain $\vec{S}$, $\vec{S} = \sum_i \vec{S}_i$ being the sum over all electron spins. We model the different contributions to the anisotropy of the magnetic grain by a single uniaxial anisotropy, assuming that this is the most dominant term (see Sec. 3.2). Assuming the anisotropy to change from state to state of the grain the anisotropy constant $k_N$ depends now on $N$, the number of electrons on the grain. To change $s_0$, the spin value of the ground state, by applying a magnetic field requires, in general, a magnetic field much larger than the magnetic field in DGR's experiments. Therefore we consider the case where the changing magnetic field only rotates the total spin moment, without changing its magnitude.

The jumps in the magnetic field dependence of the resonances measured by DGR have been attributed to the sudden reversal of the nanoparticle's magnetic moment [5], which occurs when the energy barrier between a metastable state and the true ground state is tuned to zero by the applied field [see Fig. 4(d)]. In order to illustrate the magnetic field dependence of resonances in our model, one has to calculate the tunneling energy $\Delta E^+_{fi} = E^{N+1}_f - E^N_i$ as a function of the magnetic field $h = g\mu_B\mu_0 H$. Depending on the value of $s_0$, one can either consider the spin of the grain classically (for the larger grains in DGR's experiment) or one has to treat it in a quantum mechanical framework (smaller grains in DGR's experiment). In order to calculate the ground state energies of a given grain one either calculates the classical ground state energy by looking for the orientation of $\vec{S}$ that gives a local minimum of Eq. (5) or one numerically diagonalizes $\mathcal{H}_{\text{anis}} + \mathcal{H}_{\text{Zee}}$. Figure 5 shows the ground state tunneling energy as a function of $h/k_N$ for an initial spin of $s_i = 1000$ and a final spin $s_f = s_i \pm 1/2$.

The tunneling resonances indeed show a jump at $h_{\text{sw}}$. However, if we neglect anisotropy fluctuations by choosing $k_N = k_{N+1}$ (Fig. 5,

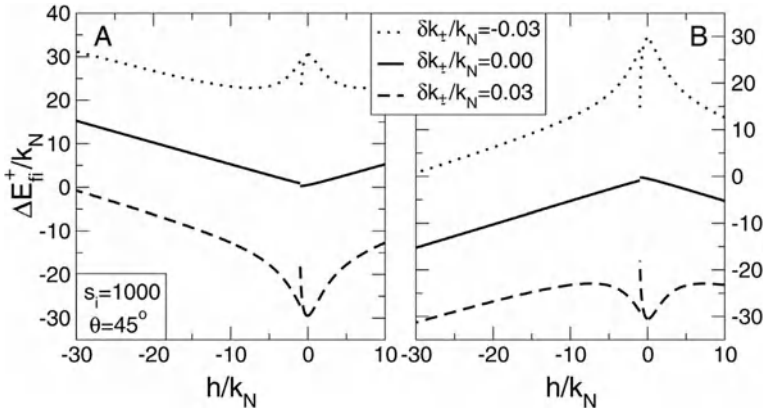


*Figure 5.* Tunneling energies $\Delta E^{+}_{fi}$ for $\mathcal{H}_{\rm anis} + \mathcal{H}_{\rm Zee}$, plotted as functions of $h/k_N$ sweeping positive to negative, illustrating the effects of anisotropy fluctuations ($\delta k_{\pm} = k_{N\pm1} - k_N$) for the transitions from ($s_i = 1000$, $N$) to (A) ($s_i - 1/2$, $N+1$) and (B) ($s_i + 1/2$, $N+1$). The magnetic field makes an angle, $\theta = \pi/4$ with the easy axis (taken from Ref. [12]).

solid lines), the $\Delta E^{\pm}_{fi}$ lines also have two unsatisfactory features: (i) An upward (downward) jump in $\Delta E^{+}_{fi}(h)$ as $|h|$ increases past $|h_{\rm sw}|$ is always followed by a positive (negative) large-$h$ slope, whereas it is observed experimentally (e.g., Fig. 3) that either upward or downward jumps can occur for states having a given large-$h$ slope; and (ii), beyond the switching field, the dependence on $h$ is monotonic (close to linear), in disagreement with Fig. 3. All attempts we made to explain such behavior by more complicated than uniaxial anisotropies, or by higher order terms, neglecting anisotropy fluctuations, were unsuccessful.

Now, the very fact that the field dependence of each resonance in Fig. 3 differs so strikingly from that of all others implies that the anisotropy energy fluctuates significantly from eigenstate to eigenstate. We shall mimic these fluctuations by simply using two different anisotropy constants in $\mathcal{H}_{\rm anis}$, say $k_N$ and $k_{N\pm1} \equiv k_N + \delta k_{\pm}$, for $N$- or $(N \pm 1)$-electron states. $k_N$ can be estimated from the switching field using Eq. (4) as $k_N \approx \mu_0 \mu_B H_{\rm sw}$ yielding $k_N \approx 0.01$ meV. Now, as illustrated in Fig. 5, $\delta k_{\pm}/k_N$ in the range of a few percent is su cient to reverse the sign of the energy jum ps at $H_{\rm sw}$. Note that $\delta k_{\pm} \neq 0$ also causes the spectral lines to exhibit rather strong nonmonotonic "kinks" near $h_{\rm sw}$, whose amplitudes are of order $s_0 \delta k_{\pm}$. Qualitatively similar nonmonotonicities have been observed (see Fig. 3), with kink amplitudes on the scale of a few 0.1 meV, in rough agreement with $s_0 \delta k_{\pm}$ for $s_0 \simeq 1000$.

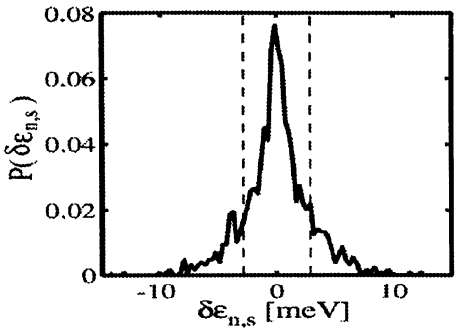


*Figure 6.* Distribution function of single-particle anisotropies for a 143 atom nanoparticle. The mean value is 15 $\mu$eV, the width of the distribution is $\Delta = 2.9$ meV (taken from [15]).

### 4.2. TIGHT BINDING MODEL

Recently, Cehovin, Canali, and MacDonald [15] used a microscopic tight-binding model including atomic spin-orbit interactions to address the mesoscopic physics of magnetocrystalline anisotropy of ferromagnetic nanoparticles. They concluded that significant fluctuations of the anisotropy energy, as conjectured in the previous section, can indeed occur in magnetic particles of nanometer size. Their calculations demonstrate that the magnetic anisotropy per atom fluctuates by several percent when the number of electrons in a particle, of the size of DGR's particles, changes by one. They can explain the surprisingly large fluctuations in anisotropy energy by the following observation: The anisotropy fluctuations in the particle are given by a single-particle contribution chosen at random from a distribution as shown in Fig. 6: $k_{N+1} - k_N \approx \delta E_{N+1}/N_a$. This distribution of single-particle anisotropies is characterized by a mean more than two orders of magnitude smaller than its variance $\Delta^2$. Therefore, the contribution of a given orbital, chosen at random from the distribution, being of order $\Delta$, can change the total anisotropy energy by a much larger amount than what a naive estimate based only on the (small) mean value would suggest, giving rise to fluctuations in $k_N$ of the order of one percent for particles containing 1000 atoms.

## 5. Conclusions

In this article we have reviewed recent experimental and theoretical results on fluctuations of anisotropy energies in magnetic particles so

small that their discrete energy spectrum must be considered. Experimental results on tunnel spectroscopy of nanoscale cobalt grains [5, 6] show very different magnetic field dependencies of individual eigenenergies of the particle. Theoretical models [6, 12, 14, 15] indicate that this behavior results from fluctuations of the anisotropy energy of the particle.

## References


1. K.E. Johnson, J. Appl. Phys. **87**, 5365 (2000).
2. S. Sun, C.B. Murray, D. Weller, L. Folks, and A. Moser, Science **287**, 1989 (2000).
3. L.F. Schelp, A. Fert, F. Fettar, P. Holody, S.F. Lee, J.L. Maurice, F. Petroff, A. Vaurés, Phys. Rev. B 56, 5747 (1997).
4. H. Shimada, K. Ono, Y. Ootuka, J. Phys, Soc. Japan **67** 2852 (1998) .
5. S. Guéron, M.M. Deshmukh, E.B. Myers, and D.C. Ralph, Phys. Rev. Lett. **83**, 4148 (1999).
6. M.M. Deshmukh, S. Kleff, S, Guéron, E. Bonet, A.N. Pasupathy, J. von Delft, and D.C. Ralph, Phys. Rev. Lett. **87**, 226801 (2001).
7. D.C. Ralph, C.T. Black, and M. Tinkham, Phys. Rev. Lett. **74**, 3241 (1995); **76**, 688 (1996); **78**, 4087 (1997).
8. K. Ono, H. Shimada, and Y. Ootuka, J. Phys. Soc. Jpn. **66**, 261 (1997); **67**, 2852 (1998).
9. J. Barnaś and A. Fert, Europhys. Lett. **44**,85 (1998).
10. J. Barnaś and A. Fert, Phys. Rev. Lett. **80**, 1058 (1998).
11. D. Weinmann, W. Háusler, W. pfaff, B. Kramer, and U. Weiss, Phys. Rev. Lett. **26**, 467 (1994).
12. S. Kleff, J. von Delft, M.M. Deshmukh, and D.C. Ralph, Phys. Rev. B **64**, 220401(R) (2001).
13. S. Kleff and J. von Delft, Phys. Rev. B **65**, 214421 (2002).
14. C.M. Canali and A.H. MacDonald, Phys. Rev. Lett. **85**, 5623 (2000).
15. A. Cehovin, C.M. Canali, and A.H. MacDonald, Phys. Rev. B **66**, 094430 (2002).
16. J. von Delft and D.C. Ralph, Phys. Rep. **345**, 61 (2001).
17. E.C. Stoner and E.P. Wohlfarth, Philos. Trans. London Ser. A **240**, 599 (1948).
18. A. Thiaville, Phys. Rev. B **61**, 12221 (2000).
19. M. Jamet, W. Wernsdorfer, C. Thirion, D. Mailly, V. Dupuis, P. Mélinon, and A. Pérez, Phys. Rev. Lett. **86**, 4676 (2001).

# Full Counting Statistics in Multi-Terminal Normal Metal Tunnel Junction Structures

J. Börlin, W. Belzig and C. Bruder
*Department of Physics and Astronomy, University of Basel, CH-4056 Basel, Switzerland*

## 1. Introduction

Current fluctuations in multi-terminal structures are at the heart of mesoscopic physics (see Ref. [1]). The current noise power in small structures depends on correlations between charge transfer events. For example, in a one-channel conductor with transparency $T$ the noise power at zero temperature is $P_I = 2e\bar{I}(1-T)$ [2, 3], where $\bar{I}$ is the average current. The suppression factor $1-T$ is a result of the Fermi correlation between electrons in different scattering events. An electron tunneling through the channel prevents the next electron from entering ('antibunching'). Thus, the noise is suppressed in comparison to fully uncorrelated charge transfer (described by Schottky noise $S_I = 2e\bar{I}$). A convenient measure of the suppression is the Fano factor defined as $F = P_I/2e\bar{I}$. In the case of two tunnel junctions in series with conductances $g_{1(2)}$, respectively, the Fano factor can be expressed as $2g_1g_2/(g_1+g_2)^2$. It is suppressed below 1 for all ratios of $g_1$ and $g_2$, again a consequence of the Pauli principle.

The extension to multi-terminal structures is an important generalization, first realized by Büttiker [4, 5, 6]. The simplest example is a beam splitter for electrons. Due to the antibunching property of the Fermions, correlations between the current fluctuations in different terminals, the so-called crosscorrelations, are always negative. This effect was experimentally veryfied [7, 8, 9].

An important step forward to extend the theory of current fluctuations was made by Levitov and coworkers [10, 11, 12]. They introduced the concept of *full counting statistics* (FCS). Here, one considers the probability $P(N;t_0)$ that $N$ charges are transfered during a certain (fixed) time $t_0$. For an $N$-terminal structure, this is generalized to the probability $P(N_1, N_2, ..., N_N; t_0)$ that $N_i$ charges are transferred into terminal $i$. All the higher moments of the current can be calculated from the full counting statistics; i.e., it provides information that is not contained in the noise. Studies of the FCS in various multi-terminal



*R. Fazio et al. (eds.), New Directions in Mesoscopic Physics,* 313–323.
© 2003 *Kluwer Academic Publishers. Printed in the Netherlands.*

structures with normal or superconducting leads have been performed [13, 14, 15, 16, 17, 18, 19, 20, 21].

In this paper we study the FCS of a particular three terminal structure. A current is passed through a series of two tunnel junction. A mesoscopic voltage probe [5, 22, 23] is attached to the region between the two tunnel junctions. Although the voltage terminal does not change the average current, it has a strong influence on the counting statistics, as we will show below.

## 2. Counting Statistics of a Multi-Tunneljunction Geometry

We will use the Keldysh-Green's function circuit theory developed by Nazarov and coworkers [24, 25, 26, 27]. We evaluate the cumulant-generating function $S(\chi_1, \chi_2, ..., \chi_N; t_0)$ defined by

$$e^{-S(\chi_1,\chi_2,...,\chi_N;t_0)} = \sum_{\vec{N}} P(N_1, N_2, ..., N_N; t_0) e^{-i\sum_j N_j \chi_j} \ . \qquad (1)$$

Below we will use the vector notation $\vec{\chi} = (\chi_1, ..., \chi_N)$ and $\vec{N} = (N_1, ..., N_N)$. A general expression of $S(\vec{\chi}; t_0)$ for star-shaped structures (left panel of Fig. 1) was derived in [28]. For normal-metal structures it boils down to

$$S(\vec{\chi}; t_0) = \frac{t_0}{2e^2} \int_{-\infty}^{\infty} dE \left[ \sqrt{g_\Sigma^2 + 4 \sum_{j \neq k} g_k g_j (e^{i(\chi_k - \chi_j)} - 1) f_k (1 - f_j)} - g_\Sigma \right], \qquad (2)$$

where $f_i$ is the Fermi occupation function of terminal $i$. Here, we introduced the abbreviation $g_\Sigma = \sum_{k=1}^{N} g_k$ for the sum of all conductances.

The current-current correlators are measures of how charge transfers in two leads $ij$ are correlated and can be calulated from $S(\vec{\chi}; t_0)$:

$$P_{Iij} = \int_{-\infty}^{\infty} dt \langle \{ \delta I_i(t), \delta I_j(0) \} \rangle = \frac{2e^2}{t_0} \left. \frac{\partial^2 S(\vec{\chi}; t_0)}{\partial \chi_i \partial \chi_j} \right|_{\vec{\chi}=\vec{0}} , \qquad (3)$$

where $\delta I_i(t) = I_i(t) - \langle I_i \rangle$ is the time-dependent current fluctuation in terminal $i$. The off-diagonal ($i \neq j$) elements of $P_{Iij}$ are called crosscorrelations, the diagonal ($i = j$) elements autocorrelations. As an immediate consequence of the permutability of the derivatives and of current conservation, we have $P_{I_{ij}} = P_{I_{ji}}$ and $\sum_i P_{I_{ij}} = 0$, i.e., the noise power $P_I$ is completely determined by $(N-1)N/2$ elements, only.

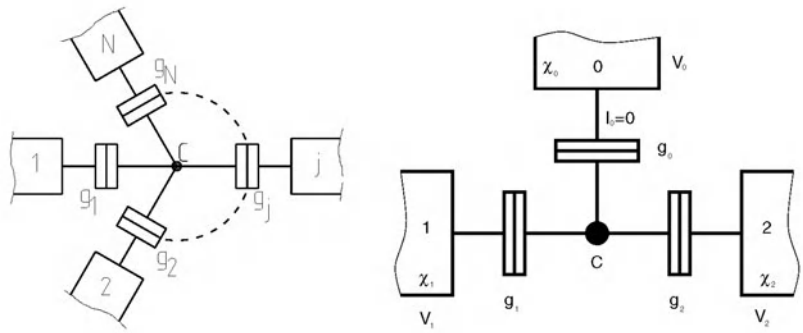


*Figure 1.* Left: Multi-terminal tunnel junction structure with $N$ terminals/tunnel junctions of conductance $g_i$ connected to the central node $C$. Right: Double tunnel junction structure with voltage probe. The counting fields $\chi_0$, $\chi_1$, and $\chi_2$ are introduced in terminals 0, 1, and 2, respectively. The structure is biased such that the mean current $\bar{I}_0$ in lead 0 vanishes.

## 3. Double Tunnel Junction with Voltage Probe

We now consider the structure shown in the right panel of Fig. 1. The potential $V_0$ is adjusted such that the mean current $\bar{I}_0$ in lead 0 vanishes, i.e., terminal 0 is a voltage probe. A voltage $V > 0$ is applied between terminal 1 and terminal 2: $V_1 = 0$, $V_2 = V > 0$. From $\bar{I}_0 = 0$ we find $V_0 = V g_2/(g_1 + g_2)$.

The average current $\bar{I} = \bar{I}_1$ from terminal 2 to terminal 1 is the same as in a simple double tunnel junction structure. However, we expect a change in the charge fluctuations: now particles can tunnel from terminal 2 to 1 either directly or via terminal 0 (see Fig. 4). To study these fluctuations, we calculate the cumulant-generating function (CGF) $S(\chi_0, \chi_1, \chi_2; t_0)$ for this configuration at zero temperature for a fixed mean number of particles $\bar{N} = \bar{I} t_0/e$ transmitted from 2 to 1 during a time interval $t_0$. The CGF $S(\chi_0, \chi_1, \chi_2; t_0)$ in Eq. (2) can be expressed as [29]

$$\begin{aligned} S(\vec{\chi}; t_0) \;=\; & -\frac{\bar{N}}{2}\Bigg(\frac{1}{g_1}\sqrt{g_\Sigma^2 + 4g_0 g_1(e^{i\chi_0 - i\chi_1} - 1) + 4g_1 g_2(e^{i\chi_2 - i\chi_1} - 1)} \\ & + \frac{1}{g_2}\sqrt{g_\Sigma^2 + 4g_0 g_2(e^{i\chi_2 - i\chi_0}) - 1) + 4g_1 g_2(e^{i\chi_2 - i\chi_1} - 1)}\Bigg) \end{aligned} \quad (4)$$

As a consequence of current conservation, $S$ depends only on the differences $\chi_1 - \chi_0$, $\chi_2 - \chi_0$. Therefore it is sufficient to study the function $S(0, \chi_1, \chi_2; t_0) \equiv S(\chi_1, \chi_2; t_0)$. In contrast to the case without voltage probe, the CGF is not symmetric under the transformation $g_1 \leftrightarrow g_2$.

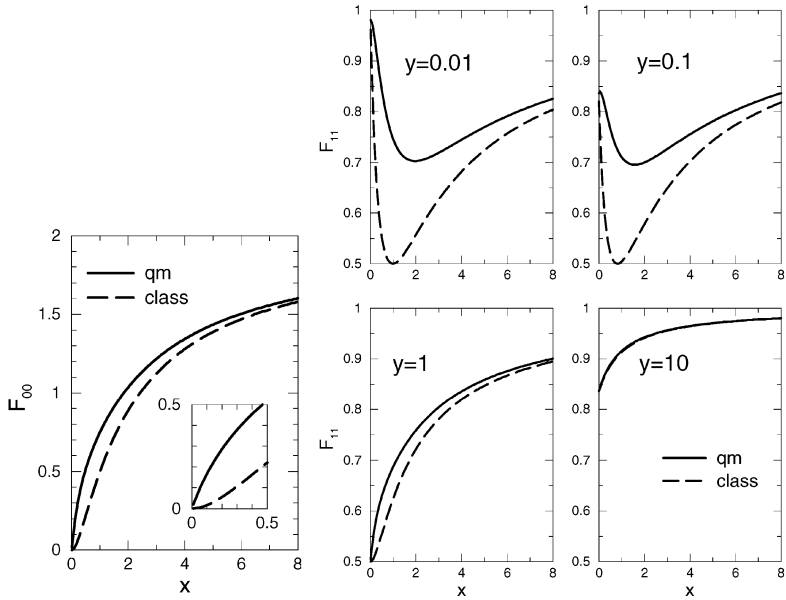


*Figure 2.* Left panel: Fano factor $F_{00}(x)$ (classical Langevin approach (dashed), quantum mechanical Keldysh Green's function approach (solid)) as a function of $x = g_0/(g_1 + g_2)$. For strong coupling $x \to \infty$, both $F_{00}$ and $F_{00}^L$ approach 2. In the weak-coupling limit $x \to 0$, where the Langevin and the Keldysh Green's function approach exhibit a qualitatively different behavior (see inset). Right panel: Fano factors $F_{11}(x, y)$ and $F_{11}^L(x, y)$ (Langevin approach (dashed), Keldysh Green's function approach (solid)) for different $y = g_2/g_1$ as a function of $x$. In the asymmetric limit $y \to 0$, $F_{11}$ has its minimum at $x = 2$, $F_{11}^L$ at $x = 1$.

In the following sections we study auto- and crosscorrelations for a fixed current $\bar{I}$ in terminal 1. It is useful to normalize the noise power by the Poisson value $2\,e\,|\bar{I}|$. We also define a generalized Fano factor $F_{ij} = P_{I_{ij}}/(2e|\bar{I}|)$ and parametrize the conductances by the two parameters $x = g_0/(g_1 + g_2)$ and $y = g_2/g_1$.

## 4. Current-Current Correlators

The autocorrelations, i.e. the diagonal elements $F_{ii}$, obtained from Eq. (4) using Eq. (3) are

$$F_{00}(x) \;=\; 2x\,\frac{x^2 + x + 1}{(1 + x)^3}\,,$$

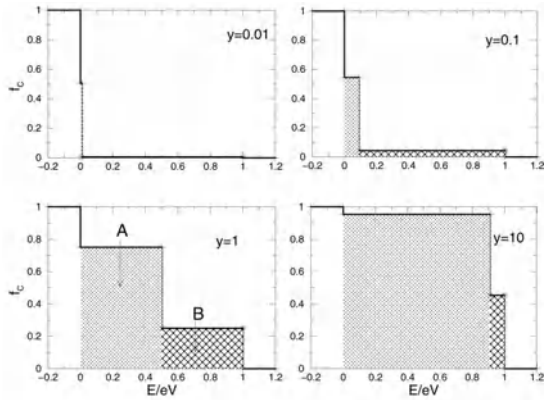


*Figure 3.* Distribution function $f_C(E)$ on island $C$ for different values of y for a coupling $x = g_0/(g_1 + g_2) = 1$. Area A indicates the fraction of particles that can go from the island to terminal 1, area B the fraction of particles that have the choice either to go to terminal 1 or terminal 0. For large values of the asymmetry $y$, A is much larger than B. For small $y$, A and B have areas of comparable size.

$$F_{11}(x,y) \;=\; 1 + \frac{2+4\,x}{(1+x)^3(1+y)^2} - \frac{2}{(1+x)(1+y)}\,. \tag{5}$$

Note that $F_{00}$ does not depend on the asymmetry $y = g_2/g_1$ of the junctions. We compare these results with the classical the Langevin approach [1, 29, 30], in which one finds

$$F^L_{00}(x) = \frac{2x^2}{(1+x)^2}\;,\; F^L_{11}(x,y) = \frac{1+(x(1+y)+y)^2}{(1+x)^2(1+y)^2}\,. \tag{6}$$

The Fano factor $F_{22}$ in terminal 2 is obtained from $F_{11}$ by interchanging indices 1 and 2 in $F_{11}$, i.e. the replacement $y \to 1/y$. This is a consequence of the special symmetry of the setup. The Fano factors $F_{00}$ and $F_{11}$ are plotted in Fig. 2 as a function of $x$ for different $y$. The following limits are easily understood:

- $x \ll 1$ ($g_0 \ll g_1 + g_2$): we recover the double tunnel junction case.
- $x \gg 1$ ($g_0 \gg g_1 + g_2$): junctions 1 and 2 are decoupled. Keldysh Green's and Langevin approaches give the same results.
- $y \gg 1$ ($g_2 \gg g_1$): noise in 1 is that of a single junction. It follows that the autocorrelation $F_{11}$ is classical.
- $y \ll 1$ ($g_2 \ll g_1$): no classical behavior of $F_{11}$ expected since junctions 1 and 0 are strongly coupled and Fermi correlations are

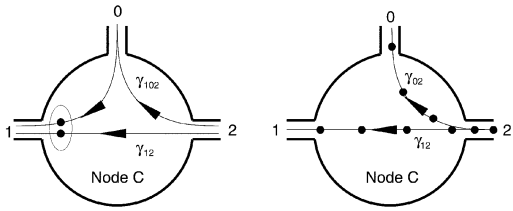


*Figure 4.* Left: two possible paths $\gamma_{102}$ and $\gamma_{12}$ from terminal 2 to 1. The circled region indicates a situation where Fermi correlations are important. Right: the electrons enter the node from 2. Then the electrons will split up in two path $\gamma_{12}$ and $\gamma_{02}$. Therefore, if an electron enters terminal 0, no electron enters terminal 1. This leads to negative crosscorrelations $F_{01}$.

important. In the Keldysh-Green's function approach, the resonant point $x_{min}$ (where $F_{11}$ has its minimum) is located at $x_{min} = 2$ in contrast to the Langevin approach, where $x^L_{min} = 1$. With growing $y$ both minima $x_{min}$, $x^L_{min}$ are shifted to the origin.

An alternative explanation to understand the discrepancy between the Keldysh Green's function and the Langevin approach can be found by considering the distribution function

$$f_C(E) = 1 - \frac{g_0}{g_\Sigma}\Theta(E - eV_0) - \frac{g_1}{g_\Sigma}\Theta(E - eV_1) - \frac{g_2}{g_\Sigma}\Theta(E - eV_2)\ , \quad (7)$$

of the node $C$. This distribution function is plotted in Fig. 3 for $x = 1$ where the deviations between Keldysh Green's function and Langevin approaches are most pronounced. The shaded area A corresponds to particles on the node $C$ which can go to terminal 1. On the other hand, the cross-hatched area B corresponds to particles which are able to go either to terminal 0 or to 1. For large $y$ the majority of particles goes directly to 1 since B is much larger than A. For small $y$ these areas become comparable to each other. Hence for $x = 1$ the fraction of particles which go to 1 via 0 (path $\gamma_{102}$ see Fig. 4) becomes comparable to the direct part (path $\gamma_{12}$). It is therefore more likely that a particle on path $\gamma_{102}$ prevents another particle on $\gamma_{12}$ from entering the node $C$ because of the exclusion principle. In this limit we expect a deviation of the statistical properties in 1 from the classical theory, which neglects Fermi correlations in agreement with Fig. 2.

The crosscorrelations, i.e. off-diagonal elements of $F_{ij}$ obtained from Eq. (4) using Eq. (3) are

$$F_{01}(x, y) \ = \ -\frac{x(1 + x^2 + (1 + x)^2 y)}{(1 + x)^3(1 + y)}\ ,$$

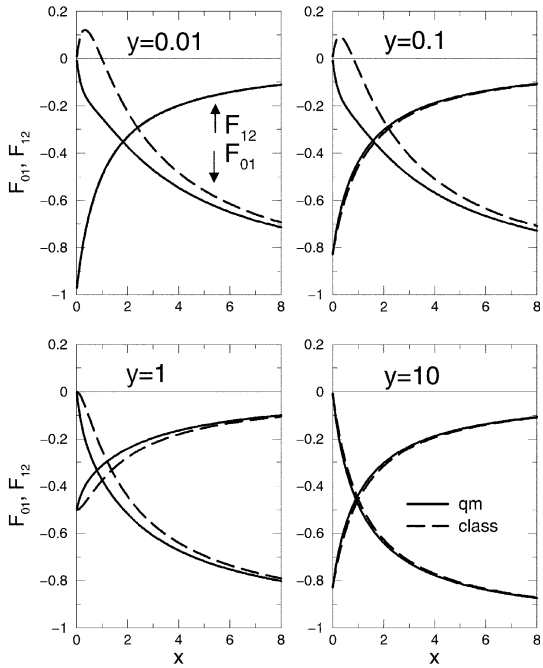


*Figure 5.* Crosscorrelations $F_{01}$, $F_{12}$ for different values of the asymmetry $y = g_2/g_1$ as a function of the coupling $x = g_0/(g_1 + g_2)$. For small values of the asymmetry $y \ll 1$ and $x \in [0, 1]$ the Langevin approach gives positive crosscorrelations $F_{01}$. In the same interval of $x$ the deviation of Langevin and Keldysh Green's function approach is largest for $F_{01}$ in the case of small asymmetries $y \ll 1$, whereas for $F_{12}$ the deviation is largest for the symmetric case $y = 1$

$$F_{12}(x, y) \;=\; -\frac{(1+x)^2(1+y)^2 + 2x^2\, y}{(1+x)^3(1+y)^2}\,. \tag{8}$$

As explained in the introduction, already three elements of $F_{ij}$ contain the full information on auto- and crosscorrelations of the system.

The Langevin approach yields:

$$\begin{aligned} F_{01}^L(x, y) \;&=\; \frac{x(1 - y - x(1+y))}{(1+x)^2(1+y)}\,, \\ F_{12}^L(x, y) \;&=\; -\frac{x(1+y)^2 + 1 + y^2}{(1+x)^2(1+y)^2}\,. \end{aligned} \tag{9}$$

In contrast to the Keldysh Green's function approach, $F_{01}^L$ gets positive for $y \ll 1$ and $x \in [0, 1]$ (see Fig. 5). As already discussed in [4] the

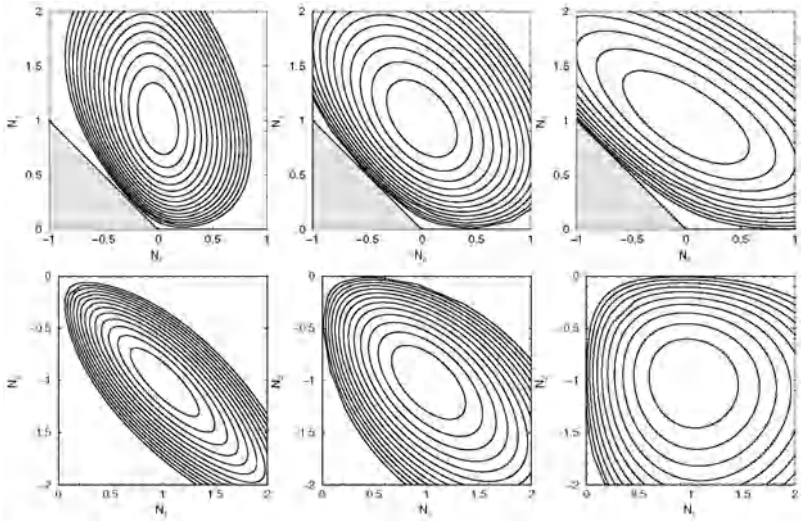

*Figure 6.* Full counting statistics of the device. Upper row: joint probability distribution for terminal 0 and 1 $P_{01}(N_0, N_1; t_0)$; Lower row: joint probability distribution for terminal 1 and 2 $P_{12}(N_1, N_2; t_0)$. Columns from left to right are for $x = 0.1, 1$ and 10. Note, that $N_0$, $N_1$ and $N_2$ are rescaled by $\bar{N}$.

strictly negative crosscorrelations in fermionic structures are due to the exclusion principle. A qualitative explanation is given in the right sketch of Fig. 4.

## 5. Full Counting Statistics

For arbitrary parameter values $x$ and $y$, we were not able to derive an analytic expression of the probability distribution function $P_{12}(N_1, N_2; t_0)$. However, in certain limits in which the square roots of the cumulant-generating function $S(\chi_0, \chi_1, \chi_2; t_0)$ can be expanded one is able to perform the integration over $\chi_i$.

In the strong-coupling limit $x \gg 1$ the square root in Eq. (3) can be expanded. To lowest order in $1/x$ we find for the CGF

$$S(\chi_1, \chi_2; t_0) = -\bar{N}\left(e^{-i\chi_1} + e^{i\chi_2} - 2\right) . \tag{10}$$

The corresponding joint probability distribution $P_{12}(N_1, N_2; t_0)$ is given by

$$P_{12}(N_1, N_2; t_0) = \frac{\bar{N}^{N_1 - N_2}}{N_1!(-N_2)!} e^{-2\bar{N}} \tag{11}$$

if $N_1 \geq 0$ and $N_2 \leq 0$, and $P_{12}(N_1, N_2; t_0) = 0$ otherwise. Thus the probability distribution is simply the product of two Poisson distributions of the charge numbers in each junction. These two processes are completely uncorrelated. The probability distributions $P_1(N_1; t_0)$ and $P_2(N_2; t_0)$ are therefore Poissonian too.

The distribution function of terminal 0 in the limit $x \gg 1$ is obtained from the $\chi_0$-dependent CGF $S(\chi_0; t_0)$. Because the CGF is only a function of the differences of the counting fields $\chi_i - \chi_j$ we can use the expression in Eq. (10) by replacing $\chi_1$ by $\chi_0$ and $\chi_2$ by $-\chi_0$. We obtain $S(\chi_0; t_0) = -\bar{N}\left(e^{i\chi_0} + e^{-i\chi_0} - 2\right)$. The corresponding probability distribution $P_0(N_0; t_0)$ is

$$P_0(N_0; t_0) = \sum_{n=0}^{\infty} \frac{\bar{N}^{|N|+m}}{n!(|N|+m)!} e^{-2\bar{N}} \tag{12}$$

This a sum of Poissonian probability distributions, a consequence of the independent electron transfers.

We now discuss the joint probability distributions for general parameters. Here, an analytic solution has been obtained numerically. Figure 6 shows contour plots of the probability distributions $P_{01}$ and $P_{12}$ for couplings $x = \{0.1, 0.5, 10\}$ in the symmetric ($y = 1$) case. Contour plots of a similar structure are studied in [27]. These contours have been calculated using the saddle-point approximation [27]. For $N_0 + N_1 < 0$ or $N_1 < 0$ the probability distribution $P_{01}(N_0, N_1; t_0)$ is zero (upper row of Fig. 6). Equivalently, in the lower row of Fig. 6, $P_{12}$ is equal zero if $N_1 < 0$ or $N_2 > 0$. This is a consequence of the fermionic statistics of the particles and the charge conservation at the node $C$. On going from weaker to stronger coupling, i.e. from $x = 0.1$ to $x = 10$, the negative crosscorrelation in $P_{01}$ increases. This can be seen either from the Fano factor, Eq. (8), or from $P_{01}$ by considering the average of $N_0$ as a function of $N_1$. This defines a line $(N_1, \bar{N}_0(N_1))$ in the figure, where $\bar{N}_0(N_1) = \sum_{N_0} P_{01}(N_0, N_1) N_0$. For curves $(N_1, \bar{N}_0(N_1))$ with negative slope, the FCS $P_{01}$ is negatively correlated. The contour plots of $P_{12}$ are symmetric around the straight line $N_1 = -N_2$ as a consequence of $y = 1$. The FCS $P_{12}$ broadens with growing coupling $x$, because for strong coupling it is more likely that a larger number of particles $N_0$ (comparable to $N_1$, $N_2$) is transfered to terminal 0. In the limit $x \to 0$ the contour plot of the FCS $P_{12}$ would be the straight line $N_1 = -N_2$.

## 6. Conclusion

We have studied the counting statistics of a double tunnel junction with a voltage probe attached to the central island. Using the Keldysh

Green's function approach we have found a the cumulant generating function at zero temperature. We have discussed noise correlations and crosscorrelations in the various terminals. The presence of the voltage probe leads to an interesting behaviour of the Fanofactor of the transmitted current, see Figure 2. The crosscorrelations are always negative as expected, however their magnitude is affected by the presence of the voltage probe. Comparing our results for the current correlator with the classical Langevin approach we have found that this approach fails to describe the weak coupling regime, whereas it gives reasonable results if the voltage probe is coupled sufficiently strongly.

## Acknowledgements

Our work was supported by the Swiss NSF and the NCCR Nanoscience.

## References

1. Ya. M. Blanter and M. Büttiker, Phys. Rep. **336**, 1 (2000).
2. V. A. Khlus, Zh. Eksp. Teor. Fiz. **93**, 2179 (1987) [Sov. Phys. JETP **66**, 1243 (1987).
3. G. B. Lesovik, Pis'ma Zh. Eksp. Teor. Fiz. **49**, 513 (1989) [JETP Lett. **49**, 592 (1989).
4. M. Büttiker, Phys. Rev. Lett. **65**, 2901 (1990).
5. M. Büttiker, Physica B **175**, 199 (1991).
6. M. Büttiker, Phys. Rev. B **46**, 12485 (1992).
7. M. Henny *et al.*, Science **284**, 296 (1999).
8. W. D. Oliver *et al.*, Science **284**, 299 (1999).
9. S. Oberholzer *et al.*, Physica (Amsterdam) E **6**, 314 (2000).
10. L. S. Levitov and G. B. Lesovik, Pis'ma Zh. Eksp. Teor. Fiz. **58**, 225 (1993) [JETP Lett. **58**, 230 (1993)].
11. L. S. Levitov, H. W. Lee, and G. B. Lesovik, J. Math. Phys. **37**, 4845 (1996).
12. H. Lee, L. S. Levitov, and A. Yu. Yakovets, Phys. Rev. B **51**, 4079 (1996).
13. B. A. Muzykantskii and D. E. Khmelnitzkii, Phys. Rev. B **50**, 3982 (1994).
14. Yu. V. Nazarov, Ann. Phys. (Leipzig) **8**, SI-193 (1999).
15. P. Samuelsson and M. Büttiker, Phys. Rev. B **66**, 201306(R) (2002).
16. P. Samuelsson, cond-mat/0210409 (unpublished).
17. M. Kindermann, Yu. V. Nazarov, and C. W. J. Beenakker, Phys. Rev. Lett. **88**, 063601 (2002).
18. Yu. Makhlin, G. Schön, and A. Shnirman, Phys. Rev. Lett. **85**, 4578 (2000).
19. H.-A. Engel and D. Loss, Phys. Rev. B **65**, 195321 (2002).
20. F. Taddei and R. Fazio, Phys. Rev. B **65**, 075317 (2002).
21. M.-S. Choi, F. Plastina, and R. Fazio, cond-mat/0208318 (unpublished).
22. M. Büttiker, IBM J. Res. Develop. **32**, 63 (1988).
23. C. W. J. Beenakker and M. Büttiker, Phys. Rev. B **46**, 1889 (1992).
24. Yu. V. Nazarov, Superlattices Microst. **25**, 1221 (1999).

25. W. Belzig and Yu. V. Nazarov, Phys. Rev. Lett. **87**, 067006 (2001).
26. W. Belzig and Yu. V. Nazarov, Phys. Rev. Lett. **87**, 197006 (2001).
27. Yu. V. Nazarov and D. Bagrets, Phys. Rev. Lett. **88**, 196801 (2002).
28. J. Börlin, W. Belzig, and C. Bruder, Phys. Rev. Lett. **88**, 197001 (2002).
29. J. Börlin, diploma thesis, University of Basel (2002).
30. S. A. van Langen and M. Büttiker, Phys. Rev. B **56**, 1680 (1997).

# Resonant Cooper-Pair Tunneling: Counting Statistics and Frequency-Dependent Current Noise

A.A. Clerk
*Departments of Applied Physics and Physics*
*Yale University, PO Box 208284, New Haven, CT 06520-8284*

## 1. Introduction

Resonant Cooper-pair tunneling, also known as Josephson quasiparticle tunneling, refers to transport cycles in superconducting single-electron transistors (SSET's) which involve the transfer of both Cooper pairs and quasiparticles [1, 2, 3]. They have recently been the subject of renewed attention, both because of their unusual noise properties [4, 5, 6] and because of their utility in measuring the state of a charge superconducting qubit [7, 8]. In terms of noise properties, it has been shown that charge fluctuations associated with these processes can induce a population inversion in a coupled two-level system (i.e in terms of its charge noise, the transistor effectively has a negative temperature) [5, 6]. The shot-noise in the current through the transistor was also found to have remarkable properties [4, 5]. By tuning the strength of the Cooper pair tunneling relative to the quasiparticle tunneling, one could effectively tune the Fano factor determining the zero-frequency shot noise. It was possible to achieve a Fano factor greater than one, which was interpreted as a consequence of the effective charge associated with the transport cycle being greater than one. Perhaps more surprisingly, it was possible to reduce the Fano factor below 1/2, behaviour that was not fully explained. The finite frequency current noise also showed interesting behaviour [4]– in the regime where the Cooper-pair tunneling dominated the quasiparticle tunneling, a coherent peak in the current noise was predicted at the Josephson energy.

In this paper, we look specifically at the statistics of transferred charge and current noise associated with the *double* Josephson quasiparticle (DJQP) process in a SSET, a process which allows for near quantum-limited measurement [5], and which has been used in a recent experiment [8]. We pay careful consideration to the fact that the breaking of gauge invariance by superconductivity can make the interpretation of counting statistics more subtle than in the normal-metal case [10, 12, 13]. One obtains phase-dependent counting statistics here despite the fact that transport is insensitive to the overall phase



*R. Fazio et al. (eds.), New Directions in Mesoscopic Physics,* 325–337.
© 2003 *Kluwer Academic Publishers. Printed in the Netherlands.*

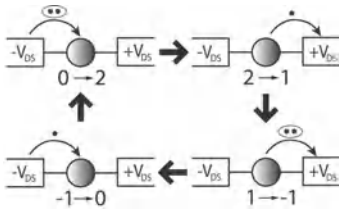


*Figure 1.* Schematic showing the four steps of the double Josephson quasiparticle process which can occur in a superconducting single-electron transistor. Circles represent the central island of the SSET, while the rectangles are the electrodes. Numbers indicate the charge of the SSET island.

difference between the two superconducting reservoirs. We identify two regimes in which there is no ambiguity in defining counting statistics, and proceed to use them to *directly* calculate the frequency-dependent shot noise, without any further approximations. This is in contrast to previous treatments both of normal and superconducting single electron transistors [14, 15, 4], where an additional Markov approximation (beyond what is needed for the counting statistics) is made to obtain the frequency-dependent current noise. The direct connection between counting statistics and frequency-dependent current noise we employ here allows one to give a simple interpretation of the latter. In particular, coherent peaks in the shot noise appearing at the Josephson energy can be directly tied to the time dependence of the counting statistics. We also suggest that the suppression of the Fano factor below 1/2 is related to the coherence of Cooper-pair tunneling.

## 2. Description and Model for Josephson Quasiparticle Tunneling

A SSET consists of a superconducting, Coulomb-blockaded island which is attached via tunnel junctions to two superconducting electrodes (Fig. 1). The SSET Hamiltonian $\mathcal{H}_S = H_K + H_C + H_V + H_T$ has a term $H_K$ describing the kinetic energy of source, drain and central island electrons (i.e. three bulk BCS Hamiltonians), a term $H_V$ which describes the work done by the voltage sources, and a tunneling term $H_T$. The charging interaction is $H_C = E_C(n - \mathcal{N})^2$, where $E_C$ is the SSET capacitive charging energy, $n$ is the number of electrons on the central island, and $\mathcal{N}$ is the dimensionless gate voltage applied to the island. We consider a SSET with identical tunnel junctions, whose dimensionless conductance $g$ satisfies $g/(2\pi) \ll 1$.

The DJQP process occurs when both the transistor gate voltage $\mathcal{N}$ and drain-source voltage $2V_{DS}$ are tuned such that two Cooper-pair tunneling transitions, one in each junction, are resonant. We label these transitions as $n = 0 \rightarrow 2$ in the left junction, and $n = 1 \rightarrow -1$ in the right junction (see Fig. 1). The double resonance point for these transitions occurs at $eV_{DS} = E_{CS}$ and $\mathcal{N}_S = 1/2$. In addition, $E_C/\Delta$ (where $\Delta$ is the superconducting gap of the SSET) must be chosen so that the quasiparticle transitions linking the two Cooper pair resonances are energetically allowed (i.e. $n = 2 \rightarrow 1$ and $n = -1 \rightarrow 0$), whereas unwanted transitions which would interrupt the cycle (i.e. $n = 0 \rightarrow 1$) are not. We take $E_C = \Delta$ to satisfy these conditions; this corresponds to the experiment of Ref. [8].

Assuming that all the above conditions are met, and that $T \ll E_C$, transport through the SSET will be dominated by the DJQP process sketched in Fig. 1. The standard theoretical description of this process [2] is obtained by looking at the dynamics of the reduced density matrix $\rho$ describing the charge $n$ of the central SSET island. Here, only four charge states are important; further, off-diagonal terms need only be retained between states involved in Josephson tunneling. Letting $\rho_{(i,j)} = \langle n = i|\rho|n = j\rangle$, we can represent the non-zero elements of this reduced density matrix as an 8 component vector:

$$\vec{\rho} \equiv \begin{pmatrix} \rho_{(-1,-1)} & \rho_{(0,0)} & \rho_{(1,1)} & \rho_{(2,2)} & \rho_{(-1,1)} & \rho_{(1,-1)} & \rho_{(0,2)} & \rho_{(2,0)} \end{pmatrix} \quad (1)$$

By starting with the von Neumann equation for the evolution of the full density matrix, treating the tunneling Hamiltonian to lowest order in perturbation theory, and then tracing out the fermion degrees of freedom (see, e.g. Ref. [15]), one obtains the an evolution equation for $\rho$. Taking both junctions to be on resonance, we have:

$$\frac{d}{dt}\vec{\rho(t)} = U^{\dagger} M U \vec{\rho(t)} \quad (2)$$

$$M = \begin{pmatrix} -\Gamma & 0 & 0 & 0 & -i\frac{E_J}{2} & i\frac{E_J}{2} & 0 & 0 \\ \Gamma & 0 & 0 & 0 & 0 & 0 & -i\frac{E_J}{2} & i\frac{E_J}{2} \\ 0 & 0 & 0 & \Gamma & i\frac{E_J}{2} & -i\frac{E_J}{2} & 0 & 0 \\ 0 & 0 & 0 & -\Gamma & 0 & 0 & i\frac{E_J}{2} & -i\frac{E_J}{2} \\ -i\frac{E_J}{2} & 0 & i\frac{E_J}{2} & 0 & -\Gamma/2 & 0 & 0 & 0 \\ i\frac{E_J}{2} & 0 & -i\frac{E_J}{2} & 0 & 0 & -\Gamma/2 & 0 & 0 \\ 0 & -i\frac{E_J}{2} & 0 & i\frac{E_J}{2} & 0 & 0 & -\Gamma/2 & 0 \\ 0 & i\frac{E_J}{2} & 0 & -i\frac{E_J}{2} & 0 & 0 & 0 & -\Gamma/2 \end{pmatrix}, \quad (3)$$

$$U = diag\left(1, 1, 1, 1, e^{-i\phi_R}, e^{i\phi_R}, e^{-i\phi_L}, e^{i\phi_L}\right) \quad (4)$$

$E_J = g\Delta/8$ is the standard Ambegaokar-Baratoff value for the Josephson energy emerging from perturbation theory in the tunneling Hamiltonian; $\phi_L$ and $\phi_R$ are the phases of the superconducting reservoirs. $\Gamma$ is the rate associated with the two quasiparticle transitions occurring the DJQP cycle, and is given by the usual expression for quasiparticle tunneling between two superconductors [16]; for simplicity, we assume the two transitions to have equal rates. We have also made a Markov approximation to obtain Eq. (2), which is valid as long we do not probe the evolution of $\rho$ on timescales smaller than $\hbar/E_C$.

The zero eigenvector $\vec{\rho}_0$ of the evolution matrix $M$ in Eq. (3) corresponds to the stationary value of the reduced density matrix describing the island charge; note that in general, it will have non-zero off-diagonal elements. The diagonal elements of $\rho_0$ (which are probabilities) can be obtained from a classical rate equation; one eliminates the off-diagonal elements from Eq. (2) by expressing them in terms of the diagonal elements. Letting $\vec{p}$ be the 4-vector of these probabilities, we are lead to the rate equation:

$$\frac{d}{dt}\vec{p}(t) = \begin{pmatrix} -\Gamma-\gamma & 0 & \gamma & 0 \\ \Gamma & -\gamma & 0 & \gamma \\ \gamma & 0 & -\gamma & \Gamma \\ 0 & \gamma & 0 & -\Gamma-\gamma \end{pmatrix} \vec{p}(t) = 0 \tag{5}$$

where $\gamma = E_J^2/\Gamma$ represents a "rate" for Cooper-pair tunneling. Eq. (5) represents an incoherent model for the DJQP process, and is sufficient for many purposes (e.g., calculating the average current $\langle I \rangle = 3\gamma\Gamma/(4\gamma+2\Gamma)$). The full stationary value of the density matrix (including off-diagonal terms) is given by:

$$\begin{aligned} \vec{\rho}_0 \;=\; & \frac{1}{4\gamma+2\Gamma}\,(\gamma, \gamma+\Gamma, \gamma+\Gamma, \gamma, \\ & iE_J e^{-i\phi_R}, -iE_J e^{i\phi_R}, -iE_J e^{-i\phi_L}, iE_J e^{i\phi_L}\Big) \end{aligned} \tag{6}$$

## 3. Counting Statistics

In order to obtain information about the number of electrons that have tunneled through one of the SSET junctions, the density matrix approach of the previous section must be embellished. The standard approach for single electron transistors [15, 4] is to employ a "counter" scheme where one explicitly tracks the dynamics of, say, $m_L$, the number of electrons which have tunneled through the left junction of the SSET. The Hilbert space of the SSET is expanded so that each state

is now also labelled by a value of $m_L$, and the tunnel Hamiltonian is modified so that it raises or lowers this index as appropriate (e.g., by introducing an auxiliary raising operator $F^\dagger$ such that $[m_L, F^\dagger] = F^\dagger$). The resulting equation for the reduced density matrix describing both $n$ and $m_L$ is simplified if one Fourier transforms in the latter variable. One finds that $\frac{d}{dt}\vec{\rho}(k) = U^\dagger M(k) U \vec{\rho}(k)$, where we have defined:

$$\rho_{(n_1,n_2)}(k) = \begin{cases} \sum_{m_L} e^{ikm_L} \langle n_1, m_L | \rho | n_2, m_L + 2 \rangle & \text{if } n_1 = 0, n_2 = 2, \\ \sum_{m_L} e^{ikm_L} \langle n_1, m_L + 2 | \rho | n_2, m_L \rangle & \text{if } n_1 = 2, n_2 = 0, \\ \sum_{m_L} e^{ikm_L} \langle n_1, m_L | \rho | n_2, m_L \rangle & \text{otherwise.} \end{cases} \quad (7)$$

$$M(k) = \begin{pmatrix} -\Gamma & 0 & 0 & 0 & -i\frac{E_J}{2} & i\frac{E_J}{2} & 0 & 0 \\ \Gamma e^{ik} & 0 & 0 & 0 & 0 & 0 & -i\frac{E_J}{2} & i\frac{E_J}{2} \\ 0 & 0 & 0 & \Gamma & i\frac{E_J}{2} & -i\frac{E_J}{2} & 0 & 0 \\ 0 & 0 & 0 & -\Gamma & 0 & 0 & i\frac{E_J}{2}e^{2ik} & -i\frac{E_J}{2}e^{2ik} \\ -i\frac{E_J}{2} & 0 & i\frac{E_J}{2} & 0 & -\Gamma/2 & 0 & 0 & 0 \\ i\frac{E_J}{2} & 0 & -i\frac{E_J}{2} & 0 & 0 & -\Gamma/2 & 0 & 0 \\ 0 & -i\frac{E_J}{2} & 0 & i\frac{E_J}{2}e^{-2ik} & 0 & 0 & -\Gamma/2 & 0 \\ 0 & i\frac{E_J}{2} & 0 & -i\frac{E_J}{2}e^{-2ik} & 0 & 0 & 0 & -\Gamma/2 \end{pmatrix} \quad (8)$$

The probability distribution for $m_L$ is thus easily obtained from the characteristic function $p(k,t)$:

$$p(m_L, t) = \int_{-\pi}^{\pi} \frac{dk}{2\pi} e^{-ikm_L} p(k,t) \equiv \int_{-\pi}^{\pi} \frac{dk}{2\pi} e^{-ikm_L} \sum_n \rho_{(n,n)}(k,t) \quad (9)$$

$$\vec{\rho}(k,t) = e^{M(k)t} \vec{\rho}(k, t=0) \quad (10)$$

It only remains to specify the initial state of the transistor (i.e. $\vec{\rho}(k, t = 0)$). The natural choice is to place the transistor $n$ degree of freedom in its stationary state, and choose $m_L = 0$ with probability one (i.e. $\vec{\rho}(k, t = 0) = \vec{\rho}_0$) [15]. $p(m_L, t)$ would then represent the stationary probability that $m_L$ electrons are transferred through the left junction in a time $t$. While this procedure is perfectly well defined for non-superconducting systems [15], it is problematic in the superconducting case. The stationary state of the SSET has coherence between different charge states– thus, one cannot have both that $m_L = 0$ *and* the coherence required in the stationary state. A possible remedy for this problem would be to suppress the off-diagonal elements of the initial density matrix; of course, this procedure needs to be justified. Note that given the linearity of Eq. (10) in the initial density matrix, we can separate incoherent and coherent contributions to $p(m_L, t)$ (i.e. those arising, respectively, from the diagonal and off-diagonal elements of the initial density matrix).

To gain further insight, it is instructive to consider an alternate to the "counter" scheme discussed above. One can also obtain a tunnelled

charge distribution for our system by following the general prescription for obtaining full counting statistics discussed in Ref. [9, 10]; we denote this distribution as $p'(m_L, t)$. The procedure here involves considering the effects of coupling an ideal measurer of current to the transistor. In practice, a gauge transformation is made to eliminate the interaction with the measurement device, resulting in a phase $e^{i\lambda(t)}$ being attached to the tunnel matrix element $t$ [11]. Using the fact that the perturbative calculation of $\rho$ in the tunneling Hamiltonian has a Keldysh structure (see e.g. Ref. [15]), one finds that $\lambda(t) = \delta + k$ on the forward Keldysh contour, and $\delta - k$ on the backwards Keldysh contour. $\delta$ is a phase which depends on the initial state of the detector; for non-superconducting systems, gauge invariance ensures that it does not play a role. This procedure results in an expression for $p'(k, t)$ which is identical in form to Eq. (10), except that now the initial state is uniquely specified as $\vec{\rho}_0$, and the evolution matrix $M$ undergoes a $\delta$-dependent unitary transformation which only affects the coherent contribution to $p(k, t)$:

$$M \to V^\dagger M V \qquad V = \mathrm{diag}\left(1, 1, 1, 1, 1, 1, e^{-i(k+\delta)}, e^{-i(k-\delta)}\right) \tag{11}$$

Thus, one has in general phase-dependent counting statistics for our system, meaning that there is a dependence on the phase shift $\delta$ introduced by the measurement. This phase-dependence exists despite the fact that the average current is not sensitive to the phase difference between the two superconducting reservoirs. As discussed in Ref. [10, 12], the results of any charge-counting experiment will now be dependent on the initial state of the detector. We thus see that the ambiguity in defining the initial state of the transistor in the "counter" scheme translates here to needing to know the initial state of the detector. Note that the incoherent part of $p(k, t)$ is the same in the two schemes, while the coherent part differs. The process of ignoring the initial coherence of the density matrix in the "counter" scheme corresponds here to assuming an initial detector state which is completely delocalized in the phase $\delta$.

Despite the above caveats, we can determine the counting statistics unambiguously in two limits where the off-diagonal elements of the stationary state $\vec{\rho}_0$ are suppressed– either $\Gamma \gg E_J$ or $E_J \gg \Gamma$ (c.f. Eq. (6)). In these limits the coherent contribution to $p(k, t)$ vanishes, implying that the counting statistics are identical in both schemes, and have no dependence on the phase shift $\delta$. Note that in general, the magnitude of the off-diagonal elements of $\rho$ in the stationary state are driven both by the size of $E_J/\Gamma$ and by the population asymmetry of the two charge states involved (i.e. $\rho_{02} \propto (\rho_{00} - \rho_{22})$). In the limit of large $E_J$, it is the lack of population asymmetry which suppresses the off-diagonal elements. In this limit, the symmetric and anti-symmetric

superpositions of charge states are equally populated, leading to a vanishing of the off-diagonal matrix elements.

### 3.1. The Limit $E_J \ll \Gamma$

In this limit, the SSET effectively gets stuck in the states $n = 0$ and $n = 1$ waiting for the relatively slow Cooper-pair transitions to occur; we can think of the rate $\gamma$ (c.f. Eq. (5)) as describing effective transitions between $n = 0$ and $n = 1$ (i.e. $\gamma$ describes both a Cooper-pair event and the subsequent quasiparticle event). We find for the probability distribution $p(m,t) \equiv p(m_L,t) = p(m_R,t)$ (i.e. the junctions are identical) :

$$p(m,t) = \begin{cases} e^{-\gamma t}\frac{(\gamma t)^{2l}}{(2l)!} & \text{if } m = 3l \\ \frac{e^{-\gamma t}}{2}\frac{(\gamma t)^{2l+1}}{(2l+1)!} & \text{if } m = 3l+1 \text{ or } m = 3l+2 \\ 0 & \text{otherwise.} \end{cases} \tag{12}$$

We have neglected terms which are small as $(E_J/\Gamma)^2$, and chosen $m = 0$ at $t = 0$. Again, as the coherent contribution to $p(m,t)$ vanishes to leading order, there is no ambiguity in defining the counting statistics. The statistics can be given a simple interpretation. Each Cooper-pair plus quasiparticle event is described by the rate $\gamma$ and a Poisson distribution. After an even number of $\gamma$ transitions, a multiple of 3 electrons must have been transferred through a junction. However, after an odd number of $\gamma$ transitions, there is an equal probability of having had an extra two electrons transferred (i.e. if we are looking at the left junction, $n = 0 \to 2 \to 1$) or of having a single extra electron transferred (i.e. $n = 1 \to -1 \to 0$ for the left junction). Note that there is an asymmetry here which favours values of $m$ which are an integer multiple of 3; this is the analog of the even-odd asymmetry found for the single JQP process [4]. Also, note that in this limit the counting statistics are identical if we use the incoherent model of Cooper-pair tunneling described by Eq. (5); coherence plays no role.

### 3.2. The Limit $E_J \gg \Gamma$

In this limit, we can think of there being long periods of coherent Josephson oscillations which are interrupted by infrequent quasiparticle transitions; note that we still assume $E_J \ll E_C = \Delta$, so that it does not effect the energetics of quasiparticle tunneling. Defining the Poisson distribution $\Lambda(l)$ as:

$$\Lambda(l) = e^{-\Gamma t/2}\frac{(\Gamma t/2)^l}{l!} \tag{13}$$

we find up to terms of order $E_J/\Gamma$:

$$p(m,t) = \begin{cases} \frac{1}{4}\left(\Lambda(2l)\left(3+\frac{\cos(E_J t)}{2^{2l}}\right)+\Lambda(2l+1)+\Lambda(2l-1)\right) & \text{if } m=3l, \\ \frac{1}{4}\left(\Lambda(2l+1)+\frac{1}{2}\Lambda(2l+2)\left(1-\frac{\cos(E_J t)}{2^{2l+2}}\right)\right) & \text{if } m=3l+1, \\ \frac{1}{4}\left(\Lambda(2l+1)+\frac{1}{2}\Lambda(2l)\left(1-\frac{\cos(E_J t)}{2^{2l}}\right)\right) & \text{if } m=3l+2, \\ 0 & \text{otherwise} \end{cases} \quad (14)$$

where again, we have assumed an initial state with $m = 0$ without any ambiguity, as the coherent contribution to $p(m,t)$ is negligible. We can again think of the quasiparticle transitions as effectively being described by a rate $\gamma = \Gamma/2$ and a Poisson distribution. Now, however, after an even number of transitions (say $2l$), it is not certain that $3l$ electrons will have been transferred through a junction; rather, due to weakly damped Josephson oscillations, there is also a probability to find $3l \pm 2$ electrons transferred. Even more remarkably, there are signatures of coherent oscillations in $p(m,t)$, this despite the fact that the initial coherence of the density matrix is irrelevant. As we will see in the next section, the time-dependence of the counting statistics has a direct impact on the frequency dependence of the current noise. Note that the oscillation serves to modulate the asymmetry which favours $m$ being a multiple of three. For $\Gamma t \gg 1$, the probability of $m$ being a multiple of 3 is given by:

$$p(m=3l) \to \frac{5+\cos(E_J t)}{8} \quad (15)$$

## 4. Current Noise and Counting Statistics

In this section, we calculate the frequency dependent current noise $S_I(\omega)$ associated with the DJQP process. As is standard, the capacitance of the junctions $C_L$ and $C_R$ may be used to connect this quantity (which includes the effects of displacement currents) to the noise associated with the tunneling currents in each contact [14]:

$$S_I(\omega) = \frac{C_L^2}{C_\Sigma} S_{LL}(\omega) + \frac{C_R^2}{C_\Sigma} S_{RR}(\omega) + \frac{C_L C_R}{C_\Sigma}\left(S_{LR}(\omega) + S_{RL}(\omega)\right) \quad (16)$$

where

$$S_{\alpha\beta} = \lim_{T\to\infty}\lim_{t_0\to\infty}\int_{-T}^{T} dt e^{i\omega t}\langle\langle\{I_\alpha(t+t_0), I_\beta(t_0)\}\rangle\rangle. \quad (17)$$

The order of limits here ensures that we are taking averages with respect to the stationary density matrix of the SSET; note also that

we are calculating the classical part of the current noise, which is a symmetric function of frequency. Previous calculations of this quantity for both normal and superconducting transistors have effectively made use of the so-called quantum regression theorem, which involves making an additional Markov approximation beyond that necessary to calculate the reduced density matrix $\rho$ [14, 15, 4]. It turns out that this is not necessary; one can directly connect the particle-current noise correlators to the counting statistics using a formula first derived by MacDonald [17] . Using the definition $I_\alpha(t) = \partial_t m_\alpha(t)$, one can show:

$$S_{\alpha\beta}(\omega) = 2e^2\omega \int_0^\infty dt\,(\sin\omega t)\,\frac{d}{dt}\langle\langle m_\alpha(t) m_\beta(t)\rangle\rangle, \tag{18}$$

where at $t = 0$, $m_L = m_R = 0$ with certainty, and the system is described by the stationary density matrix $\rho_0$. The integral in this expression should be interpreted within the theory of distributions, i.e. $\int_0^\infty dt \sin\omega t = 1/\omega$. We see from Eq. (18) that the frequency-dependent current noise is directly tied to the time-dependence of the second moment of the tunneled charge distribution. At long times, $\langle\langle m(t)^2\rangle\rangle \to fIt/e$, where $f$ is the Fano factor; this leads to the usual expression $S_{\alpha\alpha}(\omega = 0) = 2efI$. A frequency-dependent $S(\omega)$ indicates that $\langle\langle m(t)^2\rangle\rangle$ deviates from this linear in time behaviour at short times. We thus see that in addition to being useful for calculations, Eq. (18) provides a straightforward way to interpret frequency-dependent current noise in terms of counting statistics. Note that unlike approaches using the quantum regression theorem [14, 4], one does not need to add an ad-hoc term to Eq. (18) to obtain the correct noise in the high-frequency limit.

We apply Eq. (18) to the DJQP process in the limit $E_J \gg \Gamma$, where the counting statistics are well-defined and phase-independent. As noted in the previous section, the coherent Josephson oscillations at frequency $E_J/\hbar$ modulates the asymmetry in $p(m,t)$ which favours multiples of 3. This in turn modulates the second moment of the distribution (i.e. the greater the asymmetry, the smaller the width); one finds from Eq. (14):

$$\langle\langle m^2(t)\rangle\rangle = \frac{9\Gamma t}{8} + \frac{9 - e^{-\Gamma t}}{8} - \frac{\cos(E_J t)}{2}\left(e^{-\Gamma t/4} - e^{-3\Gamma t/4}\right) \tag{19}$$

Eq. (18) then implies that there should be a peak in $S_{LL} = S_{RR}$ at $\omega = E_J$ of order $e^2E_J^2/\Gamma$, which is much larger than the zero frequency noise $(9/4)e^2\Gamma$. Shown in Fig. 2 are results obtained for $S_I(\omega)$ for $E_J = 10\Gamma$, $C_L = C_R$; a sharp peak is indeed visible. Similar results for the single JQP process were found in Ref. [4]. We see here that the peak

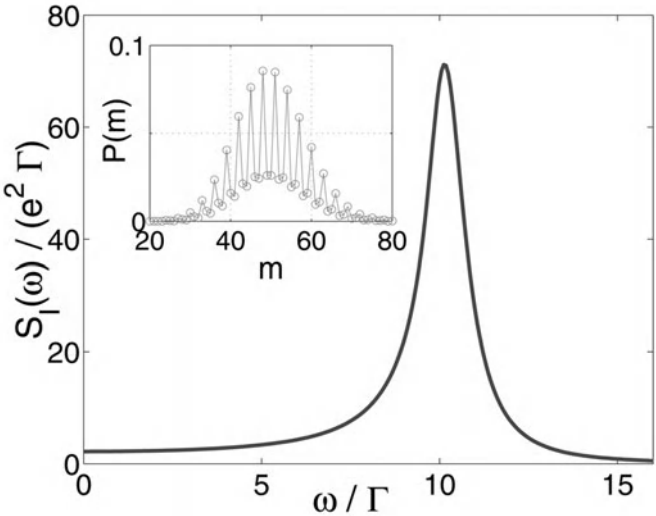


*Figure 2.* Frequency dependent current noise for the DJQP process at $E_J = 10\Gamma$; the large peak at $\omega = E_J$ is the result of oscillations in the asymmetry of the tunneled charge distribution. Inset: Distribution of tunneled charge $p(m)$ for the same parameters at $\Gamma t = 67$; the asymmetry which favours multiples of 3 is clearly visible.

in the current noise is directly related to the modulation in time of the asymmetry of the counting statistics by coherent Josephson oscillations.

## 5. The Intermediate Regime $E_J \simeq \Gamma$

The noise properties in the regime $E_J \simeq \Gamma$ are especially interesting, as it is in this regime where the DJQP process can be used to make a near quantum-limited measurement [5]. In this regime, the off-diagonal elements of the stationary density matrix $\vec{\rho}_0$ are by no means small, and thus the coherent, phase-dependent contribution to the counting statistics will play a role. While this in itself is not a problem, the resulting status of $S_I(\omega)$ as calculated using Eq. (18) becomes unclear, as the quantity $\partial_t \langle\langle m^2(t)\rangle\rangle$ is phase dependent. The conclusion would thus appear to be that for resonant Cooper-pair tunneling, *the finite-frequency current noise is phase dependent*, and consequently is sensitive to details of the measurement.

We close by pointing out that the value of the zero frequency noise remains phase independent and unambiguous regardless of the ratio $E_J/\Gamma$. At zero frequency, each of $S_{\alpha\beta}$ are equal; thus, we only need to

know $\partial_t \langle\langle m^2(t)\rangle\rangle$ in the large time limit. As discussed in Ref. [15], this is determined completely by the lifting of the zero eigenvalue of the evolution matrix $M(k=0)$ in Eq. (3) by non-zero $k$; the contribution to $\langle\langle m^2(t)\rangle\rangle$ from other eigenmodes of $M$ are damped away in the long time limit. Restricting ourselves to only this "lifted" zero-mode, we have:

$$p(k,t) \to e^{\lambda_0(k)t}(1 + A(k,\delta)), \tag{20}$$

where $A(k,\delta)$ contains all $k$-dependent terms involving the initial density matrix, and the $\delta$-dependent eigenvectors (left and right) corresponding to $\lambda_0(k)$; $A$ vanishes for $k \to 0$. As:

$$\langle\langle m^2(t)\rangle\rangle = -\frac{d^2}{dk^2}\log p(k,t) \tag{21}$$

it follows from Eq. (18) that

$$S_I(0) \equiv S_{\alpha\alpha} = 2e^2\left(-\frac{d^2}{dk^2}\lambda_0(k)\Big|_{k=0}\right) \tag{22}$$

The phase-dependent term $A$ is thus explicitly seen to play no role. Analyzing the eigenvalue $\lambda_0(k)$ of $M(k)$ in Eq. (8), one find for the Fano factor $f$ [5]:

$$f = \frac{3}{2}\left[1 - \frac{6E_J^2\Gamma^2}{\left(\Gamma^2 + 2E_J^2\right)^2}\right] \tag{23}$$

In both the limits $E_J \ll \Gamma$ or $E_J \gg \Gamma$ , $f \to 3/2$. This can be understood as an effective charge– each Cooper-pair plus quasiparticle transition transfers on average 3/2 electrons per junction. Interestingly, when $E_J \sim \Gamma$, $f$ drops below 1/2, reaching a minimum of 3/8 when $E_J = \Gamma/\sqrt{2}$. This behaviour is reminiscent of double tunnel junction systems, or of a normal SET; in both cases, there are two rates involved in transport, and the Fano factor reaches a minimum of 1/2 when these rates are equal. The behaviour in such systems can be understood completely classically by the self-averaging that occurs when one sequentially combines two independent Poisson processes. In contrast, the fact that $f$ drops below 1/2 for the DJQP process is a direct consequence of the coherence of Cooper-pair tunneling. To underscore this point, one can calculate $f$ using the incoherent model of Eq. (5). While this procedure yields the correct value of $\langle I\rangle$ and the correct value of $f$ for extreme values of $E_J/\Gamma$, it only gives a minimum $f$ of 1/2. One finds:

$$f_{\text{incoherent}} = \frac{3}{2}\left[1 - \frac{2E_J^2\Gamma^2}{\left(\Gamma^2 + 2E_J^2\right)^2}\right] = f + \frac{6E_J^2\Gamma^2}{\left(\Gamma^2 + 2E_J^2\right)^2} \tag{24}$$

Note that the incoherent calculation of $f$ is always an overestimate; as expected, *coherence between charge states suppresses the zero-frequency current noise*, as it tends to make tunnelling events more regular.

## 6. Conclusions

We have studied the counting statistics and finite-frequency shot noise of the DJQP process in a superconducting single electron transistor, attempting to clarify some of the remarkable noise features found in previous studies. In general, the counting statistics are phase-dependent, despite the fact that the average current has no phase dependent. An interesting question remains how this phase dependence impacts the finite frequency noise, given Eq. (18) which directly relates the two quantities.

## Acknowledgements

I am grateful to S. M. Girvin for useful discussions, and to L. Fedichkin for bringing Ref. [17] and Eq. 18 to my attention. This work was supported by the NSA and ARDA under ARO contracts ARO-43387-PH-QC, by the NSF under DMR-0196503 & DMR-0084501, and by the W.M. Keck Foundation.

## References

1. T. A. Fulton *et al.*, Phys. Rev. Lett. **63**, 1307 (1989)
2. D. V. Averin and V. Ya. Aleshkin, JETP Lett. **50**, 367 (1989); *ibid.*, Physica B **165 & 166**, 949 (1990).
3. A. Maasen van den Brink *et. al*, **85**, 459 (1991).
4. M-S. Choi, F. Plastina and R. Fazio, Phys. Rev. Lett. **87**, 116601-1 (2001); *ibid.*, cond-mat/0208165.
5. A. A. Clerk, S. M. Girvin, A. K. Nguyen and A. D. Stone, Phys. Rev. Lett. **89**, 176804 (2002).
6. G. Johansson, cond-mat/0210539.
7. Y. Nakamura, Y. A. Pashkin, and J. S. Tsai, Nature **398**, 786 (1999).
8. K.W. Lehnert, K. Bladh, L.F. Spietz, D. Gunnarson, D.I. Schuster, P. Delsing, and R.J. Schoelkopf, to appear in Phys. Rev. Lett., 2003.
9. L. S. Levitov, H. W. Lee and G. B. Lesovik, J. Math. Phys., **37**, 4845 (1996).
10. Yu. V. Nazarov and M. Kinderman, cond-mat/0107133
11. L. S. Levitov and M. Reznikov, cond-mat/0111057
12. W. Belzig and Yu. V. Nazarov, Phys. Rev. Lett. **87**, 067006 (2001).
13. A. Shelankov and J. Rammer, cond-mat/0207343

14. A. N. Korotkov, Phys. Rev. B **49**, 10381 (1994).
15. Y. Makhlin *et al.*, Phys. Rev. Lett. **85**, 4578 (2000); *ibid.*, Rev. Mod. Phys. **73**, 357 (2001).
16. see, e.g., M. Tinkham, *Introduction to Superconductivity*, (McGraw-Hill, New York, 1996).
17. D. K. C. MacDonald, Rep. Prog. Phys. **12**, 56 (1948)

# Influence of thermal fluctuations on an underdamped Josephson tunnel junction

I.S. Beloborodov[1,2], F.W.J. Hekking[3] and F. Pistolesi[3]
[1]*Bell Laboratories, Lucent Technologies*
*Murray Hill, New Jersey 07974*
[2]*Department of Physics, University of Colorado*
*CB 390, Boulder, Colorado 80390*
[3]*Laboratoire de Physique et Modélisation des Milieux Condensés*
*Magistère-CNRS , BP 166, 38042 Grenoble-cedex 9, France*

**Abstract.** Inspired by a recent experiment, we study the influence of thermal fluctuations on the $I$-$V$ characteristics of a Josephson junction, coupled to a strongly resistive environment. We obtain analytical results in the limit where the Josephson energy is larger than the charging energy and quasiparticles are absent.

## 1. Introduction

As it is well-known, the dynamics of a small Josephson tunnel junction is characterized by two energies: the Josephson coupling energy $E_J$ and the charging energy $E_C$ [1]. The behavior of the junction is determined by the competition between these two energy scales. If the Josephson coupling energy dominates, a superconducting state with a well-defined phase difference $\phi$ across the junction is possible. The junction will carry a Cooper pair current $I = I_J \sin\phi$ in the absence of an external voltage $V$. Here $I_J = 2eE_J/\hbar$ is the Josephson critical current ($e$ is the electron charge). If on the other hand the charging energy dominates, an insulating state with a well-defined charge $Q$ on the junction is possible. This gives rise to a gap in the $I$-$V$ characteristics of the junction, associated to Coulomb blockade [2]: the Cooper pair current $I = 0$ up to a voltage $V = 2E_C/e$. Here we defined $E_C = e^2/2C$, where $C$ is the capacitance of the junction.

The above statements are true under appropriate conditions on the impedance $Z(\omega)$ of the circuit connected to the junction, as we will discuss in some detail below. To be specific, we will consider two configurations. The voltage-biased set-up, in Fig. 1a, consists of an ideal voltage source (voltage $V_x$), connected to a series arrangement of a Josephson junction and a resistance $R$. In a current-biased set-up, see Fig. 1b, an ideal current source (bias current $I_x$) is connected to a parallel arrangement of a Josephson junction and a shunt resistance $R$. The two set-ups are equivalent if we choose $I_x = V_x/R$ [3]. The resistance $R$ plays a crucial role and determines the detailed form of the $I$-$V$ characteristics. In particular, the way in which the transition from superconducting to insulating behavior of the junction manifests itself



*R. Fazio et al. (eds.), New Directions in Mesoscopic Physics,* 339–349.
© 2003 *Kluwer Academic Publishers. Printed in the Netherlands.*

in the current-voltage characteristic depends not only on the parameters $E_J$ and $E_C$, but also on $R$.

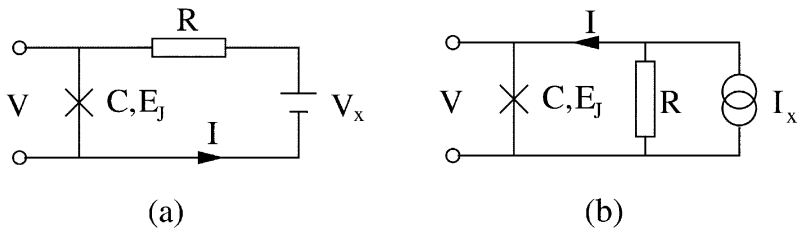


*Figure 1.* Voltage biased (a) and current-biased (b) Josephson junction.

The voltage biased set-up, Fig. 1a, has been analyzed long ago by Ivanchenko and Zil'berman [4] in the limit of strong charging effects, $E_C \to \infty$. More recently, a perturbative approach has been developed to obtain the current-voltage characteristic [3, 5]. This approach is valid for finite, but small, values of $E_J/E_C$. Specifically, in the zero temperature limit $T = 0$, a change of the position of the supercurrent peak is found upon increasing the ratio $R/R_Q$, where $R_Q = h/4e^2$. For $R/R_Q < 1$, the supercurrent peak is centered at zero bias voltage; its width increases gradually as $R/R_Q$ is increased. If $R/R_Q \gg 1$, the supercurrent peak is centered around $eV = 2E_C$. This corresponds to the transition from superconducting behavior found for small values of the external resistance to a complete Coulomb blockade of Cooper pair tunneling in the presence of a resistive environment. The range of applicability of the perturbative analysis depends on $E_J$, $E_C$, and $R$. In the low resistance limit $R/R_Q < 1$, the approach breaks down at low energy (bias voltage or temperature) for any value of $E_J$. In the opposite limit $R > R_Q$, the condition $E_J/E_C \ll (R_Q/R)^{1/2}$ needs to be satisfied. A non-perturbative analysis was developed in [6], however its validity is limited to low energies, $eV, k_BT \ll E_C R_Q/R$.

The approach discussed so far is clearly appropriate if one is interested in a small junction with $E_J \leq E_C$, coupled to an environment which is not too resistive. An example is the recent experiment by Steinbach *et al.* [7], in good agreement with the theoretical predictions of Refs. [4, 6]. However, the perturbative approach is not applicable in the case of a Josephson junction with $E_J \geq E_C$, coupled to a strongly resistive environment, $R \gg R_Q$, usually referred to as the underdamped limit [1]. Nevertheless this is a relevant situation from an experimental point of view as well. Recently, Watanabe and Haviland measured the $I$-$V$ characteristics of a small Josephson junction coupled to a tunable environment [8]. In these experiments, $E_J \sim E_C$ and the environment could be tuned to large values of the resistance such that $R/R_Q \sim 10^2$ – $10^4$. No evidence of a supercurrent peak was observed;

rather a so-called Bloch nose [9] was found for small values of the current and the bias voltage. This corresponds to an on-set of Coulomb blockade at low voltage and small current, followed by subsequent back-bending of the $I$-$V$ curve to smaller values of the voltage at higher currents which indicates a cross-over to superconducting behavior. The shape of the Bloch nose depended on the resistance $R$ as well as on temperature. The experimental findings could not be reconciled quantitatively with existing theories of Bloch nose [9, 10]. The main problem is that those theories are essentially based on the presence of dissipation due to quasiparticles. In the experiment [8], the tunable environment is a long array of superconducting junctions in the insulating regime [11], and quasiparticles are practically absent.

In this paper we analyze the finite temperature behavior of a Josephson junction with $E_J \gg E_C$, coupled to a very resistive environment, in the absence of quasiparticles. We obtain, to our knowledge for the first time, explicit formulæ for the current-voltage characteristics at finite temperature for a current-biased configuration with large $R$, see Fig. 1b. We follow the approach pioneered in Ref. [9], which is based on the periodicity of the Josephson coupling energy as a function of the phase difference $\phi$ across the junction. As a result of this periodicity, the eigenstates of the junction are of the Bloch type, and the energy spectrum consists of bands of width of the order $E_C$, separated by gaps of the order $E_J$. In the limit $E_J \gg E_C$, the gaps are large and the junction stays in the lowest Bloch band at low temperature $k_B T \ll E_J$, as long as the bias current $I_x \ll I_J$. If $R = \infty$, Bloch oscillations [9] of the voltage $V$ occur, such that its time-averaged value vanishes: the junction is in the superconducting state. If $R$ is finite, relaxation within the lowest band modifies the dynamics of the junction. This results in the appearance of the Bloch nose: if $I_x$ is so small that relaxation prevents Bloch oscillations to occur, a finite voltage state develops with no current passing through the junction (Coulomb blockade), all current passes through the resistance. If $I_x$ is increased above a threshold value, Bloch oscillations develop and the a superconducting zero-voltage state is reached. Our approach is valid for a large temperature range and our results can be compared quantitatively with the experimental data of Ref. [8].

## 2. The model

The circuit of Fig. 1b can be modelled by the Hamiltonian $\hat{H} = \hat{H}_0 + \hat{H}_{\rm coupl} + \hat{H}_{\rm env}$. Here,

$$\hat{H}_0 = \frac{\hat{Q}^2}{2C} - E_J \cos\hat{\phi} \tag{1}$$

describes the Josephson junction in the absence of the external circuit. The charge $\hat{Q}$ and the phase $\hat{\phi}$ are canonically conjugate operators, $[\hat{Q}, \hat{\phi}] = 2ie$.

Since the Hamiltonian (1) is periodic in $\phi$, the energy spectrum consists of bands $\epsilon_n(q)$ where $n$ is the band index and $q$ the quasimomentum associated to $\phi$, *i.e.*, the quasicharge. The spectrum $\epsilon_n(q)$ is a periodic function of $q$ with period $2e$. We will limit ourselves to the first Brillouin zone, $-e \leq q \leq e$. The corresponding eigenstates $\psi_{nq}(\phi)$ are of the Bloch type. In the limit of interest here, $E_J \gg E_C$, the bands are narrow compared to the gaps. Throughout this paper we will assume that all relevant energies are smaller than $E_J$ and restrict ourselves to the lowest energy band, $n = 0$, with a dispersion $\epsilon_0(q) = \hbar\sqrt{8E_C E_J} - U_0 \cos(\pi q/e)$, where the bandwidth is given by

$$U_0 = 16\sqrt{\frac{2}{\pi}} E_C [\frac{E_J}{2E_C}]^{3/4} e^{-\sqrt{8E_J/E_C}}. \tag{2}$$

The term

$$\hat{H}_{\text{coupl}} = -\frac{\hbar}{2e}\hat{I}\hat{\phi} \tag{3}$$

couples $\hat{\phi}$ to the total current $\hat{I} = I_x + \delta\hat{I}$, which contains the constant bias current $I_x$ and a fluctuating part $\delta\hat{I}$. The fluctuations are induced by the environment (the resistance $R$ in Fig. 1b) and the dynamics of $\delta\hat{I}$ is governed by $\hat{H}_{\text{env}}$.

In the absence of any current, $\hat{H}_{\text{coupl}} = 0$ and quasicharge $q$ is a well defined variable. In the limit of small bias current $I_x$ and current fluctuations $\delta I$, the effect of the coupling term (3) on $q$ can be analyzed perturbatively. As it was shown in Refs. [9], a quantum Langevin equation for the quasicharge operator $\hat{q}$ can be obtained, which reads

$$\frac{d\hat{q}}{dt} = I_x - \frac{1}{R}\frac{d\epsilon_0}{d\hat{q}} + \delta\hat{I}. \tag{4}$$

Here, $I_x$ plays the role of a driving force and $\delta\hat{I}$ of a random force. The statistical properties of the latter are determined by the Hamiltonian $\hat{H}_{\text{env}}$. Specifically, for a resistive environment at equilibrium we have [13]

$$\langle\delta\hat{I}(t)\rangle_{\text{env}} = 0 \ \ , \langle[\delta\hat{I}(t), \delta\hat{I}(t')]_+\rangle_{\text{env},\omega} = 2(\hbar\omega/R)\coth[\hbar\omega/(2k_B T)], \tag{5}$$

where $[\ldots,\ldots]_+$ denotes the anticommutator and $\langle\ldots\rangle_{\text{env}}$ an average with respect to $\hat{H}_{\text{env}}$. Finally, the derivative $d\epsilon_0/d\hat{q}$ is the voltage operator $\hat{V}$ across the junction, the corresponding term $V/R$ acts as a damping term.

We will be particularly interested in the limit of small current fluctuations. In this limit, quasicharge remains a well defined quantity and we can replace operators by classical variables in Eq. (4). In the next Section, we will analyze the resulting classical Langevin equation in some detail, using well-known methods for stochastic equations [12]. We will see under which condition current fluctuations can be considered small and we will obtain the detailed,

analytical form of $I$-$V$ characteristics, as a function of the resistance $R$ and of temperature $T$.

## 3. Current-voltage characteristics

### 3.1. Linearized Langevin equation

In the absence of fluctuations, $\delta\hat{I} = 0$, the Langevin equation (4) has a stationary solution when $I_x = (1/R)d\epsilon_0/dq \equiv V/R$, with $q = q_0 = (e/\pi)\arcsin(I_x/I_b)$. Here, $I_b = V_b/R$, with $V_b = \pi U_0/e$ the maximum voltage across the junction corresponding to the maximum slope of $\epsilon_0(q)$. The corresponding $I$-$V$ characteristic is linear, $I_x = V/R$. In other words, all the current passes through the resistance $R$, no current flows through the junction (Coulomb blockade) and the phase $\phi$ is completely undefined. This is consistent with the fact that we treat $q$ as a well-defined variable. Note that the stationary solution exists only as long as $I_x \leq I_b$; for larger current, $I_x > I_b$, the quasicharge becomes time-dependent. We will discuss that case in Sec. 3.2 below.

Let us now take into account small fluctuations $\delta\hat{I}$ such that the induced charge fluctuations $\delta q$ around the stationary solution $q = q_0$ are small. We consider the linear part of the average current-voltage characteristics and calculate

$$\langle V\rangle = \langle d\epsilon_0/dq\rangle = V_b\langle\sin(\pi q/e)\rangle. \tag{6}$$

Here the symbol $\langle\ldots\rangle$ means averaging over the fluctuations of charge. In order to find the distribution of these fluctuations, we write $q = q_0 + \delta q$, such that the linearized, classical Langevin equation takes the form

$$\delta\dot{q} = -\frac{\delta q}{\tau} + \delta I, \tag{7}$$

where we introduced the relaxation time $\tau$ such that $\tau^{-1} = (\pi/e)\sqrt{|I_b^2 - I_x^2|}$. The time $\tau$ defines the time scale characterizing the junction dynamics. Note that this is a relatively long time compared to the $RC$ time of the circuit: for $I_x = 0$, we find $\tau \sim e/I_b \sim Re^2/U_0 \gg RC$ as $U_0$ is exponentially small, see Eq. (2).

In order to solve the stochastic equation (7), we should specify the correlation function $\langle\delta I(t)\delta I(t')\rangle$, see Eq. (5). The frequencies $\omega$ of interest here are small, $\omega \sim 1/\tau$, determined by the long time scale $\tau$ characterizing the dynamics of quasicharge. For finite temperatures $k_BT \gg \hbar/\tau$, the correlation function $\langle\delta I(t)\delta I(t')\rangle_\omega \simeq 2k_BT/R$, independent of frequency and thus $\langle\delta I(t)\delta I(t')\rangle = (2k_BT/R)\delta(t-t')$. This means that the relevant current fluctuations are classical and completely uncorrelated on the long time scale $\tau$ characterizing the quasicharge dynamics.

The stochastic equation (7) can now be solved, using standard methods developed for the analysis of Brownian motion [12]. As a result, one obtains the probability distribution $W(\delta q, t; \delta q_0)$ to find the fluctuation $\delta q$ at time $t$ given that $\delta q = \delta q_0$ at time $t = 0$. In the long time limit, $t \to \infty$, this probability distribution does not depend on time and is independent of $\delta q_0$. It is given by the Gaussian distribution

$$W(\delta q, \tau) = \sqrt{\frac{1}{\pi\gamma\tau}} \exp\left(-\frac{(\delta q)^2}{\gamma\tau}\right), \tag{8}$$

where we introduced the parameter $\gamma = 2k_BT/R$.

Using Eq. (8) we immediately obtain the average square of the charge fluctuations, $\langle(\delta q)^2\rangle = k_BT\tau/R$. Quasicharge can be considered well-defined as long as these fluctuations are small, $\langle(\delta q)^2\rangle \ll e^2$. This condition gives an additional restriction on temperature, $k_BT\tau/\hbar \ll R/R_Q$. Together with the condition $k_BT \gg \hbar/\tau$ found above we obtain the temperature window

$$1 \ll k_BT\tau/\hbar \ll R/R_Q. \tag{9}$$

This means in particular that $R/R_Q \gg 1$ for the analysis presented here to be correct. If this condition is verified, quasicharge is a well-defined variable, and quantum fluctuations can be neglected. For small $I_x$ the energy scale $\hbar/\tau$ is of the order of $eV_bR_Q/R$, thus the condition (9) reads $eV_bR_Q/R \ll k_BT \ll eV_b$. This has a transparent physical interpretation: the temperature has to be much smaller than $eV_b$ in order not to smear the Bloch nose, but it must be larger than $eV_b(R_Q/R) \ll eV_b$ in order to justify the neglect of quantum fluctuations. The experiment of Ref. [8] was performed at very large values of $R/R_Q$, such that the condition (9) was verified.

With the help of Eqs. (6) and (8) we readily obtain the average voltage for the linear part of the average $I$-$V$ characteristic,

$$\langle V\rangle = I_xR\left[1 - \frac{\pi}{2}\frac{k_BT}{eR}\frac{1}{\sqrt{I_b^2 - I_x^2}}\right]. \tag{10}$$

Equation (10) represents the main result of this section. The first term on the right hand side of Eq. (10) coincides with the linear $I$-$V$ curve which was obtained above without taking into account current fluctuations. The second term is entirely due to the thermal fluctuations, which suppress the resistance. In other words, the Coulomb blockade is smeared due to thermal activation.

In this subsection we have considered the limit of small enough bias current, $I_x < I_b$, such that the Langevin equation could be linearized around a well-defined, stationary solution. For larger values of $I_x$, no stationary solution exists: quasicharge is an oscillating function of time and the full nonlinearity of the Langevin equation should be taken into account. In Section 3.2

we will use a Fokker-Planck approach to obtain the complete current-voltage characteristics.

### 3.2. Fokker-Planck approach

If the applied bias current $I_x$ exceeds $I_b$, quasicharge is a dynamical variable even in the absence of fluctuations. The corresponding non-linear equation of motion can be integrated, though, and $q(t)$ can be found. As a result, the voltage $V$ becomes an oscillating function of time, with a period given by $\tau$. Its time-averaged value $\bar{V}$ over one period of the oscillation is given by [10]

$$\bar{V} = I_b R \left[ \frac{I_x}{I_b} - \sqrt{(I_x/I_b)^2 - 1} \right]. \tag{11}$$

In other words, on measurement time scales much longer than the period $\tau$, the voltage oscillations average out and a stationary situation is reached.

In order to investigate the influence of small current fluctuations $\delta I$ on the $I$-$V$ characteristics, the full non-linear stochastic problem (4) needs to be solved. This can be conveniently done using a Fokker-Planck approach [12]. In this approach, the probability distribution $W(q,t)$ to find quasicharge $q$ at time $t$ is found , as a solution of the Fokker-Planck equation [12]

$$\frac{\partial W}{\partial t} = -\frac{\partial}{\partial q} \left( \left[ I_x - I_b \sin\left(\frac{\pi q}{e}\right) \right] W \right) + \frac{\gamma}{2} \frac{\partial^2 W}{\partial q^2}. \tag{12}$$

In writing this equation, we limited ourselves again to the case of classical fluctuations only, $k_B T \gg \hbar/\tau$. In addition, we note that this equation can be used only as long as the fluctuations are $\delta$-correlated on the time scale defined by $\tau$. Hence, we need to restrict ourselves again to the temperature interval (9).

We are particularly interested in the stationary solution of (12), $W(q)$, reached in the long time limit $t \gg \tau$. The average voltage is then given by

$$\langle V \rangle = I_b R \int_{-e}^{+e} dq \sin(\pi q/e) W(q), \tag{13}$$

where $W(q)$ is normalized, $\int_{-e}^{+e} W(q) dq = 1$. In the long time limit $t \gg \tau$, this corresponds to the measured, time-averaged voltage, $\langle V \rangle = \bar{V}$.

Let us first analyze the solution of the problem in the absence of charge fluctuations [parameter $\gamma$ equals to zero in Eq. (12)]. Solving Eq. (12) and using the normalization condition for the distribution function we obtain

$$W(q) = \begin{cases} \delta(q - q_0), & I_x \leq I_b \\ \frac{\sqrt{(I_x/I_b)^2 - 1}}{2e[I_x/I_b - \sin(\pi q/e)]}, & I_x > I_b, \end{cases} \tag{14}$$

where $q_0$ is the stationary solution found in Section 3.1. Substituting Eq. (14) into Eq. (13) for the current-voltage characteristics we immediately obtain the linear result $\langle V \rangle = I_x R$ for $I < I_b$; for the opposite case $I_x > I_b$ we reproduce the result (11). The resulting $I$-$V$ characteristic, a so-called Bloch nose, is shown in Fig. 2 as the curve corresponding to the parameter $k_B T/eV_b = 0$.

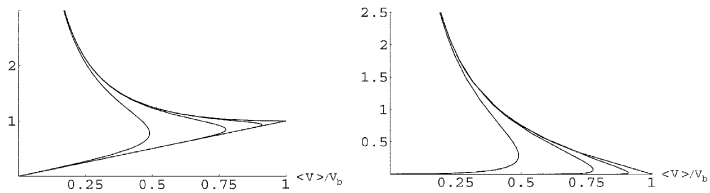


*Figure 2.* Calculated $I$-$V$ characteristics for an underdamped junction. Left panel: bias current $I_x/I_b$ as a function of voltage $\langle V \rangle/V_b$ across the junction, for various values of the parameter $k_B T/eV_b$. Curves from right to left correspond to $k_B T/eV_b = 0$, 0.004, 0.02, and 0.1. Right panel: current $I/I_b$ through the junction as a function of $\langle V \rangle/V_b$. Curves from right to left correspond to the same values of $k_B T/eV_b$.

Next we consider the current-voltage characteristics in the presence of fluctuations. To find the distribution function, $W(q)$, we use a Fourier representation

$$W(q) = \sum_{n=-\infty}^{+\infty} W_n e^{i\pi qn/e}. \tag{15}$$

Substituting the right hand side of Eq. (15) into Eq. (12) and using the periodicity condition, $W(q + 2e) = W(q)$, we obtain the following recurrence relation for the distribution function

$$2\,(n + i\eta_x)\, W_n = \eta_b\,(W_{n-1} - W_{n+1})\,. \tag{16}$$

Here we introduced the short hand notation $\eta_j = 2eI_j/(\pi\gamma)$ for $j = x, b$. To find the distribution function $W_n$ in Eq. (16) we use the analogy with the recurrence relation for the modified Bessel function [14] $2\nu I_\nu(\xi) = \xi[I_{\nu-1}(\xi) - I_{\nu+1}(\xi)]$. Here $\nu$ is the index and $\xi$ is the argument of the modified Bessel function. A comparison with (16) yields the distribution function $W_{\nu - i\eta_x} = C I_\nu(\eta_b)$, where $C = (2eI_{i\eta_x}(\eta_b))^{-1}$ is the normalization constant. Substituting this result into Eq. (13) and using the fact that the distribution function is real, $W_{-n} = W_n^*$, we obtain, upon integration over $q$, the following result for the $I$-$V$ characteristics

$$\langle V \rangle = I_x R - \frac{k_B T}{e} \frac{\sinh(\pi\eta_x)}{|I_{i\eta_x}(\eta_b)|^2}. \tag{17}$$

Equation (17) is the main result of this section. It describes the complete current-voltage characteristics in the presence of small fluctuations. The $I$-$V$ characteristics of Eq. (17) are shown in the left panel of Fig. 2 for various values of the parameter $k_BT/eV_b$. For comparison we plot the current $I$ through the junction as a function of $\langle V \rangle$ in the right panel of Fig. 2, for the same values of $k_BT/eV_b$. This would correspond to a measurement in the voltage-biased set-up, see Fig. 1a. We see that the $I$-$V$ curve corresponding to the limit without fluctuations is asymptotically reached by the finite temperature $I$-$V$ curves, both for $I_x/I_b \ll 1$ and for $I_x/I_b \gg 1$. Mathematically, this is a direct result of the asymptotics of the modified Bessel functions [14]. Physically, this can be easily understood from the fact that the point $I_x = I_b$ is unstable, separating a stationary quasicharge solution from an oscillating one. In the vicinity of $I_b$, any small current fluctuation will drastically change the nature of the dynamics. Thus the $I$-$V$ characteristic is strongly affected by fluctuations for $I_x \sim I_b$.

We finally note that the analytical form of the result (17) resembles the well-known result [15] for the $I$-$V$ characteristic of an overdamped junction with $R \ll R_Q$ and $E_C \gg E_J$. In fact, these two cases can be related by duality arguments. Here, we studied the temperature driven diffusion of quasicharge $q$, governed by Eq. (12), and found the time-averaged *voltage* across the junction as the average $\langle \sin(\pi q/e) \rangle$ over the fluctuations of $q$. In an overdamped junction, it is the dual phase variable $\phi$ that diffuses, governed by an equation similar to (12) and one is interested in the time averaged *current* $\langle \sin \phi \rangle$ over the fluctuations of $\phi$. This is why the resulting $I$-$V$ curves can be related to each other, essentially by exchanging the role of $I$ and $V$.

## 4. Discussion

In this paper we have considered the influence of thermal fluctuations on the current-voltage characteristics of an underdamped Josephson junction with $R \gg R_Q$ and $E_J \gg E_C$, in the absence of quasiparticles. To obtain analytical results for the $I$-$V$ characteristics, we have analyzed the appropriate Langevin equation using a Fokker-Planck approach. The resulting $I$-$V$ characteristic is essentially a Bloch nose [9], smeared by thermal fluctuations. Our results are valid as long as the inequality (9) is satisfied. Since we restricted our analysis to the lowest energy band we need to impose in addition $k_BT \ll E_J$ and $I_x \ll I_J$.

The present work is motivated by recent experiments [8] on a small, voltage biased Josephson junction coupled to a tunable environment. This environment consisted of a long array with a large number ($\sim 10^2$) Josephson junctions. Each junction is a small SQUID-loop, threaded by a magnetic flux $\Phi$. Thus the Josephson coupling energy $E_J^{\text{array}}(\Phi)$ of the array is flux-dependent

and the ratio $E_J^{\rm array}/E_C^{\rm array}$ could be changed during the experiment. When $\Phi$ is tuned close to $\Phi_0/2$, where $\Phi_0$ is the superconducting flux quantum, the ratio $E_J^{\rm array}/E_C^{\rm array} \ll 1$ and the array is in the insulating regime.

We ignore quasiparticles: in order for them to reach the small Josephson junction, they have to tunnel through the entire array; the corresponding probability is negligibly small. The frequency-dependent impedance $Z(\omega)$ of the array, as seen by the small junction, is then entirely due to the dynamics of Cooper pairs. In the stationary limit of interest here, we need to know the zero-frequency component $Z(\omega = 0)$. Calculations by Efetov [16] in the limit $E_J^{\rm array}/E_C^{\rm array} \ll 1$ show that the real part $R$ of $Z(\omega = 0)$ is strictly infinite at zero temperature; at finite $T$, thermal activation gives rise to a finite, large value of $R$, which depends on the ratio $E_J^{\rm array}/E_C^{\rm array}$, and thus on $\Phi$. Note that any residual quasiparticle contribution would be insensitive to the Josephson coupling and hence independent of $\Phi$. Once $R(\Phi)$ and the parameters of the small junction are known, our results can be compared in principle with the experimental data of [8].

## Acknowledgments

We thank D. Averin, K. Efetov, D. Haviland, E. Mishchenko, and M. Watanabe for valuable discussions. One of us (I. B.) thanks Laboratoire de Physique et Modélisation des Milieux Condensés for hospitality. Our research was sponsored by Institut Universitaire de France and CNRS-ATIP, Grants DMR-9984002 and BSF-9800338, as well as by the A.P. Sloan and the Packard Foundations.

## References

1. M. Tinkham, *Introduction to Superconductivity* (McGraw-Hill, New-York, 1996).
2. M.H. Devoret and H. Grabert, *Single Charge Tunneling* (Plenum, New-York, 1992).
3. G.L. Ingold and Yu.V. Nazarov, in Ref. [2].
4. Yu. M. Ivanchenko and L.A. Zil'berman, Zh. Eksp. Teor. Fiz. **55**, 2395 (1968) [Sov. Phys. JETP **28**, 1272 (1969)].
5. G.L. Ingold, H. Grabert and U. Eberhardt, Phys. Rev. B **50**, 395 (1994).
6. G.L. Ingold and H. Grabert, Phys. Rev. Lett. **83**, 3721 (1999).
7. A. Steinbach *et al.*, Phys. Rev. Lett. **87**, 137003-1 (2001).
8. M. Watanabe, and D. B. Haviland, Phys. Rev. Lett. **86**, 5120 (2001); M. Watanabe and D.B. Haviland `cond-mat/0301467` (unpublished).
9. D.V. Averin, A.B. Zorin, and K.K. Likharev, Zh. Eksp. Teor. Fiz. **88**, 692 (1985) [Sov. Phys. JETP **61**,407 (1985)]; K. K. Likharev and A. B. Zorin, J. Low Temp. Phys.**59**, 347 (1985).
10. G. Schön and A. D. Zaikin, Phys. Rep. **198**, 237 (1990).
11. R. Fazio and H. van der Zant, Phys. Rep. **355**, 235 (2001).
12. N.G. van Kampen, *Stochastic processes in physics and chemistry* (North-Holland, Amsterdam, 1992).

13. L. D. Landau and E. M. Lifshitz, *Statistical Physics*, Part 2, (Pergamon Press, Oxford, 1999).
14. I. S. Gradshteyn and I. M. Ryzhik, *Table of Integrals, Series, and Products* (Academic Press, New York, 2000).
15. K.K. Likharev, *Dynamics of Josephson junctions and circuits* (Gordon and Breach, Philadelphia, 1986).
16. K.B. Efetov, Zh. Eksp. Teor. Fiz. **78**, 2017 (1980) [Sov. Phys. JETP **51**, 1015 (1980)].

# Quantum computing with many superconducting qubits

J. Q. You[1], J. S. Tsai[1,2] and Franco Nori[1,3,*]
[1]*Frontier Research System, The Institute of Physical and Chemical Research (RIKEN), Wako-shi 351-0198, Japan*
[2]*NEC Fundamental Research Laboratories, Tsukuba, Ibaraki 305-8051, Japan*[†]
[3]*Center for Theoretical Physics, Physics Department, Center for the Study of Complex Systems, The University of Michigan, Ann Arbor, MI 48109-1120, USA*[†]

**Abstract.** Two of the major obstacles to achieve quantum computing (QC) are (i) scalability to many qubits and (ii) controlled connectivity between any selected qubits. Using Josephson charge qubits, here we propose an experimentally realizable method to efficiently solve these two central problems. Since any two charge qubits can be effectively coupled by an experimentally accessible inductance, the proposed QC architecture is *scalable*. In addition, we formulate an efficient and realizable QC scheme that requires *only one* (instead of two or more) two-bit operation to implement conditional gates.

## Introduction

Josephson-qubit devices [1] are based on the charge and phase degrees of freedom. The charge qubit is achieved in a Cooper-pair box [2], where two dominant charge states are coupled through coherent Cooper-pair tunneling [3]. Using Cooper-pair tunneling in Josephson charge devices [4, 5] and via spectroscopic measurements for the Josephson phase device [6, 7], it has been possible to experimentally observe energy-level splitting and related properties for state superpositions. In addition, using Josephson charge devices prepared in a superposition of two charge states [2], coherent oscillations were observed. While operating at the degeneracy point, the charge-qubit states are highly coherent [8] ($Q = 2.5 \times 10^4$), with a decoherence time of $\tau \sim 500$ ns. These important experimental results indicate that the Josephson charge and phase devices are potentially useful for solid-state qubits in quantum information processing. Important open problems would now include implementing a *two-bit coupling* and then *scaling up* the architecture to many qubits. Here, we propose a new quantum-computing (QC) scheme based on scalable charge-qubit structures. We focus on the Josephson charge qubit realized in a Cooper-pair box.

* Corresponding author (e-mail address: nori@umich.edu)
† Permanent address.



*R. Fazio et al. (eds.), New Directions in Mesoscopic Physics,* 351–360.
© 2003 *Kluwer Academic Publishers. Printed in the Netherlands.*

## COUPLING QUBITS

The Coulomb interaction between charges on different islands of the charge qubits would seem to provide a natural way of coupling Josephson charge qubits (e.g., to connect two Cooper-pair boxes via a capacitor). Using this type of capacitive interbit coupling, a two-bit operation [9] similar to the controlled-NOT gate was derived. However, as pointed out in [1], it is difficult in this scheme to switch on and off the coupling. Also, it is hard to make the system scalable because only neighboring qubits can interact. Moreover, implementations of quantum algorithms such as the Deutsch and Bernstein-Vazirani algorithms were studied using a system of Josephson charge qubits [10], where it was proposed that the nearest-neighbor charge qubits would be coupled by tunable dc SQUIDs. In the semiconductor literature, scalability often refers to reducing the size of the device (packing more components). In QC, scalability refers to increasing the number of qubits coupled with each other.

A suggestion for a scalable coupling of Josephson charge qubits was proposed [1, 3] using oscillator modes in a $LC$ circuit formed by an inductance and the qubit capacitors. In this proposal, the interbit coupling can be switched and any two charge qubits could be coupled. Nevertheless, there is no efficient (that is, using one two-bit operation) QC scheme for this proposal [1, 3] in order to achieve conditional gates—e.g., the controlled-phase-shift and controlled-NOT gates. In addition, the calculated interbit coupling terms [1, 3] only apply to the case when the following two conditions are met:

(i) The quantum manipulation frequencies, which are fixed experimentally, are required to be much smaller than the eigenfrequency $\omega_{LC}$ of the $LC$ circuit. This condition *limits* the allowed number $N$ of the qubits in the circuit because $\omega_{LC}$ scales with $1/\sqrt{N}$. In other words, the circuits in [1, 3] are not really scalable.

(ii) The phase conjugate to the total charge on the qubit capacitors fluctuates weakly.

## IMPROVED AND SCALABLE COUPLING BETWEEN ANY SELECTED QUBITS

The limitations listed above do not apply to our approach. In our scheme, a common inductance, but no $LC$ circuit, is used to couple all Josephson charge qubits. In our proposal, both dc and ac supercurrents can flow through the inductance, while in [1, 3] only ac supercurrents can flow through the inductance and it is the $LC$-oscillator mode that couples the charge qubits. These yield different interbit couplings (e.g., $\sigma_y\sigma_y$ type [1, 3] as opposed to $\sigma_x\sigma_x$ in our proposal).

We employ two dc SQUIDs to connect each Cooper-pair box in order to achieve a *controllable interbit coupling*. Our proposed QC architecture is scalable in the sense that *any* two charge qubits (*not* necessarily neighbors)

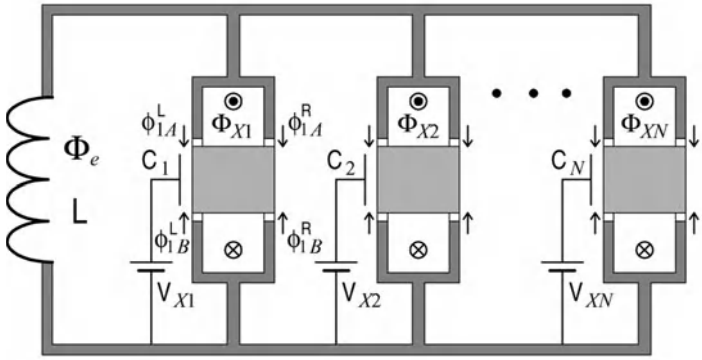


*Figure 1.* Schematic diagram of the proposed scalable and switchable quantum computer. Here, each Cooper-pair box is operated in the charging regime, $E_{ck} \gg E^0_{Jk}$, and at low temperatures $k_B T \ll E_{ck}$. Also, the superconducting gap is larger than $E_{ck}$, so that quasi-particle tunneling is strongly suppressed. All Josephson charge-qubit structures are coupled by a common superconducting inductance.

can be effectively coupled by an experimentally accessible inductance. We also formulate [11] an efficient QC scheme that requires only one (instead of two or more) two-bit operation to implement conditional gates.

This Erice summer-school presentation is based on our work in [11]. Additional work on decoherence and noise-related issues appears in, e.g., [12, 13]. Also, work more focused on entanglement and readout issues appears in [14]. Other interesting studies on charge qubits can be found in [15] for the adiabatic controlled-NOT gate, in [16] for geometric phases, and in [17, 18, 19, 20] for the dynamics of a Josephson charge qubit coupled to a quantum resonator.

## Proposed scalable and switchable quantum computer

Figure 1 shows a proposed QC circuit consisting of $N$ Cooper-pair boxes coupled by a common superconducting inductance $L$. For the $k$th Cooper-pair box, a superconducting island with charge $Q_k = 2en_k$ is weakly coupled by two symmetric dc SQUIDs and biased, through a gate capacitance $C_k$, by an applied voltage $V_{Xk}$. The two symmetric dc SQUIDs are assumed to be equal and all Josephson junctions in them have Josephson coupling energy $E^0_{Jk}$ and capacitance $C_{Jk}$. The effective coupling energy is given by the SQUIDs, each one enclosing a magnetic flux $\Phi_{Xk}$. Each SQUID provides a tunable coupling

$-E_{Jk}(\Phi_{Xk})\cos\phi_{kA(B)}$, with

$$E_{Jk}(\Phi_{Xk}) = 2E^0_{Jk}\cos(\pi\Phi_{Xk}/\Phi_0), \tag{1}$$

and $\Phi_0 = h/2e$ is the flux quantum. The effective phase drop $\phi_{kA(B)}$, with subscript $A(B)$ labelling the SQUID above (below) the island, equals the average value, $[\phi^L_{kA(B)}+\phi^R_{kA(B)}]/2$, of the phase drops across the two Josephson junctions in the dc SQUID, where the superscript $L$ ($R$) denotes the left (right) Josephson junction. Above we have neglected the self-inductance effects of each SQUID loop because the size of the loop is usually very small ($\sim 1\ \mu$m). The Hamiltonian of the system then becomes

$$H = \sum_{k=1}^{N} H_k + \frac{1}{2}LI^2\,, \tag{2}$$

with $H_k$ given by

$$H_k = E_{ck}(n_k - n_{Xk})^2 - E_{Jk}(\Phi_{Xk})(\cos\phi_{kA} + \cos\phi_{kB}). \tag{3}$$

Here

$$E_{ck} = 2e^2/(C_k + 4C_{Jk}) \tag{4}$$

is the charging energy of the superconducting island and $I = \sum_{k=1}^{N} I_k$ is the total persistent current through the superconducting inductance, as contributed by all coupled Cooper-pair boxes. The offset charge $2en_{Xk} = C_kV_{Xk}$ is induced by the gate voltage $V_{Xk}$. The phase drops $\phi^L_{kA}$ and $\phi^L_{kB}$ are related to the total flux

$$\Phi = \Phi_e + LI \tag{5}$$

through the inductance $L$ by the constraint

$$\phi^L_{kB} - \phi^L_{kA} = 2\pi\Phi/\Phi_0, \tag{6}$$

where $\Phi_e$ is the externally applied magnetic flux threading the inductance $L$. In order to obtain a simpler expression for the interbit coupling, and without loss of generality, the magnetic fluxes through the two SQUID loops of each Cooper-pair box are designed to have the *same* values but *opposite* directions. If this were not to be the case, the interbit coupling can still be realized, but the Hamiltonian of the qubit circuits would just take a more complicated form. Because this pair of fluxes cancel each other in any loop enclosing them, then

$$\phi^L_{kB} - \phi^L_{kA} = \phi^R_{kB} - \phi^R_{kA}. \tag{7}$$

This imposes the constraint

$$\phi_{kB} - \phi_{kA} = 2\pi\Phi/\Phi_0 \tag{8}$$

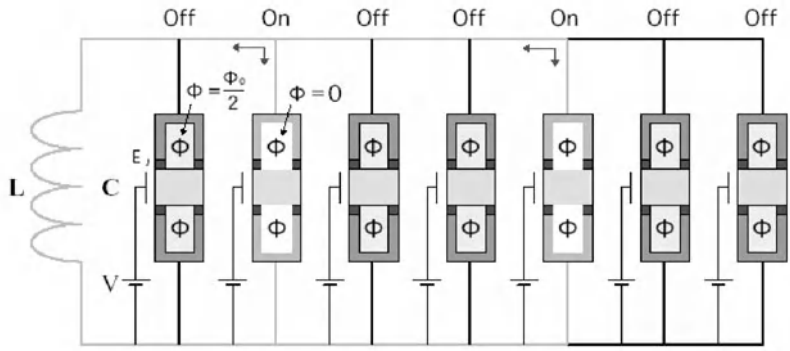


*Figure 2.* Simplified diagram of the circuit shown in Fig. 1. Here we explicitly show how two charge qubits (not necessarily neighbors) can be coupled by the inductance $L$, where the cyan SQUIDs are switched on by setting the fluxes through the cyan SQUID loops zero, and the green SQUIDs are turned off by choosing the fluxes through the green SQUID loops as $\Phi_0/2$. This applies to the case when any selected charge qubits are coupled by the common inductance [21].

for the average phase drops across the Josephson junctions in the SQUIDs. The common superconducting inductance $L$ provides the coupling among Cooper-pair boxes. The coupling of selected Cooper-pair boxes can be implemented by switching "on" the SQUIDs connected to the chosen Cooper-pair boxes. In this case, the persistent currents through the inductance $L$ have contributions from all the coupled Cooper-pair boxes. The essential features of our proposal can be best understood via the very simplified diagram shown in Fig. 2.

## ONE-BIT CIRCUIT

As seen in Fig. 3(a), for any given Cooper-pair box, say $i$, when

$$\Phi_{Xk} = \frac{1}{2}\Phi_0, \quad V_{Xk} = (2n_k + 1)e/C_k$$

for all boxes except $k = i$, the inductance $L$ only connects the $i$th Cooper-pair box to form a superconducting loop. The Hamiltonian of the system can be reduced to [11]

$$H = \varepsilon_i(V_{Xi})\,\sigma_z^{(i)} - \overline{E}_{Ji}(\Phi_{Xi}, \Phi_e, L)\,\sigma_x^{(i)}, \tag{9}$$

where

$$\varepsilon_i(V_{Xi}) = \frac{1}{2}E_{ci}[C_i V_{Xi}/e - (2n_i + 1)] \tag{10}$$

is controllable via the gate voltage $V_{Xi}$, while the intrabit coupling $\overline{E}_{Ji}$ can be controlled by both the applied external flux $\Phi_e$ through the common inductance, and the local flux $\Phi_{Xi}$ through the two SQUID loops of the $i$th

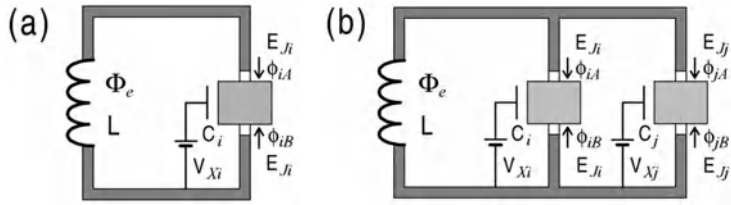


*Figure 3.* (a) One-bit circuit with a Cooper-pair box connected to the inductance. (b) Two-bit structure where two Cooper-pair boxes are commonly connected to the inductance. Here, each SQUID connecting the superconducting island is represented by an effective Josephson junction.

Cooper-pair box. Retained up to second-order terms in the expansion parameter

$$\eta_i = \pi L I_{ci}/\Phi_0, \tag{11}$$

where

$$I_{ci} = -\pi E_{Ji}(\Phi_{Xi})/\Phi_0, \tag{12}$$

we obtain

$$\overline{E}_{Ji}(\Phi_{Xi}, \Phi_e, L) \;=\; E_{Ji}(\Phi_{Xi}) \cos(\pi\Phi_e/\Phi_0)\, \xi, \tag{13}$$

with

$$\xi = 1 - \frac{1}{2}\eta_i^2 \sin^2(\pi\Phi_e/\Phi_0). \tag{14}$$

The intrabit coupling $\overline{E}_{Ji}$ in (9) is different from that in [1, 3] because a very different contribution by $L$ is considered.

## TWO-BIT CIRCUIT

To couple *any* two Cooper-pair boxes, say $i$ and $j$, we choose

$$\Phi_{Xk} = \frac{1}{2}\Phi_0, \quad V_{Xk} = (2n_k + 1)e/C_k$$

for all boxes except $k = i$ and $j$. As shown in Fig. 3(b), the inductance $L$ is shared by the Cooper-pair boxes $i$ and $j$ to form superconducting loops. The reduced Hamiltonian of the system is given by [11]

$$H = \sum_{k=i,j} [\varepsilon_k(V_{Xk})\, \sigma_z^{(k)} - \overline{E}_{Jk}\, \sigma_x^{(k)}] + \Pi_{ij}\, \sigma_x^{(i)} \sigma_x^{(j)}. \tag{15}$$

Up to second-order terms,

$$\overline{E}_{Ji}(\Phi_{Xi}, \Phi_e, L) \;=\; E_{Ji}(\Phi_{Xi}) \cos(\pi\Phi_e/\Phi_0)\, \xi, \tag{16}$$

with

$$\xi = 1 - \frac{1}{2}(\eta_i^2 + 3\eta_j^2)\sin^2(\pi\Phi_e/\Phi_0), \tag{17}$$

and

$$\Pi_{ij} = -LI_{ci}I_{cj}\sin^2(\pi\Phi_e/\Phi_0). \tag{18}$$

Here the interbit coupling $\Pi_{ij}$ is controlled by both the external flux $\Phi_e$ through the inductance $L$, and the local fluxes, $\Phi_{Xi}$ and $\Phi_{Xj}$, through the SQUID loops.

Using these two types of circuits, we can derive the required one- and two-bit operations for QC. Specifically, the conditional gates such as the controlled-phase-shift and controlled-NOT gates can be obtained using one-bit rotations and only one basic two-bit operation. For details, see Ref. [11]. A sequence of such conditional gates supplemented with one-bit rotations constitute a universal element for QC [22, 23]. Usually, a two-bit operation is much slower than a one-bit operation. Our designs for conditional gates $U_{\rm CPS}$ and $U_{\rm CNOT}$ are *efficient* since *only one* (instead of two or more) basic two-bit operation is used.

## Persistent currents and entanglement

The one-bit circuit modeled by Hamiltonian (9) has two eigenvalues $E_\pm^{(i)} = \pm E_i$, with

$$E_i = [\varepsilon_i^2(V_{Xi}) + \overline{E}_{Ji}^2]^{1/2}. \tag{19}$$

The corresponding eigenstates are

$$\begin{aligned} |\psi_+^{(i)}\rangle &= \cos\xi_i|\uparrow\rangle_i - \sin\xi_i|\downarrow\rangle_i, \\ |\psi_-^{(i)}\rangle &= \sin\xi_i|\uparrow\rangle_i + \cos\xi_i|\downarrow\rangle_i, \end{aligned} \tag{20}$$

where

$$\xi_i = \frac{1}{2}\tan^{-1}(\overline{E}_{Ji}/\varepsilon_i). \tag{21}$$

At these two eigenstates, the persistent currents through the inductance $L$ are given by

$$\langle\psi_\pm^{(i)}|I|\psi_\pm^{(i)}\rangle = \pm\left(\frac{\overline{E}_{Ji}I_{ci}}{E_i}\right)\sin\left(\frac{\pi\Phi_e}{\Phi_0}\right) + \left(\frac{\pi LI_{ci}^2}{2\Phi_0}\right)\sin\left(\frac{2\pi\Phi_e}{\Phi_0}\right), \tag{22}$$

up to the linear term in $\eta_i$. In the case when a dc SQUID magnetometer is inductively coupled to the inductance $L$, these two supercurrents generate different fluxes through the SQUID loop of the magnetometer and the quantum-state information of the one-bit structure can be obtained from the

measurements. In order to perform sensitive measurements with weak dephasing, one could use the underdamped dc SQUID magnetometer designed previously for the Josephson phase qubit [6].

For the two-bit circuit described by Eq. (15), the Hamiltonian has four eigenstates and the supercurrents through inductance $L$ take different values for these four states. The fluxes produced by the supercurrents through $L$ can also be detected by the dc SQUID magnetometer. For example, when $\varepsilon_k(V_{Xk}) = 0$ and $\overline{E}_{Jk} > 0$ for $k = i$ and $j$, the four eigenstates of the two-bit circuit are

$$\begin{aligned}
|1\rangle &= \frac{1}{2}\left(|\uparrow\rangle_i|\uparrow\rangle_j - |\uparrow\rangle_i|\downarrow\rangle_j - |\downarrow\rangle_i|\uparrow\rangle_j + |\downarrow\rangle_i|\downarrow\rangle_j\right), \\
|2\rangle &= \frac{1}{2}\left(|\uparrow\rangle_i|\uparrow\rangle_j + |\uparrow\rangle_i|\downarrow\rangle_j - |\downarrow\rangle_i|\uparrow\rangle_j - |\downarrow\rangle_i|\downarrow\rangle_j\right), \\
|3\rangle &= \frac{1}{2}\left(|\uparrow\rangle_i|\uparrow\rangle_j - |\uparrow\rangle_i|\downarrow\rangle_j + |\downarrow\rangle_i|\uparrow\rangle_j - |\downarrow\rangle_i|\downarrow\rangle_j\right), \\
|4\rangle &= \frac{1}{2}\left(|\uparrow\rangle_i|\uparrow\rangle_j + |\uparrow\rangle_i|\downarrow\rangle_j + |\downarrow\rangle_i|\uparrow\rangle_j + |\downarrow\rangle_i|\downarrow\rangle_j\right). \qquad (23)
\end{aligned}$$

Retained up to linear terms in $\eta_i$ and $\eta_j$, the corresponding supercurrents through the inductance $L$ are

$$\langle k|I|k\rangle = \mathcal{I}_k \sin\left(\frac{\pi\Phi_e}{\Phi_0}\right) + \frac{\pi L \mathcal{I}_k^2}{2\Phi_0}\sin\left(\frac{2\pi\Phi_e}{\Phi_0}\right) \qquad (24)$$

for $k = 1$ to 4, where

$$\begin{aligned}
\mathcal{I}_1 &= -(I_{ci} + I_{cj}), \qquad \mathcal{I}_2 = I_{cj} - I_{ci}, \\
\mathcal{I}_3 &= I_{ci} - I_{cj}, \qquad \mathcal{I}_4 = I_{ci} + I_{cj}. \qquad (25)
\end{aligned}$$

These supercurrents produce different fluxes threading the SQUID loop of the magnetometer and can be distinguished by dc SQUID measurements. When the two-bit system is prepared at the maximally entangled Bell states

$$|\Psi^{(\pm)}\rangle = \frac{1}{\sqrt{2}}(|\uparrow\rangle_i|\downarrow\rangle_j \pm |\downarrow\rangle_i|\uparrow\rangle_j), \qquad (26)$$

the supercurrents through $L$ are given by

$$\langle\Psi^{(\pm)}|I|\Psi^{(\pm)}\rangle = \frac{\pi L}{2\Phi_0}(I_{ci} \pm I_{cj})^2 \sin\left(\frac{2\pi\Phi_e}{\Phi_0}\right). \qquad (27)$$

These two states should be distinguishable by measuring the fluxes, generated by the supercurrents, through the SQUID loop of the magnetometer.

## Estimates of the inductance for optimal coupling

The typical switching time $\tau^{(1)}$ during a one-bit operation is of the order of $\hbar/E_J^0$. Using the experimental value $E_J^0 \sim 100$ mK, then $\tau^{(1)} \sim 0.1$ ns. The switching time $\tau^{(2)}$ for the two-bit operation is typically of the order

$$\tau^{(2)} \sim (\hbar/L)(\Phi_0/\pi E_J^0)^2.$$

Choosing $E_J^0 \sim 100$ mK and $\tau^{(2)} \sim 10\tau^{(1)}$ (i.e., ten times slower than the one-bit rotation), we have

$$L \sim 30 \text{ nH}$$

in our proposal. This number for $L$ is experimentally realizable. A small-size inductance with this value can be made with Josephson junctions. Our expansion parameter $\eta$ is of the order

$$\eta \sim \pi^2 L E_J^0/\Phi_0^2 \sim 0.1.$$

Our inductance $L$ is related with the inductance $L'$ in [1, 3] by

$$L' = (C_J/C_{qb})^2 L. \tag{28}$$

Let us now consider the case when $\tau^{(2)} \sim 10\tau^{(1)}$. For the earlier design [3], $C_J \sim 11C_{qb}$ since $C_g/C_J \sim 0.1$, which requires an inductance $L' \sim 3.6\ \mu$H. Such a large inductance is problematic to fabricate at nanometer scales. In the improved design [1], $C_J \sim 2C_{qb}$, greatly reducing the inductance to $L' \sim 120$ nH. This inductance is about four times larger than the one used in our scheme, making it somewhat more difficult to realize than our proposed $L$.

## Conclusion

We propose a *scalable* quantum information processor with Josephson charge qubits. We use a common inductance to couple all charge qubits and design *switchable* interbit couplings using two dc SQUIDs to connect the island in each Cooper-pair box. The proposed circuits are scalable in the sense that any two charge qubits can be effectively coupled by an experimentally accessible inductance. In addition, we formulate [11] an efficient QC scheme in which only one two-bit operation is used in the conditional transformations, including controlled-phase-shift and controlled-NOT gates.

## Acknowledgments

We thank Yu. Pashkin, B. Plourde and Xuedong Hu for useful discussions. This work is supported in part by ARDA, the AFOSR, and the US National Science Foundation grant No. EIA-0130383.

## References

1. See, e.g., Y. Makhlin, G. Schön, and A. Shnirman, Rev. Mod. Phys. **73**, 357 (2001), and references therein.
2. Y. Nakamura, Yu. A. Pashkin, and J.S. Tsai, Nature (London) **398**, 786 (1999).
3. Y. Makhlin, G. Schön, and A. Shnirman, Nature (London) **398**, 305 (1999).
4. Y. Nakamura, C.D. Chen, and J.S. Tsai, Phys. Rev. Lett. **79**, 2328 (1997).
5. V. Bouchiat, D. Vion, P. Joyez, D. Esteve, and M.H. Devoret, Phys. Scripta **T76**, 165 (1998).
6. C.H. van der Wal, A.C.J. ter Haar, F.K. Wilhelm, R.N. Schouten, C.J.P.M. Harmans, T.P. Orlando, S. Lloyd, and J.E. Mooij, Science **290**, 773 (2000).
7. J.R. Friedman, V. Patel, W. Chen, S.K. Tolpygo, and J.E. Lukens, Nature (London) **406**, 43 (2000).
8. D. Vion, A. Aassime, A. Cottet, P. Joyez, H. Pothier, C. Urbina, D. Esteve, and M.H. Devoret, Science **296**, 886 (2002).
9. F. Plastina, R. Fazio, and G.M. Palma, Phys. Rev. B **64**, 113306 (2001).
10. J. Siewert and R. Fazio, Phys. Rev. Lett. **87**, 257905 (2001).
11. J.Q. You, J.S. Tsai, and F. Nori, Phys. Rev. Lett. **89**, 197902 (2002).
12. E. Paladino, L. Faoro, G. Falci, and R. Fazio, Phys. Rev. Lett. **88**, 228304 (2002).
13. J.Q. You, X. Hu, and F. Nori, preprint.
14. J.Q. You, J.S. Tsai, and F. Nori, preprint.
15. D.V. Averin, Solid State Commun. **105**, 659 (1998).
16. G. Falci, R. Fazio, G.M. Palma, J. Siewert, and V. Vedral, Nature (London) **407**, 355 (2000).
17. O. Buisson and F.W.J. Hekking, cond-mat/0008275; also in *Macroscopic Quantum Coherence and Quantum Computing* (Kluwer Academic, Dordrecht, 2000), p. 137.
18. F. Marquardt and C. Bruder, Phys. Rev. B **63**, 054514 (2001).
19. A.D. Armour, M.P. Blencowe, and K.C. Schwab, Phys. Rev. Lett. **88**, 148301 (2002).
20. J.Q. You and F. Nori, preprint.
21. Additional schematic color diagrams for the proposed circuitry appear in http://www-personal.engin.umich.edu/~nori/scalable/scalableQC_figs.pdf
22. S. Lloyd, Phys. Rev. Lett. **75**, 346 (1995).
23. D. Deutsch, A. Barenco, and A. Ekert, Proc. R. Soc. London, Ser. A **449**, 669 (1995).

# Few-electron liquid and solid phases in artificial molecules at high magnetic field

Massimo Rontani (rontani@unimore.it), Guido Goldoni (goldoni@unimore.it) and Elisa Molinari
*INFM National Research Center on nanoStructures and bioSystems at Surfaces ($S^3$) and Dipartimento di Fisica, Università degli Studi di Modena e Reggio Emilia, Via Campi 213/A, 41100 Modena, Italy*

**Abstract.** Coupled semiconductor quantum dots form artificial molecules where relevant energy scales controlling the interacting ground state can be easily tuned. By applying an external magnetic field it is possible to drive the system from a weak to a strong correlation regime where eventually electrons localize in space in an ordered manner reminiscent of the two-dimensional Wigner crystal. We explore the phase diagram of such "Wigner molecules" analyzing the angular correlation function obtained by the Configuration Interaction solution of the full interacting Hamiltonian. Focus is on the role of tunneling in stabilizing different ground states.

## 1. Introduction

Semiconductor quantum dots (QDs) are zero-dimensional systems where a few electrons, typically $1 < N < 100$, are spatially confined and the energy spectrum is completely discrete [1]. Carriers can be injected one by one to the system in single-electron transport [2] or capacitance [3] experiments, based on the *Coulomb blockade* [4] phenomenon, and the energy required to add one electron can be measured if the electrostatic screening is poor and the thermal smearing is low. Measurements of such "electron affinities" [2] have revealed a shell structure for the correlated electron system and fine corrections to the energy due to exchange interaction (Hund's rule): therefore QDs are often regarded as *artificial atoms* [5, 6]. In Fig. 1 we compare the relevant parameters of natural and artificial atoms: note that for the latter the typical energy spacing is of the order of a few meV, less than the thermal energy at experimentally reacheable temperatures [1]. *Artificial molecules* can be built by coupling two QDs together in a controlled way [7, 8]: this additional degree of freedom enriches the physics of natural molecules, since for the latter the inter-nuclear coupling is almost fixed by the balance between nuclear repulsion and electrostatic attraction mediated by valence electrons, while in the former the stability of the electron system is externally imposed.



*R. Fazio et al. (eds.), New Directions in Mesoscopic Physics,* 361–371.
© 2003 *Kluwer Academic Publishers. Printed in the Netherlands.*

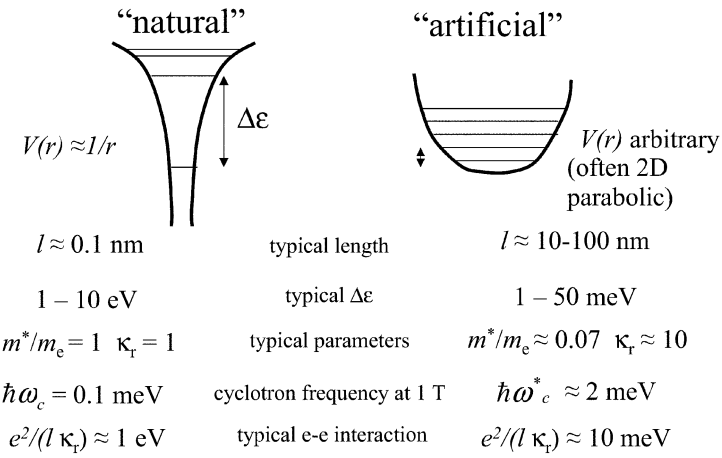


*Figure 1.* Comparison between the typical parameters and energy scales of "natural" and "artificial" atoms. $m^*$ and $\kappa_r$ are the effective mass and the static dielectric constant of the host semiconductor, respectively. The (effective) cyclotron frequency $\omega_c$ ($\omega_c^*$) is defined as $eB/mc$ ($eB/m^*c$), with $B$ applied magnetic field.

Current focus on QDs stems from their technological potentialities as optoelectronic devices (single-electron transistors [4], lasers [9], micro-heaters and micro-refrigerators based on thermoelectric effects [10]) as well as from several proposals of quantum information processing schemes in a solid-state environment [11, 12]. Here however we are more interested in basic physical principles and we look at QDs as a laboratory to explore the fundamentals of few-body strongly interacting systems.

The plan of the paper is the following: Section 2 is a primer on electron states in QDs. We show which energy scales can be artificially tailored and their effect on the interacting ground states. After, we specialize to the case of the artificial molecule in very high magnetic field as a paradigma of the strong correlation regime (Sec. 3).

## 2. Manipulating the energy spectrum

The critical issue of artificial atoms and molecules is that almost all relevant energy scales can be controlled by means of fabrication and/or

tuning of experimental parameters such as voltages or magnetic fields and made of comparable size. [1, 8, 13]. This is at difference with natural systems, where, for example, the dominant energy scale is provided by the ionic potential attracting the valence electrons, while the weaker electron-electron interactions can be treated reasonably well by mean field methods. Moreover, the orbital and spin coupling with an external magnetic field is very small (cfr. Fig. 1). The ground states are therefore determined by the successive filling of the empty lowest-energy hydrogen-like orbitals, according to the *Aufbau* theory. The open-shell configurations are well described by Hund's rules, which can be explained as the effect of the Coulomb term in the interacting Hamiltonian.

In QDs the confining potential $V(\boldsymbol{r})$ is much weaker, being provided by the electrostatic environment. Here effective parameters, such as renormalized electron mass and static dielectric constant of the host semiconductor determine the kinetic energy, the strength of the Coulomb interaction, and the coupling with the field (see Fig. 1). The overall effect is that there is no dominant energy scale (Fig. 1), making the problem of determining the electronic ground state much more difficult.

In many of the experimental realizations of artificial atoms, the system can be regarded as quasi two dimensional [1]: since the confinement along the growth direction $z$ is much tighter than in the $x-y$ plane, the $z$ degree of freedom is frozen as far as low-energy states are concerned. In the effective mass and envelope function approximation, the confinement potential $V(\boldsymbol{r})$ can be decoupled as

$$V(\boldsymbol{r}) = V(\boldsymbol{\varrho}) + V(z), \tag{1}$$

with $\boldsymbol{\varrho} \equiv (x, y)$. Lowest-energy states are very well described by a two dimensional harmonic oscillator potential

$$V(\boldsymbol{\varrho}) = m^* \omega_0^2 \varrho^2/2, \tag{2}$$

where $m^*$ is the effective mass of the host semiconductor. Adequacy of Eq. (2) has been demonstrated both by theoretical calculations [14] and far infra-red spectroscopy [1]; in addition, it is the lowest order approximation in the Taylor expansion of the weak electrostatic potential.

The single-electron Hamiltonian $H_0(\boldsymbol{r}, s_z)$ is

$$H_0(\boldsymbol{r}, s_z) = (-\mathrm{i}\hbar\nabla + |e|\,\boldsymbol{A}/c)^2/2m^* + V(\boldsymbol{r}) + g^*\mu_\mathrm{B} B s_z, \tag{3}$$

where we included a magnetic field parallel to the $z$ axis $\boldsymbol{B} = B\hat{z}$ which couples with both the spin degree of freedom, $s_z = \pm 1/2$, and

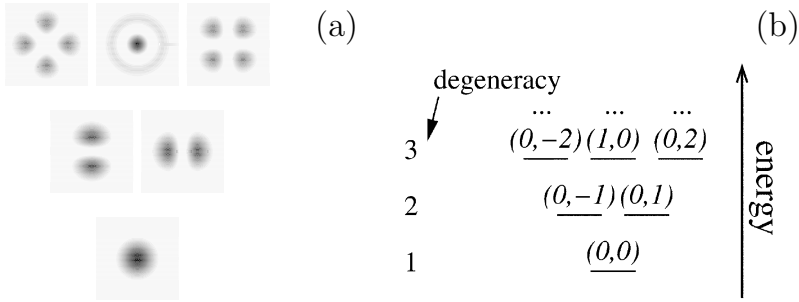


*Figure 2.* Two dimensional harmonic trap: The energy structure at zero field. (a) Contour plot in the $x-y$ plane of the probability density of the first lowest-energy single-particle orbitals. (b) Energy shell structure. The couple of numbers $(n, m)$ refer to the radial and azimuthal single-particle quantum numbers, respectively.

the orbital motion via the vector potential $\boldsymbol{A} = \boldsymbol{B} \times \boldsymbol{\varrho}/2$. Note that, since the Bohr magneton of the *free* electron $\mu_{\mathrm{B}}$ enters (3), the spin part is usually negligible with respect to the orbital part ($g^*$ is the effective giromagnetic factor).

Because of the decoupling (1), we can write the eigenfunctions of the orbital part of the Hamiltonian (3) as $\psi_{nm}(\boldsymbol{r}) = \varphi_{nm}(\boldsymbol{\varrho})\,\chi(z)$, where $\chi(z)$ is the ground state for the motion along $z$ and $\varphi_{nm}(\boldsymbol{\varrho})$ are the eigenstates of the 2D harmonic oscillator (Fock-Darwin levels, Fig. 2 and 3). The eigenvalues $\varepsilon_{nm}$ are given by

$$\varepsilon_{nm} = \hbar\Omega(2n + |m| + 1) - \hbar\omega_c^* m/2, \tag{4}$$

where $n$ ($n = 0, 1, 2, \ldots$) and $m$ ($m = 0, \pm 1, \pm 2, \ldots$) are the radial and azimuthal quantum numbers, respectively, $\omega_c^*$ is the cyclotron frequency ($\omega_c^* = eB/m^*c$), and $\Omega = (\omega_0^2 + \omega_c^{*2}/4)^{1/2}$ [1]. When $B = 0$ ($\omega_c^* = 0$) the Fock-Darwin spectrum shows a characteristic shell structure (Fig. 2): the level degeneracy linearly increases with the shell number [Fig. 2(b)], and the energy spacing between neighboring shells is constant (see Fig. 2).

A magnetic field parallel to the growth direction splits the degeneracies of the states (Fig. 3) and "squeezes" the orbitals, as it appears from the expression of the characteristic length $\ell = (\hbar/m^*\Omega)^{1/2}$, corresponding to the average value of $\varrho$ on the ground state $\varphi_{00}$: the stronger the field, the smaller the radius of the wavefunction. At intermediate fields ($\omega_c \sim \omega_0$) the energy levels may increase or decrease as a function of the field, depending whether the azimuthal quantum number $m$ is negative or positive; at large fields, however, all levels tend to the 2D

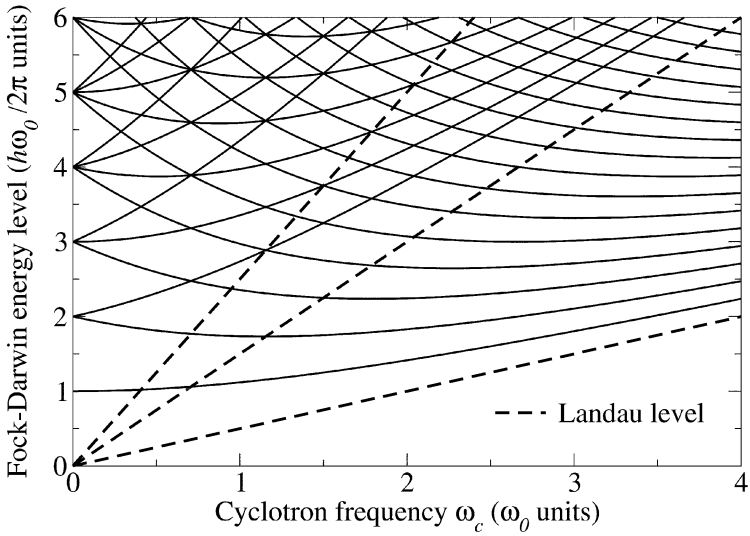


*Figure 3.* Two dimensional harmonic trap: The single-particle Fock-Darwin levels in a magnetic field $B$. The energies are given in units of $\hbar\omega_0$. The field dependence is contained in the cyclotron frequency $\omega_c^* = eB/m^*c$. The first three lowest-energy Landau levels are also depicted.

highly degenerate Landau levels. The latter can be obtained by letting $\omega_c^*/\omega_0 \to \infty$ in Eq. (4). Accordingly, at large fields only positive $m$ states are occupied ($n = 0$). In this limit, the energy separation $\Delta\varepsilon$ between levels differing on $|\Delta m| = 1$ becomes $\Delta\varepsilon \approx \hbar\omega_0^2/\omega_c^*$, which is $\propto 1/B$.

Additional flexibility in controlling the energy spectrum is given by the possibility to grow QDs coupled by quantum mechanical tunnelling. A typical "vertical" device is sketched in Fig. 4(a) (see ref. [15] for an experimental realization). In this case, the carrier dynamics is not strictly 2D anymore, as two levels $\chi_i(z)$ [symmetric ($i = \mathrm{S}$) and anti-symmetric ($i = \mathrm{AS}$) for a "homonuclear" molecule, see Fig. 4(c)] enter the relevant energy range. Correspondingly, the single particle spectrum comprises two sets of Fock-Darwin states at small [Fig. 4(d)] or high [Fig. 4(e)] magnetic fields. The energy separation between S and AS states is $2t$, $t$ being the tunneling energy which can be controlled, e.g., by varying the width $d$ or the height $V_0$ of the inter-dot potential barrier while growing the sample [Fig. 4(c)].

When we consider the Coulomb interaction between carriers, no exact solutions are available except very special cases for $N = 2$ [16].

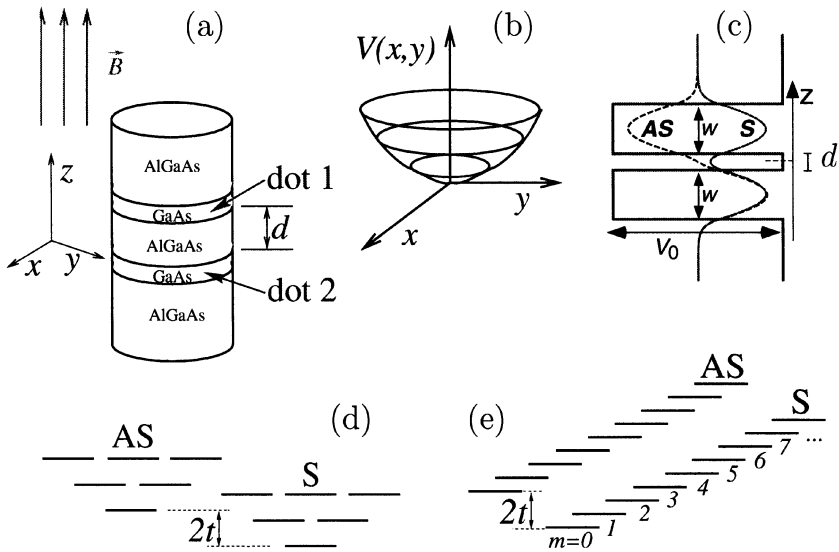


*Figure 4.* Model of the vertical artificial molecule. (a) Sketch of the model device we consider. (b) In-plane single-particle confinement potential. (c) Confinement potential along the $z$-axis. $V_0$ and $d$ are respectively the height and the width of the inter-dot potential barrier, while $w$ is the thickness of each of the two dots. (d) The symmetric (S) and antisymmetric (AS) sets of Fock-Darwin levels at zero field. $t$ is the tunneling energy. (e) The S and AS sets of Fock-Darwin levels in a high magnetic field. Only the first lowest-energy states with $n = 0$ and $m > 0$ are depicted.

The interacting Hamiltonian

$$\mathcal{H} = \sum_{i=1}^{N} H_0(\boldsymbol{r}_i, s_{zi}) + \frac{1}{2}\sum_{i\neq j} \frac{e^2}{\kappa_{\mathrm{r}}\,|\boldsymbol{r}_i - \boldsymbol{r}_j|}, \tag{5}$$

with $\kappa_{\mathrm{r}}$ static dielectric constant, must be solved numerically. Dramatic alterations of the few-body energy spectrum and wavefunctions appear, depending on the relative ratio of the magnitudes of the one- and two-body terms in $\mathcal{H}$.

If the single-electron term $H_0$ prevails, the system basically behaves as a non-interacting system, or, better, as a Fermi liquid with corrections due to the residual part of the interaction. This is the regime where the periodic table of artificial atoms has been observed [2]. If instead the Coulomb term dominates, electrons undergo a transition to a qualitatively new state where they orderly arrange themselves in

space in such a manner to minimize the electrostatic energy [1, 5, 17]. In this few-body strongly correlated regime, which is reminescent of the Wigner crystal phases in extended systems [18], the physics turns out to be classical. Asymptotically, all operators become commutative and all spin configurations tend to perfect degeneracy (except possibly the Zeeman splitting).

The Wigner regime can be artificially driven in two ways. One possibility is fabrication of QDs with weak enough lateral confinement that the average electron density $n$ is extremely small: since the 2D one-electron term in Eq. (5) goes like $n$ while the two-body term like $n^{1/2}$, in the dilute limit the former becomes negligible with respect to the latter [17]. Another possibility is to apply a magnetic field strong enough that the energy separation $\Delta\varepsilon$ becomes small compared to the typical Coulomb energy (equivalently, $\ell \ll n^{-1/2}$): again, the interaction term of $\mathcal{H}$ controls the low-energy physics. We focus on this case in Sec. 3.

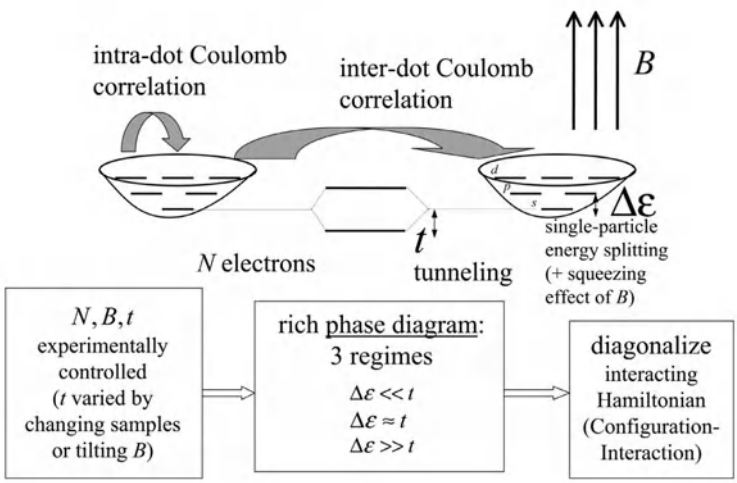


*Figure 5.* Artificial molecules: The relevant energy scales controlling the few-electron interacting ground state. Many of these energies can be artificially tuned together with the number of electrons $N$.

Figure 5 summarizes the relevant energy scales for a coupled QD system and how they can be tailored. Both single particle energies and tunneling can be independently tuned by device engineering or, more practically, by external magnetic field intensity and direction.

The "degree" of correlation of the system can be similarly controlled, as well as $N$.

## 3. Structural transitions in Wigner molecules

We now discuss the ground state of $N$ electrons in coupled QDs in a high magnetic field $B$, i.e., such that single-QD correlation functions show strong localization [8, 19]. We present results for $N = 6$ [19]. The system with $N < 6$ exhibits a similar physics. We can identify three regimes corresponding to different electron arrangements: (I) At small $d$, tunneling dominates and the system behaves as a unique coherent system. (II) As $d$ is increased, all energy scales become comparable. (III) When eventually tunneling is suppressed, only the ratio between intra- and inter-dot interaction is the relevant parameter for the now well separated QDs.

To analyze the ground state of the artificial molecule in the different regimes, we show in Fig. 6 the pair correlation function $P(\boldsymbol{\varrho}, z; \boldsymbol{\varrho}_0, z_0) = \sum_{i\neq j} \left\langle \delta(\boldsymbol{\varrho} - \boldsymbol{\varrho}_i)\delta(z - z_i)\delta(\boldsymbol{\varrho}_0 - \boldsymbol{\varrho}_j)\delta(z_0 - z_j) \right\rangle / N(N-1)$ (the average is on the ground state) [8, 19]. Since we are interested in the strong localization regime, we expect that spin texture does not alter the essential physics, therefore we assume that electrons are spin polarized [20]. Figure 6 shows $P(\boldsymbol{\varrho}, z; \boldsymbol{\varrho}_0, z_0)$ along a circle in the same dot (solid line) or in the opposite dot (dashed line) with respect to the position of a reference electron, taken at the maximum of its charge density, $(\boldsymbol{\varrho}_0, z_0)$. The right column shows the electron arrangement in the QDs as inferred by the maxima of $P(\boldsymbol{\varrho}, z; \boldsymbol{\varrho}_0, z_0)$.

At small $d$ the whole system is coherent, i.e., it behaves as a unique QD. The electrons, delocalized over the dots, arrange at the vertices and the center of a regular pentagon (Phase I). At intermediate values of the tunnelling energy electrons sit at the vertices of a regular hexagon. Contrary to the previous case peaks in the upper and lower dots have different heights (Phase II). Finally, when $d$ is sufficiently large, the structure evolves into two isolated dots coupled only via Coulomb interaction. Accordingly, three electrons in each dot sit at the vertices of two equilateral triangles rotated by 60 degrees (Phase III).

It is important to note from Fig. 6 that Phase I and III are strongly localized phases, where quantum fluctuations play a minor role, and electron configurations are basically determined by Coulomb interactions; accordingly, they have completely classical counterparts [21]. On the contrary, in Phase II tunneling fluctuations prevents electron from localizing and therefore the configuration has a "liquid" character. Such

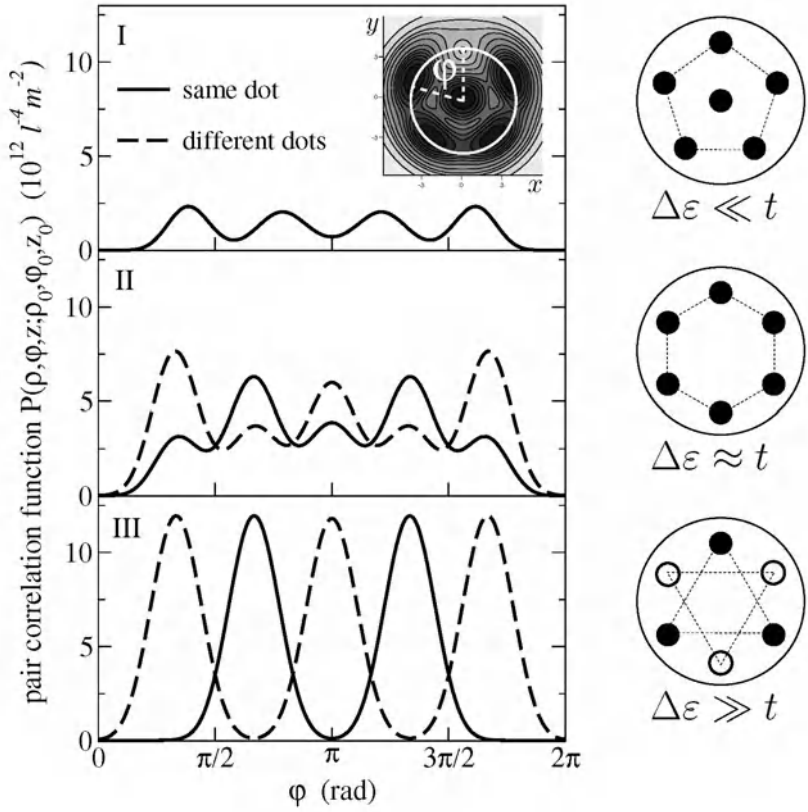


*Figure 6.* The three phases of the Wigner molecule as the critical ratio $\Delta\varepsilon/t$ is changed. Here we numerically solve the Hamiltonian of Eq. (5) by means of the Configuration Interaction method, namely we expand the few-body wavefunction as a linear combination of Slater determinants made by filling with $N$ electrons the Fock-Darwin orbitals. We consider only levels with $m > 0$ and $n = 0$. Further details in ref. [19]. $B$ is fixed (25 T) and we assume as parameters (see text and caption of Fig. 4) $\hbar\omega_0$=3.70 meV, $w$=12 nm, $V_0$=250 meV, $m^*$=0.067$m_e$, $\kappa_r$=12.4, $g^*$=-0.44 as typical values of realistic devices [15]. The three phases correspond to $d$=2, 4.6, 8 nm, respectively.

phase cannot be explained in term of Coulomb interactions solely and, in fact, the exagonal arrangement shown in Fig. 6 is classically unstable.

This example shows that in artificial molecules at high $B$ one can drive qualitative changes in the ground state of the interacting electrons that are clearly precursors of quantum phase transitions in the infinite system [22]. While the observation of such transitions in the

bulk is very difficult, QDs seem to constitute ideal systems to explore in the laboratory the fundamentals of electron correlation. For example, it is conceivable that inelastic light scattering spectroscopy is able to probe the different roto-vibrational "normal modes" of the three phases, thus allowing for their experimental detection. See ref. [19] for further details.

## Acknowledgements

This work was supported by INFM (SSQI), by MIUR (FIRB Quantum Phases of Ultra-Low Electron Density Semiconductor Heterostructures), by MAE (Progetto di Particolare Rilevanza "Controllo di stati di carica e spin in punti quantici"), and by the EC (SQID).

## References

1. For reviews see: L. P. Kouwenhoven *et al.,* in *Mesoscopic electron transport,* edited by L. L. Sohn, L. P. Kouwenhoven, and G. Schoen (Kluwer, Dordrecht, 1997), p. 105; L. Jacak, P. Hawrylak, and A. Wójs, *Quantum dots* (Springer, Berlin, 1998); D. Bimberg *et al., Quantum dot heterostructures* (Wiley, Chichester, 1998); T. Chakraborty, *Quantum dots: A survey of the properties of artificial atoms* (Nort-Holland, Amsterdam, 1999); L. P. Kouwenhoven, D. G. Austing, and S. Tarucha, Rep. Prog. Phys. **64,** 701 (2001).
2. S. Tarucha *et al.,* Phys. Rev. Lett. **77,** 3613 (1996).
3. R. C. Ashoori, Nature **379,** 413 (1996).
4. H. Grabert and M. H. Devoret, *Single charge tunneling: Coulomb blockade phenomena in nanostructures,* NATO ASI series B: physics **294** (Plenum, New York, 1992).
5. P. Maksym and T. Chakraborty, Phys. Rev. Lett. **64,** 108 (1990).
6. M. A. Kastner, Phys. Today **46,** 24 (January 1993).
7. L. P. Kouwenhoven, Science **268,** 1440 (1995).
8. For a review see M. Rontani *et al.,* Solid State Commun. **119,** 309 (2001).
9. Y. Arakawa and H. Sakaki, Appl. Phys. Lett. **40,** 939 (1982); N. Kirstaedter *et al.,* Electron. Lett. **30,** 1416 (1994).
10. H. L. Edwards *et al.,* Phys. Rev. B **52,** 5714 (1995).
11. G. Burkard, D. Loss, and D. P. DiVincenzo, Phys. Rev. B **59,** 2070 (1999).
12. F. Troiani, U. Hohenester, and E. Molinari, Phys. Rev. B **62,** R2263 (2000); E. Biolatti *et al.,* Phys. Rev. Lett. **85,** 5647 (2000).
13. M. A. Reed, Scientific American **268,** 98 (1993).
14. A. Kumar, S. E. Laux, and F. Stern, Phys. Rev. B **42,** 5166 (1990).
15. D. G. Austing *et al.,* Physica B **249-251,** 206 (1998).
16. M. Taut, Phys. Rev. A **48,** 3561 (1993).
17. G. W. Bryant, Phys. Rev. Lett. **59,** 1140 (1987).
18. E. Wigner, Phys. Rev. **46,** 1002 (1934); A. Ishiara, Solid State Phys. **42,** 271 (1989); R. Côté in *Microscopic theory of semiconductors,* edited by S. W. Koch (World Scientific, London, 1995), p. 315.

19. M. Rontani *et al.,* Europhys. Lett. **58,** 555 (2002).
20. At smaller $B$ spin plays an important role; see e.g. L. Martín-Moreno, L. Brey, and C. Tejedor, Phys. Rev. B **62,** R10633 (2000).
21. B. Partoens, V. A. Schweigert, and F. M. Peeters, Phys. Rev. Lett. **79,** 3990 (1997).
22. Here we mean phase transitions driven by continuously changing some parameter of the interacting Hamiltonian at vanishingly low temperatures: see S. Sachdev, *Quantum phase transitions,* (Cambridge University Press, 1999).

# Phase Coherence and Spin Dynamics

Martin Y. Veillette
*University of California at Santa Barbara*

## 1. Introduction

The recent advances in manipulating electronic spins in semiconductors provide a strong incentive for understanding the dynamics and transport properties of spin-based semiconducting electronics [1, 2, 3]. There has been a great deal of effort pursuing spin injection in high mobility but low dimensionality systems where spin transport is expected to be enhanced. However, most of the studies on spin transport and spin precession has been based on spin diffusive transport [4, 5]. For submicrons devices, where electronic mean free paths can easily exceed the length of the device, transport is in the ballistic regime. Furthermore, in the case of narrow conductors, only a few channels are involved in the spin transport and interchannel scattering becomes inconsequential and the electron can propagate phase coherently. It is at present unclear how the spatial part of the wavefunction can affect its spin counterpart. Indeed the quantum equation of motion for a spin in a magnetic field $\boldsymbol{B}$ is

$$\partial_t \boldsymbol{S} + \partial_x \boldsymbol{J} = g\mu_B \boldsymbol{S} \times \boldsymbol{B}, \tag{1}$$

where $\boldsymbol{S}$ and $\boldsymbol{J}$ are the spin density and spin-current density *operators* respectively and $g$, $\mu_B$ are the gyromagnetic factor and Bohr magneton. In absence of spin flip scattering, the previous equation remains valid in a semiclassical sense where the operators are replaced by their expectation values. This raises the question, "Does phase coherence affect spin dynamics?" In this paper, we investigate this question and answer by the affirmative. Using a scattering approach, we study spin dynamics in a double barrier system. The continuous transition from fully coherent to fully incoherent propagation is described by a conceptually simple approach presented by Buttiker [6, 7]. In this model, incoherent propagation is achieved by inserting localized phase randomizing scatterers between elastic scatterers. Our results, which describe spin transport in the partially coherent regime, illustrate the importance of quantum effects. We show that quantum interference between multiples partial waves shifts the semiclassical spin resonance. Moreover, we demonstrate that spin and charge can mix, a phenomena with no classical analog.



*R. Fazio et al. (eds.), New Directions in Mesoscopic Physics,* 373–379.
© 2003 *Kluwer Academic Publishers. Printed in the Netherlands.*

## 2. Model

The Buttiker-Landauer model is usually used to described ballistic transport in mesoscopic devices. The current flows into the leads in response to a net electrostatic potential between the contacts. Although the electrochemical potential in the leads is not properly defined due to the ballistic nature of the transport, each contact is in local equilibrium with a well defined electrochemical potential. For spin electronics, we consider each contact to be paramagnetic but to have two electrochemical potential: $\mu_\uparrow$ and $\mu_\downarrow$ for the spin $\uparrow$ and $\downarrow$ respectively. Hence, the contacts show a net spin polarization $\boldsymbol{S} = N_0 \boldsymbol{\mu}_s \hbar/2$ where $\boldsymbol{\mu}_s$ is defined as the spin chemical potential ($\boldsymbol{\mu}_s = |\mu_\uparrow - \mu_\downarrow|\hat{\mathbf{n}}$) and $N_0$ is the density of states per spin at the Fermi level. The spin-polarized reservoir envisioned preserved spins; each spin band internally equilibrates by energy relaxation while preserving the spin imbalance. This conceptually simple state can be achieved experimentally by optical means [8] or by injecting spins from a ferromagnet [9].

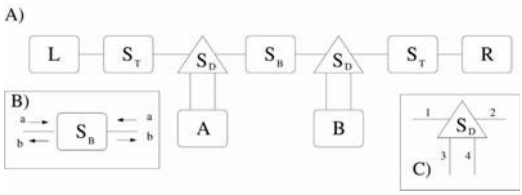


*Figure 1.* Sketch of the double barrier system: In (A), the contacts $L, R$ are connected by a wire composed of a segment in a magnetic field sandwiched between two potential barriers represented respectively by the scattering matrices $S_B$ and $S_T$ represented in (B). Dephasing centers as shown in (C) are introduced between elastic scatterers to model electron dephasing.

As a paradigm, we study spin transport in a double barrier system with a Zeeman magnetic field applied in the intrabarrier region (See Fig. 1). This choice is motivated by the fact that one might expect quantum effects on spin transport, if present, to be enhanced due to multiple reflections between the tow potential barriers [10]. For simplicity we consider a narrow wire in which current is carried by only 2 transverse subbands, one for each spin component. To determine the spin current, we use the following procedure: (A) we determine the scattering matrix of each subunit element (B) to model dephasing, we insert an inelastic scatterer between each elastic scatterer (C) we solve for the local chemical potentials in the electronic reservoirs attached to the dephasing center (D) we solve the total S-matrix of the system and determine the spin current through Buttiker's formula.

In the Buttiker-Landauer model, at low bias, the charge current $I^0$ and spin current $\boldsymbol{I}$ in the lead $i$ are given by

$$I_i^0 = \frac{e}{2\pi}\sum_\alpha \int d\epsilon \left(\langle a_{i\alpha}^\dagger(\epsilon) a_{i\alpha}(\epsilon)\rangle - \langle b_{i\alpha}^\dagger(\epsilon) b_{i\alpha}(\epsilon)\rangle\right), \tag{2}$$

$$\boldsymbol{I}_i = \frac{\hbar/2}{2\pi}\sum_{\alpha\beta} \int d\epsilon \left(\langle a_{i\alpha}^\dagger(\epsilon)\boldsymbol{\sigma}_{\alpha\beta} a_{i\beta}(\epsilon)\rangle - \langle b_{i\alpha}^\dagger(\epsilon)\boldsymbol{\sigma}_{\alpha\beta} b_{i\beta}(\epsilon)\rangle\right). \tag{3}$$

Here $a_{i\beta}^\dagger(\epsilon)$ and $b_{i\beta}^\dagger(\epsilon)$ are respectively creation operators of incoming and outgoing electrons in the lead $i$, with spin $\alpha = \uparrow / \downarrow$ and energy $\epsilon$. The occupation number of the incoming electrons in each lead is determined by the distribution function of their contact of origin.

$$\int d\epsilon \langle a_{i\alpha}^\dagger(\epsilon) a_{i\beta}(\epsilon)\rangle = \epsilon_F \delta_{\alpha\beta} + \mu_i^0 \delta_{\alpha\beta} + \frac{1}{2}\boldsymbol{\mu}_i \cdot \boldsymbol{\sigma}_{\beta\alpha}, \tag{4}$$

where $\mu^0$ is the charge chemical potential measured from the Fermi energy $\epsilon_F$ and $\boldsymbol{\sigma} = (\sigma^x, \sigma^y, \sigma^z)$ are the Pauli matrices. Furthermore, the outgoing electron operators $b$ are related to the incoming electrons $a$ via the scaterring matrix of the system, (See Fig. 1 B)

$$b_{i\alpha}(\epsilon) = S_{i\alpha,j\beta}(\epsilon, \epsilon') a_{j\beta}(\epsilon'). \tag{5}$$

Hence, in the zero temperature limit, the currents can be expressed in terms of the generalized chemical potential and the S-matrix,

$$\begin{aligned} I_i^0 &= \frac{1}{2\pi}\left[2\mu_i^0 - \sum_{j,\alpha\beta} \mu_j^0 S_{j\beta,i\alpha}^\dagger S_{i\alpha,j\beta} - \frac{1}{2}\sum_{j,\alpha\beta\gamma} \boldsymbol{\mu}_j \cdot \boldsymbol{\sigma}_{\beta\gamma} S_{j\gamma,i\alpha}^\dagger S_{i\alpha,j\beta}\right], \\ \boldsymbol{I}_i &= \frac{1}{4\pi}\left[\boldsymbol{\mu}_i - \sum_{j,\alpha\beta\gamma\delta} \mu_j^0 S_{j\beta,i\alpha}^\dagger \boldsymbol{\sigma}_{\alpha\gamma} S_{i\gamma,j\beta}\right. \\ &\quad \left. - \frac{1}{2}\sum_{j,\alpha\beta\gamma\delta} \boldsymbol{\mu}_j \cdot \boldsymbol{\sigma}_{\delta\beta} S_{j\beta,i\alpha}^\dagger \boldsymbol{\sigma}_{\alpha\gamma} S_{i\gamma,j\delta}\right]. \end{aligned} \tag{6}$$

We emphasize that this formula is valid for low bias voltage i.e. $\mu^0/\epsilon_F$, $\boldsymbol{\mu}/\epsilon_F \ll 1$. Each of the elastic scatterer elements in Fig. 1 is characterized by a $4 \times 4$ matrix. In the basis $(L\uparrow, R\uparrow, L\downarrow, R\downarrow)$, we choose the scattering matrix of the potential barrier $S_T$ and the magnetic field region $S_B$ to be given by

$$S_T = \begin{pmatrix} i\sqrt{R} & \sqrt{T} & 0 & 0 \\ \sqrt{T} & i\sqrt{R} & 0 & 0 \\ 0 & 0 & i\sqrt{R} & \sqrt{T} \\ 0 & 0 & \sqrt{T} & i\sqrt{R} \end{pmatrix}, \tag{7}$$

$$S_B = \begin{pmatrix} 0 & e^{i(\theta/2+\delta)} & 0 & 0 \\ e^{i(\theta/2+\delta)} & 0 & 0 & 0 \\ 0 & 0 & 0 & e^{i(-\theta/2+\delta)} \\ 0 & 0 & e^{i(-\theta/2+\delta)} & 0 \end{pmatrix}, \tag{8}$$

where $R$ and $T$ are respectively reflection and transmission coefficients of the potential barriers. By unitarity $R + T = 1$. The matrix $S_B$ describes a purely transmissive process where electrons accumulate a *spin dependent* phase. Microscopically, we find $\delta = k_F L$ and $\theta = g\mu_b B^z L/v_F$ where $L$ is the length over which the magnetic field is applied. Classically, the phase $\theta$ corresponds to the precession angle spins undergo upon crossing the magnetic field region.

To interpolate between the fully coherent and incoherent electron propagation, we consider phase-breaking effect in partially coherent transport. Generalizing a scheme suggested by Buttiker, we insert a dephasing scatterer coupled to a reservoir between each elastic scatterer. The local electronic reservoirs (A) and (B) can be considered fictious or real voltage probes (See Fig.1). The randomization of the phase occurs by removing electron from the phase coherent channels and reinjecting it without any phase relationships. For concreteness, we choose the dephasing scatterer to be given by a one-parameter function

$$S_D = \begin{pmatrix} 0 & \sqrt{1-\epsilon} & \sqrt{\epsilon} & 0 \\ \sqrt{1-\epsilon} & 0 & 0 & \sqrt{\epsilon} \\ \sqrt{\epsilon} & 0 & 0 & -\sqrt{1-\epsilon} \\ 0 & \sqrt{\epsilon} & -\sqrt{1-\epsilon} & 0 \end{pmatrix} \otimes \mathbf{1}_{spin}. \tag{9}$$

This $8 \times 8$ matrix connects the eight (4 channels $\times$ 2 spins) incoming amplitudes with the eight outgoing amplitudes. We note that the dephasing matrix is spin independent and therefore preserve spin currents. By construction, the limit $\epsilon = 0$ recovers the fully coherent transport equation where electron bypass the electronic reservoirs. In the opposite regime $\epsilon = 1$, all electrons are scattered into the reservoirs where their phase is randomized. We determine the chemical potentials in the reservoirs by requiring that the net current through the channels connecting the dephasing center and the reservoir to vanish, i.e. (See Fig. 1C)

$$I_3 + I_4 = 0 \text{ and } \boldsymbol{I}_3 + \boldsymbol{I}_4 = 0. \tag{10}$$

These four equations determine the four components of the chemical potentials ($\mu^0$ and $\boldsymbol{\mu}$) in each reservoir. Using standard methods, we obtained the transmission matrix of each subunit which can then be readily multiplied to obtain the total transmission matrix. Inverting this last matrix, we get the scattering matrix of the system and can determine the charge and spin current from equation (7).

## 3. Discussion

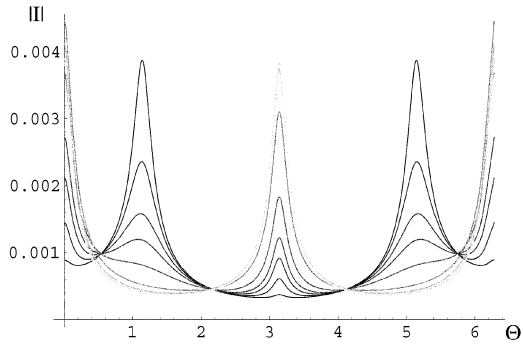


*Figure 2.* The magnitude of transmitted spin current in partial coherence regime for $\epsilon = 0.01, 0.05, 0.10, 0.15, 0.25, 0.75, 0.90, 0.95, 0.99$ (from darker to lighter) as a function of $\theta$ (or equivalently the magnetic field). The parameter used are $T = 0.1$,$\delta = 1$ and $\mu_L^x = 1$

To illustrate and contrast coherent and incoherent propagation, we present results for spin currents in the presence of spin chemical potential along the $x-y$ plane. As shown in Fig. 2, the magnitude of the spin current shows strong oscillations as a function of the applied magnetic field (or equivalently of the phase $\theta$). More interestingly, we find that the spin current shows different resonance condition depending on its degree of coherence. In the classical regime ($\epsilon = 1$), the resonance condition is realized at $\theta = n\pi$ where $n$ is an integer. This is to be contrasted with fully coherent electron propagation where the resonant condition is found to be $\theta = 2n\pi \pm (2\delta - \pi)$. This resonance shift can be understood in the following way: In the classical regime, spins merely precess in the $x - y$ plane. A strong transmission occurs when spins perfom complete revolutions upon a closed trajectory between the barrier, i.e. the acquired phase $2\theta = 2n\pi$. In this case the partial spin reflections upon the potential barrier are added in phase giving rise to a spin resonance. For coherent electron propagation, the resonance can be explained on the basis of constructive interference between multiple wavefunction *amplitudes*. Although the spin precess along the $x - y$ axis, in the quantum limit we can understand the electron as made of two spin projections: spin up and spin down along the z-axis. Due to the magnetic field aligned along the z-axis, the condition for constructive interference depends on the spin projection. For spin up electron, the condition reads $\theta + 2\delta + \pi = 2\pi n$ whereas for spin down electron it is

$\theta - 2\delta + \pi = 2\pi n$ (the extra factor of $\pi$ originates from the scattering phase shift due to the potential barriers.)

We point out that in the case of incoherent propagation the spin and charge are completely decoupled, i.e. classically the spin chemical potential does not induce charge current and vice versa,

$$\begin{aligned} I^0 &= \frac{1}{\pi}\frac{T}{2+T}(\mu_L^0 - \mu_R^0), \\ I^z &= \frac{1}{4\pi}\frac{T}{2+T}(\mu_L^z - \mu_R^z). \end{aligned} \tag{11}$$

These results are a consequence of the fact that classically the Zeeman magnetic field does not exert any torque of the z-component of the spin, therefore the z component of the spin and the electric charge are separetely conserved. This is unlike the case of coherent propagation where we find for $\epsilon = 0$, that the charge current and the spin current along z to be

$$\begin{aligned} I^0 &= \frac{T^2}{2\pi}\left(\frac{1}{|\Delta_1|^2} + \frac{1}{|\Delta_2|^2}\right)(\mu_L^0 - \mu_R^0) + \\ &\quad \frac{T^2}{4\pi}\left(\frac{1}{|\Delta_1|^2} - \frac{1}{|\Delta_2|^2}\right)(\mu_L^z - \mu_R^z), \\ I^z &= \frac{T^2}{8\pi}\left(\frac{1}{|\Delta_1|^2} + \frac{1}{|\Delta_2|^2}\right)(\mu_L^z - \mu_R^z) + \\ &\quad \frac{T^2}{4\pi}\left(\frac{1}{|\Delta_1|^2} - \frac{1}{|\Delta_2|^2}\right)(\mu_L^0 - \mu_R^0), \end{aligned} \tag{12}$$

where $\Delta_{1/2} = \exp(-i\delta \pm i\theta/2) + (1-T)\exp(i\delta \mp i\theta/2)$. Hence, the magnetic field has a filtering effect on the spin up/down transmission. The constructive interference condition being different for the spin components, the transmission shows strong magnetic field dependence. However, since the charge an spin are carried by the same particle, applying a spin chemical potential leads to a charge current and vice versa. This is a result of the particle-wave duality of the electron.

## 4. Conclusion

In summary, we have generalized Buttiker dephasing scheme to include spin degrees of freedom. We have shown that electron phase coherence can alter the dynamics and transport properties of spins. We stress that the effects are purely quantum mechanical and cannot be taken into

account by a Boltzmann transport treatment but require full quantum mechanical effects.

## 5. Acknowledgments

I wish to acknowledge fruitful discussion with Cristina Bena and Leon Balents.

## References

1. S. Datta and B. Das, Appl. Phys. Lett. **56**, 665 (1990).
2. D.D. Awschalom, D. Loss and D. Samarth, *Semiconductor Spintronics and Quantum Computation*, Springer Berlin, (2002) and references therein.
3. J.M. Kikkawa and D.D. Awschalom, Science, **287**, 473 (2000); R. K. Kawakami et. al., Science, **294**, 131 (2001).
4. M. Johnson, Science **260**, 320 (1993).
5. F.J. Jedema, A.T. Filip, B.J. van Wess, Nature **410**, 345 (2001).
6. M. Buttiker, Phys. Rev. **B33**, 3020 (1986); IBM J. Res. Dev. **32**, 63 (1988).
7. I. Knittle, F. Gagel and M. Schreiber, Phys. Rev. B. **60**, 916 (1999).
8. I. Malajovich, J.M. Kikkawa, D.D. Awschalom, J.J. Berr and N. Samarth, Phys. Rev. Lett. **84**, 1015 (2000).
9. M. Johnson, R.H. Silsbee, Phys. Rev. B **37**, 5712 (1988).
10. S. Datta, *Electronic Transport in Mesoscopic Systems*, Cambridge University Press, Cambridge, (1995).